

DTIC FILE COPY

SECURITY CLASSIFICATION OF THIS PAGE (When Data Entered)

REPORT DOCUMENTATION PAGE		READ INSTRUCTIONS BEFORE COMPLETING FORM
1. REPORT NUMBER NR 659-801-1/87	2. GOVT ACCESSION NO.	3. RECIPIENT'S CATALOG NUMBER
4. TITLE (and Subtitle) Picosecond Studies of Condensed-Phase Energetic Materials		5. TYPE OF REPORT & PERIOD COVERED 3/14/82-3/14/85 Final Technical Report
		6. PERFORMING ORG. REPORT NUMBER
7. AUTHOR(s) John H. Clark		8. CONTRACT OR GRANT NUMBER(s) N00014-82-K-0349 NR659-801
9. PERFORMING ORGANIZATION NAME AND ADDRESS Prof. John H. Clark Dept. of Chemistry, University of California Berkeley, CA 94720		10. PROGRAM ELEMENT, PROJECT, TASK AREA & WORK UNIT NUMBERS
11. CONTROLLING OFFICE NAME AND ADDRESS Dr. Richard Miller, Office of Naval Research Dept. of the Navy, Code 432P 800 No. Quincy St., Arlington, VA 22217		12. REPORT DATE 1/21/87
		13. NUMBER OF PAGES 328
14. MONITORING AGENCY NAME & ADDRESS (if different from Controlling Office) Office of Naval Research Ms. Roberta Lutz, Resident Representative University of California, Berkeley, Richmond Field Station, Richmond, CA 94804		15. SECURITY CLASS. (of this report)
		15a. DECLASSIFICATION/DOWNGRADING SCHEDULE
16. DISTRIBUTION STATEMENT (of this Report)		
<div style="border: 1px solid black; padding: 5px; text-align: center;"> This document has been approved for public release and sale; its distribution is unlimited. </div>		
17. DISTRIBUTION STATEMENT (of the abstract entered in Block 20, if different from Report)		
18. SUPPLEMENTARY NOTES		
19. KEY WORDS (Continue on reverse side if necessary and identify by block number) Condensed-Phase Energetic Materials, Raman Spectroscopy, Picosecond Lasers, Picosecond Absorption Spectroscopy, Picosecond Emission Spectroscopy, Rotational Reorientation		
20. ABSTRACT (Continue on reverse side if necessary and identify by block number) This report describes a series of picosecond spectroscopic investigations aimed at studying the reaction dynamics of condensed-phase energetic materials. (continued) to J. L.		

DD FORM 1 JAN 73 1473

EDITION OF 1 NOV 65 IS OBSOLETE
S/N 0102-LF-014-6601

unclassified

SECURITY CLASSIFICATION OF THIS PAGE (When Data Entered)

87 4 16 134

It was originally anticipated that Raman techniques could be utilized to study of free radical reactions in solutions. Such reactions are of great importance with regard to energetic materials and it was hoped that the relatively high specificity attainable with Raman spectroscopy could be used to address questions about various reaction pathways in these materials. Unfortunately, there were unforeseen difficulties that prevented this from occurring. In particular, it was concluded after a great deal of effort that, with the exception of a very few fortuitous cases, it was not possible to detect any Raman signal at all using the available equipment. This generally precluded using Raman spectroscopy as a detection method in subsequent experiments. Raman spectra were obtained for several pure liquids and for a few species with exceptionally large resonant Raman cross-sections. However the difficulty and slowness of the Raman system made it impractical to search through a large class of energetic materials in search of the few molecules that might yield detectable photoproducts.

The origin of this difficulty appears to be related to the high peak powers typical of a picosecond experiment. With conventional CW Raman spectroscopy relatively high sensitivities can be achieved despite the weakness of the Raman scattering. This is because there are generally no extraneous background signals to interfere with the detection process, and sensitive photon counting techniques can be employed. In a picosecond measurement the laser energy is concentrated in a short pulse, resulting in peak powers that are many orders of magnitude higher than those in a CW experiment with similar average power, and, hence, similar data rates. This greatly increases the likelihood of multi-photon and other nonlinear processes occurring. Such processes, including stimulated Raman scattering and two-photon fluorescence, give rise to spurious signals that severely degrade the experimental sensitivity. In general these nonlinear background signals made it impossible to detect the extremely weak Raman signals arising from low concentrations of transient molecules. Increasing the laser intensity by focussing will increase the Raman signal, but it will also simultaneously increase the background, generally obliterating any increase in the signal levels. It became clear that with the low repetition rate laser used here it simply was not possible to achieve the average powers required for producing detectable Raman scattering without simultaneously producing large nonlinear background signals.

The possibility of using stimulated and other nonlinear Raman techniques to exploit the inherently high powers found under these experimental conditions were also considered. This is a tempting possibility, since high peak powers tend to increase the nonlinear signals. Unfortunately, it was determined that although large nonlinear Raman signals could be obtained from pure compounds, no currently known method is capable of providing a viable detection method for low concentrations of transient species in the presence of high concentrations of solvent molecules. In general, a combination of nonlinear background signals and nonresonant scattering processes led to situations where the detection levels were no better than those for spontaneous Raman scattering. Thus, the effort to use Raman spectroscopy was ultimately abandoned, largely because no usable signals could be found. As discussed below, it is possible that with somewhat different conditions Raman scattering might be detectable. Unfortunately, none of these techniques were adaptable to the existing equipment in our laboratory. (continued)

The emphasis of the experimental work was thus shifted primarily to emission spectroscopy, and focussed on ~~studies of~~ rotational reorientation of excited state molecules in solution. A number of results of relevance to the understanding of condensed-phase energetic materials were obtained. Studies were made at elevated pressures (up to 10kbar). The short time behavior of molecules under such conditions may be relevant to shock wave chemistry, and therefore, to energetic materials. The rotational behavior of molecules under these and other conditions were observed and compared with a variety of theoretical approaches. In general, it was found that hydrodynamic models, which are fundamentally macroscopic in character, could be used to describe the short-time behavior of molecules. It was found that on this timescale, dielectric relaxation plays an important role in determining the behavior of polar molecules. It was also observed that the molecular rotation times were independent of the excitation frequency. This was used to estimate the microscopic thermal conductivity of the solvent. Since the emission spectra are not observed to change with excitation energy, the excess vibrational energy in the molecule must be dissipated into the solvent in a few picoseconds. Once there, this heat might be expected to decrease the solvent viscosity. This in turn would decrease the measured rotation time. That this was not observed sets an upper bound on the time a local hot spot can be maintained. Note that this result is also consistent with macroscopic expectations, based on simple thermal conductivity arguments. This finding is believed to be of considerable importance with regard to the initiation of thermal reactions as a shock wave passes through a condensed-phase energetic material.



Little on file

A1

FINAL TECHNICAL REPORT

PREPARED FOR THE OFFICE OF NAVAL RESEARCH

ARLINGTON, VIRGINIA.

FOR CONTRACT N00014-82-K-0349, NR 659-801

by Professor John H. Clark

DEPARTMENT OF CHEMISTRY

UNIVERSITY OF CALIFORNIA

BERKELEY, CALIFORNIA 94720

Soc. No. 550-84-0492

February 18, 1987

PICOSECOND STUDIES OF CONDENSED PHASE

ENERGETIC MATERIALS

I. INTRODUCTION

The purpose of this report is to summarize the results obtained over the last several years as a part of an ONR-funded effort to apply picosecond spectroscopic techniques to the study of energetic materials. The intent of this report is to give a broad overview of the work, and its importance to our understanding of condensed-phase energetic materials. This work was carried out by several graduate students over a period of years and formed the basis for their thesis projects. In particular, the dissertations of Laura A. Philips and Douglas W. Anthon describe virtually all the work carried out in pursuit of this project. Rather than paraphrasing these works, it seemed preferable to simply include the Lawrence Berkeley Laboratory reports derived from these theses as appendices to this report. They will be referred to as LAP and DWA, respectively. It should be noted that although all the information contained in these reports has relevance to the question of the picosecond behavior of energetic materials, not all of it was sponsored by ONR. In particular, the chapter in DWA describing solvation and hydrogen bonding in 9,9'-bianthryl was sponsored by the Gas Research Institute, and the chapter in LAP describing picosecond Raman spectroscopy of electronically excited ruthenium-tris-bipyridine was sponsored by the United States Department of Energy.

It was originally anticipated that Raman techniques could be utilized to study free radical reactions in solutions. Such reactions are of great importance with regard to energetic materials and it was hoped that the relatively high specificity attainable with Raman spectroscopy could be used to address questions about various reaction pathways in these materials. Unfortunately, there were unforeseen difficulties that prevented this from occurring. In particular, it was concluded, after a great deal of effort, that with the exception of a very few fortuitous cases, it was not possible to detect any Raman signal at all using existing equipment. This generally precluded using Raman spectroscopy as a detection method in subsequent experiments. Raman spectra were obtained for several pure liquids and for a few species with exceptionally large resonant Raman cross-sections. However the difficulty and slowness of the Raman system made it impractical

to search through a large class of energetic materials in search of the few molecules that might yield detectable photoproducts.

The origin of this difficulty appears to be related to the high peak powers typical of a picosecond experiment. With conventional CW Raman spectroscopy relatively high sensitivities can be achieved despite the weakness of the Raman scattering. This is because there are generally no extraneous background signals to interfere with the detection process, and sensitive photon counting techniques can be employed. In a picosecond measurement the laser energy is concentrated in a short pulse, resulting in peak powers that are many orders of magnitude higher than those in a CW experiment with similar average power and Raman signal level. This greatly increases the likelihood of multi-photon and other nonlinear processes occurring. Such processes, including stimulated Raman scattering and two-photon fluorescence, give rise to spurious signals that severely degrade the experimental sensitivity.

In general these nonlinear background signals made it impossible to detect the extremely weak Raman signals arising from low concentrations of transient molecules. Increasing the laser intensity by focussing will increase the Raman signal, but it will also simultaneously increase the background, generally obliterating any increase in the signal levels. It became clear that with the low repetition rate laser used here it simply was not possible to achieve the average powers required for producing detectable Raman scattering without simultaneously producing large nonlinear background signals.

The possibility of using nonlinear Raman techniques to exploit the inherently high powers found under these experimental conditions were also considered. This is a tempting possibility, since high peak powers tend to increase the nonlinear signals. Unfortunately, it was determined that although large nonlinear Raman signals could be obtained from pure compounds, no currently known method is capable of providing a viable detection method for low concentrations of transient species in the presence of high concentrations of solvent molecules. In general, a combination of nonlinear background signals and nonresonant scattering processes led to situations where the detection levels were no better than those for spontaneous Raman scattering. Thus, the

effort to use Raman spectroscopy was ultimately abandoned, largely because no usable signals could be found. As discussed below, it is possible that with somewhat different conditions, Raman scattering might be detectable. Unfortunately, none of these techniques were adaptable to the existing equipment in our laboratory.

The emphasis of the experimental work was thus shifted primarily to emission spectroscopy and focussed on studies of rotational reorientation of excited-state molecules in solution. A number of results of relevance to the understanding of condensed phase energetic materials were obtained. Studies were made at elevated pressures (up to 10 kbar). The short time behavior of molecules under such conditions may be relevant to shock wave chemistry, and therefore to energetic materials. The rotational behavior of molecules under these and other conditions was observed and compared with a variety of theoretical approaches. In general, it was found that hydrodynamic models, which are fundamentally macroscopic in character, could be used to describe the short-time behavior of molecules. It was found that on this timescale, dielectric relaxation plays an important role in determining the behavior of polar molecules. It was also observed that the molecular rotation times were independent of the excitation frequency. This was used to estimate the microscopic thermal conductivity of the solvent. Since the emission spectra are not observed to change with excitation energy, the excess vibrational energy in the molecule must be dissipated into the solvent in a few picoseconds. Once there, this heat might be expected to decrease the solvent viscosity. This in turn would decrease the measured rotation time. That this was not observed sets an upper bound on the time a local hot spot can be maintained. Note that this result is also consistent with macroscopic expectations, based on simple thermal conductivity arguments. This finding is believed to be of considerable importance with regard to the initiation of thermal reactions as a shock wave passes through a condensed phase energetic material.

II. OVERVIEW OF PICOSECOND CHEMISTRY

Before discussing the specific contents of these two reports, it is of interest to consider

the type of processes that occur on this timescale, and how they can be studied. To obtain this type of time resolution, it is necessary to make use of ultrafast spectroscopic techniques. Both the initiation and detection must be carried out optically to achieve this time resolution. Techniques of this sort have been used many times to study dynamic processes in a variety of different materials¹, and they can be usefully applied to the study of energetic materials as well. Although the major processes of interest in such materials, such as detonation, occur on a somewhat slower (nanosecond or microsecond) timescale, the fundamental chemical and physical events associated with the initiation of these phenomena occur much more rapidly. It might be hoped that by investigating systems on the picosecond timescale, information about these crucial initial steps might be obtained.

In many cases, the types of phenomena that can occur on this timescale are limited by the relative slowness of various transport processes. Estimates of the types of processes that will be observed on this timescale can be obtained by extrapolating macroscopic results to short times. In the case of chemical reactions, rates are largely governed by diffusion; a typical diffusion constant (ethanol at room temperature) is on order of $10^{-5} \text{ sec}^{-1}\text{cm}^2$. A characteristic length in this case is given by $l = (\tau D)^{1/2}$. Given a typical time domain of 10-1000 picoseconds this leads to distances of 1-10 Å. When this is compared to typical molecular dimensions of a few Å, this suggests that for the first 100 picoseconds after excitation, only quasi-unimolecular processes such as isomerization, geminate recombination and reactions with adjacent solvent molecules will be seen. Only on longer timescales will more conventional diffusion-controlled reactions be seen. Thus, in liquids, the picosecond time domain is where one observes the crossover between geminate cage reactions and diffusion-controlled reactions. It is thus the time domain in which initially-formed, isolated reactive species begin to interact with other reactive species in the solvent, and possibly with the solvent itself, giving rise to, among other things, the early stages of chain reactions.

There are unique advantages to working in this time domain. Being limited to quasi-unimolecular reactions, it is possible to study early stages of complex reactions without interfer-

ences from the secondary photolysis of diffusion-formed products. In a sense, one might hope to be able to study reactions before the onset of complexity. In addition, the transition between quasi-unimolecular and bimolecular reactions is of interest in its own right. It is in this time domain that the details of relatively low energy solvation and solvent-solute interactions can play an important role in determining the course of chemical reactions². For example, it is possible to identify cases where, in the equilibrium solvation geometry, reactive solvent functional groups are oriented away from potentially reactive solute moieties. When the solute in such a system is photolysed to become a reactive species, it is then possible to observe the finite solvent rearrangement time associated with the onset of reaction. It is also possible to observe even more extreme cases in solvent mixtures, where reactive solvent and solute molecules can be separated by a layer of a chemically inert solvent⁴. Chapter 4 of DWA discusses such a system, that of 9,9'-bianthryl. Studies of other similar systems have also been made. In particular, because of their experimental simplicity, low energy processes involving electronically-excited molecules have been widely studied. Such processes include solvation, hydrogen bond formation, and proton transfer.

Such low-energy processes are generally not the processes of greatest interest in energetic materials. Instead, the relatively high energy processes associated with the initiation of exothermic chemical reactions take precedence. Low energy process still remain important in these systems, since they may make it possible to either enhance or suppress possible reaction pathways in the initiation of reactions in energetic materials. Relatively low energy reversible process are also of importance as probes of the molecular environment; although rotational reorientation is not in and of itself important in energetic materials, it provides a very convenient way of studying the dynamic behavior of solvents over a wide range of conditions. Nonetheless the study of exothermic, irreversible phenomena are crucial to the understanding of energetic materials.

For purely experimental reasons, such irreversible systems are very difficult to study. In a reversible system, the same sample can be irradiated repeatedly. Samples of only a few milliliters are sufficient, since they can be subjected to repeated laser shots. On the other hand, if a highly

energetic irreversible process is being studied, each laser shot causes the irreversible degradation of the sample. It is necessary to use flowing sample cells and much larger sample volumes. This introduces a variety of experimental difficulties including the problem of preparing and purifying the requisite sample. In a Raman experiment it is necessary to use thousands of laser shots to obtain any data at all. Even if only a few microliters of sample are destroyed with each shot, hundreds or thousands of milliliters of suitably purified sample will still be needed. This can actually be a serious limitation on the types of systems that can be studied, as large amounts of highly purified energetic materials can be both difficult and dangerous to prepare.

III. RAMAN SPECTROSCOPY OF TRANSIENT MOLECULES

The original goal of this project was to devise methods for following chemical reactions in the picosecond time domain using Raman spectroscopy. Although the range of possible reactions is limited by the slowness of diffusion, a variety of dissociation and isomerization reactions might be accessible. With this in mind, the development of techniques for measuring such reactions was begun. One of the first things to become apparent in this effort was that the available lasers were not adequate for this purpose. The commercial passively mode-locked lasers suffered from large intensity fluctuations and variety of more subtle problems. Chapter two of LAP and chapter two of DWA both describe in some detail the optimizations required to convert the lasers into reliable, stable sources of picosecond pulses⁵. A number of surprising results were obtained from the laser itself. For example, self-phase modulation in the laser cavity made it possible to produce laser pulses approaching the laser bandwidth transform limit, that is roughly nine picoseconds. This was a novel result and made it possible to obtain pulses from the YAG system that were useful in a variety of experiments.

A further extension of the range of the optical system was achieved through the use of an optical parametric source⁶. This device made it possible to generate nearly transform-limited pulses throughout the visible and near infrared. As described in chapter two of DWA, this source was characterized in detail and was found to be a simple and reliable tunable source.

The existence of this tunable source made it possible to consider several types of experiments. For example, it was used for making the wavelength dependent rotational¹ reorientation measurements described in the appendix of LAP. Another application for which the tunable source was considered was the possible use of both resonance Raman and coherent Raman spectroscopy for monitoring species in solution.

Initial efforts were devoted to the use of resonance Raman spectroscopy for the study of free radical intermediates. Although a considerable effort was devoted to this project, it was ultimately found that the inherently low signal levels of Raman spectroscopy were incompatible with the high peak powers of a picosecond laser pulse. The weak Raman scattering was generally lost in the background signals generated by various nonlinear processes such as stimulated Raman, continuum generation or dielectric breakdown. A detailed description of these considerations is given in chapter three of DWA. A number of Raman spectra were successfully measured for stable molecules with large Raman cross sections (mostly aromatic or chlorinated hydrocarbons). In general the conclusion drawn from these results was that with the equipment used here it would not be possible to detect nonresonant Raman spectra at molecular concentrations below a few percent. Since this is several orders of magnitude greater than the populations attainable with photoinitiation, it was clear that only species with very large resonant enhancements could be detected. One molecule with an exceedingly large Raman cross section that was successfully detected at low levels was the excited state of ruthenium-tris-bipyridine⁷. This is described in chapter five of LAP. Although this molecule is of little relevance to energetic materials chemistry, it does illustrate the sensitivity which could be obtained under favorable circumstances. It was initially hoped that it would be possible to investigate some classes of energetic materials with this method. In particular the free-radical dissociation of nitromethane was considered; the fact that NO₂ absorbed in the visible suggested that an enhanced Raman cross section might be found⁸. Unfortunately, efforts to detect Raman scattering from low concentrations of NO₂ in various solvents using both pulsed and CW techniques were unsuccessful, making it impossible to pursue this project further. Efforts to find other free radicals that might be detectable were

made. It was found, for example, that despite a strong absorbance near 532 nm, it was not possible to observe any Raman signal from the perylene radical cation. As described in chapter three of DWA, the extremely slow scan rates imposed by the low signal levels and the low laser repetition rate made the system largely unsuitable for survey work. Because of this it was extremely difficult to identify systems that might be amenable to study.

The prospects for improvements in picosecond Raman spectroscopy are discussed in chapter three of DWA. It appears that although the work carried out here was unsuccessful, there may yet be methods for making Raman spectroscopy useful for transient detection. It appears that higher repetition rates and correspondingly lower peak powers might lead to order-of-magnitude increases in the sensitivity of spontaneous Raman methods. This speculation has been confirmed by recent work in other laboratories^{9,10}, where resonance Raman spectra have been successfully obtained at kilohertz and megahertz repetition rates. Alternatively, if coherent Raman techniques, such as CARS, could be used, then the high peak powers of picosecond pulses could be used to good advantage since the signal levels scale with the peak power rather than with the average energy. Although a variety of techniques exist, these methods generally are limited by a combination of nonresonant interactions and other background signals. The merits of several alternative coherent Raman techniques are discussed in chapter three of DWA. It was ultimately decided that no currently available technique would offer any significant advantages over spontaneous Raman scattering for the detection of trace species in solutions. In general, the inherent weakness of Raman scattering means that picosecond Raman will never be a simple technique, although it is possible that it will be useful for studying transients with large resonantly enhanced Raman cross sections.

In view of the difficulties with Raman techniques and vibrational spectroscopy, various forms of electronic spectroscopy were investigated, including both time-resolved absorption and emission¹¹. Absorption provides a method for studying the evolution of the ground-state species found in free-radical dissociation processes. Unfortunately, the broad, featureless spectra seen in absorption make it a far less specific technique than Raman. It is thus difficult to use when more

than one absorbing species is present. The sensitivity of absorption is somewhat higher than that of Raman, but there are still a number of experimental difficulties. For example, it was still impossible to detect any NO_2 generated when nitromethane was photolysed at 355 nm. This is a result of the relatively low absorption cross section for NO_2 ; transient absorption spectra were successfully measured for several other organic and organometallic species¹². These results are described in chapter three of DWA.

It is difficult to monitor reactive intermediates using time-resolved emission spectroscopy, since most photochemical methods for producing free radicals produce them in the ground state. This is a simple result of energy conservation; the energy remaining after bond cleavage is rarely enough to permit the production of excited-state fragments. Indirect evidence for the formation of reactive intermediates can sometimes be obtained from fluorescence quenching measurements. For example, the fluorescence lifetime of 9,9'-bianthryl excited at 355 nm was found to be much shorter in nitromethane (tens to hundreds of picoseconds rather than tens of nanoseconds) than in other solvents of comparable polarity. Furthermore, the lifetime varied with the intensity of the excitation pulse. This suggests that the fluorescence was being quenched by a diffusion-controlled reaction between bianthryl and the solvent photolysis products. This type of measurement was not pursued in detail here, as it was difficult to interpret and because it appeared to correspond simply to a diffusion constant measurement. However, in systems where such measurements are of interest, this technique provides a relatively sensitive method for detecting such reactive intermediates.

Overall, the effort to use picosecond spectroscopy to study reaction dynamics in condensed-phase energetic materials was not successful. Using Raman and absorption methods it was not possible to detect reactive intermediates at the low concentrations at which they could be photolytically produced. The results are summarized in chapters two and three of DWA and in chapter five of LAP. Although some encouraging results were obtained, it was not possible to actually apply them to interesting chemical systems, much less to any energetic materials. It is believed that with a higher repetition rate, higher average power system it might be possible to

increase the sensitivity of the system sufficiently to make it possible to obtain useful results. In particular, increasing the rate of data acquisition might make it possible to carry out some of the exhaustive survey work required to identify systems that are conducive to study. Thus, while Raman shows some promise¹⁰, the fact remains that it is an extremely difficult technique which can only readily be applied to the small class of molecules that show large resonant Raman cross-sections. Because it is difficult to predict which molecules these will be, it will still be a matter of luck whether Raman can be applied to a particular chemical system.

IV. ROTATIONAL REORIENTATION AND SOLUTION DYNAMICS

In addition to the chemical reactions of condensed phase energetic materials, it is also important to understand the dynamics of the solvent environment in which these reactions occur. Simply studying chemical reactions at ambient temperature and pressure may not be sufficient for understanding the processes that occur at the extremes of temperature and pressure found in a shock wave. For studies of this type, time-resolved emission spectroscopy provides a relatively simple and direct method for detecting probe molecules. There are several ways of exploiting excited-state molecules to probe the solvent environment. Molecules whose excited-state properties are significantly different than those of the ground state often make it possible to detect solvent-solute interactions such as proton transfer, dielectric relaxation, and hydrogen bond formation. The change in solvent environment is reflected in the emission spectrum so that the dynamics can be inferred from the time-dependent emission spectrum. Such studies were carried out here^{2,3}, but will not be discussed here at length.

It is also possible to use unreactive molecules to study solvent properties such as the effective viscosity or local temperature of a solution. The method used here for carrying out such studies involved the use of rotational reorientation¹³ as a probe. The details of this method are described in chapter three of LAP. Experimentally, it corresponds to exciting a sample with polarized light, and then measuring the rate of depolarization of the resulting emission. This approach has the advantage of being a rather general technique that can be applied to a wide

range of molecules in many different solvent environments. Studies were carried out here in which the rotational reorientation of several molecules as a function of pressure (up to several kilobar), solvent composition, temperature, and excitation wavelength. Systematic variation in the probe molecules and solvents made it possible to observe the effects of molecular size and dipole moment as well as solvent properties such as viscosity and dielectric relaxation. A variety of such results are given in chapter three of LAP. Rotational reorientation is a relatively simple process and is therefore amenable to a variety of theoretical approaches. Chapter three of LAP compares the results obtained here with a variety of theoretical approaches. In particular, hydrodynamic models can be used to describe the observed relaxations¹⁵. It might be expected that the continuum approximations implicit in these models would prevent these results from being applicable. In effect, the finite molecular sizes should matter when the solvent and solute molecules are of comparable dimensions. In fact, this is not the case; strong local correlations that might be expected to interfere with the continuum models do not appear to be significant. Those deviations which do occur can be largely accounted for by using terms related to the (macroscopic) dielectric relaxation to take into account the role of solvent-solute dipole correlations. In general, it appears that, contrary to what one might initially expect, extrapolations of macroscopic solvent properties to the molecular scale do a remarkably good job of describing the observed behavior. This information is believed to be of considerable importance to the understanding of reaction dynamics in condensed-phase energetic materials, where it is generally necessary to extrapolate reaction rates in temperature and pressure to match shock wave conditions.

In addition to chemical pathways, it is also important to observe the rates of energy transport. Chemical reactions in energetic materials are often supposed to be initiated in highly localized "hot spots" in the material. Such induced thermal inhomogeneities, if they exist, could provide a mechanism for the initiation of chain reactions in the fluid. For example, the energy released by the isomerization of one molecule might heat the surrounding molecules enough to induce a second isomerization, ultimately leading to thermal runaway and the beginning of a detonation

wave. For this to be significant, the thermal confinement time must be greater than the reaction time. It is possible that in systems with low thermal conductivity, low reaction barriers and large energy releases, such a process might occur. The extent to which a uniform solvent can support such a hot spot is of interest. An order-of-magnitude estimate of the rate of thermal relaxation can be obtained from the macroscopic thermal diffusion constant $D_T = (kM)/(\rho C_P)$, where k is the thermal conductivity, M is the molecular weight, ρ is the density and C_P is the heat capacity. Typical values for this quantity are on the order of $10^{-3} \text{ sec}^{-1} \text{ cm}^2$; this gives characteristic lengths on the order of 10–100 Å for the 10–1000 ps experimental timescale. This suggests that a hot spot associated with a single excited molecule might be expected to dissipate in a few picoseconds. If an energy of 6000 cm^{-1} is deposited in a volume of 1000 Å^3 (corresponding to a timescale of $\sim 10 \text{ ps}$) a temperature rise of roughly 60 C should occur.

Such temperature effects were investigated indirectly using rotational reorientation, by measuring the change in the rotational relaxation rates as the excitation wavelength was decreased. This is described in detail in Appendix A of LAP. Since the amount of excess energy lost to the solvent as heat will increase with increasing excitation photon energy, on some timescale the solvent molecules adjacent to the probe molecule will be hotter than the bulk solvent. This in turn could lead to a local solvent “melting”, which might be expected to decrease the local viscosity and lead to more rapid relaxation. The thermal conductivity calculations would suggest that temperature rises of 2–200 C, more than sufficient to change the local viscosity, could be produced by the amount of excess energy deposited in the solution by the excitation techniques employed in these experiments. However, our experimental results showed no change in any rotational reorientation parameters for Rhodamine 6G in ethanol, for excitation wavelengths between 460 and 550 nm, indicating that local heating is not significant on the 10–100 picosecond timescale. This confirms that a single-molecule hot spot will only persist for a few picoseconds. Note that this result is consistent with other picosecond experiments in molecules¹⁶. In these cases it was observed that intramolecular vibrational redistribution in dye molecules occurred on a subpicosecond timescale and that solvent-solute temperature equilibration occurred in less than

10 ps. This clearly suggests that the rapid dissipation of local hot spots predicted by macroscopic calculations is in reasonable agreement with what is observed.

The question of whether even this limited, very short-lived, local heating is sufficient to initiate a chain reaction can be approached using these transport laws in conjunction with a RRKM rate calculation. The type of process considered here would be one in which the energy released by one event remained localized for long enough to induce a second reaction. Such a pathway might be envisioned for a process such as the isomerization of methyl isocyanide, where a low barrier, highly exothermic isomerization is involved. In this case the excess energy resulting from the first isomerization might be sufficient to activate a neighboring molecule which could also isomerize ultimately producing a thermal chain reaction.

The question is whether thermal transport is slow enough to allow this sort of concentration of energy to persist. The time required for a bond to break in a vibrationally activated molecule is given by

$$\tau = \tau_0 \left[\frac{E}{E - E^*} \right]^{n-1}$$

where E is the available energy, E^* is the barrier height and n is the number of vibrational degrees of freedom. Typically, for a highly exothermic reaction, $E/E^* \sim 10$ and τ_0 is 10^{-13} sec. The thermal conductivity given above suggests that after 10 picoseconds, the energy released by a molecule will have dissipated over approximately 1000 \AA^3 , which can be arbitrarily partitioned into 7, 10 atom molecules. This gives seven systems with $E/E^* \sim 10/7$ and $n = 24$ degrees of freedom, corresponding to RRKM reaction times on the order of milliseconds. Similar results are obtained for other possible partitions; in general, the excess energy will have fully thermalized long before the reaction occurs. Only if the energy could be localized on one or two molecules with a few degrees of freedom immediately upon formation could such a mechanism be effective. The evidence from rotational reorientation suggests that the thermal conductivity is rapid enough to completely thermalize the environment in less than 10 picoseconds. If local "hot spots" are the site of initiation, then they must be "hot" in some sense other than thermal. For example, if

resonant energy transfer or some similar process is occurring on a subpicosecond timescale, it might be possible to cause adjoining molecules to dissociate rapidly enough to initiate a chain reaction.

V. CONCLUSION

As can be seen in the two attached reports, picosecond spectroscopic techniques have been developed, refined, and applied to several areas of potential interest with regard to energetic materials. In terms of directly usable results, the most successful area of investigation has been time-resolved emission spectroscopy, and its application to rotational reorientation. Studies of rotational reorientation have been used to provide information on the thermal properties of materials on short timescales as well as to probe the dynamic properties of solvents at elevated pressures. The results of these studies have been interpreted in terms of hydrodynamic models that include both macroscopic viscosity and dielectric relaxation. Despite the fact that the interactions being studied are occurring on molecular dimensions, the results are in good agreement with the predictions of macroscopic, hydrodynamic theories. Some of the other, more speculative work undertaken here, especially that involving Raman spectroscopy, has been less successful. Nonetheless, useful information can still be obtained. The reasons for our lack of success have been analyzed, and methods for increasing the chances of success have been proposed. Despite our lack of success in obtaining information on transient intermediates using Raman spectroscopy with existing equipment, the possibility remains that with somewhat more sophisticated equipment it may be possible to balance the constraints of peak and average power to obtain reasonable results. Raman spectroscopy may in fact be best suited to the 0.1–100 nanosecond regime where diffusion controlled reactions can begin to play a role. In this case, longer pulses and higher repetition rates may improve the odds of success considerably.

VI. REFERENCES

1. See for example, M. J. Soileau, ed., *Ultrashort Pulse Spectroscopy and Applications (Proc. SPIE, V. 533)*, SPIE, Bellingham WA, 1985; D. H. Auston and K. B. Eisenthal, eds., *Ultrafast Phenomena IV*, Springer-Verlag, New York, 1984).
2. S. W. Yeh, Ph.D. thesis, University of California, Berkeley, 1985; Lawrence Berkeley Laboratory Report 20662.
3. D. W. Anthon, Ph.D. thesis, University of California, Berkeley, 1986; Lawrence Berkeley Laboratory Report 21612.
4. D. W. Anthon and J. H. Clark, Submitted to *J. Phys. Chem.*
5. H. Nathel, Ph.D. thesis, University of California, Berkeley, 1986; Lawrence Berkeley Laboratory Report 20446.
6. D. W. Anthon, H. Nathel, D. M. Guthals and J. H. Clark, Submitted to *Review of Scientific Instruments*.
7. L. A. Philips, W. T. Brown, S. P. Webb, S. W. Yeh, and J. H. Clark, in *Ultrafast Phenomena IV*, D. H. Auston and K. B. Eisenthal, eds., (Springer-Verlag, Berlin, 1984) 390-392.
8. P. Robrish and H. Rosen, *Study of the Spectroscopy of NO₂ by Selective Excitation with a Tunable Laser*, Lawrence Berkeley Laboratory Report 3229, Berkeley, 1975.
9. J. B. Hopkins and P. M. Rentzepis, *Chem. Phys. Lett.* **124** (1986) 79-83.
10. T. L. Gustafson, D. M. Roberts and D. A. Chernoff, *J. Chem. Phys.* **79** (1983) 1559-1564.
11. D. W. Anthon, S. W. Yeh and J. H. Clark, Submitted to *Review of Scientific Instruments*.
12. P. Chen, T. D. Westmoreland, K. S. Schanze, D. W. Anthon, P. E. Neveux and T. J. Meyer, Submitted to *Inorganic Chemistry*.
13. L. A. Philips, Ph.D. thesis, University of California, Berkeley, 1985; Lawrence Berkeley Laboratory Report 19511.
14. L. A. Philips, S. P. Webb, S. W. Yeh and J. H. Clark, *J. Am. Chem. Soc.* **106** (1984) 7286-7288.
15. L. A. Philips, S. P. Webb, and J. H. Clark, *J. Chem. Phys.* **83** (1985) 5810-5821.
16. P. O. J. Scherer, A. Seilmeier, F. Wondrazek, and W. Kaiser, in *Ultrafast Phenomena IV*, D. H. Auston and K. B. Eisenthal, eds., (Springer-Verlag, Berlin, 1984) 351-354.

**Picosecond Spectroscopy in Solutions:
The Excited-State Solvation Dynamics
of 9,9'-Bianthryl**

Douglas William Anthon

Ph.D. Thesis

**Lawrence Berkeley Laboratory
University of California
Berkeley, California 94720**

May 1986

**The United States Department of Energy has the right to use
this thesis for any purpose whatsoever including the right
to reproduce all or any part thereof.**

**This work was supported by the
U.S. Department of Energy under
Contract Number DE-AC03-76SF00098.**

**Picosecond Spectroscopy in Solutions:
The Excited-State Solvation Dynamics
of 9,9'-Bianthryl**

Douglas William Anthon

Abstract

Several aspects of picosecond spectroscopic measurements in solution are described. Picosecond pulses at 1064 nm at a repetition rate of 10 Hz were provided by an active-passive mode-locked Nd:YAG laser. Pulse trains of 15 pulses with 5 mJ/train and 5% amplitude stability were obtained, as were amplified single pulses of 10 mJ with 10% amplitude stability. The variation in the pulse duration from 40 to 8 ps through the pulse train was attributed to the interaction of self-phase modulation and the limited laser gain bandwidth. A 355 nm-pumped single-pass optical parametric source (OPS) made from two 37 mm type II potassium dihydrogen phosphate crystals, generating tunable visible (455–650 nm) and infrared (780–1610 nm) light was characterized. Conversion efficiencies of up to 44% were achieved; pulses approaching the transform limit were produced at lower efficiencies. Injection locking of the OPS with scattered laser light improved the stability and spectral linewidth of the device at 532 nm. A type I OPS covering the range 455–1610 nm is also described. Details of the systems used for obtaining picosecond emission, absorption and Raman spectra are described. Emission from samples excited with a single laser pulse were measured in 10 nm bandwidths with 6 ps resolution using a computer-controlled streak camera system. Absorption measurements made with the same system measured, with a resolution of .01 OD, the time-dependent attenuation of the emission from a dye solution by a second, excited sample. Limited results from a Raman spectrometer in a pump-probe configuration are also described, as are the limitations inherent in such measurements. The applicability of coherent Raman techniques to solution measurements is discussed. Measurements of the solvation dynamics

of 9,9'-bianthryl in alcohols, deuterated alcohols and alcohol-alkane mixtures at several temperatures are described. Complex triexponential decays were observed, correlating with dielectric relaxation, alcohol concentration and solvent viscosity. No dynamics were observed in nonhydrogen-bonding solvents irrespective of polarity. These results combined with evidence of excited-state proton transfer suggest that BA initially (~ 20 – 50 ps) forms an unsolvated charge transfer state which then forms hydrogen bonds to the solvent (~ 50 – 500 ps, increasing with viscosity). Other interpretations are discussed.

John D. Coe

Acknowledgements

It is my pleasure to acknowledge all the people who, in one way or another, played a role in making the work described here possible. There is not room here to explicitly acknowledge the roles of everyone who contributed to the process of my getting involved in this project in the first place. A variety of friends, family and co-workers contributed to this process. Special thanks should be accorded to Arnie Falick and the late Craig Hollowell, both of whom were instrumental in getting me started in research and who worked persistently to nudge me in the direction of graduate school.

It is important to note the contribution of all the members of my research group. Special thanks should be accorded to John Clark who has been the source of countless new ideas, and who has encouraged me to pursue a variety of different projects. As long as this thesis is, it omits a significant number of smaller projects, all of which contributed to the diversity of the last few years. All the work described here was to some extent a collaborative effort, and the support and assistance of all my fellow graduate students should be noted. The streak camera system was originally the handiwork of Sheila Yeh and Steve Webb; thanks are in order for both of them for getting me started on the system. Ward Brown and Cindy Buhse were responsible for the fluorimeter used for steady-state fluorescence measurements, as well as some of the later Raman work. The efforts to improve and characterize the laser and optical parametric source began with Dennis Guthals and Howard Nathel. Without their efforts, much of the work carried out here would not have been possible. Other members of the group who made significant contributions to the various projects I pursued included Don Sipes, Bill Hopewell and Li-Wen Xu. Their contributions are somewhat less clearly delineated than those just mentioned, but all of them provided a combination of technical expertise and moral support at some crucial stage of the project. One other noteworthy collaborator has been Kirk Schanze, who provided the transition metal complexes used for the excited-state

absorption measurements in chapter three.

Both personal and professional thanks are in order for Leah Zebre, who not only put up with having an occasionally ill-tempered graduate student for a roommate for the last few years, but who was also responsible for the mass spectral measurements in chapter four. Important though those mass spectra might be, her role in keeping me (almost) sane through all this is by far her greatest contribution to this project.

Finally, it must be noted that the work described in chapters two and three, especially that involving Raman spectroscopy and the optical parametric source, was supported by the Office of Naval Research under contract N00014-82-K-0349, NR 659-801. Support for the work on solvation in chapter four was from the Gas Research Institute under contract 5081-260-568. Both of these sources of support are gratefully acknowledged.

Contents

	Page
Abstract	1
Preface	i
Table of Contents	iii
List of Figures	iv
List of Tables	viii
Chapter 1	
Introduction	1
Chapter 2	
Picosecond Optical Sources	8
A. Introduction	8
B. The Laser System	9
1. Hardware and Optics	10
2. System Characterization	22
3. Effect of Self-Phase Modulation	26
4. Effect of an Intra-Cavity Etalon	28
C. Optical Parametric Source	30
1. Introduction	30
2. Optical Hardware	36
3. Pulse Characterization	42
4. Comparison with Theory	56
D. Conclusion	62
E. References for Chapter 2	63

Chapter 3

Picosecond Spectroscopic Techniques	65
A. Introduction	65
B. The Streak Camera	68
C. Time-Resolved Emission Spectroscopy	70
1. Hardware and Optics	70
2. Data Transfer and Correction	76
3. Results	90
D. Time-Resolved Absorption Spectroscopy	93
1. Introduction	93
2. Hardware and Optics	95
3. Data Handling	101
4. Results	107
E. Time-Resolved Raman Spectroscopy	112
1. Introduction	112
2. Measurements and Results	117
3. Time-Resolved Raman: Future Prospects	125
4. Coherent Raman Techniques	133
F. Conclusion	141
G. References for Chapter 3	142

Chapter 4

Picosecond Solvation Processes in 9,9'-Bianthryl	144
A. Introduction	144
B. Excited-State Solvation	147
1. Overview	147
2. Previously Studied Systems: 1-Naphthol, DMABN and 4AP	153

3. 9,9'-Bianthryl	160
C. Experimental Procedure	164
D. Picosecond Emission Measurements: BA in Alcohols	167
E. Short Time Behavior	175
1. Time-Resolved Emission	175
2. Time-Resolved Absorption	178
F. Intermediate Time Behavior	183
1. Pure Alcohols	183
2. Alcohol-Alkane Mixtures	185
3. Deuterated Alcohols	193
4. Rotational Reorientation	196
G. Long Time Behavior	202
1. Polarity Dependent Lifetimes	202
2. Proton Quenching and Proton Transfer	206
H. Discussion	208
1. Bianthryl Photophysics	208
2. Polarity, Solvation and Dielectric Relaxation	217
3. Solvation as a Diffusion Controlled Reaction	223
I. Conclusion	228
J. Appendix on Data fitting	230
K. References for Chapter 4	242
 Chapter 5	
Conclusion	247

List of Figures

Figure	Page
2.1 Active-passive Nd:YAG laser schematic	12
2.2 Laser relaxation oscillations	15
2.3 Pulse trains of the passive and active-passive mode-locked laser	17
2.4 Pulse selector, spatial filter and amplifier schematic	21
2.5 Spectral and temporal profiles of pulses at various positions in the pulse train	24
2.6 Laser pulse properties versus position in the pulse train	25
2.7 Effect of an intra-cavity étalon on the laser pulse	29
2.8 Optical system used for characterization of OPS pulses	38
2.9 Crystal orientation and polarizations for the OPS	41
2.10 Angle tuning curve for the OPS	43
2.11 Visible OPS energy output at 540 nm versus the pump energy	45
2.12 Output energy of the OPS as a function of wavelength	46
2.13 OPS spectral and temporal profile at 540 nm, ~15% conversion	48
2.14 OPS spectral and temporal profile at 540 nm, ~1% conversion	49
2.15 OPS spectral and temporal profile at 532 nm, ~20% conversion	50
2.16 OPS spectral and temporal profile at 532 nm, ~1% conversion	51
2.17 OPS spectral and temporal profile at 358 nm, ~1% conversion	54
3.1 Optical system for time-resolved emission	71
3.2 Instrument response function of the streak camera	74
3.3 Uncorrected time-base étalon traces	80
3.4 Normalized étalon spacing versus channel number	82
3.5 Emission data for intensity calibration	83
3.6 Corrected étalon traces	86
3.7 Corrected fluorescence decay curve for aqueous RUTBY	87
3.8 Optical system for emission/absorption spectrometer	97

3.9 Schematic of the time resolved absorption process	102
3.10 Time-resolved absorption in BOSCO	108
3.11 Absorption Instrument response function	110
3.12 Time-resolved absorption data for the compound RE-PTZ	111
3.13 Time-resolved Raman apparatus	118
3.14 Raman spectrum of neat CCl ₄	119
3.15 Raman spectrum of benzene in a CCl ₄ solution	120
3.16 Raman spectrum of I ₂ in cyclohexane	121
3.17 Raman spectrum of of the excited state of RUTBY	123
4.1 Potential for continuous solvation along a single solvation coordinate	149
4.2 Potential for two-state relaxation along a single coordinate	151
4.3 Conformations of DMABN in the ground and first singlet states	156
4.4 Structure of 9,9'-Bianthryl	161
4.5 Emission spectra of BA in a series of linear alcohols	169
4.6 Time-resolved emission at 20 C for BA in a series of linear alcohols	170
4.7 Fluorescence decay of BA at 500 nm in <i>n</i> -hexanol at 20 C	172
4.8 Fast components of the emission of BA in <i>n</i> -hexanol at 0 C at 20 nm intervals	174
4.9 Time resolved emission spectra for BA in <i>n</i> -hexanol at 0 C	176
4.10 Time-zero spectra of in <i>n</i> -hexanol between 0 and 60 C.	179
4.11 Intensity and excitation wavelength dependence of BA emission	180
4.12 Room-temperature time resolved absorption of BA	182
4.13 Time-resolved emission of BA in mixtures of <i>n</i> -butanol and <i>n</i> -hexadecane	189
4.14 Spectral relaxation time versus viscosity for BA in alcohol-alkane mixtures	190
4.15 Rotational reorientation data for BA in <i>n</i> -butanol at 400 nm	199
4.16 The states and point groups related to the CT state in BA	211
4.17 Parameters used in fitting the emission data	234

List of Tables

Table	Page
2.1 Wavelengths and Approximate Energies from the OPS	55
4.1 Spectral relaxation time constants for BA versus Temperature	173
4.2 Relaxation Properties of Alcohols at 20 C	184
4.3 Relaxation Properties of Butanol-Hexadecane Mixtures at 20 C	187
4.4 Relative Relaxation Properties of Alcohols and Alcohol-Alkane Mixtures . .	192
4.5 Relative Properties of Protonated and Deuterated Alcohols at 20 C	194
4.6 Rotational and Spectral Relaxation in alcohols and alcohol-alkane mixtures .	200
4.7 Fluorescence Yields and Lifetimes for BA at 20 C	203
4.8 Parameters of fits for BA in n-hexanol at 0 C	238
4.9 Parameters of fits for BA in n-hexanol at 20 C	239
4.10 Parameters of fits for BA in n-hexanol at 36 C	240
4.11 Parameters of fits for BA in n-hexanol at 60 C	241

Chapter 1

Introduction

Since a majority of all chemical reactions occur in solution, the study of chemistry in liquids is of great fundamental and practical importance. Despite this, relatively little is known about the detailed molecular dynamics of liquid phase chemical reactions. This lack of detailed knowledge is especially striking when compared with the detailed theoretical and experimental results available in the gas phase or in solids. The properties of gas phase molecules are essentially the same as those of isolated molecules, so that a combination of spectroscopy and theory can often be used to understand detailed molecular properties. In addition to this, the only significant intermolecular interaction arises from bimolecular collisions. Since these are also accessible theoretically and experimentally, an extremely detailed description of gas phase processes at low pressures is often possible. Solids are also relatively tractable, since molecules are located at fixed sites on rigid lattices. Although each molecule interacts with several nearest neighbors, the interactions remain relatively constant, so the behavior of the system will resemble that of isolated molecules interacting with a static potential.

Unfortunately, the dense, disordered environments found in liquids do not lend themselves to any such simplifications. Because of the lack of long-range order, the methods applied to solids cannot be used in liquids. In general, liquids tend to be approached as if they were very dense gases. Although this gives qualitatively correct results, it is difficult to take into account the detailed intramolecular interactions. For gases at atmospheric pressure the bimolecular collision rate is roughly 10^{10}sec^{-1} ; extrapolating to liquid densities indicates that the nominal collision rate will increase by three orders of magnitude. In a liquid, molecules are no longer well-separated entities interacting through infrequent collisions. Instead, the intermolecular distances are comparable to molecular diameters, and every molecule interacts continuously with several nearest neighbors. It is difficult to

interpret the nominal collision rate directly, but the implication that time resolution on the order of picoseconds or femtoseconds is required to measure collision-related phenomena in solution appears to be correct. For example, dye molecules excited to any electronic state typically relax to the lowest vibrational level of the first singlet state in less than a picosecond. Similarly, the vibrational dephasing time for many organic liquids is on the order of a few picoseconds. Note that the spectral broadening associated with this rapid dephasing (as well as other sources of inhomogeneous broadening) makes it difficult to identify individual states, since in most cases electronic spectra are broadened into continua. Not all processes in liquids are this rapid. Unlike gases, the mean free path of a molecule in a liquid is comparable to a molecular diameter. This leads to the cage effect, where a given pair of molecules collides many times per encounter. This has the effect of limiting the rate of chemical reactions; rather than being governed by the collision rate, reaction rates are now diffusion controlled. Collision-mediated relaxation processes tend to be much more rapid than chemical reactions in solution, and the reaction rates tend to be well described in terms of equilibrated molecules diffusing together. Quasi-equilibrium theories involving diffusion controlled transport and simple transition states tend to work quite well in solutions.

This leads to the situation where the measured reaction rate is much slower than the reaction itself. This makes it difficult to study directly the fast processes associated with chemical reactions. For example, a typical method for studying the reactions of reactive species in solution is to dissolve precursor and scavenger molecules in an inert solvent. Photolysis of the precursor generates the reactive species which then react with the scavenger. Although it is possible to carry out this type of experiment using picosecond pulses, the rates measured this way will correspond to diffusion constants rather than reaction rates. If one is interested in looking at the reaction itself, it is necessary to study systems where the effects of diffusion can be eliminated. To do this it is necessary to study systems where the reactive species can be generated in close proximity to one

another. This can be most readily accomplished if all the reactive species are generated from the same precursor molecule, or if the excited species react with the solvent. The first case is exemplified by the caged recombination of free radicals, including both reversible cases such as the recombination of iodine atoms to form I_2 and irreversible cases such as the formation of ethane from azomethane. Simple intramolecular reactions such as intramolecular charge transfer or conformational changes can also be considered. Reactions with the solvent once again range from simple reversible solvation to proton transfer to irreversible free radical reactions.

There are two basic reasons for wanting to investigate chemical reactions on a picosecond timescale. The information obtainable on these timescales reflects the fundamental processes which constitute solution phase chemistry, including molecular solvation and reactions between specific molecules. The difference between the liquid and gas phases is the difference between an isolated molecule and a molecule surrounded by weakly interacting neighboring molecules; these weak interactions determine the difference in properties between an isolated and a solvated molecule. A thorough understanding of these interactions is clearly necessary if one is to have any hope of bridging the gap between what is known about isolated molecules and their behavior in solutions. The ultimate goal of this type of work would be to extend the rather detailed understanding of gas-phase reactions into the liquid phase; unfortunately, this remains a rather distant goal.

A second reason for wanting to observe chemical reactions in solution with picosecond time resolution is related to the complexity of typical solution-phase free-radical reactions, especially those involving the solvent itself. Although the initial process in such reactions presumably corresponds to a relatively simple process such as cleavage of some molecule to reactive radicals, the subsequent reaction can be quite complex. Steady-state photolysis of such systems typically leads to a complex product distribution which depends not only on the photochemistry of the initially present species but

also on the photoreactivity of any of the subsequently formed species. This makes the interpretation of the data rather difficult. This is unfortunate, since reactions involving liquids are important in areas as diverse as organic synthesis and combustion. Using ultrafast techniques should simplify the study of such systems, by making it possible to study the early stages of the reaction before the onset of more complicated behavior. For example, if a single short exciting pulse is used, there will be virtually no secondary photolysis. Furthermore, with time-resolved detection it should be possible to watch the development of the the product distribution directly, and it should be possible to distinguish rapid cage reactions from the slower diffusion controlled reactions. Note that in this case the selectivity of the detection method is very important, since it must be possible to distinguish between the various species which have been created. This was one of the primary motivations for attempting to use time-resolved Raman spectroscopy for this purpose.

There is clearly sufficient motivation for studying solution-phase reactions on the picosecond timescale. The fact remains that carrying out measurements on this timescale involves the use of rather sophisticated laser and electrooptic technology. Because of this a considerable amount of effort went into the laser itself, and into related optical techniques. This is reflected in the content of the following chapters, which contain roughly equal amounts of both optics and chemistry.

The laser itself consisted of an active-passive mode-locked Nd:YAG laser (based on a commercial system from Quantel) which operated with a repetition rate of 10 Hz. As described in the following chapter, numerous modifications were required to bring it into its final form. By using different conditions and generating harmonics of the laser frequency, it was possible to obtain pulses varying in duration from 8 to 40 ps with millijoules of energy at 1064, 532, 355, and 266 nm. The generation of pulses as short as 8 ps from a Nd:YAG laser has never been reported before. They are generated in this system through the unusual interaction of self-phase modulation and the finite

gain bandwidth of the laser. The shortest pulses are relatively weak and are consequently somewhat difficult to use, but they provide a relatively simple source of short pulses when they are needed. In addition to the laser itself, an optical parametric source was developed as a source of tunable infrared and visible light. Picosecond parametric generation is relatively simple, since the laser peak power is high enough that a single pass through two nonlinear crystals is sufficient to generate the tunable output. The external cavity normally used in the nanosecond regime is not required. The parametric source was found to be a convenient and reliable method for generating tunable light.

The development of spectroscopic techniques for use with solution phase measurements as one of the major efforts in this project, as described in chapter three. Systems were developed for carrying out time-resolved emission, absorption and Raman spectroscopy. There is an unfortunate tradeoff between the ease of measurement and the generality of these measurements. Emission measurements are relatively easy to make, but can only be applied to excited state relaxation. Absorption is more difficult to use, and much less sensitive, but it should make it possible to follow processes involving ground-state molecules. Raman spectroscopy was only marginally possible with the current laser system, and could not be usefully applied to any chemical system. However, if it could be made to work, it would provide a method for observing the behavior of individual ground-state species in complex mixtures.

A streak camera based detection system was used to make both time-resolved emission and absorption measurements. Triggering the streak camera in the presence of a time-varying optical signal, such as the fluorescence from an excited dye solution, produces a time-resolved image of the signal. This is detected with a photodiode array, digitized and sent directly to a microcomputer for real-time signal averaging. Because of the weak signals and the limited dynamic range of the streak camera, such signal averaging was essential if reliable emission and absorption data were to be obtained. In the case of emission, the sample being investigated was excited with a single picosecond pulse,

and the resulting fluorescence imaged through a bandpass filter into the streak camera. Spectral resolution of 10 nm and time resolution of 6 ps were attainable. These measurements of time resolved emission at fixed wavelengths were combined with steady-state emission spectra to produce time-resolved emission spectra. To measure time-resolved absorption, a two pulse system was employed. A dye solution was excited with an initial laser pulse and the long-lived emission was imaged through a second sample into the streak camera, making use of the same bandpass filters and optics used for emission. Excitation of the second sample with a delayed pulse created an excited-state population which would attenuate the dye fluorescence. The excited-state absorption corresponds to the difference in the fluorescence intensity measured with and without the second excitation pulse. Changes in absorption of ~ 0.01 could be detected this way. Raman spectra were measured using a pump-probe method using a conventional double monochromator in a geometry comparable to that normally used for a CW Raman spectrometer. Although spectra could be obtained from pure solvents, the signal levels were generally too low to permit measurements in more dilute samples. Nonlinear background signals including stimulated Raman were a major difficulty. Coherent Raman techniques were considered, but no useful measurements were made.

Chapter four describes the studies which were made of solvation processes involving 9,9'-bianthryl (BA) in alcohols, deuterated alcohols and alcohol-alkane mixtures. These studies represent a continuation of other solvation studies which have been carried out in this laboratory using other probe molecules, including 4-aminophthalimide and 4-(N,N-dimethylamino)benzonitrile. All of these molecules are characterized by a large change in dipole moment between the ground and excited states. This causes the equilibrium solvation to be quite different in the two states. Since the emission spectrum depends on the solvation configuration, the solvation process will be detectable in the emission spectrum. This is a very important feature from an experimental point of view, since it means that useful results can be obtained using simple time-resolved emission. It is also

possible to observe these processes using absorption spectroscopy, although the quality of the data is poorer and little additional information can be obtained. Upon excitation in polar solvents, BA undergoes a transition from a symmetric, rigorously nonpolar ground state, to an asymmetric intramolecular charge transfer state with a large dipole moment, and an appreciable rate of proton transfer. This represents a rather extreme change in molecular properties, and large changes in solvation including the formation of excited-state hydrogen bonds are expected. This molecule is unusual in that it makes it possible to look at both the intramolecular charge transfer process and the intermolecular solvation. Analysis of the tri-exponential decays observed in emission suggest that both processes are observable; in hexanol at 20 C, for example, time constants of 50 and 320 ps were observed, the first value being comparable to what would be expected from a dielectric relaxation-controlled charge transfer process, and the latter being consistent with a diffusion-controlled reaction with the solvent. The extent to which the observed data is consistent with the occurrence of excited-state hydrogen bonding is discussed, as are other alternative explanations. Despite the relative simplicity of this molecule, it is still difficult to come to definitive conclusions about its behavior.

Chapter 2

Picosecond Optical Sources

A. Introduction.

The central component of virtually any experiment involving measurements on the picosecond timescale is a mode-locked laser, and the work done here is no exception. In particular, a flashlamp-pumped Nd:YAG laser with active-passive mode-locking operating at a repetition rate of 10 Hz was employed. The laser system used here is based on a commercial system, although after numerous modifications, only a small fraction of the original parts remained in use. The modifications were made primarily to improve the stability of the laser output and to increase the overall reliability of the system. Some of these modifications were required to undo shortcuts taken by the manufacturer, especially with regard to the mechanical and thermal stability of the cavity; others, such as the use of the acoustooptic modulator represented an overall improvement in the laser design. The mechanical stability of the laser was improved markedly through the use of a floating Invar rail system and kinematic mounting hardware. Using specially designed optical mounts for the cavity optics simplified the alignment and operation of the laser. Amplitude fluctuations arising from thermal fluctuations were eliminated with the use of a properly regulated temperature bath for the laser cooling water. Further modifications were made to improve the performance of the laser. The original stirred dye cell was replaced with a redesigned flowing dye cell which improved the uniformity of the saturable absorber and led to greater output stability. Adding an acoustooptic modulator (AOM) to the cavity led to active-passive mode-locking, and another increase in stability. An intra-cavity étalon could be added to modify the effective gain bandwidth of the laser and leading to shorter or longer pulses as needed.

An interesting aspect of this work was the discovery that with the active-passive con-

figuration, self-phase modulation in the laser rod was significant, leading to the formation of chirped pulses with a spectral width comparable to the laser amplification bandwidth. This, combined with the presence of the saturable absorber led to the formation of pulses very close to the transform limit of the gain bandwidth of laser medium. The stability of the laser as well as the high peak power of a picosecond pulse made it feasible to use of an optical parametric source (OPS) to generate tunable light in the visible and near-infrared. These sources rely on nonlinear interactions in a crystal to generate the tunable light, and have few of the difficulties associated with dye lasers. To obtain reasonable output powers, it is necessary to use laser intensities close to the damage threshold of the crystal. Good intensity stability is essential if the nonlinear crystals are not to be damaged.

The system shown here underwent several stages of evolution, beginning as a passively mode-locked system with very poor ($\pm 100\%$) energy stability and poor beam quality and ending up as a much more stable active-passive system producing a nearly diffraction limited beam. The full development of this system, as well as the process of setting up and aligning the system is described in detail elsewhere¹. In its final form, the energy of the pulse trains varied by less than 5% from shot to shot, and the energy of the selected single pulse varied by only 10%. The increased stability of the system is important for several reasons. All of the nonlinear optical processes used to convert the laser frequency to usable visible and UV frequencies (especially the OPS) have nonlinear power dependences, and greatly amplify the laser fluctuations. Fluctuations in the pulse trains will also cause the pulse selector to act erratically, introducing additional fluctuations into the system. The improved beam quality was reflected in a decrease in optical damage and an improvement in conversion efficiency of high power components such as the OPS. Only the final version is described here.

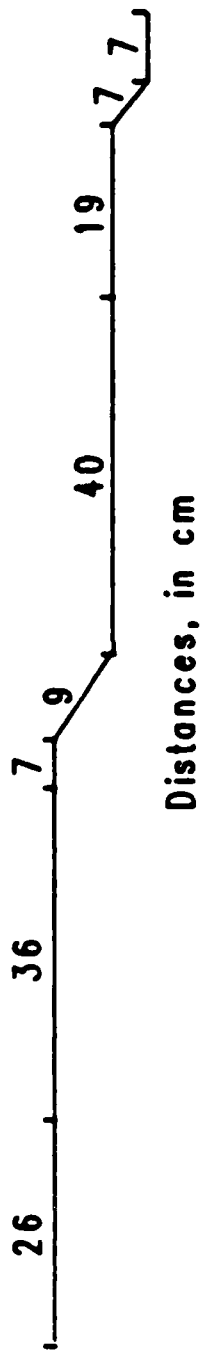
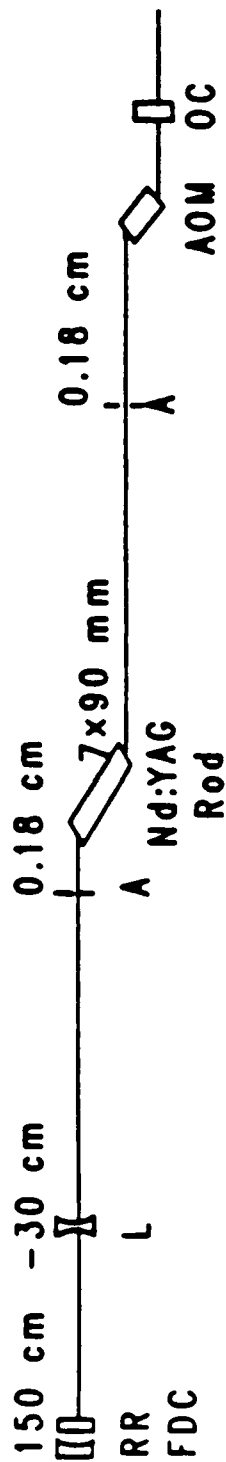
B. The Laser System

1. Hardware and Optics

The laser cavity itself is shown in figure 2.1. The cavity hardware is mounted on floating Invar rails to maximize the mechanical stability of the system. Rail plates were used to attach the optical mounts to the rail system; these employed three-point kinematic mounting to facilitate the removal and replacement of the optics. The optical components were mounted in a mixture of commercial and custom-made hardware. In general, the mounts were similar to those sold by NRC, although in many cases significant modifications were required to adapt the mounts for specific applications. To simplify alignment of the cavity, all critical adjustments are controlled with low-hysteresis differential micrometers (NRC).

The optical configuration of the cavity is hemispherical, with the curved dye cell reflector being focused with the output coupler. This arrangement results in a beam waist at the output coupler and a relatively large beam diameter at the dye cell. The active medium consists of a 90 mm rod of Nd:YAG (1% Nd by weight) cut at Brewster angle, optically pumped at ten hertz with a pair of krypton flashlamps at using a commercially-available laser head and power supply (Quantel YG400AP). The acoustooptic modulator (Intra-action Inc. ML-1870) consists of a quartz crystal cut at Brewster angle, with an acoustic resonance of approximately 50 MHz, coinciding with the cavity length. The piezoelectric crystal is driven electronically at this resonant frequency, to generate the time-varying diffraction loss required for active mode-locking². The cavity optics (Optics for Research) are flat to $\lambda/10$ and are coated (CVT) as necessary. All optics are wedged to avoid unwanted étalon effects. The flat output coupler is coated to be 70% transmitting; this large cavity loss is required to allow the rapid evolution of the pulse shape through the pulse train. A more reflective output coupler will lead to longer pulses. The flowing dye cell consists of a 200 μm thick machined nickel shim sandwiched between the curved, 99% reflector and the AR coated window. A solution of a saturable absorber, (Eastman 9740

Figure 2.1. Optical configuration of the active-passive Nd:YAG laser system.



RR: Rear Reflector	A: Aperture
FDC: Flowing Dye Cell	AOM: Acousto-optic Modulator
L: Lens	OC: Output Coupler

Figure 2.1

in 1,2 dichloroethane, see below) is pumped through a channel in the shim, resulting in a well-controlled, flowing dye region. The dye cell is mounted in an ordinary mirror mount. Two 1.3 mm diameter apertures made of machinable ceramic are placed in the cavity to ensure TEM₀₀ operation. The use of smaller apertures decreased the output energy, while larger apertures allowed higher-order transverse mode operation to occur. The AR coated, -30 cm lens is placed in the cavity to compensate for the thermal lens in the laser rod. The thermal lensing is large enough that the laser is very sensitive to small thermal effects. In particular, variations of a few degrees in the cooling water temperature were directly reflected in the laser output. To minimize this effect, the cooling water temperature was controlled to within 0.1 degrees with a refrigerated recirculator (Neslab). Thermal effects arising from variations in the laser repetition rates were eliminated by only operating the laser at 10 Hz. This is why, for example, the streak camera system described in the next chapter was used with the laser at 10 Hz even though data collection proceeded at less than 3 Hz.

The laser system used here uses both an acoustooptic modulator and a saturable absorber in the laser cavity to produce mode-locked pulses³. Picosecond pulses will still be produced if either element is removed from the cavity, but the combination of the two leads to an optimal combination of pulse length and stability. Consider first the case where only active mode-locking is occurring. This corresponds to the case where pure solvent is passing through the flowing dye cell. The behavior of the laser in this case is much like a CW mode-locked laser, and is well described by the conventional theory of mode-locking². The laser cavity consists of a Fabry-Perot étalon with longitudinal modes at frequency spacings $\Delta\omega = \pi c/L$; this is exactly equal to the frequency of the AOM. In the frequency domain, the AOM can simply be treated as a means of coherently scattering photons from one cavity mode to another. Repeated Brillouin scattering in the AOM coherently couples all the oscillating cavity modes. It can be shown that the interference of these oscillating modes will give rise to a single pulse travelling back

and forth through the cavity, with a duration inversely proportional to the number of oscillating modes, which in turn reflects the bandwidth of the gain medium². The time-dependent behavior of the AOM is important as well. In general, the pulses produced in a mode-locked laser are longer than those predicted from the laser gain alone, suggesting that other, time-dependent phenomena control the pulse length. In the time domain, the AOM acts as a time dependent loss. The diffraction efficiency of the acoustic grating varies with the phase of the driving field and a pulse travelling through the cavity will experience essentially no loss if it passes through the AOM in phase with the nodes of this field. The width of the pulses in this case will be related to the effective width of these nodes, which in turn depend on the modulation depth of the AOM.

In order for this to work correctly, it is necessary that the AOM crystal be properly oriented with respect to the laser axis, and that the resonant frequency of the crystal be accurately matched to the cavity length. The first of these requirements arises because the diffraction efficiency of the acoustic grating depends strongly on the angle of incidence, and strong coupling is required for efficient mode-locking. An alternative view of this angle adjusting procedure is that it corresponds to an adjustment of the phase-matching angle for Brillouin scattering from one cavity mode to another². To simplify these adjustments, the output coupler is placed on a micrometer-controlled translation stage, and the AOM is mounted on a mirror mount. To set the angle, the cavity length is adjusted to be a few percent out of resonance with the AOM frequency and an aperture is placed in the beam outside the cavity so the intensity of the diffracted or undiffracted beam can be measured. The number of diffracted spots varies with the AOM angle and the optimum angle corresponds to the presence of only one intense diffracted spot in addition to the undeflected beam. This allows coarse adjustment of the angle; fine adjustment consists of adjusting the angle until the intensity of the undeflected spot is minimized.

Once this angle has been found, the cavity length is adjusted. As the length of the

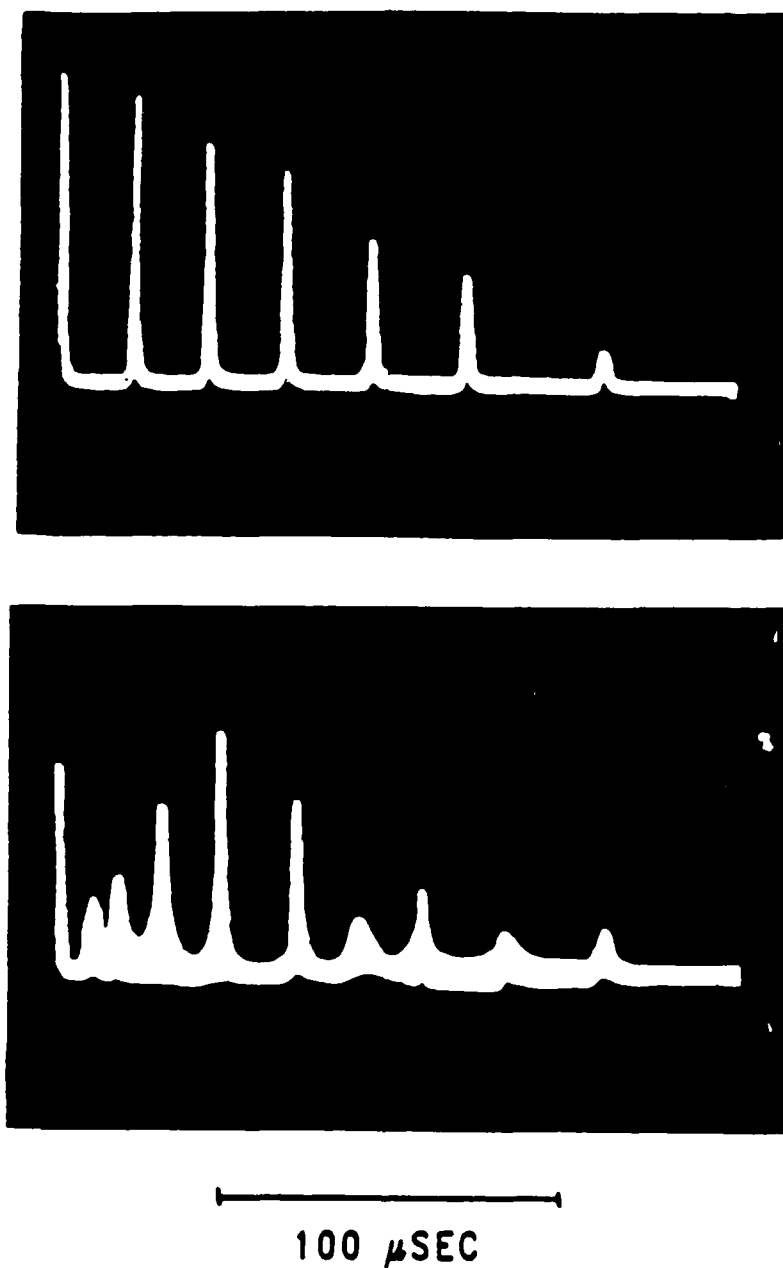


Figure 2.2. Relaxation oscillations from the passively mode-locked Nd:YAG laser. Upper curve shows the system with the cavity in resonance. Lower figure shows the system 100 ppm out of resonance. In both curves, the laser was operated without dye with a flashlamp voltage of 1200 V.

cavity approaches resonance, the diffracted intensity will decrease, until, at resonance, it is almost entirely eliminated. This corresponds to the fact that the single pulse is in phase with the acoustic field so that the pulse "misses" the diffraction grating. Since the flashlamps remain on for approximately 100 μ s, while the cavity round-trip time is 10 ns, the cavity length must be matched to the AOM frequency to within a few ppm. For a 3 M cavity, this corresponds to varying the cavity length to tens of microns³. With the cavity length properly adjusted, the laser output will consist of the smoothly decaying relaxation oscillations shown in figure 2.2. The number of oscillations will depend on the total energy in the laser rod. Note that these relaxation oscillations themselves consist of long trains of pulses. This can be seen in figure 2.3, which shows a single relaxation oscillation on a faster timescale. Each of these pulses is roughly 100 ps long, and the inter-pulse separation is equal to the cavity round-trip time. The smooth relaxation oscillations appear to result because the system never goes below threshold. The circulating pulse persists at very low levels between relaxation oscillations, so that when the gain builds up again, there is a smooth transition to larger pulses. Note that the presence of this circulating pulse prevents the buildup of other modes, so that the second relaxation oscillation arises from a well-defined initial condition, and not from noise. When the cavity is out of resonance, this does not occur. The lower half of figure 2.2 shows the effect of adjusting the cavity 100 ppm out of resonance. The smoothly decaying relaxation oscillations are replaced by a chaotic series of relaxations. While the resonant case is stable from shot to shot, the nonresonant case fluctuates randomly from shot to shot. It appears that with the cavity this far out of resonance, the weak circulating pulse does not remain in phase with the AOM between oscillations. As a result, the later relaxation oscillations are not driven by the previous oscillation, but instead arise from noise, giving rise to the chaotic decay observed in the lower half of figure 2.2. The presence of well-defined relaxation oscillations can be used to verify that the correct cavity length has been found.

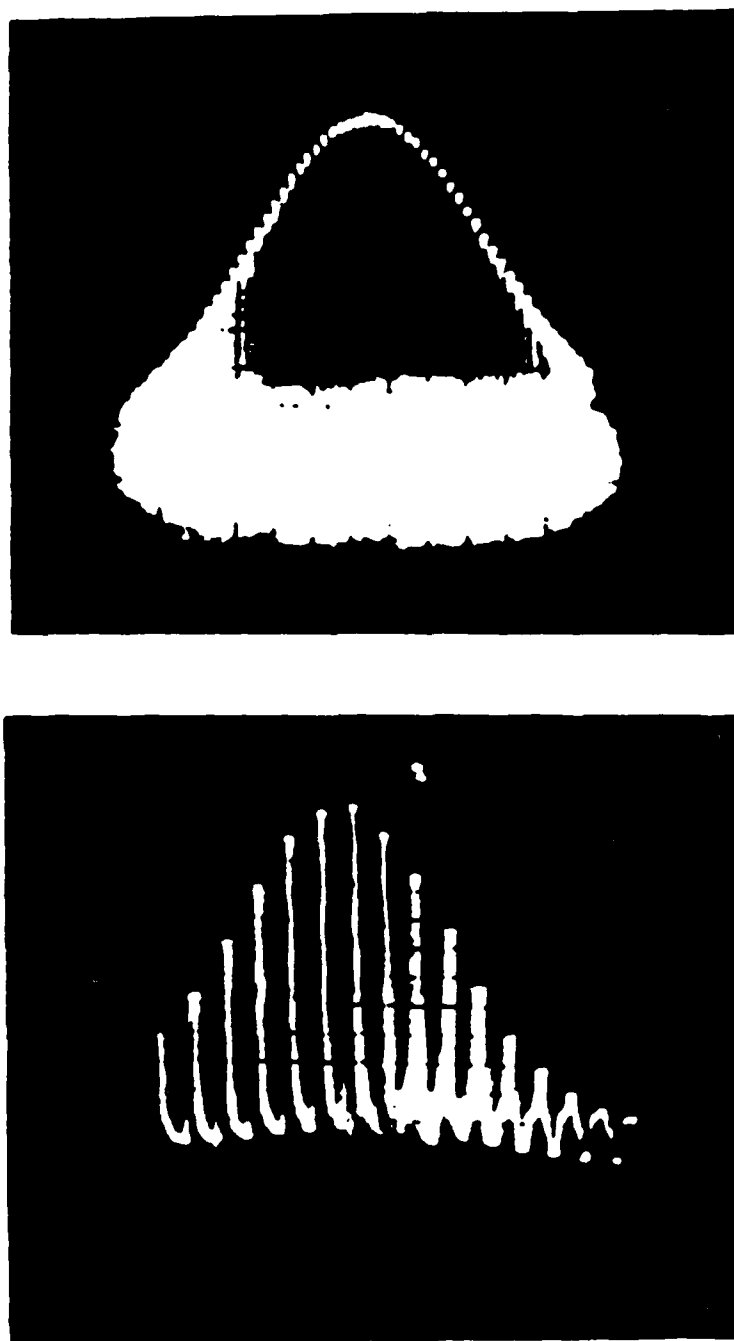


Figure 2.3. Pulse trains seen with purely active mode-locking (upper figure), and active-passive mode-locking (lower figure). Conditions for the upper curve are the same as figure 2.2. Conditions for the lower curve are described in text.

Adding dye to the system results in active-passive mode-locking. The dye solutions used here are less concentrated than those used for simple passive mode-locking. In the linear absorption regime, the dye solution is 70% transmitting, so the dye cell is significantly less lossy than the output coupler. When the dye is added, it has the initial effect of simply increasing the threshold for oscillation. This loss can be readily overcome by increasing the energy in the flashlamps so as to increase the gain, and the system will begin oscillating just as it did before. This leads to a gradual buildup of pulses which are approximately 100 ps wide exactly as before. However, above a certain threshold, the intensity reaches the point that saturable absorber begins to bleach. This has the effect of greatly increasing the gain available in all the cavity modes. Consequently, the pulse intensity begins to grow very rapidly, as one would expect from such a Q-switching process. This also increases the effective gain bandwidth of the system, so modes formerly below threshold can begin to oscillate, causing the pulse width to decrease correspondingly. The saturation of the dye leads to a rapid increase in the intensity of the pulses, a decrease in the pulse duration and a rapid depletion of the gain in the rod. Rather than the approximately 100 pulses seen in the upper half of figure 2.3, the pulse train is transformed into that seen in the lower figure, with fewer than 20 pulses per train, and pulse durations less than 40 ps.

The performance of the laser varies with the dye concentration, and it is necessary to adjust this concentration empirically. There are two interrelated variables in this adjustment, the dye concentration, and the flashlamp energy. Initially, with no dye present, the flashlamp voltage is set to produce three or four relaxation oscillations. Dye is then added until only one remains, and still more is added until there are roughly 25 pulses in the train. The voltage is then increased until the second relaxation oscillation reappears, and then dye is added until it is suppressed again. This sequence was continued until the desired combination of pulse train length and output energy was achieved. As ultimately used, the pulse trains resembled those in figure 2.3. There were approximately 15 pulses

per train (counted to the 10% points), with a total energy of approximately 5 mJ in the train. As described below, the length of the pulses varied throughout the pulse train. The dye tended to degrade with time, resulting in the gradual lengthening of the pulse train and a loss of total energy. This could generally be overcome by simply adding more dye, although it was necessary to change the dye solution every few weeks of operation.

The optical system used to convert the pulse train emitted by the cavity into a usable single pulse is shown in figure 2.4. This figure also shows the system used to characterize the output of the laser, as discussed below. After leaving the cavity, the pulse train is passed through a 1.25x expanding telescope and into a single pulse selector. This device consists of a Pockels cell placed between two crossed Glan-Thompson polarizing prisms². The Pockels cell consisted two pieces of deuterated potassium dihydrogen phosphate (KD*P) placed between two electrodes, with the beam propagating along the crystal optic axis. With no voltage on the crystals, the crossed polarizers reject at least 99.999% of the incident beam. However, with the quarter-wave voltage (3300 Volts for KD*P) across the crystals, the field-induced birefringence rotates polarization of the incident light so it passes through the crossed polarizers. The bulk of the pulse selector consists of the electronics required to generate a suitably synchronized high voltage pulse which will cause the Pockels cell to pass a single pulse. This pulse is generated by discharging two transmission lines of different lengths through a Krytron tube. The trigger for the Krytron is generated by a train of avalanche transistors which in turn is initiated by a threshold comparator driven by a fast photodiode sensing the laser pulse intensity. The pulse selector is thus triggered by the rapidly increasing pulse intensity seen early in the train. Which pulse is actually chosen can be varied by adjusting the light intensity at the photodiode or by increasing the cable length between the photodiode and the trigger circuit. Since the pulse length varies with the position in the train, it is desirable to be able to pick pulses anywhere in the train. A variable cable delay makes this possible. The pulse selector is the least reliable component of the entire system, and it often behaved

Figure 2.4. Optical layout of the pulse selector, spatial filter and amplifier used to generate single pulses, as described in the text. Also shown are the optics used to characterize the output of the laser.

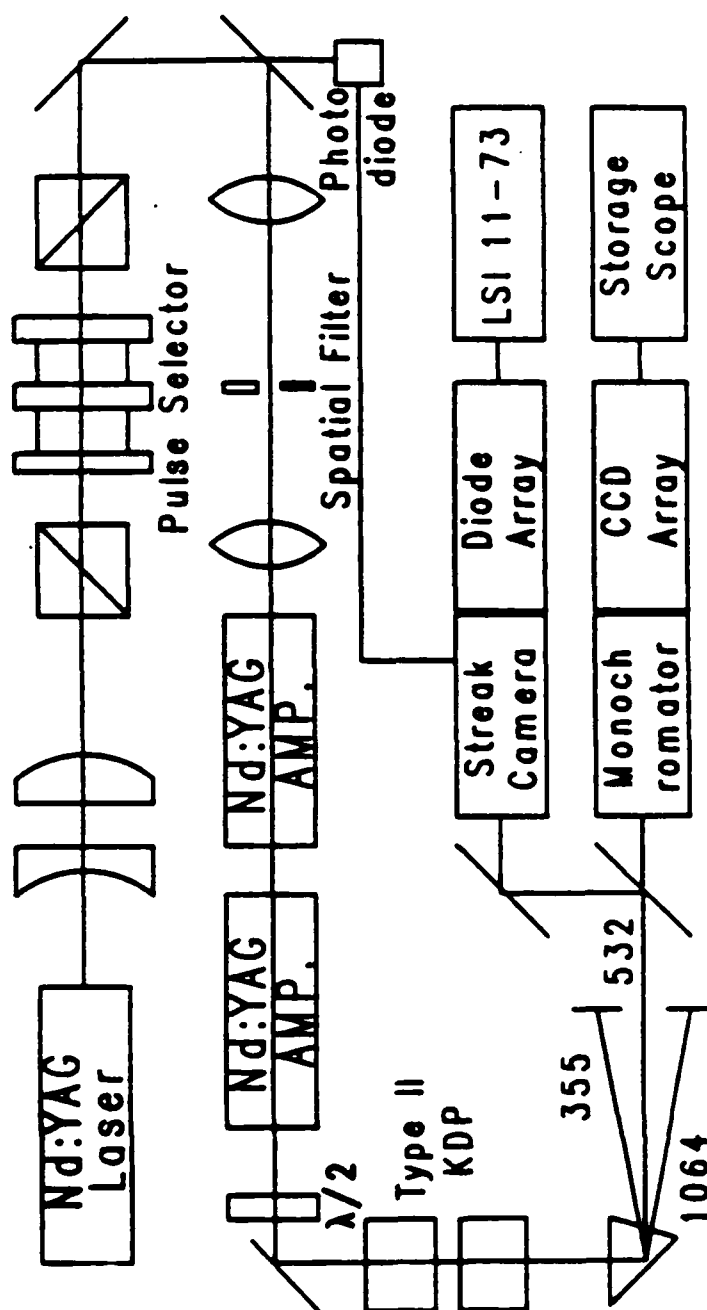


Figure 2.4

erratically, especially if pulses very early or very late in the train were being selected. This is important in connection with the results presented below which show that very short pulsed occur at the end of the train. Limitations imposed by the pulse selector made it difficult to use these pulses, since they were not selected consistently.

After the pulse selector, the single pulse is passed through another expanding telescope, spatially filtered and amplified by one or more flashlamp-pumped Nd:YAG amplifiers. With a single amplifier, single pulse energies of 5–10 mJ were achieved, and multiple amplifiers could increase this by a factor of 10 or 20. The polarization of the amplified single pulse is rotated and the beam is passed through a pair of KDP crystals (type II, 58 degrees) to generate the second and third harmonics (532 and 355 nm, respectively) of the laser frequency, with the polarizations shown. Conversion efficiencies of roughly 40% into the second harmonic and 30% into the third harmonic could be achieved. Note that with an identical arrangement, but with a different second crystal (Type I, 77 degrees), the fourth harmonic (266 nm) will be generated instead of the third; conversions of up to 10% were observed in this case. If the second crystal is removed altogether, the system can be optimized for production of the second harmonic.

2. System Characterization

In order to use the laser for time-resolved experiments, it is important that the spectral and temporal properties of the system be known. The system used for measuring these characteristics is shown in figure 2.4. This arrangement allows the simultaneous measurement of both the spectral and temporal properties of a single laser pulse. The streak camera and associated hardware are discussed below in connection with emission and absorption spectroscopy, and will not be discussed here. It should be noted that all these measurements were made on the fastest available streak speed, so that 12 channel slit function corresponds to a resolution of 4 ps. Spectral measurements are obtained with a .85 M double monochromator with 1800 l/mm gratings (Spex 1404). It is the

same monochromator described below in conjunction with Raman spectroscopy. The array detector used here is a 256 channel linear CCD array (Fairchild 111A), with $13\text{ }\mu\text{m}$ square pixels. The triggering of the streak camera, the scan of the CCD array, and the triggering of the storage oscilloscope were all carried out in such a way that all the data from a single shot could be obtained simultaneously. Note that the second harmonic is used rather than laser fundamental. This is due to the spectral limitations of both the streak camera and the CCD array. When measuring the pulses, the amplifiers were run with very low gain and only the second harmonic crystal was used, so as to minimize any distortion of the pulse. Ideally, the spectral width of the doubled pulse will be twice that of the original pulse, while the temporal width will be cut in half.

The characteristics of the laser pulse as a function of position in the pulse train is shown in figure 2.5 and figure 2.6. The first figure shows the spectral widths obtained from individual pulses as well as temporal width obtained by averaging 100 pulses. These averages are close to the behavior of the individual pulses, but are somewhat less noisy. Figure 2.6 shows the behavior of several quantities as a function of the position in the pulse train. The first plot shows intracavity energy of the pulses. This is essentially the same data as in the lower half of figure 2.3, except that the relative energies measured by the photodiode have been converted into actual energies. This was done by measuring the total energy in the pulse train using a disk calorimeter (Scientech 360001), correcting for the 30% reflectivity of the output coupler, and assuming that the photodiode output is proportional to the energy. Similar measurements could be made by simply measuring the energy of the single pulses after the pulse selector. However, these measurements were less accurate, and included any erratic behavior attributable to the pulse selector. Using the photodiode output appeared to offer better internal consistency. The second curve shows the intracavity intensity calculated from the aperture cross-section, the output energy and the pulse width obtained from the streak camera. This curve shows an interesting trend, that although the pulse energy is decreasing late in the train, the pulse

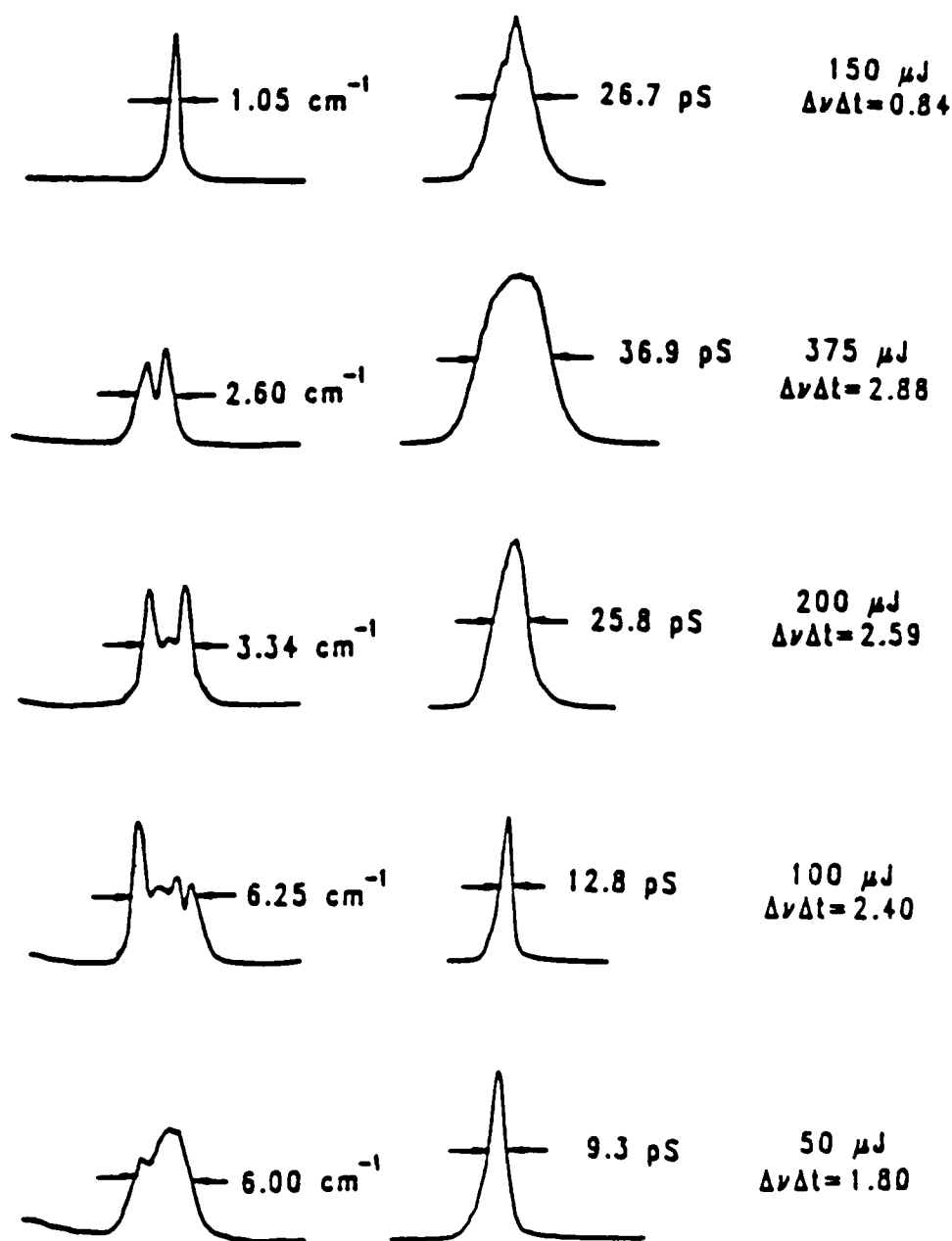


Figure 2.5. Spectral and temporal profiles of pulses at various positions in the pulse train. The spectra represent individual laser shots; the time-resolved data is the average of 100 shots.

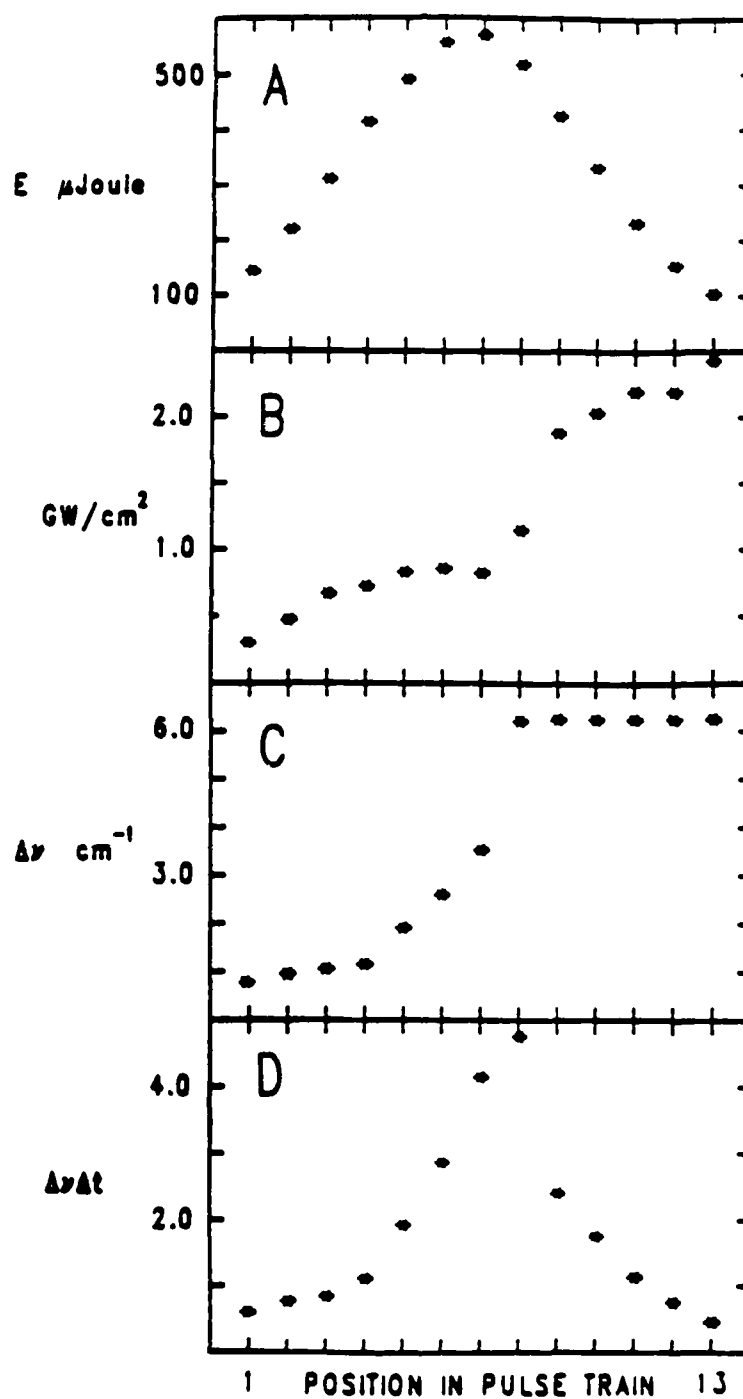


Figure 2.6. Variation of several laser pulse properties as a function of position in the pulse train. A: Pulse energy, B: Pulse intensity, C: pulse width, $\Delta\nu$ and D: Transform product (for ideal gaussian pulses, $\Delta\nu\Delta t = 0.44$).

intensity is relatively constant. This is equivalent to saying that the pulses are getting shorter the further into the train one looks. The curve below this shows the measured spectral width. This curve also shows unusual behavior at the end of the train. Here it is seen that the spectral width starts relatively small, but rapidly increases near the peak of the pulse train and then remains constant from then on. Note that the asymptotic spectral width (6 cm^{-1}) is equal to the fluorescence bandwidth of the laser medium. This suggests that the process occurring in this case is limited by the bandwidth of the laser. The final curve shows the uncertainty product $\Delta\nu\Delta t$. This curve also exhibits unusual behavior. Initially, the pulses are relatively close to the transform limit (for an ideal gaussian pulse, $\Delta\nu\Delta t$ will be equal to 0.44). As the pulse energy increases, this product increases, until near the peak the pulse is a factor of ten away from the transform limit. This increase is due to increases in both the spectral and temporal profiles of the pulse. After the pulse, however, a remarkable decrease in the transform product occurs; this is because the pulses are getting shorter without a concomitant increase in the spectral width. Indeed, at the end of the train, the pulses are even closer to the transform limit than they were at the beginning.

3. Effect of Self-Phase Modulation

In order to explain this rather unusual behavior, it is necessary to note that self-phase modulation is occurring in the laser. Self-phase modulation is a consequence of the third-order polarizability of a substance. It can be shown that the effective index refraction of a medium varies with the optical intensity, so that

$$n = n_0 + n_2|E|^2 \quad (2.1).$$

This nonlinear index is responsible for a number of phenomena including self-focusing² and self-phase modulation⁴. In order to model self-phase modulation, consider the prop-

agation a linearly polarized optical pulse in the z direction,

$$E(z, t) = A(z, t) \exp[i(k_0 z - \omega_0 t)] \quad (2.2).$$

In this case, the wave equation will take the form

$$\frac{\partial^2 E}{\partial z^2} - \frac{n^2}{c^2} \frac{\partial^2 E}{\partial t^2} = \frac{2n_2 n_0}{c^2} \frac{\partial^2}{\partial t^2} (|E|^2 E) \quad (2.3).$$

Making use of the slowly-varying-envelope approximation and ignoring group velocity dispersion (that is, neglecting all derivatives of A except the the first spatial derivative), gives

$$\frac{\partial A}{\partial z} = \frac{in_2 \omega_0}{c} |A|^2 A \quad (2.4).$$

If $A(z, t) = a(z, t)e^{i\phi(z, t)}$, where a and ϕ are real, it can be shown that a is independent of z and $\phi = n_2 \omega_0 a^2 z / c$. By definition, the instantaneous frequency is given by

$$\omega = \omega_0 - \frac{\partial \phi}{\partial t} = \omega_0 - \frac{n_2 \omega_0 z}{c} \frac{\partial a^2}{\partial t} \quad (2.5).$$

Thus, after passage through the nonlinear medium, a chirped pulse with the frequency distribution proportional to the derivative of the pulse envelope will result. The leading edge of the pulse will be red-shifted, and the trailing edge, blue-shifted.

This neglects the effects of the finite amplification bandwidth and the presence of the saturable absorber. At the beginning of the pulse train, it is reasonable to neglect these effects, since the spectral width is narrower than that of the laser. The effect of self-phase modulation alone is to simply broaden the spectrum of the pulse. For pulses with reasonably sharp edges, it should lead to pulses with a bimodal frequency distribution, just like those observed in figure 2.5. This breaks down when the bandwidth of the chirp exceeds the gain bandwidth of the laser. In this case, the unshifted center and wings of the pulse should receive the greatest amplification, while the intermediate chirped regions are expected to lose intensity. In fact, due to the large losses in the cavity, these regions

will be rapidly attenuated. Ideally, the regions at the ends of the pulse should continue to be amplified, since the chirp is small there. This should lead to a trimodal pulse. This is not observed. It appears that the gap between the center pulse and the edges is such that the saturable absorber can recover enough to suppress the satellite pulses. The combination of self-phase modulation, frequency-dependent gain and time-dependent loss will therefore tend to produce a short, spectrally broadened pulse. Unfortunately, there is no simple way to incorporate a frequency dependent gain term or a saturable loss term into the equations describing self-phase modulation. Because of this, no simple expressions for the pulse shapes can be obtained. Some numerical work on this subject has been presented elsewhere^{1,5}. Since this phenomenon is somewhat peripheral to the further development of the system, it will not be discussed further. The main feature of these results is that short pulses are obtainable if necessary.

4. Effect of an Intra-Cavity Etalon

A second method for modifying the output of the laser is to introduce an étalon into the cavity. Other investigators have demonstrated that by using an étalon to increase or decrease the effective bandwidth of the system, it is possible to shorten or lengthen the pulses as needed⁶. Figure 2.7 shows the effect of placing an étalon with a free spectral range of 4.13 cm^{-1} and a finesse of 4.94 into the cavity. The pulses shown are both from the leading edge of the pulse train, and have energies of roughly $125 \mu\text{J}$. The upper pulse shows what happens when a transmission minimum of the étalon coincides with the gain peak. The transmission minimum will have the effect of "flattening" the apparent gain profile. This will lead to spectrally broadened pulses which are shortened in time. The pulse seen at the transmission maximum shows the opposite effect, as the spectral bandwidth is narrowed, and the duration of the pulse increased. The fact that these pulses are very near the transform limit is a result of the fact that they were picked very early in the train, before self-phase modulation becomes significant. Pulses near the peak of the

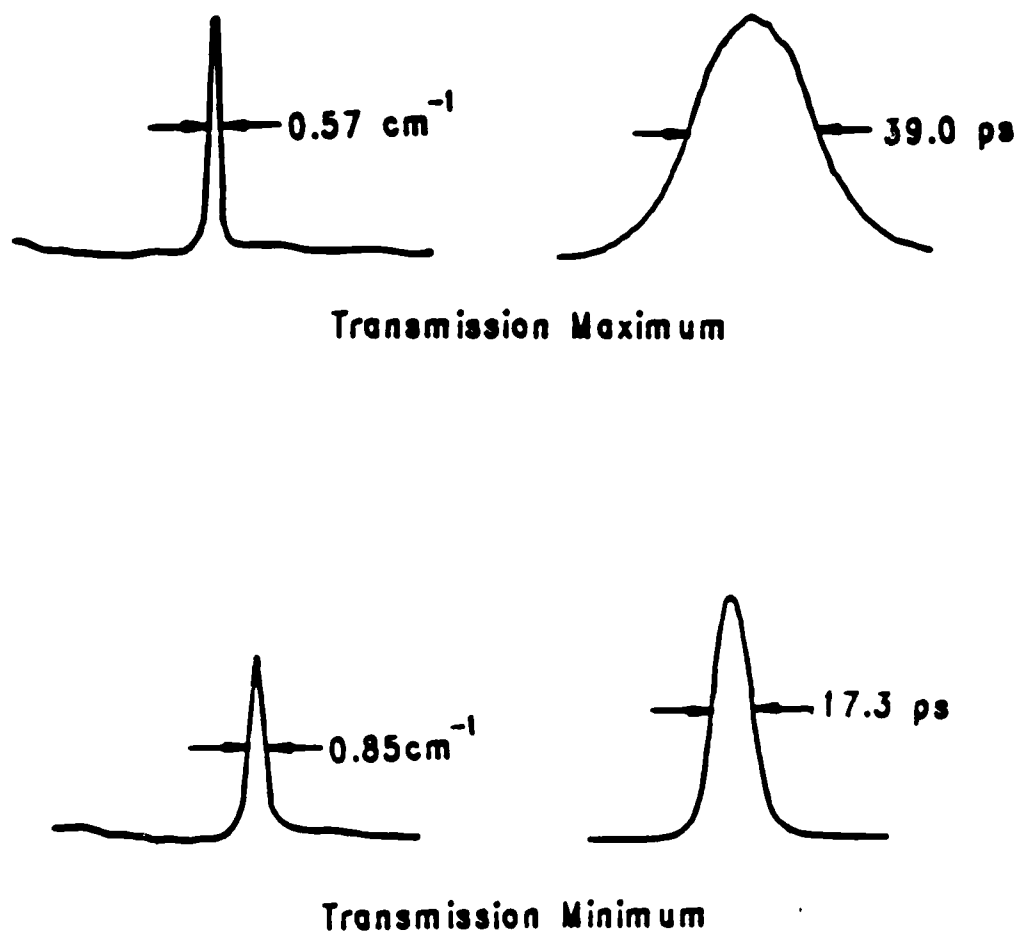


Figure 2.7. Effect of an intra-cavity étalon on the laser pulse. Upper curve, étalon transmission maximum aligned with laser frequency. Lower curve, étalon minimum aligned with laser peak. The étalon minimum will "flatten" the gain curve, causing the apparent spectral width to increase, causing the pulses to shorten. The maximum has the opposite effect, and leads to longer pulses.

train will be similar to those seen without the étalon, and will be far from the transform limit. Placing the étalon in the cavity clearly has some desirable effects. However, since the pulses at the peak of the train were relatively unchanged, there was no reason for using such an étalon on a regular basis. The pulse shortening observed with the étalon was less significant than that caused by self-phase modulation at the end of the train, so the latter pulses were used when short pulses were required.

C. Optical Parametric Source

1. Introduction

One of the most obvious limitations of the laser system described so far is that only frequencies available are the four laser harmonics. Although these wavelengths do span much of the visible and ultraviolet spectrum, and there are many experiments which can be performed with them, the lack of tunability limits both the variety of systems which can be studied, and the range of methods which can be used. The lack of a tunable laser source significantly restricts the range of detection methods which can be considered. Without a tunable source, it is necessary to rely on the fortuitous overlap of molecular spectra with the laser wavelengths, to make use of such basic techniques as absorption or fluorescence spectroscopy. This can be a significant limitation. In addition, it is necessary to have a tunable laser source to make use of other more sophisticated forms of laser spectroscopy. Techniques which fall into this category include multi-photon ionization, resonance Raman, and the non-linear Raman spectroscopies, such as coherent anti-Stokes Raman spectroscopy (CARS). Since the high peak powers which are present in a picosecond experiment tend to favor multi-photon effects, it is only reasonable to try to exploit them whenever possible. This necessitates the use of a tunable source.

There are several ways of approaching the problem of generating tunable light. Stimulated Raman shifting is widely used to generate light at a fixed frequency shift from

the laser line. Under favorable conditions, conversion efficiencies as great as 80% have been reported⁷. The basic tradeoff in stimulated Raman shifting is between having enough scattering cross-section to efficiently generate the Stokes frequency without inducing other undesired nonlinear effects. These include higher order Raman shifting (Stokes or anti-Stokes), which spreads the pump laser energy into multiple output frequencies, and self-focusing or self phase-modulation which lead to degradation of the beam quality. To avoid these effects, while retaining enough Raman cross section to be useful one is led to the use of symmetric gases at pressures of tens of atmospheres. They provide a single Raman active vibrational mode with a relatively narrow linewidth. They can be made sufficiently dense to give appreciable Raman scattering, and are dispersive enough that collinear phase matching for anti-Stokes generation is minimized. All of this results in the shifted energy being concentrated in the first Stokes line. The densities used are sufficiently low, however, to minimize other nonlinear effects. Efficient Raman shifting is generally limited to nitrogen (2331 cm^{-1}), deuterium (2942 cm^{-1}), or hydrogen (4161 cm^{-1}), although methane and oxygen can also be used. Since the laser harmonics are separated by 9398 cm^{-1} , Raman shifting can be useful for generating frequencies between the laser harmonics, especially when high power is more important than the exact frequency. This is often the case for emission spectroscopy, for resonance Raman spectroscopy⁸, and for sum frequency generation, when, for example, tunable visible light is being summed with a fixed frequency to produce a tunable ultraviolet source⁹.

Raman shifting is only a partial solution, since it does not provide a means of generating continuously tunable wavelengths. To achieve this, it is necessary to produce tunable radiation over some small spectral region, typically in the visible or near infrared. Once this is available, it is possible to use a variety of nonlinear optical techniques to shift the light into other frequency regimes. By combining Raman shifting with sum and difference generation in nonlinear crystals, a relatively narrow tuning range can be extended to cover the ultraviolet through near-infrared¹⁰. By using more exotic

techniques, such as sum generation in metal vapors or rare gases, this can be extended into the mid-infrared and vacuum ultraviolet¹¹. In any case, it is an important first step to develop a suitable tunable visible source.

The conventional method for generating tunable visible light is the dye laser. Picosecond (and femtosecond) dye lasers are well established¹², but they are generally not compatible with the type of laser used here. In general, they are CW devices which require a CW pump laser and have an output which consists of a continuous pulse train. Although it is possible to conceive of ways of using the pulse train of this laser as a quasi-continuous source to synchronously pump a dye laser, from which a single pulse could be picked for amplification, it is clear that such a system would not be ideal. It is not obvious that the pulse trains are long enough for effective synchronous pumping, and it is unlikely that any system which requires two pulse selectors will be reliable enough to use. It would be desirable to have a system which takes the single amplified pulse out of the laser and converts it to a tunable wavelength.

The lifetimes of most laser dyes are on the order of a few nanoseconds. With a single picosecond pump pulse this sets an upper bound of a few centimeters on the dye laser cavity length. To obtain a single pulse which is comparable in length to the pump pulse it is necessary to use a cavity configuration in which both oscillation and gain depletion occur on this timescale. This requires that the cavity round trip time be on the order of picoseconds, corresponding to a cavity length of less than a millimeter. This leads to the idea of a short cavity dye laser, which is essentially an étalon filled with a dye solution¹³. By adjusting the free spectral range of the étalon to be comparable to the gain bandwidth of the laser dye, it is possible to achieve single wavelength operation. Tuning can be achieved by adjusting the mirror spacing just as in an ordinary étalon. A significant amount of work has been carried out in this laboratory to characterize the output of such a device. There are two major difficulties encountered when using a short cavity dye laser. It is difficult to obtain reliable single mode operation; several

longitudinal modes usually have sufficient gain to for oscillation to occur, leading to multiple wavelength outputs. The short cavity also leads to a highly divergent output beam. This is unavoidable in this configuration, although it is possible to minimize this by amplifying the output through several additional dye stages. This adds significantly to the complexity of the system, but it eventually leads to a beam whose spatial properties are determined by the gain profile of the amplifiers, which in turn reflects the shape of the pump beam¹⁴. Although the short cavity dye laser can be used as a tunable source, the overall complexity of the system makes it unappealing to do so on a continuing basis.

As it turns out, one of the most efficient ways of solving the problem of generating tunable light from a pump laser of the type used here is to dispense with the dye laser entirely, and to use optical parametric generation instead. Parametric generation is essentially the inverse of sum generation, and arises from the same second-order interaction. Under suitable conditions, the second order polarizability will lead to the annihilation of a photon of a pump beam at frequency ω_3 , with the simultaneous creation of a photon pair at ω_1 (idler) and ω_2 (signal), such that energy and wavevector are conserved. This process is stimulated by photons at ω_1 or ω_2 , and can be used to amplify weak input signals. In the absence of any inputs, the process will be stimulated by quantum noise, and spontaneous parametric fluorescence will result. To convert a "few" photons of parametric fluorescence into useful output energies, a gain on the order of 10^{13} (e^{30}) is required. The gain depends on both the pump intensity and the interaction length. The pump intensity is limited by the crystal damage threshold, which in turn depends largely on the energy per pulse, or equivalently, on the pulse length. In the nanosecond regime, peak intensities are limited to tens of MW cm^{-2} , and it is necessary to use an external cavity resonant at ω_1 or ω_2 to obtain sufficient gain¹⁵. Because of this, optical parametric generation tends to be difficult in most cases, and is rarely used except at infrared frequencies where dye lasers cannot be used¹⁶. With a picosecond laser, this is no longer true. Pump intensities can be on the order of GW cm^{-2} , and the required gain

can be obtained in a single pass through a few centimeters of crystal. This eliminates the need for the external resonator, and permits the construction of a simple single pass OPS. In this form, the OPS is as simple to use as a doubling crystal, and constitutes a viable solid-state replacement for a dye laser.

Unlike dye lasers, there are no resonances involved in parametric generation, and tuning of an OPS is achieved by varying the phase-matching condition, that is, by exploiting the fact that wavevector must be conserved². The tuning range of an OPS is limited only by the transparency of the crystal, the wavelength of the pump beam, and the phase-matching conditions in the crystal. It is clear that in an ordinary isotropic material, with normal dispersion, it will never be possible to simultaneously conserve energy and wavevector. This can be overcome by using a birefringent crystal, and exploiting the differences in the phase velocities for the ordinary and extraordinary rays. Specifically, for the negative uniaxial crystals used here, there are two possible phase matches. The pump beam will always be an extraordinary ray, the signal will always be an ordinary ray, and the idler can either be an ordinary or extraordinary ray. These are known, respectively, as type I and type II phase matches. Since the magnitude of the wavevector of an extraordinary ray depends on the orientation of the propagation direction with respect to the crystal optic axis, it is possible to vary the wavelengths of the outputs by rotating the crystal. It is also possible to vary the phase-matching condition by adjusting other variables such as the temperature of the crystal. Using a variety of different pump wavelengths and nonlinear crystals, wavelengths from 300 nm to 10 μm ¹⁵ have been produced.

The nonlinear crystal used for the OPS described here was potassium dihydrogen phosphate (KDP). This is an excellent material for for this purpose. Although the nonlinear coefficient is smaller than that of other materials, such as lithium niobate or lithium iodate², the high damage threshold ($\sim 50 \text{ GW cm}^{-2}$ for picosecond pulses¹⁷) compensates for this, since the pump beam can be more tightly focused. The phase-matching

conditions are not strongly temperature dependent, so precise temperature control is not needed and the crystal is not so hygroscopic as to require protection from the atmosphere. It is relatively inexpensive, and large crystals of excellent optical quality are readily available. KDP is transparent from 230 to 1650 nm, and is sufficiently birefringent that phase matching is possible over most of this range.

There have been several reports of picosecond optical parametric sources using KDP. In most cases, type II phase matching was used, with the second harmonic of a mode-locked Nd:YAG laser (532 nm) used as a pump source^{9,17,18,19,20,21}. Using this combination, it is possible to tune from 780 to 1680 nm. The output of these devices has typically been at least a factor of six from the transform limit. Third harmonic (355 nm) pulses from mode-locked Nd:YAG lasers have also been used to pump type II optical parametric sources^{9,22} but little work has been done to characterize the performance of such devices. Spectral widths of $\sim 10 \text{ cm}^{-1}$, conversion efficiencies of $\sim 10\%$, and spectral coverage from 448 to 640 nm and from 792 to 1687 nm have been reported. Type I phase matching has not been widely used with KDP, although numerous reports exist of type I phase matching in the closely related ammonium dihydrogen phosphate (ADP) crystal. In this case, pumping with the third²³ and fourth²⁴ harmonics have been reported. In the latter case, a single OPS can be used to cover the entire visible spectrum. An additional feature of a picosecond OPS is the fact that under some circumstances, the pulses generated this way can be dramatically shortened by nonlinear gain effects²⁵, leading to pulses much shorter than the pump pulse.

Three different combinations of pump wavelength and phase-matching type were used here. Type II KDP was pumped with both the second and third harmonics, and Type I KDP was pumped with the third harmonic. The type II crystal worked quite well when pumped with the second harmonic, giving results in good agreement with the literature. However, the spectral regions of greatest interest were the visible and near UV, and work was concentrated on the third-harmonic pumped systems which produce

visible light directly. Type II phase matching was emphasized, since the angle tuning curve is much less sensitive in this case, resulting in a narrower spectral output, and a much smaller dependence on the exact focussing of the beam. Type I phase matching is preferable only in the 600–800 nm spectral region where the Type II OPS cannot be phase matched.

The results obtained from this system are actually somewhat better than those reported in the literature. Under ideal circumstances, the OPS can produce tunable pulses which are very near the transform limit, although as might be expected, there was a tradeoff between pulse quality and conversion efficiency. At low conversion efficiency ($\sim 1\%$), pulses of 8 ps duration with a spectral width of 2 cm^{-1} were observed, indicating that a $\Delta\nu\Delta t$ product within a factor of two of the transform limit could be achieved. Conversion efficiencies approaching 50% could also be achieved, albeit with much broader spectral and temporal profiles. This performance is significantly better than that previously reported. Evidently, the use of the stable active-passive mode-locked pump laser with its diffraction-limited output enhanced the performance of the OPS. It also increased the conversion efficiency by making it possible to use somewhat higher pump intensities without risking crystal damage.

2. Optical Hardware

The third-harmonic pumped type II OPS appeared to be the best suited to most of the problems encountered here, so it was characterized in some detail. The system used to characterize the OPS is shown in figure 2.8. The laser system is exactly like that shown in figure 2.4, and the horizontally polarized third harmonic pulse used to pump the OPS is obtained from the output of the Pellin-Broca prism. This beam was sent through the beamsplitter [B] which passed $\sim 1\%$ of the beam to a calibrated large-area photodiode (Silicon Detector Corp., SD380-23-21-251) for energy measurement. The photodiode was calibrated with a calibrated disk calorimeter (Sciencetech 360001). A small fraction of

Figure 2.8. Optical system used for characterization of OPS pulses.

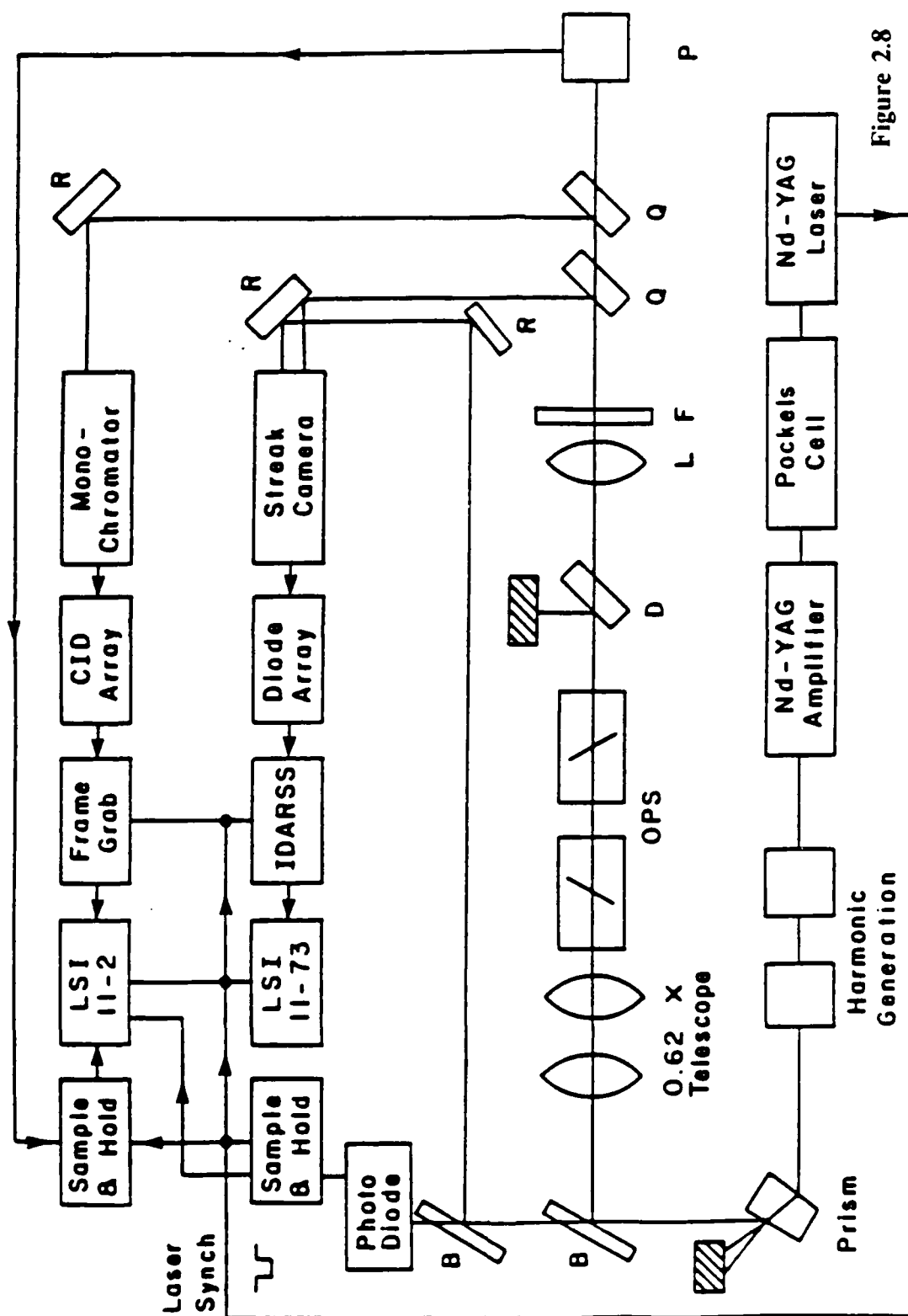


Figure 2.8

this beam is also sent to the streak camera. The remaining 99% of the beam was passed through a .62x telescope to the OPS. At this point, the beam typically had an energy of $1.35 \pm .14$ mJ, a spectral width of 2 cm^{-1} , a pulse duration of 35 ps, and a diameter of 1.36 mm (FWHM). This corresponds to a peak input intensity of $1.7 \times 10^9 \text{ W cm}^{-2}$.

The Type II OPS consisted of two KDP crystals (Cleveland Crystals), 37 mm in length, cut for type II phase matching at an angle of 59 degrees with respect to the optic axis. The crystals were mounted 15 cm apart on stepper-motor-controlled rotation stages. Figure 2.9 shows schematic diagrams of the crystal orientation, beam polarizations, and phase-matching angle used. The same crystals could be used with either second or third harmonic pumping, although the latter was ordinarily used. A type I OPS consisting of two 40 mm crystals cut at 50 degrees was also made. It was ordinarily used with third harmonic pumping. In what follows, the OPS used was the type II, third harmonic pumped version.

The OPS was aligned by rotating the first crystal so that the pump beam was at normal incidence. The second crystal was then rotated until the residual pump beam and the two parametric outputs were collinear. This also corresponds to the configuration which maximizes the intensity of the parametric outputs. The two crystals could then be counter-rotated throughout the entire tuning range with no significant deflection in the direction of either the output or the pump beam. Tilts of a few degrees about either of the other two axes of rotation had no significant effect on the OPS outputs.

The residual third harmonic output was separated from the OPS beams with a dichroic reflector [D]. The OPS beams were then collimated using a 40 cm focal length lens placed such that its focal point was at the front (input) face of the first crystal. Colored glass filters [F] (Schott BG18, KG3, GG395 or RG715) were used to select the visible or infrared beam for characterization. Calibrated glass neutral density filters (Schott) were used to attenuate the OPS beams as necessary. Two uncoated quartz beamsplitters were used to send a portion of the tunable outputs to the monochromator and the streak

Figure 2.9. Crystal orientation and polarizations for the Type II OPS.

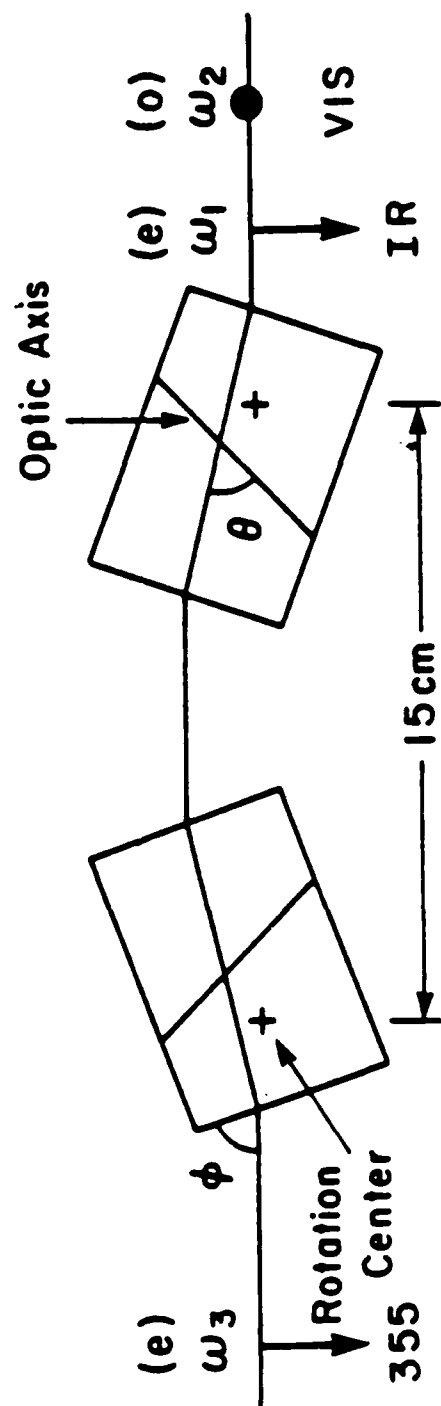


Figure 2.9

camera. The remaining output beam was sent to a pyroelectric detector [P] (Molelectron J3-05DW) for energy measurements. The energy values quoted include corrections for all the optics between the OPS and the pyroelectric detector.

The detection system is similar to that used to characterize the laser. The streak camera system is described below; measurements made here were made with a resolution of 4 ps. The spectral measurements were made with the same .85 m double monochromator used to characterize the laser output, with a different detector. Spectra were recorded using a two-dimensional CID array (General Electric, TN2505-A) placed at the image plane of the spectrometer, digitized with a frame grabber (Poynting, 505-RM) and transferred to a microcomputer (DEC LSI 11-2) for subsequent display and analysis. Throughout the visible tuning range, spectra could be measured over a range of at least 100 cm^{-1} with a resolution of 1.3 cm^{-1} .

3. Pulse Characterization

The measured tuning curves for both the visible and infrared OPS outputs are shown in figure 2.10. A crystal rotation of less than 40 degrees allowed the visible and infrared outputs to be continuously tuned from 450 to 650 and from 780 to 1675 nm, respectively. The tuning curve was generated by measuring the visible output wavelength as a function of the rotation angle of the two crystals with respect to the propagation direction of the pump beam (ϕ in figure 2.9). The infrared tuning curve was calculated from the measured visible and pump wavelengths. The presence of the infrared beam was verified by direct observation with the pyroelectric detector. The tuning curves measured here agree well with both previous experimental results ²² and with the curve calculated from the known dispersion constants for KDP ²⁶. Figure 2.11 shows the OPS output as a function of the pump beam energy. The sharp increase in output energy with increasing pump energy is a result of the exponential pump intensity dependence of the parametric amplification process, as described below. Figure 2.12 shows the energies of the visible and infrared

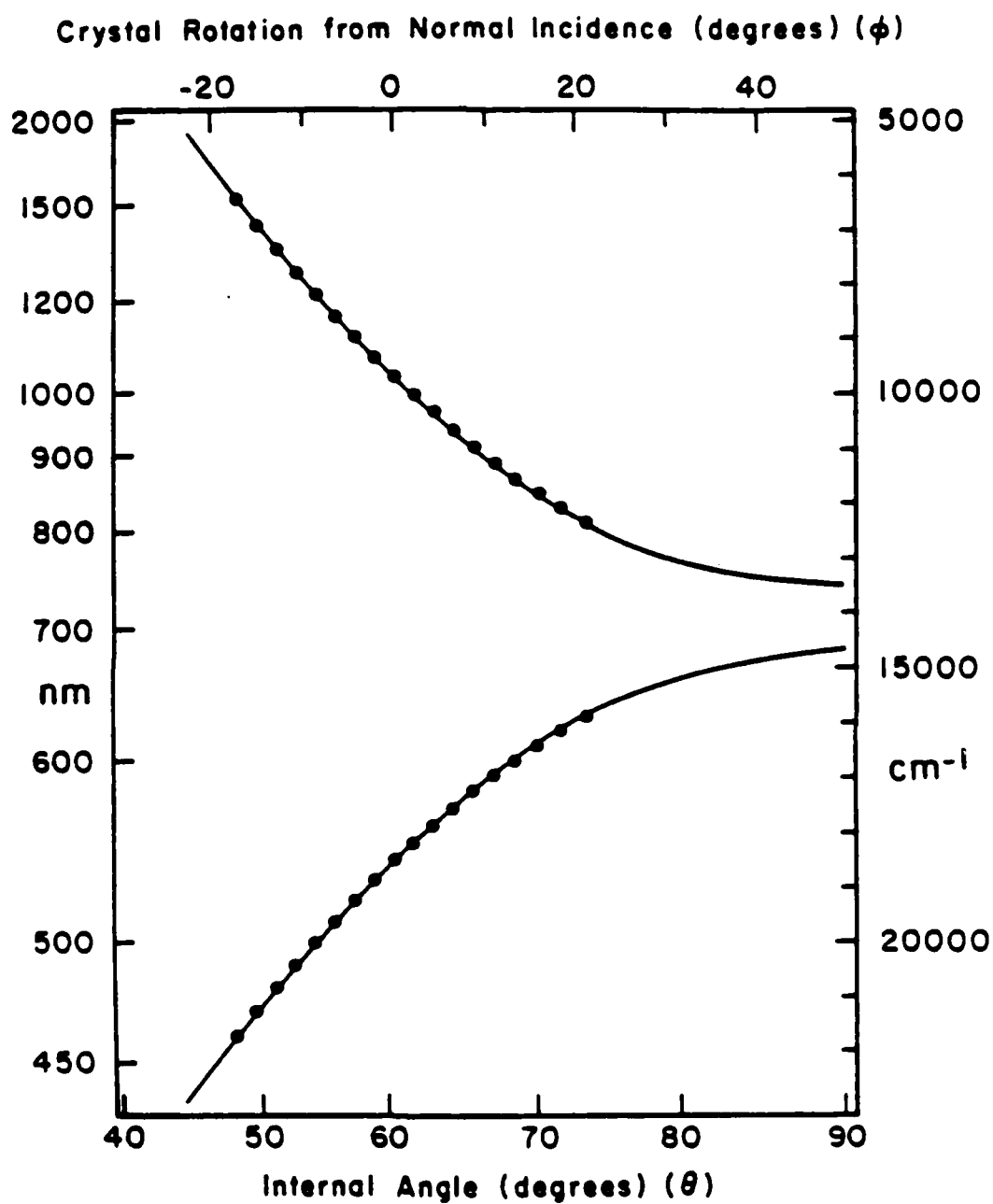


Figure 2.10. Angle tuning curve for the OPS. Solid curve calculated from reference 26.

OPS outputs as a function of the output wavelength. The energies shown in figure 2.12 were measured for selected laser shots such that the 355 nm input energy was in the range of 1.35 ± 0.04 mJ. Similarly shaped curves were obtained at other pump energies. It can be seen that an energy conversion efficiency of more than 10% into the visible can be obtained over the spectral range 470–570 nm, with a maximum of 26% at 532 nm. If the energy of the infrared output is included and if allowance is made for reflection losses at the crystal surfaces, this corresponds to an overall conversion efficiency of 44%.

Simultaneous spectral and temporal measurements of single visible OPS pulses were made under a variety of conditions. Note that the pulse widths are given as both the FWHM and RMS values. Although the FWHM is what is usually cited, the RMS values are less ambiguous for pulses like figure 6a. In addition, the uncertainty relationship $4\pi c \Delta\nu \Delta t \geq 1$ is rigorously true for all pulse shapes if the RMS values are used. All $\Delta\nu \Delta t$ values quoted here are based on the RMS values. For a gaussian pulse, the FWHM value is 2.35 times as large as the RMS value.

At high conversion efficiencies ($\sim 10\%$), the spectral and temporal profiles were typically like those in figure 6. The temporal width is equal to that of the pump pulse (30–35 ps, FWHM), while the spectral width is $10\text{--}15\text{ cm}^{-1}$, FWHM. While the overall spectral profile and center frequency of the output pulses remain relatively constant, the complex sub-structure varies randomly from shot to shot. Under the operating conditions depicted in figure 2.13, the output pulses typically have a $\Delta\nu \Delta t$ product that is 15–30 times the transform limit. As shown in figure 2.14, both the temporal and spectral characteristics of the visible pulse improve significantly at low conversion efficiencies. figure 2.14 shows the temporal and spectral profile of a single 540 nm pulse obtained at $\sim 1\%$ conversion efficiency. This pulse has a $\Delta\nu \Delta t$ product within a factor of four of the transform limit. Such pulses are quit common, especially at the ends of the tuning range where the conversion efficiency is relatively low. Unfortunately, they do not occur consistently. Under pumping conditions nominally identical to those in figure

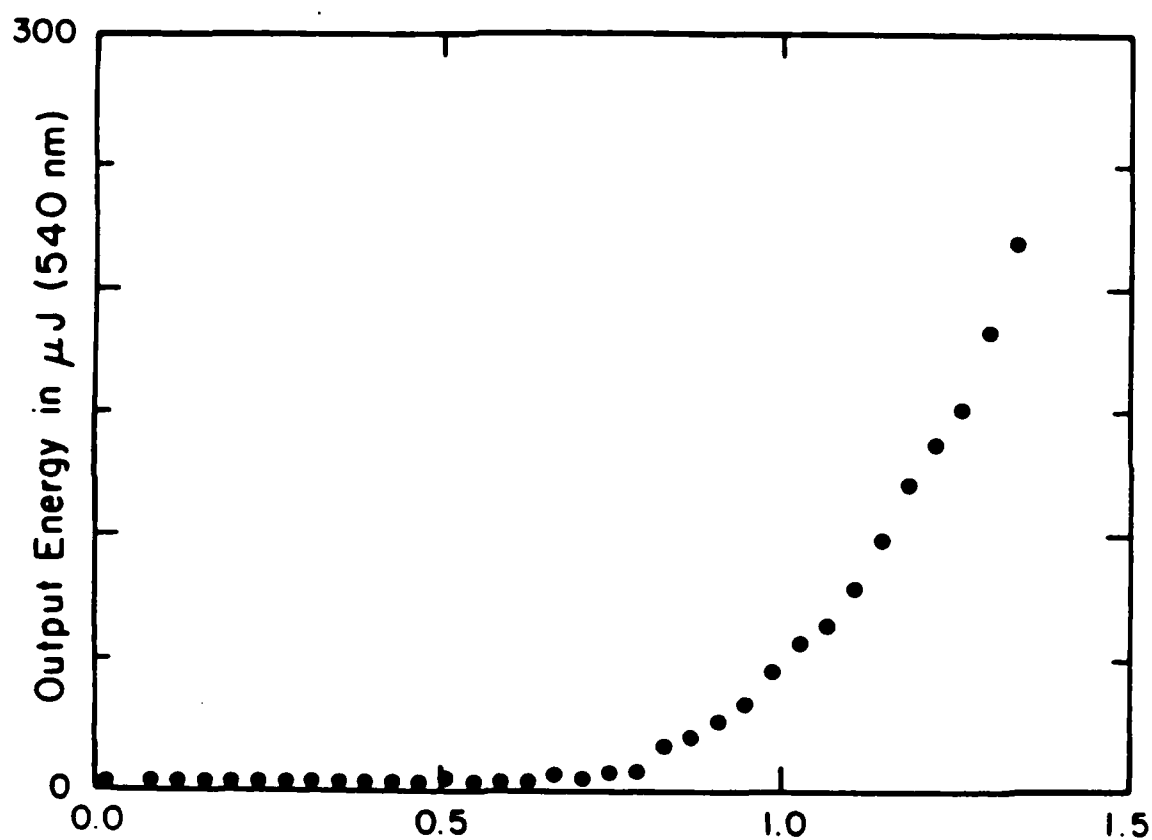


Figure 2.11. Visible OPS energy output at 540 nm versus the pump energy. This figure was obtained by collecting several hundred datapoints while the laser energy was varied by detuning the doubling crystal. Every point is the average of 5–50 points, with a vertical standard deviation of ~20%.

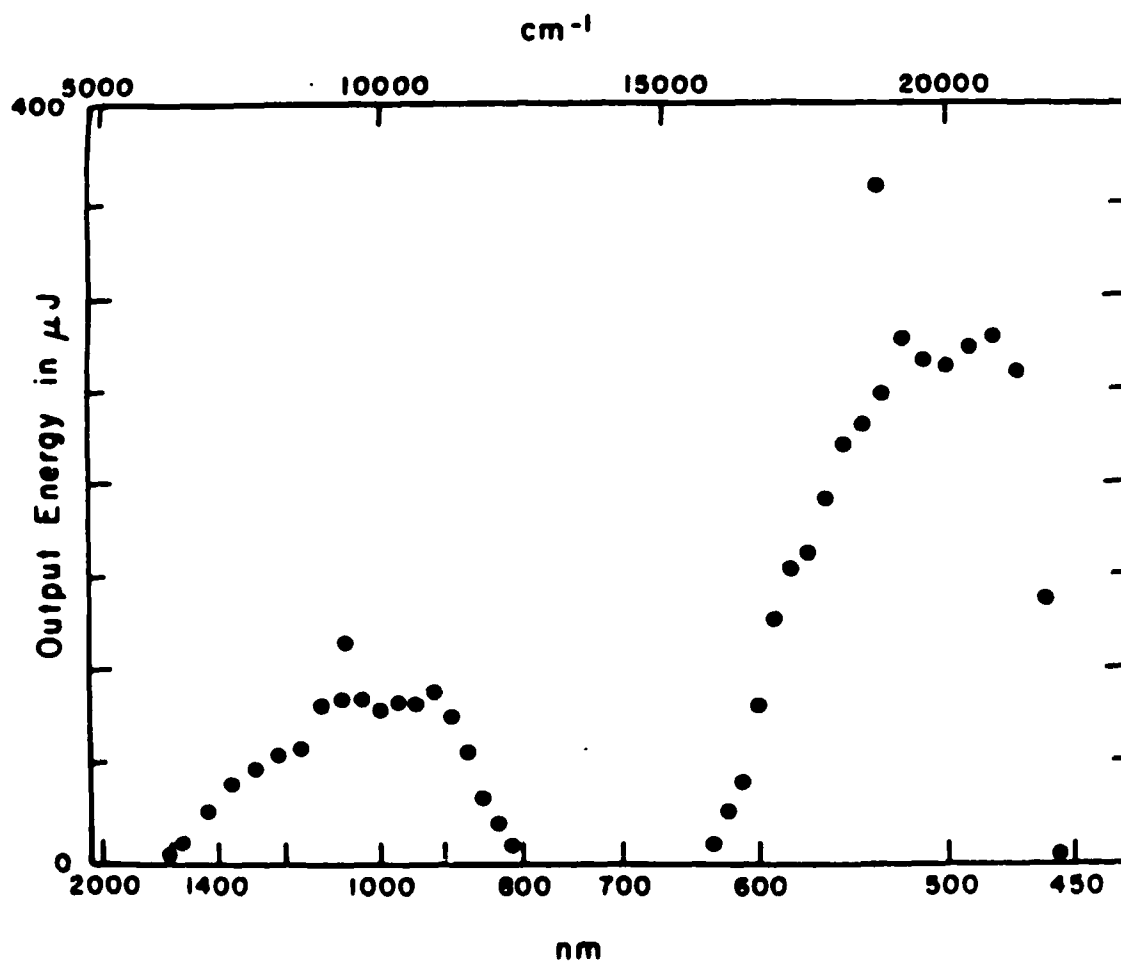


Figure 2.12. Output energy of the OPS as a function of wavelength with a pump energy of $1.35 \pm .04$ mJ. The vertical standard deviation is $\sim 20\%$ at all points.

2.14, significant fluctuations in both the spectral and temporal widths were observed with the $\Delta\nu\Delta t$ product ranging from 2-15 times the transform limit.

Figure 2.15 and figure 2.16 show low and high conversion spectral and temporal profiles obtained with the OPS tuned to produce a visible output at 532 nm, coincident with the wavelength of the second harmonic of the pump laser. Under these conditions, the temporal profile of the visible OPS output remains similar to that at nearby frequencies but the spectral width is reduced to $\sim 3 \text{ cm}^{-1}$, even at high conversion efficiencies. In the case of low conversion efficiency, the pulse is within a factor of two of the transform limit. This result appears to indicate that scattered laser light is a more intense input than is spontaneous parametric fluorescence, so that the output results from the amplification of spectrally narrow scattered laser light rather than broadband parametric fluorescence. This was confirmed by placing glass filters in the pump beam ahead of the OPS to absorb the scattered light at 1064 nm (Schott KG-3) and/or 532 nm (Schott BG-1). As expected, the spectral narrowing persisted if only one of the two filters was used, but it disappeared entirely when both filters were used. It appears that seeding the OPS with spectrally narrow scattered light can be used to both increase the conversion efficiency of the OPS and to narrow the spectral output, although this was not investigated at other wavelengths. This is consistent with what has been observed in other cases where weak input lasers have been used to injection-lock parametric sources²⁷. It is noteworthy, however that the weak, incoherent scattered light is enough to cause injection locking.

Using the second harmonic to pump the type II OPS is quite feasible, since the phase-matching angles are quite similar to those required for third harmonic pumping. Setting up for this mode of operation was essentially identical to using the third harmonic, except that neither output frequency is visible, so an infrared viewer is needed for aligning the crystals. The overall behavior of this type of OPS is quite similar to that described above and to that described in the literature¹⁸. If only the infrared output is needed, second harmonic pumping is usually preferable, since somewhat higher powers can be

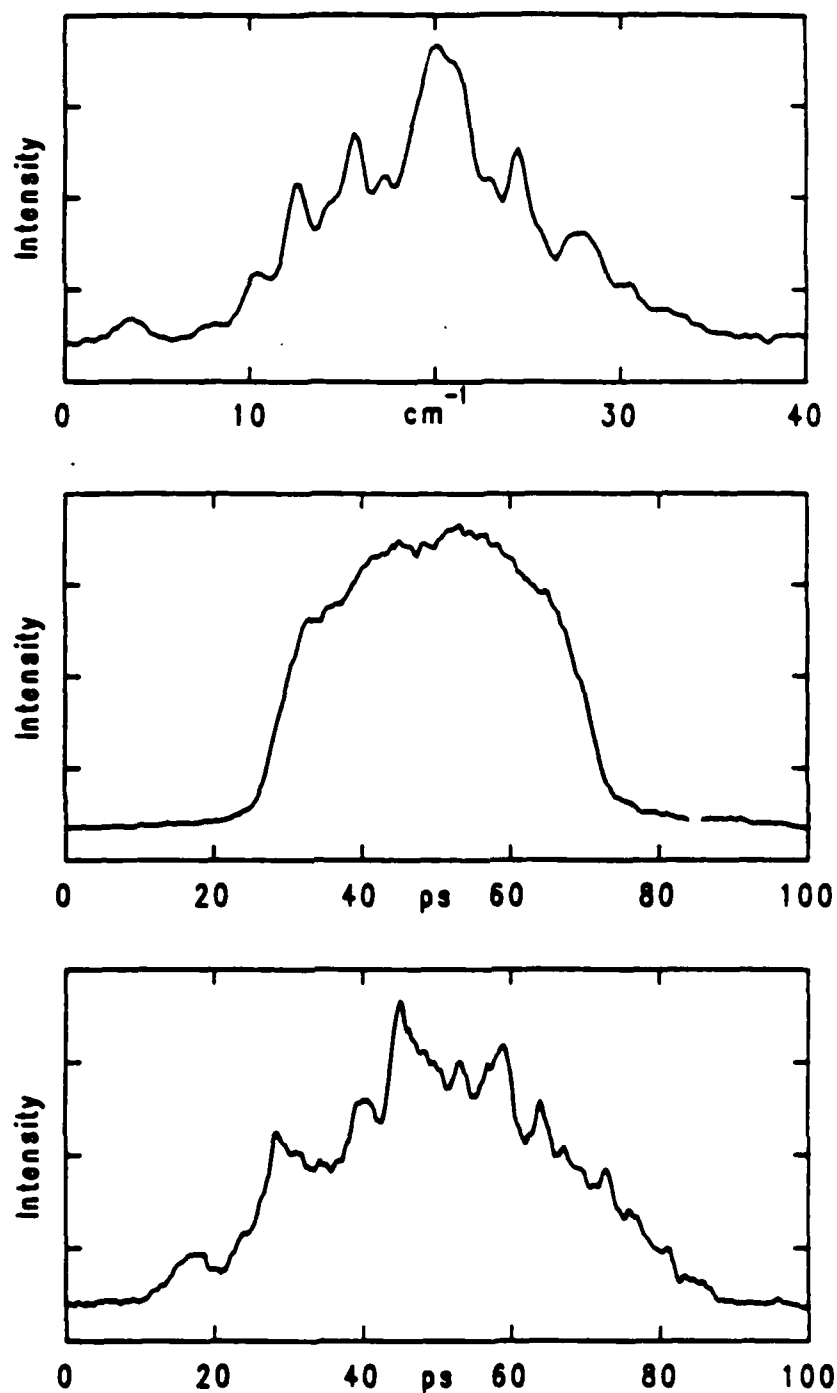


Figure 2.13. Upper curve: Spectral profile, 540 nm, $\Delta\nu=12.8 \text{ cm}^{-1}$ FWHM, 5.35 cm^{-1} RMS. Middle curve: Temporal profile, 540 nm $\Delta t=39.0 \text{ ps}$ FWHM, 14.5 ps RMS. Lower curve: Temporal profile, 355 nm $\Delta t=39.6 \text{ ps}$ FWHM, 16.4 ps RMS. For the tunable output, $4\pi c\Delta\nu\Delta t=29.3$, conversion efficiency $\sim 15\%$.

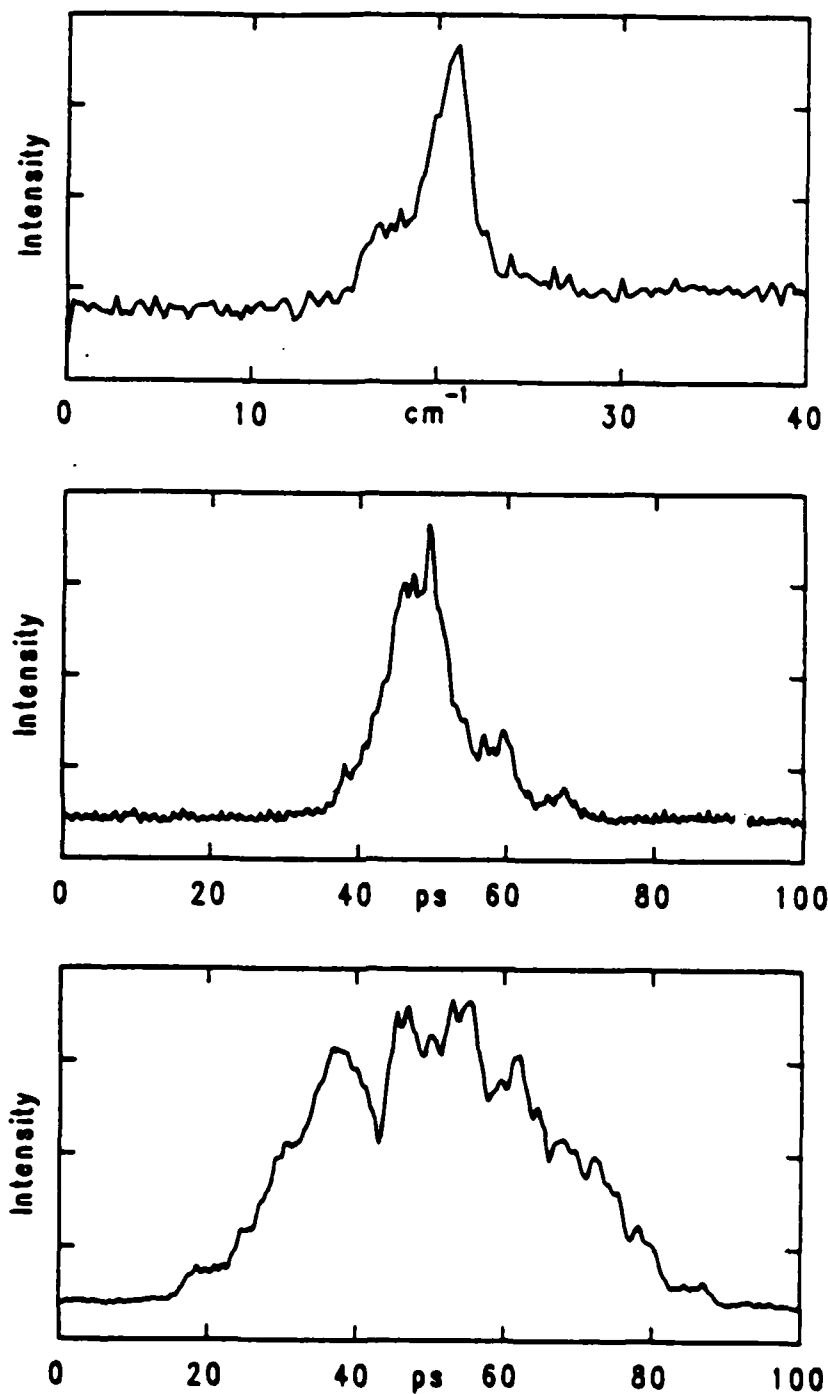


Figure 2.14. Upper curve: Spectral profile, 540 nm, $\Delta\nu=2.6 \text{ cm}^{-1}$ FWHM, 1.3 cm^{-1} RMS. Middle curve: Temporal profile, 540 nm $\Delta t=8.4 \text{ ps}$ FWHM, 7.6 ps RMS. Lower curve: Temporal profile, 355 nm $\Delta t=39.6 \text{ ps}$ FWHM, 17.2 ps RMS. For the tunable output, $4\pi c \Delta\nu \Delta t=3.8$, conversion efficiency $\sim 1\%$.

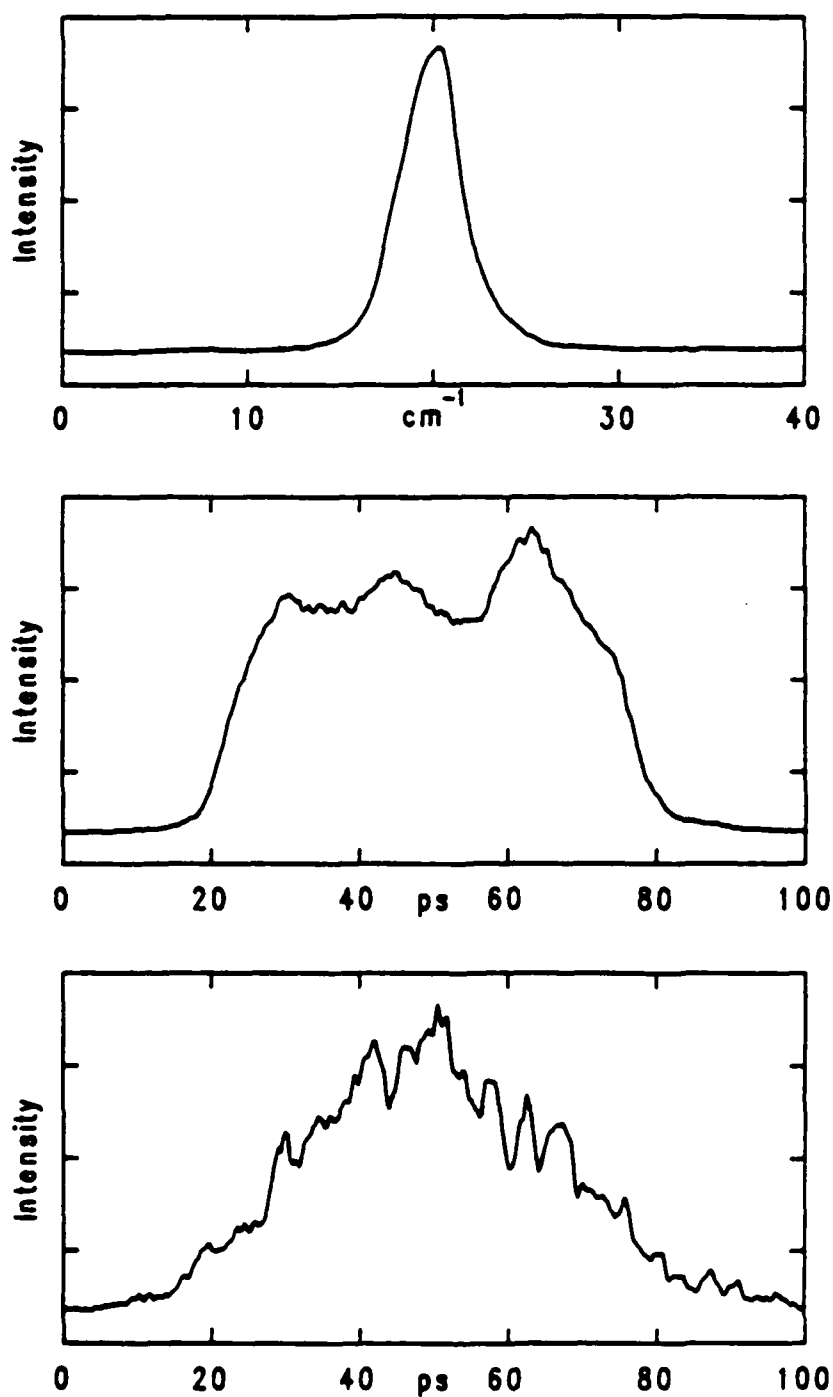


Figure 2.15. Upper curve: Spectral profile, 532 nm, $\Delta\nu=3.8 \text{ cm}^{-1}$ FWHM, 2.3 cm^{-1} RMS. Middle curve: Temporal profile, 532 nm $\Delta t=51.2 \text{ ps}$ FWHM, 16.9 ps RMS. Lower curve: Temporal profile, 355 nm $\Delta t=39.9 \text{ ps}$ FWHM, 16.9 ps RMS. For the tunable output, $4\pi c \Delta\nu \Delta t=14.4$, conversion efficiency $\sim 20\%$.

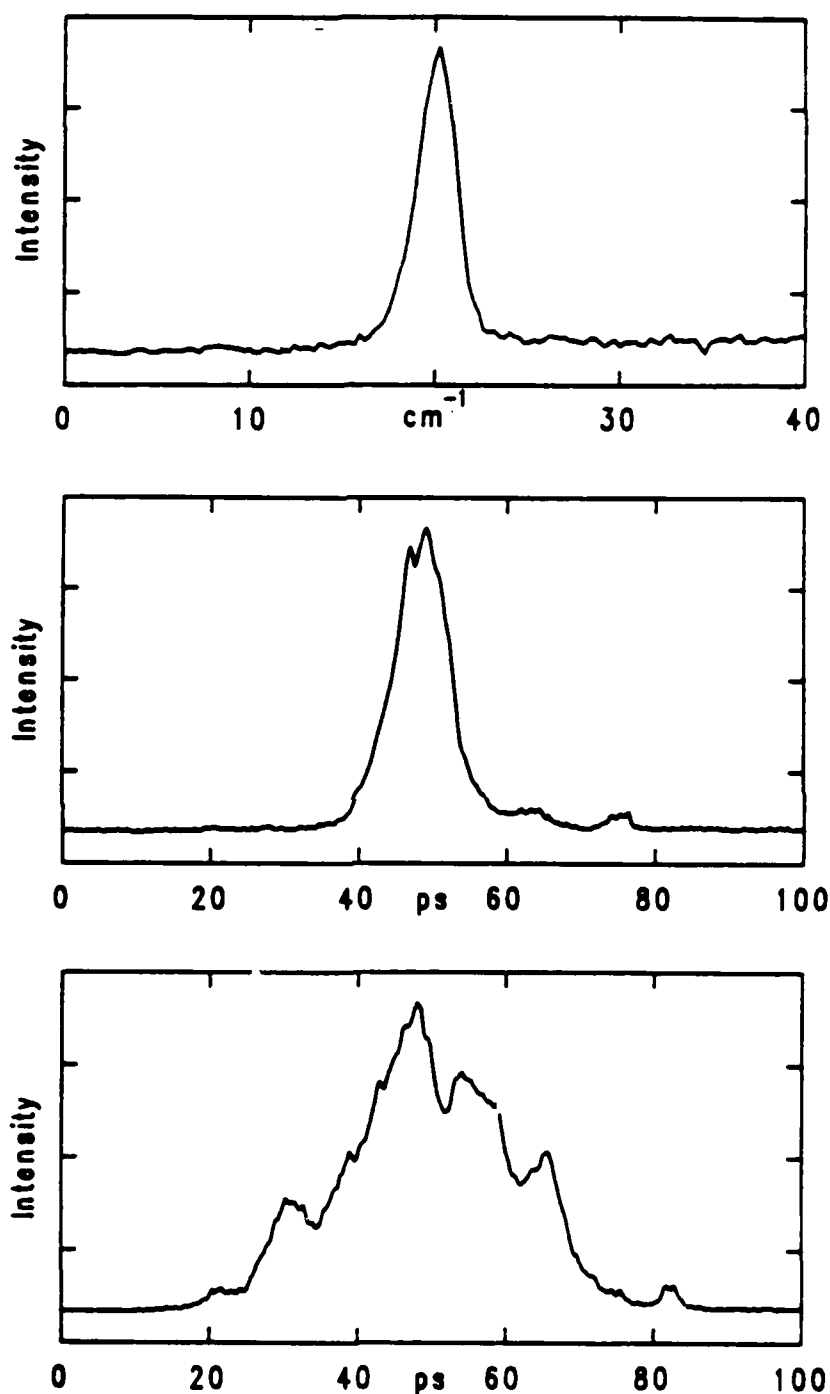


Figure 2.16. Upper curve: Spectral profile, 532 nm, $\Delta\nu=2.43 \text{ cm}^{-1}$ FWHM, $.67 \text{ cm}^{-1}$ RMS. Middle curve: Temporal profile, 532 nm $\Delta t=8.37 \text{ ps}$ FWHM, 8.29 ps RMS. Lower curve: Temporal profile, 355 nm $\Delta t=27.2 \text{ ps}$ FWHM, 12.5 ps RMS. For the tunable output, $4\pi c\Delta\nu\Delta t=61/44$, conversion efficiency $\sim 1.5\%$. Note that the pump pulse is shortened compared to the other curves. It was picked further into the train than the others.

obtained. One interesting possibility is to combine second and third harmonic pumping to produce a narrow-band visible source. The output of the second harmonic pumped OPS is dispersed through a spectrometer to obtain a weak, distorted but spectrally narrow infrared beam. If this is matched to the idler frequency of the third-harmonic pumped OPS, it can serve to injection-lock the frequency of the visible output. The resulting visible output should have the spectral characteristics of the IR beam and the temporal and spatial properties of the usual visible beam. Tunable pulses approaching the transform limit should be achievable in this way.

The type I OPS was also investigated briefly using the third harmonic as the pump beam. The main reason for wanting to use this phase match is that spectral coverage is better. Unlike the type II interaction where the output intensity falls dramatically in the red, the type I OPS is most efficient between ~ 600 and 710 nm (or in terms of the idler, 870 – 710 nm). The type I OPS can be used to fill the spectral gaps associated with the type II phase-match. The primary difficulty with the type I phase match is that the angle tuning curve is much more sensitive than is the type II curve. To scan from 450 to 710 nm requires only a few degrees rotation. In and of itself this is not a problem, since small angle adjustments are readily made. The problem is that this type of tuning curve causes the output frequency and spectral width to be very sensitive to small changes in the beam focus or position. Unless extreme care is taken, spectral widths of several hundred wavenumbers can result. Small spatial drifts associated with long delay lines can cause significant spectral shifts as well. For time-resolved emission these problems can be tolerated, and useful results have been obtained²⁸. Spectral widths of a few wavenumbers have been reported²³, but only under ideal circumstances. In general, when applicable the type II phase match is much easier to use, and gives better results.

An effort was made to investigate the range of frequencies which could be generated by sum generation using the laser harmonics and the tunable outputs. In particular, reasonably intense sources between 250 and 400 nm were of interest, since these are often

desirable for time-resolved emission. Appreciable output energies could be obtained by doubling the idler, by summing the idler with the laser fundamental, by summing the signal with the laser fundamental, by summing the signal with the laser second harmonic, and by doubling the signal. Several of these combinations produce outputs at frequencies already well covered by the OPS itself. These were not studied in detail. Most of the effort was devoted to studying the outputs which result from summing the signal with the laser fundamental, since this appeared to be a promising method for producing a significant amount of power at wavelengths in the neighborhood of 355 nm. Temporal and spectral measurements were made of these pulses. Figure 2.17 shows a typical pulse at 358 nm obtained this way. It can be seen that the pulse has structure similar to what is seen with the corresponding 540 nm pulses. The $\Delta\nu\Delta t$ product indicates that the pulse is a factor of 28 from transform limited. This is well in line with what was observed in the visible.

A summary of the available wavelengths and the powers attainable are shown in table 2.1. With the pump powers available, adequate energies for purposes such as emission spectroscopy or possibly resonance Raman are available in the visible. It would clearly be desirable to have a more intense or more readily produced UV source. The simplest method for achieving this appears to be to amplify the visible output using dye amplifiers pumped with the second harmonic, and then use sum generation to produce the desired wavelength. This was attempted briefly, but it was not pursued systematically. The use of a dye amplifier is in some ways undesirable, since it limits the available tuning range. The conditions required for amplification should be very much like those used to amplify the short cavity dye laser output¹⁴. Other variations include summing the tunable infrared output with the Raman shifted fourth harmonic⁹, or using other laser amplifiers to generate other fixed frequencies. One interesting possibility in this regard, is to use OPS pumped with either the second or third harmonic to generate an output at 1320 nm, and then amplify this with the Nd:YAG amplifier. The harmonics of this frequency can

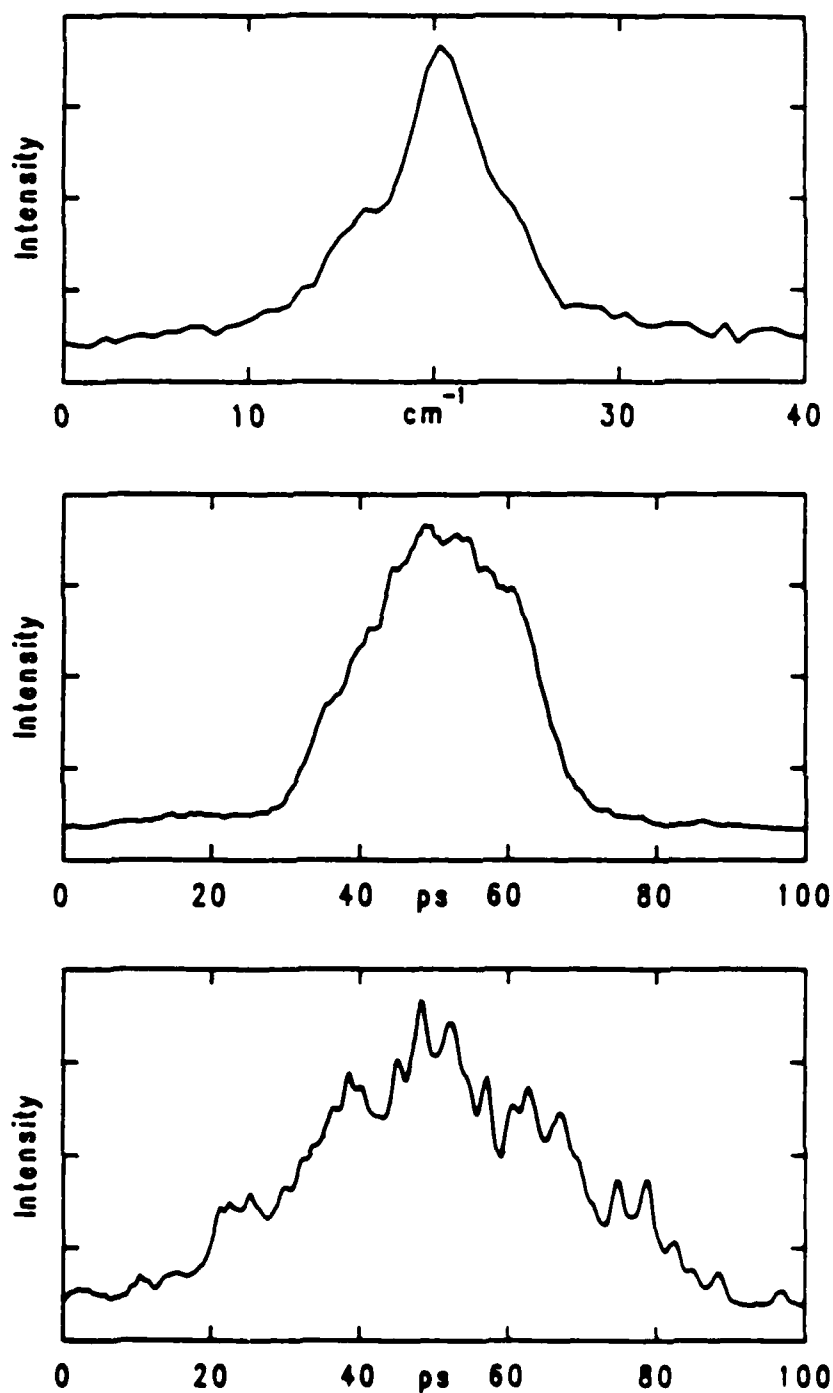


Figure 2.17. Upper curve: Spectral profile, 358 nm, $\Delta\nu=6.20 \text{ cm}^{-1}$ FWHM, 5.36 cm^{-1} RMS. Middle curve: Temporal profile, 358 nm $\Delta t=26.0 \text{ ps}$ FWHM, 12.0 ps RMS. Lower curve: Temporal profile, 355 nm $\Delta t=35.3 \text{ ps}$ FWHM, 18.4 ps RMS. For the tunable output, $4\pi c \Delta\nu \Delta t=28.0$, conversion efficiency $\sim 1\%$

Table 2.1

Wavelengths and Approximate Energies for the OPS System.

OPS Visible:	$\sim 100 \mu\text{J}$	470–620 nm
OPS Infrared:	$\sim 50 \mu\text{J}$	850–1300 nm
1064 nm + OPS Infrared:	$\sim 10 \mu\text{J}$	470–620 nm
1064 nm + OPS Visible:	$\sim 10 \mu\text{J}$	325–390 nm
Doubled OPS Infrared:	$\sim 1 \mu\text{J}$	420–550 nm
Doubled OPS Visible:	$\sim 1 \mu\text{J}$	250–310 nm
Type I OPS:	$\sim 100 \mu\text{J}$	500–1200 nm
532-pumped Type II OPS:	$\sim 100 \mu\text{J}$	850–1400 nm
532-pumped Dye + OPS Visible:	$\sim 500 \mu\text{J}$	570–610 nm
OPS Infrared + YAG Amplifier:	$\sim 1000 \mu\text{J}$	1320 nm

be summed with the harmonics of the 1064 beam to produce a variety of visible and infrared frequencies. A fully tunable source could be obtained by summing these outputs with the output of a second-harmonic-pumped OPS. Tens or hundreds of microjoules of tunable UV might be available by this method, although it is rather complex to set up. Another possibility is to use a XeCl amplifier to amplify pulses at 308 nm²⁹. These possibilities were not investigated in detail, but they suggest that a variety of reasonably powerful UV sources can be achieved.

4. Comparison with Theory

The theory of parametric amplification is well understood. The coupling of three plane waves of known polarization by the second order polarizability tensor can be described by explicitly including the nonlinear polarization in the classical wave equation. This is described in detail in reference 2. The derivation is identical to that given below in connection with coherent Raman scattering, and will not be repeated. Making use of the usual slowly-varying-envelope approximation, results in the desired coupling equations. In this case, using the conventional notation that the subscripts 1,2 and 3 refer respectively to the infrared (idler), visible (signal) and ultraviolet (pump) wavelengths, and making the nondepleted pump approximation, the equations describing the growth of the signal and idler waves are (in the notation of reference 2)

$$\frac{dA_1}{dz} = \frac{-\alpha_1}{2} A_1 - \frac{ig}{2} A_2^* \exp(-iz\Delta k) \quad (2.6a),$$

$$\frac{dA_2^*}{dz} = \frac{-\alpha_2}{2} A_2^* + \frac{ig}{2} A_1 \exp(iz\Delta k) \quad (2.6b).$$

A_j is proportional to the electric field amplitude so that the intensity I_j is given (in MKSA units) by

$$I_j = \frac{\omega_j}{2} \left(\frac{\epsilon_0}{\mu_0} \right)^{\frac{1}{2}} |A_j|^2 \quad (2.7).$$

The absorption coefficient α_1 corresponds to the infrared adsorption in KDP; α_2 is assumed to be negligible. The maximum gain coefficient g depends on the crystal symmetry and the phase matching configuration. For type II KDP it is given by

$$g = 2d_{36} \sin 2\theta \left(\frac{2\omega_1\omega_2 I_3}{n_1 n_2 n_3} \right)^{\frac{1}{2}} \left(\frac{\mu_0}{\epsilon_0} \right)^{\frac{1}{4}} \quad (2.8).$$

The phase mismatch Δk is defined by

$$\Delta k = k_3 - k_2 - k_1 \quad (2.9),$$

the second order susceptibility of KDP is d_{36} , θ is the same as in figure 2.10, and the n_i refer to the effective indices of refraction for the three beams.

These equations can be solved exactly, giving for the idler,

$$A_1(z) = A_1(0) \exp(Bz) \quad (2.10),$$

where

$$B = \frac{-1}{2} \left[\left(\frac{\alpha_1}{2} + i\Delta k \right) \pm \left(\frac{\alpha_1^2}{4} + g^2 - \Delta k^2 - i\alpha_1 \Delta k \right)^{\frac{1}{2}} \right] \quad (2.11a).$$

Only the negative solution is physically reasonable, corresponding to parametric amplification. In the case that α_1 can be neglected, the expression for B reduces to

$$B = \frac{1}{2} \left[-i\Delta k + \left(g^2 - \Delta k^2 \right)^{\frac{1}{2}} \right] \quad (2.11b).$$

If Δk can be ignored and g is much greater than α_1 ,

$$B = g/2 - \alpha_1/4 \quad (2.11c).$$

In terms of intensities, the solutions can be expressed as

$$I_1(z) = I_2^0 \frac{\omega_1}{\omega_2} \left| \frac{2B + \alpha_1}{g} \right|^2 \exp(2bz) \quad (2.12a),$$

$$I_2(z) = I_2^0 \exp(2bz) \quad (2.12b),$$

where I_2^0 is the visible intensity at the front of the first crystal (in the absence of an input beam, this corresponds to the parametric fluorescence), b is the real part of B and z is the crystal length. The factor in the first equation involving α_1 is a correction for the photons absorbed by the crystal.

Many of the observed performance characteristics of the OPS are explained by equation 2.12. The strong dependence of the output power on the pump beam intensity (see figure 2.11) means that any amplitude fluctuations in the pump beam will be greatly amplified in the output beam. The linear pump intensity dependence of g^2 leads to a square root power dependence in the exponent b in equation 2.12. Thus, small changes in the input power lead to large changes in the output power, as observed. The measured fluctuations in the output energy observed for an essentially constant pump energy appear to correspond to quantum noise associated with spontaneous parametric fluorescence. The presence of fluctuations in the temporal, spectral, and spatial distribution of the spontaneous parametric fluorescence would also account for the observed variations in the temporal and spectral profiles of the OPS at low conversion efficiencies.

The variation in the output energy through the tuning range is also described by the theory. It can be seen from the tuning curve that the $\sin(2\theta)$ dependence of g will result in a decrease in the gain for longer wavelengths. The phase-matching condition can be satisfied for values of λ_2 up to 680 nm, but because of the decreasing value of g , no output is observed beyond 650 nm. The increasing value of α_1 in the infrared ³⁰ leads to a decrease in b for the corresponding visible wavelength. This causes the blue cutoff at 450 nm. It is interesting to note that although KDP is strongly absorbing in the region above 1200 nm, the idler beam can be seen out to 1650 nm. This is because the unattenuated visible beam can function as the carrier of the parametric process, so the loss of most of the infrared beam is not a problem. Furthermore, since the bulk of the

amplification occurs in the last few mm of the crystal, the effective attenuation of the infrared output will be relatively small. Only when the absorption becomes comparable to the gain does the parametric process cease.

When literature values for α_1 ³⁰, n_i ²⁶ and d_{36} ² are substituted into the above equations, the calculated curve agrees only qualitatively with the measured values. The calculated curve is more sharply peaked than the measured curve, and falls too rapidly at the red end of the tuning range. This is not surprising, since the simple model used here neglects such important factors as pump beam depletion, the finite beam size, and the spatial walk-off of the three beams caused by refraction and birefringence. It has been shown in similar systems that taking these factors into account can lead to much more nearly quantitative agreement³¹.

The observed shortening of the visible OPS pulse relative to the pump pulse at low conversion efficiencies is primarily due to the power dependence of the parametric gain²⁵. For a pump pulse with a gaussian intensity envelope with a width τ_3 , it can be shown that the output pulse will have a gaussian profile with a width τ_2 given by

$$\tau_2 = \tau_3(bz)^{-1/2} \quad (2.13).$$

For $2bz \sim 30$, this equation predicts an output pulse duration .26 times τ_3 . Pump pulses of 35 ps would thus lead to a visible output pulse of 9.0 ps. This agrees well with what was observed at low conversion efficiency. At higher conversion efficiencies, the center of the pump beam will be depleted, and the width of the output pulse will broaden until it matches that of the pump pulse.

Pulse broadening due to group velocity dispersion is a general feature of the interaction of ultrashort pulses with a dispersive medium³². In the present case, group velocity dispersion does not significantly broaden the output pulse duration, primarily because the pulses are relatively long. Since the bulk of the output pulse energy arises from parametric amplification in the last few mm of the crystal, any group velocity broadening

effects must occur over a pathlength of a few mm. Using the known group velocities of KDP (at 532 nm, in the phase-matched geometry with $v \equiv d\omega/dk$, $v_3 = .9916v_1$, $v_2 = .9535v_1$ and $v_1 = .6419c$)²⁶, a pulse broadening of ~ 2 ps would be predicted for passage through 10 mm of KDP. This is much smaller than the pulse width, even at low conversion efficiency.

The phase matching condition $\Delta k = 0$ plays a key role in determining both the spectral and spatial profiles of the OPS beam. The first crystal emits broad-band parametric fluorescence at any frequency and in any direction for which the phase matching condition is satisfied². The space between the crystals acts as a spatial filter, since only the narrow cone of parametric fluorescence which overlaps the pump beam in the second crystal will be amplified. The spectral width of the output beam would thus be expected to decrease as the spacing between the crystals is increased, until a spectral width corresponding to the limit set by the bandwidth for collinear amplification is reached. In the present work it was found that the spectral width of the output changed very little for crystal spacings greater than 10 cm.

The amplification bandwidth for collinear amplification corresponds to the range of Δk for which significant amplification will occur³³. From the above equations it can be seen that the half width of the bandwidth is given by the condition

$$\exp(2bz) = 1/2 \exp(gz) \quad (2.14).$$

Neglecting absorption and using equation 2.11b, this can be solved to give

$$\Delta k = \left(\frac{2g \ln 2}{z} \right)^{\frac{1}{2}} \quad (2.15).$$

For $gz \sim 30$ and $z = 7.4$ cm, this gives Δk as $.87 \text{ cm}^{-1}$. The full spectral width can then be determined from the group velocities, since $v = d\omega/dk$,

$$\Delta \nu = \frac{2\Delta k}{2\pi} \left[\frac{dk_1}{d\omega} - \frac{dk_2}{d\omega} \right]^{-1} = \frac{v_1 v_2 \Delta k}{\pi c(v_1 - v_2)} \quad (2.16).$$

Substituting the values given above for Δk and the group velocities into this equation gives a bandwidth of 4.6 cm^{-1} . This is consistent with the spectral widths observed at low conversion efficiencies, as shown in figure 2.14. The broadening observed at higher conversion efficiencies (see figure 2.13) is presumably a result of the pump pulse depletion.

As might be expected from these arguments, the spatial divergence of the OPS is determined by both the crystal separation and the noncollinear phase matching. The latter effect appears to have the dominant effect in determining the shape of the final output beam. The visible output beam is not the round shape that would be expected from the spatial filtering argument presented above, but instead has the crescent shape characteristic of a noncollinear phase matching cone³⁴. Since careful investigation of the spectrum of selected portions of the OPS beam showed no evidence of spectral inhomogeneity, it appears that the spatial broadening occurs in the second crystal after the spatial and spectral effects of the crystal separation. This can be explained by assuming that the off-axis light results from parametric amplification of light scattered into the phase matched directions.

Although they are clearly visible, the more divergent parts of the beam are relatively weak, containing no more than a few percent of the total power. The bulk of the power is concentrated in an oblong spot with a divergence of 0.6 mrad in the plane of the optic axis and 1.2 mrad in the perpendicular direction. Extrapolating this output back into the crystals suggests that the parametric output arises from an approximate point source near the front surface of the first crystal. This is reasonable, since the parametric output will correspond to light emitted from the most intense part of the beam and passing through the full length of both crystals. A similar argument has been made to explain the spatial properties of light generated by stimulated Raman scattering³⁵. It is possible to compensate for this divergence by placing a lens in the output, one focal length away from the crystal front surface. Using a 40 cm lens produced a 3 mm diameter beam

which remained collimated for many meters.

D. Conclusion.

The combination of the active-passive mode-locked laser and the OPS have been found to be a very satisfactory source of picosecond pulses. As described in the next two chapters, this system has been used to carry out a variety of time resolved measurements. Despite the successes with this system, there are still many aspects of the system which could be improved further. With regard to the laser, there are reasons for wanting both higher repetition rates and higher powers. As described in the next chapter, many spectroscopic measurements can be made more efficiently with a repetition rate of tens of kilohertz. Repetition rates this high require a somewhat different approach than was used here (i.e. a CW or quasi-CW laser) so this was not pursued. Repetition rates of 20–50 Hz are more approachable and might be considered a logical next step with this system. Increasing the laser power is of interest primarily in regard to making more efficient use of nonlinear optical processes. As noted above, there is still a significant lack of a conveniently tunable source in the ultraviolet. Several approaches are possible within the framework of a pulsed Nd:YAG system, ranging from elaborate summing schemes involving the use of both Nd:YAG frequencies and an OPS output, to simply boosting the 1064 nm output to hundreds of millijoules and generating the various harmonics of a second-harmonic-pumped OPS.

E. References for Chapter 2

1. H. Nathel, Ph.D. thesis, University of California, Berkeley, 1986
2. A. Yariv, *Quantum Electronics, Second Edition*, Wiley, New York, 1975.
3. H. P. Kortz, *IEEE J. Quantum Electron.* QE-19 (1983) 578-584.
4. D. Anderson and M. Lisak, *Phys. Rev. A* 27 (1983) 1393-1398.
5. T. Tomie, *Japan. J. Appl. Phys.* 9 (1985) 1008-1017.
6. H. Graener and A. Laubereau, *Optics Comm.* 37 (1981) 138-142.
7. J. L. Carlsten, J. M. Telle and R. G. Wenzel, *Optics Lett.* 9 (1984) 353-355.
8. S. M. Beck and L. E. Brus, *J. Chem. Phys.* 75 (1981) 4934-4940.
9. Y. Takagi, M. Sumitani, N. Nakashima, D. O'Connor and K. Yoshihara, *Appl. Phys. Lett.* 42 (1983) 489-491; D. A. Angelov, G. G. Gurzadyan and D. N. Nikogosyan, *Sov. J. Quantum Electron.* 9 (1980) 1334-1335.
10. G. A. Massey, *Appl. Phys. Lett.* 24 (1974) 371-373.
11. J. F. Reintjes, *Nonlinear Optical Parametric Processes in Liquids and Gases*, Academic, New York, 1984.
12. See for example, M. J. Soileau, ed., *Ultrashort Pulse Spectroscopy and Applications (Proc. SPIE, V. 533)*, SPIE, Bellingham WA, 1985; D. H. Auston and K. B. Eisenthal, eds., *Ultrafast Phenomena IV*, Springer-Verlag, New York, 1984).
13. G. W. Scott, J. H. Clark, M. A. Tolbert, S. P. Webb, A. J. Cox and G. Renz, *IEEE J. Quantum Electron.* QE-19 (1983) 544-550.
14. H. P. Kortz, P. Pax and R. Aubert, in *Ultrashort Pulse Spectroscopy and Applications (Proc. SPIE, V. 533)*, M. J. Soileau, ed., (SPIE, Bellingham WA, 1985) 32-37.
15. R. Fischer and L. A. Kulevskii, *Sov. J. Quantum Electron.* 7 (1977) 135-159; R. Fischer and L. A. Kulevskii, *Sov. J. Quantum Electron.* 7 (1977) 798.
16. B. Bareika, G. Dikchyus, E. D. Isyanova, A. Piskarskas and V. Sirutkaitis, *Sov. Tech. Phys. Lett.* 6 (1980) 301-302; T. Elsaesser, A. Seilmeier and W. Kaiser, *Opt. Comm.* 44 (1983) 293-296.
17. R. Danelyus, G. Dikchyus, V. Kabelka, A. Piskarskas, A. Stabinis and Ya. Yasevichute, *Sov. J. Quantum Electron.* 7 (1977) 1360-1368.
18. R. Danelus, A. Piskarskas, V. Sirutkaitis, A. Stabinis and Y. Yasevichute, *Optical Parametric Oscillators and Picosecond Spectroscopy*, Mokslas, Vilnius, USSR, 1983.

19. P. Kryukov, Yu. Matveets, D. Nikogosyan, and A. Sharkov, *Sov. J. Quantum Electron.* 8 (1978) 1319-1322.
20. R. Danelyus, A. Piskarskas, and V. Sirutkaitis, *Sov. J. Quantum Electron.* 12 (1982) 1626-1632; R. Gadonas, R. Danelyus and A. Piskarskas, *Sov. J. Quantum Electron.* 11 (1981) 407-408.
21. V. Kabelka, A. Kutka, A. Piskarskas, V. Smil'gyavichyus and Ya. Yasevichyute, *Sov. J. Quantum Electron.* 9 (1979) 1022-1024.
22. R. Danelyus, V. Kabelka, A. Piskarskas, and V. Smil'gyavichyus, *Sov. J. Quantum Electron.* 8 (1978) 398-400.
23. F. Wondrazek, A. Seilmeier and W. Kaiser, *Appl. Phys.* B32 (1983) 39-42.
24. A. Kung, *Appl. Phys. Lett.* 25 (1974) 653-654.
25. A. Akhmanov, S. Akhmanov, R. Khokhlov, A. Kovrigin, A. Piskarskos and A. Sukhorukov, *IEEE J. Quantum Electron.* QE-4 (1968) 828-831; W. Glenn, *Appl. Phys. Lett.* 11 (1967) 333-335.
26. F. Zernike, *J. Opt. Soc. Am.* 54 (1964) 1215-1220.
27. S. A. Magnitskii, V. I. Malachova, A. P. Tarasevich, V. G. Tunkin and S. D. Yakubovich, *Optics Lett.* 11 (1986) 18-20.
28. S. W. Yeh, Personal communication.
29. J. H. Glowina, G. Arjavalasingam, P. P. Sorokin and J. E. Rothenberg, *Optics Lett.* 11 (1986) 79-81.
30. V. I. Bespalov, I. A. Batyрева, L. A. Dmitrenko, V. V. Korolikhin, S. P. Kuznetsov and M. A. Novikov, *Sov. J. Quantum Electron.* 7 (1977) 885-887.
31. B. Schröder, *Opt. Comm.* 49 (1984) 75-78; B. Schröder, *Opt. Quant. Electron.* 15 (1982) 57-63; H. Bergner, V. Brückner and B. Schröder, *Sov. J. Quantum Electron.* 11 (1981) 952-953.
32. A. M. Weiner, *IEEE J. Quantum Electron.* QE-19 (1983) 1276-1283.
33. A. Seilmeier and W. Kaiser, *Appl. Phys.* 23 (1980) 113-119.
34. H. Bates, *J. Opt. Soc. Am.* 63 (1973) 146-151.
35. B. Bobbs and C. Warner, *Optics Lett.* 11 (1986) 88-90.

Chapter 3

Picosecond Spectroscopic Techniques

A. Introduction.

The purpose of building the picosecond laser system described in the previous chapter was to make it possible to monitor chemical processes in solution on a picosecond timescale. In order to study such processes, it is necessary to identify and develop spectroscopic techniques which are compatible with both the laser hardware and the liquid-phase environment. With the range of wavelengths available from the system, it is possible to imagine using all the conventional forms of visible and infrared spectroscopy (absorption, emission and Raman) as well as nonlinear techniques such as coherent anti-Stokes Raman spectroscopy (CARS) or multi-photon ionization (MPI). Each method clearly has its own set of advantages and difficulties, and the choice of spectroscopic technique will depend on the system under study. Visible emission and absorption are clearly the easiest methods for problems involving solution-phase problems. These wavelengths are easy to generate and detect, and this is a frequency range where most solvents are transparent. Spontaneous Raman scattering is another potentially useful technique which makes use of visible light. Unfortunately, as will be seen below, using this method in conjunction with the laser system described in the last chapter has proven to be quite difficult. The combination of high peak power and low average power tends to maximize nonlinear background noise while minimizing signal levels. Possible methods for overcoming this problem, including the use of nonlinear spectroscopy and different laser systems will be discussed below. Infrared methods are potentially valuable, but the difficulty of generating and detecting these wavelengths, as well as the strong absorptions found in many solvents, limits the potential usefulness of this method for the present. The more exotic coherent and multiphoton spectroscopic techniques tend to be nonlinear, so the signal

levels often increase dramatically with increasing laser peak power. Since high peak powers are inevitable with picosecond pulses, such methods seem ideally suited to picosecond work. Unfortunately, these methods are usually only workable in the gas phase; in solutions, the signal is either quenched by collisions or overwhelmed by nonresonant signals arising from the solvent. MPI is useless for the first reason; CARS fails for the second. Variations on CARS which alleviate this difficulty do exist, but they are quite complex, and often lead to a loss of signal.

In general, there are two methods for making optical measurements with picosecond time resolution. A streak camera can be used to directly time-resolve an optical signal, or a two beam pump-probe measurement can be used to sample a signal at various fixed delays. Both methods have their advantages and disadvantages. Streak camera methods tend to be very efficient and easy to use, and they allow data to be collected quite rapidly. In particular, they are extremely well suited to time-resolved emission measurements¹ at repetition rates of up to tens of hertz. The time resolution of a streak camera measurement is typically in the range of 1–10 ps, limited by the streak camera itself. This was not a limitation here, but it precludes streak camera measurements in the femtosecond time domain. Signal averaging greatly improves the quality of streak camera data. Unfortunately, time-consuming computer corrections are necessary and at present these constitute the rate-limiting step in data collection. With the computer system used here repetition rates of almost 3 Hz could be achieved; with a more sophisticated system rates of 20–50 Hz are feasible. Streak cameras are well matched in this regard to pulsed Nd:YAG lasers which have comparable repetition rates. The spectral limitations of a streak camera are comparable to those of a photomultiplier tube.

The pump-probe technique was used here for Raman spectroscopy. In a pump-probe measurement, two pulses are obtained by splitting the laser output into two beams. Each beam is directed to the sample via different paths with the time delay determined by the pathlength difference. In a Raman measurement the pump beam

ω_2 are used; these are generated in nonlinear optical crystals just before the beams are recombined ahead of the sample. Ideally, the first pulse at ω_1 will excite the sample, and photochemically generate some species with a large Raman cross section. This will then lead to Raman scattering of the second pulse at ω_2 . By varying the delay between the two pulses, it should be possible to map out the density of scattering molecules as a function of time. This is actually an example of a much more general type of measurement, where a two photon process is time-resolved by a sampling technique. The two photons can either interact in the sample, as in the Raman measurement, or the probe photon can interact in some way (e.g. in a Kerr shutter) with light scattered from the sample. In the second case, the probe pulse is used, in effect, to drive an optical sampling circuit³.

The time resolution of a pump-probe experiment is limited only by the duration of the laser pulses, so with a suitable laser, femtosecond time resolution is possible. Detection in a pump-probe measurement can be quite simple, and a photomultiplier tube or a photodiode is often used. In some cases, multichannel detection is possible as in absorption or Raman spectroscopy, where data may be collected at several wavelengths simultaneously. Note that the lack of jitter in a spectrometer makes signal averaging much simpler here than it was with the streak camera. The signal in a pump-probe measurement scales as the product of the power of the two beams. In principle, this favors high powers and low repetition rates. However, in many cases (e.g. Raman scattering) high peak powers lead to nonlinear background effects which obscure the desired signal. In these cases, high repetition rates, rather than high powers are desirable. Since simple detection systems are generally used, signal averaging can be quite simple, and tends not to limit the rate of data collection. The very high (~ 100 MHz) repetition rates achieved with CW mode-locked lasers are well suited to this type of experiment in reversible systems. With these very high repetition rates, the question of signal averaging takes on a rather different character. Instead of using elaborate multichannel detection schemes to maximize the yield of data per laser shot, it is often more profitable to employ

CW techniques involving amplitude modulation, lock-in amplifiers and simple detectors to enhance the signal quality⁴. As discussed below, for Raman experiments in reactive solutions, a somewhat lower repetition rate (~ 50 KHz) is often desirable. It represents the compromise between high data collection rates and the rate at which the sample volume can be purged.

In what follows, descriptions will be given of the methods used here to obtain time-resolved emission, absorption and Raman spectra. Not all of the systems described were developed to the fullest extent possible; indeed, significant improvements are possible in all cases. Some such improvements will be discussed briefly in order to show the range of possible future measurements. In general, as the systems were developed, it became clear that the optical system should be arranged to maximize flexibility so as to simplify the process of switching from one form of spectroscopy to another. This can be seen with the streak camera system, where both emission and absorption spectroscopy coexist with most of the same hardware, and it is quite simple to switch back and forth between the two. If everything had gone according to plan, there would ultimately have been a generalized pump-probe spectrometer with available delays up to several nanoseconds and the capability of being used for Raman and absorption spectroscopy. By combining a computer controlled delay line with a multichannel detector, a pump-probe system with an efficiency comparable to that of the streak camera should have been obtainable. Unfortunately, time and circumstances did not permit the completion of this system.

B. The Streak Camera

The vast majority of all work carried out in this laboratory has been carried out using a streak camera. Work has centered on time-resolved emission, but absorption measurements have been carried out as well. Most of the techniques used for operating and calibrating the streak camera were developed with emission spectroscopy in mind. The absorption system was something of an afterthought and can be best described as a

modification of the emission system. Signal averaging plays a crucial role in acquiring high-quality data from the streak camera. Indeed, the data collection rate is limited by the rate at which data can be corrected and averaged. In emission spectroscopy, the desired signal is directly proportional to the light intensity, so signal averaging corresponds to simply summing the data. In absorption, Beer's law must be taken into account, and it turns out to be necessary to sum the logarithm of the datasets. This will be discussed below.

The operation of the streak camera emission system naturally divides itself into three timescales: The picosecond timescale over which the data is generated, the millisecond timescale over which the data is transferred to the computer, corrected and summed, and the timescale of minutes or hours over which the data is actually collected. The fast time regime is perhaps the most important, since it is where the limitations of the data originate. In this time regime, the details of the streak camera are important, since they determine the nature and limitations of the data. Improvements in this time regime could lead to great simplifications at the slower timescales. For example, if the jitter or nonlinearities of the streak camera could be eliminated, much of the work involved with correcting the data on the millisecond timescale would be eliminated, leading to much more rapid data collection rates. Unfortunately, streak camera development was beyond the scope of this project, and a commercially available streak camera (Hadland Photonics Ltd., Imacon 500) was used without modification.

Given that some corrections are necessary, many of the limitations of the system as it currently exists, manifest themselves on the millisecond timescale. The combination of computer systems used at the present time represents a somewhat inefficient mixture of relatively incompatible hardware. Because of this, the present system can collect data at only 3 Hz, a factor of three slower than the laser repetition rate. As described below, a somewhat faster system (up to perhaps 25 Hz) is possible with a more efficient configuration of the existing hardware. Even with a faster computer system, increasing

the rate beyond this point is difficult with the existing optical system, since the phosphors in the streak camera and image intensifiers have lifetimes of tens of milliseconds. Even if it is an order of magnitude slower than it could be, three hertz is still a respectable data collection rate. It is at least an order of magnitude faster than many other systems presently in use. When compared to systems based on the Nd:Glass laser (which is limited by thermal effects to rates much less than one hertz), it is extraordinarily fast². Nonetheless, it is still slower than one might like, and the collection of multiple datasets can be a long and tedious process.

The reasons for wanting to increase the data collection rate are most apparent on the minute or hour timescale. Many experiments require the collection of dozens of datasets under nominally identical conditions. With the present system, this can take many hours. Unfortunately, over this timescale the room temperature, the laser output and the streak camera calibrations can all show significant variations. A higher repetition rate is clearly desirable, since it allows complex measurements to be made more efficiently. In what follows, the operation and limitations of the streak camera itself are discussed, as are the detection system and the computer interfacing used to handle the data. The methods used to calibrate both the time and intensity response of the entire detection system are included, as are the methods used to overcome the streak camera time jitter. In addition, methods for increasing the repetition rate of the system are discussed.

C. Time-Resolved Emission Spectroscopy

1. Hardware and Optics

The optical system used for time-resolved emission is shown in figure 3.1. The pulse from the laser is initially split into two components. The first pulse (less than 1% of the beam energy) is sent to a photodiode (Hewlett-Packard, HP 5082-4220) which is used to trigger the streak camera. This must occur many nanoseconds before the beam reaches

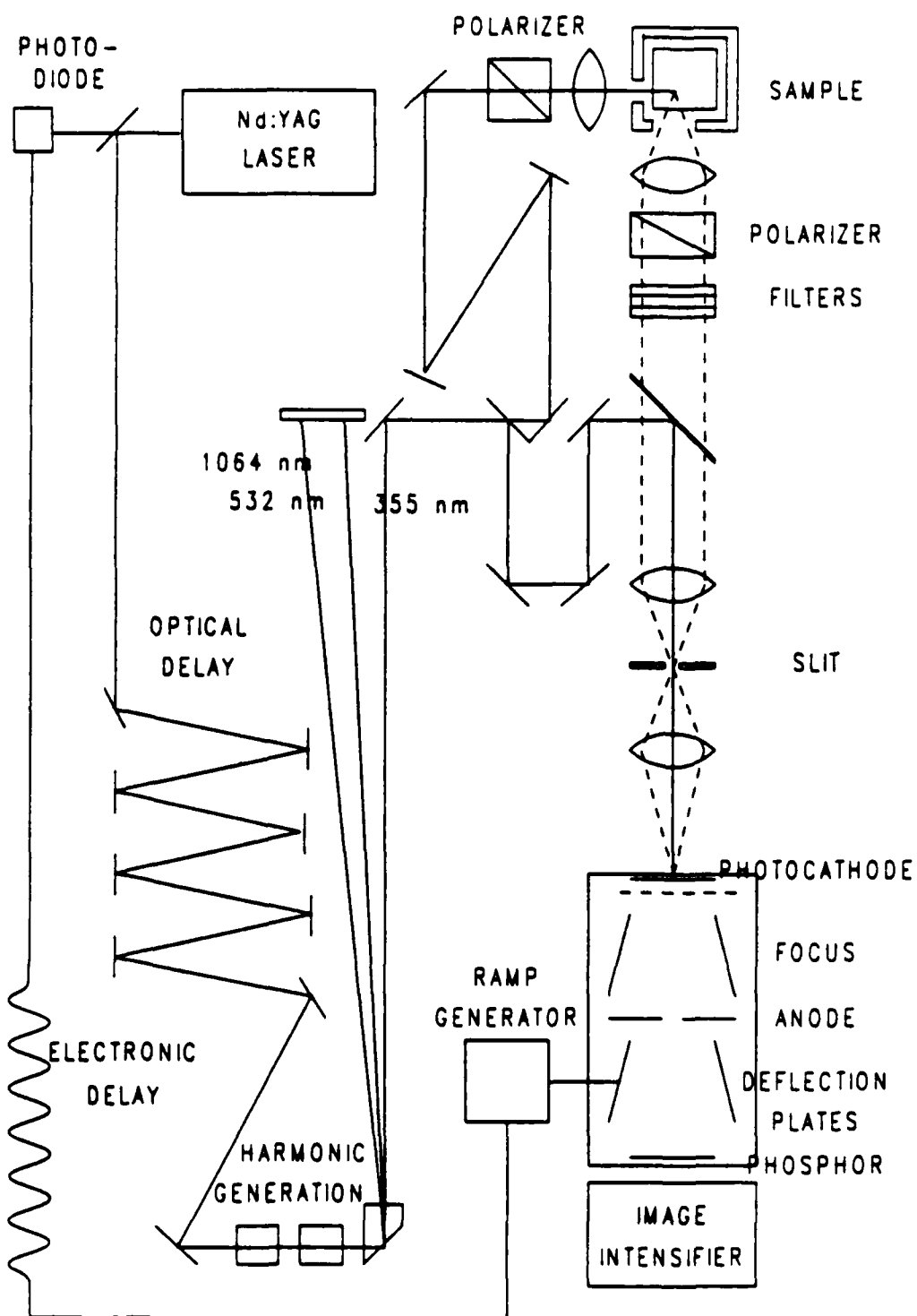


Figure 3.1. Optical system for time-resolved emission, as described in the text.

the sample, to compensate for the transit time in the streak camera trigger circuitry. The purpose of the optical and electronic delays shown is ultimately to synchronize the arrival of the optical signal with the triggering of the streak camera. The optical delay consists of five passes up and down the three meter optical table for a delay of 30 m or 100 ns. The electronic delay consists of a variable length of coaxial cable. Note that this 30 meter delay greatly amplifies small drifts in the pointing axis of the laser. This results in a gradual drift in the position of the beam at the sample. This could be corrected by placing a quadrant detector (SDC SD-10053-S) behind the final mirror of the delay to sense the beam position, and then using the resulting signals to drive a servo motor attached to a differential micrometer on a mirror mount early in the delay. This system made it possible to keep the laser aligned with the sample over a period of hours, despite the drift of the laser.

After passing through the delay line, the beam is passed through a series of nonlinear crystals to produce the frequency needed for sample excitation. This is usually the third or fourth laser harmonic, but the second harmonic or an output from the OPS can also be used. After a small fraction of the beam is split off, the excitation beam is then passed through a short delay line and allowed to impinge on the sample, which then begins to fluoresce. Light from the sample is then collected and reimaged through a series of relay lenses onto the streak camera photocathode. The same optical system is also used to transfer a small fraction of the excitation pulse to the photocathode, timed to arrive just before the fluorescence signal. As described below, this "prepulse" is used to facilitate signal averaging.

The figure shows the details of the streak tube. Despite the expense of the device, it is little more than a modified image intensifier. Light striking the photocathode causes the prompt formation of photoelectrons. An extraction grid placed directly behind the photocathode surface generates a local field of tens of KV/cm which accelerates the electrons toward the anode. The large field is needed to produce a uniform electron

velocity, since the final velocity must be much greater than the initial (thermal) velocity distribution of the electrons. The focus cone is an electron lens which focuses the collimated electron beam through the aperture in the anode. The electron lens is focussed so that the photocathode is reimaged directly onto the phosphor screen. After passing through the anode, the electron reaches the deflection plates. If no field is present, the electrons pass directly through this region and strike the phosphor at the back of the tube, producing a fixed image of the slit. This time-independent image is used to align and focus the camera. The position of the slit image depends on the deflection plate voltage, with larger voltages increasing the deflection from the center of the phosphor. In normal operation, a field of approximately 10 KV is left on the deflection plates so the beam is deflected away from the the phosphor screen when not in use. Time-resolved measurements are obtained by applying a linear voltage sweep to the deflection plates. This causes the electron slit image to be swept across the phosphor as a function of time. Spatial variations in the intensity of the phosphor image correspond to time variations in the electron beam intensity which in turn correspond to time variations in the optical signal. In this manner, the streak camera converts the temporal variation of an optical signal into a spatially resolved phosphor image.

The time resolution of the streak camera is determined by many factors¹. The "technical" resolution is determined by the ratio of the streak rate to the spatial resolution of the phosphor. Streak rates approach the speed of light, while a spatial resolution of approximately 10 microns is possible. This corresponds to an ultimate resolution of less than 100 femtoseconds. This is not observed in practice as several effects serve to degrade the the time resolution. "Chromatic" dispersion arises from the finite distribution of electron velocities. This can be minimized (but not completely eliminated) by using a large accelerating voltage. At high signal intensities there will be effects due to space charge within the beam. This debunching effect will tend to blur the image and degrade the time resolution. Finally, the time resolution will be limited by the duration of the

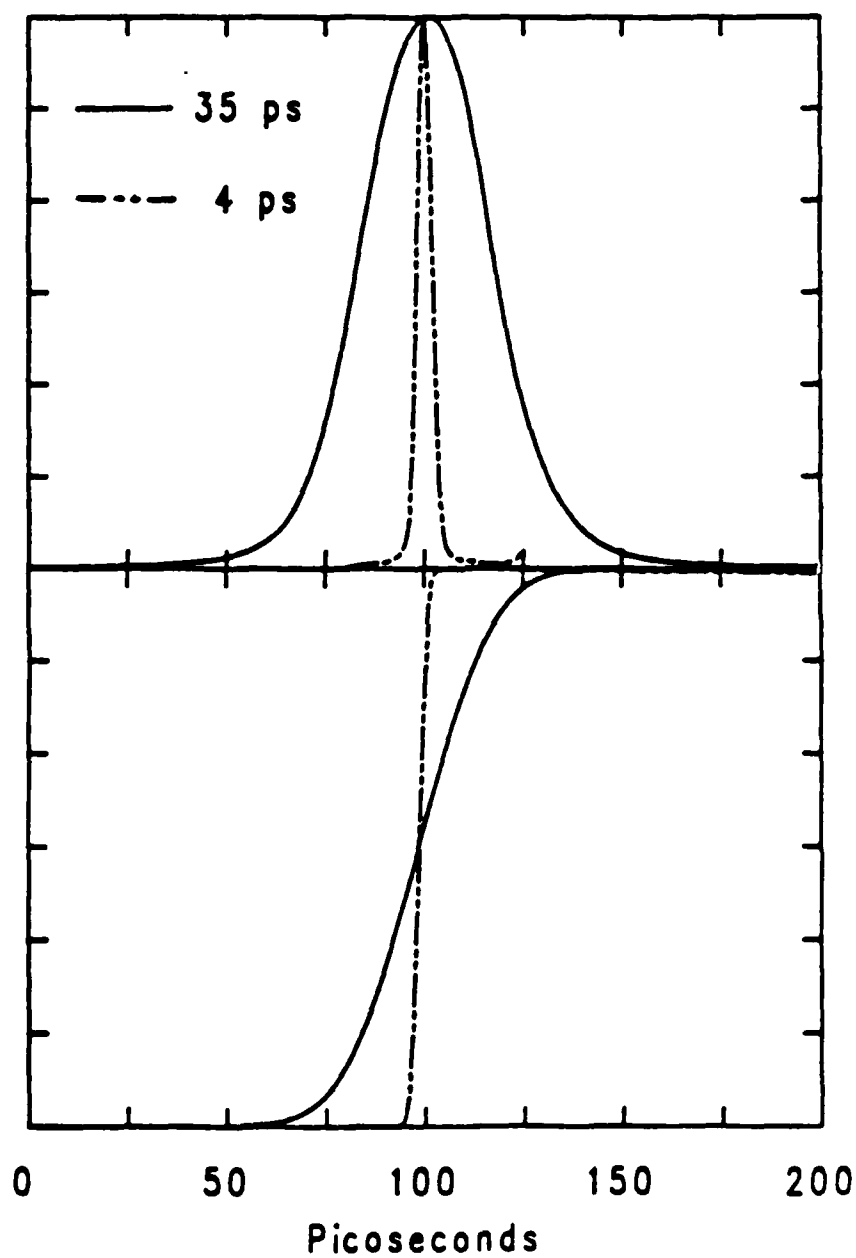


Figure 3.2. Pulse width and instrument response function with the fastest available streak speed. The solid curve shows the 35 ps average of 500 laser pulses, the dashed curve shows the slit image obtained with no voltage on the deflection plates. The lower curve shows the integral of the upper curve.

laser pulse, the finite width of the entrance slit, and the degree to which the phosphor image is degraded in the image intensifiers. These last effects appear to be the actual limiting factors in the existing system. The actual resolution of the system at the fastest streak rate can be seen in figure 3.2. This shows that the focussed slit image seen with no field on the deflection plates has a width of approximately 12 channels or 4 ps, while the laser pulse has a width of 35 ps. On this scale the slit function has essentially no effect on the observed pulse width. Only when slower streak speeds are used will the pulse width begin to be affected by the slit function. Deconvolution of the excitation pulse will result in a deconvolution of the slit function. When deconvolution is used, the resolution of the system is typically on the order of five channels.

The electronics associated with the ramp generation are another problem. As shown in the figure, the process begins with the laser pulse impinging on the photodiode. The resulting electronic signal is sent to a series of avalanche transistors which in turn generate the voltage ramp. Associated with this process are both a relatively long transit time (tens of nanoseconds) and an appreciable amount of jitter (tens of picoseconds). To compensate for the first of these effects, it is necessary to include many nanoseconds of optical delay between the trigger photodiode and the sample. Since the transit time varies with the streak speed, it is convenient to have an excess of optical delay which can be compensated with a variable electronic delay. Synchronization of the optical signal with the streak camera trigger is then accomplished without optical adjustment by varying the electronic delay of the trigger pulse; in practice, this corresponds to varying a length of coaxial cable.

The time jitter is a more serious problem, since it varies randomly from shot to shot. Unless corrections are made, it will interfere with efficient signal averaging. This is the reason for including the "prepulse" in the data, since it can be used as a time marker to provide the basis for such a correction. As described below, the signal averaging program identifies the prepulse and shifts the data accordingly before the data is summed. The

timing is adjusted so that the pulse arrives before the fluorescence, leading to data like that in figure 3., where there is a prepulse followed by the fluorescence data. It is important that the prepulse not overlap with the data itself, so the adjustment of the optical delay is important. The optimal spacing changes with the streak speed, so the optical delay must be changed whenever the timebase is changed. Note that other types of time markers can be used. For example, with absorption spectra, a system, based on the rising edge of a dye fluorescence signal is used. This produces equivalent results.

At the back of the streak camera, the signal consists of the weak emission emanating over a few milliseconds from the streak camera phosphor. It is necessary to amplify this emission and convert it to an electronic signal for digitizing and signal processing. This is accomplished with a fiber-coupled microchannel plate image intensifier (Hadland Photonics, Ltd. Imacon 20/30) optically coupled to an intensified, cooled 1024 channel photodiode array (Tracor-Northern, IDARSS 6300). Within a few tens of milliseconds after the laser has fired, all of the information associated with that laser shot will have passed through the image intensifiers and will be stored on the photodiode array. From this point on the problem becomes one of efficiently digitizing the photodiode signal, transferring the data to the computer, and correcting and summing the data.

2. Data Transfer and Correction

In a sense, the details of the data transfer are not important, since the results will be independent of signal processing hardware. As a practical matter the efficiency with which the data is transferred is extremely important. It is the factor controlling the rate at which the data is collected, and hence it determines the scope of experiments which can be carried out. There are a number of ways of transferring the data and the method used at present is not the most efficient possible. The hardware controlling the digitization and transfer of the data consists of a Tracor-Northern photodiode array controller (TN-1710), which includes a 12 bit A-D converter and a DEC LSI 11-2 microprocessor. This in

turn is connected to a DEC LSI 11-73 microcomputer which is used for correcting and summing the data. In the present system, the the photodiode array is read out and digitized five times after each laser shot at eight millisecond intervals. This rate is used, since it corresponds to the maximum A-D rate possible with this hardware. In particular, the 12 bit A-D performs a conversion every $8\ \mu\text{s}$, so that the 1024 channel diode array can be fully digitized in 8 ms. The five scans are summed by the LSI 11-2, a previously stored dark background is subtracted, and the data is stored in the LSI 11-2 memory. This is repeated for seven laser shots, and then the seven resulting datasets are transferred to the LSI 11-73 via a 9600 baud interface. In order to minimize the wear on the streak camera, a shutter is closed to block the laser whenever no data is being collected. Once transferred to the LSI 11-73, the individual datasets are corrected for the streak camera trigger jitter, and the nonlinearities of the time and intensity response, and then summed and stored. A suitably scaled version of the running sum is also generated and stored in a separate buffer. This is accessed by a DMA D-A converter (Data Translation Inc., DT2771) and displayed on Tektronix 2215 monitor oscilloscope.

The process results in an average data collection rate of 2.9 Hz, corresponding to less than one third the rate of the laser. The rate of data collection itself is not the limiting factor, as the the A-D can readily handle data at much higher repetition rates. In addition to this, the data collection is occurring simultaneously with the correction of the previous set of data. Since it takes approximately 230 ms to correct and sum a dataset on the 11-73 using the corrections described below, it is clear that the 11-2 has completed the data collection and is waiting for the 11-73 to finish the corrections before the data transfer can begin. The transfer time for the seven datasets is 770 ms, or 110 ms per dataset. The overall cycle time consists of the sum of transfer time and the correction time, that is 340 ms, or 2.9 Hz.

To increase the data collection rate it is necessary to improve both the transfer time and calculation time. The latter will be discussed below in conjunction with the normal

correction procedure. As for the former, it has been found that it is possible to reduce the effective transfer time to 8 ms per dataset by eliminating the LSI 11-2 from the data handling cycle altogether, and using a DMA transfer from the A-D converter to the LSI 11-73 instead. In this configuration the 11-2 serves only as a clock for gating the photodiode array exposure time and timing the A-D cycles. In its existing form, the controller can be made to operate so that the photodiode readout is synchronized with the laser shot. In this mode, the photodiodes are allowed to integrate the phosphor emission for the full phosphor lifetime (tens of milliseconds), so only one readout is required to obtain the entire dataset. At the end of the integration time, the photodiode controller begins reading the data out through the A-D converter. At this point the digitized outputs of the individual pixels, as well as the requisite synchronization pulses, are all readily accessible. They appear sequentially at 8 μ s intervals in the form of TTL signals which are readily buffered for external use. This rate is slow compared to the LSI 11-73 bus cycle time, so synchronization of the A-D output with the LSI 11-73 is relatively simple. To accomplish a DMA transfer it is necessary only that the 11-73 be ready and waiting for the transfer to begin when the integration time ends. The synchronization pulse can be used to initiate the transfer of each word and the 11-73 will have stored the data well before the next synch pulse arrives. That this is possible is not surprising, since such a transfer is precisely what is occurring inside the controller as the data is transferred to the 11-2. The minor preprocessing functions performed by the 11-2 (i.e. baseline subtraction) must now be handled by the 11-73. The requisite 1024 integer additions can be performed in less than 10 ms. To make full use of this data transfer method, it is necessary to be able to carry out the corrections in less than 80 ms. As shown below, this can be accomplished with a simplified correction scheme which does not significantly degrade the data quality.

To make the best use of the streak camera, extensive signal averaging is required. The dynamic range of a streak camera is a function of the desired time resolution. For

the work carried out here, where a time resolution of approximately 10 ps is desired, the effective dynamic range is around 200^5 . If better signal-to-noise is desired, it is necessary to signal average. Several corrections must be applied to the data in order for successfully signal averaging to occur. First, it is necessary to correct for the system dark signal. This is the simplest of the four corrections, since it corresponds to simply subtracting off a background signal. To obtain a suitable average background signal, all that is necessary is to collect a set of data with no light impinging on the streak camera photocathode. The resulting data will correspond to any background signals arising from the streak tube, the image intensifiers or the photodiode array. These datasets can be summed without correction, since they correspond to the actual background for the fixed channels.

The second correction to be made is for the nonlinearity of the streak camera time base. This correction is generated with the use of an etalon consisting of two flat, parallel 99% reflectors at a fixed spacing. A single laser pulse (usually the second harmonic) is introduced in the direction perpendicular to the reflective surfaces. 99% of the beam is lost at the first surface, and only 1% of the beam is transmitted by the second. The beam reflected by the second surface makes another round trip through the cavity, and another 1% pulse is generated. Continuing this process leads to a series of pulses with a gradually decreasing intensity and a time separation governed by the mirror spacing. The time interval between pulses can be calculated from the etalon spacing Δx and the speed of light, with $\Delta t = 2\Delta x/c$. After suitable attenuation, this pulse sequence is focussed onto the streak camera photocathode (via the prepulse optical system) and a large number of datasets are collected. The individual datasets resemble the sum shown in figure 3.3, although they are somewhat noisier. (The data in the figure represents a sum of 50 datasets. The only correction applied in the figure is to compensate for the timing jitter; the datasets were aligned on the basis of the first pulse on the left.) It is clear that the timebase is not linear, but varies by roughly 10%. A systematic correction

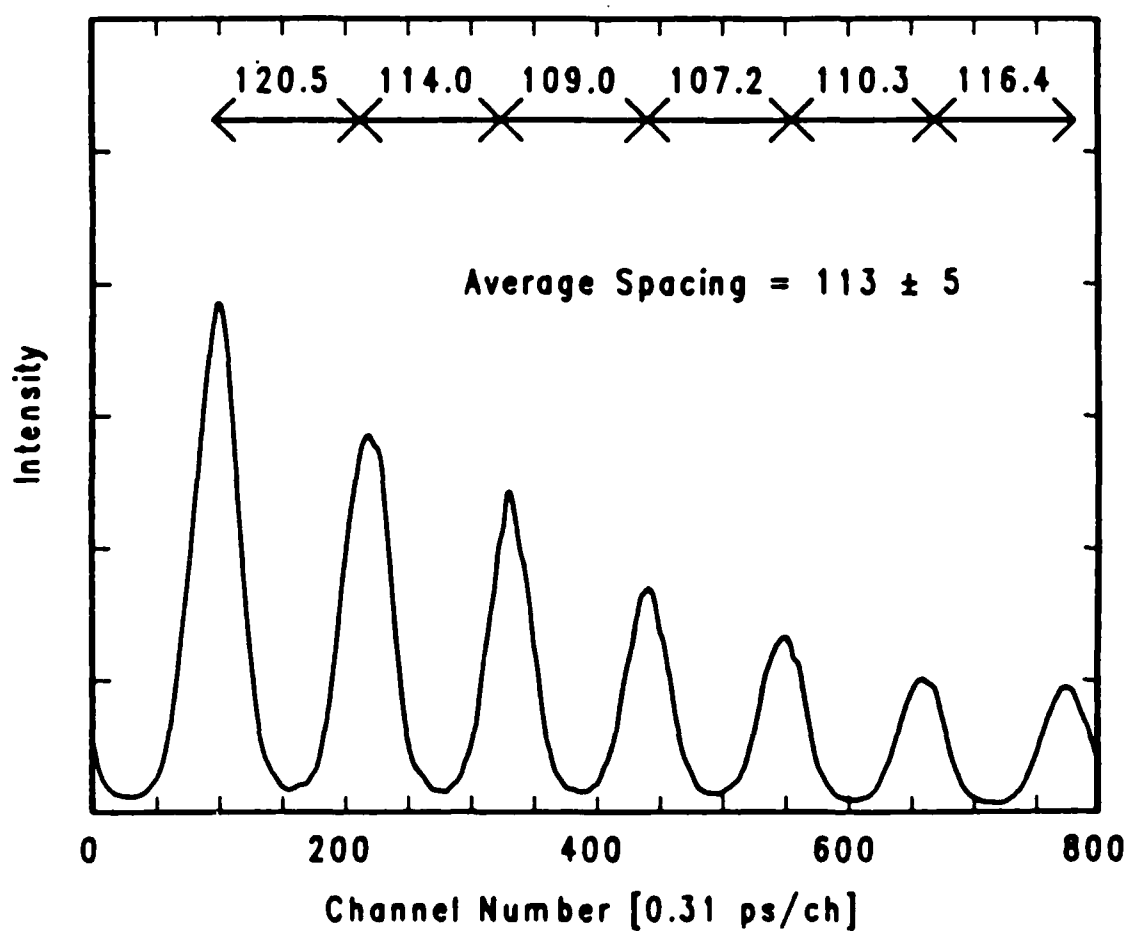


Figure 3.3. The sum of 50 uncorrected étalon traces. The data has been shifted for summing based on the left-most peak, but no timebase correction has been applied. Note that there is a systematic variation in the peak spacing due to pincushion distortion.

function can be obtained measuring the spacing (in channels) between all of the pairs of peaks in all of the datasets, and plotting these values versus the channel number at the center of each interval. This is shown in figure 3.4. Similar plots were made for all streak rates. Since the time interval between the peaks is known from the etalon spacing, this corresponds to a plot the local streak rate, $\Delta t / \Delta x$ as a function of channel number. Note that this required pulse pairs centered at all channels. This is a case where the streak camera jitter works to one's advantage, since the positions of the individual datasets will fluctuate considerably from shot to shot, giving the desired distribution. This fluctuation is sufficient at the faster streak speeds, but at the slowest streak speeds, it was necessary to vary the electronic delay to scan the full range of channels.

Once the streak rate $\Delta t / \Delta x$ is known as a function of channel, it is possible to linearize the timebase of the data. The data in figure 3.4 can clearly be approximated by a smooth function which corresponds to the reciprocal streak rate (dx/dt) as a function of x . This in turn can be integrated to give x as a function of t . Direct linear interpolation of the dataset can now be used to linearize the timebase. The time scale is divided into units corresponding to the average streak rate, and suitable linear combinations of the original data based on the function $x(t)$ become the new data. In general, no more than three old datapoints contribute to the new datapoints. This generates a dataset with the same number of channels as before, but with a fixed number of picoseconds per channel. This correction procedure is equivalent to multiplying the dataset (a column vector), by a band-diagonal correction matrix (T) with no more than three non-zero elements per row. The timebase was found to be quite stable, and it changed only when the avalanche transistors in the ramp generator were changed. It was not measured on a regular basis unless there was some evidence that it had changed.

The next correction to be applied compensates for the nonlinear intensity response of the detection system. This is generated by recording the time- and baseline-corrected response of the system to an essentially constant signal. Such a signal can be obtained

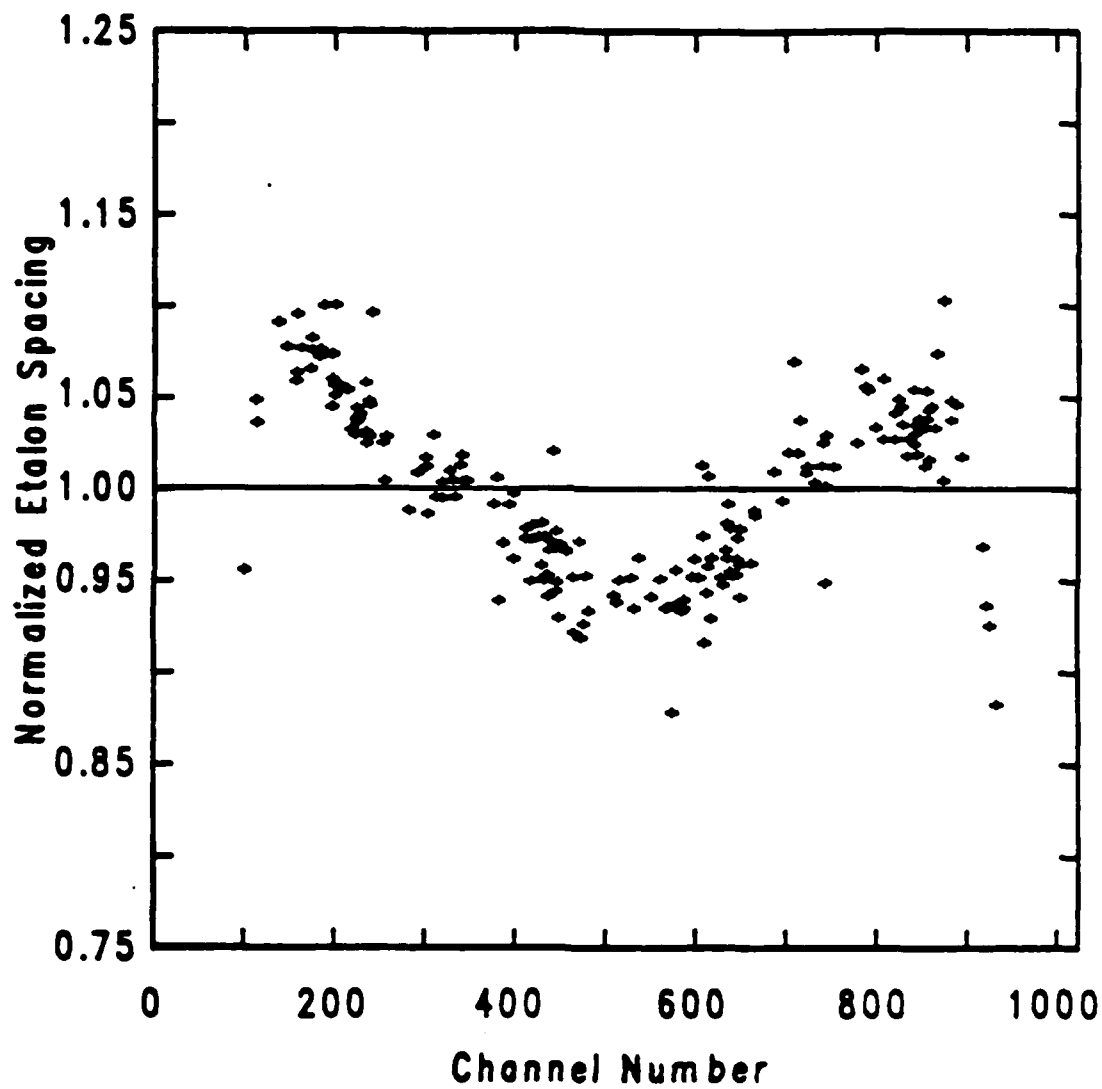


Figure 3.4. Normalized étalon spacing versus channel number. This corresponds to a plot of the reciprocal streak rate (dx/dt) as a function of x .

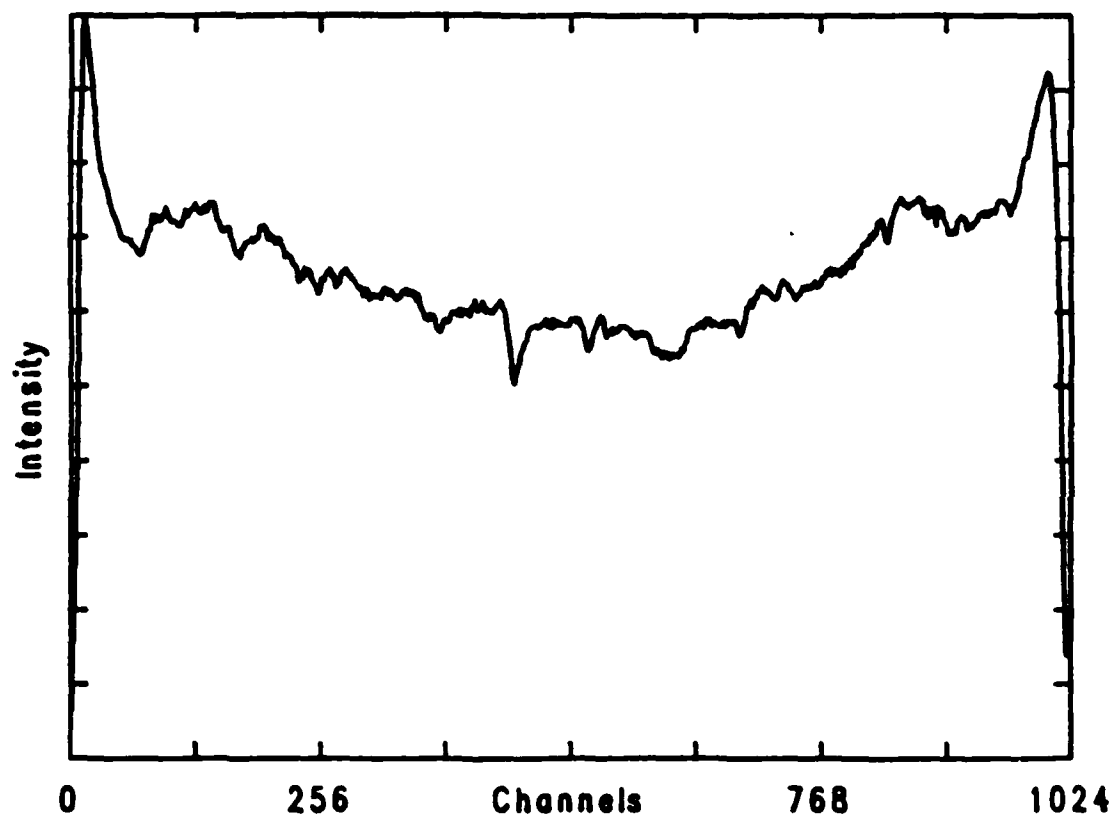


Figure 3.5. Data used for intensity correction. This shows the sum of 1000 datasets of the decay of the fluorescence of RUTBY, several nanoseconds after excitation. The streak rate is 1.97 ps/channel.

by looking at the fluorescence emitted at long times from a sample with a fluorescence lifetime much longer than the streak time. An ideal solution for this purpose is an aqueous sample of the ruthenium(II) tris-(2,2'-bipyridine) complex (RUTBY), which absorbs at wavelengths below 550 nm, and has a red emission with a lifetime of 600 ns. In some instances, notably when the fourth harmonic was used for excitation at a fast streak speed, the emission from this compound was too weak to be used. In this case a deoxygenated sample of 9,9'-bianthryl in butanol with a lifetime of 27 ns was used instead. The procedure followed for generating these datasets was to take each dataset, subtract the averaged baseline and right multiply the resulting difference by the time correction matrix T . These datasets were summed with no further correction, giving a result like that shown in figure 3.5. This data is supposed to correspond to an exponential decay with a known lifetime τ . To correct for this, each datapoint is multiplied by $\exp(jR/\tau)$ where j is the channel number, R is the streak rate and τ is the (known) fluorescence lifetime. Ordinarily, the lifetime greatly exceeds the streak range, and these correction rarely exceed 10%. These corrected values are averaged, and a table of corrections corresponding to the ratio of the average value to the individual corrected values is obtained. These values are placed along the diagonal of a square matrix, leading to an intensity correction matrix I . The overall correction matrix C is given by the product IT , which has the same form as T . Only one matrix multiplication is thus necessary to linearize both the time and intensity response of the system, and that matrix is band-diagonal so that it only involves roughly $2N$ multiplications. The intensity correction was less stable than the timebase correction, and it varied somewhat from day to day. This type of correction dataset was measured every time the system was used, and a new correction matrix was generated.

At this point the dataset is fully corrected for the nonlinearities of the system, and the process of including the dataset in the running average can begin. To do this, it is necessary to find the prepulse and shift the data accordingly, to test the dataset to make sure it has no unacceptable features, and to add data to the sum. This process is based on

a number of user-entered criteria. The first thing to be specified is the range of channels in which to look for the prepulse. This width w depends mainly on the degree of jitter, which in turn depends on the streak rate. For a streak rate of 1.97 ps/ch, the range of 100 to 200 was normally used. This choice avoided the poorly calibrated edge channels, but still left more than 700 channels for data. The process of testing the data begins by finding the most intense datapoint in the specified range. If this intensity is less than a specified value, the dataset is rejected as having too little intensity. If it is acceptable, then the width (FWHM) of the pulse is found by searching away from the peak in both directions until datapoints with less than half the intensity of the peak are found. The average off these two channels is defined to be the prepulse center. If the pulse is less than three channels wide, it is presumed to be electronic noise, and is rejected. If a pulse is wider than a specified width, typically 50 channels, it is also rejected. This rejects anomalously wide pulses, and also minimizes the chance that the data will be mistaken for the prepulse. A final test is whether there is any intensity in a specified region typically 50-70 channels above the peak. This is supposed to be the "valley" between the pulse and the data, and intensity in this region usually indicates a prepulse with an anomalous shoulder. Such pulses are also rejected. If a dataset is acceptable, it is shifted down so the center of the prepulse is located at the lower end of the search range, truncated at channel $(1024-w)$, and added to the running sum. This process continues until a specified number of datasets have been accumulated.

The effectiveness of the correction and signal-averaging procedure in eliminating time and intensity nonlinearities can be seen in figure 3.6 and figure 3.7. The first of these figures shows the same data as shown in figure 3.3 after it has been corrected and summed using the standard correction scheme. The data was treated as if it were a fluorescence dataset, with the left-most pulse serving as the prepulse. The effectiveness of the timebase correction is clear, since the systematic variation in the peak spacing seen in figure 3.3 has been eliminated. The effectiveness of the intensity correction can

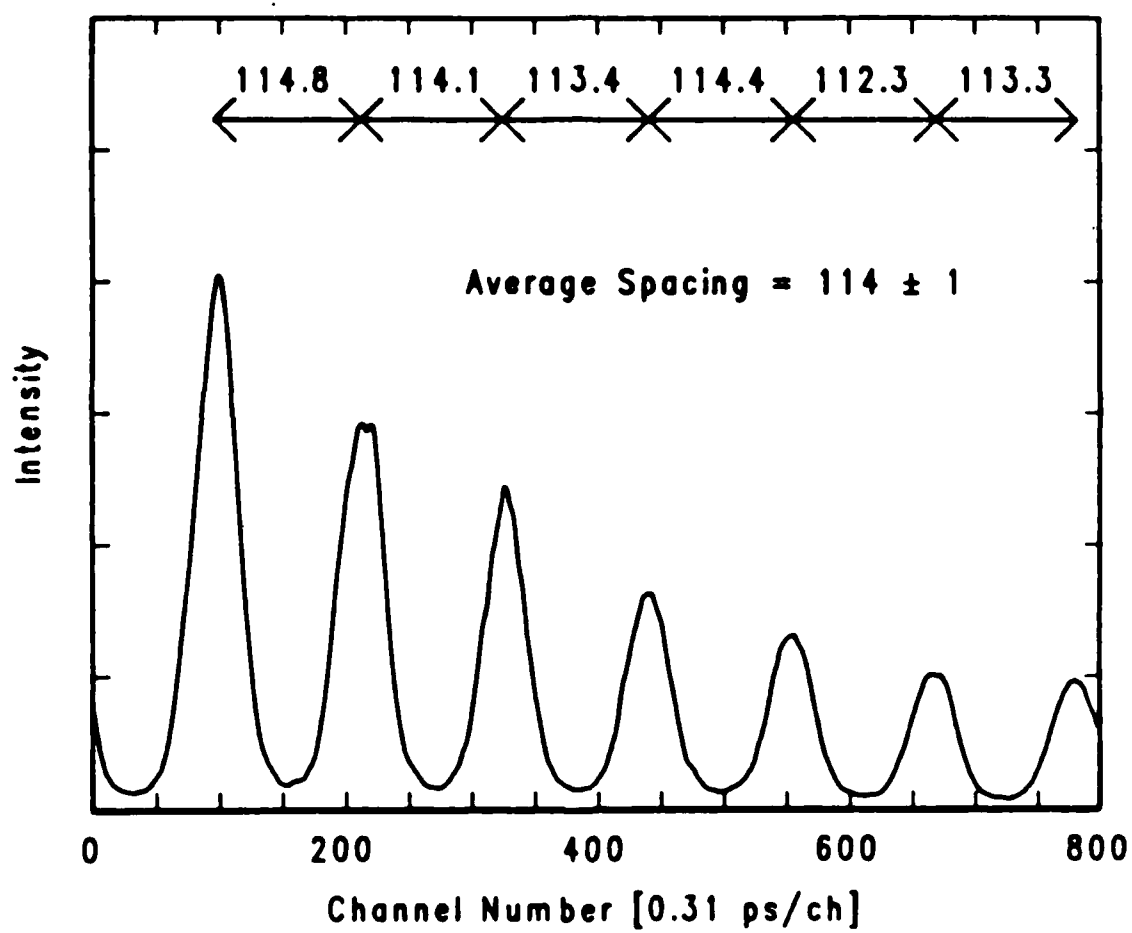


Figure 3.6. Corrected étalon traces. This is the same data as in figure 3.3, treated as a fluorescence dataset. The left pulse is treated as the prepulse in the shifting process.

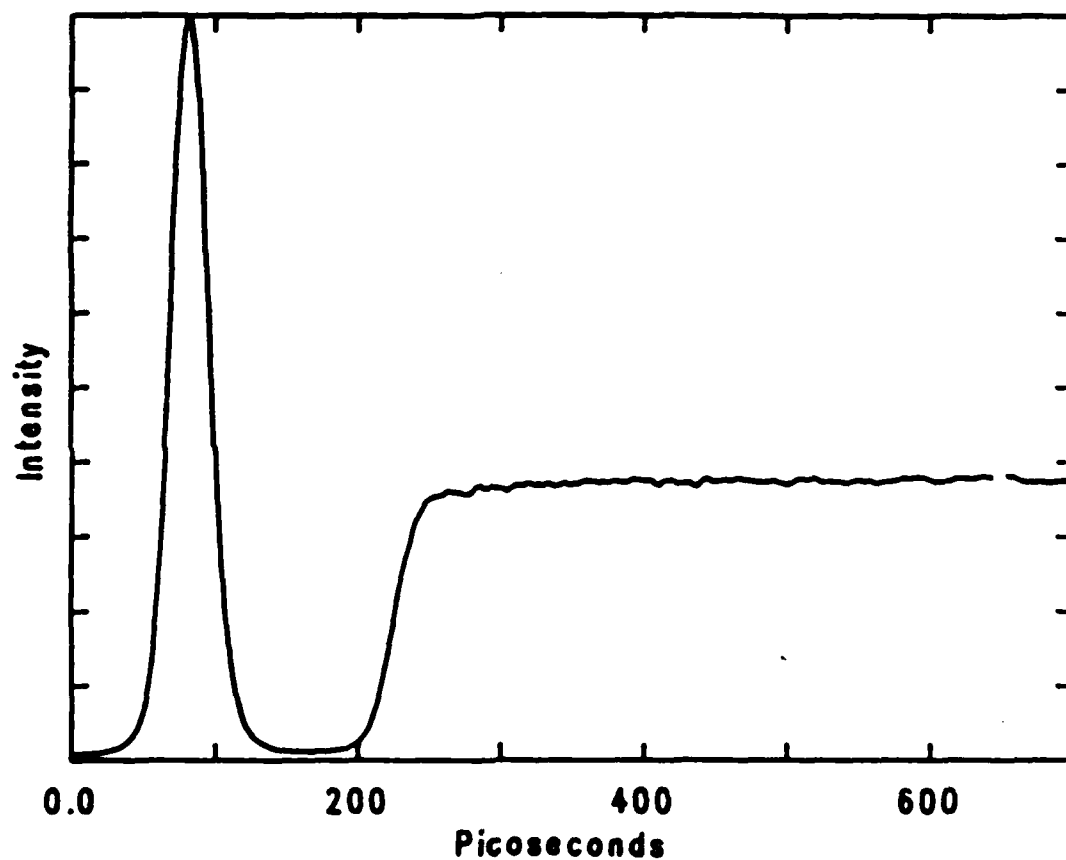


Figure 3.7. Corrected fluorescence decay curve for aqueous RUTBY. The observed flat decay is consistent with the 600 ns lifetime of this compound. Note that the intensity variations seen in figure 3.5 have been eliminated.

be seen in figure 3.7, which shows the time-resolved emission of an aqueous solution of RUTBY. The intensity variations seen in figure 3.5 have clearly been eliminated, and the decay curve appears absolutely flat, as expected from the 600 ns lifetime.

Before leaving the subject of the correction procedure, it is of interest to see how it can be made more efficient. At present, the 12 bit data is converted to real form, and all the multiplications required for the correction are made using Fortran with real numbers. This preserves the nominal precision of the data, but takes a relatively long time. There are two ways of shortening the data correction process. Either the correction algorithm can be simplified by means of a less sophisticated interpolation procedure or the precision of the data can be reduced so that the calculations can be done more rapidly using integer multiplication.

The present interpolation algorithm takes linear combinations of two or perhaps three original datapoints to produce each corrected datapoint. Equally accurate corrections should be obtainable by considering only the data channel which makes the largest contribution to the corrected point. Rather than interpolating the data, this procedure is equivalent to "stretching" the old grid to match the new one. The time correction in this case corresponds to multiplying the data in each channel by the ratio of nominal channel width to the real channel width. Since the two grids are not the same it is necessary to occasionally adjust the grid by one step to maintain alignment. This corresponds to occasionally repeating a datapoint when the original data is too sparse or neglecting a point when the data is too dense. From figure 3.4, it is clear that the channel width is generally within 5% of the average, so no more than one channel in 20 will be affected. Furthermore, the regions with the greatest channel density, where most of the data neglect will occur, are at the edges of the dataset, where the time calibration is poor in any case. The effect of using the simplified correction will be to neglect perhaps 10 datapoints near the center of the image, and perhaps 20 more at the edges while repeating a comparable number of points over the rest of the image. When data corrected using the simplified

procedure was compared with data collected under identical conditions using the standard corrections, the results are virtually indistinguishable.

A further simplification can be achieved by truncating the data and the corrections to 8 bit accuracy, and using integer multiplication in the corrections. The dynamic range of a streak camera⁵ is ~ 200 , so digitizing the data to only 8 bits is quite reasonable. (A fast method for preserving the full 12 bit accuracy is to shift the data into the 12 most significant bits, to scale the corrections to be $2^{13} < C_{ij} < 2^{16}$, and to save the overflow word rather than the data. This is relatively fast, but it is complicated to program and is probably unnecessary.) On the LSI 11-73, integer multiplication is almost an order of magnitude faster than real multiplication, and 1024 multiplications take only 16 ms. This indicates that the correction procedure can be implemented quite rapidly. The times required to carry out the full process of data collection and correction are estimated to be as follows: Data transfer, 8 ms; baseline subtraction (1024 additions), 10 ms; time and intensity corrections (1024 additions and 1024 multiplications), 26 ms; Identifying the prepulse (roughly 1000 comparisons), 10 ms; and data summing (1024 additions), 10 ms. This gives a cycle time of 64 ms, for a potential repetition rate of 15 Hz. The exact cycle time depends on the details of the program.

Note that the time required for the monitor scope has been neglected so far. The time required to dump the data to the scope is only about 3 ms, so the screen can be updated after every shot. Rescaling the data for display is rather time consuming, and would slow the collection process. Rather than updating the display on every shot, it is possible to do so only on laser shots which are unacceptable. This can be accomplished by testing the first 200 or so channels of the dataset for peak intensity before the data is corrected. If no pulse is present and the dataset is invalid, the time usually spent on the corrections can be used to update and normalize the display register instead. Since some of the datasets are always unacceptable, this means the display register will be updated relatively often. From an experimental point of view, if the data is so good that the

display is not updating, it would only be necessary to block the beam momentarily to obtain an updated record.

If 15 Hz is still too slow, still another shortcut is possible, that of lumping the data in groups of two or three to decrease the number of channels in the calculation. This can be incorporated into the baseline subtraction step, so that all subsequent steps are proportionally shorter. This sounds like an excessively drastic simplification, but since the slit image is 12 channels wide, it will have essentially no effect on the final data. In fact, it will smooth the data, improve the signal to noise and (if done correctly) eliminate the need to neglect or repeat datapoints in the correction procedure. With this system a repetition rate of 25 Hz appears to be feasible. This is comparable to the limits imposed by the laser repetition rate and by the lifetimes of the image intensifier phosphors.

All of this could have been carried out with relatively minor and inexpensive modifications of the existing hardware. Although this method takes several shortcuts as compared to the present method, it appears to have the potential of producing a significant increase in the data collection rate without sacrificing the quality of the results. If the modifications described here could have been carried out, and the laser repetition rate increased, the data collection rate would have been increased by an order of magnitude. At that rate, the slowest step in data collection would be the time required to change the filters and adjust the signal intensity between samples. Methods for automating this step to make a true scanning spectrometer are conceivable (e.g. a filter holder resembling a slide projector), but would only make sense in conjunction with the higher data collection rate. The relative slowness of the current system gave anyone involved in collecting data many hours to contemplate such system renovations. Unfortunately, by the time all of these modifications had been worked out, the project had entered a declining phase where it was impossible to justify spending any more time on system improvements.

3. Results

The discussion so far has centered primarily on the streak camera and signal processing system, with little emphasis on the sample itself. Figure 3.1 shows the sample and associated hardware in detail. The pump beam first passes through a Glan-Thompson prism to ensure that it is vertically polarized. The beam is then brought to a cylindrical focus near the center of the sample cell with a 50 mm focal length cylindrical lens. The sample is contained in an ordinary 1 cm quartz cuvette. Depending on the sample, either stoppered cuvettes or vacuum cuvettes were used. The sample itself was placed in a temperature-regulated copper block and stirred magnetically. A temperature controlled water recirculator (Neslab) was used to vary the sample temperature from -15 to 80 C. As shown in the figure, the pump beam enters the sample near the front face of the cuvette, and the fluorescence is sampled a short distance from the edge of the cuvette. This arrangement minimizes the effect of cuvette fluorescence and fluorescence reabsorption by the sample while sampling the most intense region of the emission. Normally, samples with an optical density greater than two were used, so that more than 90% of the light was absorbed in the first millimeter of the sample. This maximized the signal and helped to suppress nonlinear processes such as stimulated Raman scattering.

The emission is collected at $f/2$ using a 50 mm focal length quartz lens. Fast collection optics have the advantage of efficiently sampling a small volume of the emission. The short depth of field minimizes loss of resolution due to pathlength variations. The collimated fluorescence passes through a polarizing prism. As discussed below in connection with 9,9'-bianthryl, it is necessary to collect the sample at "magic angle" polarization (54.7 degrees from vertical) to avoid the effects of rotational diffusion in the sample. The detection polarizer could also be varied to measure the rotational anisotropy, as discussed below.

The fluorescence then passes through a series of filters to block scattered laser light, to attenuate the fluorescence and to select the desired bandwidth. A variety of colored glass filters (Schott and/or Corning) were used to block the scattered laser light or to select

relatively broad bandpasses. For narrow bandwidths, 10 nm interference filters (Corion Inc.) were used. A vastly more elaborate optical system in which the filters would be replaced with a double monochromator with subtractive dispersion was considered. In addition to allowing the use of narrower and more readily adjustable bandwidths, it would also make it possible to have an all-reflective, achromatic collection system. It was not constructed, however, and bandpass filters were used for all the work described below. The collimated and filtered emission is now transferred to the streak camera exactly as shown in figure 3.1.

The signal averaging scheme described above is all based on simply summing the data to obtain an average. As described below for absorption spectroscopy, this is not always the correct procedure, and it is important to show that in the case of emission it is in fact correct. The emission signal $I(t)$ from a single laser shot will be given by

$$I(t) = kAEP(t) \quad (3.1),$$

where A is the sample optical density, E is the energy of the pump pulse and k is a factor which incorporates the collection geometry and the spectral bandwidth. $P(t)$ is fluorescence decay convolved with the excitation pulse profile. If various spatial fluctuations are ignored, the only one of these quantities which varies from shot to shot is E . When many shots are summed, the result for $P(t)$ will be

$$P(t) = \frac{\sum I(t)}{kA \sum E} \quad (3.2).$$

Thus the desired quantity $P(t)$ will be proportional to the simple sum of the datasets. If this seems trivial, it should be compared with the results given below for absorption spectra.

The process of analyzing the observed fluorescence decays depends in large measure on the system under consideration and is really separate from the process of data collection. In general, the procedures used consisted of fitting the data to multiexponential decays, and deconvolution of the excitation pulse. These procedures, as well as the

process used for transforming the time-resolved decays and steady-state emission spectra into time-resolved emission spectra are discussed below in connection with 9,9'-bianthryl and will not be discussed here.

D. Time-Resolved Absorption Spectroscopy

1. Introduction

The system described so far makes it relatively simple to obtain time resolved emission data. Unfortunately, the number of systems which undergo significant changes while in the excited state is relatively small. This is why the bulk of all studies done with time resolved emission have concentrated on proton transfer, electron transfer and solvation. They are among the very few processes which occur in the excited state manifold. The normal pattern in a system undergoing photochemistry is that the chemically interesting step (e.g cleavage to form free radicals or reaction with solvent) occur with the simultaneous deactivation of the molecule. Thus, with fluorescence it is usually only possible to monitor the unreacted molecules. Studying fluorescence quenching can be useful, since it reflects the relative rates of the radiative and nonradiative processes, but it would also be valuable to be able to look at the ground state products being formed. This is especially true in systems such as nitromethane where absolutely no emission is observed, despite an extensive free-radical photochemistry. In order to overcome this limitation, a system for time resolved absorption was constructed.

Picosecond absorption spectra can be measured with either pump-probe methods or with a streak camera. There are two variations on the first approach. In one technique, the broad-band continuum generated by focussing a picosecond laser into a non-fluorescent solvent such as water, is used for probing². The major advantage of this method is that, when used in conjunction with an array detector, absorption spectra can be measured over a broad frequency range in a single shot. This advantage is offset by the low signal-

to-noise levels typically seen with this method, a result of the fact that the continuum itself is very weak and varies considerably from shot to shot. This is primarily because the continuum arises from a poorly defined combination of nonlinear effects such as self-phase modulation and parametric scattering⁶. Because of this it depends very strongly on such poorly-controlled factors as the exact beam power and spatial profile. This has been overcome to some degree by using a double beam technique where both the attenuated and unattenuated intensities are measured on each shot, allowing corrections to be made for these fluctuations. Even when this is done, the signal-to-noise is often quite poor.

A second variation of this technique is to use a laser beam as a probe source. These methods tend to offer relatively large signals and high sensitivity, although there can be some difficulties associated with coherent artifacts arising from higher order interactions between the two beams⁷. If the pump and probe beams are the same frequency, ground state recovery experiments are possible. In this case the pump beam must be sufficiently intense to partially depopulate the ground state, decreasing the absorptivity of the sample. The rate at which the sample transparency returns to its initial value is then determined. This is commonly done, although it provides a rather limited amount of information, and can only be applied to reversible systems. It is also possible to use a second laser frequency as the probe beam. Many authors have considered the case of pumping with one laser harmonic and probing with another². This is another workable but limited technique, since it is difficult to assess the true nature of the spectral changes occurring with a limited set of probe frequencies. Clearly it would be desirable to have a continuously tunable source of probing light. This can be done using two synchronously-pumped dye lasers⁴ or by using a tunable parametric source as a probe beam⁸. Using the OPS, it has been reported that 10^{-4} absorption changes can be detected this way. In view of the work which had already been carried out with the OPS, this was a very tempting option for an absorption system. Most of the delay hardware and electronics would be precisely the same as for a Raman system; if a new Raman system had been built, there would have

undoubtedly been a provision for absorption work as well. However, since most of the required Raman-related hardware and software were not available, a method based on the streak camera was used.

The system which was actually constructed was an outgrowth of the time-resolved emission system, and uses the streak camera to measure the time dependent attenuation of the fluorescence of a dye solution. This is essentially a pump-probe experiment with time-resolved detection. The first pulse excites a dye solution. The rising edge provides the marker pulse and the subsequent emission is used as a probe beam. A second, delayed pulse is used to excite a sample in the beam path of the fluorescence. The sudden attenuation of the fluorescence due to excited-state absorption can be seen in the streak camera output. A major advantage of the system is that most of the required hardware and software was already in place for the emission system. Because of this the system was assembled fairly quickly with a minimum of unforeseen difficulties. Since the system shared a great deal of hardware with the streak camera system, there was the possibility that the two systems would interfere with each other. This was not the case, and it was generally possible to switch between the two modes of operations in a few minutes. Although it has a number of shortcomings, and is not as sensitive an OPS based system would be (a lower detection limit of approximately .01 optical density was achieved), it has made it possible to collect useful absorption data relatively easily.

2. Hardware and Optics

Figure 3.8 shows the optical system used for the combined emission and absorption system. As shown the system is the mirror image of that in figure 3.1. All the optics before the reflector [A] are exactly as described above and all the electronics used to trigger the streak camera and the computer remain unchanged. If the reflector [A] is installed and the emission sample is placed at the focus [B], the third harmonic beam will be directed into the sample, the prepulse will go into the streak camera, and the

Figure 3.8. Optical system for emission/absorption spectrometer. The two beams coming in from the top left of the figure are the same as shown in figure 3.1 after the Pellin-Broca prism. If the reflector [A] is in place, the third harmonic beam will be sent to the focus [B] where an emission sample would ordinarily be; the prepulse will go to the streak camera as before (note that this drawing is a mirror image of figure 3.1). If reflector [A] is removed, the emission spectrometer will be disabled, and the beam will go to the absorption system. If the reflector [D] is removed, then the beamsplitter [C] directs ~90% of the beam to the sample, and 10% to the dye cell [E]. If the reflector [D] is installed, the dye will be excited by the second harmonic beam. In either case, the fluorescence is imaged through the sample, refocussed at [B] and sent into the streak camera. The beam passing through the sample is mixed with and the separated from the fluorescence with a pair of dichroic reflectors. See the text for details.

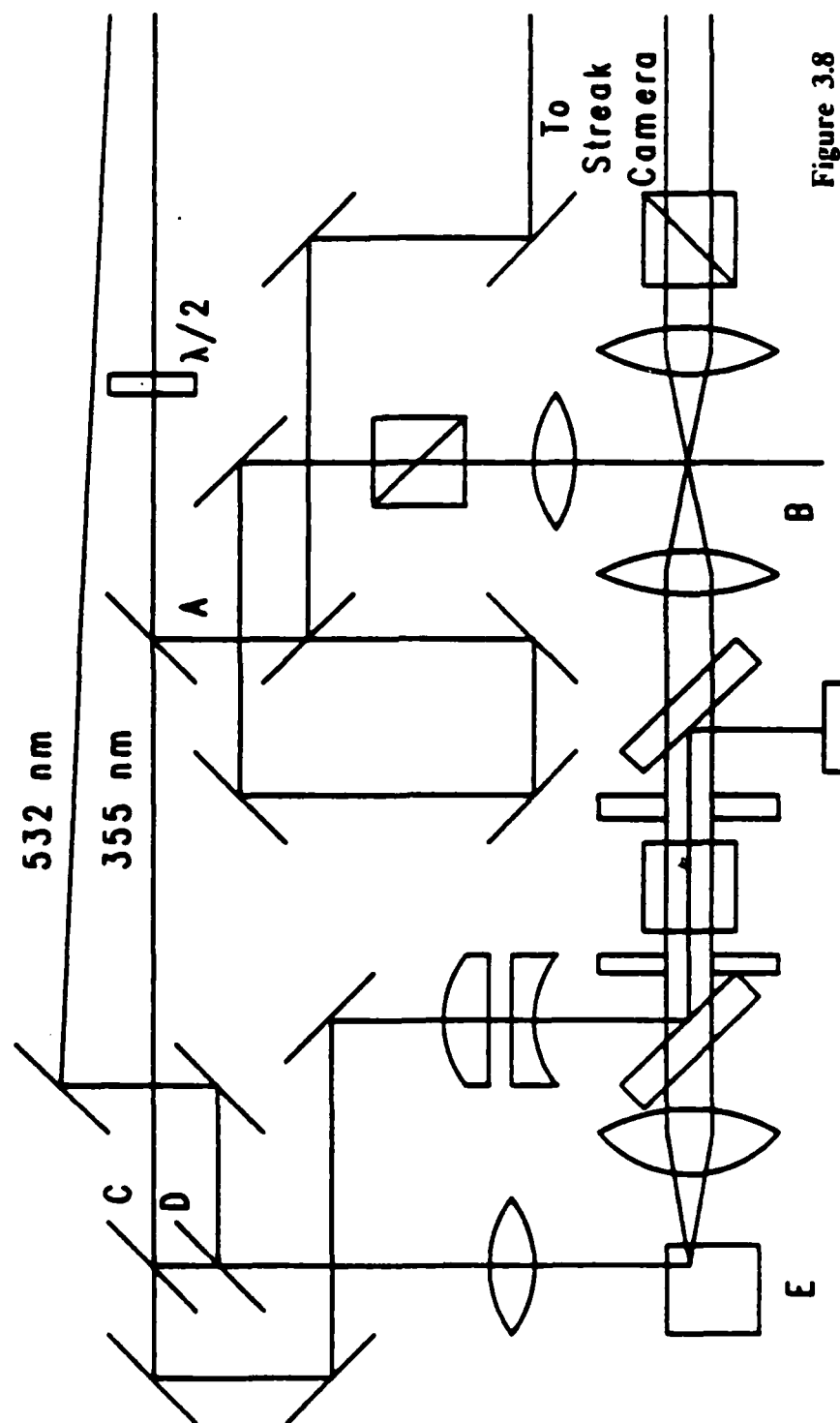


Figure 3.8

system can produce emission spectra exactly as described above. If the reflector and sample are removed, then the beam will continue into the remainder of the optics and absorption measurements can be made.

The vertically polarized third harmonic beam is split at the beamsplitter [C] to form the two excitation beams. Approximately 90% of the beam is transmitted by the beamsplitter and is passed through a short optical delay to form the pump beam. The beam is reduced through the telescope to a diameter of approximately 3 mm, brought into parallel with the probe light by means of a pair of dichroic reflectors, and passed through the 3 mm apertures and the sample. The sample itself consists of a strongly absorbing solution (see below) held in magnetically stirred, 1 cm pathlength quartz cuvette [E]. After the sample, any remaining pump beam is deflected with a second dichroic reflector. Note that a reflector is used rather than an absorbing filter to avoid any artifacts which might arise from excite-state absorption in the filter. Several additional UV absorbing filters were placed after the dichroic reflector to make absolutely certain that it was not possible to inadvertently focus the pump beam into the streak camera.

A second exciting beam is used to excite the dye solution. Two different beams can be used. If the reflector [D] is removed, the the third harmonic beam ($\sim 100 \mu\text{J}$) from the beamsplitter [C] is sent to the dye solution, while if the reflector is in place, the ($\sim 1 \text{ mJ}$) second harmonic beam will be used instead. For probe wavelengths longer than 532 nm, second harmonic excitation is clearly preferable. It is better matched to the absorption spectra of red-emitting dyes and the more intense beam produces correspondingly more fluorescence. At shorter wavelengths, third harmonic excitation is necessary. Since the absorption signal will ultimately be proportional to the intensity of the pump beam, only a small fraction of the beam can be diverted for dye excitation. As a result, the fluorescence obtained this way is an order of magnitude weaker than that obtained with the second harmonic. Fortunately, the sensitivity of the streak camera improves greatly at shorter wavelengths, largely compensating for the weaker fluorescence intensity.

In either case, the excitation beam is focussed into a strongly absorbing dye solution contained in a magnetically stirred, 1 cm pathlength quartz cuvette. The beam is typically absorbed in less than 1 mm. The resulting fluorescence is then collected with a 12 mm aspheric lens and passed through the aperture into the sample. The apertures ensure that pump and probe signals are spatially overlapped. The fluorescence emerging from the sample is brought to a focus where the emission sample would ordinarily be. From here on the system is optically identical to the emission system. The probe beam is vertically polarized, so monitoring the dye signal through a magic angle polarizer will compensate for polarization effects just as it did in emission. Wavelength selection is accomplished with the same bandpass filters used in emission.

It is clear that for this method to work correctly a suitable dye solution must be available. There are several features which a successful dye solution must have. It is extremely important that the dye exhibit a sharp risetime so that the leading edge can be unambiguously identified, since this is used as the time marking pulse in the shifting procedure. This is usually not a problem, since relatively few compounds exhibit slow fluorescence risetimes. Once initiated, the dye emission should decay slowly across the timescale of interest. It is not important that the decay be exponential, merely that it be smooth and reproducible. Initially, several unsuccessful efforts were made to use solutions of the more common laser dyes, such as rhodamine 6G as probe sources. In general, the very same features which make these dyes good laser dyes made them into poor probe sources. Laser dyes generally combine a short lifetime with a narrow emission band to produce relatively high gain. In extreme cases (e.g. solutions of Rhodamine 6G) an ordinary cuvette can function as a laser resonator, driven by the Fresnel reflections at the parallel cuvette surfaces. Such lasing is extremely undesirable, since it rapidly depletes the excited state population, leaving only a very weak fluorescence decay. This problem could be avoided by blocking two of the cuvette surfaces with a thin piece of teflon. Unfortunately, even in the absence of a laser resonator, most laser dyes exhibit

large amounts of amplified spontaneous emission (ASE). This appears as a sharp spike at the leading edge of the fluorescence decay with a large and randomly fluctuating intensity. The maximum allowable signal intensity will be governed by the ASE, which unfortunately leaves only a relatively weak signal for the absorption probe.

The solution to this problem was to make use of a long-lived fluorescing compound as a sensitizer. This compound absorbs the pump pulse, and then slowly transfers energy to a suitable short-lived laser dye which then emitted the desired wavelength. When the second harmonic was used as the dye excitation source, Uranine, a fluorescein dye with a lifetime of approximately 10 ns was used as the sensitizer. By itself, this compound exhibits the usual undesirable features of a laser dye. However, if a second dye with a slightly redder spectrum is added to the mixture (in this case rhodamine 6G), it tends to reabsorb the emission, quenching the ASE and giving a reasonably smooth decay. The emission could be shifted further into the red by adding other laser dyes such as cresyl violet or Nile blue to the mixture. Sufficient emission intensity could be achieved at any wavelength out to 700 nm. For third harmonic excitation, 9,9'-bianthryl was found to be an excellent sensitizer. As described in the following chapter, alcoholic solutions of this compound do exhibit finite fluorescence risetimes at some wavelengths but this was not found to be a problem. It is more important that the compound has a long lifetime (10–40 ns) and does not exhibit any ASE. Bianthryl (~ 1 mM in ethanol) works quite well by itself as a probe source between 390 and 460 nm. The combination of a high quantum yield, moderate solubility and long lifetime are almost ideal. Reasonably intense sources centered on any desired wavelength from 400 to 550 nm can be achieved by adding a laser dye with the desired emission peak (typically a coumarin dye, $\sim 10^{-3}$ M in methanol) to the bianthryl solution. These solutions are prepared by trial-and-error methods, with the dye solution being added dropwise to the bianthryl solution until a suitable emission decay is found at the desired wavelength. Many other compounds could undoubtedly be used as sensitizers. All that matters is that the compound have a long fluorescence

lifetime, a high quantum yield, a low laser gain and a reasonable solubility in alcohols.

3. Data Handling

The method used for treating the data in absorption is somewhat different than that used in emission. In emission signal averaging consisted of summing the data itself; in absorption it is necessary to sum the logarithm of the data instead. This is what one might expect from a naïve application of Beer's law, although the situation for excited-state absorption is somewhat more complicated, since the concentration of excited molecules varies in both space and time. Consider the case depicted in figure 3.9. A pump and a probe pulse with intensity envelopes $I_P P(z, t)$ and $I_R R(z, t)$ are propagating in the z direction through a sample of length ζ beginning at the point $z = 0$. The sample, with a concentration C and a ground-state absorption cross-section σ at the pump frequency, is initially transparent at the probe frequency. Absorption of a pump photon gives rise to an absorbing excited-state; the absorption cross-section of this excited state decays as the function $w(t)$, which includes any intramolecular relaxations as well as the excited-state lifetime. In general, this is the quantity of interest. Now, assume absorption in both the ground and excited states is linear and that ground-state depletion is never a significant problem (the validity of these assumptions is discussed below). In this case, for $0 < z < \zeta$, the excited-state absorptivity of the sample $\alpha(z, t)$, is proportional to the convolution of the pump pulse and the decay function,

$$\alpha(z, t) = I_P \sigma C e^{-\sigma C z} \int_{-\infty}^t P(0, \tau) w(t - \tau) d\tau \quad (3.3).$$

The attenuation of the probe beam is given by

$$\frac{\partial R(z, t)}{\partial z} = R(z, t) \alpha(z, t) \quad (3.4);$$

this can be integrated over the sample length to give

$$\ln \frac{R(0, t)}{R(\zeta, t)} = \int_0^\zeta \alpha(z, t) dz \quad (3.5).$$

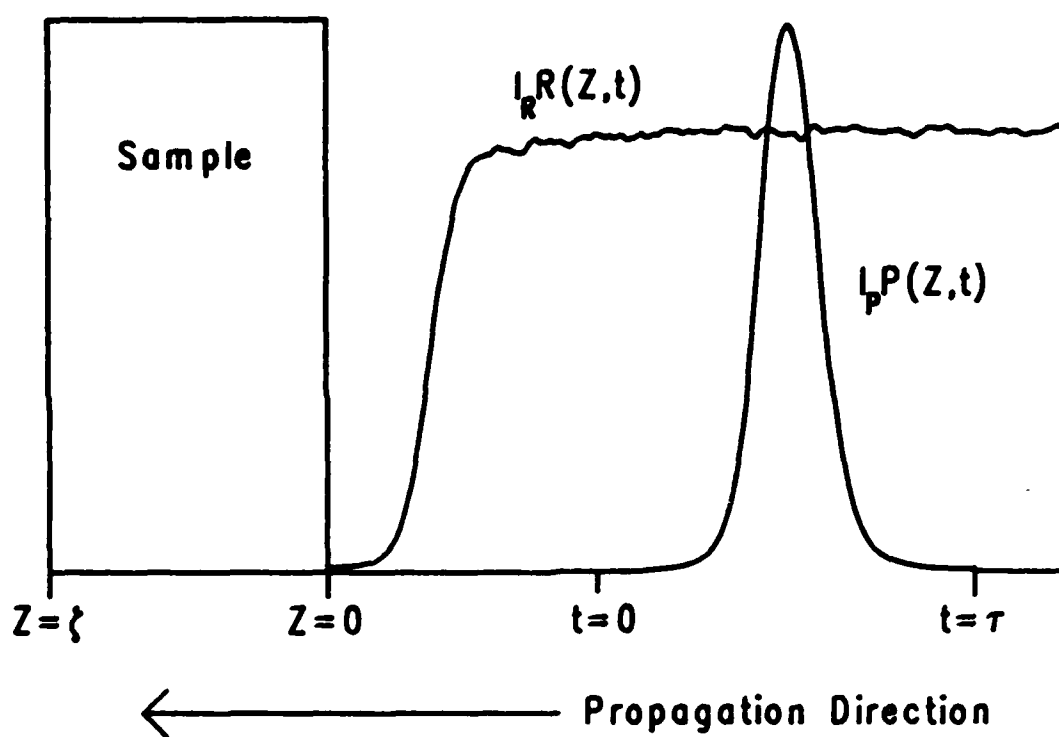


Figure 3.9. Schematic of the time resolved absorption process. The pump pulse is propagating to the right followed at a distance τ by a probe pulse. The coordinate t is pulse-fixed, while z is space-fixed.

For strongly absorbing samples, the upper limit of the integral is effectively infinite; making this approximation and substituting for $\alpha(z, t)$ gives

$$\ln \frac{R(0, t)}{R(\zeta, t)} = I_P \int_{-\infty}^t P(0, \tau) w(t - \tau) d\tau \quad (3.6).$$

The data obtainable from the streak camera is in the form

$$D(t) = I_R R(\zeta, t) \quad (3.7).$$

If $I_P = 0$, that is, if the pump beam is blocked, then there is no absorption and

$$D'(t) = I'_R R(0, t) \quad (3.8).$$

Substituting equation 3.7 and equation 3.8 into equation 3.6 gives

$$I_P \int_{-\infty}^t P(0, \tau) w(t - \tau) d\tau = \ln D'(t) - \ln D(t) - \ln I'_R + \ln I_R \quad (3.9).$$

If it were possible to measure I_R , I'_R , $D(t)$ and $D'(t)$ for each shot using multiple detectors, then the left side of equation 3.8 could be calculated after each shot, allowing direct signal averaging. This is not possible with the single-beam system used here, and measurements of $D(t)$ and $D'(t)$ must be made on separate shots. It is reasonable to assume that the major shot-to-shot variation is in the intensities I_P and I_R and that $R(0, t)$, $P(0, t)$ and $w(t)$ remain essentially unchanged from shot to shot. Making this assumption and summing over n shots of each type,

$$\int_{-\infty}^t P(0, \tau) w(t - \tau) d\tau \sum I_P = \sum \ln D'(t) - \sum \ln D(t) - [\sum \ln I'_R - \sum \ln I_R] \quad (3.10).$$

The term in brackets is simply a time-independent offset which can be found by noting that the excited-state population is zero before the pump pulse arrives. In other words, for $t < 0$,

$$[\sum \ln I'_R - \sum \ln I_R] = \sum \ln D'(t) - \sum \ln D(t) \quad (3.11).$$

The order of the n shots is not specified; it is most convenient to sum n shots both with and without sample excitation and to take the difference of the two datasets afterwards. This leads to data like that shown in figure 3.10. The absorption signal is the difference between the signal and the baseline established in the first nanosecond. The desired decay, $w(t)$ can be obtained by deconvolution of equation 3.10. Note that the time-resolved optical density $A(t)$ is also directly available, since

$$A(t) = \log \frac{R(0,t)}{R(\zeta,t)} = \frac{1}{n \ln 10} \int_{-\infty}^t P(0,\tau) w(t-\tau) d\tau \sum I_P \quad (3.12).$$

This derivation explicitly assumes that that $R(0,t)$, $P(0,t)$ and $w(t)$ can be treated as constants. Because of this, this method does not correct for real shot-to-shot variations in the spatial or time profiles of the laser pulses, the fluorescence decay curve, or the excited-state absorption curve. Such variations could be corrected in a true double beam experiment. However, it is not clear that such fluctuations are significant. The the laser itself is quite stable so $P(0,t)$ does not change greatly; except for the ASE contribution to $R(0,t)$, the excited-state decays governing $R(0,t)$ and $w(t)$ arise from allowed single-photon transitions, which tend to be well-behaved and reproducible as well. This is in sharp contrast to measurements involving continuum generation, where large shot-to-shot variations arise because of the poorly-defined nonlinear nature of the generating process, and where double beam measurements are essential. In this case the dominant source of noise appears to be the streak camera and image intensifiers. Using two detectors would tend to increase this source of error, since correlated, channel-specific errors from the streak camera itself would not cancel. That this type of error is occurring can be seen from the fact that the curve obtained by subtracting two nominally identical datasets is less noisy than the original datasets. This suggests that the noise seen in the absorption data arises primarily from systematic errors in calibrating the streak camera rather than from shot-to-shot fluctuations.

Several other things can also cause data distortions. In the derivation presented

above, it was assumed that the ground state population was never significantly perturbed, so that ground state absorption did not vary. This is reasonable only if the number of molecules in the excited region of the sample exceeds the predicted number of absorbed photons. A 3 mm diameter, 1 mJ pulse at 355 nm corresponds to an incident photon intensity (I_0) of 2.5×10^{16} photon cm^{-2} . A typical sample used here (.001 M bianthryl) has an absorption cross section (σ) of 3.1×10^{-17} cm^2 molecule $^{-1}$, and a concentration (C) of 6.0×10^{17} molecules cm^{-3} . The product $I_0\sigma$ corresponds to the fraction of molecules excited at the leading edge of the sample; in this case it equals 0.78. Clearly, in this case, significant ground state depletion will have occurred and the sample will no longer be in the linear regime.

This is not as serious as it might seem. The primary reason why this result occurs is that the absorption length (.5 mm) is so short. This corresponds to 2.5 ps, well below the time resolution of the camera. As long as the entire pulse can be absorbed in a length shorter than the time resolution of the camera divided by the pulse group velocity, (2 mm in this case), no time resolution will be lost, and the data will still appear as the convolution of the pulse shape and a decay function. The pulse profile will still enter into the results because of the spread in the arrival time of the pulse, and not because of the absorption depth of the sample.

The ultimate sensitivity of the method is limited by the number of excited state molecules which can be created in the sample. This can be limited by either the number of photons in the pump beam or the number of molecules in the sample. Generally, samples with optical densities of 2-20 are used, limited usually by the solubility of the sample. As the pump beam intensity is increased, there are two useful regimes of operation. For molecules with small absorption cross sections, (i.e. $I_0\sigma \leq .1$), the absorption will be linear, and, if the pump and probe beams propagate in the same direction, cells with long pathlengths can be used. In the case of molecules with large absorption cross sections, (i.e. $I_0\sigma \geq .1$), the absorption will be nonlinear and the useful pathlength will be limited

by the transit time of the probe beam to ~ 2 mm for 10 ps resolution. Increasing pump energies (or increasing cell lengths) will result in stronger excited-state absorption, but only at the cost of time resolution.

The spectroscopy of the sample can also limit the sensitivity of the method. In particular, if the molecule has a strong excited-state absorption at the probe wavelength, the latter part of the pulse is likely to be absorbed by the excited molecules rather than those in the ground state. In most cases, the higher excited states created this way decay back to the first singlet state very rapidly (~ 100 femtoseconds⁹), so they have little effect on the measured absorption spectrum. However, this is a rather efficient mechanism for wasting the pump beam photons, so it can ultimately limit the excited state population, and hence the sensitivity. It will also distort the apparent shape of the pump pulse and interfere with the deconvolution process. This may be the cause of the unusual pulse shape seen in figure 3.11.

All of the discussion given above relating to the calibration of the streak camera applies here as well. Since the absorption measurements are made by measuring emission as a function of time, the usual methods of calibrating the streak camera could still be used. The time calibrations remained unchanged, and the intensity corrections could be carried out by replacing the dye solution with a suitable long-lived fluorescing sample such as 9,9'-bianthryl. A significant difference between the absorption and emission systems relates to the computer averaging of the data. In emission, the instrumental jitter is compensated for with a marker pre-pulse, and the data is simply summed for the averaging. In absorption, there is no prepulse. Instead, the sharp rising edge of the dye emission is used as a marker. Finding this edge is somewhat more difficult than finding the prepulse. The algorithm ultimately used defined the edge as the average of the first channel to exceed 75% of the maximum and the last channel to be less than 25% of the maximum. A pulse was acceptable if these two points were within 5 channels of one another. Provided the probe light is sufficiently intense, this system was found to work

reasonably well.

Once the data had been corrected and shifted, it was summed. In the actual program, the quantity summed is $2048 \log_2(\text{data})$. This could be rapidly calculated using an interpolation algorithm, and it maps the 16 bit integer data into a 16 bit integer. The same integer summation routine used for emission could be used without modification. Although these may sound like major changes in the program, they in fact correspond to small changes in two subroutines. In practice the only difference between the two methods is that calculations required for absorption (especially the logarithms) lead to a somewhat slower data collection rate than in emission. Otherwise, the two systems are virtually identical.

4. Results

A typical set of data resulting from this procedure is shown in figure 3.10. The sample in this case is a solution of osmium compound BOSCO¹⁰ in acetonitrile. This compound has been studied on the nanosecond timescale, and is known to have a large excited-state absorption cross section at 600 nm, so the measurements were carried out at this wavelength. Previous studies have shown that emission from this excited state is prompt, so that no observable time dependence in the absorption is expected. The dye solution used in this case is mixture of Uranine and Cresyl Violet excited with the second harmonic (~ 1 mJ). The upper curve shows the sum of the logarithm of the dye emission for the dye sample with the sample excitation beam blocked. This data represents the sum of 1000 shots. It shows the sharp risetime used for time-referencing the data. Note that the fluorescence decay is not linear, as would be expected for an exponential decay. Instead, as noted above, it exhibits a peak at short times characteristic of amplified spontaneous emission. The second curve shows logarithmic sum of 1000 shots with the same dye conditions, when the sample is excited with ~ 1 mJ at 355 nm. The excited state absorption beginning near 1500 ps is clearly evident. The bottom curve

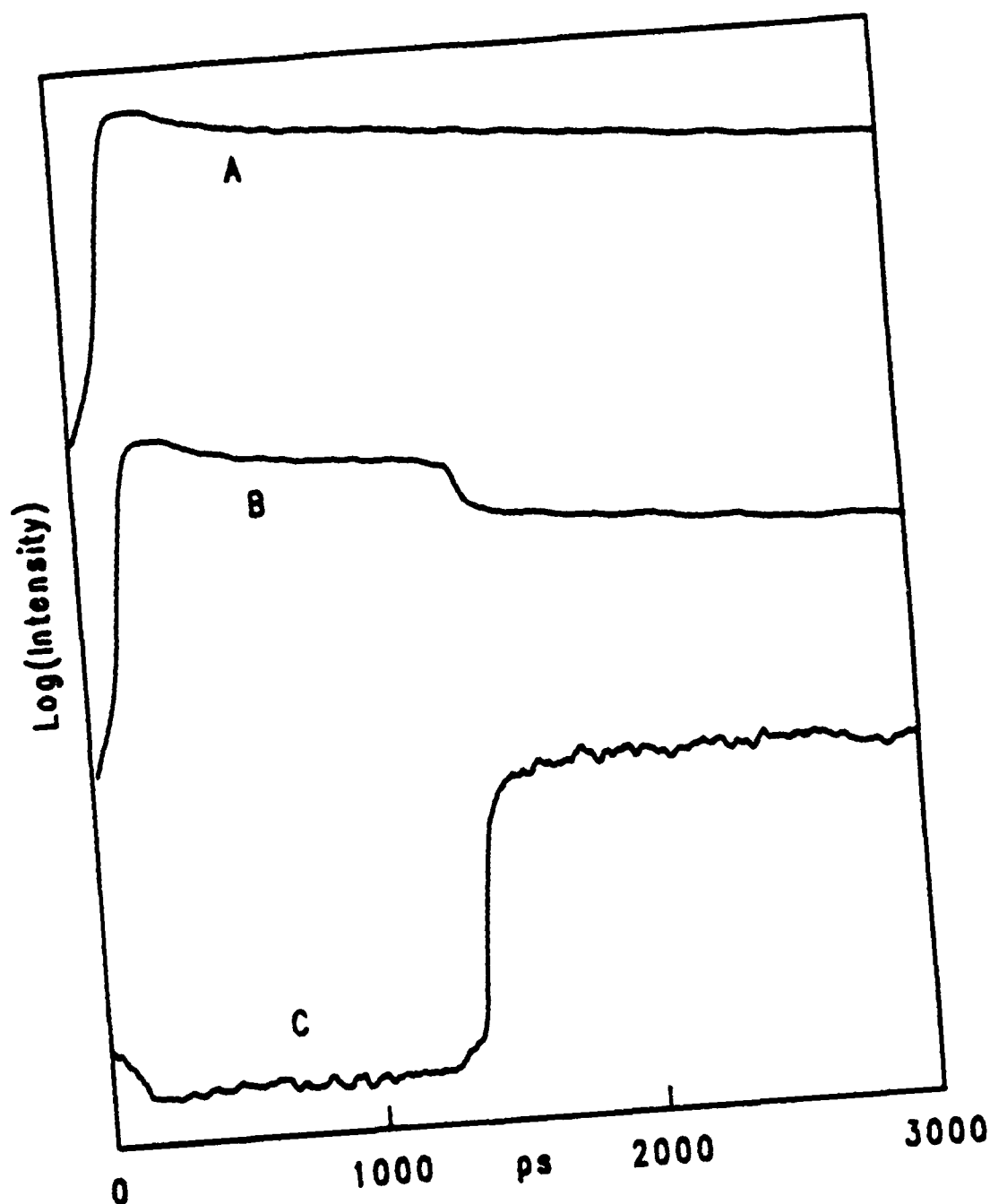


Figure 3.10. Time-resolved absorption in BOSCO. The upper curve shows the sum 1000 shots of the logarithm of the dye emission for the dye sample with the sample excitation beam blocked. It shows the sharp risetime used for time-referencing the data, and the non-exponential dye decay. The second curve shows logarithmic sum of 1000 shots with the same dye conditions, when the sample is excited with ~ 1 mJ at 355 nm. The excited state absorption beginning near 1500 ps is clearly evident. The bottom curve shows the difference between the two curves, which is proportional to the sample optical density.

shows the difference between the two curves with the vertical scale being proportional to the sample optical density. Optical densities approaching .3 were obtained in this case.

The time resolution of the absorption system can be inferred from the risetime of the absorption. Figure 3.11 shows a pulse obtained from an emission dataset at the same streak speed (3.54 ps/ch). This can be compared to the derivative of the BOSCO absorption risetime seen in the lower figure. Although the absorption curve is significantly noisier than the emission dataset, both show the same 16 channel width. When this is corrected for the 12 channel slit function, this gives a risetime of 37 ps, in good agreement with the measured pulsewidth.

A second set of data illustrating the results obtainable with a blue laser dye are shown in figure 3.12. The dye solution used in this case was a roughly equimolar (~ 10 mM in ethanol) mixture of 9,9'-bianthryl and Coumarin 500. It was excited at 355 nm, and the emission was collected through a 500 nm bandpass filter. The sample in this case, is a solution of the Rhenium complex Re-PTZ¹¹ in both DMF and methylene chloride. This compound is characterized by having both electron-donating and electron-accepting ligands. An initially formed metal-ligand charge transfer state (similar to that in RUTBY) decays at a finite rate into an inter-ligand charge transfer state with an absorption peaked at 500 nm. The rate of this relaxation depends on the polarizability of the solvent. This is seen in the data where the risetime in seen in DMF is much slower than that seen in methylene chloride. The signal-to-noise is comparable to that seen in the BOSCO complex, although the excited-state absorption cross section of this compound is somewhat smaller. The peak optical density is $\sim .16$ for both curves. The smooth curves shown in the figure represent biexponential fits. These were obtained by the methods described in the next chapter. To fit and deconvolute the data, the same programs used for emission data can be used. To make the data identical to a fluorescence dataset, it is only necessary to append a prepulse obtained from a fluorescence dataset at the same streak speed to the beginning of the dataset.

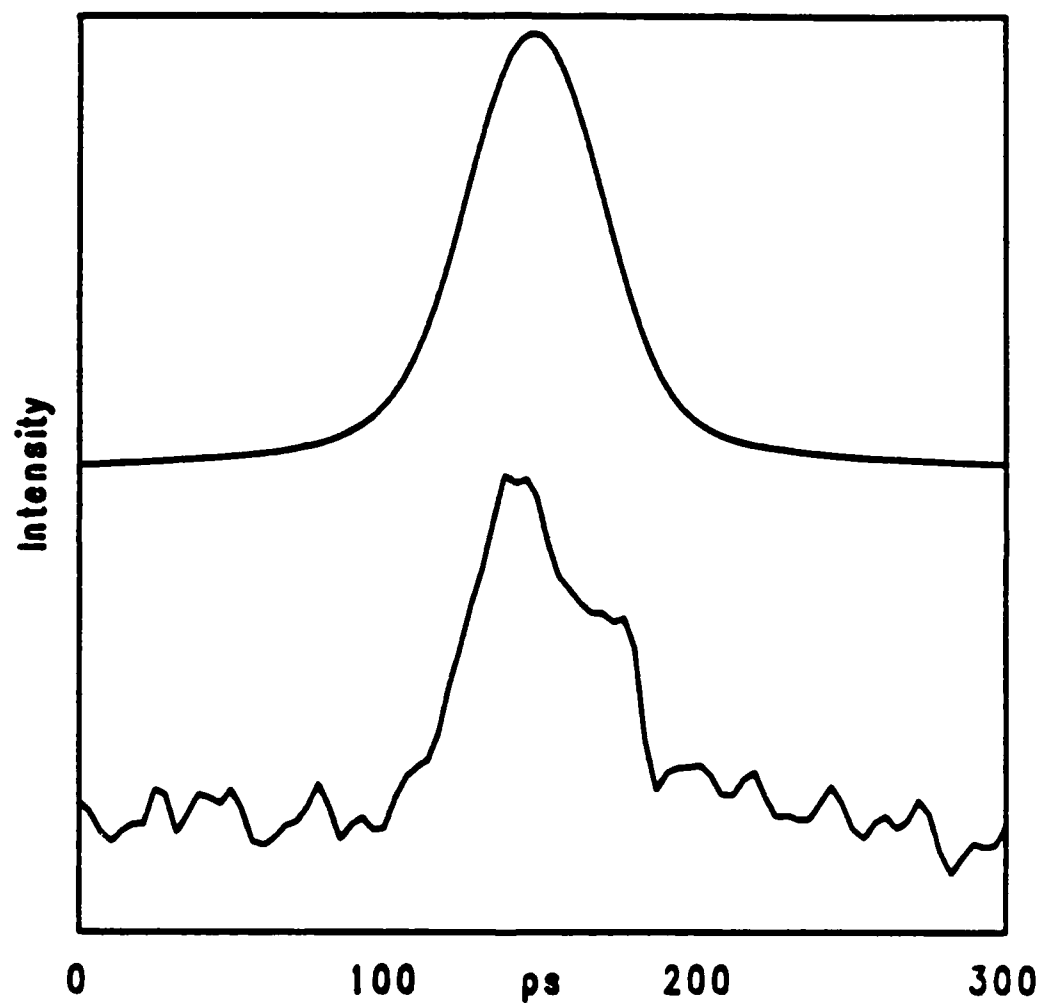


Figure 3.11. The upper curve shows a typical pulse obtained using the fluorescence apparatus at a streak rate of 3.54 ps/ch. Lower curve shows the derivative of the BOSCO risetime (see figure 3.10). The similarity of the two curves indicates that the time resolution of the absorption and emission systems are comparable.

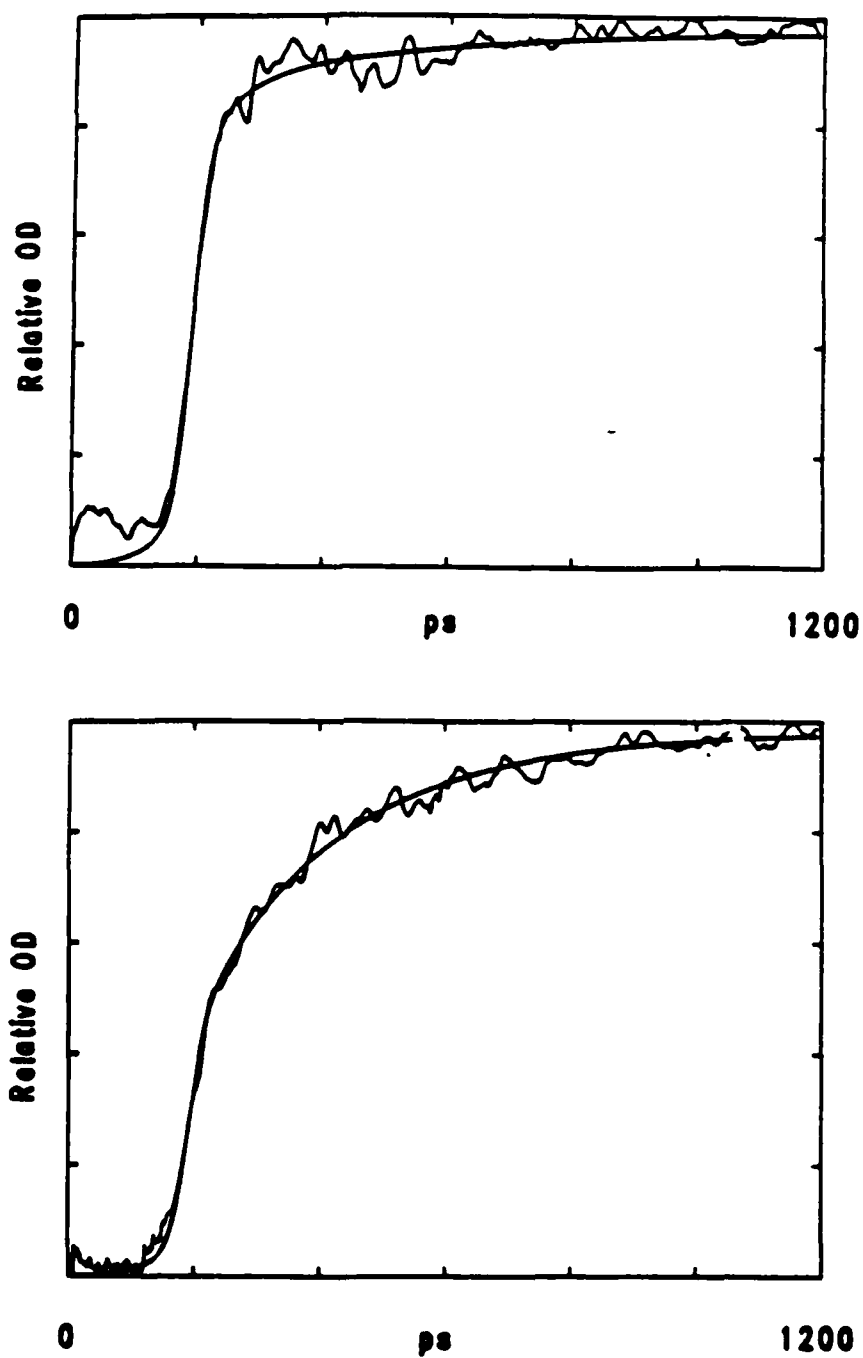


Figure 3.12. Time-resolved absorption data for the compound RE-PTZ, as described in text. Upper curve in methylene chloride, lower curve in DMF. Note that the intramolecular charge transfer step is faster in the more polarizable chlorinated solvent.

E. Time-Resolved Raman Spectroscopy

1. Introduction

A final spectroscopic technique which was employed here was time-resolved Raman scattering. If everything had gone according to plan, most of this thesis would have centered on this technique. Unfortunately, a number of virtually insurmountable experimental difficulties arose so that it simply was not practical to use Raman for any type of experiments. There are several reasons for this, mostly relating to the high peak power and low average power of a picosecond laser. Because of this, there was a continuing problem with nonlinear backgrounds which were more intense than the desired Raman signal. A viable Raman system appears to be possible, provided that a laser with lower peak powers and a higher average power (i.e. a laser with a much higher repetition rate) is used. Further development of a tunable source should enhance the possibilities of using resonance Raman as well. A generally unsuccessful effort was made to find a suitable nonlinear Raman technique for use in solutions to exploit the high peak powers. Although it is tempting in principle to use such techniques, it appears that with the present equipment, such methods are not practical.

There are several reasons for wanting to make use of Raman techniques. A majority of all work done with solution-phase chemistry on the picosecond timescale has been carried out using ultraviolet and visible spectroscopic techniques². As noted above these are convenient methods to use, since the signals are large and the solvents are usually transparent. There are also some well known drawbacks to these methods. Electronic spectra tend to be broad and featureless, with similar molecules often exhibiting similar, overlapping spectra. This makes it difficult to identify unknown species, and greatly complicates the study of systems involving several similar molecules. Many of these problems can be avoided with the use of vibrational spectroscopy. Unlike the broad, featureless electronic spectra, vibrational spectra are characterized by narrow lines and

by spectral features which can be associated in a reasonable way with structural features of the molecule. Vibrational spectroscopy, and in particular Raman spectroscopy, has the potential for allowing one to study complex solution reactions even when several molecules with similar electronic spectra are involved. An example of this type of problem would be the study of the formation different isomeric species in a geminate recombination process¹². In addition to this, using Raman spectroscopy would make it more likely that any unknown species which were encountered could be unambiguously identified.

The difficulties with Raman spectroscopy encountered here centered on three problems:

1. In the case of species with "normal" Raman cross-sections, it is generally difficult to measure spectra in samples any more dilute than $\sim .01$ M. This is because the background scattering from the solvent tends to be of this order of magnitude, and the desired signal is often obscured by the solvent background. Since it is difficult to generate transient species at high concentrations, this intrinsic lack of sensitivity severely limits the usefulness of transient Raman spectroscopy. In the absence of resonantly enhanced Raman cross sections, the only way around this problem is to use solvents with extremely low Raman cross-sections. For example, Brus et.al. carried out some relatively successful nanosecond studies at approximately $.001$ M in aqueous systems, exploiting the small Raman cross section of water¹³. Another approach to this problem would be to make use of liquid rare gas solvents where there no vibrational spectrum; obviously, this technique is rather limited, since it is difficult to use and can be applied only to a very small class of systems.

2. The use of resonance Raman is often proposed as a way around these problems. When Raman spectra are measured in the neighborhood of an electronic resonance, the spectra begin to take on some of the properties of fluorescence. In general, there is an increase in the scattering cross section, and an increase in the intensity of overtone and

combination bands. This phenomenon can be traced to an increase in the lifetime of the intermediate state associated with the scattering process. As one approaches resonance, the virtual state responsible for Raman scattering is replaced by a real state, and fluorescence can result. In the gas phase this actually occurs, but in solution collisional deactivation often occurs so rapidly as to preclude fluorescence. This leads to emission from the unrelaxed Franck-Condon state on a timescale comparable to the collision rate (tens of femtoseconds). This unrelaxed fluorescence reflects only the ground state molecular Hamiltonian, and thus is equivalent to the Raman spectrum. As discussed by Heller et al., there is in fact a continuum between fluorescence and Raman, depending on the lifetime of the upper state¹⁴.

In the context of transient Raman spectroscopy, the increase in the scattering cross-section associated with resonance Raman makes it possible to look at species at relatively low concentrations. Thus resonance Raman looks like the logical method to use in order to extend the conventional gas-phase, pump-probe, laser-induced-fluorescence experiment into solutions. Unfortunately, the degree to which a molecule exhibits a resonantly enhanced Raman cross section is not easily predicted. At present there is relatively little known about the resonance Raman cross sections of reactive solution species such as free radicals. The fact that they often absorb in the visible means that that resonance Raman will occur in some cases, but detailed predictions are not possible. Resonance Raman spectra of several free-radical species have been measured, and there is no reason to believe that many other radicals will not exhibit similar spectra¹⁵. Unfortunately, there are many radicals which show no resonance enhancement. For example, one system which was studied, NO_2 , shows significant absorption in the visible, and is known to show resonance Raman in the gas phase¹⁶, but gives no detectable Raman scattering in any solvent tried. In other words, before any experiment involving Raman studies of transient species can be carried out, a significant amount of survey work will be necessary just to identify systems which are amenable to study. The Raman system described here

was extremely slow and difficult to use, and as such, was particularly ill-suited to survey work. Actually, much of the survey work required could be done without picosecond resolution, suggesting that a nanosecond resolution system such as that used by Brus et.al.¹³ might be a valuable adjunct to a picosecond Raman system.

3. The problems described so far apply to Raman spectroscopy in general, and in many cases, these types of problems have been successfully overcome. The experimental difficulties encountered here were exacerbated by the use of picosecond pulses. In essence, the problem of measuring Raman spectra on the picosecond timescale corresponds to putting enough energy into the sample to get detectable Raman scattering without raising the power density above the threshold for nonlinear effects. This is not a trivial problem. In a typical laser Raman spectrometer a CW beam of roughly one watt is focussed as tightly as possible onto a sample, giving rise to power densities on the order of tens of kilowatts per square centimeter, and a useful amount of scattering from a convenient near-point source. In comparison, the second harmonic of the picosecond laser output consists of 10, 30 picosecond duration, 1 mJ pulses per second. When this beam is focussed, the average power is only 10 mW, but the peak power is on the order of many GW cm^{-2} . There will be only 1% as much Raman signal, but the peak power densities are high enough to cause sample breakdown, stimulated Raman scattering and continuum generation. Note that virtually all materials, even the nominally transparent materials used for solvents and sample cells emit to some degree under these conditions. Thus the relatively weak Raman signal can be easily overwhelmed by the nonlinear processes. In a pump-probe experiment, things will be even worse, as two high power beams will be present. The pump beam is typically in the ultraviolet and will tend to excite processes normally only seen in the vacuum ultraviolet. Unfortunately, this means that virtually all substances absorb to some degree, leading to a significant background fluorescence. To minimize the nonlinear effects, one is forced to defocus or attenuate the beams. This will lead to a further loss of Raman signal.

This is not to say that it is impossible to measure Raman spectra with a picosecond laser. Several examples of Raman spectra obtained with picosecond excitation are shown below. With one exception, they are of relatively concentrated solutions of stable molecules. The problem is basically that as it existed, the Raman system was too cumbersome to use for anything except measuring spectra of stable species. This made it difficult to apply Raman spectroscopy to any type of chemically significant question. However, as the system was used, a number of improvements suggested themselves. Most of them were impossible to implement with the existing hardware, but they suggested directions for further development. In addition to this, other investigators have made some progress in time resolved Raman spectroscopy using alternative techniques¹⁷. Although time and circumstances did not permit the construction of the next generation of picosecond Raman spectrometer, it appears that some more useful results might have been obtainable, especially with regard to resonance Raman. It seems worthwhile to review what was learned from this system, and to see how it might have been used to make a more workable system.

As discussed below, it did not appear that significant progress could be made with spontaneous Raman spectroscopy without major changes in the system, including a different laser. In an effort to find alternative methods, especially ones using existing equipment, the use of coherent Raman techniques was explored. Coherent techniques have the advantage that the signal scales in a nonlinear fashion with increasing power, so that the high peak powers inevitable in a picosecond experiment enhance the signal, rather than obliterating it. Of course, there remain serious obstacles in applying coherent Raman techniques to solution-phase measurements. These arise primarily from the presence of the non-resonant susceptibility of the solvent. This leads to a large background signal which can interfere with the Raman signal, distorting the lineshape and ultimately obliterating the signal. Methods of eliminating this problem have been proposed where a sequence of picosecond pulses can be used to isolate the resonant component of the signal

and recover the Raman signal. Initially it appeared that using this method in conjunction with the shortened pulses obtained from the OPS might lead to a useful spectroscopic technique. When further, detailed characterization of the OPS revealed that the output pulses were too temporally unstable to be useful, the project was discontinued.

2. Measurements and Results

The first thing to describe is the system which was actually constructed, so that its weaknesses can be assessed. Figure 3.13 shows the apparatus used to obtain the Raman spectra shown below. A pump and a probe beam were generated from the laser output (either as a laser harmonic or the result of Raman shifting in hydrogen), passed through the delay lines and recombined ahead of the sample. The combined beams were then focussed through a 100 mm quartz cylindrical lens onto the sample in a .5 mm i.d. quartz capillary tube. The sample was placed just ahead of the focus to prevent stimulated Raman from occurring. This resulted in a .5 mm wide, 2.5 mm tall line image. This was then relayed into the spectrometer through the lens pair shown, with an overall magnification of eight. The monochromator (Spex model 1404) was operated with 1 mm slits, providing relatively low resolution (2 cm^{-1}) but still preserving most of the nominal $1:10^{12}$ stray light rejection. A 1P28 photomultiplier tube was used for detection. The tube voltage was sampled by a gated integrator (100 ns gate) and sent to the LSI 11-2 microcomputer.

The following figures show typical examples of Raman spectra obtained with the picosecond spectrometer. Figure 3.14 shows the spectrum of CCl_4 obtained in a 20 minute scan with 532 nm excitation, using 2.5 mm slits, .1 nm increments and 16 shots per point. This spectrum shows that under ideal conditions, a reasonable looking Raman spectrum can be obtained. Figure 3.15 shows the spectrum of benzene in CCl_4 as a function of concentration, using conditions the same as figure 3.15. It is clear that under non-resonant conditions even a molecule with a relatively large Raman cross section such

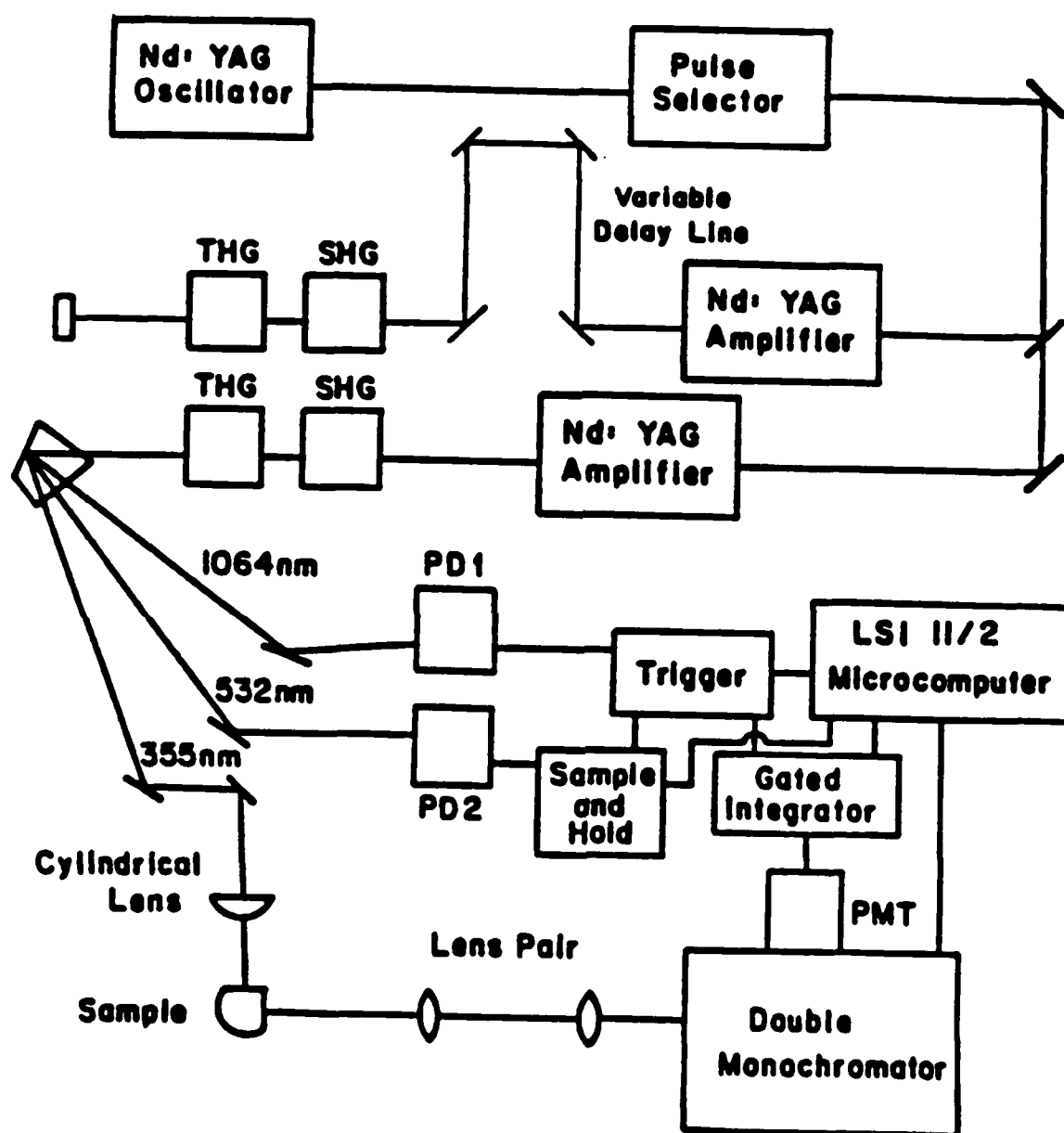


Figure 3.13. Time-resolved Raman apparatus, as used for the RUTBY spectrum. As shown, the system uses the 355 nm beam for a probe, and uses no pump beam. The blocked beam passing through the delay line would ordinarily be used for sample excitation.

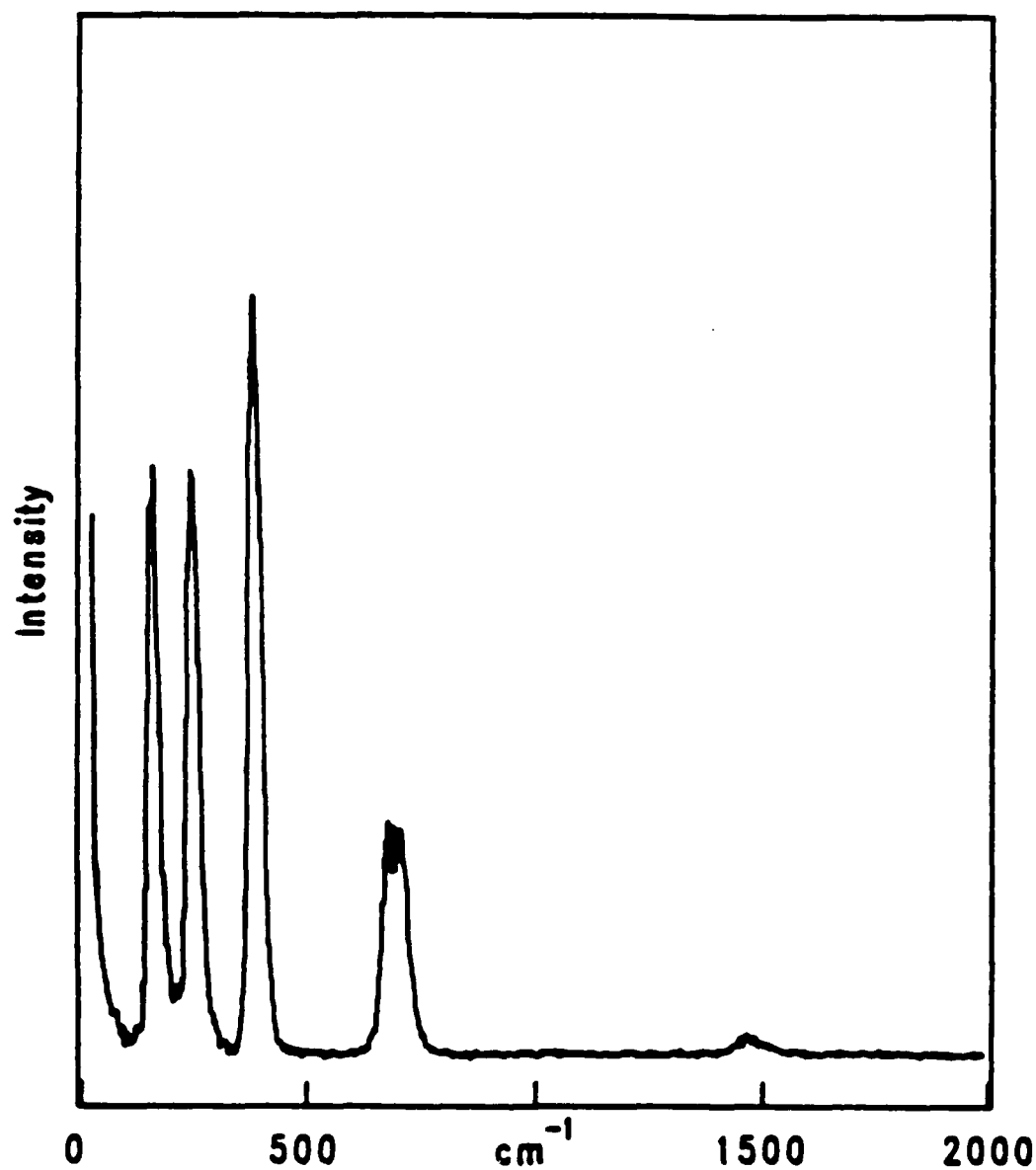


Figure 3.14. Spectrum of neat CCl_4 obtained in a 20 minute scan with 532 nm excitation, using 2.5 mm slits, .1 nm increments and 16 shots per point, using charge integration for detection.

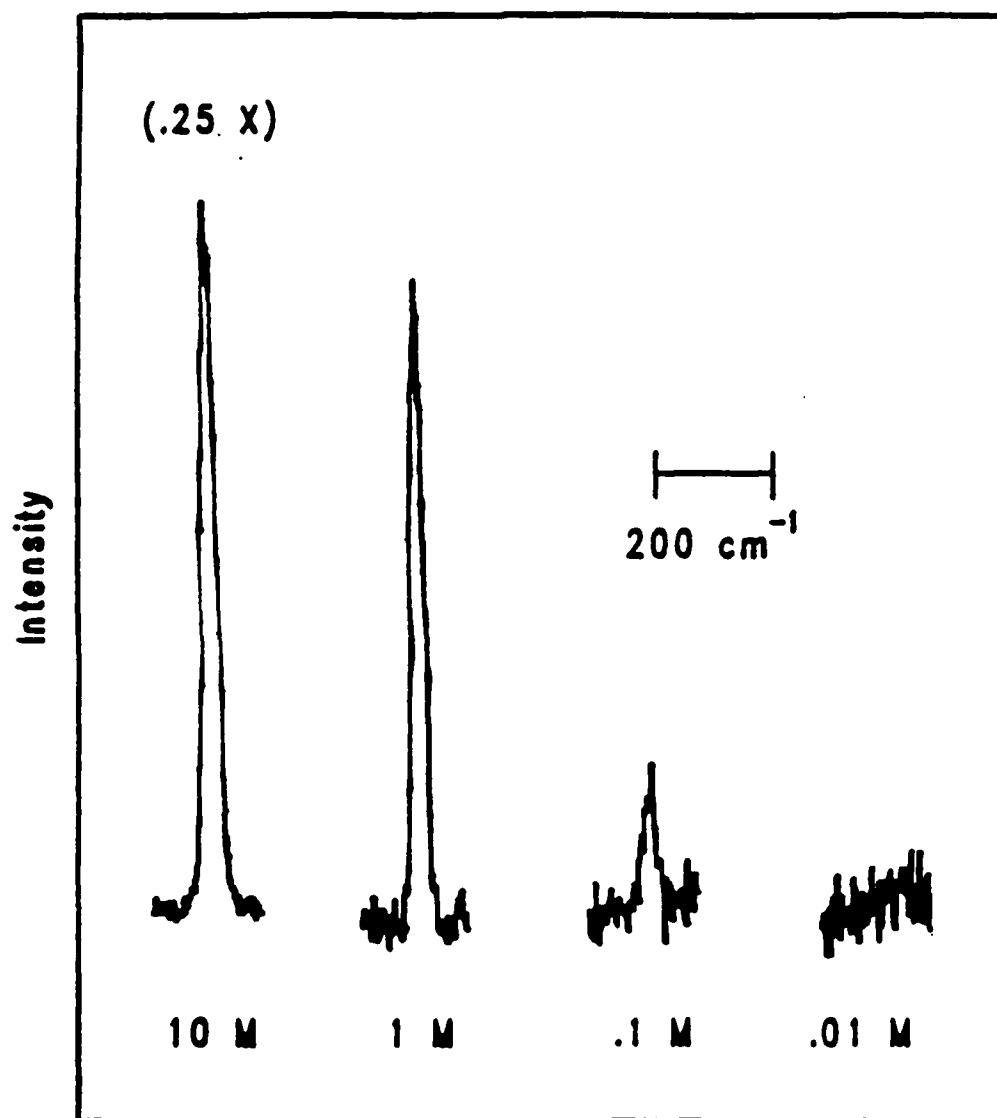


Figure 3.15. Spectrum of the 992 cm⁻¹ line of benzene in a CCl₄ solution as a function of concentration, using conditions the same as figure 3.14.

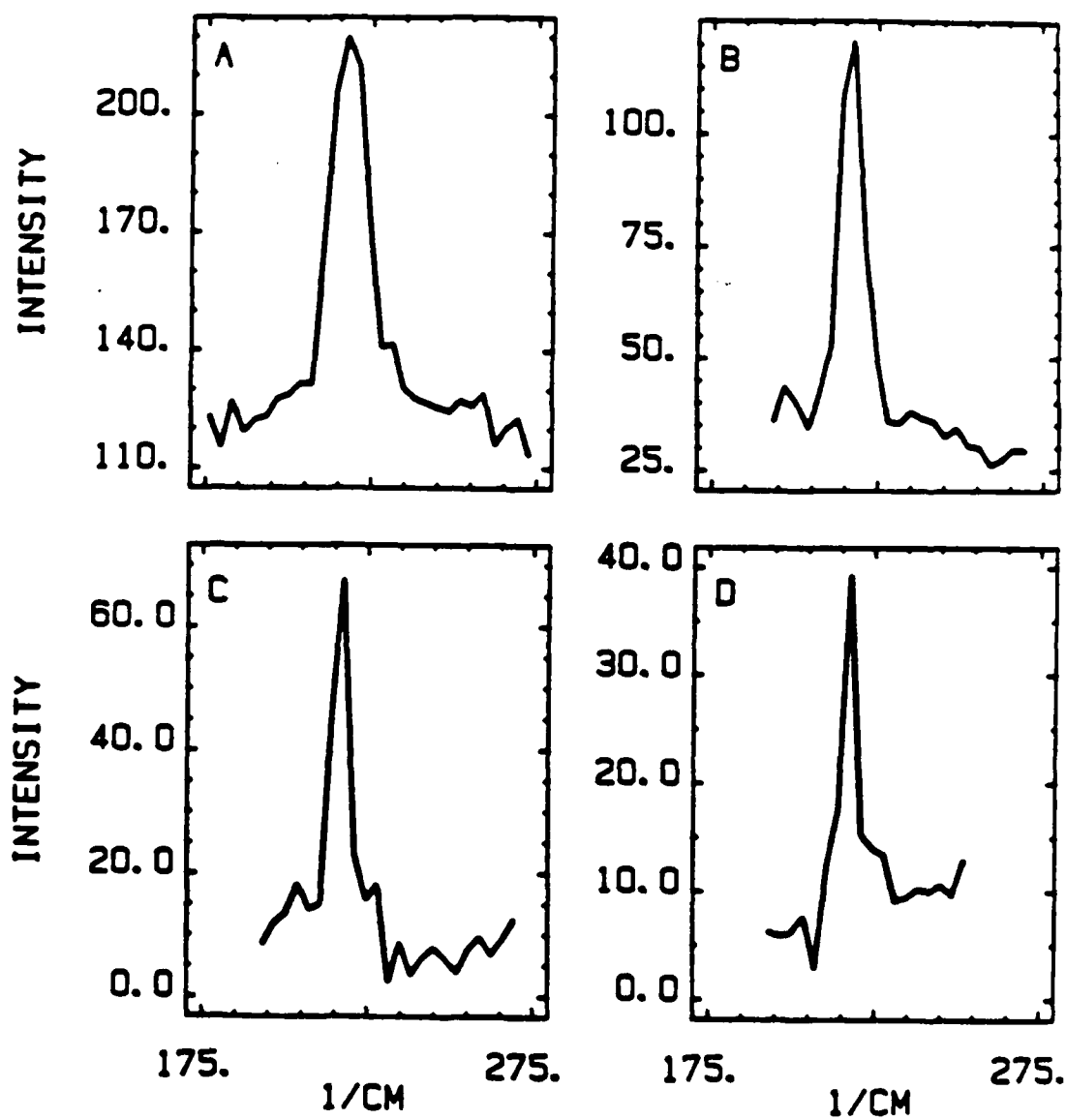


Figure 3.16. Spectrum of I_2 in cyclohexane excited at 532 nm, at several different slit widths. The excellent signal-to-noise in these spectra is due to both the large cross section and to the use of photon counting.

as benzene, cannot be detected much below 1%. Figure 3.16 shows the spectrum of I_2 in cyclohexane excited at 532 nm. Iodine has a significant degree of resonant enhancement at this wavelength so the cross section is perhaps an order of magnitude larger than that of benzene. The excellent signal-to-noise in these spectra is due to both the large cross section and to the use of photon counting detection.

The spectra in figure 3.14 and figure 3.15 were obtained by integrating the total charge on the photomultiplier tube after each shot. In principle, this charge is proportional to the number of photons impinging on the photocathode. Unfortunately, the accuracy of the analog charge measurement is rather poor, especially in the presence of the electronic background generated by the laser. Ordinarily, in a low signal measurement with a photomultiplier tube, a photon counting technique is used. A large dynamic range can be obtained, with count rates ranging from a few hertz to tens of megahertz. In a picosecond experiment, fast counters are of no help; all the signal photons from a given laser shot arrive at the phototube within a few picoseconds, so they will appear as a single pulse which cannot be counted in the time domain. In the picosecond time domain, a photon counting measurement consists of determining whether or not a single photon arrived after each laser shot. This leads to a maximum meaningful count rate of around 5 Hz, when using a 10 Hz laser. The spectra in figure 3.16 resulted from a photon counting technique. Essentially the same collection system as before was used, except instead of summing the individual signals, the data was recorded as the fraction of the shots in which a certain signal level was exceeded. Under identical conditions using this technique resulted in more than an order of magnitude improvement in the signal to noise. Unfortunately, measuring spectra this way is extremely slow, as thousands of laser pulses are needed for each point.

Figure 3.17 shows the Raman spectrum of the excited state of RUTBY excited at 355 nm. This molecule was studied with both emission and Raman techniques, and as noted above is used for calibrating the streak camera. The details of this system

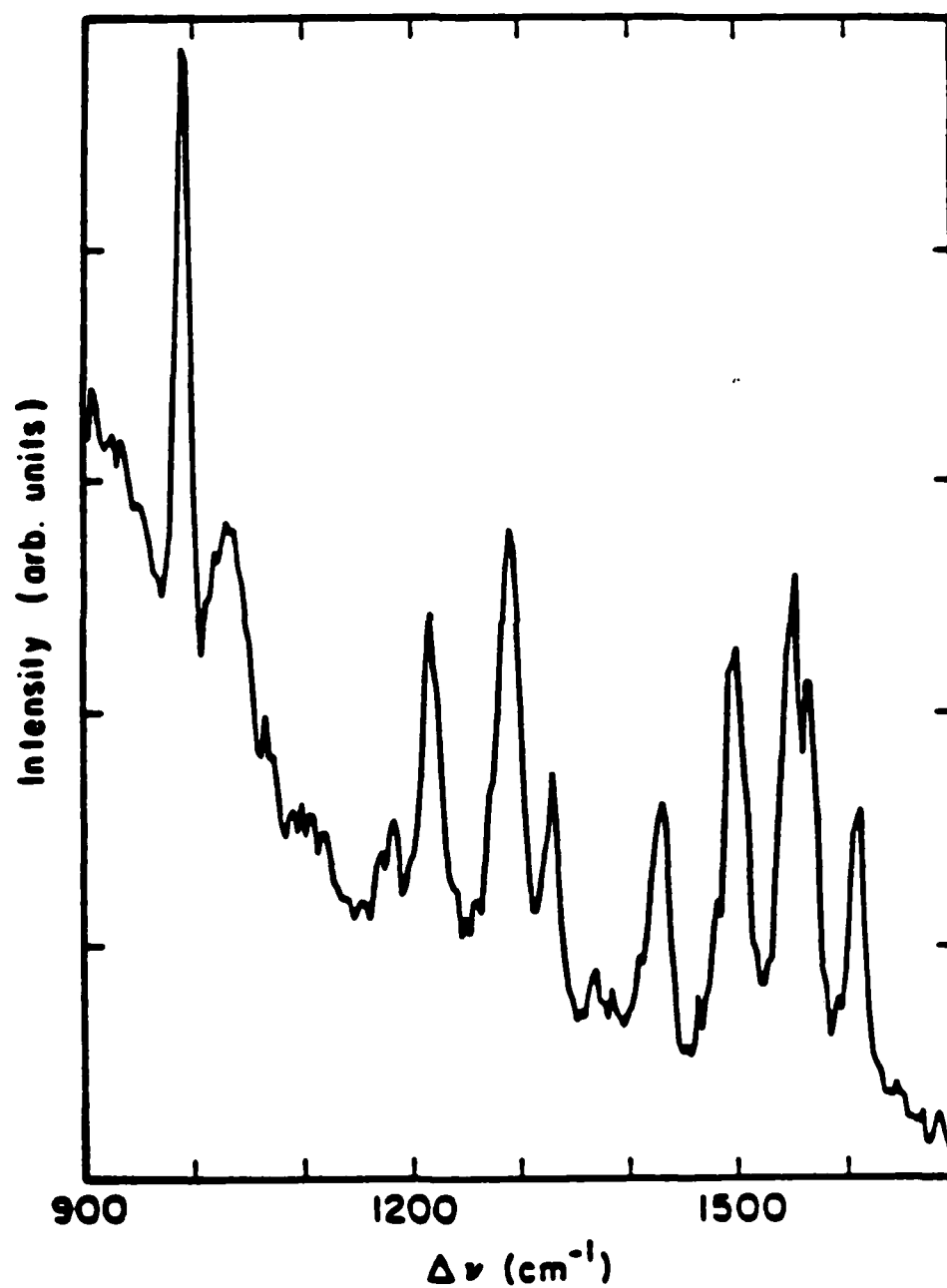


Figure 3.17. Raman spectrum of the excited state of RUTBY excited at 355 nm.

are discussed in detail elsewhere¹⁸. The main reason for showing this spectrum is that it represents the one successful transient Raman spectrum recorded with this laser system. As it happens this system is almost perfectly well suited to this process. When the third harmonic is used for excitation, the molecule is excited by the leading edge of the pulse, producing an excited state which has a Raman cross section orders of magnitude larger than benzene. Thus the excited state spectrum is obtained with a single pulse experiment. Luminescence occurs only at much longer wavelengths with a lifetime of nearly a microsecond, and so is easily eliminated. This spectrum demonstrates how efficient resonance Raman can be if suitable systems can be identified.

So far little has been said about time-resolved measurements. In principle, time-resolved measurements can be carried out using a pump-probe technique, as alluded to above. This was because the difficulties in obtaining usable spectra made the question of time-resolved measurements largely irrelevant; there was no signal to time resolve. In the case of RUTBY, some efforts were made to time-resolve the absorption and Raman scattering steps, but no conclusive results were obtained. The reason for this can be seen in figure 3.7, which shows that the time-resolved emission from this compound. If no dynamics can be observed in emission, it is not surprising that nothing can be seen with Raman. Assuming that a reasonable system for measuring the spectra can be developed, it is important to have a reliable system for generating the pump and probe beams. In general, if transient species are to be studied, the relevant timescale will vary from picoseconds to tens of nanoseconds. Thus, a reliable means of generating a delay varying from millimeters to meters was required.

For most applications it is important that the beam passing through the variable delay line not change spatially as the delay is changed. This is a rather stringent requirement, since it means producing a stable delay line with a lever arm of several meters. These problems can be largely overcome by using a corner cube reflector on the moving delay. It can be shown that with this type of reflector, the input and output beams will always

be parallel, so that lever arm effects will be minimized. It is also generally important that the focal properties of the beam not change. This can be achieved only if the beam is a high quality gaussian beam with a sufficiently large beam waist that a pathlength variation of a few meters has little effect on the beam. This suggests that the beam should be expanded through a telescope before the delay and recollimated afterwards. It also indicates that the laser fundamental, rather than one of the harmonics should be delayed. The optical quality of the laser harmonics tends to be significantly poorer than that of the fundamental. This arises not only the relatively poor optical quality of the nonlinear crystals, but from the nature of beam propagation in birefringent crystals as well. In addition, scattering and wavefront distortion problems will be minimized at longer wavelengths. One additional problem which can arise is due to self-focussing in the corner cube. Since a solid corner cube involves a rather long pathlength through glass, a corner cube constructed from front-surface reflectors might be desirable.

A long delay line incorporating most of these features was built from a commercial translation stage (Thompson SCF). With the addition of a stepper motor driven screw feed it was possible to generate any desired delay under computer control. In general, it was found that the reproducibility of the beam position was excellent when a corner cube reflector was used, although some degree of self-focussing was occasionally observed.

3. Time-Resolved Raman: Future Prospects.

Most of the data presented so far is relatively self-explanatory. In essence it shows that while Raman spectroscopy can be useful, the Raman system constructed here does not provide a practical way for exploring these possibilities. The most significant question about these results is how one might go about modifying the system to obtain more reasonable results. From an experimental point of view, this corresponds to the question of devising a spectrometer which can obtain reasonable results in a finite time. The unpredictable nature of resonance Raman makes it essential that a rapid data collection

rate commensurate with the needs of survey work be achieved. Two different approaches to the problem can be made, either with an improved system for detecting spontaneous scattering, or with the use of coherent methods. Since it was not possible to carry out either of these projects with existing equipment, the systems described here represent an educated guess as to how to go about measuring Raman spectra with a with the maximum possible efficiency.

The key to increasing the usefulness of the Raman system would be to increase the rate of data collection while keeping the power levels as low as possible. The obvious way to go about doing this is by increasing the repetition rate. Not only does doing this make it possible to increase the average power substantially with no increase in the peak power, it makes it reasonable to consider the use of photon counting in the detection system. The only question is how high a repetition rate can be used. An actively mode-locked CW laser has a repetition rate on the order of 100 MHz. There have been reports of picosecond resonance Raman spectroscopy at these repetition rates, notably the work of Gustavson et.al. with the excited state of stilbene¹⁷. Unfortunately, there are significant drawbacks to working at this high a repetition rate. This rate is actually too high for many purposes, since only systems which return to equilibrium in less than 10 ns can be studied. This requirement is satisfied by relatively few systems, and is never true when actual photochemistry occurs. Repetition rates of tens of kilohertz seem to be more practical, especially when the sample is being degraded photochemically. This is essentially the limiting rate at which the sample volume can be flushed out in a flowing sample cell.

The power densities required for these experiments suggest that a laser producing ~ 20 ps pulses at a repetition rate of ~ 100 KHz, and an average power of ~ 10 W would be optimal. Such a system could be produced with a CW mode-locked Nd:YAG laser using a fiber compressor to produce pulses with ~ 6 μ J in each pulse at 80 MHz¹⁹. Pulses could be selected at 100 KHz, and amplified through a series of CW-pumped Nd:YAG

amplifiers to produce the desired $\sim 100 \mu\text{J}$ per pulse. Somewhat higher powers would be available by cavity dumping the oscillator at 100 KHz, but unless some method were to be found for shortening the pulses at higher powers, pulses as long as 150 ps would result. Note that the very long radiative lifetime of Nd in YAG ($\sim 500 \mu\text{s}$) means that any repetition rate above a few KHz can be amplified as if it were a CW beam. There are several other methods for achieving this combination of repetition rate, pulse width and average power, including, for example the use of a copper vapor laser to pump dye amplifiers at a kilohertz repetition rate¹⁹. The point of this is to show that such a system is well within the range of current technology.

It is also possible to decrease the peak power by increasing the focal volume or, at some cost in resolution, by increasing the pulse widths in time and/or frequency. None of these options are nearly as promising as increasing the repetition rate. Increasing the frequency width is barely possible, since the spectral width of the 532 nm beam is already several cm^{-1} . Further broadening would be quite detrimental to the spectrum. Nonetheless, some improvement might be made. In particular, using the OPS as an excitation source would greatly increase the chances of finding species with resonantly enhanced Raman cross sections. One feature of the OPS is a bandwidth of $\sim 15 \text{ cm}^{-1}$. Although such a bandwidth might seem excessive, the tunability of the beam might make up for this. The resonantly enhanced species will stand out from the rest of the spectrum, so that spectral clutter might be less of a problem, and the larger bandwidth might be tolerable.

Temporal broadening is readily accomplished, and might indeed be valuable for survey work. Actually, for survey work, pulses in the nanosecond range might be useful, as noted above. Unfortunately many nonlinear processes increase with increasing pulse length, as resonant two-photon processes begin to occur. For example, the damage threshold in KDP decreases linearly as the pulse length goes from picoseconds to nanoseconds. Longer pulses may not be as advantageous as they appear, since the background signals

may also increase. Finally, there is the possibility of increasing the focal volume. In principle, it could be possible to retain the 10 Hz laser, while increasing the laser energy and sample volume greatly. In a sense, this would correspond to doing a number of low power measurements simultaneously, and then analyzing all the results with the same spectrometer. Since it appeared that in principle this approach could be used to construct a viable system based on the existing ten hertz laser, this possibility was considered in some detail.

The questions which arise in this approach relate to the size and shape of the irradiated volume, and to the efficiency with which the scattered light can be transferred through the spectrometer and to be detected. In a typical a Czerny-Turner monochromator, light is passed through the slits, collimated by the first reflector, dispersed through the grating and finally reimaged onto the exit slits by the second reflector. The acceptance angle of the system is principally determined by the set of rays which pass through the slits and strike the first reflector. This ignores such things as vignetting on the grating, but for a well designed spectrometer, this is not a problem. High resolution spectrometers are characterized by small slits and large f numbers, resulting in a narrow image with a large depth of field. Because of this the a narrow sample volume narrow volume with an aspect ratio matched to the depth of field of the spectrometer will optimize the collection process. For the $f/8.5$ monochromator used here, an aspect ratio of $\sim 1:20$ is called for. The depth of field is proportional to the slit width, so the collected volume increases with the square of the slit width. There is clearly a great potential benefit associated with sacrificing resolution for slit width. For this monochromator, a slit width of ~ 1 mm is appropriate.

Of course, the emitting sample is not located at the slits, but instead is transferred there with a collection lens. The only real variable in designing a suitable set of collection optics, is the extent to which the real source is magnified by the optics. The relative proportions of the sampled area will remain the same, irrespective of magnification, but

the size will vary. The amount of light reaching the slits will scale with the volume of the sample, V , the collected solid angle Ω and the density of emitting molecules, D . Clearly, V is inversely proportional to the cube of the magnification M , and, assuming the lens diameter is large enough, Ω is proportional to M^2 . For Raman scattering in the linear regime, D will scale as the product of the laser intensity and the concentration of scattering molecules. Assuming that the excitation laser is focussed to a size comparable to the sampled volume, D will scale as $M^2 P$, where P is the average laser power. The overall signal will be proportional to MP , which suggests that to maximize the Raman signal, one should focus the laser to as small a spot as possible and magnify the resulting image into the spectrometer. This is precisely the optical system used in a CW Raman spectrometer.

The conditions for a pump-probe experiment are more complex. The volume and solid angle arguments are still the same, but the term for D changes. For linear absorption, $D \propto M^4 P_1 P_2$ where the subscripts refer to the pump and probe beams. This results in $S \propto M^3$, which still suggests that strong focussing and high collection magnification are apropos. Unfortunately, the real quantity of interest is the signal to noise ratio S/N . The noise in this case arises from nonlinear scattering processes such as two-photon fluorescence or stimulated Raman; these quantities scale with the square of the laser power. This leads to terms where $N \propto V \Omega P_1^2 P_2 \propto M^5$. The signal-to-noise will then scale as M^{-2} , which of course means that a low collection magnification is favored. This argument only applies if the nonlinear terms dominate the noise; if linear scattering is the dominant noise term, then S/N will be independent of power, and maximizing S again becomes reasonable.

The optimum geometry is ultimately determined by two quantities, $I_1^{(M)}$ and $I_2^{(M)}$, the maximum pump and probe laser intensities for which nonlinear scattering does not dominate the noise. The signal will be proportional to $V \Omega I_1^{(M)} I_2^{(M)}$ or $M^{-1} I_1^{(M)} I_2^{(M)}$. For most samples, $I^{(M)}$ will be on the order of tens of MW cm^{-1} . It will be necessary

to disperse the laser energy into a large enough volume that this magnitude of intensity will result. There is a practical limit to the size of the irradiated volume. There are two inescapable features of any real system which would be amenable to study with resonance Raman, namely that it would absorb at both the pump and probe wavelengths. This sets a limit on the irradiated sample thickness, perhaps a millimeter or two. In addition, if too large a volume is used, all the signal emanating from the back of the sample will probably be reabsorbed by the sample and lost, negating the benefits of the large depth-of-field. These features set a practical upper limit on the size of the irradiated volume in the neighborhood of $1 \times 10 \times 10$ mm. The transfer optics would have to have roughly unit magnification to transfer this image into the spectrometer. The irradiated area associated with this geometry is $\sim 1 \text{ cm}^2$. If a peak intensity of $\sim 100 \text{ MW cm}^{-2}$ can be tolerated, a pulse energy of $\sim 3 \text{ mJ}$ is indicated for a 30 ps pulse.

This is very close to the existing energy, so it appears that any further increase in the sample volume or laser power would not be especially fruitful. One would need joules per pulse before significant signal levels would be reached; at this point the required sample volumes would be too large to be practical. Actually, what is suggested by this calculation is that the system described above would have benefitted greatly from a larger sample volume and collection optics with smaller magnification. Unfortunately, by the time that this was realized, it was no longer feasible to try this approach.

All of these arguments with regard to focus and sample size apply equally well to systems with higher repetition rates as well. One difference between the two cases is that the maximum repetition rate is to some extent governed by the rate at which the sample volume is flushed. Clearly larger volumes will tend to decrease the allowable repetition rate. In this case, it is clearly desirable to increase the repetition rate at the expense of sample volume, so long as the average power does not suffer appreciably. This is because the image of the smaller volumes will be collected at higher magnification, and hence more efficiently, making better use of the existing average power. It is also advantageous

to increase the rate of photon counting if at all possible.

At this point it is clear that the most efficient way of measuring Raman spectra is to work at high repetition rates with moderate peak powers. One question which remains is that of how to go about detecting the signal. There are two well-established choices. A system with single channel detection very much like the system described above can be used. In this case, a double monochromator is used with a photomultiplier tube for signal detection. It should be possible to use either charge integration or photon counting in this case. As noted above, single photon counting tends to give better results, so it is likely to be preferred. At high repetition rates, single-photon counting is relatively simple, since one merely counts the number of pulses above a specified threshold value. If sample fluorescence is a problem, using a channel plate photomultiplier and the same electronics normally utilized in time-correlated single photon counting, should make it possible to gate the signals with a resolution of of hundreds of picoseconds. This should make it possible to discriminate against the longer-lived fluorescence signals.

A second alternative is to make use of a multichannel detector such as an intensified photodiode array. This approach is not new, having been suggested by Bridoux and Delhay²⁰ for picosecond work and by Brus et.al.¹³ in the nanosecond domain. In order to make efficient use of the array detector, it is necessary to use a significantly different optical system. The spectrometer used for this purpose is not the same as that used with single channel detection. Instead of the large double monochromator used with a photomultiplier tube, a triple monochromator consisting small, double monochromator with subtractive dispersion coupled to a highly dispersive single monochromator is used. The first stage acts as a prefilter to eliminate most of the stray light from the system. In terms of transfer optics it acts as a unit magnification system and a bandpass filter. Since it is operated at low resolution, the slit widths can be comparable to those used in the final stage monochromator. There will be a minimum of light loss in the first stage, and most of the previous discussion of the optimum arrangement of the relay optics can

be carried over directly into this configuration. The final stage of this system takes this filtered output and disperses it onto an image plane, where the array detector can be placed. By changing gratings in this stage, the dispersion of the array channels can be varied as needed.

Actually, a case can be made both for and against the use of such a detector. Although the multichannel detector increases the rate at which data can be collected, the quantum efficiency of the associated image intensifier is generally lower than that of the phototube, so at low signal levels both systems become comparable. In addition, photon counting with an array is somewhat uncertain, so that there may be yet another loss of signal at this point. In terms of overall sensitivity, the two systems are comparable. The array is better for large signals, since entire spectra can be accumulated in a few or even in a single shot²¹. The photomultiplier may have the edge for detecting very weak signals. Since transient spectra are expected to fall into the latter group, the photomultiplier approach appears to have a very slight edge. Since the quality of image intensifiers is still improving, this may not be a permanent advantage; if a multichannel detector which could be used for single photon counting for each channel were to be used, the array detector could ultimately have an order of magnitude advantage over the single channel system.

A different approach to the problem of increasing the throughput of the spectrometer is to use a different type of monochromator. An interesting possibility is the time-of-flight spectrometer described by Ross²¹. In this device, the dispersion present in an optical fiber is used as an optical dispersing element. It is in essence an optical chromatograph; light is injected into one end of the fiber, dispersed with respect to wavelength and then detected with respect to time. In many ways, such a device is ideally suited to the picosecond regime, since the time resolution is the crucial factor in determining the spectral resolution. The appeal of this system for Raman spectroscopy is that the sample could be placed in a hollow waveguide cell and coupled directly into the fiber

monochromator. In this way all the losses associated with the small numerical aperture of the monochromator could be eliminated, greatly increasing the signal reaching the detector. Unfortunately, most optical fibers are designed to minimize dispersion, so rather long fibers (several kilometers) are needed to yield the necessary dispersion; because of this, losses in the fiber tend to be a problem. In addition, it is necessary to have very high time resolution in the detection system (~ 50 ps) to attain the necessary ($\sim 10 \text{ cm}^{-1}$) spectral resolution. This would necessitate the use of a streak camera, or alternatively, an optically gated detection system. Although this is possible, it is not easy to do. Besides, both of these detectors are much less sensitive than a photomultiplier tube, negating any advantage generated by the collection system. Thus, while this concept remains appealing, and may well be applicable to picosecond problems, the requirements imposed by Raman spectroscopy are too stringent for this system to be used profitably.

4. Coherent Raman Techniques.

The last aspect of Raman spectroscopy to have been considered is that of coherent Raman spectroscopy. There are actually a large number of techniques which are considered under this heading, including Coherent Anti-Stokes Raman Spectroscopy, Stimulated Raman (gain/loss) Spectroscopy (SRS) and the Raman Induced Kerr Effect (RIKES). A rather thorough review of these techniques is given in reference 23. From the point of view of picosecond dynamic studies, the most important features of a spectroscopic method are going to be the sensitivity, ease of operation and the extent to which the method will be affected by the presence of a large pump pulse a few picoseconds earlier. Under most circumstances it has been found that spontaneous Raman is more sensitive and easier to use than any of the coherent techniques. It has a lower intrinsic background and is much easier to use than any of the methods involving multiple beams²³. Nonetheless, there is a case to be made for using these techniques for picosecond detection. The main reason why spontaneous Raman is as sensitive as it is derives from the lack

of any background signal. The large nonlinear background observed in the picosecond experiments tends to degrade this sensitivity badly. A general feature of the coherent techniques is that the signal levels scale with the incident laser powers, so that using powerful picosecond pulses will tend to increase the signals. Of course, background signal increase as well, so this is not as advantageous as it might seem. Nonetheless, this is in sharp contrast to spontaneous scattering, where high powers simply obliterate the signal. Nonlinear fluorescence is no longer a major problem, since the coherent output beam can be easily distinguished from fluorescence. Indeed, Using coherent Raman techniques, it is possible to measure the Raman spectra of fluorescing dye solutions²³. Ultimately, the appeal of the coherent techniques was that they appeared to be better suited to picosecond measurements. Unlike the case of spontaneous Raman, where high peak powers were an endless source of difficulties, power requirements of the coherent methods seemed perfectly suited to the laser system's limitations.

Coherent Raman interactions can be derived from the the third order polarizability of a material²³. Consider the third-order interaction of four time-harmonic electric fields of the form

$$\mathbf{E}(\mathbf{r}, t) = \frac{1}{2} [E(\mathbf{r}) \exp i(\omega t - \mathbf{k} \cdot \mathbf{r}) + \text{c.c.}] \quad (3.13),$$

in an isotropic medium. In general, the polarization of the medium resulting from any three of these waves will be of the form

$$P_i^{NL} = \sum_{jkl} \chi_{(ijkl)}^{(3)} (-\omega_i, \omega_j, \omega_k, -\omega_l) \mathbf{E}_j \mathbf{E}_k \mathbf{E}_l^* \quad (3.14).$$

In principle, there can be 81 components in the $\chi^{(3)}$ tensor, but in an isotropic medium, the symmetry only allows 4 components. One corresponds to all four polarizations in the same plane, and the other 3 to permutations of pairs of polarizations in perpendicular planes. At this point, consider the case where all three input fields have the same polarization; in this case $\chi^{(3)}$ reduces to a scalar.

It is desirable to see how this relates to Raman spectroscopy, that is to explicitly consider the Raman contribution to $\chi^{(3)}$. By considering a two-level system in the presence of an electric field, it is possible to derive an expression for the polarizability of the system in the neighborhood of a two-photon resonance. This includes both two-photon absorption resonances and Raman resonances. In general, it can be shown that $\chi^{(3)}$ takes the form

$$\chi^{(3)} = \chi_{NR}^{(3)} + \frac{\alpha N \Delta \omega}{(\Delta \omega)^2 + \Gamma^2} + \frac{i \alpha N \Gamma}{(\Delta \omega)^2 + \Gamma^2} \quad (3.15).$$

$\chi_{NR}^{(3)}$ is a real offset analogous to the real index of refraction, arising from the contributions of all the other system resonances. Thus, the real part of $\chi^{(3)}$ has both resonant and nonresonant contributions, while the imaginary part must be resonant²³. This is physically reasonable, since imaginary polarizations correspond to absorptions, and the system must be at a resonance for energy to be absorbed.

To see how the nonlinear polarization gives rise to Raman scattering, substitute the polarization component at frequency ω_i into the source term of the classical wave equation:

$$\nabla^2 \mathbf{E}_i - \frac{n^2}{c^2} \frac{\partial^2 \mathbf{E}_i}{\partial t^2} = \frac{4\pi}{c^2} \frac{\partial^2 \mathbf{P}_i^{NL}}{\partial t^2} \quad (3.16).$$

Here c is the speed of light and n is the index of refraction. Since the purpose of this is to generate a polarization at the fourth frequency ω_i , it is only necessary to consider frequencies which obey the relationship

$$\omega_i = \omega_j + \omega_k - \omega_l \quad (3.17).$$

It is also reasonable to define the phase mismatch

$$\Delta \mathbf{k} = -\mathbf{k}_i + \mathbf{k}_j + \mathbf{k}_k - \mathbf{k}_l \quad (3.18).$$

Assume that \mathbf{k}_i is along the z axis and the second spatial derivative of E can be neglected.

Then the wave equation reduces to

$$\frac{\partial E_i}{\partial z} = \frac{2\pi i \omega_i}{n_i c} \chi_{(ijkl)}^{(3)} E_j E_k E_l^* \exp i(\Delta \mathbf{k} \cdot \mathbf{z}) \quad (3.19).$$

Integrating this equation with the initial condition $E_i(0) = 0$ yields the appropriate output signal.

Stimulated Raman scattering can be derived by considering the case where $\omega_i = -\omega_j$, $\omega_k = -\omega_l$, $k_i = -k_j$ and $k_k = -k_l$. These conditions correspond to ω_k and ω_l being the pump beam and ω_i and ω_j being in the same (arbitrary) direction. Without loss of generality, the phase is chosen so that $E_i(0)$ is real. It is also assumed that the depletion of the pump beam is negligible, so E_k is not a function of position. In addition, $\omega_k - \omega_i = \omega_S$ corresponds to the Raman Stokes shift. In this case, the coupling equation becomes

$$\frac{\partial E_i}{\partial z} = \frac{2\pi i \omega_i}{n_i c} \chi^{(3)} |E_k|^2 E_i \quad (3.20),$$

which becomes

$$E_i(z) = E_i(0) \exp\left(\frac{2\pi i \omega_i}{n_i c} \chi^{(3)} |E_k|^2 z\right) \quad (3.21).$$

Only the real part of the exponential contributes to the observed output, and only if the imaginary susceptibility is negative, will gain be observed. Spontaneous Raman scattering can be recovered by treating the initial value of I_i as quantum noise, exactly as with parametric scattering. It can be shown²⁴ that the Raman cross-section $d\sigma/(d\Omega d(1/\lambda))$ $\text{cm}^2 \text{sr}^{-1}$ is related to the imaginary susceptibility $\chi_{IM}^{(3)}$:

$$\chi_{IM}^{(3)} = \frac{2\pi N c^3}{48\hbar \omega^4} \frac{d\sigma}{(d\Omega d(1/\lambda))} L(\Delta\omega) \quad (3.22),$$

where L is a lineshape function. It can also be shown²⁴ that for confocal gaussian beams with powers P_i and P_k in the limit of low conversion,

$$\frac{\Delta P_i(z)}{P_i} = \frac{384\pi^4}{\lambda^2 c n} P_k \chi_{IM}^{(3)} \quad (3.23).$$

The major features of SRS can be seen from this derivation. The signal is linear in the concentration of scattering molecules, and in both the laser powers. Phase matching is not a problem; no matter what axis the two lasers are on, the interaction can still occur

SRS is readily used as a spectroscopic technique in transparent solvents, and can be detected in several ways. If a stable CW²⁴ or CW mode-locked²⁵ laser is used, then it is possible to monitor either the gain at the Stokes frequency or the loss at the pump laser frequency. Peak powers on the order of a watt are typically used in these measurements, and power gains/losses of 1 ppm can be detected. It is also possible to use a pulsed laser and detect the absorbed energy by optoacoustic methods²⁶. These methods can typically detect spectral features with an intensity .001 times that of benzene. A numerical estimate of the potential sensitivity of the method used with the YAG system can be obtained. For pure benzene at 992 cm^{-1} , $\chi_{IM}^{(3)} = 1.6 \times 10^{-13}\text{ cm}^3/\text{erg}$; a typical laser power for the YAG system is 10 MW. This gives a value in excess of 5000 for $\Delta P_i(z)/P_i$. This is clearly beyond the low conversion limit, but it indicates that the ppm concentration range might be accessible with power changes near 1%. It is not clear that these powers can actually be focussed through a liquid without giving rise to other nonlinear losses related to sample breakdown or two photon absorption.

In terms of pure spectroscopy, SRS has a number of desirable features, including large signals, immunity to sample fluorescence and potentially high resolution, but it is not clear that these features will survive in a pump-probe experiment. The possibilities for the method are reasonable, but there are several potential pitfalls. In particular, if Raman loss or Raman gain are being detected, the method will fail in a pump-probe experiment if there is any induced absorption or scattering losses, since it will not be possible to distinguish the various loss mechanisms. Optoacoustic detection will be at even more of a disadvantage, since the signal will be buried under the energy deposited in the sample by the pump laser, and will probably be impossible to detect. Thus, although SRS looks like a reasonable method on paper, it appears that it will suffer from even worse problems than does spontaneous Raman. As a result it was not pursued experimentally.

A second nonlinear Raman spectroscopic technique is CARS²³. This can be derived from the general expression by considering the case where $\omega_k = -\omega_l$ and $-\omega_i + \omega_s =$

$\omega_j = \omega_l - \omega_S$ where ω_S is the Stokes shift. In this case, Δk depends on the dispersion of the medium. The angles of the incident beams must be adjusted until the condition $\Delta k \cdot z = 0$ is achieved. The coupling equation becomes

$$\frac{\partial E_i}{\partial z} = \frac{2\pi i \omega_i}{n_i c} \chi^{(3)} E_j E_k E_l^* \quad (3.24).$$

This can be solved to yield (in terms of intensities)

$$I_i = \frac{64\pi^3 \omega^2 z^2}{n^3 c^3} |\chi^{(3)}|^2 I_j I_k I_l \quad (3.25).$$

This is clearly a less desirable result than that for SRS, since the signal will scale with the absolute value of $\chi^{(3)}$ which includes the nonresonant term. For all practical purposes this restricts the use of CARS to pure compounds, since the spectrum of a solution will represent primarily the nonresonant polarizability of the solvent rather than the solute of interest. As a practical matter, two other difficulties are involved with CARS. The first is the phase matching condition, since liquids have sufficient dispersion that noncollinear phase matching is required. This makes the method difficult to align, and results in a short interaction length. The second problem is that the resonant signal scales with the square of the concentration. This is readily compensated for, but it means that the sensitivity falls off rapidly with decreasing concentration. In general, CARS is well suited to measuring spectra of major components in gases in the small focal volumes of the laser. Because of this, it is widely used for such things as measuring N_2 vibration-rotation spectra to determine flame temperatures²³. It is not well suited to liquid solution measurements. This is unfortunate, because it is otherwise a reasonable method for use in a pump-probe experiment. It is not overwhelmingly sensitive to the small sample perturbations associated with the excitation pulse, and the output is in the form of a conveniently accessible beam. Were it not for the nonresonant susceptibility, it would be a reasonable method.

A variety of tricks have been proposed for getting around the nonresonant susceptibility, but none have been terribly successful. It is possible to use the polarization

dependence of CARS to generate beams with differing amounts of resonant and nonresonant scattering. By heterodyning these two beams, it is possible to cancel most of the nonresonant scattering, and increase the sensitivity by roughly an order of magnitude²⁷. Unfortunately, this method is difficult to use, and will suffer from any birefringence induced in the sample by an excitation pulse. In addition, the order-of magnitude improvement in signal is not enough to make it useful for solutions at concentrations below a few per cent.

A second method for eliminating the nonresonant contribution exploits the real lifetime of the induced polarization to separate the resonant and nonresonant processes²⁸. Two beams are initially passed through the sample to excite a vibrational population via SRS. This population is allowed to evolve for a time, and then a second beam is sent through the sample and scattered off the remaining polarization. This provides a method for detecting the energy left in the sample by SRS. Although in principle, this method seems to be applicable to picosecond measurements, there are enormous complexities involved. The question of generating transient polarizations and studying their decay has been widely studied²⁹. In general, the dephasing time of the polarization is on the order of a few picoseconds, and to carry out a pulse-sequenced CARS measurement, it is necessary to generate a population with one pulse and then use a second pulse within a few picoseconds to observe the resonant scattering. This severely constrains the widths of the pulses used. Not only must they be on the order of a few picoseconds in length, but there can be no wings to the pulse, since the nonresonant interaction stemming from the edges of the pulse will still overwhelm the weak and decaying resonant signal. Note that the signal will not simply be a function of the concentration, but will depend on the dephasing time as well. This in turn has a strong concentration dependence³⁰. As a method for measuring the dephasing time of liquids, this type of measurement is reasonable. It is essentially the only way of making such measurements, so the difficulty is justified. Successful measurements have been made with both Nd:glass lasers³⁰ and

CW mode-locked dye lasers³¹; in both cases pulses of less than 5 ps are available. The method also has some unique aspects as a spectroscopic technique, and some unusual line narrowing effects have been observed in some liquids³². When the OPS was first constructed here, it appeared that transform-limited pulses with virtually no wings could be generated and that pulse-sequenced methods might be viable. On further characterization, it was found that the OPS pulses were neither as short nor as reliable as had been initially believed. It became clear, that a pulse-sequenced method could not be used here. Whether these methods are useful for anything besides dephasing measurements is debatable. They appear to be an extremely difficult method for generating nonlinear signals that can often be obtained by other methods.

In general, the only coherent method which appears to have any real potential value for pump-probe picosecond experiments is SRS. This method is linear, requires no special phase matching and has no contribution from the nonresonant susceptibility. It has in fact been successfully implemented using CW mode-locked lasers, although not in a pump-probe type experiment. The limitation in this method is the ability to measure the small change in the transmitted signal accurately. The stability of the CW laser is high enough that this is possible; whether comparable measurements are possible with the noisier pulsed lasers is difficult to say. One feature which may ultimately prevent this method from working is the presence of excite-state absorption in the sample. This is not a problem in the purely spectroscopic measurements, but it may be inevitable in a pump-probe measurement. Thus, while the coherent methods make it possible to generate much larger Raman signals than can be obtained from spontaneous Raman, the measurements are susceptible to several types of background problems which appear to be worse than those encountered with spontaneous Raman scattering. Coherent methods are wonderful from the point of view of resolution, and can be made to work reasonably well in well-behaved, nonabsorbing samples or in pure compounds. However, in the relatively hostile environment of a flowing liquid cell of a dilute solution undergoing a pump-probe

measurement, coherent Raman appears to be at a severe disadvantage.

F. Conclusion.

Of the three spectroscopic techniques discussed here, time-resolved emission is clearly the easiest to use and produces the best results. In systems where it can be used it is clearly the method of choice. The technique used for absorption is more difficult to use than the emission technique, and does not match the signal-to-noise ratios attainable with emission. Nonetheless, useful results, which are often unobtainable with emission, can be obtained this way. The results obtained here are relatively respectable for a single beam absorption technique. While pump-probe techniques appear to offer better sensitivity, they are correspondingly more complex to carry out. The method used here provides a simple way to extend the range of the emission system. Time-resolved Raman was much less successful. A combination of fundamental and instrumental limitations made it difficult to make any progress with this technique. There is no doubt that with a better-designed system it will be possible to obtain useful picosecond Raman spectra. The results will probably be limited to species which show significant resonant enhancement, but it appears that a large number of free-radical species may fall into this class. Thus, with sufficient development, picosecond Raman may become a usable, if still difficult, technique.

G. References for Chapter 3

1. A. J. Campillo and S. L. Shapiro, *IEEE J. Quant. Electron.* QE-19 (1983) 585-603; S. W. Yeh, Ph.D. thesis, University of California, Berkeley, 1985; Lawrence Berkeley Laboratory Report 20662.
2. R. M. Hochstrasser and R. B. Weisman, in *Radiationless Transitions*, S. H. Lin, ed., (Academic, New York, 1980) 317-362; See also references cited therein.
3. E. P. Ippen and C. V. Shank, *App. Phys. Lett.* 26 (1974) 92-93.
4. P. Bado, C. G. Dupuy, G. P. Bergsma and K. R. Wilson, in *Ultrafast Phenomena IV*, D. H. Auston and K. B. Eiseenthal, eds., (Springer-Verlag, New York, 1984) 296-299.
5. D. J. Bradley, S. F. J. R. Taylor and W. Sibbet, *Rev. Sci. Instrum.* 49 (1978) 215-219.
6. A. Penzkofer, W. Kaiser, *Opt. Quant. Electron.* 9 (1977) 315-349.
7. S. L. Palfrey, T. F. Heinz and K. B. Eiseenthal, in *Ultrafast Phenomena IV*, D. H. Auston and K. B. Eiseenthal, eds., (Springer-Verlag, New York, 1984) 216-219.
8. R. Danelyus, A. Piskarskas, and V. Sirutkaitis, *Sov. J. Quantum Electron.* 12 (1982) 1626-1632; R. Gadonas, R. Danelyus and A. Piskarskas, *Sov. J. Quantum Electron.* 11 (1981) 407-408.
9. C. V. Shank, E. P. Ippen, O. Teschke and K. B. Eiseenthal, *J. Chem. Phys.* 67 (1977) 5547-5561.
10. T. D. Westmoreland, Ph.D. thesis, University of North Carolina, Chapel Hill, 1985; BOSCO is $[(2,2'\text{-bpy})_2\text{Os}^{II}(\text{CO})(4,4'\text{-bpy})][\text{PF}_6]_3$, where bpy is bipyridine.
11. T. D. Westmoreland, K. S. Schanze, P. E. Neveux, E. Danielson, B. P. Sullivan, P. Chen and T. J. Meyer, *Inorg. Chem.* 104 (1984) 2596-2597; Re-PTZ is $[(2,2'\text{-bpy})\text{Re}^I(\text{CO})_3(\text{py-PTZ})]^+$ where bpy is bipyridine, and py-PTZ is a methyl pyridine substituted phenothiazine.
12. S. M. Beck and L. E. Brus, *J. Amer. Chem. Soc.* 104 (1982) 1805-1808.
13. S. M. Beck and L. E. Brus, *J. Chem. Phys.* 75 (1981) 4934-4940.
14. S. Y Lee and E. J. Heller, *J. Chem. Phys.* 71 (1979) 4777-4788.
15. See, for example S. M. Beck and L. E. Brus, *J. Amer. Chem. Soc.* 104 (1982) 4789-4792; M. Forster and R. E. Hester, *Chem. Phys. Lett.* 85 (1982) 287-292; G. N. R. Tripathi and R. H. Schuler, *J. Phys. Chem.* 85 (1983) 1706-1710; Also references cited therein.

16. P. Robrish and H. Rosen, *Study of the Spectroscopy of NO₂ by Selective Excitation with a Tunable Laser*, Lawrence Berkeley Laboratory Report 3229, Berkeley, 1975.
17. T. L. Gustavson, D. M. Roberts and D. A. Chernoff, *J. Chem. Phys.* **79** (1983) 1559-1564.
18. L. A. Philips, Ph.D. thesis, University of California, Berkeley, 1985; Lawrence Berkeley Laboratory Report 19511.
19. B. H. Kolner, D. M. Bloom, J. D. Kafka and T. M. Baer, in *Ultrafast Phenomena IV*, D. H. Auston and K. B. Eisenthal, eds., (Springer-Verlag, New York, 1984) 19-22; W. H. Knox, M. C. Downer, R. L. Fork and C. V. Shank, *Optics Lett.* **9** (1984) 552-554; P. Bado, I. N. Duling, T. Sizer, T. B. Norris and G. A. Mourou, in *Ultrashort Pulse Spectroscopy and Applications (Proc. SPIE, V. 533)*, M. J. Soileau, ed., (SPIE, Bellingham WA, 1985) 59-62.
20. M. Bridoux and M. Delhay, in *Adv. Infrared Raman Spectros.*, (Heyden, New York, 1976) Vol. 2, 140-152.
21. P. Valat and H. Tourbez, *J. Raman Spec.* **8** (1979) 139-144.
22. W. B. Whitten and H. H. Ross, *Anal. Chem.* **52** (1980) 101-104.
23. M. D. Levinson, *Introduction to Nonlinear Laser Spectroscopy*, Academic, New York, 1982.
24. A. Owyong *IEEE J. Quant. Electron.* QE-14 (1978) 192-203.
25. J. Baran, D. Elliott, A. Grofcsik, W. Jeremy Jones, M. Kubinyi, A. Langley and V. U. Nayar, *J. Chem. Soc., Faraday. Trans.* **79** (1983) 865-883; R. A. Beaman, J. Baran, A. Grofcsik, M. Kubinyi, A. Langley, V. U. Nayar and W. Jeremy Jones *J. Mol. Struct.* **115** (1984) 237-240.
26. C. K. N. Patel and A. C. Tam, *App. Phys. Lett.* **34** (1979) 760-763.
27. J. L. Oudar, R. W. Smith and Y. R. Shen, *App. Phys. Lett.* **34** (1979) 758-760.
28. F. M. Kamga and M. G. Sceats, *Optics Lett.* **5** (1980) 126-128.
29. A. Laubereau and W. Kaiser, *Rev. Mod. Phys.* **50** (1978) 607-665.
30. M. L. Geirnaert and G. M. Gale, *Chem. Phys.* **86** (1984) 205-211.
31. J. P. Heritage, *App. Phys. Lett.* **34** (1979) 470-472.
32. W. Zinth, M. C. Nuss and W. Kaiser, in *Ultrafast Phenomena IV*, D. H. Auston and K. B. Eisenthal, eds., (Springer-Verlag, New York, 1984) 263-265.

Chapter 4

Picosecond Solvation Processes in 9,9'-Bianthryl

A. Introduction

There has always been a very strong connection between chemistry and the study of liquid solutions, since such solutions provide the medium in which the majority of chemical processes of practical interest occur. There is a very good reason for this, since liquid solutions constitute an excellent environment for chemical reactions, with a combination of high density and facile molecular motion which maximizes the collision rates between potentially reactive molecules. Since collisions constitute the primary events in most chemical reactions, it is apparent why solution-phase processes play such a large role in chemistry. Solvents are more than just an inert medium to support the reacting species, and the outcome of a given reaction is often strongly dependent on the solvent used. By changing the solvent it is possible to completely change both the rate and the product distribution of a given reaction. A number of factors ordinarily go into the choice of a solvent. Such a choice is often based on experience and intuition, with empirical rules-of-thumb such as "like dissolves like", playing a major role. Solvent physical properties such as polarity, acidity, viscosity or volatility, as well as practical properties such as purity, toxicity or price are often the determining factors. Since a large number of solvents with a variety of physical properties are commercially available, a resourceful chemist can generally combine these empirical considerations to find a solvent or solvent mixture suited to a particular application¹. Such pragmatic rules are difficult to interpret physically, since they are related to macroscopic properties of the solvents, and do not pertain directly to microscopic solvent-solute interactions. From a physical point of view, it is these microscopic interactions which are responsible for determining the roles which solvents can play in chemistry. Elucidating the connections between the

empirical, macroscopic rules used in practice and the fundamental nature of solvation is essential to a physical understanding of condensed phase chemistry.

The nature of the liquid phase makes it difficult to extract information about the underlying microscopic processes. The very properties which make liquids so well suited to chemistry (high density, high collision rates and a disordered environment) are the same properties which make liquids so difficult to study. To obtain information about the microscopic dynamics occurring in the liquid, measurements with time resolution comparable to intermolecular collision rates are necessary. Liquid densities are intrinsically high, on the order of 10^{22} molecule cm^{-3} , and a molecule experiences a collision approximately every 100 femtoseconds². Even though this number is somewhat artificial (a molecule in a liquid does not undergo discrete collisions, but is always in close contact with *several* neighboring molecules), it defines the relevant microscopic time scale. In the gas phase, collision rates can be reduced to convenient levels by changing the pressure. In solids, a combination of low temperatures and a rigid, ordered environment often lead to a similar slowing of the important dynamic processes. Since liquids are intrinsically dense and disordered, there is no obvious way to effect such a simplification in this case, and high time resolution is an inescapable requirement. This need for high time resolution severely constrains the range of experimental techniques which can be used to investigate microscopic processes in solution. Only with the development over the last two decades of of picosecond (ps) and, more recently, femtosecond (fs) spectroscopic techniques have measurements of microscopic solvation processes become possible.

In view of the experimental difficulties associated with probing the microscopic properties of liquids, theoretical studies might be considered as a means of clarifying the situation. Unfortunately, theoretical studies of liquid properties have not yet achieved the degree of sophistication required for dealing with real systems. To properly model the liquid state, it is necessary to simultaneously consider a large number of molecules interacting through poorly defined potentials for a large number of collisions³. This is clearly

a difficult problem, and it immediately leads to almost insurmountable computational difficulties. Even for simple, relatively tractable systems such as liquid rare gases, calculations which go beyond a few picoseconds (i.e. thousands of collisions per molecule) are all but impossible. The theoretical study of solutions of more complex molecules under realistic conditions is simply beyond the range of the current technology⁴.

A number of experimental methods have been devised for studying the nature of solvation. One of the most direct methods for studying solutions and the nature of solvent-solute interactions is that of observing spectroscopically the behavior of an isolated probe molecule in solution. In a dilute solution, the interactions between such a probe molecule and the surrounding solvent are reflected in the internal energy levels of the probe molecule, and thus in the spectroscopic properties of the system. The use of such spectral shifts to clarify the nature of solvent-solute interactions is an old and well-established technique, dating back to the work of Hildebrand and co-workers on the solvent dependence of the spectra of iodine complexes⁵. In this case, the observed spectral shifts arose from the formation of charge-transfer complexes; the magnitude of the spectral shift was thus an indicator of the Lewis acidity of the solvent. This approach can be extended to measurements of many other solvent properties. By determining the spectral properties of various probe molecules in different solvents, scales reflecting various combinations of solvent properties been developed. Such diverse spectroscopic techniques as ³¹P-NMR, visible circular dichroism, and UV absorption applied to suitable probe molecules have all yielded useful information⁶. Since these scales are based on steady-state measurements, they reflect the equilibrium properties of the solvents. However, the spectra themselves correspond to the instantaneous, microscopic behavior of individual probe molecules. With suitable time resolution, such measurements can yield information about the dynamic nature of solvent-solute interactions. Such dynamic information is important because chemical reactions are fundamentally dynamic processes. To understand the dynamics of condensed-phase chemical reactions, it is first necessary

to understand the dynamics of the environment in which they occur.

B. Excited-State Solvation

1. Overview

The measurements described below emphasize the solvation processes of excited-state molecules in solution. There are several reasons for using excited molecules as solvation probes. First of all, they can be created very rapidly; the process of photon absorption occurs on the timescale of a single optical cycle, (a few femtoseconds for visible light), so with a suitable excitation pulse, it should be possible to create a population of excited-state molecules on this timescale. Once an excited state molecule is formed, its physical properties are often quite different from what they were in the ground state. The electronic distribution can change greatly on going from one electronic state to another. Since many molecular properties, such as acidity⁷, polarity⁸, and Lewis acidity⁹ are very sensitive to subtle changes in the electronic distribution, large changes in these properties can be expected. Cases exist where the pK_a of a molecule either increases⁷ or decreases¹⁰ by many orders of magnitude on excitation. Similarly, dipole moments can also increase or decrease greatly, depending on the system in question¹¹. Molecules are also known to undergo major conformational changes in the excited state¹², even if no dipole change is involved. These types of changes simply reflect the different potential surfaces found in the excited state, and they can occur even in the absence of any solvent. When such changes do occur in the presence of solvent, they result not only in a change in the probe molecule, but also in a modification of the solvent-solute potential surface. This in turn leads to solvent-solute relaxation and dynamic solvation. For example, if exciting a molecule in a polar solvent causes a large increase in the dipole moment, then the solvent dipoles will tend to reorient themselves to counteract the new charge distribution. Since this change will also serve to stabilize the excited state, this relaxation will be

reflected in spectroscopic properties of the probe molecule. By performing time-resolved spectroscopy, it will then be possible to follow this relaxation as it occurs.

A final reason for working with excited-state molecules is that they are spectroscopically convenient. The fluorescence associated with decay to the ground state provides a simple way to observe the evolution of the excited-state population. This naturally leads to the use of time-resolved emission spectroscopy as an experimental method. When this method is applicable, it provides a very simple, direct way of following relaxation processes. It is restricted to molecules which fluoresce and can only be used to follow relaxation channels which are not accompanied by radiationless conversion to the ground state. In general, these channels are limited to those which do not significantly perturb the molecular chromophore; photochemical processes such as dissociation are almost always accompanied by internal conversion. As a practical matter, this distinction can be considered as the divide between solvation and photochemistry. Time-resolved absorption spectroscopy is also potentially useful in studying solvation, providing a second, often complementary method for observing the probe molecule. Although both absorption and emission measurements reflect the same underlying physical processes, the different spectra can emphasize different aspects of the process. An example of this can be seen in figure 4.1, where the emission spectrum shows much greater changes than the excited-state absorption spectrum. Absorption spectroscopy also has the advantage of being usable for detecting molecules in their ground states. This makes it applicable to a wide range of photochemical processes.

The process of solvation is shown schematically in figure 4.1. The curves shown here are drawn for the case that the ground state (S_0) is non-polar while the next two excited states (S_1 and S_2) exhibit significant and roughly equal dipole moments. Point A gives the equilibrium solvent-solute configuration for the ground state, while C gives the corresponding point for the S_1 state. Upon absorbing a photon, a molecule undergoes a Franck-Condon transition from point A into an unrelaxed vibronic level, possibly in-

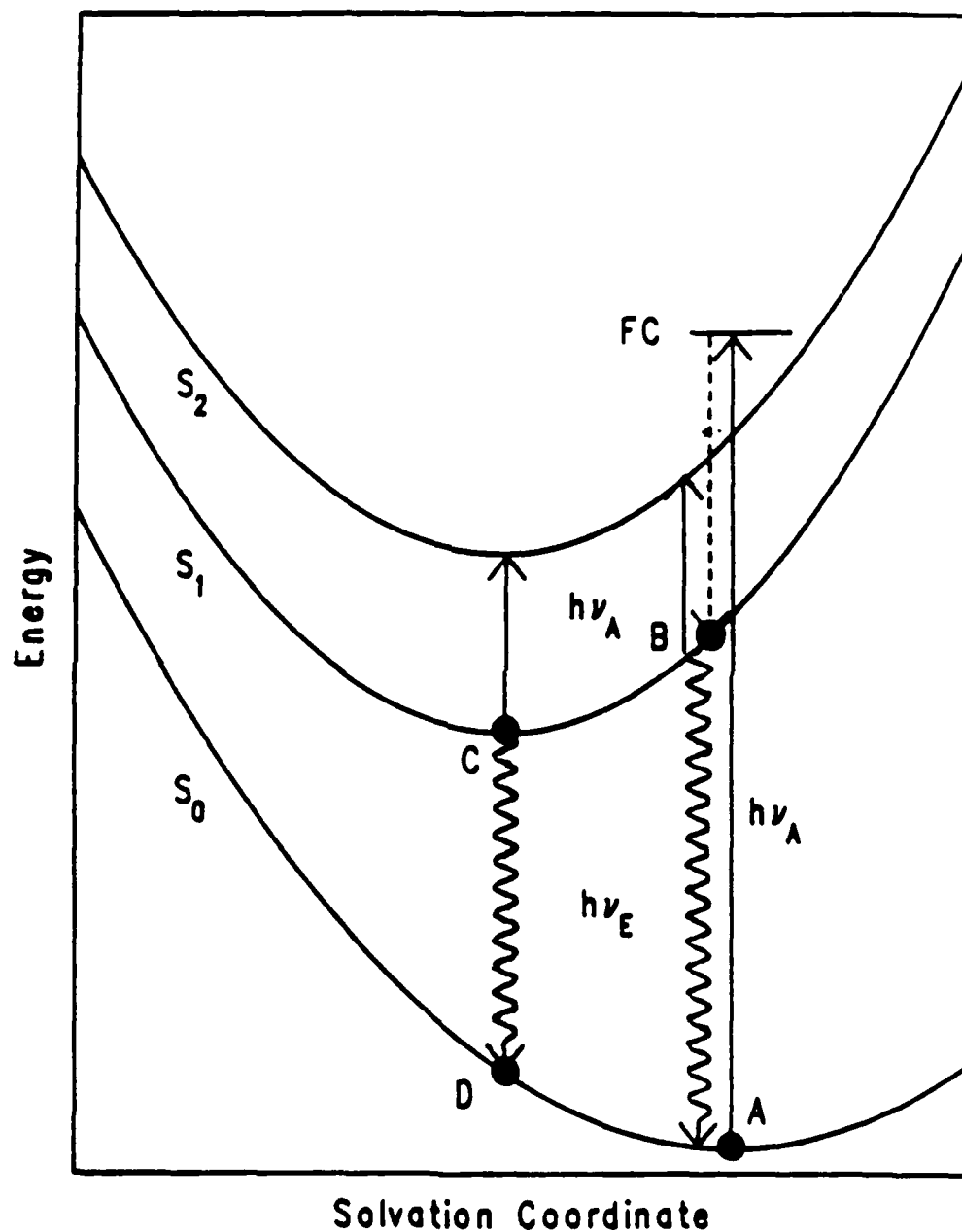


Figure 4.1. Potential energy diagram for a continuous solvation process along a single solvation coordinate, as described in the text.

volving a higher electronic state, as shown. Emission occurring at this point is unrelated to the structure of the excited states and corresponds to resonance Rayleigh or Raman scattering¹³. The molecule rapidly relaxes (~ 100 fs¹⁴) into the lowest vibrational level of the S_1 manifold at point B. The system then begins to propagate down the S_1 potential curve from B to C as shown. In this case, this process would correspond to the polarization of the solvent in response to the imposed solute dipole moment. Note the effect that this has on the other two states. The S_2 state, having a similar dipole moment is stabilized by this process, so that the $S_2 \leftarrow S_1$ absorption spectrum would show very little change. On the other hand, the $S_1 \rightarrow S_0$ emission spectrum shows a significant red shift as the excited state is stabilized and the ground state is destabilized by the solvent relaxation. The observed emission depends on the lifetime of the S_1 state. If it is shorter than the relaxation time from FC to B, then only resonance Rayleigh and Raman scattering will be seen. If it is shorter than the relaxation time from B to C, the unrelaxed fluorescence will predominate. If the lifetime is longer than the other relaxation processes, the full relaxation process will be detectable, subject only to the time resolution of the detector. If such a process can be monitored, it will be a real-time measurement of solvation.

This potential curve is only a qualitative approximation and is not necessarily applicable to all excited-state solvation processes. The model just described assumes that dipole-dipole interactions are the only form of solvent-solute interaction, and ignores the presence of multiple interacting excited states. These assumptions are often not correct. Figure 4.2 shows a second commonly proposed model for solvation of polar excited states¹⁵. In this case, excitation to a Franck-Condon state and rapid relaxation leaves the molecule at the point B in the nonpolar LE potential well. The energy of the polar CT state on the right depends on the local polarization of the solvent, that is, the degree to which the solvent can interact with the solute dipole moment. In the Franck-Condon state, the solvent is still configured to stabilize the nonpolar ground state, so at short times the nonpolar excited state will be the most stable. In a polar solvent, however, the

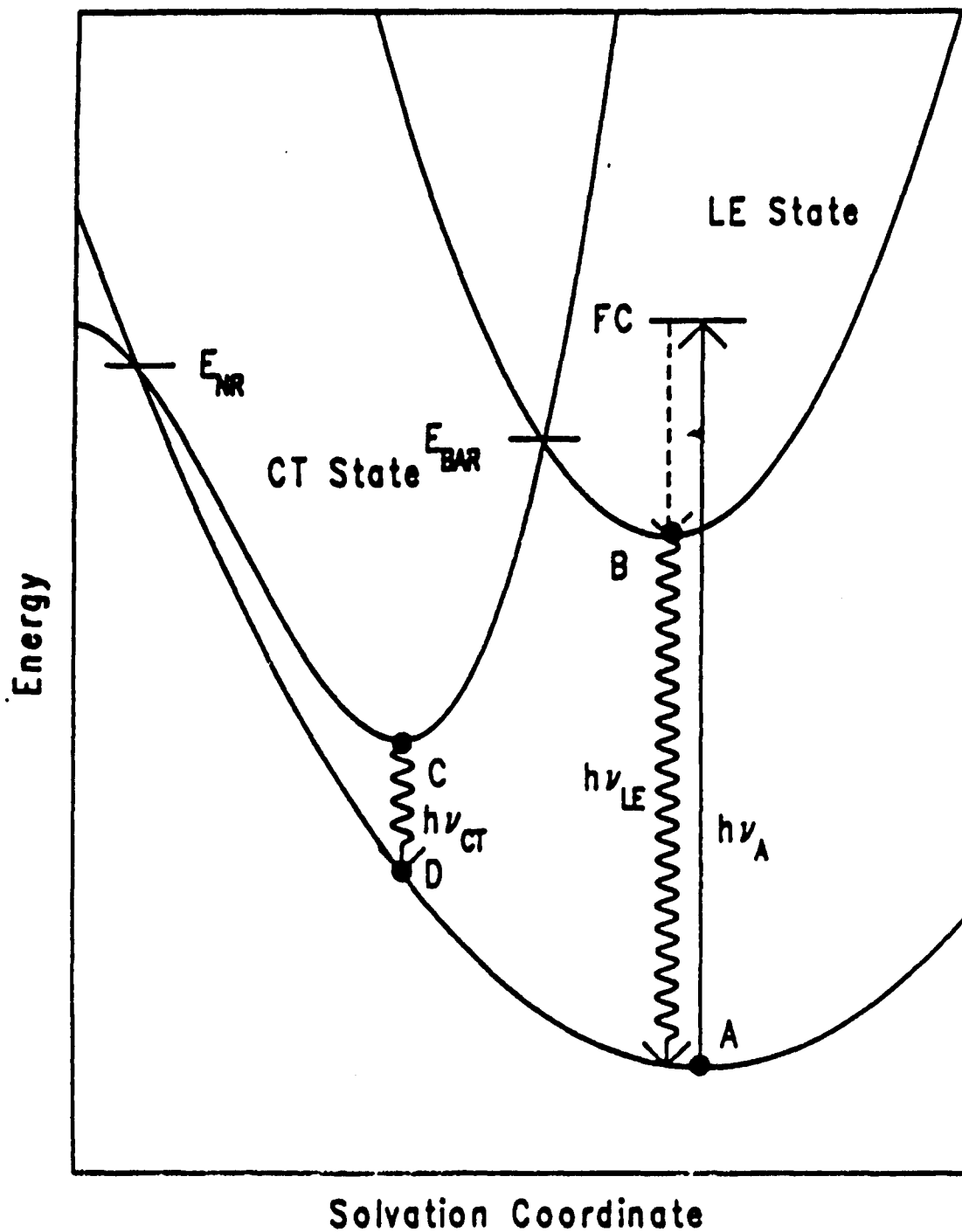


Figure 4.2 Potential Energy Diagram for a two-state relaxation process along a single configuration/solvation coordinate, as described in the text.

CT state will ultimately be favored, as the polar solvent can stabilize the dipolar excited state. A rather complex relaxation process involving both solvent and solute motions is required to transfer a molecule from B to C. Not only will the energy C vary with the solvent polarization, but the barrier between the two states will also change. The details of how the solvent-solute system makes this transition are not clear, since there is no longer a simple separation between solvent and solute relaxation processes. There is no longer the solute dipole moment "pushing" the solvent into a new configuration. Instead, the transition between the two excited states now involves a cooperative motion of both the solvent and solute. It is no longer clear whether the solvent is rearranging around solute, or whether the solute is responding to the polarization of the solvent. This process resembles a barrier crossing process in a molecule with many degrees of freedom, except in this case, the "molecule" consists of a solvent-solute complex. Note that as drawn there are two barriers to be crossed, one for LE-CT interconversion, and one for the internal conversion of the CT state. Changing the polarity will consequently have an affect on the excited-state equilibration and the overall lifetime. As will be seen, both of these are real effects.

The extent to which one will be able to observe solvation processes will depend on the time resolution of both the excitation source and the detector. With infinite time resolution, the example of figure 4.1 would show the details of vibrational relaxation and the gradual process of solvation. With pulses of finite duration excited state molecules will be generated over the entire pulsewidth, blurring any fast processes taking place. In this example, as time resolution is lost, the details of vibrational relaxation would disappear first, with more of the fine details of solvation gradually washing out until only the slower components of solvation remained visible. The present state of laser technology is such that optical pulses in the visible with a duration of only a few optical cycles can be produced. Using such a pulse it should be possible to generate a large population of excited state molecules in less than 20 fs. The rapidly developing field of

femtosecond spectroscopy has been reviewed in detail elsewhere¹⁶. In general, measurements are carried out using pump-probe techniques very much like those often used in the picosecond time regime¹⁷. Unfortunately, such a laser system was not available, so that a somewhat slower system, based on the approximately 30 ps pulses of a Nd:YAG laser was used instead. Use of this system for both absorption and emission spectroscopy have been described in the previous chapters. Various instrumental limitations restrict the time resolution of this system to about 10 ps, even when deconvolution techniques are used¹⁸. Although this is much slower than the process of excitation, it is still rapid enough to detect significant solvation processes in many molecules.

2. Previously Studied Systems: 1-Naphthol, DMABN and 4AP

The process of solvation in solutions containing electronically excited molecules has been studied for a number of years. With picosecond time resolution it has not been possible to monitor all aspects of this process. In general, vibrational relaxation of the solute¹⁴ or simple polarization of the solvent¹⁹ are too rapid to be observed on a picosecond timescale, but in many cases changes in solvent-solute interactions, notably proton transfer⁷ and hydrogen bonding²⁰ can be detected. In addition to this, many systems exhibiting conformational changes have been investigated²¹. Since such conformational changes are often accompanied by large changes in the molecular charge distribution, major solvent reorientation often takes place. In these cases, it is generally difficult to distinguish the rate of conformational change from the rate of solvent relaxation. Much confusion has resulted from the failure to distinguish between the two¹⁹.

Excited-state proton transfer is one of the most extreme examples there is of excited state solvation. Not only does the solvent stabilize the solute, it reacts with it. Numerous examples of excited-state proton transfer are known to exist²², characteristically involving large phenolic compounds as excited-state acids, or aromatic carbonyl compounds as excited-state bases¹⁰. It is convenient to classify proton transfer as a solvation process

because, unlike virtually any other dissociation process, it can occur entirely on the excited state manifold, suggesting that despite the proton transfer, the probe molecule remains relatively unperturbed. Proton transfer is readily reversible, and in aqueous solution, it often represents little more than a shift in a pre-existing hydrogen-bonded solvent complex. Thus it has much in common with other solvation processes such as hydrogen-bond formation. Systems involving proton transfer are often regarded as a relatively clear example of two-state relaxation. In the case of 1-naphthol in aqueous solution, studied in this laboratory, the excited state of 1-naphthol readily transfers a proton to the solvent with a single exponential time constant of 32 ± 5 ps⁷. The emission spectra for both the naphthol and the naphtholate ion are known from steady-state measurements and the observed time constant corresponds to both the fall time for naphthol emission and the risetime for the naphtholate emission. This seems to indicate that these are the only states involved in the relaxation process. However, even in this seemingly simple case there is evidence that other, more complex processes are occurring. When deuterated water is used as a solvent, there is isotopic exchange between the solvent and the hydrogens at the 5 and 8 positions of the naphthyl group. This demonstrates the unusual properties of excited-state molecules. Not only is the pK_a of the hydroxy group affected, but the ordinarily unreactive aromatic system becomes a strong base as well. This unusual protonation scheme can be related to observed proton-induced quenching of the naphtholate emission²³. It is important to note that aromatic systems can take on completely unexpected properties in the excited state. This example serves as a warning that even a seemingly well-understood two-state system may contain hidden complexities.

One of the most thoroughly investigated cases of conformational changes coupled to charge redistribution and solvation is the case of the formation of twisted intramolecular charge transfer (TICT) states¹¹. This is essentially the process described in figure 4.2, with the additional fact that the reaction coordinate involves an intramolecular rotation. Many examples of this type of behavior have been observed. The most widely studied

of these molecules is 4-(N,N'-dimethylamino)benzonitrile (DMABN). Early picosecond studies¹⁹ were interpreted in terms of solvent reorganization around the large dipole of the excited state, in a manner reminiscent of figure 4.1. Subsequent studies have suggested that figure 4.2 provides a better description. Experimentally, the spectroscopy of these molecules reflects the fact that both excited states are present, subject to an equilibrium which varies with solvent polarity. Figure 4.3 shows the conformations of this molecule in the ground and excited states. The ground state of DMABN can exist in either a planar (a) or a twisted (b) geometry. The experimental dipole moment of 7.6 Debye suggests that the planar form predominates. The excited states of both forms also exist, as shown in (c) and (d). The planar state maximizes the interaction between the amino nitrogen and the aromatic ring at the expense of the dipole moment, while the twisted state maximizes the dipole moment at the expense of π orbital interaction. In the absence of solvation the planar state is slightly more stable, but if the charge stabilization associated with a polar solvent is included, the twisted state is favored. This is directly analogous to the double well potential of figure 4.2.

The nature of the TICT state is relatively well understood, although there is some question as to whether the formation of this state is better thought of as a simple barrier crossing problem with a polarity-dependent barrier, or whether it is necessary to include other solvent effects such as viscosity or dielectric relaxation. Extensive studies in linear nitriles and alkane-nitrile mixtures have shown that in isoviscous solutions, the observed isomerization process can be well described by a polarity-dependent barrier crossing problem²⁴. For nitriles somewhat less polar than butanol (e.g. valeronitrile) a time constant of 16 ps was observed. Although it is not absolutely certain that this type of behavior persists when a hydrogen-bonding solvent is used, it clearly indicates that a rapid equilibration between the two excited states is possible. Numerous studies have been carried out regarding the internal rotation of aromatic compounds such as 1,1'-Binaphyl¹⁷ or various triphenylmethane dyes¹². In these cases, a relatively rapid

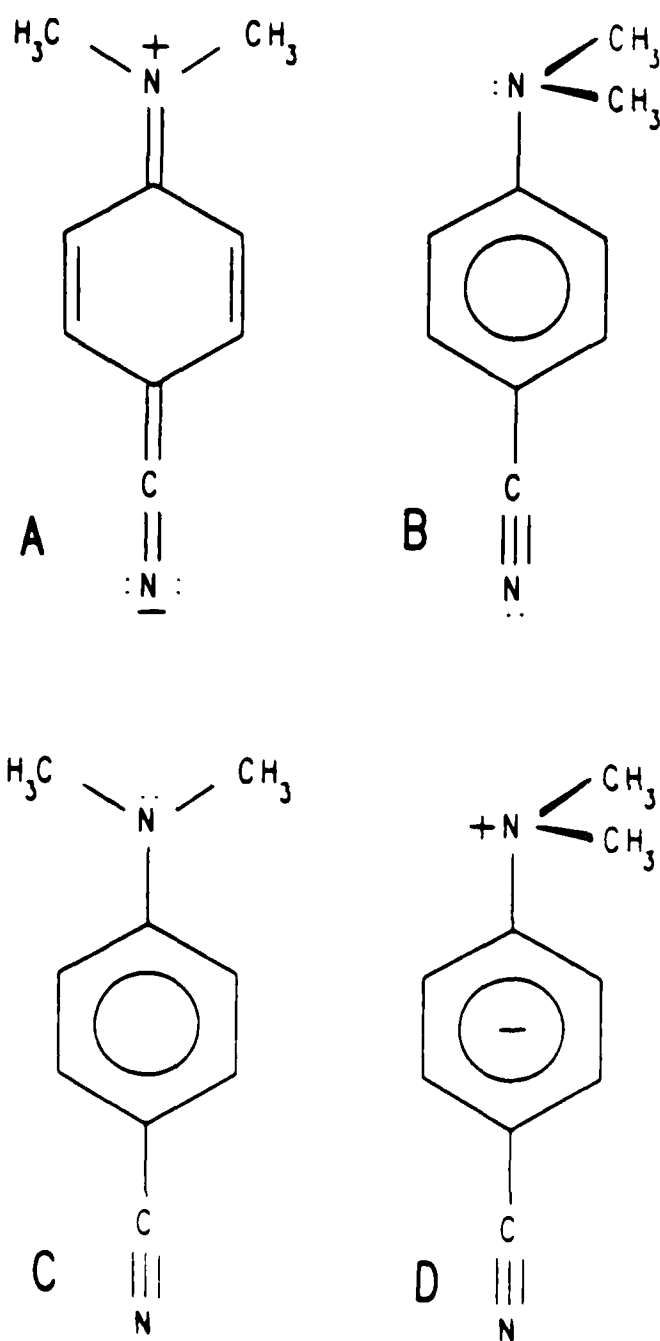


Figure 4.3. Conformations of DMABN in the ground and first singlet states. Structure A is the normal ground state conformation, and accounts for the ground-state dipole moment. In the excited state, C predominates in nonpolar solvents and D in polar solvents. The potential in figure 4.2 describes the interconversion of C and D.

(1-10 ps) relaxation has been observed with a nonlinear viscosity dependence. Such behavior can be successfully modelled using the Fokker-Planck equation which takes into account both a barrier and the solvent viscosity²⁵. A similar approach might be feasible for modelling the fast relaxation in DMABN.

Recent work by Eisenthal et.al. has suggested that other processes may be detectable as well. In particular, it appears that complex formation between the excited state of DMABN and alcohol solvents can represent the rate limiting step in the formation of the TICT state. A likely mechanism for this process involves hydrogen bonding between the solvent and the solute. When DMABN emission was studied in alcohol-alkane mixtures, a triexponential decay was observed; in pure butanol short time constants of 30 and ~95 ps were observed²⁶. The intermediate time constant varied inversely with the alcohol concentration, suggesting a diffusion-controlled reaction between the alcohol and the DMABN. The magnitude of the intermediate time component was quite small in the pure alcohols, but became increasingly prominent as the alcohol concentration was decreased. At low alcohol concentration, only a fraction of the ground-state molecules are initially complexed. Thus, on excitation significant solvent reorganization is required to form the complexes necessary for stabilizing the polar excited state. Note that the nonpolar and TICT states are always close to equilibrium in this model; the slow process corresponds to the rearrangement of the solvent to stabilize the latter state. This model does not distinguish between the charge transfer followed by solvation or solvent rearrangement followed by charge transfer. Instead, it describes the simultaneous evolution of both the solute and the solvent leading to an increase in the population of the CT state.

A second example involving excited-state solvation and hydrogen bond formation is found in the case of 4-aminophthalimide (4AP) in protic solvents²⁷. In this case, a solvation process quite similar to that which would be expected from figure 4.1 is seen. A continuous spectral shift is observed with increasing Stokes shift in the fluorescence becoming evident on a timescale of tens to hundreds of picoseconds²⁰. In pure alcohols,

this spectral shift occurs more rapidly than the molecular rotation time inferred from the fluorescence depolarization, so this process is attributed to solvent polarization about a quasi-stationary solute molecule. This appears to be consistent with the assumptions inherent in figure 4.1, where the solvation involves a continuous rearrangement of the solvent about a stationary molecule. The Stokes shift varied exponentially with time, and this exponential time constant was taken as the solvation time. This solvation time was found to correlate well with the longitudinal dielectric relaxation time described below²⁸. Note that this is precisely the behavior predicted theoretically²⁹ for a system like that in figure 4.1.

Despite this correlation, it is also possible to fit the behavior of 4AP to a model like that in figure 4.2. Several reasons exist for considering such a possibility. The relative orientations of the amino and carbonyl groups are analogous to the amino and cyano groups of DMABN, so similar behavior in the two systems seems like a reasonable possibility. In addition, it appears that 4AP is hydrogen bonding to the solvent. This is suggested by both the behavior of similar molecules³⁰ and by the isotope effect seen in 4AP, where the singlet lifetime increases by a factor of two in deuterated alcohols³¹. Although changes in solvent-solvent hydrogen bonding play an important role in dielectric relaxation in alcohols³², this is not the same as solvent-solute hydrogen bonding. The former process can be described in terms of a continuum dielectric; the latter in terms of a solvent-solute reaction. It appears reasonable to suppose that the processes being observed in 4AP can be described in terms of an initial charge transfer equilibrium followed by diffusion-limited hydrogen bond formation. Such a model would predict triexponential decay kinetics, with wavelength-independent time constants, and indeed if the experimental data²⁰ is reanalyzed, it is found that an excellent fit can be obtained with such a decay. In pure *n*-butanol time constants of 25 and 100 ps were found. These are almost identical to the values found for DMABN, and as will be seen, are also close to the values obtained for 9,9'-Bianthryl. In a practical sense, the difference between the two

models is largely semantic. Although the theoretical descriptions are quite different, the qualitative results are basically the same. Both models describe a relatively slow solvent reorientation, in which hydrogen bonding plays a major role. In either description, this process tends to scale with the same external parameters, in particular, with viscosity and alcohol concentration. As will be shown below, this makes it difficult to distinguish between the two experimentally.

A feature which both 4AP and DMABN have in common is that in the ground state, both molecules are capable of strong interactions with the solvent. Both molecules have a ground-state dipole moment of several Debye, a value comparable to that seen in such polar molecules as acetone or chlorobenzene. In addition, as has just been noted, these molecules (especially DMABN) are known to form hydrogen bonds in the ground state. This is reasonable, since both molecules have several heteroatomic sites which could function as hydrogen bond acceptors³³. Because of these features, the change in solvation associated with the formation of the more polar excited state may not be overwhelmingly large. If, for example, there is a change in the solvent configuration associated with the presence of a nearby dipole, (e.g. a reorientation of a polar functional group on an adjacent solvent molecule), it will have occurred at least partially in the ground state. Furthermore, if solvent-solute hydrogen bonding occurs, the presence of ground-state hydrogen bonding means that the hydrogen bond donating solvent moieties will already be oriented towards the solute molecule, eliminating the slow diffusive process of solvent reorientation. When nonpolar molecules are solvated in hydrogen bonding solvents, the solvent is expected to favor a "micellular" configuration in which the nonpolar ends of the solvent molecule would be expected to associate with the nonpolar solute thus maximizing the number of "outer shell" hydroxyl groups available for hydrogen bonding to the solvent. If the solute molecule forms hydrogen bonds, then this configuration will not be especially favorable, and a more random configuration may well occur³⁴.

Because of these features, it is not accurate to characterize the excitation of 4AP

or DMABN as being "nonpolar to polar" transitions, as has sometimes been done¹⁹. Instead, it is necessary to consider both the ground state and excited state in detail. This is especially true with respect to solvation processes, since even a small ground-state dipole moment will tend to orient the solvent and obscure the relatively slow reorientation processes which are expected to occur in a true "nonpolar to polar" transition. It is clearly of interest to identify probe molecules which in fact undergo such a transition, and to observe whether such solvent reorganization processes do in fact occur. Such systems would have to be completely nonpolar in the ground state with essentially no possibility of forming ground state hydrogen bonds. In essence, what would be needed would be a symmetric hydrocarbon which nonetheless gives rise to a large dipole moment in the excited state.

3. 9,9'-Bianthryl

The unusual charge transfer properties of the excited states of large aromatic double molecules such as 9,9'-Bianthryl (BA) or 1,1'-Bipyrene (BP) are well known³⁵. In the ground state, these molecules act very much like any other sterically hindered aromatic double molecule, and can be thought of as being analogous to a 2,5 disubstituted biphenyl. As shown in figure 4.4, steric interference forces the two rings apart, resulting in a nonplanar geometry with an internal angle of approximately 65 degrees³⁶. In this nominally perpendicular configuration, interactions between the two pi electron systems are relatively weak, and the double molecules have essentially the same properties as the constituent halves. The absorption spectrum of BA is almost identical to anthracene, and remains essentially unchanged in different solvents. This reflects the fact that the same noninteracting, noncoplanar structure occurs irrespective of the solvent.

In contrast to this, the emission spectrum depends strongly on the solvent³⁷. In nonpolar solvents the emission spectrum of BA resembles that of anthracene and, as discussed below, can be assigned to a nonpolar exciton resonance state directly analogous

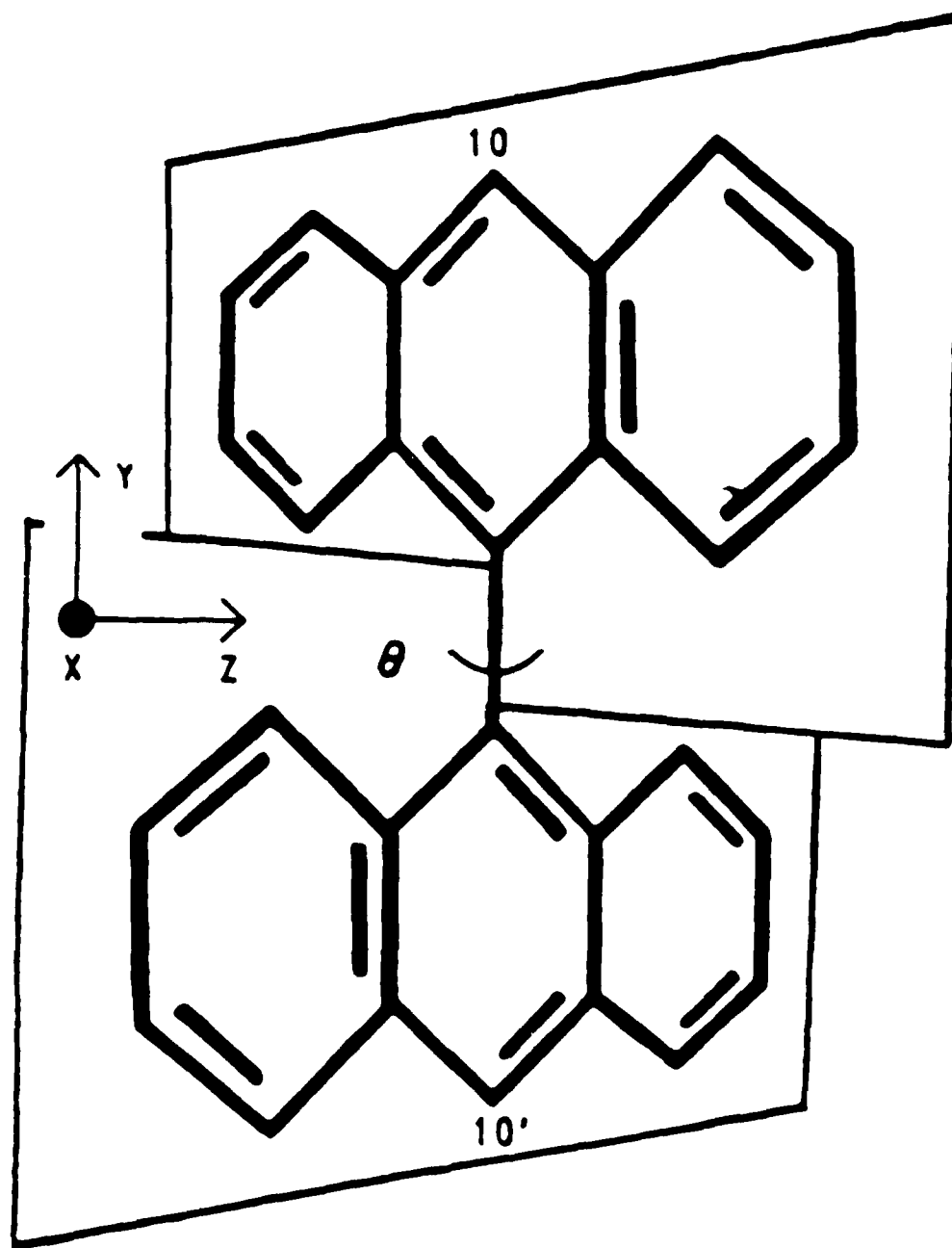


Figure 4.4. Structure of 9,9'-Bianthryl. The internal angle θ is approximately 65 degrees in the ground state and varies in the excited states. The coordinate system shown is conventional for a molecule in the point group D_2 .

to the excited state of anthracene. This is sometimes referred to as the locally excited (LE) state. Note that BA does not show the spectral broadening seen with 1,1'-Binaphthyl (BN) in fluid solutions. This is attributable to the differing energy levels of naphthalene and anthracene and not to solvent polarity or solvation. So far, the properties of BA are precisely what one would expect for a nonpolar aromatic system. A sharp departure from this behavior is seen in the emission spectrum in polar solvents. Although some of the features of the LE state emission can still be seen, a broad unstructured peak begins to appear, with a polarity-dependent spectral shift characteristic of a polar excited state. From this shift, an excited-state dipole moment of roughly 20 Debye can be inferred. This corresponds to a full charge transfer (CT) between the two anthryl groups, resulting in a state which has many similarities to a radical anion-cation pair. The appearance of this highly polar CT state is rather unexpected in a symmetrical molecule such as this, but from the point of view of solvation, it represents a near-perfect example of a "nonpolar-to-polar" transition. These aromatic double molecules, and BA in particular, are thus ideally suited to studying solvation processes in polar solvents.

A considerable volume of literature concerning BA exists, although very little of it addresses the question of solvation directly. The strong polarity dependence of the emission spectrum of BA was first reported in steady-state emission studies³⁷. It was shown that the emission consisted of two components, a strongly structured LE component similar to that seen in nonpolar solvents and a broad, featureless CT emission with a strong polarity dependence. The relative quantum yield of the CT state decreased with increasing solvent viscosity (in ethanol and glycerol/methanol), suggesting a slow, viscosity dependent relaxation from the LE to the CT state. The formation of the CT state was attributed to a large excited-state polarizability, with the idea that electric field fluctuations in the polar solvent induced the initial asymmetric dipole moment which could then interact with the solvent polarizability to produce the observed state. They also carried out a limited molecular orbital calculation and suggested that the CT state

could be identified with the so-called 1L_b level, shifted to lower energies by the electric field. This is the same state which is responsible for the excited-state behavior of BN noted above. It is also similar to models used at that time to explain what is now attributed to TICT formation in DMABN¹¹.

Several subsequent sets of measurements cast doubt on various aspects of this interpretation. Time resolved absorption studies³⁸ indicated that there were no slow equilibration processes occurring in BA. They found that with ~ 50 ps time resolution, the excited-state absorption spectrum remained essentially unchanged for the entire 25-35 ns lifetime in various polar solvents. They interpreted this as indicating an equilibrium between the two excited states. The excited-state polarizability of BA in the Franck-Condon state was measured using electrooptic absorption techniques³⁹ and was found to be quite similar to anthracene itself. This suggested that the simple model proposed earlier was not complete, and that a more sophisticated barrier crossing theory was probably needed.

The work of Grabowski et.al.¹¹ with TICT molecules has greatly clarified the nature of the BA excited states. Although their work focussed on DMABN and related molecules, they noted that BA exhibited many of the same features as DMABN and might well be a TICT-type molecule as well. A more systematic study of the steady-state emission spectrum of BA and several closely related molecules in a variety of polar solvents has recently been carried out³⁵. By using a microstructural model of the solute molecules⁴⁰, the dipole moments of BA and several similar, asymmetric compounds were compared. Their results indicate that the charge transfer states in all of these molecules are TICT states. This conclusion was supported by calculations. In another study, the pressure dependence of BA fluorescence spectrum in various solvents showed a similar dependence to that seen for DMABN, once again indicating that the same process is occurring⁴¹. Both of these papers use curve fitting procedures to estimate the relative quantum yields of the two states. As discussed below, such methods can only produce crude estimates of the relative quantum yields.

Finally, a variety of data tend to suggest that detectable solvation processes are occurring with BA, especially in alcohols. Several picosecond time-resolved measurements were made using both absorption and emission spectroscopy. In aprotic solvents, notably acetonitrile and acetone, there was no detectable spectral relaxation except for the overall fluorescence lifetime, indicating that all relaxation processes occurred in a few picoseconds. In alcohols, such as glycerol/methanol⁴² or 1-propanol⁴³ relaxation processes were observed with lifetimes of a few hundred picoseconds. These times were attributed to the formation time of the CT state with no consideration given to the possible role of solvation. The fact that measurable relaxation times were only seen in protic solvents was attributed to dielectric relaxation⁴⁴. A puzzling aspect of these results is that such relaxation times were not observed using absorption spectroscopy in cyclohexanol⁴⁵. It was of interest to determine if this carried over into other alcohols, or indeed, whether it was simply an artifact associated with the poor signal-to-noise of the absorption measurements. Another unusual aspect of BA in alcohols is seen in the steady-state spectra. It has been shown that for a given solvent polarity ($E_T(30)$ value) the Stokes shift obtained in protic solvents is approximately 2500 cm^{-1} less than that obtained for aprotic solvents⁴⁶. Since this is comparable to the energy of a hydrogen bond, this suggests that the protic solvents are hydrogen bonding to BA. The fact that the CT emission is strongly quenched by protons also indicates that proton transfer and/or hydrogen bonding may occur⁴⁷. Although this would be unusual behavior for a hydrocarbon, it is within reason for a radical cation or anion²³. It is also similar to the behavior noted above for 1-naphthol.

C. Experimental Procedure

At the present time it is not possible to obtain BA commercially, but it is readily synthesized by the zinc amalgam reduction of anthraquinone. The procedure of Magus et.al.⁴⁸ was used without modification. 100 g of zinc amalgam (prepared by stirring

100 g mossy zinc, 7 g HgCl_2 , and 5 ml concentrated HCl in 125 ml H_2O for 5 minutes at room temperature⁴⁹) was added to a mechanically stirred, refluxing suspension of 30 g anthraquinone in 350 ml glacial acetic acid. Over the course of the next five hours, 200 ml concentrated HCl was added dropwise to the refluxing mixture. At the end of this time, the mixture was cooled to room temperature and filtered. The solids were extracted with boiling chlorobenzene, and crystallized. Mass spectroscopic analysis of the resulting yellowish-white crystals indicated that the crude product was approximately 95% BA, with anthracene and an anthracene dimer (MW 356) as the only detectable impurities. The overall yield of the reaction was not determined exactly, but was approximately 50%.

Further purification was necessary, since anthracene has spectral properties which are very similar to bianthryl, and would interfere with subsequent measurements. Analysis by HPLC⁵⁰ indicated that two impurities absorbing at 266 nm were present, with one (identified by retention time as anthracene), which absorbed at 355 nm as well. Recrystallization from chlorobenzene, as suggested by Magus et.al. was not successful. BA appears to be more soluble than anthracene, since recrystallization led to the isolation of pure anthracene. Recrystallization from mixtures of acetic acid and acetic anhydride, as suggested by Mataga et.al.³⁸, was more successful. Anthracene is much more soluble than BA, and BA crystals form readily on cooling. Actual purification is complicated by the fact that anthracene tends to adhere to the crystals. To overcome this problem it was necessary to cool the saturated solutions slowly in an ultrasonic bath. This led to the formation of microscopic crystals from which the adsorbed anthracene could then be removed. By repeatedly dissolving the sample in the boiling solvent mixture (approximately 80% acetic acid, and 20% acetic anhydride), cooling to 0 C in an ultrasonic bath, and washing the resulting crystals repeatedly with cold methanol, samples were produced in which no impurities could be detected by HPLC. A purity of at least 99.9%, at least with regard to UV absorbing impurities, was indicated. No indication of any impurity was found in the fluorescence, proton NMR or mass spectra, confirming the HPLC result.

These samples were used in subsequent experiments.

It has been suggested by Shizuka et.al.⁴⁷ that recrystallization from ethanol can be used to purify BA. Although it was not tried here, it is consistent with the observed solubility of anthracene and bianthryl in alcohols. Other than the odor, the main advantage of ethanol would be that it freezes well below 0 C, so there is no possibility of the solvent freezing during cooling. This was a problem with the acetic acid mixtures if too little acetic anhydride was present. Butanol or pentanol might be even better than ethanol, since their lower polarity and higher boiling points should make it possible to use less solvent.

The solvents used for the spectroscopic measurements were all of the highest commercially available purity. Acetonitrile, DMSO, *n*-hexadecane *n*-propanol and *n*-butanol were HPLC grade, obtained from Burdick and Jackson. Methanol, benzene, *n*-heptane and *n*-pentane were spectroscopic grade from Mallinckrodt. Anhydrous ethanol was from Rossville. *n*-Pentanol (99%), *n*-hexanol (98%), *n*-Octanol(99+%) as well as methan(*ol-d*) (99.5 atom%), ethan(*ol-d*)(99.5 atom%), *n*-butan(*ol-d*) (98 atom%) and 20% w/w DCl in D₂O (99 atom%) were the highest available grade for Aldrich. All solvents were dried over 5A molecular sieve prior to use. All samples used for spectroscopic purposes were placed in vacuum cuvettes prior to use and were degassed in vacuum.

Picosecond absorption and emission measurements were made using the apparatus described in chapter two. Sample excitation was with the 355 nm beam in both cases, except as noted. Except when measuring polarization anisotropies, "magic angle" detection was used for emission and absorption measurements. The emission intensity was adjusted to produce a similar signal level in all datasets. This ensured that any power-dependent distortion of the data, such as that arising from electron debunching in the streak tube would at least be consistent. Such adjustment is also necessary to accommodate the finite dynamic range of the streak camera. To reduce the signal, the pump beam was attenuated rather than the emission itself, since this minimized sample degradation and stimulated

Raman scattering, without distorting the signal. For the absorption spectra shown, the fluorescence dyes were those described earlier; dye excitation was with the 532 nm beam.

Steady-state absorption spectra were measured on a Cary 219 spectrophotometer. Steady state emission spectra were measured on a Spex Fluorolog II, using Rhodamine B for quantum corrections. Steady-state emission spectra were measured with right angle detection in .002 mM solutions; this eliminated most of the reabsorption of the fluorescence below 400 nm. Time-resolved emission used .4 mM solutions, and time-resolved absorption was carried out using 1 mM BA concentrations. Mass spectra were measured on an AEI MS-12 magnetic sector instrument. Proton NMR spectra were measured on a Nicolet 250 FTNMR. An IBM HPLC was used for sample analysis.

Time resolved data was analyzed using the procedure described in the appendix. This entire procedure was combined into a single set of programs and implemented using a Digital Equipment Corporation VAX-780 computer. This program takes a series of decay curves with comparable peak intensities, deconvolutes the excitation pulse from the datasets and fits the resulting curves to a set of triexponential decays with wavelength-dependent amplitudes and wavelength-independent time constants. This is the functional form expected from a simple three-state relaxation process, although it can be used to approximate a variety of other processes as well. The program then proceeds to combine a steady-state emission spectrum with the time-resolved emission data to produce time-dependent spectra.

D. Picosecond Emission Measurements: BA in Alcohols

It is known from previous work that BA undergoes detectable excited-state relaxation processes in alcohols, so the first solvents to be investigated were the simple linear alcohols. These represent a very convenient set of solvents with which to work, since they have been characterized in detail, and are readily available in high purity. The steady state emission spectra of BA in a series of alcohols is shown in figure

4.5, along with the excitation spectrum in *n*-butanol and the emission spectrum in *n*-hexadecane. The excitation spectrum shown is essentially the same as the absorption and excitation spectra seen in other solvents. These spectra are essentially the same as those reported previously³⁷, and they clearly show the increasing red shift in more polar solvents characteristic of the CT state. Note the persistence of the vibrational structure at the blue edge of the band. This structure is characteristic of the LE state, and it persists to some degree even in the most polar solvents. Since the CT state is not formed in nonpolar solvents, the spectrum seen in *n*-hexadecane corresponds to that of the LE state spectrum. Note that the peak in the spectrum of *n*-hexadecane spectrum does not line up with the shoulder seen in the alcohols. Although not shown here, the same peak is seen in *n*-hexane, but not in diethyl ether where the vibrational structure is well aligned with that of the alcohols⁴¹. A similar shift is seen in other nonpolar solvents³⁸. It is not clear why this occurs, but it can have a significant effect on some of the methods used to interpret the data, especially the curve fitting procedures sometimes used to estimate the relative quantum yields for the LE and CT states³⁵. Hexadecane was used for comparison with the alcohols because its viscosity is comparable to the larger alcohols.

Time-resolved emission for BA in *n*-propanol, *n*-butanol and *n*-hexanol are shown in figure 4.6 at the blue and red edges of the emission. Similar curves were observed in other alcohols and in other protic solvents such as acetic acid. The data for propanol is quite similar (albeit less noisy) than the data reported previously in the same solvent⁴³. These earlier results were interpreted in terms of a simple two-state system. This requires that the same exponential decay be seen at all wavelengths. To support this interpretation, it was emphasized that the risetime at 540 nm, treated as a single exponential, was equal to the falltime seen at 400 nm. Looking at the newer, less noisy data, it is not altogether clear that this interpretation is correct. In particular, the description of the risetime seen at 540 nm as a single exponential appears to be an incorrect, since the data appears to include a significant prompt component. When this is included, the agreement between the

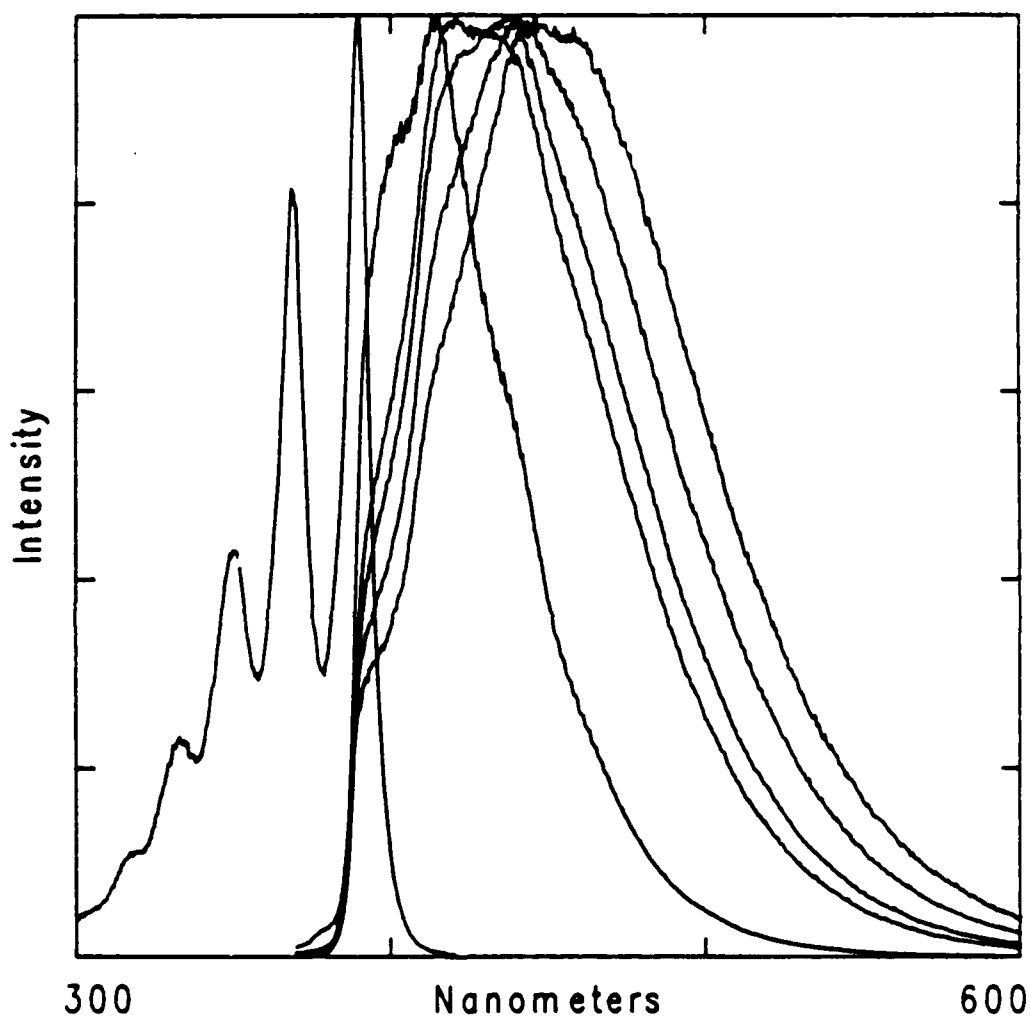


Figure 4.5. Corrected emission spectra for BA in a series of linear alcohols at 20 C. From right to left solvents are methanol, ethanol, *n*-butanol, *n*-hexanol and *n*-hexadecane. It can be seen that the Stokes shift increases with the solvent polarity. Curve at far left is the excitation spectrum in *n*-butanol. The absorption spectrum in all these solvents is essentially constant, and closely resembles the excitation spectrum shown.

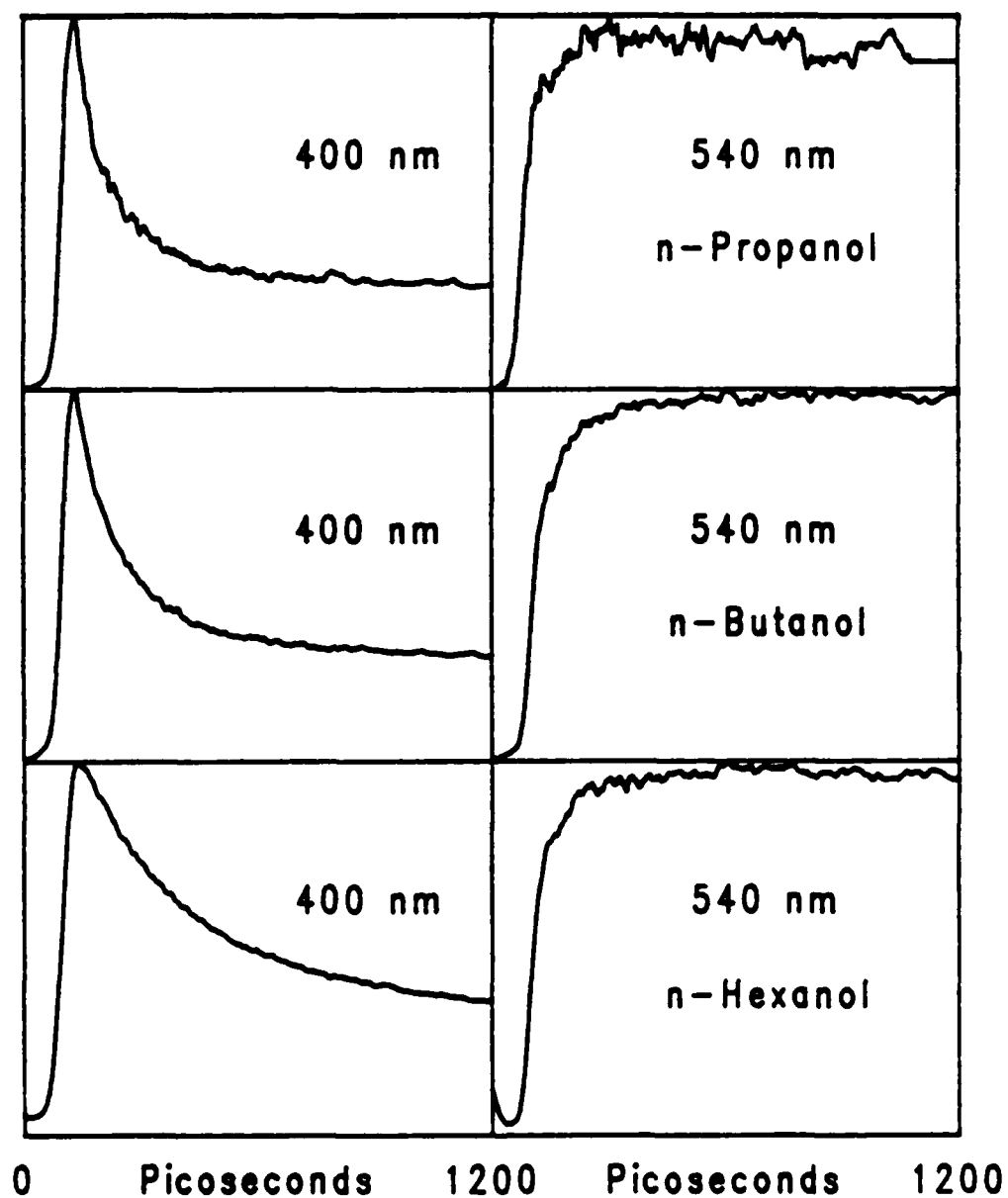


Figure 4.6. Time-resolved emission at 20 C for BA in *n*-propanol, *n*-butanol and *n*-hexanol at 400 and 540 nm.

risetime and the falltime becomes much poorer, and a simple two-state decay seems less likely. Figure 4.6 also shows data for *n*-butanol and *n*-hexanol at the same wavelengths. In these cases the data looks even less like a single exponential than it does for propanol.

In an effort to clarify the nature of the processes occurring in BA, it was necessary to generate time resolved spectral data. This requires both the steady-state emission spectrum and time-resolved data taken at 10 nm intervals over the entire spectral band, from 390 to 600 nm. These initial studies were carried out in solutions of BA in *n*-butanol and *n*-hexanol. Spectra were measured in both of these solvents at 20 degree intervals between 0 and 60 C. This leads to an order of magnitude variation such solvent parameters as viscosity, in an otherwise relatively constant solvent environment. Because the lifetime of BA is so much longer than the initial equilibration times, two measurements are necessary. One, at a slower streak speed is used to determine the overall fluorescence lifetime, while the second at a much faster streak speed to measure the fast relaxation times. A typical decay curve for BA in *n*-hexanol at 20 C made with the slower streak speed (100 ps/ch) is shown in figure 4.7. After the initial equilibration, the data at all wavelengths could be fit to a single exponential decay of 22 ns. This is in reasonable agreement with previous lifetime measurements for BA³⁸. The data for BA in *n*-hexanol at 0 C as a function of wavelength, measured at the faster streak speed (1.97 ps/ch) is shown in figure 4.8. The smooth curves shown are the calculated curves resulting from the triexponential fitting procedure. It can be seen that they fit the data quite well. All the data in both alcohols was fit by this procedure, and the fits in all cases were quite good. Table 4.1 gives a summary of the resulting time constants.

The next step in this procedure is to generate the time-dependent spectra. The steady-state data provides the relative quantum yield in a given spectral bandwidth, and the time-resolved data can then be used to apportion this between the different exponential components, so that the full time-resolved spectrum can be calculated. The scanned steady-state spectra is matched to the 10 nm bandpass filters by by integrating the spectrum

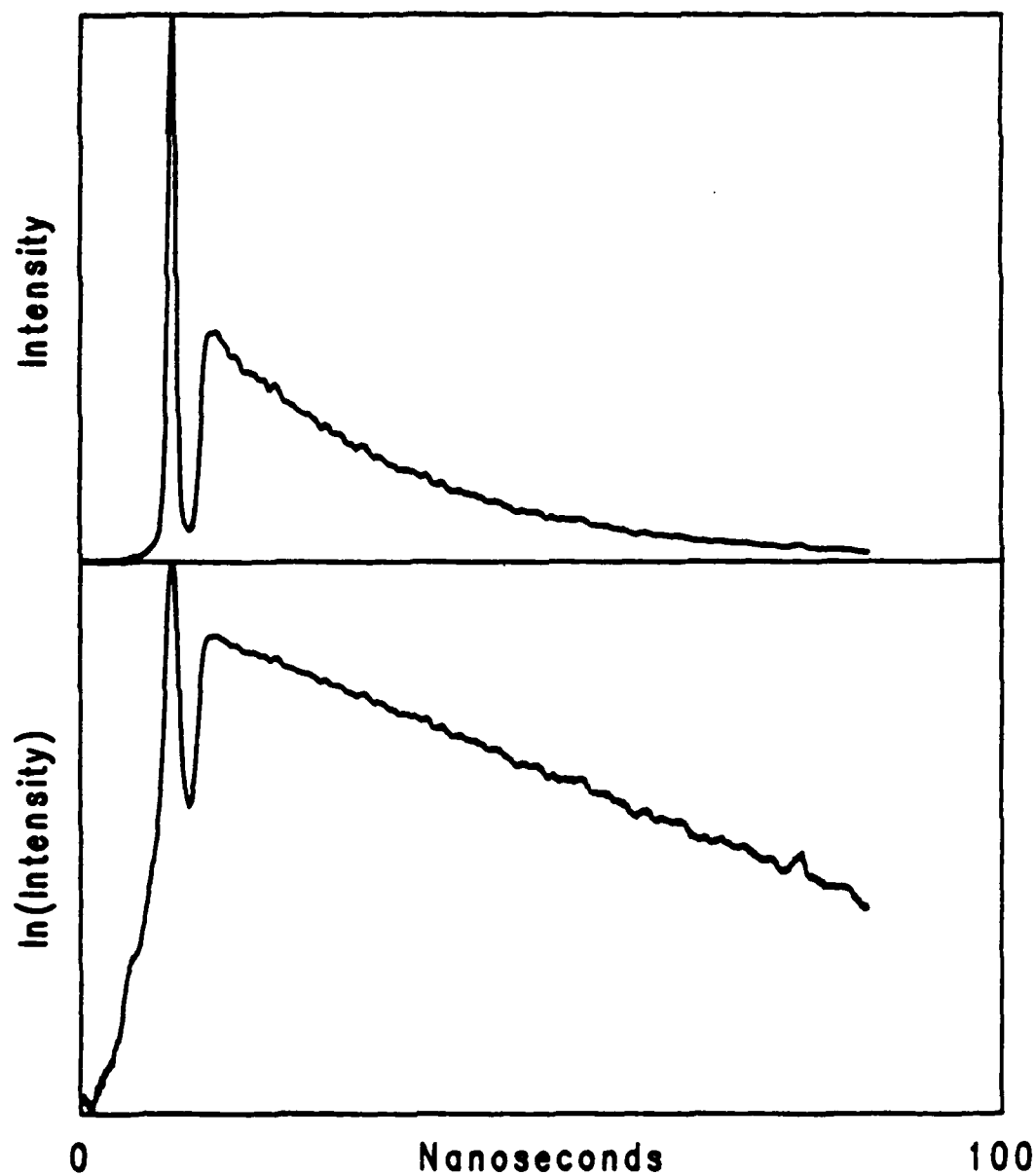


Figure 4.7. Linear and semi-log plots of the fluorescence decay of BA at 500 nm in *n*-hexanol at 20 C. The decay is clearly a single exponential. After the initial dynamics, the decays observed at all wavelengths showed the same 22 ns exponential decay.

Table 4.1

Time constants resulting from the triexponential fitting procedure for BA in *n*-butanol and *n*-hexanol as a function of Temperature.

Solvent	°C ^a	$\tau_1(\text{ns})^b$	$\tau_2(\text{ps})^c$	$\tau_3(\text{ps})^c$
<i>n</i> -Butanol	-15 C	*	425	60
<i>n</i> -Butanol	0 C	28	330	60
<i>n</i> -Butanol	20 C	27	160	40
<i>n</i> -Butanol	40 C	26	110	†
<i>n</i> -Butanol	60 C	*	60	†
<i>n</i> -Hexanol	0 C	25	520	60
<i>n</i> -Hexanol	20 C	22	320	60
<i>n</i> -Hexanol	36 C	21	200	70
<i>n</i> -Hexanol	60 C	22	100	†

†. Single exponential fit.

*. Not measured

a. Reproducible to $\pm 2^\circ \text{C}$.

b. Reproducible to $\pm 2 \text{ ns}$.

c. Reproducible to $\pm 20 \text{ ps}$. or $\pm 10\%$.

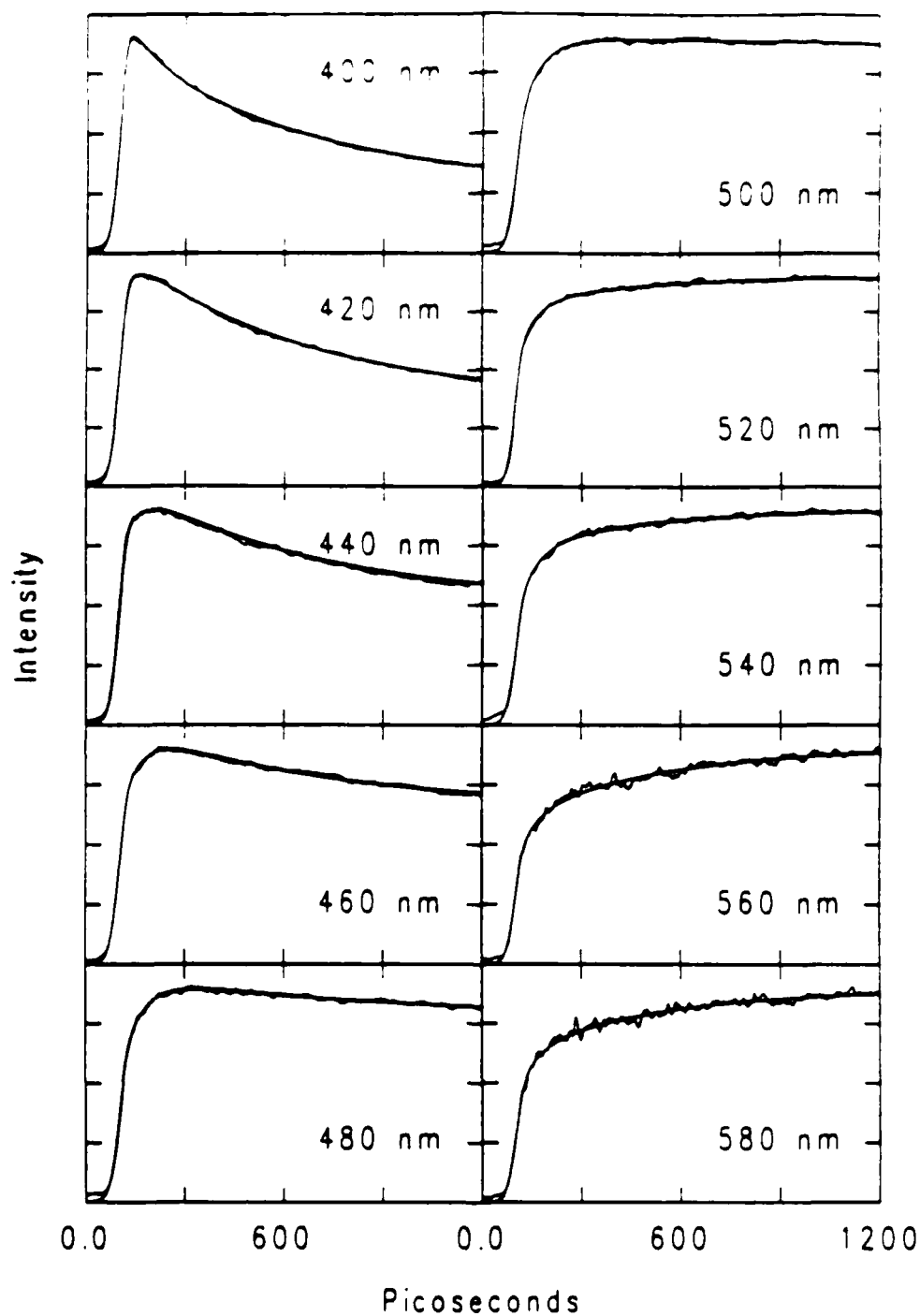


Figure 4.8. Fast components of the time-resolved emission of BA in *n*-hexanol at 0°C at 20 nm intervals. The smooth curves represent fits to fast biexponential process with relaxation times of 62 and 519 ps.

in 10 nm sections (e.g. from 395–405 nm) giving the discrete spectrum $I(\lambda)$. This, in turn can be set equal to the time integral of the time-resolved decay. For the triexponential decays used here with amplitudes a_i and time constants τ_i this becomes

$$I(\lambda) = a_1\tau_1 + a_2\tau_2 + a_3\tau_3 \quad (4.1).$$

This can then be solved for a_1 , and a time resolved spectrum can be obtained. Time resolved spectra for *n*-hexanol at 0 C are shown in figure 4.9.

E. Short Time Behavior

1. Time-Resolved Emission

It is clear from the time-resolved spectra that the major portion of the spectral shift is governed by the fast time constant. In the case of *n*-hexanol at 0 C, the the shift is essentially complete in less than 100 ps. This is in good agreement with what one would expect from an equilibration between the two excited states. Note that there is even an isosbestic point near 470 nm on this time scale, in agreement with a two-state model. After 100 ps, the spectrum changes very little, but the emission intensity continues to decrease. Note that this process is governed by the intermediate time constant, and is *not* simply due to the overall fluorescence decay. This type of behavior is consistent with solvation. The fact that there is only a small red shift associated with the second decay process indicates that the solvent relaxation process does not greatly perturb the energy of the CT state. One possibility is that the second relaxation time is associated with the formation of solvent-solute hydrogen bonds. Calculations²³ tend to suggest that a rotation into a perpendicular geometry is accompanied by a decrease in fluorescence cross-section, an increase in the internal energy and an increase in the likelihood of hydrogen-bond formation. As discussed below, this one effect would explain much of the observed data.

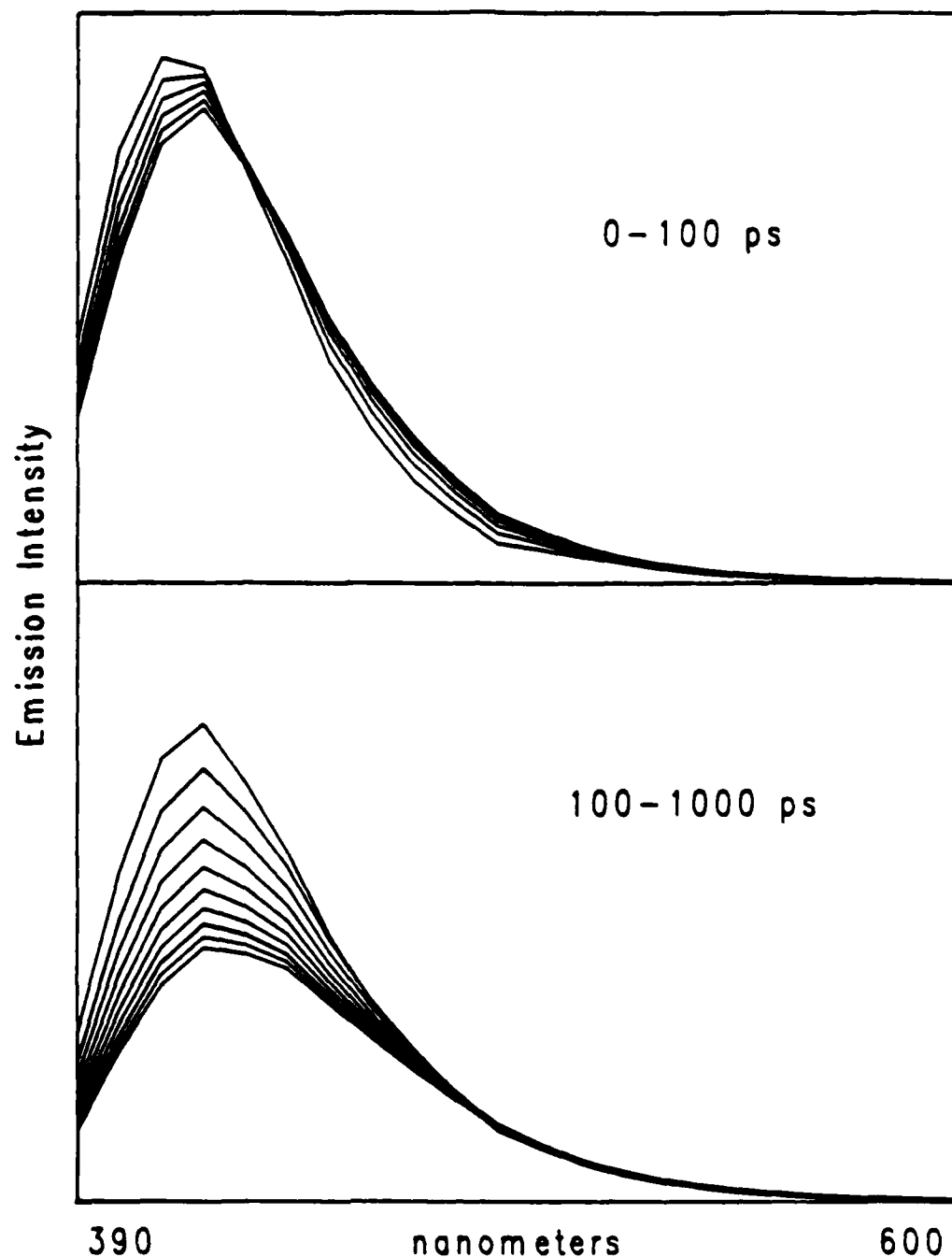


Figure 4.9. Time resolved emission spectra for BA in *n*-hexanol at 0°C reconstructed from the data in figure 4.5 and figure 4.8. Upper figure, 0–100 ps in 20 ps increments; lower figure 100–1000 ps in 200 ps increments. The peak intensity is uniformly decreasing with time. Note the presence of the isosbestic point in the upper curve, suggesting that an initial two-state relaxation process is occurring. The lack of an isosbestic point in the lower curve suggests that at later times, an intramolecular solvation process is taking place.

It would be desirable to take the time resolved spectra and separate out the effects of the LE and CT states. From the persistence of the LE state emission in the steady-state spectrum, it is evident that the steady-state mixture consists of several excited states in equilibrium with one another. Separating these spectra into their various contributions is not easy. Since nothing is known about the relative free energies of the states, it is not possible to separate the different emissions directly. It is possible to crudely decompose the steady-state spectrum into a LE component and a CT component, by assuming that the vibrational structure of the LE emission is constant, and that the CT band is completely unstructured³⁵. This gives a spectrum for the overall CT band, but does not distinguish between the possible variations in solvation. There are also some potential problems with this technique. As can be seen from the spectra for BA in heptane and hexadecane, the LE spectrum is subject to variation. If the vibrational structure is not constant, then these procedures may well fail. Since these procedures can only be used to get a crude idea of the relative yield of the LE state, they were not pursued in detail.

There appears to be no reliable way of measuring the fast time constant τ_3 . It never appears as an isolated decay, and although it is needed to fit the data especially near 400 and 520 nm, its exact value is uncertain. Indeed, a reasonable fit for the data will result if any value between 30 and 60 ps is used. It does appear the τ_3 is decreasing in the less viscous solutions. In the least viscous solvents, this time constant cannot be resolved at all, although there is still spectral evidence for the fast relaxation. Figure 4.10 shows the spectra corresponding to time-zero as well as the spectrum observed in *n*-hexadecane. In the more viscous solvents, where two time constants could be resolved, the time-zero spectra are very close to that in *n*-hexadecane, in agreement with the idea that the system is initially in the LE state. In the less viscous solvents there is a significant red shift in the time-zero spectrum. This indicates that as the temperature increases, there is an increase in the "prompt" formation of the CT state. There is nothing unreasonable about this, since is what is normally observed in aprotic polar solvents. It suggests that a

fast partial polarization occurs, so the alcohol acts much like a weakly polar, effectively aprotic solvent on short timescales.

The fast time constant is very badly resolved, and the value close enough to the pulse width that the value found in the fitting process will be strongly affected by any sources of scattered light, such as stimulated Raman scattering (SRS). The possibility that the short time constant was indeed an artifact arising from SRS was considered in detail. Using the 355 nm excitation beam, SRS in the 380–420 nm range can be a real problem, since this region corresponds to the CH and OH stretch resonances of the solvent. In pure solvents, SRS is quite intense, and it can be readily observed. However, SRS is suppressed when a relatively strongly absorbing solution is used instead. This is one of the reasons why the solutions used for time-resolved emission are so much more concentrated than those used for the steady-state measurements. Evidence that SRS is not a problem can be seen in figure 4.11. In the upper half of the figure, the time-resolved emission observed from a solution of BA in *n*-butanol at 400 nm and 40 °C is shown as the power density is increased by nearly three orders of magnitude from ~ 1 to $\sim 200 \text{ MWcm}^{-2}$. Except for an increase in the noise levels, there is no detectable change in the shape of the decay. Besides indicating that SRS is not a problem in this case, this data also shows that it is reasonable to adjust signal levels by adjusting the pump power. The lower half of the figure shows the decay at 400 nm for a BA solution in *n*-hexanol using both 355 and 266 nm for excitation. Once again there is no difference, indicating that SRS is not a problem. Thus it appears that the shorter time constant is indeed a real phenomenon, although it is not clear if it represents one process or many.

2. Time-Resolved Absorption

Further investigation of the short-time processes in alcohols using emission spectroscopy was precluded by the difficulty of isolating a reproducible time constant. It was conceivable that the short time behavior might be more pronounced in the absorption

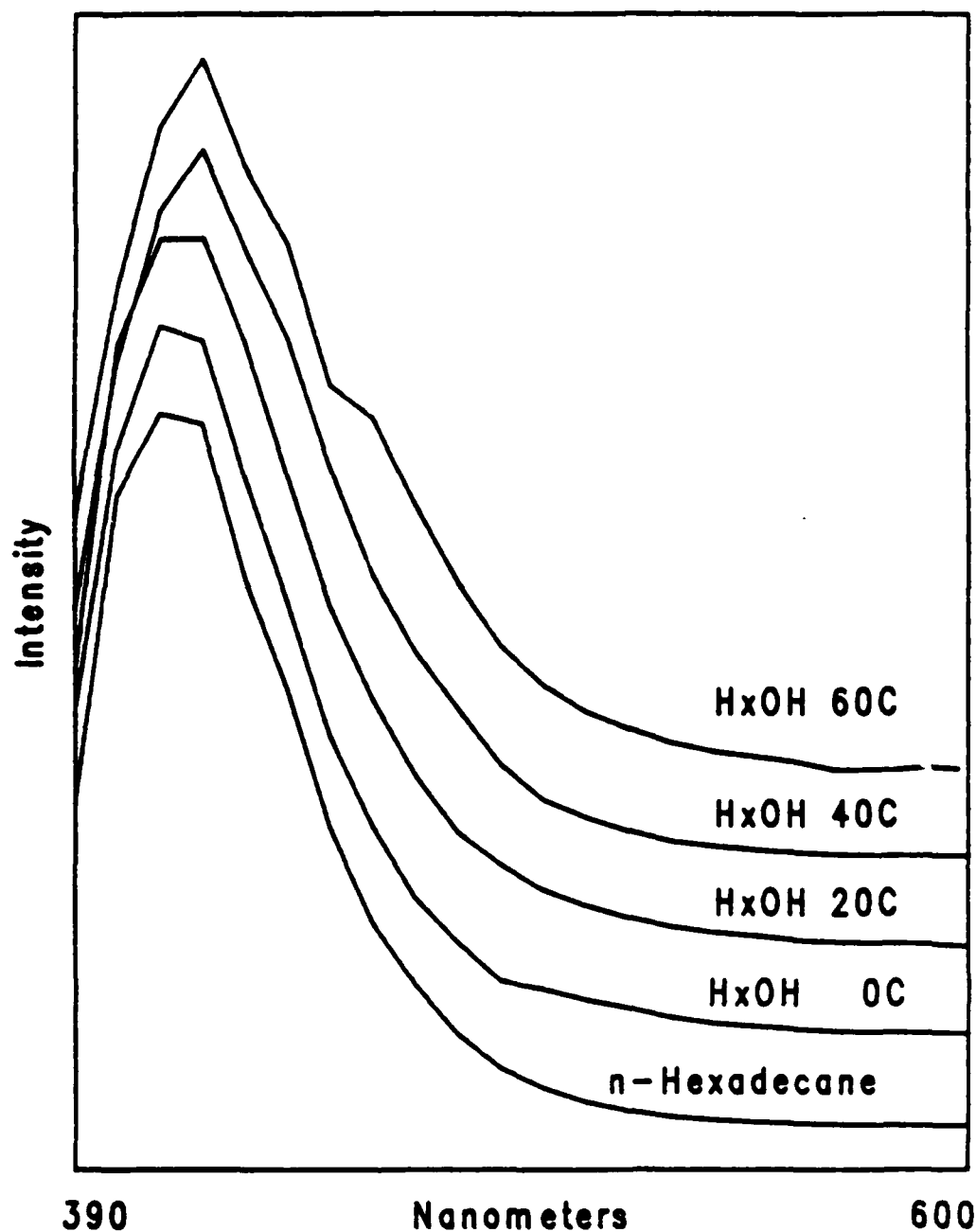


Figure 4.10. Time-zero spectra of in *n*-hexanol between 0 and 60 C. Also shown is the smoothed emission spectrum for BA in *n*-hexadecane. At 0 C the alcohol and the alkane spectra are almost identical, but as the temperature increases the alcohol spectral width increases considerably. This suggests that at higher temperatures an unresolved fast relaxation process is occurring. The spectra have been offset vertically for clarity.

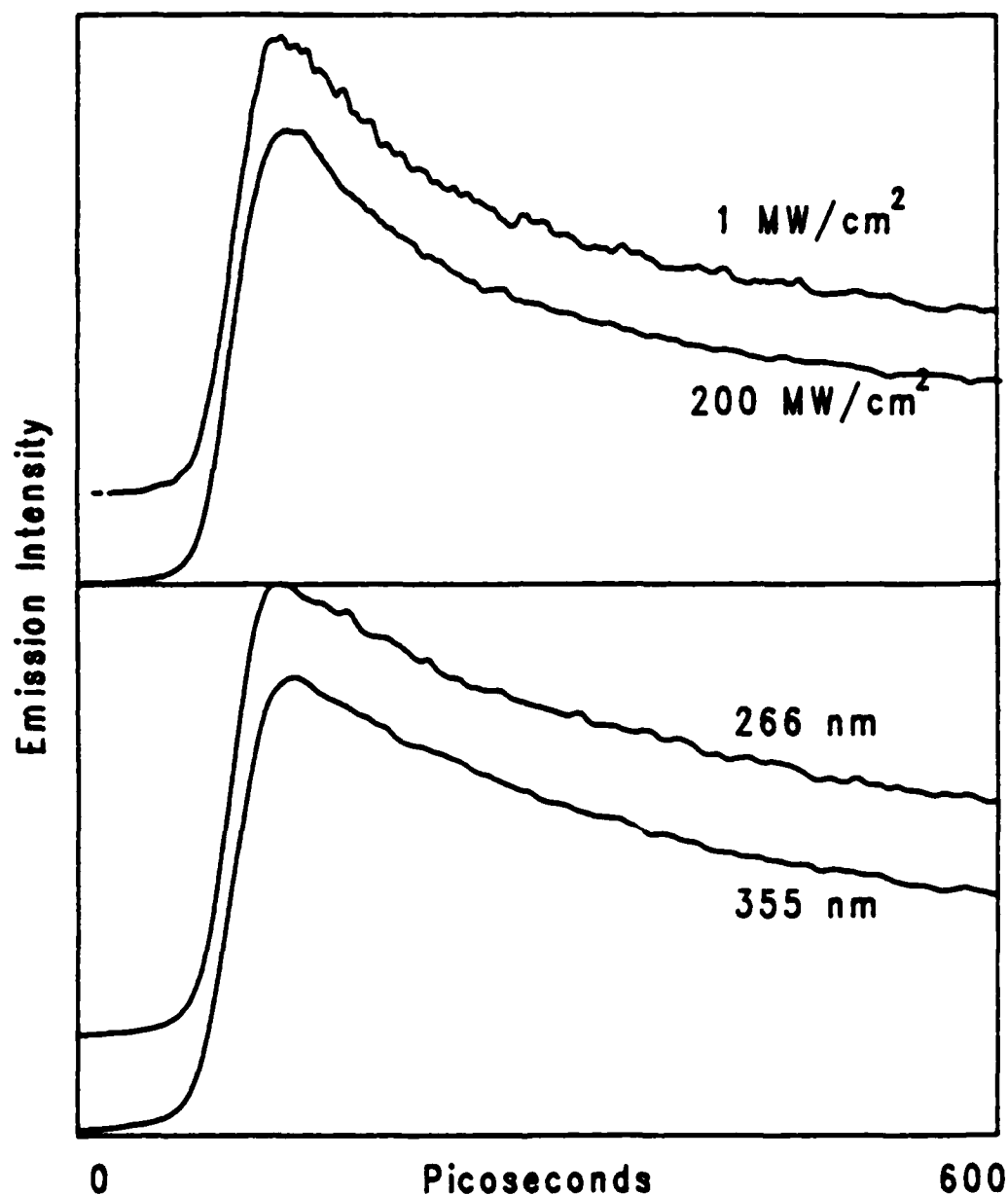


Figure 4.11. Upper figure: Time resolved emission at 400 nm of BA in *n*-butanol at 40 C, as the laser intensity is varied from 1 to 200 MW cm⁻². Lower figure: Time resolved emission at 400 nm of BA in *n*-hexanol at 20 C, with both 266 and 355 nm excitation. Laser intensity is approximately 50 MW cm⁻² for both excitation wavelengths. That the fluorescence shows no appreciable power or wavelength dependence indicates that stimulated Raman scattering is not occurring.

spectrum. This was suggested by the fact that previous investigators had not seen any time development in cyclohexanol⁴⁵. It has been shown that in nonpolar solvents, BA has an absorption extending from 500 to 650 nm, with a peak near 590 nm. This matches the absorption seen in anthracene. In polar solvents, the absorption cross-section increases by roughly a factor of three, and the spectrum is shifted to the 650 to 700 nm region³⁸. Reliable time-resolved absorption measurements for BA in *n*-butanol could only be made at wavelengths between 600 and 700 nm. The long wavelength limit results from the diminishing sensitivity of the streak camera photocathode, while the short wavelength limit is imposed by the increasing intensity of the sample fluorescence. Figure 4.12 shows the absorption profiles obtained for BA at 600 and 700 nm. Also shown is the curve for anthracene at 600 nm in cyclohexane, and the integral of a pulse measured at the same streak speed using the emission configuration. It can be seen that the pulse integral agrees quite well with the data at 600 nm for both BA and anthracene. This is expected for anthracene, since, in this case, there is no evidence in emission for spectral relaxation. The BA data is somewhat confusing, since one might expect some relaxation to be detectable if the LE-CT equilibration is occurring. The spectra⁴⁵ suggest that near 600 nm the two states have comparable absorption cross-sections, so the amplitude of any relaxation would be small. Measurements at shorter wavelengths might be expected to show a decay, but they could not be measured here due to fluorescence. A risetime is clearly evident in the 700 nm curve. Using the pulse shown for deconvolution, a risetime of 120 ps is found, although the fit is not good. A somewhat better fit can be obtained with a biexponential risetime. In this case all the usual cautions about not taking the values of the time constants literally apply, since only one curve is being fit⁵¹. The data can be quite well fit with a combination of a 60 and 160 ps risetime, that is with the same values found in emission. These are by no means the only values which will give reasonable fits, but they indicate that no new information can be obtained from the absorption spectra, at least with at these wavelengths.

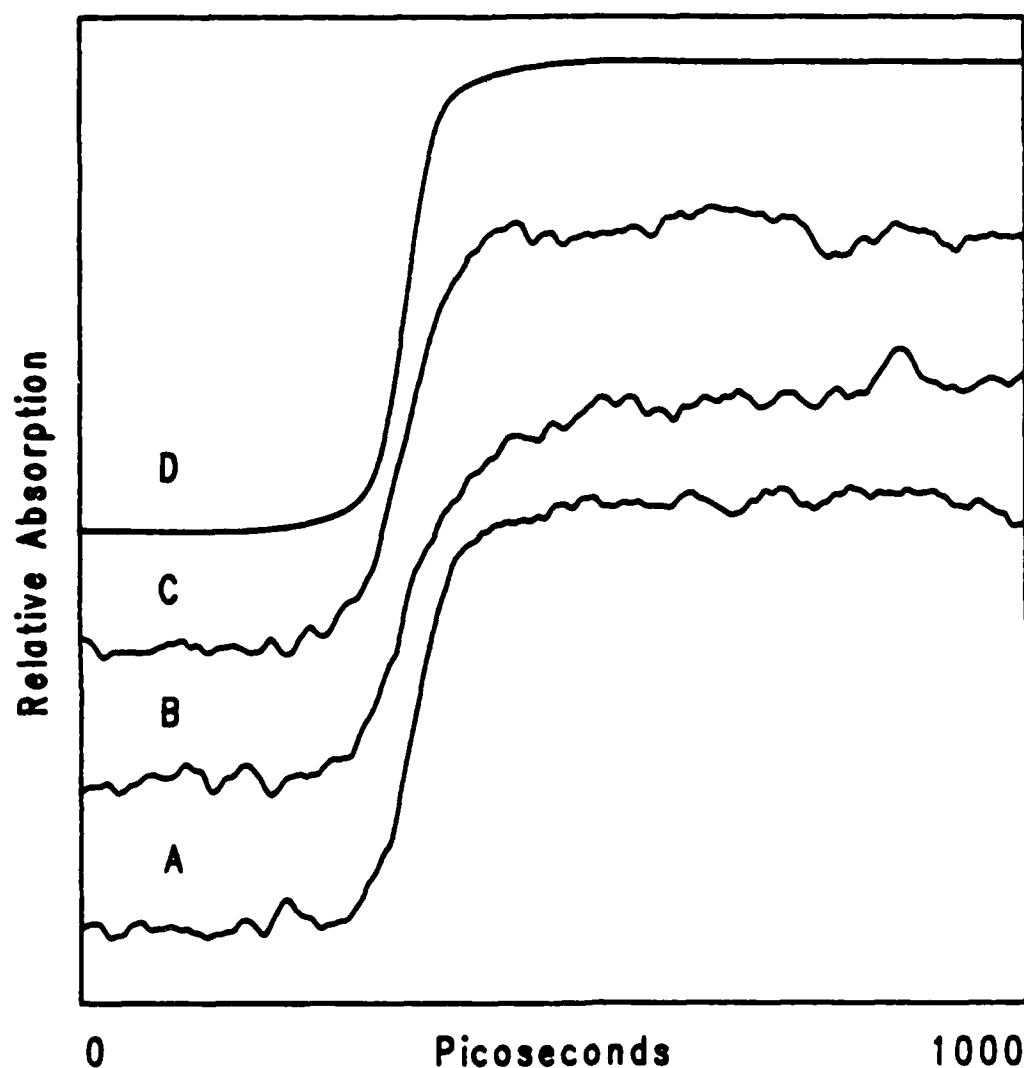


Figure 4.12. Room-temperature time resolved absorption curves for (A) BA in *n*-butanol at 600 nm, (B) BA in *n*-butanol at 700 nm and (C) anthracene in cyclohexane at 600 nm. Curve (D) shows the integral of a typical pulse as measured with the emission configuration. Note that curve B has an appreciable risetime compared with the other curves, as would be expected from the excited-state absorption spectrum.

It appears that if one is interested in investigating the charge-transfer process itself, the use of non-hydrogen bonding solvents is necessary. Unfortunately, with the time resolution available here, no detectable time behavior was observed in acetonitrile, DMSO, DMF or acetone, preventing any further study. It would be of interest to look at these processes with femtosecond time resolution, using either absorption or emission spectroscopy. Absorption spectroscopy is particularly appealing, since it is possible to generate femtosecond pulses in the neighborhood of 725 nm⁵². It would thus be a relatively simple experiment to generate the second harmonic of this pulse (362 nm) and use it to excite the sample, and then use the 725 nm pulse as a probe beam¹⁷. Unfortunately, this sort of measurement was not possible, since such a laser was not available here. One question which comes up in connection with aprotic solvents is why, if the charge transfer step appears as 60 ps "fast" relaxation process in alcohols, is there no detectable relaxation in aprotic solvents. In other words, why is the charge transfer step so much slower in alcohols. A possible reason for the greater rate of charge transfer is that dielectric relaxation still plays a role in determining this rate. Dielectric relaxation in alcohols is orders of magnitude slower for alcohols than it is for aprotic solvents (430 ps for propanol³² versus 5 ps for acetonitrile⁵³), so that to even partially polarize the alcohol takes much longer than the entire charge transfer process would in an aprotic solvent.

F. Intermediate Time Behavior

1. Pure Alcohols

From the data in Table 4.1 it is clear that as the temperature of a sample is changed, τ_2 scales directly with the solvent viscosity. This indicates that whatever process is involved in this time constant involves molecular motion. This is consistent with a model involving diffusion controlled hydrogen bonding and torsional relaxation, but it is also consistent with several other interpretations. In particular, the idea that this time constant is related

Table 4.2

Relaxation Properties of Alcohols at 20 C^a.

Solvent	η^b (cp)	τ_L^c (ps)	[OH] ^d (M)	τ_2^e (ps)	τ_2/τ_L^f	[OH] τ_2/η^g
Ethanol	1.20	37	17.13	30	.81	428
<i>n</i> -Propanol	2.25	83	13.37	100	1.20	594
<i>n</i> -Butanol	2.95	136	10.92	160	1.18	592
<i>n</i> -Pentanol	3.70	202	9.24	200	0.99	499
<i>n</i> -Hexanol	5.30	293	7.96	320	1.09	481
<i>n</i> -Octanol	8.90	525	6.35	610	1.16	435

a . Temperatures uncertain to $\pm 2^\circ$ C.

b . See reference 54.

c. Longitudinal dielectric relaxation time; see text for definition. Ethanol data from reference 55, other solvents from reference 32. Many other measurements exist; see reference 57. Most literature values are within 10% of the values shown.

d. Calculated from data in reference 55.

e. Spectral relaxation time for BA in the alcohol solution. Determined from the relaxation time at 420 nm. These values were reproducible to ± 20 ps.

f. Average value: $1.07 \pm .15$ (14%).

g. Average value: 505 ± 73 (14%).

to the solvent longitudinal dielectric relaxation time τ_L (see below) is also consistent with the viscosity dependence. In contrast to the situation for τ_3 , accurate values for τ_2 can be obtained from a limited number of measurements. Over much of the spectrum, τ_2 is the dominant time constant. Fitting a single dataset taken between 420 and 450 nm to a single exponential decay provides a reasonable value for τ_2 . Furthermore, the fact that τ_2 scales directly with viscosity for a given solvent suggests that measurements at one temperature can be combined with known viscosity values to obtain reasonable values for τ_2 at other temperatures. This greatly simplifies data collection, and makes it possible to look at a wider range of solvents. Table 4.2 gives values for τ_2 as well as values for both $(\tau_2/\eta)[\text{OH}]$ and τ_2/τ_L for several alcohols. The first of these quantities should be constant if the process is diffusion controlled, while the second will be constant if dielectric relaxation is the controlling factor. As can be seen, both quantities are constant to within 15%, so that it is not possible to distinguish between the two models.

2. Alcohol-Alkane Mixtures

Since there are many alcohol properties which vary simultaneously as the chain length increases, it is difficult to single out the factors controlling the variation in τ_2 . Among the properties which vary with alcohol chain length are the viscosity, and viscosity-dependent processes including dielectric relaxation and diffusion; the hydroxyl group concentration and related properties including the solvent polarity⁵⁸; and the degree of hydrogen bonding in the solution. It is desirable to be able to vary the solvent parameters in a more independent manner. One method of doing this is to make use of mixed solvents. Unlike the pure alcohols, where many properties scale together, the properties of mixed solvents can be made to vary in rather different ways so there is the possibility that their effects can be distinguished. In choosing solvent mixtures, it is clearly desirable to find mixtures in which it is possible to keep some solvent properties constant while varying others. The solvent mixtures used here were chosen to variously

keep the viscosity, the polarity or the alcohol concentration fixed. Alcohol-alkane mixtures are especially reasonable for use in comparison with linear alcohols. The only difference between the mixtures and the pure solvents is the distribution of bonds in the linear alkane chains.

The first solvent system to be investigated was the same one used previously to study the relaxation of DMABN²⁶, namely mixtures of *n*-butanol and *n*-hexadecane. This mixture has the advantage that both compounds have similar viscosities so that the viscosity of mixtures remain at an almost constant value of $3.2 \pm .2$ cp for all concentrations. Table 4.3 once again gives values for both $(\tau_2/\eta)[\text{OH}]$ and τ_2/τ_L for these mixtures. The dielectric relaxation data is estimated based on the properties of butanol-paraffin oil and butanol-decalin mixtures, corrected for the hydrocarbon viscosity⁵⁹. Given the rather approximate values for the dielectric properties, it is surprising how well the measured relaxation times correlate with the corrected dielectric relaxation times, with all values of τ_2/τ_L being within a factor of two of one another. A comparable correlation can be obtained between the decay times and the ratio of the alcohol concentration to the viscosity, the two quantities expected to correlate for a diffusion-controlled reaction. Neither of these correlations is especially good; they certainly do not make it possible to choose between the two processes.

It is of interest to consider other factors which will affect these correlations. A serious problem associated with this particular experiment is the fact that the polarity of the solvent changes with each solvent mixture. In a molecule like DMABN this is not a serious problem, since emission spectra of the two excited states are well separated from each other, and can be clearly observed even at relatively low alcohol concentrations. With DMABN, measurements could be made with alcohol concentrations as low as 200 mM²⁶. In BA, the LE and CT emissions tend to overlap each other, so that it becomes increasingly difficult to separate the two emissions as the alcohol concentration, and solvent polarity decrease. The decays observed at 400 nm for the butanol-hexadecane

Table 4.3

Relaxation Properties of Butanol-Hexadecane Mixtures at 20 C^a.

Mixture ^b	η^c (cp)	τ_L^d (ps)	[OH] (M)	τ_2^e (ps)	τ_2/τ_L^f	[OH] τ_2/η^g
<i>n</i> -butanol	2.95	136	10.92	160	1.20	577
B-H	3.1	226	8.19	380	1.68	1004
B-H	3.2	360	5.46	650	1.81	1109
B-H	3.3	315	2.72	830	2.63	686
<i>n</i> -hexadecane	3.44	*	0.00	*	*	*

a. Temperatures uncertain to $\pm 2^\circ$ C.

b. Butanol-hexadecane mixtures with the alcohol concentrations shown.

c. See reference 54 for the pure compounds; viscosities for the mixtures were interpolated.

d. Longitudinal dielectric relaxation time; see text for definition. Data for mixtures estimated from the data in reference 59 for butanol mixtures with decalin and paraffin oils.

e. Spectral relaxation time for BA in the alcohol solution. Determined from the relaxation time at 450 nm. These values were reproducible to ± 20 ps.

f. Average value: $1.83 \pm .60$ (33%).

g. Average value: 848 ± 248 (29%).

mixtures are shown in figure 4.13. As the polarity decreases, the amplitude of the decaying component clearly becomes smaller, so that for alcohol concentrations below ~ 2.5 M, it is no longer possible to distinguish the decay with any accuracy. In alcohol-alkane mixtures, the presence of various alcohol oligomers is expected to have a profound effect on the alcohol diffusion rates. A simple linear dependence on alcohol concentration can only be expected at low alcohol concentrations. Thus it is unfortunate that with BA measurements can only be made at relatively high concentrations where only crude correlations can be expected. That a simple linear correlation is seen in DMABN is actually rather surprising²⁶.

To overcome some of these difficulties, a second set of measurements in which the solvent composition and temperature were varied while leaving unchanged both the alcohol concentration and the $E_T(30)$ value⁵⁸. The data in figure 4.14 shows the results obtained at several temperatures with *n*-hexanol and several alcohol-alkane mixtures with the same alcohol concentration (8.0 M). It is interesting to note that for each solvent mixture the relaxation time is directly proportional to the viscosity, although the proportionality constant varies by an order of magnitude on going from *n*-hexanol to *n*-pentane/methanol. In the simple reaction model this proportionality constant should remain unchanged for fixed alcohol concentrations. That such a large change in this quantity occurs, suggests that the detailed solvent structure plays an important role in determining the solvation dynamics. The fact that both propanol-containing mixtures fall on the same line suggests suggests that the relaxation time depends primarily on the size of the alcohol, with the exact structure of the alkane being relatively unimportant except for its influence on the solvent viscosity. This is what would be expected for a system consisting of micelle-like alcohol oligomers suspended in a hydrocarbon solution, where the volume fraction of the hydrocarbon determines the average solute-hydroxyl distance.

All of the rate data for both alcohols and alcohol-alkane mixtures is compared in table 4.4, which gives values for $[\text{OH}]\tau_2/\eta$. Literature values for DMABN²⁶, 4AP²⁰ and for a

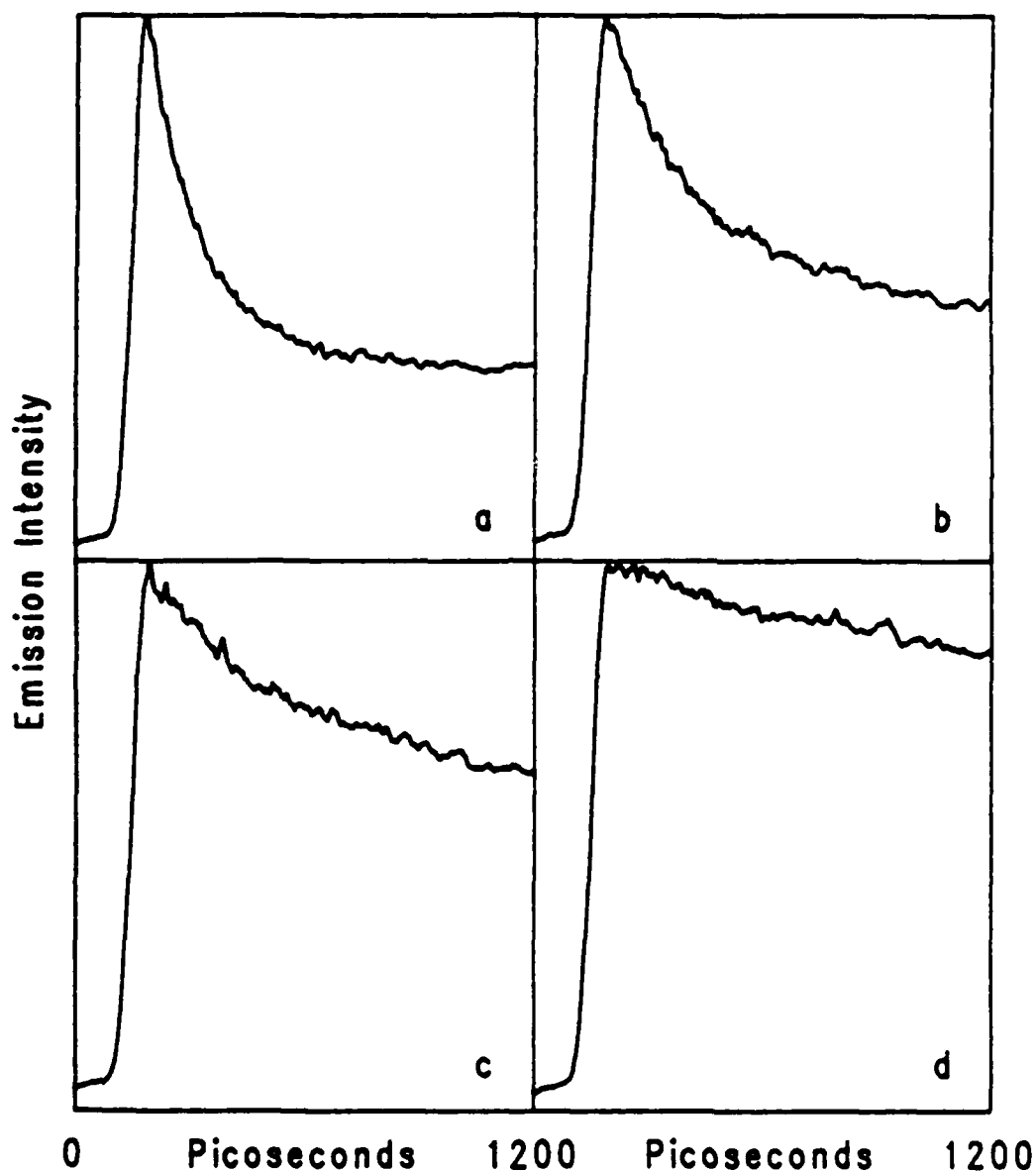


Figure 4.13. Time resolved emission curves at 400 nm for BA in mixtures of *n*-butanol and *n*-hexadecane. *n*-Butanol concentrations are 10.92 M in (a), 8.2 M in (b), 5.5 M in (c) and 2.7 M in (d). While the decay time increases with decreasing alcohol concentration, the amplitude of the decaying component decreases. Thus the decay is difficult to measure at lower alcohol concentrations.

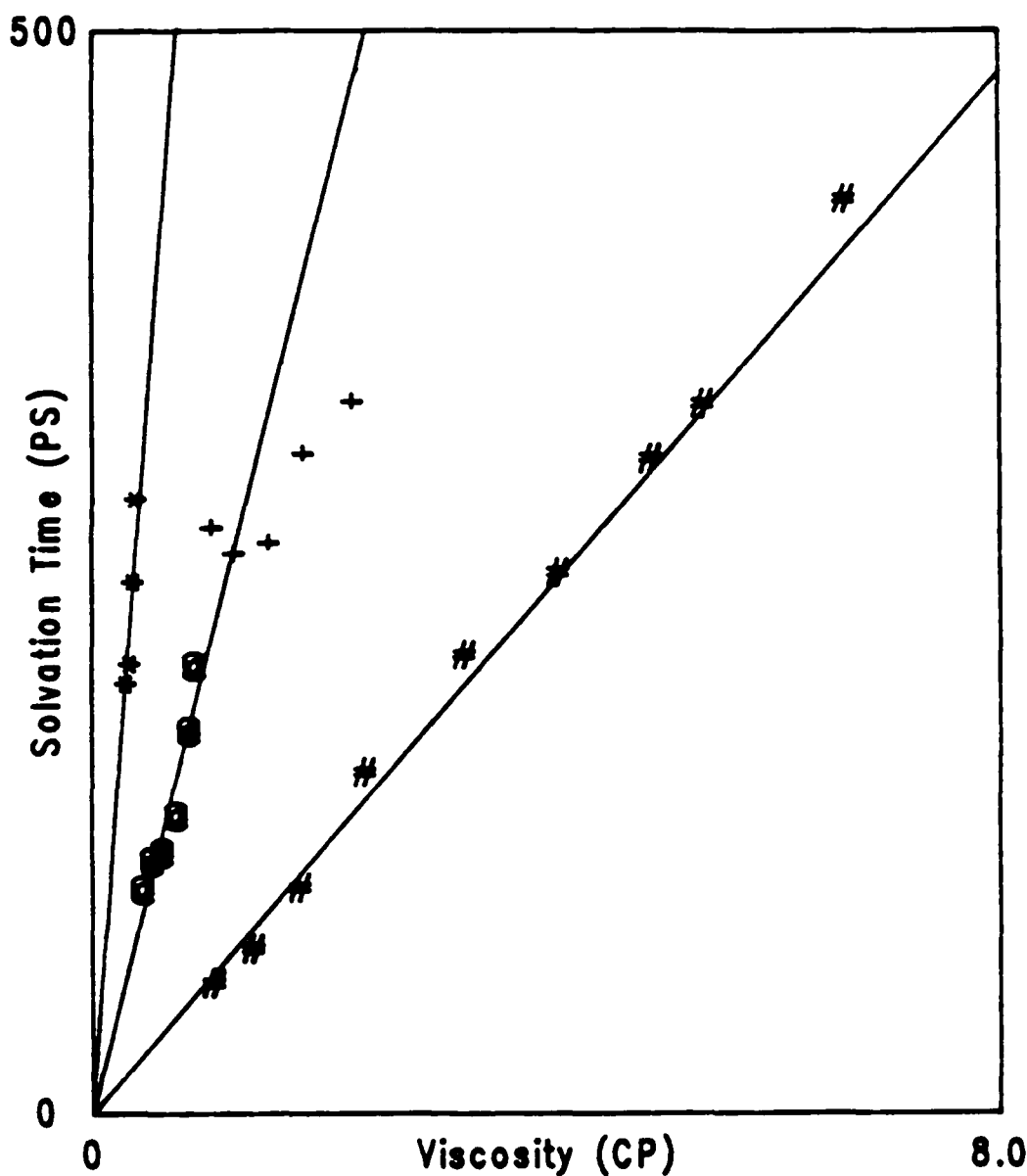


Figure 4.14. The intermediate spectral relaxation time τ_2 plotted against the viscosity for a series of 8.0 M alcohol solutions in alkanes. Temperatures were varied from 15 to 60 C to provide a range of viscosities. (#): *n*-hexanol; (+): *n*-propanol in *n*-hexadecane; (@): *n*-propanol in *n*-pentane; (*): methanol in *n*-pentane. The slopes of the solid lines are given table 4.4.

simple diffusion controlled process in butanol are also shown. It is clear that the nonpolar BA molecule and the polar DMABN molecule behave quite differently. While the data for DMABN scales linearly with alcohol concentration even in the butanol-hexadecane mixtures, only the data for the pure alcohols scales this way for BA. In BA the mixed solutions all show dramatically reduced relaxation rates relative to the corresponding pure alcohols. In both cases it appears that essentially the same process is occurring, that is the rearrangement of the solvent about a newly formed CT state. In both cases there is circumstantial if not unambiguous evidence that hydrogen bonding constitutes the primary form of solvation. The difference between the two systems appears to lie in the nature of the ground state solvation. In DMABN, the solvent dipole has polarized the alcohol so that the local environment has an anomalously large alcohol concentration. Even in the pure alcohols, the hydroxy groups should tend to be directed toward the molecule. This argument has to be reversed for BA since the hydrophobic ground state will tend to minimize the local alcohol concentration. Thus the hydroxy groups of the pure alcohols should be oriented away from the molecule, and the mixed solvents should be primarily hydrocarbon near the BA molecule. Of course other factors such as the differences in the size and geometry of the two molecules may also contribute to the differences. Nonetheless the result appears to be quite consistent with the idea that much of the difference is caused by variations in the local solvent environment.

The presence of local solvent inhomogeneities induced by the presence of a polar solute molecule have been reported before, primarily in relationship to the anomalously large spectral shifts seen in mixtures of polar and nonpolar solvents. These measurements tended to suggest that there was an increased concentration of the polar solvent molecules near the solute dipole, so that the solvent acted more polar than would be expected from the bulk dielectric constant. Calculations of the magnitude of this effect have been carried out, based on the model of a spherical dipole placed in a polar-nonpolar solvent mixture. The extent to which the local environment is enriched in the polar

Table 4.4

Relative Relaxation Properties of Alcohols and Alcohol-Alkane Mixtures.

Solvent	Solute	[OH] τ_2/η
<i>n</i> -Alkanols ^a	BA	505±73
Butanol-hexadecane ^b	BA	1050±100
Propanol-alkanes ^c	BA	1600±200
Methanol-pentane ^d	BA	5500±500
<i>n</i> -Alkanols ^e	DMABN	370±30
<i>n</i> -Alkanols ^f	4AP	370±30
<i>n</i> -Alkanols ^g	Diffusion Control	114

a . Based on the data in table 4.2.

b. Based on the data in table 4.3 for concentrations comparable to hexanol.

c. See figure 4.14.

d. See figure 4.14.

e. Data from reference 26 for *n*-butanol.

f. Data from reference 20 for butanol and propanol.

g. See text.

component can be calculated by balancing the electrostatic stabilization caused by the increased local dielectric constant against the entropy associated with the concentration inhomogeneity. The results suggest that over distances comparable to the molecular radius, a large enrichment will be seen, but that this enrichment will fall off rapidly at longer distances. This dependence on molecular size may be responsible for some of the anomalies seen in the spectra of different molecules. With the relatively small 4-nitroaniline molecule, a large spectral shift was seen³⁴, whereas for the much larger E_T(30) dye, there was no spectral evidence of local polar solvent enrichment⁵⁸.

The problem associated with BA is more complex, since it involves the exclusion of polar molecules from the neighborhood of a nonpolar solute. This is of interest since it corresponds to the biologically important hydrophobic interaction⁶⁰. The force behind this interaction is generally taken to be the strong association between the polar solvent molecules which tends to force the excluded nonpolar molecules together. Such forces are extremely difficult to quantify, since they result from microscopic solvent inhomogeneities. The measurements reported here tend to confirm this picture, and provide an independent, dynamic method for assessing the magnitude of this effect. It would clearly be of interest to observe the behavior of BA in a micellar environment. In this case, the "nonpolar to polar" nature of BA might be expected to produce radical changes in the structure of the micelle, helping to clarify the dynamic nature of such systems.

3. Deuterated Alcohols

One additional set of time-resolved emission measurements were carried out using identical solutions of BA in *n*-butanol and *n*-butan(ol-*d*), with detection at 420 nm. The decay curves are essentially identical to those in figure 4.6, except that the decay time in the deuterated alcohol is 24% longer than that seen in the protonated alcohol. Table 4.5 gives representative physical properties for several deuterated alcohols, including the

Table 4.5

Relative Properties of Protonated and Deuterated Alcohols (X_D/X_H) at 20 C.

	Methanol	<i>n</i> -Propanol	<i>n</i> -Butanol	<i>n</i> -Octanol
Viscosity Coefficient (η)	1.025 ^a	1.015 ^a	1.015 ^a	*
Self-Diffusion Constant (D)	1.09 ^b	*	*	*
Dielectric Relaxation Time (τ_L)	1.34 ^{c,†}	1.15 ^{d,†}	*	1.09 ^e
Bianthryl Rotational Relaxation Time (τ_R)	*	*	1.24	*
Bianthryl Spectral Relaxation Time (τ_2)	*	*	1.23	*
Bianthryl Fluorescence Lifetime (τ_1)	1.0	*	1.0	*
Dielectric Constant (ϵ_S)	0.958 ^c	*	*	1.016 ^e
Refractive Index (n_D)	0.999 ^a	0.999 ^a	0.999 ^a	0.999 ^e
Polarity (Δf)	0.998 ^{a,c}	*	*	1.006 ^e

* Data unavailable.

† Extrapolated from temperatures below 200 K.

^a See reference 62.^b See reference 61.^c See reference 63.^d See reference 63.^e See reference 57.

rotational reorientation time for BA described in the next section. Despite the paucity of the data it is clear that deuteration affects τ_2 in a significantly different manner than it affects the viscosity. The scaling of the spectral relaxation time more closely resembles that of rotational reorientation, dielectric relaxation or, to a lesser extent, self-diffusion. Although this might be taken as an argument against a diffusion-controlled mechanism especially one involving hydrogen bond formation, such is not the case. Note that this scaling is virtually identical to that observed for solutions of 4AP in deuterated alcohols, suggesting that the spectral relaxation process seen in both compounds is the same. In view of the fact that hydrogen bonding to the solute is rather well substantiated in 4AP, the observed isotope effect cannot be used to rule out such behavior in BA.

The isotope effects observed here are much larger than would be expected from classical arguments. A simple kinetic energy argument predicts that the transport properties of the solution should scale with $(M_D/M_H)^{1/2}$. Deuteration of a molecule as large as *n*-butanol would be expected to induce changes of less than 1%. This molecular weight argument is strictly true only in the case where the weights of *all* the atoms increase in the same proportion. It neglects effects which can arise from changes in the intramolecular potentials or in internal parameters such as the moments of inertia. All available evidence indicates that deuteration has a relatively minor effect on the hydrogen bond strength and molecular dimensions in alcohols⁶², so it is not reasonable to attribute the slower behavior of deuterated alcohols to hydrogen-bonding effects. One factor which does scale in an appropriate manner, at least in small alcohols is the moment of inertia, especially that associated with the rotation of the OH group about the O-C bond. This is expected to have an effect primarily on the rotational behavior of the solvent, that is on the angular momentum. Longitudinal diffusion can be described in terms of a linear momentum autocorrelation function. In real molecules, the "roughness" of molecules leads to a coupling between translational and rotational motions which leads to dephasing effects, and a reduced diffusion constant⁶⁴. Isotopic substitution modifies the angular

momentum of the solvent, and so influences the diffusion constant via this coupling. Rotational diffusion processes will feel an even greater effect, since since they directly depend on angular momentum autocorrelation functions which will be directly affected by isotopic substitution. Both the rotational reorientation time and the dielectric relaxation time relate to the rotational reorientation of a dipole. The first corresponds to a free rotation, while the latter includes the influence of an external field, but both processes can be reasonably well modelled by the diffusional rotation of a spherical molecule. That both scale in roughly the same manner indicates that similar processes are involved. The fact that the solvation time also scales this way indicates the importance of a rotational process such as the rotation of an alcohol molecule so as to better solvate the CT state. As shown below, this can be related to either hydrogen bond formation or dielectric relaxation.

4. Rotational Reorientation

The data in both the alcohol-alkane mixtures and in *n*-butan(ol-*d*) indicate that the local dynamic solvent environment is subject to influences not reflected in the macroscopic properties of the solvent. It would clearly be desirable to have an independent measurement which can be used to characterize the microscopic solvent environment. The rotational relaxation time provides just such a measurement, since it can be used to determine a local viscosity for the molecular environment. The rotational relaxation time is derived directly from polarized, time-resolved emission measurements. When a molecule is excited with polarized light, only those molecules with an excitation dipole in the direction of a component of the electric field will be excited. If the emitting dipole is parallel to the excitation dipole, a similarly asymmetric distribution of emission dipoles will have been produced. As a result, the polarization of the emission will initially be anisotropic, with a large fraction of the emission being polarized parallel to the direction of the excitation polarization. As a function of time, rotational Brownian motion will

tend to randomize the physical orientation of the excited molecules. This in turn will lead to a randomization the emission dipoles so that at long times, the initial anisotropy in the emission polarization will disappear. The only requirement for the probe molecule is that the excitation and emission dipoles not be perpendicular. As will be discussed later, the transition dipole associated with the BA absorption feature at 355 nm is polarized along the short axis of the anthracene moieties. The dipole for both the LE and CT emission is also along this axis. Thus measurements of rotational reorientation is possible in BA. Note that the transition corresponding to excitation at 266 nm is polarized perpendicular to the emission dipole, so that a completely depolarized spectrum is observed at all times.

The rotation problem can be treated hydrodynamically in terms of an Einstein sphere of volume V , with a single absorption and emission dipole, immersed in a continuum fluid of viscosity η ⁶⁵. More sophisticated treatments involving more general molecular shapes, more elaborate treatments of viscosity and the hydrodynamic boundary conditions, and a more general relationship between the emission and absorption dipoles are possible⁶⁶, but this simple treatment is adequate for discussing the behavior of BA. Consider such a spherical molecule placed at the origin of a three dimensional coordinate system. The excitation beam is propagating along the the x axis, with the electric field vector in the z direction. Fluorescence propagating along the y axis will be observed in both the z axis ($I_{||}$) and x axis (I_{\perp}) polarizations. The transition dipole μ of the molecule is pointed in the direction defined by the polar angles (θ, ϕ) . Initially, probability of a given dipole being excited is proportional to the projection of the electric field onto the dipole axis. This leads to an initial dipole distribution function

$$W(\theta, \phi, 0) = \frac{3 \cos^2 \theta}{4\pi} \quad (4.2).$$

This distribution will evolve with time due to both rotational diffusion and the finite lifetime of the excited state. The diffusion problem can be readily solved for this initial condition to yield the time-dependent angular distribution; this is multiplied by the

excited-state decay function $P(t)$, to produce the time-dependent dipole distribution:

$$W(\theta, \phi, t) = \frac{P(t)}{4\pi} \left[1 + (3 \cos^2 \theta - 1) \exp\left(\frac{-kTt}{V\eta}\right) \right] \quad (4.3).$$

The probability of a given dipole direction producing emission in a given polarization depends once again on the projection of the dipole direction onto the electric field vector. For emission along the y axis, I_{\parallel} will be proportional to $\cos^2 \theta$ and I_{\perp} will be proportional $\sin^2 \theta \cos^2 \phi$. Substituting the angular distribution function into the expressions for I_{\parallel} and I_{\perp} and integrating over all angles yields the time-dependent expressions for the emission intensity:

$$I_{\parallel}(t) = P(t) \left[\frac{1}{3} + \frac{4}{15} \exp\left(\frac{-kTt}{V\eta}\right) \right] \quad (4.4a),$$

$$I_{\perp}(t) = P(t) \left[\frac{1}{3} - \frac{2}{15} \exp\left(\frac{-kTt}{V\eta}\right) \right] \quad (4.4b).$$

The fluorescence anisotropy function

$$r(t) = \frac{I_{\parallel} - I_{\perp}}{I_{\parallel} + 2I_{\perp}} = \frac{2}{5} \exp\left(\frac{-kTt}{V\eta}\right) \quad (4.5)$$

then relates the diffusion parameters to the observed emission profiles. Note that the denominator of this expression is equal to $P(t)$, and is independent of the diffusion parameters. This is equivalent to the mixture of the two polarizations obtained when the fluorescence is detected through a polarizer set at an angle ω with respect to the z axis, such that $\sin^2 \omega = 2 \cos^2 \omega$. Detection at this angle, (54.74 degrees from the z axis, also known as "magic angle") was used for all the other measurements presented here. An example of this can be seen in figure 4.15.

Table 4.6 shows the values obtained for the rotational time constant $\tau_R = (V\eta/kT)$ in a series of solvents at 20 C. Also shown are values for the viscosities and spectral relaxation times. That the molecular volume is not expected to change greatly between solvents, so that changes in τ_R appear to be attributable to changes in the microscopic or local viscosity. Several trends are apparent. The behavior of the solutions of BA in

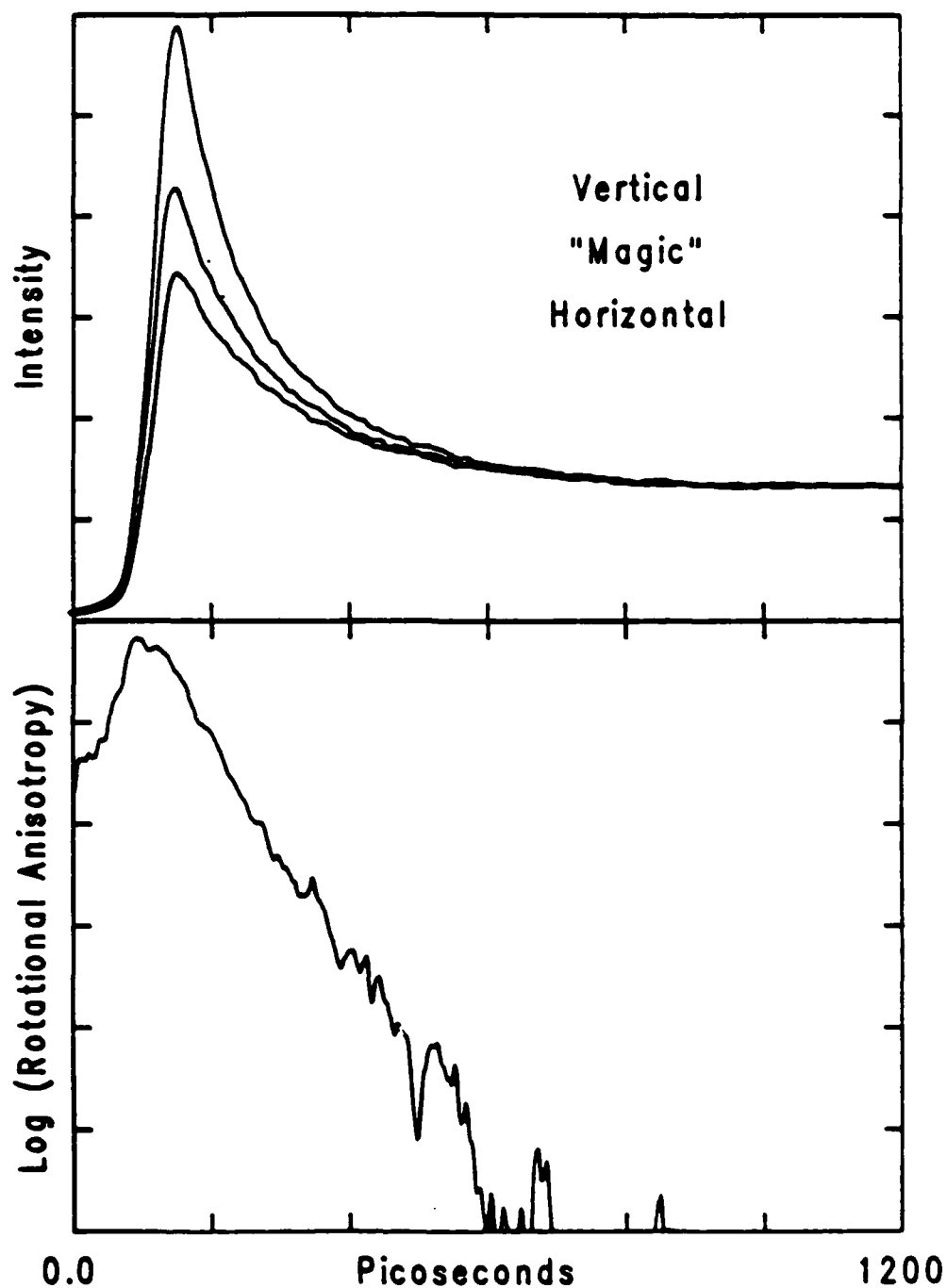


Figure 4.15. Rotational reorientation data for BA in *n*-butanol at 400 nm. The upper curves show the decays observed at the parallel, magic and perpendicular angles, while the lower curve shows the logarithm of the anisotropy function. The linearity of this curve indicates that a single exponential fit will be adequate.

Table 4.6

Rotational and Spectral Relaxation Properties alcohols and alcohol-alkane mixtures at 20 C^a.

Solvent ^b	η^c (cp)	τ_R^d (ps)	τ_2^e (ps)	τ_R/η	τ_2/τ_R
<i>n</i> -butanol	2.95	122	156	41.4	1.27
<i>n</i> -butan(ol- <i>d</i>)	2.99	151	192	50.5	1.27
<i>n</i> -hexanol	5.38	214	284	39.8	1.33
A3C16	2.43	160	264	65.8	1.65
A3C5	.86	67	151	77.9	2.25
A1C5	.36	36	202	100.0	5.61
DMSO	2.16	178	*	82.4	*

*. Not measurable.

a. Temperatures uncertain to $\pm 2^\circ$ C.b. A3C16 refers to an 8.0 M solution of *n*-propanol in *n*-hexadecane, A3C5 to the comparable mixture of *n*-propanol and *n*-pentane, and A1C5 to a mixture of methanol and *n*-pentane. These solutions all have the same alcohol concentration as *n*-hexanol.c. See reference 54 for the pure compounds and reference 62 for *n*-butan(ol-*d*). Viscosities for the mixtures were measured with an Ostwald viscometer.

d. Rotational reorientation time for BA determined at 420 nm; see text for details.

e. Spectral relaxation time for BA measured at 420 nm. Sequential measurements of the emission polarized in the parallel, perpendicular and magic-angle directions were made of the same sample. The first two were used to calculate the rotational reorientation time, and the last one for calculating the spectral relaxation time. This ensures that the measurements were made under the same conditions, so direct comparisons were feasible. Some values for τ_2 differ slightly from those in the other tables, probably because of temperature variations.

n-butanol and *n*-butan(*ol-d*) have already been discussed, and strongly suggest that the observed solvation processes correspond to a molecular rotation.

The data for the nondeuterated alcohols indicates that both relaxation times scale in essentially the same way as the viscosity. This is quite reasonable and is what is expected from the theory. The values obtained for these rotation times are quite close to those obtained for molecules of similar sizes in comparable solvents⁶⁶. Given the uncertainties in these values, one might suspect that the two relaxation times are in fact equal. If this were the case, it would be possible to argue that both decays arose from the same process. This would occur, for example, if the second relaxation time corresponded to a transition to a nonpolarized state. This is a troubling possibility when only data for pure alcohols is available. However, if one includes the data for the aprotic solvents and the solvent mixtures, this possibility seems remote. The similarity of the two values appears to be a coincidence.

The alcohol-alkane mixtures provide the most interesting set of data. The large change in the values of τ_2/η has already been noted, and it has been suggested that it relates to the local solvent composition. A second effect which may be related to the local solvent composition is the fact that as the hydrocarbon fraction increases, the rotational reorientation time increases more rapidly than the bulk viscosity. The origin of this trend is not altogether clear. It might be expected that the relative rotation time would decrease in the local hydrocarbon environment, owing to a decrease in dipole-dipole interactions. On the other hand, the hydrocarbon chains are somewhat longer than those of the alcohols. It is possible that the intertwining of the alkane chains will impede local rotational motion more efficiently than it does long range shear effects. Such behavior would lead to the observed viscosity effects. It is also consistent with the observed isotope effect in butanol. Dielectric relaxation scales in a somewhat similar way in alcohol-alkane mixtures⁶⁷. Since this is also a rotational process, it tends to support this argument. The value of τ_2/τ_R increases consistently the hydrocarbon fraction increases. This indicates

that even if one allows for the difference between rotational and bulk viscosity, the rate of solvation in these mixtures is still anomalously slow. This is once again consistent with the notion that there is a local depletion of the alcohol concentration in the neighborhood of the BA molecule. The value for DMSO is somewhat anomalous, with the value for τ_R/η being twice as large as that seen in alcohols. It is possible that this effect arises from the rapid formation of the CT state, and the correspondingly greater dipole-dipole interaction, but this is once again uncertain.

G. Long Time Behavior

1. Polarity Dependent Lifetimes

If the relaxation processes in BA include the formation of solvent-solute complexes, then the presence of these complexes should be most apparent in the long-time emission properties of the system. Once the fast relaxation processes are complete, the emission will be from molecules in the quasi-equilibrium solvent-solute configuration, and whatever complexation is occurring should be detectable. Table 4.7 gives a summary of the the fluorescence lifetimes and quantum yields for a variety of solvents. The temperature dependences observed in both *n*-butanol and *n*-hexanol are also shown. It is clear that in these solvents the lifetime decreases only slightly with temperature. This is consistent with the potential curve in figure 4.2, since assuming a relatively large barrier for radiationless deactivation results in a small decrease in the lifetime with increasing temperature.

The most pronounced trend in this data is the relationship between the lifetime and the solvent polarity. In nonpolar solvents a lifetime of 10 ns is seen. This appears to correspond to the lifetime of the LE state. In protic solvents (including the butanol-hexadecane mixtures) the lifetime increases linearly with alcohol concentration, until a lifetime of 37 ns is found for methanol. In these solvents, both the LE and CT states exist simultaneously. Even if only a small amount of the nonpolar state is present, the larger

Table 4.7

Fluorescence Yields and Lifetimes for BA at 20 C^a.

Solvent ^b	τ_1^c	Φ_f^d	[OH] ^e	Φ_f/τ_1
Methanol	37 ^f	.21 ^f	24.69	.0057
Ethanol	33 ^g	*	17.13	*
<i>n</i> -butanol	27 ^h	*	10.92	*
<i>n</i> -pentanol	25	*	9.24	*
B-H	23	*	8.19	*
<i>n</i> -hexanol	22 ^h	*	7.96	*
B-H	18	*	5.46	*
B-H	13	*	2.73	*
<i>n</i> -hexadecane	10	*	0.0	*
<i>n</i> -hexane	8 ^g	.55 ^g	0.0	.0688
Acetonitrile	46 ^f	.42 ^f	0.0	.0091
DMSO	26	*	0.0	*

*. Not measured.

a. Temperatures uncertain to $\pm 2^\circ$ C.b. B-H is a solution of *n*-butanol in *n*-hexadecane with the alcohol concentration shown.c. Fluorescence lifetime in ns; typical uncertainty $\pm 10\%$.

d. Fluorescence Quantum Yield; literature values from the references cited.

e. Molar alcohol concentration.

f. Values from reference 47

g. Values from reference 38

h. $(d\tau_1/dT) = -(.06 \pm .01)$ ps/C for *n*-butanol and *n*-hexanol.

emission probability associated with this state (as reflected in the shorter lifetime) will cause decay via this channel will be significant. As the solvent polarity is increased, the relative amount of the CT state will increase, leading to an increase in the fluorescence lifetime. Despite the fact that they are less polar than alcohols, aprotic solvents give rise to even longer lifetimes. This is not surprising if the LE-CT equilibrium is controlling the lifetime. Not only do the aprotic solvents give rise to longer lifetimes for a given polarity, but the spectral shifts are larger as well. This can be interpreted in terms of a lowering of the CT state energy. This will both increase the Stokes shift and decrease the rate at which the excited state population decays via the LE state. This data tends to confirm the idea that there is a qualitative difference between the excited state seen in protic and aprotic solvents. The idea that a hydrogen-bonded state slightly higher in energy is occurring in the alcohols is consistent with the data.

The lifetimes and quantum yields are strongly dependent on the solvent purity, with both sample dryness and the presence of oxygen leading to a significant decrease in the measured lifetimes. Lifetimes measured in air-saturated solutions were on the order of 10 ns for all solvents, consistent with diffusion-controlled oxygen quenching. Samples containing oxygen were also prone to photo-oxidation and such samples acquired a yellowish cast after a few hours of exposure to light. Mass spectroscopic analysis of such decomposed samples showed the presence of a peak at mass 386, corresponding to the addition of two oxygen atoms. This suggests the presence of a quinoid oxidation product, consistent with an increased reactivity at the 10 and 10' positions, although the details of this reaction were not investigated further. The effect of water on the lifetimes is more subtle, but it is clearly detectable. In *n*-butanol at 20 C the lifetime decreased from 27 to 23 ns when the solvent was not dried before use. The effect was even more pronounced in the aprotic solvents. A value of 26 ns is shown for DMSO; this value was obtained after repeated drying of the solvent over 5A molecular sieve. Without drying the solvent, lifetimes as short as 10 ns were obtained. Similarly, with acetonitrile, both

the lifetimes and quantum yield reported for unpurified spectroscopic grade acetonitrile³⁸ are considerably less than those reported for dry acetonitrile⁴⁷.

If hydrogen bonding is important, then the use of deuterated solvents might yield useful information. It might be expected that the replacement of the solvent OH with an OD group will have a greater effect on a hydrogen-bonded system than on a system with no hydrogen bonds. Unfortunately, most existing evidence suggests that the changes will be small, generally less than 20%, so they can be difficult to detect. Deuteration of alcohols not only affects solvent-solute interactions, but solvent-solvent interactions as well. Under these circumstances, it is quite difficult to separate changes in bulk solvent properties from changes in the detailed solvent-solute interactions. Table 4.5, gives representative physical properties for several deuterated alcohols. Dielectric data for deuterated alcohols is surprisingly rare, and the reliability of some of the data, especially that for octanol, is uncertain. The dielectric relaxation and viscosity data appear to be internally consistent, since deuteration uniformly leads to slower relaxation times. The dielectric constants and polarity data may be less reliable; deuteration decreases the apparent polarity of methanol while increasing that of octanol. This may be an artifact resulting from the fact that the differences in dielectric constant are comparable to the uncertainties in the measurements. In any case the change in polarity is quite small, being much less than the effect associated with increasing the alcohol chain length. The emission spectra of BA in methan(ol-*d*) and *n*-butan(ol-*d*) were measured, and no isotope effect was observed. The spectra were essentially indistinguishable from the spectra shown in figure 4.5. The spectral shifts were certainly no larger than those expected from the polarity change. The effect which the deuterated solvent has on the fluorescence lifetime and quantum yield of BA in either methanol and *n*-butanol is equally small. No change in either quantity could be detected. This data offers little support for the idea that hydrogen-bonding plays an appreciable role in the excited-state properties of BA, although, once again the results are not conclusive.

2. Proton Quenching and Proton Transfer

The evidence which exists for a strong interaction between the CT state of BA and protic solvents is primarily based on three results. First of all, the spectral shift seen in protic solvents is significantly smaller than would be expected on the basis of polarity⁴⁶. As described below, this agrees theoretically with what has been predicted for a hydrogen bonded state. The second set of evidence involves the quenching of BA fluorescence by protons. The data of Shizuka et.al.⁴⁷ demonstrates that there is a strong interaction between BA and protons, with appreciable fluorescence quenching being observed in methanol solutions with H_2SO_4 concentrations less than .2 M. Their data at these concentrations can be interpreted in terms of a reaction between BA and protons, and a rate constant of $1.5 \times 10^9 \text{ M}^{-1}\text{sec}^{-1}$ is obtained in methanol-sulfuric acid mixtures. This is slower than a diffusion-controlled rate for this solvent, although it is somewhat faster than what was observed for the relaxation of BA in butanol-hexadecane mixtures. This difference is attributable to the higher diffusion constant for protons and the lower viscosity of methanol. Similar measurements in acetonitrile-sulfuric acid solutions gave a rate constant of $2.2 \times 10^8 \text{ M}^{-1}\text{sec}^{-1}$ for proton quenching and a rate of $1.5 \times 10^8 \text{ M}^{-1}\text{sec}^{-1}$ for deuteron quenching. This isotope effect suggests the presence of a protonated BA complex, similar to the solvent complex indicated for 4AP. Shizuka described the interaction in terms of an ion-pair process, with the proton interacting with the anionic half of BA via a charge-transfer mechanism. Such a mechanism was invoked to account for the large (30%) quantum yield for intersystem crossing associated with the proton quenching process. In this model, an radical pair $\text{BA}^+ \cdots \text{H}$ is formed by electron transfer in a loosely associated complex, with the triplet BA being formed by geminate recombination. This model was formulated before the existence of the TICT state was proposed, so that this complexation scheme was needed to generate a radical ion pair which could recombine to form the triplet state. This may be unnecessary, since

the CT state itself corresponds to radical ion pair.

More recent theoretical work has related the electron density at specific carbon atoms with the rate of proton quenching²³. Note that this work included the behavior of both BA and 1-naphthol, and suggested that the proton quenching was related to the formation of a weakly bound proton complex at an electronegative carbon atom, and to subsequent proton transfer. In general, in aromatic systems which exhibit proton fluorescence quenching also show evidence of proton transfer, albeit with a relatively low quantum yield. It was suggested that the barrier to protonation in the ground state is so large that the S_0 potential would cross the S_1 surface. The resulting avoided crossing leads to a barrier which limits the rate of excited-state proton transfer and also leads to a high rate of fluorescence quenching via internal conversion. According to the calculations the site of complexation will be the carbon atom with the greatest electron density. In the case of BA, this is the 10 position of one of the anthracene moieties.

Evidence confirming the prediction that protonation is occurring at the 10 position of BA was obtained through isotopic substitution measurements. A saturated solution of BA in a solvent mixture made from 1.0 ml of 20% DCl in D_2O and 9.0 ml ethan(*ol-d*), corresponding to a deuterium concentration of 0.6 M. After degassing the sample with repeated freeze-pump-thaw cycles, the sample was irradiated overnight through a pyrex filter with ordinary fluorescent lights. The solvent was pumped away, and the mass spectrum of the resulting solid was measured. The normal molecular ion at 354 was completely eliminated and replaced with a peak at 356, suggesting that two protons had been replaced with deuterium. The symmetry of BA is such that only substitution at the 10 position will result in two protons being exchanged, confirming the theoretical prediction. Further confirmation came from the proton NMR spectrum. The hydrogens at the 10 position ordinarily result in an isolated singlet corresponding to two protons at δ 8.67. While the remainder of the spectrum remained unchanged, this peak disappeared completely in the deuterated sample⁶⁸. An identical sample stored in the dark showed

no evidence of isotopic exchange. Irradiating a similar sample made from nonacidified methan(ol-*d*) also produced no isotopic exchange

These measurements clearly indicate that BA can act as an excite-state base. In principle, either the singlet or the triplet state could be involved, although in studies of related excited-state bases the singlet state has generally been implicated⁶⁹. This appears to be the case here as well. It has been found⁴⁷ that while protons had a large influence on the singlet relaxation, there was no observable proton quenching of the triplet state. This suggests that protons interact much more strongly with the singlet. Furthermore, there is no evidence that the triplet state is polar, making it unlikely that proton interaction will occur. Only the highly polar TICT state has the charge characteristics normally associated with proton transfer. This is consistent with the behavior of a number of other compounds where proton transfer and proton quenching appear to be attributable to singlet state²³. That no isotopic exchange was observed in the nonacidified solution, indicates that if excited-state hydrogen bonding is occurring, it is not accompanied by proton transfer to any significant degree.

H. Discussion

1. Bianthryl Photophysics

The most surprising feature of the charge transfer state in BA is that it exists at all. There is nothing in the behavior of smaller aromatic systems which would lead one to suspect that a symmetry-breaking charge transfer process would occur. Nonetheless, it is not altogether unreasonable that such a state should exist. The formation of charge transfer states in symmetric molecules is not unknown; the metal-ligand charge transfer states seen in tris-bipyridine complexes of transition metals certainly fall in this class⁶⁶, and other examples can be found. The relative stability of the radical ions of larger aromatic systems such as perylene or tetracene is also well known⁷⁰, so it is clear that

aromatics can function as electron donors or acceptors. Because of these features, it is not as unreasonable as it first appears that BA should form a CT state. Most of the unusual properties found in the excited state of BA, such as the large dipole moment and the proton exchange reaction are quite reasonable for a CT state. Because of the relative simplicity of the π electron systems found in symmetric aromatic hydrocarbons, a relatively good theoretical understanding of the states in question is possible. A variety of aromatic double molecules, have been investigated theoretically, including BA, BN and BP. The results of these calculations make it relatively simple to understand the underlying process in BA.

A discussion of the photophysics of BA should begin with the ground state. The equilibrium conformation of BA has been studied by several methods primarily in regard to the structure of substituted biphenyls in general. In the ground state, BA consists of two noncoplanar essentially noninteracting anthracene moieties. This lack of interaction reflected in a variety of electrochemical⁷¹, thermochemical⁴⁸ and spectroscopic³⁷ measurements, all of which show that in the ground state, BA acts very much like two noninteracting anthracene molecules. One way of rationalizing this situation is to assume that the two aromatic groups are perpendicular so that the two π electron systems cannot interact. An internal angle as large as 90 degrees has been suggested for both BA and BN, primarily to account for the similarity between the absorption spectra seen in the single and double molecules⁷². Calculations for BN suggest that this is unnecessary, and that any angle larger than ~ 60 degrees will reproduce the observed spectra⁷³. In the case of BA, there are other independent measurements to support this interpretation, at least for nonpolar solvents. These include measurements of the solution Kerr effect tensors⁷⁴, the Cotton-Mouton (magnetic Kerr effect) tensors³⁶ and dipole moment measurements of halogenated analogs⁷⁵. In all of these cases a vector property of anthracene (or a halogenated analog in the case of the dipole moment) is measured, and compared to that of the double molecule. Since the two anthryl groups are essentially unperturbed in the

double molecule, its properties are just the vector sum of those of the constituent halves. The internal angle is then adjusted until this sum matches the result obtained for the real molecule. Such measurements all indicate an angle of 65 ± 10 degrees. A similar value (67 degrees) has been obtained theoretically, in good agreement with experimental and theoretical values for a variety of sterically hindered biphenyls⁷⁶. (Note that a previously reported value of 89 degrees for a fluorinated analog of BA, cited by Lippert and Schneider³⁷ as evidence for a perpendicular geometry was retracted by the original authors and revised to 65 degrees in a subsequent errata.⁷⁵)

As might be expected, the properties of the double molecules are closely related to those of the individual halves. The spectroscopy of the linear polyacenes have been studied extensively for many years. Although the structure of a large number of excited states have been characterized, it is only necessary to look at the two lowest lying singlet states in naphthalene and anthracene to understand the fluorescence behavior of the double molecules. In the D_{2h} point group of these molecules, these correspond to states of the B_{2u}^+ and B_{3u}^- representations, also known respectively as the 1L_a and 1L_b states⁷⁷. In naphthalene the latter state has the lowest energy, and thus dominates the fluorescence spectrum. Transitions from this state to the ground state are symmetry-forbidden and this accounts for the relatively long fluorescence lifetime of naphthalene. The electron configuration corresponding to this state is not a simple HOMO-LUMO transition, instead it results from configuration interaction (CI) of several higher-lying transitions⁷⁸. In anthracene 1L_a state dominates. The transition to this state is strongly allowed, corresponding to a simple HOMO-LUMO transition, with the transition dipole lying along the short axis of the molecule. One of the few remaining controversies regarding the spectroscopy of anthracene regards the exact location of the 1L_b state. As a symmetry-forbidden transition lying slightly above the strongly allowed 1L_a state, it is so thoroughly obscured as to be almost undetectable⁷⁹.

The spectroscopy of double molecules in general is dominated by exciton resonance

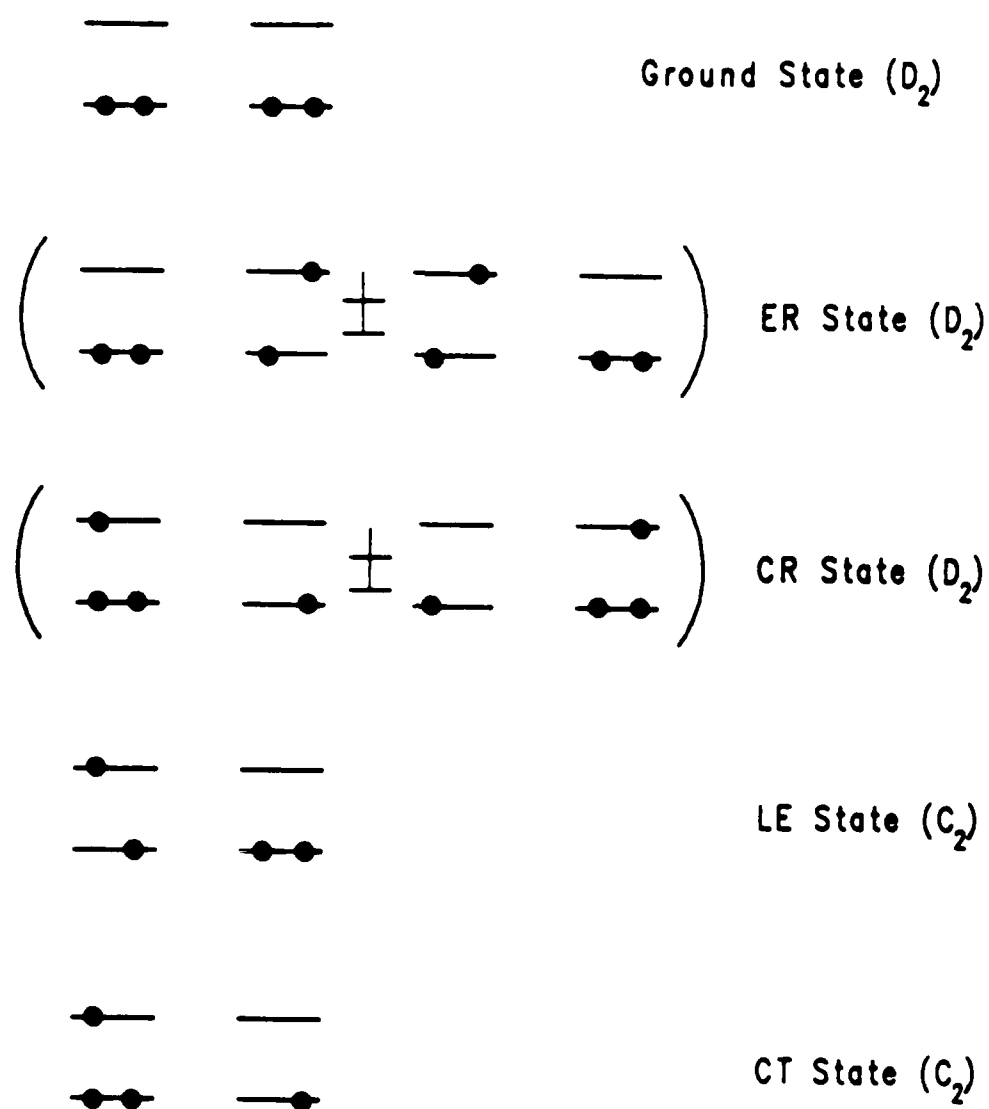


Figure 4.16. Energy level diagram showing the states and the symmetry point groups related to the CT state in BA. In this figure, the individual anthracene moieties are treated as essentially noninteracting two-state systems. In this admittedly crude approximation, all the excited states shown are isoenergetic. The ER and CR states are the linear combinations of the LE and CT states required to maintain the ground-state symmetry.

(ER) and charge resonance (CR) states. The spectroscopy of these systems has been extensively discussed⁷². Published results have emphasized BN and BP, but the discussion is applicable to BA as well. In a simple case, such as BA, where the S_1 level of the single molecule is derived from a HOMO-LUMO two level transition, the states of the double molecule can be thought of as arising from a pair of identical two level transitions. When the two halves do not interact (i.e. 90 degree internal angle) the resulting states divide into ER states (HOMO and LUMO on the same half) and CR states (HOMO and LUMO on opposite halves), with pairs of ER and CR states having the same symmetry. This is shown schematically in figure 4.16 In BN and BP (point group C_2) the symmetries for the symmetric ER and CR states are A (long axis polarized) and B (short axis polarized)⁷². In BA (point group D_2) they are A (inactive) and B_2 (short axis polarized). This corresponds to the allowed transitions in BA being along the $9,9'$ axis. Away from 90 degrees, significant CI between these states occurs, resulting in an S_1 level with a mixed ER-CR character. In both BN and BP (and presumably in BA as well) this leads to a decrease in the dihedral angle and a red shift in the emission relative to the single molecules⁸⁰. The case of BN is complicated by the presence of the 1L_b state, since at angles near 90 degrees this is the S_1 level, but with decreasing dihedral angle, there is a crossing to the mixed ER-CR state described above. This crossing is responsible for the observed spectroscopic and polarization properties observed in BN in fluid solutions¹⁷. The 1L_b level is shifted to higher energies in anthracene, so this spectral complexity is not observed BA. In nonpolar media, the equilibrium configuration for BA, BN and BP should all be quite similar. With BN and BP there is also the question as to whether this configuration is cis or trans. Calculations tend to suggest that both orientations are nearly equal in energy, with no clear indication as to which is the most favorable⁷³. In the case of BA, the configurations are identical, so this question does not come up.

To extend this discussion to BA first consider the relaxation processes in nonpolar solvents. Here one expects relaxation processes comparable to those in BN. Thus some

torsional relaxation is expected, with the corresponding increase in the CR character of the state, although the final configuration is sufficiently similar to that of a noninteracting configuration that the anthracene-like vibrational structure is still visible. At any angle other than 90 degrees, the S_1 state consists of a combination of ER and CR components. Since the transition is strongly allowed, the relevant states appear to be the short-axis polarized B_2 states. The time-resolved emission in nonpolar solvents is found to be strongly polarized when excited at 355 nm and totally depolarized at 266 nm. This is to be expected, since the higher-lying transition is to a B_1 or B_3 state with the transition moment lying perpendicular to the emitting S_1 state. Thus in this case, there will be no correlation between the excitation and emission dipoles so the emission will be unpolarized.

Up to this point the existence of the CT state has not been discussed. This is principally because the behavior of BA has been discussed in terms of the ground-state symmetry, which automatically precludes a charge transfer between the rings. It seems clear that the CT state is of CR parentage. After all, the CR states are just symmetric linear combinations of the polar states, and an electric field induced asymmetry would tend to split them into the polar components. Returning to figure 4.16, the nature of the CT state can clearly be seen. It corresponds to the direct transfer of an electron from one ring to the other. In the absence of electron repulsions, this state should be exactly equal in energy to that of the local excited state. Note that this state is rigorously defined for a 90 degree internal angle, where interactions between the pi electron systems will be minimized, leading to a complete electron transfer. It should be noted that experimentally, the emission retains the same polarization as the LE state. This is not altogether surprising, since the LE emission is polarized along the 9,9' axis, and so is parallel to the charge separation in the TICT state. Thus the emission dipoles will lie along the same axis, resulting in polarized emission.

The CT state of BA differs significantly from that seen in DMABN. In DMABN,

the existence of two excited states was rationalized in terms of a solvent-dependent equilibrium between two excited-state conformations. The conformational change in this case corresponded to a 90 degree rotation of the amino nitrogen about the C-N bond. In one configuration, the nonbonding orbital on the nitrogen atom is oriented in a direction perpendicular to the plane of the aromatic ring. This maximizes the interaction between π electron system and the nitrogen orbital, but it minimizes the degree of charge transfer. A rotation of 90 degrees eliminates the possibility of π electron interactions, but maximizes the degree of charge transfer. At angles between these two extremes, a mixture of conjugation and charge transfer would be expected. Calculations by Grabowski et al.¹¹ indicate that in DMABN the rotational potential has minima at 0 and 90 degrees. The intermediate states are not formed and the molecule can be understood in terms of a planar and a twisted form. The nature of the CT state in BA is somewhat different, since no heteroatoms or nonbonding electrons are involved. In addition, steric considerations make a 90 degree rotation unlikely, since a coplanar geometry is not going to be stable. Finally, it is not clear whether the excited state is truly perpendicular.

In a nonpolar solvent the CT state will be destabilized by its large dipole moment, since there are no electrostatic interactions to stabilize the large charge separation. In this case the molecule will presumably retain its ground-state symmetry and eventually form a mixed ER-CR state with an internal angle comparable to that in BN, that is ~ 40 degrees. In polar solvents, the polarization of the solvent will tend to compensate for the large charge separation in the CT state, and this state will predominate. This is the usual tradeoff between "resonance stabilization" associated with the greater π - π interaction in the more coplanar, nonpolar geometry and the "electrostatic stabilization" associated with a large dipole moment in a polar solvent. This model tends to predict two rather different types of conformational relaxation, even in polar solvents. Starting from a ground-state angle near 65 degrees, the molecule in the unrelaxed solvent environment will initially rotate toward a more planar geometry; in nonpolar solvents this configuration

will persist, but in polar solvents, as the solvent polarizes, the CT state will form, causing a rotation back toward 90 degrees. Unfortunately, there is no way to follow this process, and it is not clear to what extent it occurs. In particular, it is not clear how close to a perpendicular geometry the CT state really is.

The configuration of the BA CT state has been considered in some detail in connection with the process of proton quenching of the fluorescence. The total energy of the system is found to vary somewhat with angle, with an increase of 730 cm^{-1} occurring on going from 60 to 90 degrees. Thus, it is possible that an angle less than 90 degrees might in fact be the preferred configuration. Two other features are associated with the rotation from 60 to 90 degrees. The oscillator strength of the transition to ground decreases by at least a factor of 8, and the negative fractional charge density at the 10 position increases by a factor of ten to almost 0.2. It is interesting to note that these facts can be used to generate an internally consistent picture of the difference between the observed spectral behavior in protic and aprotic solvents.

Based on the fluorescence quenching and isotopic exchange experiments, it appears that the 10 position of the CT state of BA can function as base. In most cases, molecules which can function as bases can also function as hydrogen bond acceptors, since both processes involve interactions with protons³³. It appears therefore, that in protic solvents, solvent-solute hydrogen bonds should be formed. Their formation will be accompanied by a rotation into the perpendicular configuration, since this maximizes the degree of charge separation and hence the hydrogen bond strength. Note that the typical energy of a hydrogen bond is about 2500 cm^{-1} . This is almost exactly equal to the value (2520 cm^{-1}) obtained by Kosower et.al.⁴⁶ for the difference in energy between the excited state seen in protic and aprotic solvents. This strongly indicates that a perpendicular hydrogen-bonded state is occurring in protic solvents. In aprotic solvents, there will be no such tendency to form hydrogen bonds, so the molecule may well adopt a somewhat more coplanar geometry, since in the absence of hydrogen bonds this is a more stable

geometry. A second aspect of the data which agrees with this interpretation is the time-resolved emission spectrum shown in figure 4.9. In this case after the initial formation of the charge transfer state, there is a gradual loss of fluorescence intensity, associated with the intermediate time constant. It has been shown that this time constant scales in the way one would expect for either dielectric relaxation or a diffusion controlled reaction between BA and the solvent. That this process is also associated with a large loss in fluorescence intensity corresponds to the fact that in the perpendicular, hydrogen bonded geometry, the emission cross-section is much less than it is in other geometries. This suggests that what is occurring is hydrogen bond formation coupled to a rotation into a less intensely emitting geometry.

In aprotic solvents, the molecule may favor a more coplanar geometry, since there is no stabilization associated with maximizing the local charge densities. Because of this, a lower energy state with a larger oscillator strength might be expected in aprotic solvents. The lowering of energy is consistent with what is observed, although hydrogen bond formation may be a more significant factor in the observed Stokes shifts. The relative oscillator strength can be estimated from the the lifetime and quantum yield data in table 4.7. The emission rate will correspond to the ratio of the quantum yield to the lifetime. As can be seen, this quantity is significantly larger in acetonitrile than it is in methanol, indicating that, as predicted, the oscillator strength is larger in acetonitrile than it is in methanol. Note that both values are an order of magnitude smaller than that seen in *n*-hexane. Since the electron distribution and symmetry of the CT state are quite different from the ground state, it is reasonable that the Franck-Condon factors associated with emission from the CT state (in any geometry) will be smaller than those associated with the LE emission. Note that a decrease in oscillator strength does necessarily not lead to a longer lifetime, since the lifetime depends on both the emission rate and the the rate of other relaxation processes such as LE emission and internal conversion. The barriers to the nonradiative processes are governed primarily by the level of the CT state, and it is

indeed found that the lifetime does scale with the spectral shift. This tends to suggest that the lifetime is governed by the nonradiative channels, rather than the oscillator strength.

On additional reason to believe that BA in aprotic solvents is in a somewhat less polar geometry is the relative rates of proton quenching seen in methanol and acetonitrile. It was found that that the rate was at least a factor of five faster in methanol⁴⁷. Since this rate was found to correlate with the maximum charge density, it suggests that in acetonitrile, a state with less localized charge is occurring. This is precisely what results from decreasing the internal angle. These results also may be related to the quenching of fluorescence by traces of water in aprotic solvents, i.e. the shorter lifetimes seen in wet DMSO. Traces of water should not affect the polarity greatly, but might have a significant effect on the lifetime by forming a perpendicular hydrogen-bonded state with a lower barrier for nonradiative relaxation. Only small concentrations of this state would be expected, so it might not be seen spectroscopically. This possibility was not studied in detail, but if this interpretation is correct, such studies might lead to direct evidence of hydrogen bond formation.

Thus, on both experimental and theoretical grounds there is reason to believe that the process underlying solvation of BA in alcohols is hydrogen bond formation, with a hydrogen-bonded perpendicular CT state dominating in protic solvents, and a more coplanar, nonhydrogen-bonded state occurring in aprotic solvents.

2. Polarity, Solvation and Dielectric Relaxation

In understanding the behavior of BA, it is important to keep in mind the nature of solvent polarity. The observed behavior of BA can to some degree be explained either in terms of a reaction between the solvent and the BA molecule or in terms of the polarization of a dielectric fluid. The two models appear to be quite different, since one emphasizes the microscopic diffusion of individual solvent molecules while the other relates to the relaxation of a continuous fluid. Nonetheless, the underlying processes

are quite similar and the two theories lead to similar behavior. The dielectric relaxation theory has received a great deal of attention recently²⁹, so it would be of interest if it applies here. At the same time, the microscopic reaction picture is much clearer in some respects, and also appears to describe the data reasonable well. In essence, the difference between the two approaches is the relative importance of non-specific, long-range dipole interactions, and short range interactions such as hydrogen bonding.

Solvent polarity, that is the tendency of solvent dipoles to stabilize polar and charged species in solution, is an extremely valuable guide to the behavior of a solvent. Polarity affects many aspects of solvent behavior from solubilities to the spectroscopy of dissolved species. Spectral shifts come about when the states involved in a transition have different dipole moments and so are stabilized to differing degrees in polar solvents. For example, the absorption spectrum of a molecule whose dipole moment is large in the ground state and small in the Franck-Condon excited state, will be increasingly blue-shifted as the solvent polarity is increased. This reflects the fact that the energy of the ground state is lowered by dipole-dipole interactions in the polar solvent, while the energy of the excited state remains essentially unchanged. This leads to an increase in the energy difference between the two states, and hence to a blue shift in the absorption spectrum. By measuring the spectral shift of a single molecule in a range of solvents, an empirical polarity scale can be obtained. This is the origin of the commonly used $E_T(30)$ polarity scale, based on the absorption spectrum of a betaine dye. Many other properties show similar variations indicating that to a good approximation, polarity is a real, definable property of a solvent⁶.

Of greatest interest here is the relationship between the macroscopic solvent dielectric properties and the solvent-dependent spectral shift. The theory of polar molecules in solution as developed by Onsager, Lippert, Mataga and many others⁸¹ treats the problem of a spherical dipolar object with radius a immersed in a continuous polarizable dielectric. For fluorescence spectra, this theory gives the following relationship between the Stokes

shift and the dielectric properties of the solvent:

$$\Delta\nu_{st} = \frac{2}{a^3hc}(\mu_e - \mu_g)^2 \left(\frac{\epsilon - 1}{2\epsilon + 1} - \frac{n^2 - 1}{2n^2 + 1} \right) \quad (4.16).$$

The cavity radius a is not well defined and must be treated as an empirical parameter. It can vary from solvent to solvent and between closely related solute molecules in the same solvent. There has been some success in developing microstructural models which make it possible to obtain reliable relative values of a (and hence relative dipole moments) for closely related molecules, but the problem is by no means solved⁴⁰. The spectral shift depends on the difference between the dipole moments μ_e and μ_g in the two states. A similar result applies for absorption spectra, with the dipole moment terms reversed. The term on the right involving ϵ and n is referred to as Δf and can be used as an empirical polarity scale. In general, it has been found that the correlation between the $E_T(30)$ value and Δf is reasonably good within a homologous series, but changes with different families of solvents. This simply reflects the variation in a ⁸².

A number of efforts have been made to extend this approach to time-dependent processes²⁹. The expression given here for the Stokes shift can be generalized to include the time dependence of the dielectric constant. The macroscopic variable which is ordinarily used to describe this time dependence is the dielectric relaxation. The dielectric relaxation properties of many liquids have been investigated⁸³, characteristically by measuring the microwave dispersion and absorption properties. As shown by Debye⁸⁴, the dielectric response of a polar liquid includes relatively slow components arising from the reorientation of molecular dipoles. This leads to a decrease in the polarizability with increasing frequency, and is reflected in both the real and imaginary parts of the electric susceptibility. In the time domain, the process of dielectric relaxation is described in terms of a polarization with a finite response time. In isotropic media, where the tensor nature of ϵ can be neglected, this takes the form of the convolution integral

$$D(t) - E(t) = \int_{-\infty}^t E(u) \alpha(t - u) du \quad (4.7),$$

where the displacement, \mathbf{D} and the electric field \mathbf{E} have their usual meanings.

In a real liquid, the response function $\alpha(t)$ includes both fast and slow components, which arise from a variety of mechanisms and correspond to the various absorption features of the liquid. From the point of view of the experiments carried out here, all components which relax faster than ~ 10 ps cannot be detected, and so can be lumped into a "high frequency" polarizability, $\epsilon_\infty - 1$, and a slow polarization $\alpha'(t)$. Equation 4.4 now becomes

$$\mathbf{D}(t) - \epsilon_\infty \mathbf{E}(t) = \int_{-\infty}^t \mathbf{E}(u) \alpha'(t-u) du \quad (4.8).$$

For many liquids, there is no appreciable dielectric absorption below this cutoff, so dielectric relaxation will not be observed with this time resolution. The principal exception to this rule is in the case of hydrogen-bonded solvents, such as alcohols, where a slow relaxation of hundreds of picoseconds is seen. This slow relaxation is usually expressed in the form

$$\alpha'(t) = \left(\frac{\epsilon_S - \epsilon_\infty}{\tau_D} \right) \exp\left(\frac{-t}{\tau_D}\right) \quad (4.9).$$

The preexponential factor takes this value so that for static fields, the polarization given by equation 4.2 agrees with that given by the static dielectric constant, i.e. $\mathbf{D} = \epsilon_S \mathbf{E}$. This form, due to Debye, is largely phenomenological, although it can be derived by considering the reorientation of spherical dipoles in a viscous fluid, in a manner analogous to that used for rotational reorientation. In this case the dielectric relaxation time takes the form $\tau_D = (3V\eta/kT)$, where the variables take the same definitions as they did in the case of rotational relaxation⁸⁴. Note that this formulation only takes into account a single dielectric relaxation time τ_D . The mathematics are readily extended to the case of multiple exponential decays, but for the systems considered here (linear alcohols and alcohol-alkane mixtures) this was found to be unnecessary. Although multiple relaxation times are observed, the higher frequency components are generally either too fast or too weak to be of any significance. Their contributions are represented in the value for ϵ_∞ .

Substituting the form of a single Debye relaxation into equation 4.2 and subtracting the time derivative of this equation from itself, leads to a differential equation to describe dielectric relaxation:

$$\tau_D \frac{d}{dt}(\mathbf{D} - \epsilon_\infty \mathbf{E}) + (\mathbf{D} - \epsilon_\infty \mathbf{E}) = (\epsilon_S - \epsilon_\infty) \mathbf{E} \quad (4.10).$$

There are several conditions under which this equation can be solved. If \mathbf{E} and \mathbf{D} are taken to be of the form $Ee^{i\omega t}$ and $De^{i\omega t}$, and the frequency-dependent complex dielectric constant is defined by $\epsilon(\omega) = D/E$, then equation 4.2 becomes

$$\epsilon(\omega) = \epsilon_\infty + \frac{\epsilon_S - \epsilon_\infty}{1 + i\omega\tau_D} \quad (4.11).$$

This form of solution reflects the method normally used to measure dielectric relaxation, in which the real and imaginary parts of ϵ are measured using sinusoidal electric fields at microwave frequencies. Clearly there will be a Lorentzian resonance at $\omega = \tau_D^{-1}$; this is the value tabulated for the dielectric relaxation time. On the other hand, it is also possible to solve the equation with the assumption that \mathbf{D} is a constant. In this case, equation 4.2 becomes

$$\frac{d\mathbf{E}}{dt} = \frac{-\epsilon_S}{\tau_D \epsilon_\infty} \left(\mathbf{E} - \frac{\mathbf{D}}{\epsilon_S} \right) \quad (4.12).$$

This yields an exponential decay with a time constant given by $\tau_L = \epsilon_\infty \tau_D / \epsilon_S$. This time constant, the longitudinal relaxation time, corresponds to the relaxation of a system in response to an imposed charge distribution, and is the case which is often used to describe the relaxation of the solvent in the field of a molecular dipole⁸⁵. A more sophisticated analysis²⁹ suggests that instead of τ_L , one should expect the relaxation rate to scale with the slightly different time constant τ'_L defined by

$$\tau'_L = \frac{2\epsilon_\infty + 1}{2\epsilon_0 + 1} \tau_D \quad (4.13).$$

This difference arises from the fact that the simple derivation of τ_L is literally true only for a parallel-plate capacitor; it ignores the effects due to the spherical molecular cavity

as per the Clausius-Mossotti equation. The difference between the two values is small and is of little real significance. Note that the value of τ_L depends strongly on the value of ϵ_∞ . In particular, the common practice of using the optical dielectric constant n_D^2 in place of ϵ_∞ , is not correct⁴⁴. Doing so typically leads to values for τ_L which are a factor of two too small.

The relevance of these calculations to BA is unclear. Calculations relating time-dependent spectral shifts to dielectric relaxation often explicitly assume that a potential diagram comparable to figure 4.1 is applicable, with a fixed excited-state dipole moment appearing instantaneously, and the solvent then rearranging to accommodate it²⁹. This leads to a continuously shifting spectrum with a with an exponentially varying Stokes shift, as is seen in 4AP. Since BA appears to be a molecule with a CT state, with a potential analogous to figure 4.2, such an interpretation is doubtful. If the potential in figure 4.2 can be taken literally, then solvent polarization corresponds to a lowering of the CT potential curve, with only minor changes in the nonpolar LE and ground states. If the timescale for LE-CT interconversion is much faster than the dielectric polarization, then the solvent relaxation will correspond to a gradual shift in the LE-CT equilibrium and to a shift in the CT spectrum. The shifting equilibrium will result in a given molecule spending more time in the CT state, which in turn will increase the tendency of the solvent to polarize further. In the simple electrostatic derivation given above, this corresponds to the case where D varies in a nonlinear fashion with E . Such a system is expected to give a relaxation time intermediate between τ_D and τ_L , although it is not possible to give a definite value. Once again, this relaxation would correspond to a shift in the position of a fixed spectral feature, and not a two-state relaxation process.

The basic problem with applying the theories based on dielectric relaxation to the observed behavior of BA is that the theories predict a type of behavior which is not observed in BA. They predict that the relaxation corresponding to τ_L will involve a continuous shift in the position of a fixed spectral feature. This is what would be expected

If the polarity of the solvent were continuously increasing, since it is what is seen in a series of increasingly polar solvents. What is observed instead in BA is an initial spectral shift followed by an exponential loss of intensity. Because of this phenomenological mismatch, it is difficult to directly associate the observed spectral decay with dielectric relaxation or an increase in the solvent polarity. As noted above, a reasonably good phenomenological description of the observed spectral relaxation can be obtained from a model involving hydrogen bonding. In this model, the high frequency components of the dielectric relaxation cause the solvent to act initially like a weakly polar, aprotic solvent (comparable to an ester or an ether). This leads to the observed rapid formation of the CT state. The slow, diffusive component of dielectric relaxation is not seen directly; it manifests itself as the formation of hydrogen bonds. This leads to the conclusion that dielectric relaxation is not what is being observed, despite the fact that the observed time constants are quite close to the predicted values.

3. Solvation as a Diffusion Controlled Reaction.

If dielectric relaxation and a concomitant increase in the solvent polarity is not the mechanism responsible for the observed spectral relaxation, then an alternative model is needed. If possible, it would be desirable to both account for the experimental results and to show why dielectric relaxation, an evidently incorrect model, correctly predicts the observed relaxation times. As has been suggested, a diffusion controlled reaction between the protic solvent and the BA CT state leading to the formation of a hydrogen-bonded state seems to account for most of the observed features of the decay. The existence of the hydrogen bonded state cannot be shown directly, but it is consistent with the observed spectroscopic and proton-transfer properties of the molecule. The nature of the diffusion controlled formation of this state is more complicated than a simple diffusion controlled reaction. The conventional Einstein-Smoluchowski rate for a diffusion controlled reaction between equal sized, spherical molecules would give the following time constant for the

reaction of BA with the surrounding solvent,

$$\tau = \frac{\eta}{[\text{OH}]} \frac{3}{8kT} \quad (4.14).$$

For butanol at 20 C, this corresponds to 42 ps, which is somewhat faster than the observed decay time. This is not a serious disagreement, since this model ignores any electrostatic effects associated with the adjacent dipoles, and makes unreasonable assumptions about the molecular geometry. It also ignores the orientation effects which must arise due to the site-specific nature of hydrogen bonding. In effect, this model ignores rotational diffusion and describes the relaxation process in terms of translational diffusion.

A second approach to the diffusion controlled mechanism is to ignore translation and concentrate on rotational diffusion. To do this, it is necessary to obtain the rotational relaxation times. For BA, this can be readily obtained from the fluorescence depolarization measurements. In general, these rates are proportional to the solvent viscosity and the molecular volume; for BA in pure alcohols, the spectral and rotational relaxation times are almost equal. For the solvent relaxation, the rotation time for a solvent molecule in the presence of the solute dipole is needed. This is identical to the problem of dielectric relaxation, and leads to the same result, that $\tau = \tau_L$. In terms of the Debye theory, this is given by

$$\tau = \frac{3V\eta\epsilon_\infty}{kT\epsilon_0} \quad (4.15),$$

where V is an empirically determined molecular volume. One might expect that it would be related to the molecular size and would be inversely proportional to the molar alcohol concentration. This is not true for pure alcohols; dielectric relaxation in alcohols is generally attributed to the motion of individual molecules within a hydrogen-bonded structure. The rate limiting step in this case is believed to be the rate of hydrogen bond formation³². The value for V is thus not directly related to the molecular size and is roughly constant for all linear alcohols. The alcohol concentration does, however enter into the picture. For alcohols and alcohol-alkane mixtures it is generally true that the

static dielectric constant is close to a linear function of the alcohol molarity. In fact, in all but the most dilute solutions, it can be treated as being directly proportional to the alcohol concentration, so $\epsilon_0 \sim \beta[\text{OH}]$. With this approximation, the relaxation time takes the form

$$\tau = \frac{\eta}{[\text{OH}]} \frac{3V\epsilon_\infty}{\beta kT} \quad (4.16).$$

Because of the nature of dielectric relaxation in pure alcohols, this corresponds to the reorientation time of a single molecule.

The observed spectral relaxation time in pure alcohols takes the form

$$\tau \propto \frac{\eta}{[\text{OH}]} \quad (4.17).$$

In the alcohol-alkane mixtures this is still roughly true, but the proportionality constant varies with the volume fraction of the alcohol. Note that this is the functional form assumed by both the translational and rotational diffusion times. Because of this, the data can be fit to any model which includes some combination of these two effects. This is why it is so difficult to distinguish "diffusion control" and "dielectric relaxation" models; to a reasonable approximation, they give exactly the same functional form. Differences arise only in the more subtle concentration effects. After correcting for the bulk concentration and viscosity, the Einstein-Smoluchowski relaxation time will vary in different solvents as the size and shape of the solvent changes. It will also be affected by local solvent inhomogeneities, as the effective concentration will vary in the neighborhood of the probe molecule. The dielectric relaxation time varies in different ways, as the molecular volume changes and longitudinal diffusion begins to play a role. At low concentrations, dielectric relaxation represents the rotation of individual alcohol molecules. As the concentration increases alcohol oligomers begin to form, leading to increased volumes and longer dielectric relaxation times. Finally, at very high concentrations, the oligomers give way to an extended hydrogen bonded structure which allows cooperative motions of several molecules to play a greater role. Because of this, the dielectric relaxation time decreases

for alcohol mole fractions above 0.5. Because of this, in relatively concentrated solutions, both models predict that the viscosity- and concentration-corrected relaxation time will increase significantly as the alcohol volume fraction decreases; this is precisely what is observed. At lower concentrations a greater effect might be expected, as the dielectric relaxation time becomes smaller again. Unfortunately, as noted above, it is not possible to measure relaxation times in BA at low alcohol concentrations, owing to the lower polarity and the smaller Stokes shift. Thus there is no clear phenomenological difference between the two approaches.

Both of these models represent a gross oversimplification of the molecular environment, since both describe the behavior of spherical molecules in a continuum fluid and ignore the finite size of the solvent molecules. This hydrodynamic approximation is quite reasonable when considering macroscopic measurements, such as diffusion over relatively long distances, but it becomes difficult to accept when processes on a molecular scale are considered. After all, at this level the solvent and solute molecules are approximately the same size so that treating one group of molecules as a continuum seems inherently unreasonable. Nonetheless, hydrodynamic models are widely used and have been found to give relatively reliable descriptions of molecular phenomena such as rotational reorientation, even though the motions being described occur over molecular dimensions. This success can be attributed to the nature of statistical averaging. Diffusion acts like a random walk; it can be shown, that provided the motions are not correlated, a random walk with small equal steps will give the same distribution as one with large, randomly distributed steps. In other words, the coarseness of the motion associated with the equal sizes of the solvent and solute motions will average out when a large ensemble of molecules is considered. What will remain are effects arising from non-random features of the solution such as oligomer formation or local solvent inhomogeneities.

Treating the relaxation process according to the Einstein- Smoluchowski theory as a diffusion controlled reaction minimizes the affect of this simplification, since the solvent

and solute are treated as having finite sizes. The continuum fluid simply maintains the viscosity. Diffusion in alcohols is a complex process, since it involves the motion of a variety of oligomeric species. Nonetheless, Fick's law is obeyed so that an average diffusion constant can be defined. The diffusion controlled rate will be affected by spatial inhomogeneities around the BA molecule. In pure alcohols these effects are limited; only the orientation of the neighboring alcohol molecules can be changed. Translational diffusion cannot play a major role in this case, since the reacting species are already in contact. If it is assumed that the rotational time is proportional to the molecular volume and the viscosity, and that the molecular volume is proportional to the reciprocal of the alcohol concentration, then the observed viscosity and concentration dependences are accounted for. They are also accounted for if the dielectric relaxation time is taken as being the single-molecule reorientation time. In alcohol-alkane mixtures, greater inhomogeneities are possible because of the presence of the hydrocarbon molecules, and the nonpolar BA molecule is expected to induce such inhomogeneities. Translational diffusion will be needed to bring the reacting species together; smaller alcohols will typically be farther apart, leading to the longer relaxation times. Rotational diffusion is still needed to account for the relative orientations of the molecules, but since both rates scale in the same way, the rotational and translational components will be difficult to distinguish.

The difference between the dielectric relaxation model and the diffusive model can be seen to be quite small. This is primarily because the dielectric relaxation time corresponds to a rotational relaxation time, and not because of the electrostatic nature of the relaxation process. The underlying physical processes are much better explained in terms of the diffusive model. In particular, the behavior of the alcohol-alkane mixtures is quite reasonable. By invoking a diffusion controlled reaction, it is quite easy to describe the difference between what was observed in DMABN with a polar ground state and with BA and a nonpolar ground state. The simplicity of this interpretation makes its use seem preferable to invoking dielectric relaxation. The latter method appears to give reasonable

results as well, but only because it is closely related to the diffusion process.

I. Conclusion

The data presented here all tends to support the following interpretation for the solvation processes observed in BA. In nonpolar solvents, the molecule behaves just as would be predicted for BN, except for the absence of the low-lying 1L_b state. Solvation in this case should take the form of torsional relaxation to a more planar geometry, in a manner analogous to BN. In polar aprotic solvents, the CT state is rapidly formed. Presumably, with femtosecond time resolution, it might be possible to follow this process. It is expected in this case that dielectric relaxation will be the limiting factor, and that a time-dependent spectral relaxation process, similar to what is predicted theoretically, might be seen. Finally, in protic solvents, the sequence of events appears to be an initial formation of a CT state in a partially polarized solvent environment followed by diffusion-controlled hydrogen bond formation. The first part of this is reasonable; on timescales short compared to the hydrogen bond rearrangement time, alcohols might well be expected to exhibit a polarity comparable to an ester or an ether. As for the second step, as unlikely as it appears, a variety of spectroscopic, theoretical and chemical evidence all point to the CT state of BA as both a base and a hydrogen bond acceptor. Although the longitudinal dielectric relaxation time agrees quite closely with the observed solvation times, a mechanism involving dielectric relaxation *per se* does not account for the observed spectral behavior. It appears that the close similarity of the two time constants arises because both arise from rotational reorientation of a solvent molecule in the presence of an electric field.

The most unusual feature of BA, the fact that it goes from a rigorously nonpolar molecule to a highly polar charge transfer state, is reflected in its behavior in alcohol-alkane mixtures. In these solvents, the solvation times are as much as an order of magnitude slower than would be predicted for a pure alcohol with the same alcohol con-

centration and viscosity. This effect is readily accounted for by considering the presence of a nonpolar ground state will have resulted in a local enrichment of the nonpolar solvent. Solvation, in the form of hydrogen bond formation will thus be much slower than would be predicted from the bulk alcohol concentration. An area which was not investigated, but would clearly be of interest would be the behavior of BA in micelles. In particular, the long lifetime and hydrogen bond acceptor properties of the CT state of BA might be expected to yield interesting results.

The data presented here have by no means exhausted the experiments which can be carried out using BA and analogous compounds as probe molecules. For example, the anomalously large isotope effect observed in the solvation time and in the rotational reorientation time suggests that studies in other deuterated alcohols might be of interest. The difference in behavior between the nonpolar BA molecule and the polar DMABN molecule suggest that a great deal can be learned about the local solvent environment of the ground state. A significant limitation on comparing the results of BA and DMABN is the differing molecular geometries. BA has the advantage that many closely related molecules with significantly different ground state properties can be synthesized. The asymmetric compounds used by Rettig et. al.³⁵ can be used to provide a range of ground state dipole moments. These compounds include a variety of 10 substituted analogues of BA, as well as the compounds in which one of the anthryl groups is replaced by a 9-carbazolyl or 9-acridinyl group. An equally interesting group of analogues are the symmetric compounds such as 1,1'-bipyrene, 9,9'-bicarbazole or 9,9'-biacridine. The last of these compounds is nonpolar, but is expected to be a strong hydrogen bond acceptor at the 10 and 10' positions. It is thus expected to act much like DMABN, since the solvent molecules needed for excited-state hydrogen bonding are already in place. The results obtained so far demonstrate the unusual behavior of this molecule, and further studies can be expected to yield further unusual results.

J. Appendix on Data fitting

Most of the conclusions reached here are based on the existence of wavelength-independent time constants which can describe a multiexponential decay. This section will consider the reasons for expecting that such a fit will occur, what it corresponds to physically, and the limitations and cautions which must be applied when interpreting such results. In addition, the mechanics of how to go about obtaining such a fit for multiple datasets is included, mostly to provide an unambiguous description of how these results were obtained.

Ideally, the systems studied here will undergo a series of relaxation processes where a molecule in one state will undergo a transition into another state. It is of interest to consider how to go about describing the behavior of a system undergoing a multi-state decay. For the molecules described here, it was sufficient to consider a four-state process (the ground state and three excited states), but the generalization is obvious. Since dilute solutions of the probe molecules are being studied on timescales much shorter than the time between bimolecular encounters, it is expected that all processes will be first order. Assuming this sort of kinetic scheme leads to the rate laws of the following form:

$$\frac{d}{dt} \begin{pmatrix} C_1 \\ C_2 \\ C_3 \\ C_4 \end{pmatrix} = \begin{pmatrix} k_{11} & k_{12} & k_{13} & k_{14} \\ k_{21} & k_{22} & k_{23} & k_{24} \\ k_{31} & k_{32} & k_{33} & k_{34} \\ k_{41} & k_{42} & k_{43} & k_{44} \end{pmatrix} \begin{pmatrix} C_1 \\ C_2 \\ C_3 \\ C_4 \end{pmatrix} \quad (4.18),$$

where the vector C corresponds to the concentrations of the four states and k corresponds to a matrix of rate constants. Such systems have solutions which are linear combinations of four exponentials, with the time constants given by the reciprocals of the eigenvalues of the matrix k . To make the system physically reasonable, it is necessary that the components of k obey the usual constraints of microscopic reversibility, that the number of molecules be conserved and that all the molecules eventually return to the ground state. The last of these conditions is equivalent to setting the last column of k equal to

zero. This causes one of the eigenvalues to be zero, so that there is a time-independent term corresponding to the ground state at long times. The time-dependent spectrum (absorption or emission) is given by the sum of the concentrations of the four states, weighted by their relative spectral intensity:

$$S(\lambda) = \sum_{j=1}^4 I_j(\lambda) c_j \quad (4.19)$$

where $I_j(\lambda)$ is the spectrum of the j th component. The contribution from the time-independent term is ordinarily included in a background term and ignored. This then leads to a triexponential decay with wavelength-independent time constants and wavelength-dependent amplitudes.

There are many pitfalls associated with fitting experimental data to multiexponential decays. In general, the fits are not unique, and many different combinations of time constants and amplitudes can be used to fit a given set of data⁸⁶. It has been shown repeatedly that it is far simpler to obtain a plausible fit than it is to assign any real significance to the resulting time constants. The existence of a relatively simple two or three exponential fit does not automatically indicate the existence of an underlying simple two or three state decay process⁵¹. At best, a lower bound on the number of excited states might be obtained; the possibility that a complex or nonexponential process is occurring cannot be ruled out. For the present problem, the constraint that the time constants not be a function of wavelength removes some of the arbitrariness from the problem by minimizing the number of free parameters in the system. Now, instead of fitting a single decay, it is necessary that the lifetimes chosen fit up to twenty different decays. This does not rule out the possibility that a given time constant is representing a distribution of similar time constants. However, if the data can be fit over the entire spectrum with only a few time constants having significantly different values, then it is probably reasonable to infer that different processes are occurring on different timescales and that the exponential time constants obtained from the fitting procedure are valid

estimates of the relevant timescales.

There is a question of how one goes about defining the best fit for a group of datasets. Clearly it is just a generalization of the usual procedures used to fit individual datasets, but there are some new questions about weighting the data and comparing data from different datasets. For fitting single datasets, the noise characteristics of the streak camera are such that Poisson statistics are ordinarily used. In this case the weaker datapoints will receive greater weight. This is reasonable within a single dataset, but when used with multiple datasets, it will give an inordinate weight to any datasets with the low signal levels. To avoid this, it is important that all the datasets have comparable signal levels. It is actually rather difficult *not* to satisfy this condition experimentally, due to the finite dynamic range of the detector. In practice, either the pump beam or the sample fluorescence was attenuated until peak intensities slightly below the detector saturation level were obtained. If the differences in overall intensity between datasets is small, then the overall deviation between the data and a set of fitting functions (the quantity to be minimized) is simply the sum over all the datasets of the squares of the individual deviations, divided by the individual signal intensities. This corresponds to treating all the datapoints in all the datasets as being equally valid.

The purpose of the fitting procedure is to find a set of wavelength-independent time constants, and wavelength-dependent amplitudes and time-zero values which generate a set of positive-definite triexponential decays which, when convolved with the excitation pulse and normalized to the same area as the corresponding datasets, minimize the overall deviation defined above. The method used to find the parameters corresponding to the best fit combined a simplex search for the time constants, a grid search for time-zero (varied for each dataset), and a constrained linear fit for the amplitudes of the various exponential components. In addition to this, a modified version of the Grinvald-Steinberg iterative convolution procedure was used to speed up the calculations⁸⁶ In most cases, it was not actually necessary to vary all three time constants simultaneously. For example,

the fluorescence lifetime of BA in alcohols is so much longer than the short time constants, that measurements at two different streak speeds are needed to measure all three times. Lifetime measurements were made at a relatively slow streak speed. They could be fit as single exponentials and were found to be independent of wavelength. When the data at higher streak rates was fit, this time constant was fixed at this value. Thus the actual fitting procedure consisted of varying the two fast time constants until the overall offset was minimized.

Figure 4.17 shows a "typical" dataset. By inspecting the curve it is possible recognize the "pulse" region (channels m_1 to m_2) and the "data" region (channels n_1 to n_2). These are best determined manually, so they are treated as given by the fitting routine. They are taken to be the same for an entire group of datasets. The data offset, or time-zero is determined by the difference between t_1 and t_2 . Because of the way in which the data is collected, t_1 is invariant from dataset to dataset. On the other hand, t_2 tends to vary by a few channels from dataset to dataset, because of the differences in the thickness of the bandpass filters and because of general chromatic aberrations. Because of this it must be left as a free parameter in fitting each dataset. The data shown is for the simple case where the data is the integral of the pulse. In this case, t_1 represents the center of the pulse, while t_2 corresponds to the 50% point of the data.

Each data set can be divided into an n -vector D_i taken from the "data channels" of the dataset, and an m -vector P , taken from the "pulse channels". Since this pulse remains essentially unchanged over an entire group of datasets, a "typical" pulse is generated by averaging the individual P_i vectors. The averaged pulse vector P is defined only at the m grid points, but it can be transformed to a continuous function $P(t)$ by setting all the undefined grid points equal to zero, interpolating the datapoints and correcting the timescale using the streak rate of R ps/ch. In order to carry out the fitting procedure, it is necessary to convolute the pulse function $P(t)$ with each of the exponential decays. This

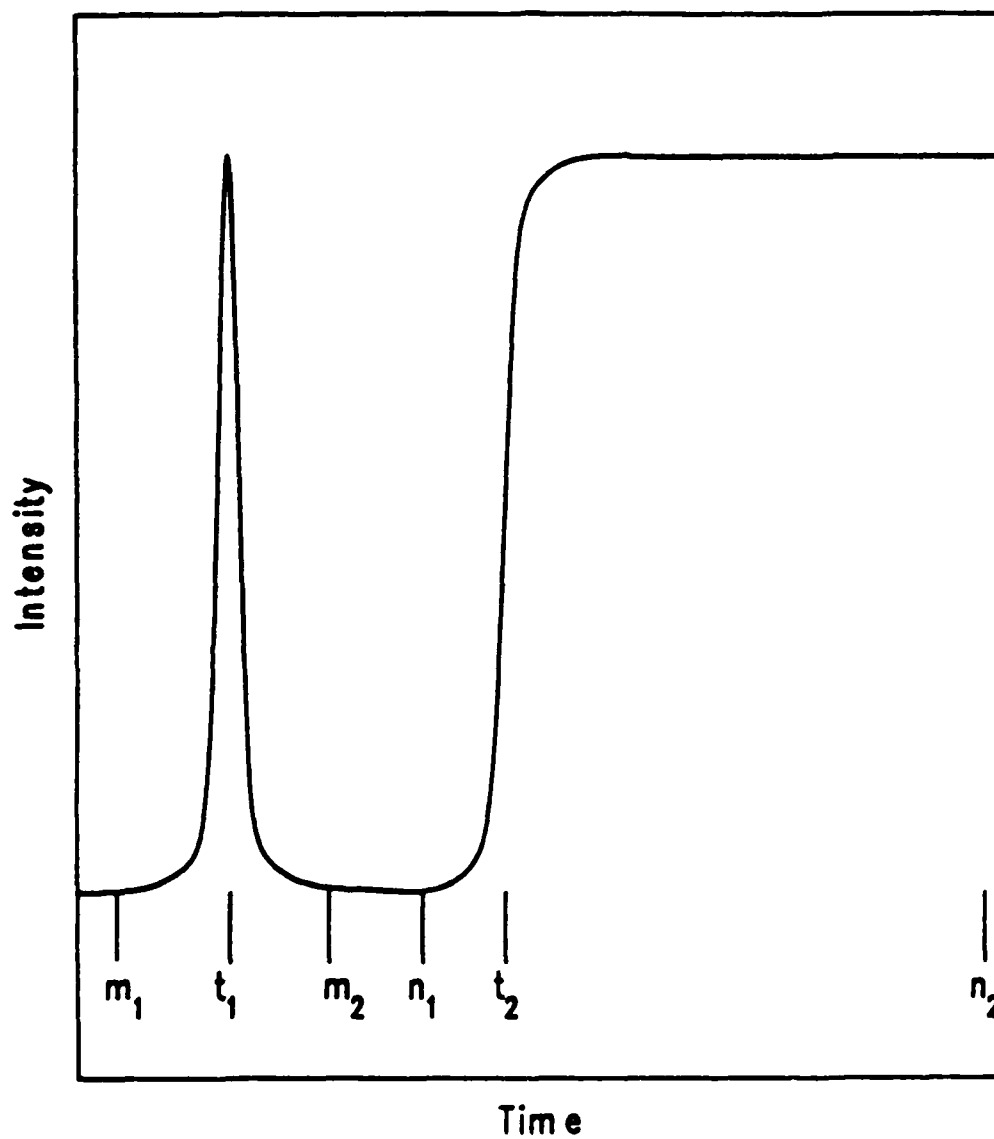


Figure 4.17. A "typical" dataset obtained from the streak camera. The "data" shown is simply the integral of the pulse. The points marked on the figure relate to the fitting process, as described in the text.

leads to a new function $Q(t)$:

$$Q_j(t) = \int_0^t P(x) \exp\left(\frac{(x-t)}{\tau_j}\right) dx \quad (4.20).$$

To compare this with D_j , it is necessary to convert this function back into a vector. This is accomplished by evaluating $Q(t)$ at the grid points. Making use of the fact that $P(t)$ is linear between these points leads to a simple iterative method for carrying out this calculation. It is clear from the definitions of P and Q that for the value of t corresponding to P_i ,

$$Q_j(t+R) = Q_j(t) + \int_t^{t+R} [(P_{i+1} - P_i)(x - t_i) + P_i] \exp\left(\frac{(x-t)}{\tau_j}\right) dx \quad (4.21);$$

Solving the integral and rearranging, leads to the following iterative formula for the components of $Q_{i,j}$.

$$Q_{i+1,j} = Q_{ij} + A_j P_i + B_j P_{i+1} \quad (4.22),$$

with

$$A_j = 1 + \beta_j^2 - (1 + \beta_j + \beta_j^2)e^{-1/\beta_j} \quad (4.23),$$

$$B_j = -\beta_j^2 + (\beta_j + \beta_j^2)e^{-1/\beta_j} \quad (4.24),$$

and

$$\beta_j = \frac{R}{\tau_j} \quad (4.25).$$

These are an extension of the formulae⁸⁶ given by Grinvald et.al., using slightly different assumptions as to how one should interpolate the pulse. Note that A and B should be calculated in double precision to avoid roundoff errors. Applying this formula is straightforward, since P_0 and $Q_{0,j}$ are equal to zero. These formulas look complex, but since A and B need only be calculated once for each value of τ_j , they make it possible to calculate the convolutions quite rapidly, so the relatively complex fitting scheme used here converges in a reasonable time. In the actual fitting routine, it is necessary to know

the integral of Q so the areas of the calculated curves can be matched to those of the actual data. This is quite conveniently done at the same time that the iterative calculation is being carried out.

There is one more detail to be worked out before the problem is reduced to a simple linear fit, that of time-zero. As it stands, the Q vectors are calculated as if t_2 were equal to t_1 . This is obviously not the case, so Q must be shifted before it is fit to D . In principle, Q can be shifted continuously, it being possible to evaluate $Q(t)$ at any point desired. In fact, this is unnecessary. Restricting the shifts to integral channels saves an appreciable amount of calculation by facilitating the use of the iterative formula for Q , and does not noticeably affect the results. This is reasonable, since the streak camera response function is several channels wide, and that it is unlikely that fractional channel resolution would be possible in any case. In what follows the notation Q_j^s is used to describe the vector defined by convolving the pulse with the i th exponential, and then shifting the result by an integral number s channels.

The fitting problem for i_0 datasets and j_0 exponentials now becomes that of finding a_{ij} , τ_j , and s_i such that the weighted norm

$$\sum_{i=1}^{i_0} \|D_i - \sum_{j=1}^{j_0} a_{ij} Q_j^{s_i}\|^2 = \epsilon^2 \quad (4.26)$$

is minimized, subject to the constraints

$$\sum_{j=1}^{j_0} a_{ij} (Q_j^{s_i} \cdot I) = (D_i \cdot I) \quad 1 \leq i \leq i_0 \quad (4.27).$$

$$\sum_{j=1}^k a_{ij} \geq 0, \quad 1 \leq k \leq j_0 \quad (4.28),$$

The vector I is unity for the channels in the "data range", and zero elsewhere. The dot products shown correspond to taking the integral of the data and the fit curve over the "data range", and are used in the equality constraints to conserve area. The set of

inequality constraints provide a sufficient (though not absolutely necessary) condition that the fit curves be positive definite, provided that $\tau_1 > \tau_2 > \dots > \tau_{j_0}$.

All the nonlinear aspects of the problem are now concealed in Q . At this point, given values for τ_j and s_i , the values for a_{ij} and ϵ^2 can be found immediately by standard methods⁸⁷. Taking the partial derivatives of (8) with respect to the a_{ij} and setting them equal to zero leads to a set of linear normal equations. Each value of i corresponds to a different dataset, so the problem in fact separates into i_0 individual constrained optimizations. The first constraint is an equality constraint, so it can be included immediately to eliminate one of the a_{ij} . Having done this, the remaining constraints are ignored and the problem is solved directly. If the constraints are satisfied, the new values for a_{ij} are accepted and the fit is complete. If not, a simplex search among the constraints can be carried out until the optimum set of active constraints is found. In reality, the only inequality constraint which ever matters for this problem is that with $k = j_0$, since it is almost impossible to construct curves which are even qualitatively similar to the data if the other constraints are violated. Therefore, if the unconstrained fit fails, invoking this constraint almost always solves the problem.

At this point, it is easy to vary s_i ; since only integral values of the shift are allowed, such changes correspond only to changing the subscripts of Q . Furthermore, since the integral of Q was calculated at all points at the same time as Q , the dot product involving Q is also calculated immediately. A grid search for the best value of s is thus carried out for each dataset along with the linear optimization. This is not as inefficient as it sounds, since the search starts from the previous best value, and s rapidly converges to the best value. Doing this leads to a problem where ϵ depends only on τ_j . A simplex optimization for $\epsilon(\tau_j)$ thus completes the solution of the optimization problem.

The type of data resulting from the fitting process can be seen in table 4.8 through table 4.11, which show the fits for BA in *n*-hexanol at several temperatures.

Table 4.8

Parameters of fits for BA in n-hexanol at 0 C. Viscosity = 10.6 cp

Wavelength (nm)	24600 ps a_1	519 ps a_2	62 ps a_3	$t=0$ $\sum a_i$
390	0.031974	0.063389	0.035786	0.131148
400	0.065646	0.126312	0.045158	0.237116
410	0.096223	0.167755	0.021313	0.285291
420	0.115652	0.173341	-0.011478	0.277515
430	0.116881	0.136704	-0.032332	0.221253
440	0.113960	0.095972	-0.039295	0.170637
450	0.099330	0.059652	-0.041945	0.117037
460	0.083925	0.034671	-0.037275	0.081321
470	0.068510	0.019091	-0.033949	0.053652
480	0.054008	0.006623	-0.024608	0.036053
490	0.040933	-0.000692	-0.019433	0.020809
500	0.030821	-0.000923	-0.012223	0.017675
510	0.022571	-0.002093	-0.006845	0.013633
520	0.016495	-0.002919	-0.003211	0.010364
530	0.011801	-0.002342	-0.002530	0.006929
540	0.008559	-0.002001	-0.002022	0.004535
550	0.006080	-0.001885	-0.000924	0.003271
560	0.004334	-0.001582	-0.000647	0.002105
570	0.003109	-0.001068	-0.000700	0.001341
580	0.002244	-0.000771	-0.000352	0.001121
590	0.001615	-0.000659	-0.000121	0.000835
600	0.001162	-0.000558	0.000002	0.000607

Table 4.9

Parameters of fits for BA in n-hexanol at 20 C. Viscosity = 5.37 cp

Wavelength (nm)	22400 ps a_1	323 ps a_2	62 ps a_3	$t=0$ $\sum a_i$
390	0.035590	0.055418	0.019774	0.110782
400	0.069168	0.131377	0.044132	0.244677
410	0.098836	0.185434	0.002751	0.287021
420	0.117395	0.194773	-.038362	0.273807
430	0.116806	0.167760	-.053459	0.231108
440	0.113114	0.130407	-.054808	0.188713
450	0.097862	0.081791	-.044108	0.135545
460	0.082441	0.050109	-.034329	0.098221
470	0.066588	0.030733	-.029387	0.067934
480	0.052450	0.016649	-.023945	0.045154
490	0.039674	0.007930	-.015191	0.032413
500	0.029936	0.002211	-.009627	0.022520
510	0.021875	0.000064	-.005646	0.016292
520	0.016074	-.001751	-.002919	0.011404
530	0.011471	-.000005	-.003425	0.008040
540	0.008294	-.000866	-.001743	0.005685
550	0.005896	-.001180	-.000496	0.004221
560	0.004252	-.000997	-.000837	0.002418
570	0.003040	-.000726	-.000492	0.001821
580	0.002184	-.000420	-.000300	0.001464
590	0.001585	-.000316	-.000085	0.001184
600	0.001141	-.000255	0.000065	0.000952

Table 4.10

Parameters of fits for BA in n-hexanol at 36 C. Viscosity = 3.32 cp

Wavelength (nm)	21100 ps a_1	202 ps a_2	73 ps a_3	t=0 $\sum a_i$
390	0.039743	0.049939	0.012211	0.101894
400	0.072167	0.091206	0.040807	0.204180
410	0.100930	0.124647	0.040402	0.265978
420	0.118549	0.130896	0.040901	0.290346
430	0.116488	0.106461	0.025056	0.248006
440	0.112102	0.083999	0.015576	0.211677
450	0.095977	0.056746	0.005981	0.158704
460	0.080565	0.038272	-0.004321	0.114516
470	0.065515	0.020334	-0.002265	0.083584
480	0.051443	0.011137	-0.002116	0.060465
490	0.038815	0.004641	-0.005551	0.037905
500	0.029168	0.002927	-0.008415	0.023681
510	0.021309	0.000466	-0.005300	0.016475
520	0.015585	-0.001160	-0.003480	0.010945
530	0.011150	-0.001089	-0.003159	0.006902
540	0.008060	-0.001142	-0.002136	0.004782
550	0.005725	-0.001290	-0.001180	0.003254
560	0.004142	-0.001088	-0.001012	0.002041
570	0.002949	-0.000774	-0.000821	0.001354
580	0.002121	-0.000591	-0.000554	0.000976
590	0.001538	-0.000671	0.000010	0.000877
600	0.001110	-0.000484	0.000007	0.000633

Table 4.11

Parameters of fits for BA in n-hexanol at 60 C. Viscosity = 1.78 cp

Wavelength (nm)	21800 ps a_1	101 ps a_2	(0 ps) a_3	t=0 $\sum a_i$
390	0.043684	0.029709	0.000000	0.073392
400	0.076041	0.069549	0.000000	0.145590
410	0.104645	0.087644	0.000000	0.192289
420	0.121443	0.090788	0.000000	0.212231
430	0.116992	0.063101	0.000000	0.180093
440	0.111522	0.045008	0.000000	0.156530
450	0.094525	0.019923	0.000000	0.114448
460	0.078611	0.025865	0.000000	0.104477
470	0.063451	0.015067	0.000000	0.078519
480	0.049443	0.005822	0.000000	0.055265
490	0.037082	-.000366	0.000000	0.036716
500	0.027793	-.002638	0.000000	0.025154
510	0.020276	-.003044	0.000000	0.017232
520	0.014708	-.002525	0.000000	0.012183
530	0.010530	-.002456	0.000000	0.008074
540	0.007588	-.002255	0.000000	0.005333
550	0.005403	-.001717	0.000000	0.003686
560	0.003871	-.001777	0.000000	0.002094
570	0.002747	-.003324	0.000000	-.000578
580	0.001990	-.002408	0.000000	-.000419
590	0.001409	-.000733	0.000000	0.000676
600	0.001030	-.001240	0.000000	-.000210

K. References for Chapter 4

1. C. Reichardt, *Solvent Effects in Organic Chemistry*, (Verlag-Chemie, Weinheim, West Germany, 1979).
2. S. F. Fischer and A. Laubereau, *Chem. Phys. Lett.* **35** (1975) 6.
3. W. G. Hoover, *Ann. Rev. Phys. Chem.* **34** (1983) 103–27.
4. J. P. Boon and S. Yip, *Molecular Hydrodynamics* (McGraw-Hill, Inc., New York, 1980), Chapter 1.
5. J. H. Hildebrand, J. M. Prausnitz and R. L. Scott, *Regular and Related Solutions* (Van Nostrand Reinhold Co., New York, 1970), Chapter 1.
6. C. Reichardt, *Angew. Chem. Int. Ed.* **18** (1979) 98–110; K. Dimroth and C. Reichardt, *Liebigs. Ann. Chem.* **727** (1969) 93; T. R. Griffiths and D. C. Pugh, *J. Sol. Chem.* **8** (1979) 247–258.
7. S. P. Webb, S. W. Yeh, L. A. Philips, M. A. Tolbert and J. H. Clark, in *Ultrafast Phenomena IV*, D. H. Auston and K. B. Eisenthal, eds., (Springer-Verlag, New York, 1984) 371; S. P. Webb, S. W. Yeh, L. A. Philips, M. A. Tolbert and J. H. Clark, *J. Am. Chem. Soc.* **106** (1984) 7286; S. P. Webb, S. W. Yeh, L. A. Philips, L. M. Tolbert and J. H. Clark, *J. Phys. Chem.*, in preparation.
8. R. S. Mulliken, *J. Am. Chem. Soc.* **72** (1950) 600; *ibid.* **74** (1952) 811.
9. A. Weller, *Z. Elektrochem.* **56** (1952) 662; Th. Förster, *Z. Elektrochem.* **54** (1950) 531; Th. Förster, *Naturwissenschaften* **36** (1949) 186.
10. J. F. Ireland and P. A. H. Wyatt, *Adv. Phys. Org. Chem.* **12** (1976) 131; A. J. Campillo, J. H. Clark, S. L. Shapiro, K. R. Winn and P. K. Woodbridge, *Chem. Phys. Lett.* **67** (1979) 218.
11. Z. R. Grabowski, K. Rotkiewicz, A. Siemiarzuk, D. J. Cowley and W. Bauman, *Nouv. J. Chimie* **3** (1974) 443–454.
12. V. Sundstrom, T. Gillbro and H. Bergström, *Chem. Phys.* **73** (1982) 439–458.
13. S. Y. Lee and E. J. Heller, *J. Chem. Phys.* **71** (1979) 4777–4788.
14. C. V. Shank, E. P. Ippen and O. Teschke, *Chem. Phys. Lett.* **45** (1977) 291.
15. A. Rollinson and H. Drickamer, *J. Chem. Phys.* **73** (1980) 5981–5996.
16. *Ultrafast Phenomena IV*, D. H. Auston and K. B. Eisenthal, eds., (Springer-Verlag, New York, 1984).
17. C. V. Shank, E. P. Ippen, O. Teschke and K. B. Eisenthal, *J. Chem. Phys.* **67** (1977) 5547–5561.

18. Calculations related to the sensitivity of the streak camera system to short time scale decay components are given in L. A. Philips, W. T. Brown, S. P. Webb, S. W. Yeh and J. H. Clark, in *Ultrafast Phenomena IV*, D. H. Auston and K. B. Eisenthal, eds. (Springer-Verlag, New York, 1984) 477; see also L. A. Philips, Ph.D. Thesis, University of California, Berkeley, 1985; Lawrence Berkeley Laboratory, Report LBL-19511.
19. W. S. Struve, P. M. Rentzepis and J. Jortner, *J. Chem. Phys.* **59** (1973) 5014.
20. S. W. Yeh, Ph.D. thesis, University of California, Berkeley, 1985; Lawrence Berkeley Laboratory Report 20662.
21. G. Rothenberger, D.K.Negus and R. M. Hochstrasser, *J. Chem. Phys.* **79** (1983) 5360-5367.
22. S. L. Shapiro, K. R. Winn and J. H. Clark, in *Picosecond Phenomena II* R. M. Hochstrasser, W. Kaiser and C. V. Shank, eds. (Springer-Verlag, Berlin, Germany, 1980) p. 227.
23. S. I. Druzhinin and B. M. Uzhiniov, *Chem. Phys.* **78** (1983) 29-39.
24. J. Hicks, M. Vandersall, Z. Babarogic and K. B. Eisenthal, *Chem. Phys. Lett.* **116** (1985) 18; Y. Wang, M. McAuliffe, F. Novak and K. B. Eisenthal, *J. Phys. Chem.* **85** (1981) 3736; D. Huppert, S. D. Rand, P. M. Rentzepis, P. F. Barbara, W. S. Struve and Z. R. Grabowski, *J. Phys. Chem.* **75** (1981) 5714.
25. J. S. McCaskill, R. G. Gilbert, *Chem. Phys.* **44** (1979) 389-402.
26. Y. Wang and K. B. Eisenthal, *J. Chem. Phys.* **77** (1982) 6076-6082.
27. 4-Aminophthalimide is the trivial name for the compound. Official nomenclature is: 5-amino-1H-isoindole-1,3(2H)-dione.
28. H. Fröhlich, *Theory of Dielectrics* (Oxford University Press, Oxford, England, 1958), 2nd ed.
29. G. van der Zwan and J. T. Hynes, *J. Phys. Chem.* **89** (1985) 4181-4188; B. Bagchi, D. W. Oxtoby, G. R. Fleming, *Chem. Phys.* **86** (1984) 257-267.
30. A. Declémy, C. Rullière and P. Kottis, *Chem. Phys. Lett.* **101** (1983) 401-406.
31. Th. Förster and K. Rokos, *Z. für Phys. Chemie N. F.* **63** (1969) 208-211. See reference 20..
32. S. K. Garg and C. P. Smyth, *J. Phys. Chem.* **69** (1965) 1294-1301.
33. G. C. Pimentel and A. L. McClellan, *The Hydrogen Bond* (W. H. Freeman and Company, San Francisco, 1960).
34. J. Midwinter and P. Suppan, *Spectrochim. Acta* **25A** (1968) 953-958.

35. W. Rettig and M. Zander, *Ber. Bunsenges. Phys. Chem.* **87** (1983) 1143–1149
36. C. L. Cheng, D. S. N. Murthy and G. L. D. Ritchie, *J. Chem. Soc., Farad. Trans. II* **1972** (1972) 1679–1690.
37. F. Schneider and E. Lippert, *Ber. Bunsenges. Phys. Chem.* **72** (1968) 1155–1160; *Ber. Bunsenges. Phys. Chem.* **74** (1970) 624–630.
38. N. Nakashima, M. Murakawa and N. Mataga, *Bull. Chem. Soc. Jpn.* **49** (1976) 854–858.
39. W. Liptay and G. Walz, *Z. Naturforsch.* **26a** (1971) 2007–2019; W. Liptay, G. Walz, W. Baumann, H. J. Schlosser, H. Deckers and N. Detzer, *Z. Naturforsch.* **26a** (1971) 2020–2038.
40. W. Rettig, *J. Mol. Struct.* **84** (1982) 303–327.
41. K. Hara, T. Arase and J. Osugi, *J. Am. Chem. Soc.* **106** (1984) 1968–1972
42. T. Kobayashi, S. Nagakura and M. Swarc, *Chem. Phys.* **39** (1979) 105–110; T. Kobayashi, in *Picosecond Phenomena I* C. V. Shank, E. P. Ippen and S. L. Shapiro, eds. (Springer-Verlag, Berlin, Germany, 1978) p. 339–345.
43. M. Migata, T. Okada, N. Mataga, Y. Sakata, S. Misumi, N. Nakashima and K. Yoshihara, *Bull. Chem. Soc. Jpn.* **54** (1981) 3304–3311.
44. E. M. Kosower, *J. Am. Chem. Soc.* **107** (1985) 1114–1118; E. M. Kosower and D. Huppert, *Chem. Phys. Lett.* **96** (1983) 433; D. Huppert, H. Kanety and E. M. Kosower, *Discuss. Faraday Soc.* **74** (1982) 161–203.
45. R. W. Anderson, in *Advances in Laser Chemistry* A. H. Zewail, eds. (Springer-Verlag, Berlin, Germany, 1978) p. 149–154.
46. E. Kosower and K. Tanizawa, *Chem. Phys. Lett.* **16** (1972) 419–425.
47. H. Shizuka, Y. Ishii and T. Morita, *Chem. Phys. Lett.* **51** (1977) 40–44.
48. A. Magnus, H. Hartmann and F. Becker, *Z. Phys. Chem.* **197** (1951) 75–91.
49. E. L. Marun, *Org. React.* **1** (1942) 155–209.
50. S. A. Wise, W. J. Bonnett, F. R. Guenther and W. E. May, *J. Chrom. Sci.* **19** (1981) 457–465.
51. D. R. James and W. R. Ware, *Chem. Phys. Lett.* **120** (1985) 455–459.
52. K. Smith, N. Langford, W. Sibbett and J. R. Taylor, *Optics Lett.* **10** (1985) 559–561.
53. M. Evans, *J. Mol. Liq.* **25** (1983) 149.

54. Viscosities for pure compounds as a function of temperature are from reference 55. These values compared reasonably well with measurements made at 20 C with a temperature-controlled Wells-Brookfield Cone/Plate Digital Viscometer. Viscosities of the alcohol-alkane mixtures were measured with an Ostwald viscometer.
55. *Landolt Bořnstein Zahlenwerte und Funktionen*, (Springer Verlag, Berlin, 1969); *CRC Handbook of Chemistry and Physics*, 62nd Edition, Robert C. Weast, ed. (CRC Press, Boca Raton, Florida, 1981).
56. M. W. Sagal, *J. Chem. Phys.* **36** (1962) 2437-2442.
57. M. Corval and L. Reinisch, *Compt. Rend.* **234** (1952) 724-726; R. Dalbert, M. Magat and A. Surdet, *Bull. Soc. Chim. France*. **1949D** (1949) 345-352.
58. H. Langhals, *Nouv. J. Chem.* **6** (1982) 265-267; *Angew. Chem. Int. Ed.* **21** (1982) 724-733.
59. J. Crossley and S. C. Srivastava, *Adv. Molec. Relax. Proc.* **8** (1976) 111-116; F. F. Hanna and I. K. Hakim, *Z. Naturforsch.* **26a** (1971) 1194-1198.
60. L. R. Pratt and D. Chandler, *J. Chem. Phys.* **67** (1977) 3683-3704.
61. R. L. Hurle and L. A. Woolfe, *Aust. J. Chem.* **33** (1980) 1947-1952.
62. I. B. Rabinovich, *The Influence of Isotopy on the Physicochemical Properties of Liquids* (Consultants Bureau, New York, 1970).
63. D. W. Davidson, *Can. J. Chem.* **35** (1957) 458-472; D. W. Davidson and J. Wheeler, *J. Chem. Phys.* **36** (1959) 1357-1358.
64. D. Chandler, *J. Chem. Phys.* **62** (1975) 1358-1363.
65. T. Tao, *Biopolymers* **8** (1969) 609-632.
66. L. A. Philips, Ph.D. thesis, University of California, Berkeley, 1985; Lawrence Berkeley Laboratory Report 19511.
67. C. Campbell, J. Crossley and L. Glasser, *Adv. in Mol. Relax. Proc.* **9** (1976) 63-77; T. Koshii, E. Arie, M. Nakamura, H. Takahashi and K. Higasi, *Bull. Chem. Soc. Jpn.* **47** (1974) 618-622; R. Minami, K. Itoh, H. Sato, H. Takahashi and K. Higasi, *Bull. Chem. Soc. Jpn.* **54** (1981) 1320-1323; See reference 59..
68. B. Bock, M. Kuhr and H. Musso, *Chem. Ber.* **109** (1976) 1184-1194.
69. M. G. Kuz'min and Yu. Yu. Kulis, *Dokl. Akad. Nauk. SSSR.* **200** (1971) 630-633.
70. I. C. Lewis and L. S. Singer, *J. Chem. Phys.* **43** (1965) 2712-2727.
71. J. Honjink, *J. Recl. Trav. Chim. Pays-Bas.* **74** (1955) 1525.

72. M. F. M. Post, J. K. Eweg, J. Langelaar, J. D. W. Van Voorst and G. Ter Maten, *Chem. Phys.* 14 (1976) 165-176.
73. K. Gustav, J. Sühnel and U. P. Wild, *Chem. Phys.* 31 (1978) 59-65.
74. E. D. Bergmann, M. Rabinovitz, M. J. Aroney, R. J. W. Le Febre, L. Radom and G. L. D. Ritchie, *J. Chem. Soc. B* 1968 (1968) 1551-1554.
75. H. Weiler-Feilchenfeld, E. D. Bergmann, A. Hirschfeld, *Tetrahedron Lett.* 1965 (1965) 4129-4131; 1966 (1966) 992.
76. H. J. Hofmann, *Z. Chem.* 15 (1975) 78-79.
77. H. B. Klevins and J. R. Platt, *J. Chem. Phys.* 17 (1949) 470-481.
78. R. Pariser, *J. Chem. Phys.* 24 (1956) 250-268.
79. D. M. Friedrich, R. Mathies and A. C. Albrecht, *J. Mol. Spec.* 51 (1974) 166-188; P. Tavan and K. Schulten, *J. Chem. Phys.* 70 (1979) 5414-5421.
80. M. F. M. Post, J. Langelaar and J. D. W. Van Voorst, *Chem. Phys. Lett.* 42 (1976) 133-136; M. F. M. Post, J. Langelaar and J. D. W. Van Voorst, *Chem. Phys. Lett.* 32 (1975) 59-62.
81. L. Onsager, *J. Am. Chem. Soc.* 33 (1936) 1486-1493; E. Lippert, *Z. Naturforsch.* 10a (1955) 541; N. Mataga, Y. Kaifu and M. Koizumi, *Bull. Chem. Soc. Jpn.* 28 (1955) 690.
82. E. M. Kosower, *J. Am. Chem. Soc.* 80 (1958) 3253-3260.
83. C. P. Smyth, *Dielectric Behavior and Structure* (McGraw-Hill Book Co. New York, 1955).
84. P. Debye, *Polar Molecules* (Dover, New York, 1928).
85. A. Mozumder, *J. Chem. Phys.* 50 (1969) 3153; R. Schiller, *J. Chem. Phys.* 43 (1965) 2760; *ibid.* 47 (1967) 2278; J. Hubbard and L. Onsager, *J. Chem. Phys.* 67 (1977) 4850; J. Hubbard, *J. Chem. Phys.* 68 (1978) 1649.
86. J. N. Demas, *Excited State Lifetime Measurements* (Academic Press, New York, 1983).
87. C. L. Lawson and R. J. Hanson, *Solving Least Squares Problems* (Prentice Hall, New York, 1974).

Chapter 5

Conclusion

It should be clear from the work presented in the last three chapters that picosecond spectroscopic techniques can be profitably used for the study of dynamic processes in solution. The studies carried out with bianthryl point out both the types of results which can be achieved, as well as the inherent difficulty involved in interpreting them in a meaningful or unambiguous way. Although it is clear that bianthryl undergoes a variety of interesting relaxation processes in alcohols and other hydrogen-bonding solvents, there remain some uncertainties in describing the origins of these processes. The fact that BA acts as an excited-state base and undergoes detectable proton transfer, along with the fact that detectable relaxation occurs only in protic solvents, tends to suggest that a combination of solvent mediated intramolecular charge transfer and excited-state hydrogen bond formation are occurring. Nonetheless, it is difficult to rule out the possibility that the observed relaxation is simply a manifestation of the simple solvent dielectric relaxation. The behavior of the molecule in alcohol-alkane mixtures tends to suggest that the role of ground-state solvation is important. The observed slowing of the measured relaxation time is consistent with the idea that the nonpolar alkane molecules tend to concentrate in close proximity to the nonpolar ground-state bianthryl molecule, so that when the molecule is excited it must first diffuse through this boundary layer before reacting (i.e. forming a hydrogen bond) with the alcohol fraction of the solvent. Unfortunately, this cannot be directly differentiated from dielectric relaxation, because of the similar concentration dependence of the solvent dielectric constant. It is possible that by comparing the behavior of bianthryl to analogous molecules such as 9,9'-biacridine (which should hydrogen bond in the ground state), a more definitive conclusion might be obtained. In addition, the study of bianthryl and related compounds in aprotic solvents with femtosecond time resolution might also provide information on the formation of the

charge transfer state itself. Nonetheless, with the information that is available, it is clear that bianthryl constitutes an interesting probe molecule which might be well suited to the study of polarity related dynamic processes in a wide range of chemical systems.

The choice of this chemical system was dictated more by experimental limitations than by its overwhelming chemical interest. It is one of the relatively few systems which can be studied using time resolved-emission. There are a tremendous number of chemical processes of great practical interest which are not accessible by this method, most notably those involving ground state free-radical chemistry or complex mixtures. Nonetheless the relative ease with which time-resolved emission measurements could be made dictated that an emitting system be used.

Time-resolved emission spectroscopy is, within limits, a simple, reliable method for studying excited-state dynamic processes. The system used here represents a reasonable and convenient method for making such measurements. Several experimental limitations exist. The fact that the laser pulses are almost an order of magnitude longer than the streak camera resolution means that the pulse shape must be deconvoluted from all the data. This complicates the analysis of the data. The lack of a convenient tunable source in the 250–400 nm range is also a problem, and limits the range of systems which can be studied. For example, investigating the behavior of bianthryl in nitromethane would require a pump wavelength near 390 nm to avoid the long wavelength tail of the solvent absorption. Similarly to study binaphthyl in chlorinated solvents would require a source near 300 nm. A final limitation stems from the rate of data acquisition; at ~ 3 Hz, collection of a single dataset takes several minutes, so acquiring time-resolved spectra (which require tens of datasets) can be very time consuming. In addition, the mechanical stability of the system is such that perfect optical alignment cannot be maintained over this period of time, so that several adjustments must be made in the course of acquiring the spectral data. These problems can be readily overcome by increasing the laser repetition rate and data collection rate, as described above. With essentially no changes in hardware,

the system can be made to operate at rates approaching 25 Hz. This repetition rate would largely eliminate the difficulties involved in collecting spectral data, although one could undoubtedly devise more elaborate experiments which would make this data collection rate seem too slow to be useful. Ultimately, by using the second harmonic of a cavity-dumped synchronously-pumped dye laser as a pump beam, and using a faster image intensifier, a faster A-D converter, and a bigger, faster computer system, one could approach the KHz repetition rates imposed by the streak camera itself. At this point, one could obtain spectra with signal averaging much better than that used here with a repetition rate limited only by the rate at which the sample and bandpass filters could be changed. Note that the short tunable pulses from this system would eliminate the other difficulties described above as well. In addition, the pulse peak powers would be lower; this would necessitate more signal averaging, but would minimize the possibility of nonlinear effects in the sample.

Further development of time-resolved emission would be more of a convenience than anything else, since it is not altogether clear that the method is general enough to be of value in studying a wide range of processes. There is a limit to what information one can obtain from excited state measurements, simply because so few systems undergo excited-state relaxation; there are other processes of interest besides proton transfer, electron transfer and solvation. Time-resolved absorption makes it possible to study a much broader range of problems, most notably those involving ground state molecules. Unfortunately, the sensitivity and selectivity of absorption are rather low, so that the results obtained this way are often ambiguous or difficult to interpret. The streak camera-based absorption system described here is not especially noteworthy in terms of the quality of the data. Although it appears to be better than reported using picosecond continua as probe sources, it lacks the sensitivity which can be obtained by using a tunable laser as a probe source. Nonetheless, the system is extremely easy to use, and complements the time-resolved emission system. Any improvements in one would likely be reflected in

the other. The absorption system is perhaps best regarded as a useful accessory to the fluorimeter, not as the ultimate in absorption technology.

Raman spectroscopy provides a potentially useful method for studying complex mixtures of ground-state molecules in solutions. Unfortunately, the low signal levels in conjunction with the high laser peak powers, make it extremely difficult to carry out these measurements on this timescale. The use of parametric generation to produce tunable light greatly improves the prospects for using resonance Raman for this purpose, although the high peak powers and low repetition rates are still a problem. Further development of this method will most likely come only with the use of a higher repetition rate laser with a higher average power. As noted above, either a quasi-CW Nd:YAG laser used in conjunction with a parametric generator or a cavity-dumped, synchronously pumped dye laser appear to be the best candidates. At this point it should be noted that infrared absorption may also become more feasible in the future. In particular, the combination of Nd:YAG pumped parametric sources utilizing crystals such as Proustite in conjunction with high efficiency HgCdTe detectors may ultimately make this a more practical method than Raman for measuring vibrational spectra.

Time-resolved emission is the only method used here which does not suffer from severe technical limitations. The results presented for bianthryl reflect this fact. Indeed, only with emission was it possible to reach the point that chemical system being studied received more attention than the hardware used to acquire the data. The efforts to stabilize the laser as well as the development of the OPS all represent efforts to overcome these technical difficulties so as to make other methods of spectroscopy possible. Although significant improvements were made, resulting in a stable laser and convenient tunable visible light, these were not enough to make Raman spectroscopy into a viable method, especially with regard to irreversible phenomena. They mostly served to simplify emission measurements. At present, a higher repetition rate laser (1–100 KHz) appears to be the most likely means for making this type of study possible. Unfortunately, it is at

present a relatively untried panacea, so that it is difficult to gauge the extent to which it will actually work.

LBL-19511

Picosecond Studies of Structure and Dynamics
of Electronically Excited Molecules in Solution

Laura Alma Philips
Ph.D. Thesis

Lawrence Berkeley Laboratory
University of California
Berkeley, California 94720

April 1985

Picosecond Studies of Structure and Dynamics
of Electronically Excited Molecules in Solution

Laura Alma Philips

Abstract

Picosecond spectroscopy was used to probe the liquid phase dynamics of two different chemical systems. In the first study, the rotational reorientation times of rhodamine 6G (R6G) and p-terphenyl (PTP) were measured as a function of solvent viscosity. The viscosity was varied either by changing the solvent or by changing the pressure in a single solvent. The differences between the two molecules PTP and R6G provided a means of evaluating the role of solute structure and solute-solvent interactions on the dynamics on rotational reorientation. For example, the rotational behavior of PTP was well described by simple hydrodynamic models as embodied in the Stokes-Einstein-Debye equation. In contrast, the rotational reorientation dynamics of the charged molecule R6G were not well described by these models. High pressure (> 6 kbar) techniques were developed for this study to provide a means of varying the viscosity of a single solvent. The new information from these experiments demonstrated that dielectric friction plays an important role in governing the rotational motion of charged solute molecules in polar solvents. Models incorporating the role of dielectric friction accurately predicted the observed experimental trends. The validity of this dielectric friction model was confirmed in studies of the effect of added salt on rotational reorientation dynamics. The dielectric friction model also adds new insight into the role of hydrogen bonded complexes in rotational behavior.

The second study employed both time resolved emission and time resolved resonance Raman spectroscopies to examine the ultrafast photophysics of ruthenium tris-2,2' bipyridine in aqueous solution. The structural specificity of Raman spectroscopy enabled the identification of the electronically excited species. It was determined that in the excited state, the electron undergoing the metal-to-ligand-charge-transfer (MLCT) is localized on a single bipyridine ligand within 25 ps of excitation. Additional information from the time resolved emission studies provided insight into the rate of relaxation through the manifold of excited electronic states. It was determined that the emitting state, which is of triplet parentage, is formed in less than 1 ps after excitation into a state of singlet parentage. This extremely fast intersystem crossing rate indicates that spin-orbit coupling dominates the relaxation process. This conclusion should be generally applicable to any MLCT excited states of any transition metal complex that contains a heavy central metal atom such as ruthenium.

John P. Caul

ACKNOWLEDGMENTS

Many people have contributed to this thesis in a variety of ways. My parents instilled in me the inquisitive mind necessary for a scientist. My father taught me the perserverence required to ask difficult questions and then to find the answers. From my mother's appreciation of nature I learned the sensitivity to understand the implications of the questions asked. Encouragement from my brothers was always available and their thoughtful questions help me to keep the goals of science in perspective.

Upon coming to Berkeley and joining the newly formed Clark group, I was faced with the additional challenges that come with building a new research group. The optimism and enthusiasm of my research director, John Clark, was invaluable in overcoming this and many other obstacles. Many members of the Clark group participated in my graduate career, on both personal and professional levels. Steve Webb played an instrumental role in most of the work contained in this thesis. In addition he is a good friend and a constant source of support. Ward Brown collaborated with me on the construction of the Raman apparatus and the work on $\text{Ru}(\text{bpy})_3^{++}$. Howard Nathel and Maggie Tolbert, who joined the group with me have been both good friends and colleagues. Howard Nathel also developed the OPS used in the wavelength dependent studies. Other members of the group who helped make graduate school fun were Marion Helfand, our newest graduate student, and Steve Finkel, an undergraduate in the group performed many thankless tasks for which I am grateful.

Much of the work in this thesis would not have been possible without the expert machining available from the machine shop at Berkeley.

In particular, I would like to thank Fred Wolfe for patiently evaluating many designs to optimize the performance of many pieces of apparatus.

Helpful scientific discussions took place which provided insights at crucial stages of this work. For this help I would like to thank Prof. D. Kivelson, Prof. G. T. Evans, Prof. R. H. Harris, and Prof. R. Boehler.

Finally, I want to thank Mark Maroncelli, who is a source of inspiration as well as insight. His passionate dedication to science is a model I try to emulate and his love and support help give me the power to do so.

This work was supported by the Director, Office of Energy Research, Office of Basic Energy Sciences, Chemical Sciences Division of the U.S. Department of Energy under Contract No. DE-AC03-76SF00098 and the Office of Naval Research under Contract No. N00014-82-K-0349.

TABLE OF CONTENTS

Chapter	Page
I. Introduction.....	1
II. Experimental.....	7
A. Laser.....	7
B. Time Resolved Emission.....	15
C. High Pressure Cell.....	25
D. Time Resolved Resonance Raman.....	40
E. Solutions.....	41
1. Rhodamine 6G and p-Terphenyl.....	41
2. $\text{Ru}(\text{bpy})_3^{++}$	45
III. Rotational Reorientation.....	46
A. Introduction.....	46
B. Theory.....	48
1. Models.....	48
i) Hydrodynamic Models.....	49
ii) Molecular Models.....	61
iii) Dielectric Friction Model.....	65
2. Methods for Determining Rotational Reorientation Times.....	66
3. Literature Review.....	74
C. Results.....	94
1. Molecular Structure.....	94
2. Fluorescence Lifetimes.....	98
3. Rotational Reorientation Times.....	106
D. Discussion.....	122
1. p-Terphenyl.....	122

TABLE OF CONTENTS (continued)

Chapter	Page
2. Rhodamine 6G.....	155
3. Dielectric Friction.....	162
4. Salt Effect.....	170
5. Previous Results and the Dielectric Friction Model.....	176
6. Conclusions.....	180
IV. Ultrafast Charge Transfer Photophysics in $\text{Ru}(\text{bpy})_3^{++}$	182
A. Introduction.....	182
B. Results.....	185
1. TR^3 Spectral Data.....	185
2. Time Resolved Emission Data.....	188
C. Discussion.....	190
V. Conclusion.....	204
Appendix	
A. Excitation Wavelength Study of Rotational Reorientation..	208
1. Introduction.....	208
2. Experimental.....	209
3. Results and Discussion.....	210
B. Tables.....	211
References.....	212

LIST OF TABLES

Table		Page
1	Rotational Reorientation Times of Rhodamine 6G (R6G), Rhodamine B (RhB), and Rose Bengal (RB) from Previous Work.....	81
2	Rotational Reorientation Times Normalized to Solvent Viscosity - Oblate and Asymmetric Cation Xanthene Dyes.	82
3	Rotational Reorientation Times Normalized to Solvent Viscosity - Prolate Xanthene Dyes.....	83
4	Rotational Reorientation Times Normalized to Solvent Viscosity - Oblate Dianion Xanthene Dyes.....	84
5	Rotational Reorientation Times Normalized to Solvent Viscosity - Non-Xanthene Dyes.....	85
6	Fluorescence Lifetimes of R6G as a Function of Solvent and Pressure.....	104
7	Fluorescence Lifetimes of PTP as a Function of Solvent and Pressure.....	105
8	Rotational Reorientation Times of R6G as a Function of Solvent.....	114
9	Rotational Reorientation Times of R6G in Ethanol as a Function of Pressure.....	114
10	Rotational Reorientation Times of PTP as a Function of Solvent.....	115
11	Rotational Reorientation Times of PTP in Hexane as a Function of Pressure.....	116
12	Rotational Reorientation Times of PTP in Octane as a Function of Pressure.....	117
13	Rotational Reorientation Times of PTP in Ethanol as a Function of Pressure.....	118
14	Rotational Reorientation Times of PTP in Chloroform as a Function of Pressure.....	119
15	Linear Regression Fits of the Results of PTP Data.....	129
16	Rotational Reorientation Times of PTP Normalized to Solvent Viscosity.....	130

LIST OF TABLES (continued)

Table		Page
17	Rotational Reorientation Times of PTP Normalized to Solvent Viscosity for Solvents Under Pressure: Hexane and Octane.....	131
18	Rotational Reorientation Times of PTP Normalized to Solvent Viscosity for Solvents Under Pressure: Ethanol and Chloroform.....	132
19	Rotational Reorientation Times of R6G Normalized to Solvent Viscosity.....	159
20	Rotational Reorientation Times of R6G Normalized to Solvent Viscosity for Ethanol Under Pressure.....	160
21	Components of Rotational Reorientation Times of R6G due to Dielectric Friction for Alcohol Solvents.....	166
22	Components of Rotational Reorientation Times of R6G due to Dielectric Friction for Ethanol Under Pressure.....	166
23	Rotational Reorientation Times of R6G in Ethanol as a Function of LiCl Concentration.....	171
24	Rotational Reorientation Times of PTP in Ethanol as a Function of LiCl Concentration.....	171
25	Component of Rotational Reorientation Times of R6G due to Dielectric Friction for Ethanol with Added LiCl.....	173
26	Component of Rotational Reorientation Times of R6G due to Dielectric Friction for Ethanol Temperature Variation.....	179
27	Rotational Reorientation Times of R6G in Ethanol as a Function of Excitation Wavelength.....	213
B1	Thermodynamic Constants of Selected Solvents at Ambient Pressure.....	221
B2	Thermodynamic Constants of Selected Solvents as a Function of Pressure.....	222
B3	Calculations of PTP Rotational Reorientation Times as a Function of Solvent for a Solute Volume of 341 \AA^3	224
B4	Calculations of PTP Rotational Reorientation Times as a Function of Solvent for a Solute Volume of 224 \AA^3	225

LIST OF TABLES (continued)

Table	Page
B5 Calculations of PTP Rotational Reorientation Times as a Function of Pressure for a Solute Volume of 341 Å ³	226
B6 Calculations of PTP Rotational Reorientation Times as a Function of Pressure for a Solute Volume of 341 Å ³	227
B7 Calculations of PTP Rotational Reorientation Times as a Function of Pressure for a Solute Volume of 224 Å ³	228
B8 Calculations of PTP Rotational Reorientation Times as a Function of Pressure for a Solute Volume of 224 Å ³	229
B9 Calculations of R6G Rotational Reorientation Times as a Function of Solvent for a Solute Volume of 461 Å ³	230
B10 Calculations of R6G Rotational Reorientation Times as a Function of Pressure.....	230

LIST OF FIGURES

Figure		Page
1	Laser Cavity.....	8
2	Time Resolved Emission Apparatus.....	17
3	Plot of Viscosity versus Pressure for Ethanol.....	26
4	Fluorescence Decay of Ethyl Violet as a Function of Pressure.....	28
5	High Pressure Hydrostatic Press.....	30
6	High Pressure Cell.....	32
7	High Pressure Cell: Cross Section View.....	33
8	Time Resolved Raman Apparatus.....	39
9	Absorption and Emission Spectra of Rhodamine 6G.....	42
10	Absorption and Emission Spectra of p-Terphenyl.....	43
11	Diagram of Time Resolved Rotational Reorientation Experiments.....	68
12	Molecular Structures of Oblate Cation Xanthene Dyes.....	75
13	Molecular Structures of Prolate and Asymmetric Xanthene Dyes.....	76
14	Molecular Structures of Dianion Xanthene Dyes.....	78
15	Molecular Structures of Non-Xanthene Dyes.....	79
16	Molecular Structure of Rhodamine 6G.....	95
17	Molecular Structure of p-Terphenyl.....	96
18	Fluorescence Decay of Rhodamine 6G in Ethanol.....	99
19	Fluorescence Decay of p-Terphenyl in Octanol.....	100
20	Semi-Log Plot of the Fluorescence Decay of p-Terphenyl in Acetonitrile.....	103
21	Vertical and Horizontal Components of the Fluorescence Decay of Rhodamine 6G in Ethanol.....	107
22	Vertical and Horizontal Components of the Fluorescence Decay of p-Terphenyl in Various Solvents.....	109

LIST OF FIGURES (continued)

Figure	Page
23 Vertical and Horizontal Components of the Fluorescence Decay of p-Terphenyl in Ethanol at Various Pressures...	110
24 Rotational Anisotropy for Rhodamine 6G in Ethanol at 5.4 kbar.....	111
25 Semi-Log Plots of the Rotational Anisotropy of Rhodamine 6G in Ethanol at Various Pressures.....	112
26 Plots of τ as a Function of η for p-Terphenyl in Various Solvents.....	123
27 Plots of τ as a Function of η for p-Terphenyl at Various Pressures.....	125
28 Gierer-Wirtz Model Plots of τ as a Function of η for p-Terphenyl in Various Solvents.....	136
29 Gierer-Wirtz Model Plots of τ as a Function of η for p-Terphenyl at Various Pressures.....	138
30 Kivelson-Dote Model Plots of τ as a Function of η for p-Terphenyl in Various Solvents.....	140
31 Kivelson-Dote Model Plots of τ as a Function of η for p-Terphenyl at Various Pressures.....	142
32 Plots of τ as a Function of $V_S/\Delta V$ for p-Terphenyl in Various Solvents.....	146
33 Plots of τ as a Function of $V_S/\Delta V$ for p-Terphenyl at Various Pressures.....	148
34 Plots of τ as a Function of $\eta \times V_S/\Delta V$ for p-Terphenyl in Various Solvents.....	151
35 Plots of τ as a Function of $\eta \times V_S/\Delta V$ for p-Terphenyl at Various Pressures.....	153
36 Plots of τ as a Function of η for Rhodamine 6G.....	156
37 Plots of $\Delta\tau$ as a Function of η for Rhodamine 6G.....	167
38 Expanded Plots of $\Delta\tau$ as a Function of η for Rhodamine 6G.	174
39 Absorption and Emission Spectra of $\text{Ru}(\text{bpy})_3^{++}$	186
40 Picosecond Time Resolved Resonance Raman Spectrum of $\text{Ru}(\text{bpy})_3^{++}$	187

LIST OF FIGURES (continued)

Figure		Page
41	Time Resolved Emission Spectra of $\text{Ru}(\text{bpy})_3^{++}$	189
42	Comparison of Picosecond and Nanosecond Raman Spectra of $\text{Ru}(\text{bpy})_3^{++}$	192
43	Kinetic Model of Emission.....	199
44	Kinetic Model Fits to the Experimental Data.....	201
45	Kinetic Model Fits to the Experimental Data.....	202
46	Vertical and Horizontal Components of the Fluorescence Decay of Rhodamine 6G in Ethanol, 476 nm Excitation....	211
47	Plot of τ as a Function of Excitation Wavelength.....	214
48	Plot of $r(0)$ as a Function of Excitation Wavelength.....	217

Chapter I

INTRODUCTION

A large majority of chemical reactions occur in liquids, yet surprisingly little is known about molecular dynamics in this complex phase of matter. In the gas phase, intermolecular interactions consist predominantly of isolated collisions between two, or at most three molecules. An individual molecule spends most of its time in isolation from other molecules. Collisions can be treated as an instantaneous perturbation of the molecular trajectories. In solids, a single molecule exists in a particular site on a rigid lattice. Although a given molecule is constantly interacting with all of its nearest neighbors, these interactions can be well characterized since the local environment of the lattice is both relatively static, and typically highly ordered. In contrast, a given molecule in a liquid is constantly interacting with a multitude of other molecules in an environment which is perpetually changing. A molecule in one atmosphere of gas typically undergoes ~ 10 collisions per nanosecond (ns). If one modeled a room-temperature, atmospheric pressure liquid as a dense gas, the effective collision rate would be $\sim 10^3$ times higher, on the order of 10 collisions per picosecond (ps). It is important to realize, however, that in a liquid, a single molecule is virtually always in contact with at least one other molecule in the solution.

To understand dynamics in solution, it is necessary to probe events which occur on a timescale corresponding to the timescale of molecular collisions. Standard techniques of nanosecond spectroscopy are sufficient to perform time resolved studies of the simple binary

collisions which occur in the gas phase. Similarly, picosecond spectroscopy provides a powerful probe of liquid phase phenomena. In liquids, events such as chemical reactions occur on a picosecond timescale, but rates are limited by the time it takes for individual molecules to diffuse through the liquid medium towards one another. The timescale of diffusion is many orders of magnitude slower than that of collisional processes. Thus, it is necessary to design experiments to specifically probe microscopic collisional events, rather than the macroscopic diffusion process.

Collisional phenomena can be probed by instantaneously perturbing the molecular environment. At any given moment prior to such a perturbation, it is assumed that the system of interest is at equilibrium. Equilibrium consists of an ensemble of molecules in a variety of molecular environments at various stages of interaction. If such an ensemble of molecules is instantaneously perturbed from equilibrium, intramolecular relaxation and intermolecular collisional events act to move the system back towards equilibrium. The response of the system can then be monitored as it relaxes to equilibrium.

In the studies described here, the perturbation is electronic excitation of the solute molecules. Prior to excitation, both the solute and the surrounding solvent molecules are in the appropriate ground state equilibrium environment. Upon electronic excitation, some of the solute molecules are instantaneously transferred to an excited state. In the excited state, the molecules are no longer at equilibrium, and therefore undergo relaxation. The dynamics of the relaxation processes are the focus of the present study.

Two systems were studied in these experiments. The events that

were probed occurred on substantially different timescales, and were produced by fundamentally different physical phenomena. One study explored the rotational reorientation dynamics of rhodamine 6G (R6G) and p-terphenyl(PTP) as a function of solvent and pressure. The other study examined the roles of spin-multiplicity and charge localization on the ultrafast photophysics of electronically excited ruthenium tris(2,2'-bipyridine) (II) dichloride ($\text{Ru}(\text{bpy})_3^{++}$).

Rotational reorientation was studied by selective electronic excitation of an ensemble of molecules which were preferentially oriented in a specific direction. The relaxation of the resulting anisotropic distribution of excited state species was monitored using time resolved fluorescence techniques. Rotational reorientation times for the intermediate size molecules studied here are on the order of tens to hundreds of picoseconds. Thus, rotational motion studied here occurred on a timescale intermediate between collisional and diffusional timescales. One question we address is whether bulk diffusion or molecular collisions control the rotational reorientation process.

Rotational reorientation depends on the viscosity of the solvent. The nature of this viscosity dependence has been widely studied, but is not yet completely understood. A number of methods can be used to vary the solvent viscosity and to observe its effect on molecular rotation. This study demonstrates the effectiveness of the use of pressure as a novel method of varying the solvent viscosity. High pressure experiments yield new information that provides new insight into the dynamics of rotational reorientation. The results of this study are used to evaluate existing models of molecular rotation, with

particular emphasis on the predictive power of macroscopic approaches for modelling microscopic phenomena.

The second study involves the investigation of the photophysics of the transition metal complex $\text{Ru}(\text{bpy})_3^{++}$. Transition metal complexes display a rich variety of chemical phenomena in solution. Especially important is the photoinduced reactivity of many complexes. The photophysics of the excited states of these molecules, however, is not well understood, in part because it occurs on a very fast timescale. In the case of $\text{Ru}(\text{bpy})_3^{++}$ the primary events occur on a timescale on the order of collisional events in liquids. This study addresses the following questions: What are the dynamics of the relaxation behavior in the manifold of electronically excited states? What is the nature of the states which are populated via the relaxation process? The rate of the relaxation processes provides information concerning excited state properties such as spin multiplicity. Both time resolved emission and time resolved resonance Raman experiments are employed to evaluate the structure and dynamics of electronically excited $\text{Ru}(\text{bpy})_3^{++}$.

The structure of this thesis is as follows. In Chapter II the various techniques and apparatus used in these experiments are described. A detailed account of the picosecond laser system used in all of the experiments is given in Section II.A. In Section II.B., the time resolved emission apparatus is described, followed in Section II.C. by the details of the design, construction, and application of the high pressure cell. Section II.D. describes the time resolved resonance Raman apparatus. The final section of Chapter II gives the methods of sample preparation.

The rotational reorientation experiments are described in Chapter

III. Following the introduction, some of the existing models that describe rotational motion in solution are discussed. The methods used to extract the rotational reorientation times from the experimental data are described in Section III.B.2. Section III.B.3. reviews much of the existing experimental literature and outlines the current interpretations of the existing data. This section is not an exhaustive review, but rather focuses primarily on picosecond, time resolved experiments carried out on molecules similar to those used in our study. The results from the present study are given in Section III.C. A discussion of these results is contained in Section III.D. The discussion is organized in the following manner. The results of the experiments on PTP and R6G are discussed in separate sections within the framework of the existing models. The effects of dielectric friction are introduced in Section III.D.3. to help explain the present experimental results. Further experiments on the effects of added salt are discussed Section III.D.5. The results of this study are compared to those of previous studies in Section III.D.4. The results of previous studies are then analyzed in the context of the models suggested by the present study. Conclusions are presented in the final section of Chapter III.

Chapter IV covers the experiments on $\text{Ru}(\text{bpy})_3^{++}$. The introduction provides the general background information about $\text{Ru}(\text{bpy})_3^{++}$. The results of both the emission and Raman experiments are presented in Section IV.B. A discussion of the results of these experiments is given in Section IV.C., including an evaluation of existing models.

The conclusions of the thesis are presented in summary in Chapter V. This thesis also contains two appendices to the text. Appendix A

presents a study of the effect of excitation wavelength on the rotational reorientation dynamics of R6G in ethanol. Appendix B consists of tables of constants used in model calculations for the rotational reorientation experiments as well as the results of those calculations.

Chapter II

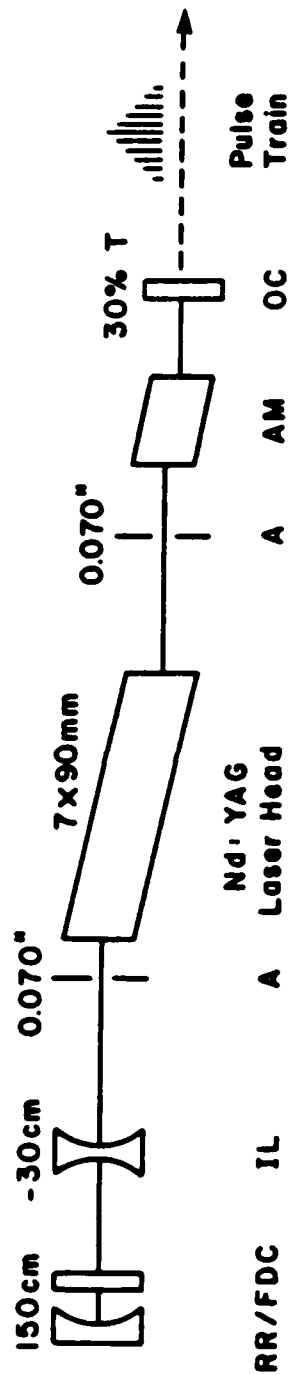
EXPERIMENTAL

A. Laser

The excitation source for all of the experiments described here, was a modified, passively modelocked, Nd:YAG, picosecond laser (Quantel, Model YG400). The basic cavity design is shown in Fig. 1. The cavity consists of an end mirror which also acts as part of the dye cell, a diverging lens, an aperture, the laser head containing a 7mm diameter X 90 mm long Nd:YAG rod, a second aperture, and an output coupler. Later experiments incorporated the use of an active, acousto-optic modelocker positioned between the second aperture and the output coupler.

The original Quantel design was modified in four major ways. First, the stirring dye cell for passive modelocking was replaced by a flowing dye cell. The use of a flowing dye cell improved the pulse-to-pulse amplitude stability of the laser output and decreased the occurrence of burning of the dye cell window. The dye cell and mount were designed for easy repositioning following the occasional instances in which a burn did occur. Although it was possible to vary the pathlength of the dye cell, it was usually maintained at 100 microns, considerably shorter than the approximately 2 mm pathlength of the Quantel design. The shorter pathlength requires an increased concentration of modelocking dye (Eastman 9740). A systematic study of the performance of the laser over a range of dye cell pathlengths was not performed, primarily because the configuration described above resulted very stable, reproducible performance and required minimal remodelocking.

Laser Cavity



Real Dimensions (cm. not to scale)

- IL: Intracavity Lens AM: Active Mode-Locker
- A: Aperture OC: Output Coupler
- RR/FDC: Rear Reflector/Flowing Dye Cell

Figure 1 - Diagrammatic representation of the laser cavity. The diagram is not drawn to scale but the actual dimensions are given below the diagram.

For example, when the laser was under constant use, the dye needed to be replaced approximately once a week.

The second modification was to replace the Quantel cooling group with a recirculating bath (Neslab). It was observed that the laser output energy fluctuated in a regular pattern corresponding to the opening of a solenoid valve in the Quantel cooling group. When the cooling group was replaced, the stability of the laser cavity output improved. The temperature of the cooling water was maintained at approximately 27°C. The fluctuation in temperature was less than $\pm 0.1^\circ\text{C}$.

The third improvement was to replace all of the optics in the cavity with higher quality optics. The optics were purchased from Optics for Research and were coated by CVI. The end mirror was coated to be >99% reflective at 1064 nm. The dye cell window was antireflection (AR) coated on the outer face of the window, as were the surfaces of all other non-reflecting optics in the cavity, including the lens, and the output coupler. The end mirror had a radius of curvature of 75 cm and a corresponding focal length of 150 cm. The diverging lens had a focal length of -30 cm, to help compensate for the thermal lensing which occurs in the laser rod. The output coupler had a 1° wedge and a flat reflective surface. Both the laser rod and the acoustoptic crystal were cut at Brewster's angle to minimize reflective losses in the cavity.

The apertures were made of machinable ceramic and varied in diameter. The approximate aperture sizes used were 0.06, 0.07, and 0.08 inches in diameter. Different combinations of sizes were used at various times. Typically, the two apertures were either the same size

the first aperture was one size smaller (0.01 inch) than the second aperture. In either case, larger apertures resulted in an increase in the output power of the laser and made alignment easier. If the apertures became too large, however, the beam quality began to deteriorate. Thus, the size of the apertures was selected to ensure single mode, TEM_{00} operation.

The final improvement in the cavity design was perhaps the most important. All of the optical mounts in the cavity were replaced with mounts that were both more stable and were easier to align. All of the cavity elements were mounted on optical rail plates which in turn were mounted on a floating Invar rail system. The rail plates contacted the rails at three points which insured kinematic replacability when an element was temporarily removed during the course of alignment.

The optical rail system allowed for the independent translational adjustment of any optical element in the cavity. This flexibility was particularly useful in optimizing the position of the lens and the apertures. The output coupler and the dye cell had micrometer controlled angular adjustments. Precise lateral adjustments of these elements proved unnecessary. Micrometer control of adjustments of the lens and apertures, however, were invaluable in optimizing the alignment of the cavity and in maintaining a TEM_{00} output. The lens in particular was extremely sensitive to small adjustments in the alignment. The most important features of the optical mounts were their stability and the lack of hysteresis in adjustments. These features were obtained by using quality micrometers and by maximizing the rigidity of the optical mounts.

Careful alignment of the cavity was always reflected in improved

performance of the laser. Initial alignment was performed on the unmodelocked cavity. Before modelocking, cavity alignment was evaluated by monitoring the output power using a power meter (Scientech, Model 362) or a photodiode and oscilloscope. A HeNe alignment laser (Uniphase, Model 1803P) was used to position the apertures and the lens such that the HeNe beam was centered on the laser rod. The back reflections of the HeNe beam from the end mirror and from the output coupler aided in the angular adjustment of these elements.

Once the initial alignment was complete, dye was added to the solvent in the dye cell. The dye used was Eastman #9740 and the solvent was 1,2 dichloroethane (Kodak, Q-switch grade). Both the dye and the solvent were used as received. The solvent was redistilled for repeated use as needed. During the modelocking process there was an initial drop in the output power as dye was added to the solvent. The power increased at the onset of modelocking. Dye was added until the pulse trains contained approximately 10-12 pulses per train. The final alignment consisted of minor adjustments of the cavity to optimize the quality and stability of the output beam. The second aperture and the output coupler played a critical role at this stage of alignment. The beam quality was monitored with IR sensitive paper. When the cavity was optimally aligned, between 90-100% of the pulse trains were acceptable. The nominal repetition rate was 10 Hz. The beam also appeared perfectly round, reflecting the Gaussian power distribution of the TEM₀₀ mode.

For later experiments, an acoustoptic active modelocker was added to the cavity. The above alignment procedure was modified in the following manner. During the initial alignment, it was crucial

that the cavity be aligned such that the beam was parallel to the longitudinal axis of the cavity (i.e. parallel to the optical rail system). The length of the cavity must be adjusted in the course of alignment to match the acoustic frequency of the active modelocker, and this was accomplished by longitudinal translation of the output coupler. Since the active modelocking process is very sensitive to cavity length, it was necessary to incorporate micrometer adjustment of translational motion of the output coupler. The loss of stability accompanying this modification was deemed necessary in order to achieve suitable performance from the active modelocker. Alignment of the active modelocker entailed the iterative adjustment of the cavity length and the angle of the active modelocker. The angle of the modelocker was first adjusted to orient the crystal at Bragg's angle. This adjustment was made by observing the diffraction pattern after the output coupler. The angle was set to yield the greatest diffracted intensity while the cavity length was adjusted out of resonance to provide adequate diffracted intensity. The length was then adjusted such that diffraction was minimized and the bulk of the power was in the central spot. Proper alignment was reflected in pulse trains that have approximately Gaussian shaped pulse envelopes and did not exhibit multiple trains. Once alignment of the active modelocker was complete, dye was added to passively modelock the cavity as described above.

Passive versus active/passive modelocked laser systems have disadvantages as well as advantages. When the cavity is only passively modelocked, the cavity must be extremely carefully aligned in order to obtain useful output trains 90-100% of the time. In contrast, the active/ passive system always produces useful pulse

trains, and precise alignment was less critical. The disadvantages of the active/passive system are twofold. First, there is an additional element in the cavity to be aligned. Further, parallel alignment of the cavity becomes important. This disadvantage is compensated by the fact that performance is slightly less sensitive to alignment. The second disadvantage is that in standard operation, the active/passive system produces longer pulses. This problem can be overcome by using pulses later in the train, since later pulses are shorter¹. These later pulses, however, are also less intense. Using later pulses in the passive system is more difficult since the pulse-to-pulse amplitude stability is reduced. Further information on the design and operation of this laser may be found in references 1 and 2.

The output of the laser cavity consisted of a train of 10-12 pulses. A single pulse is extracted from the pulse train by an electro-optic pulse selector (Quantel, Model PF302). Immediately before the pulse selector is a telescope which expands the beam by 1.5 times. The beam expansion is a precautionary measure to decrease the power density before introducing the beam to the sensitive optical elements in the pulse selector. The major component of the pulse selector is a Pockels cell. Birefringent crystals (KD*P) in the Pockels cell act to rotate the polarization of a laser pulse when subjected to a voltage gradient. For 1064 nm light, a voltage drop of 3.6 kV rotates the polarization of the light by 90°. A short voltage pulse across the crystal (<10 ns) rotates the polarization of only a single pulse in the train. This pulse is then separated from the train by a Glan prism polarizer.

Performance of the pulse selector was somewhat unstable, and was a constant source of difficulty. Typical problems included mismatched or worn out avalanche transistors, open-circuit resistors adjacent to the krytron tube, unstable power supplies, worn out krytron tubes, and unstable triggering. The krytron needed to be replaced regularly, as evidenced by erratic performance. When the krytron was replaced the voltage levels which trigger the avalanche train and, hence, the high voltage to the krytron, had to be readjusted. There was a burn-in time for the krytron during which these voltages had to be constantly monitored. As the krytron begins to wear out, increasing the high voltage often increased the life of the krytron. Erratic triggering of the pulse selector was partially eliminated by adjusting the intensity of light at the trigger photodiode by the use of neutral density filters. When it was necessary to pick pulses late in the train, an electronic delay was added to the trigger line in the form of extra lengths of BNC cable. Another cause of trigger jitter was shot-to-shot fluctuations in the laser output power, a factor that was especially important when picking late in the train. There was also an additional component of trigger jitter that was intrinsic to the pulse selector itself. On some occasions, the pulse selector would select all of one pulse plus a fraction of a second pulse. Although this behavior was annoying, it did not normally interfere with any of the experiments described here. The pulses are spaced at approximately 10 ns intervals (the round trip time of the cavity), which is much longer than the timescales of interest here.

After the pulse selector, the pulse was expanded a second time by a 1.5 x telescope before amplification. An aperture placed at the

focus of this telescope served as a spatial filter. The amplifier was a Nd:YAG laser head (Quantel, Model SF400) that contained a rod 7 mm in diameter by 115 mm long. The rod was cut with a 2° wedge to eliminate back reflections along the optical path and was AR coated at 1064 nm. The voltage to the amplifier was varied from 1.2-2.0 kV depending on the amplification required for each particular experiment.

The 1064 nm beam was doubled to 532 nm just after the amplifier using a type II KDP crystal. When the third harmonic at 355 nm was required, summing of the 1064 nm light with the 532 nm beam also occurred at this point using a second type II KDP crystal. At one time a reducing telescope was placed between the amplifier and the KDP crystals in an attempt to optimize conversion efficiency. This telescope proved to be unnecessary when it was found that the beam could be appropriately adjusted using the telescope before the amplifier. Typical energy conversion efficiencies from 1064 nm were 30-40% for 532 nm generation and 30% for 355 nm generation. The harmonics were separated by a Pellin-Broca prism. The appropriate beam was selected for each particular experiment.

B. Time Resolved Emission Apparatus

A complete diagram of the picosecond, time resolved emission apparatus is shown in Fig. 2. After separation at the Pellin-Broca prism, the desired harmonic was injected into the delay line. The 1064 nm beam and a fraction of the 532 nm beam were used as triggers for the streak camera and the detector, respectively. A clean, sharp leading edge was required for optimal triggering of the streak camera.

Figure 2 - Diagrammatic representation of the time resolved emission apparatus. SHG - Second harmonic generator (KDP crystal); DM - Dichroic mirror; FHG - Forth harmonic generator(KDP crystal); BS - beam splitter; F - Filter; GT - Glan Thompson prism; L - Lens.

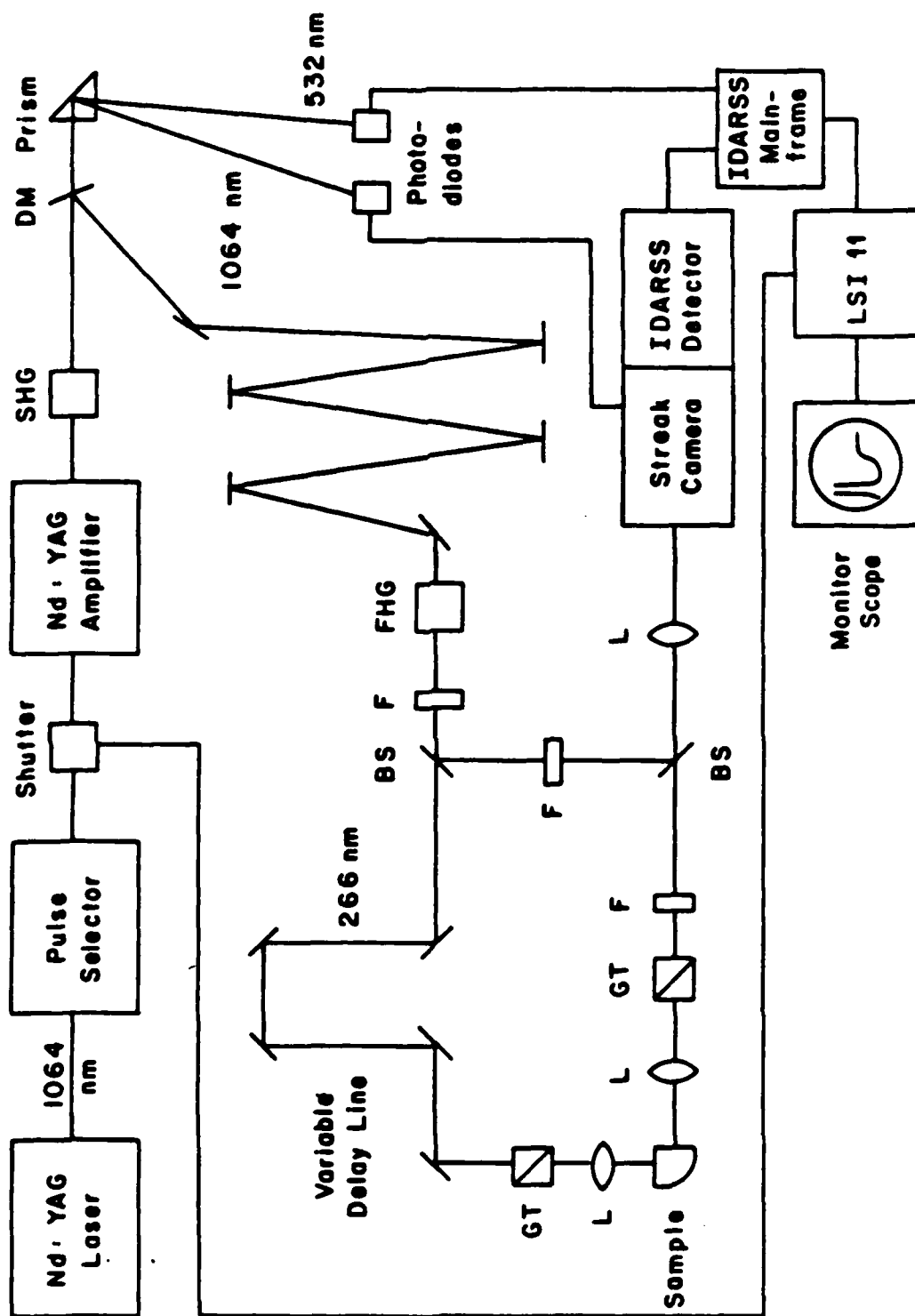


Figure 2

Therefore, the 1064 nm beam was sent through a saturable absorber (Eastman #9740 in 1,2 dichloroethane) prior to the trigger photodiode (Hewlett Packard, Model 5082-4220). The 532 nm trigger beam was sent directly into a similar photodiode. Both photodiodes were biased with a 90 V battery, adjustable by a 100 k Ω potentiometer.

The main beam traversed the table several times to delay the beam by 70-80 ns. This delay was necessary to provide sufficient time for triggering of the the streak camera and detector prior to the arrival of the emission signal. The beam quality was monitored at the end of the delay line. If necessary, minor improvements in the beam quality were made by small adjustments in either the telescope directly before the amplifier, the spatial filter, or the KDP crystals.

The final modification of the beam occurred in the last leg of the delay line, just before the sample cell. The beam was sent through a 1/4 inch diameter aperture to eliminate the diffraction fringes which developed over the course of the delay line. Next, a reducing telescope (0.5 x) was used to recollimate the beam, compensating for the slight divergence of the beam at this point. This telescope also provided flexibility to control the focus of the beam if necessary. For example, when the fourth harmonic at 266 nm was required, the telescope was adjusted so as to slightly focus the 532 nm beam into the type I KDP crystal used for 266 nm generation. Similarly, the 355 nm beam was slightly focused into the optical parametric source (OPS) crystals when tunable light was required. Details of the OPS are given elsewhere³, but a brief description is given here. The OPS consisted of two type II KDP crystals of dimensions 1.3 cm X 0.9 cm X 4 cm. From the annihilation 355 nm photons, pairs of difference

frequency photons are created and amplified in the crystals. The tuning range was 450-650 nm in the visible, with a complementary range of 780-1680 nm in the near IR. The beam quality was significantly degraded by the OPS. To improve the beam quality after the OPS, a series of three cylindrical lenses and an aperture were used. The focal length of these lenses varied as necessary to achieve adequate beam quality at the sample. The energy conversion efficiency for the OPS was ~ 2 to 3 % of the 355 nm beam. The energy conversion efficiency was about 5% for the 266 nm generation with respect to the 532 nm beam.

Before the beam was sent into the sample, filters were used to remove any unwanted frequencies and to adjust the intensity of the excitation beam. Four per cent of the beam was split off with a quartz flat for use as a time marking pulse. The excitation beam passed through a Glan prism polarizer to insure that the excitation light was purely vertically polarized. The light was finally imaged into the sample by a 2 inch focal length cylindrical lens. For the high pressure experiments, the focusing lens was eliminated. The high pressure cell window aperture was 1/8 inch, which sufficiently limited the excitation spot size.

For room pressure studies, the sample was contained in a 1 cm square quartz cuvette. Sample solutions were continuously stirred by a magnetic stirring bar. The excitation beam was imaged into the sample at the front edge of the sample cell to minimize reabsorption artifacts. The image size was <1 mm in width, and 2-3 mm in height. The fluorescence from the sample was collected through a slit 1 mm wide by about 1 cm in height. The slit was placed at the edge of the

cell nearest the excitation window. The cell used for high pressure experiments is described in detail below.

The light from the sample was collected with f2 collection efficiency using a 50 mm focal length spherical lens. The collimated light passes through a Glan prism polarizer to select the desired polarization for observation. To eliminate rotational effects, the polarizer was placed at magic angle (54.7°) with respect to the excitation beam polarization. For the rotational reorientation experiments, data was taken with the polarizer set both parallel and perpendicular to the input beam polarization.

After the Glan polarizer, filters are used to select the desired wavelength for observation. The filters served two functions and were different for each set of experiments. The first function of the filters was to eliminate any scattered light from the excitation beam. For experiments with 266 nm excitation, high-pass filters (Shott, KV370 or KV380) were used. The second function of the filters was to select the appropriate wavelengths and intensity of the fluorescence from the sample. If a specific, narrow wavelength range was desired, a 10 nm bandpass interference filter (Corion) was used. For most of the rotational reorientation experiments, bandpass filters were not needed. Neutral density filters were used as needed to limit the intensity of the fluorescence.

Once the wavelength, polarization, and intensity of the fluorescence signal had been appropriately adjusted, the signal was ready to image into the streak camera. The time-marking fraction of the excitation beam was recombined with the fluorescence the signal and imaged into the streak camera. Before being recombined with the fluorescence

signal, the time-marking pulse was adjusted in intensity by neutral density filters. The two signals were combined by an adjustable quartz plate set at approximately 45° with respect to the fluorescence path. The time-marking pulse was sent in at 90° to the fluorescence path and was deflected off of the quartz plate to become collinear with the fluorescence signal. A lens focused both signals onto the entrance slit of the streak camera (Hadland Photonics Ltd., Imacon 500). The details of the streak camera, the diode array detector (Tracor Northern, IDARSS), and the signal processing are given elsewhere² but are described briefly here. After the slit, a one to one telescope imaged the light onto the photocathode of the streak camera. At the output of the streak camera, a compound lens imaged the signal from the streak camera phosphor to the diode array detector. The signal from the diode array was sent into a signal processing computer (DEC, LSI 11/2, 11/23, or 11/73 as the computer was upgraded over the course of these experiments).

The streak camera is capable of operation over a wide range of streak speeds. The nominal streak rates were 20 ps/mm, 50 ps/mm, 100 ps/mm, 200 ps/mm, 500 ps/mm, 1 ns/mm, and 2 ns/mm. These streak speed typically translated into 0.31 ps/ch, 0.84 ps/ch, 1.81 ps/ch, 3.21 ps/ch, 8.80 ps/ch, 17.4 ps/ch, and 34.4 ps/ch (ch being a single channel of the diode array). These assignments were made by a calibration procedure using etalons. The etalon calibration was also used to eliminate non-linearities in the time base of the streak camera. At least two different etalon spacings and at least twenty etalon traces were used to calibrate each streak speed. The etalon spacing was measured at each position across the streak camera screen, and the re-

sulting points were fit to a smooth function using either a polynomial least squares fit or a spline smoothing routine. The inverse of the resulting function acted as a time base correction for data collected. Once the time base correction was applied to the etalon traces, the streak speeds could be calibrated to determine the time spacing of the diode array channels.

Each streak speed required a different delay time between triggering and accepting data. To vary the trigger delay in a simple manner, additional lengths of cable were introduced between the trigger photodiode and the streak camera. Shorter delays were needed for the faster streak speeds (i.e. less ps/ch). The cables were placed in a trigger delay box which allowed variation of the cable length to introduce delays from 0.5 ns to 64 ns at 0.5 ns intervals by a series of switches. In addition, each streak speed required a different spacing between the time-marking pulse and the fluorescence signal. The optical paths of both the excitation pulse and the time-marking pulse were variable to facilitate the adjustment of this spacing.

There were non-linearities in the intensity response of the streak camera/detector system as well as time base non-linearities. The intensity corrections were made by a calibration procedure using signals from samples of known lifetimes. Calibration data sets were taken using samples which had lifetimes which were long compared to the time window across the detector. For example, for fast streak speeds (e.g., 0.31 ps/ch or 0.84 ps/ch), where there was less than a 1 ns time window, rubrene in benzene or cyclohexane was used for these calibrations. Rubrene has a fluorescence lifetime of >10 ns in these solvents, so the decay over 1 ns is very small ($<10\%$). Thus, the trace

of rubrene fluorescence on the fast streak speeds was virtually flat. $\text{Ru}(\text{pby})_3^{++}$ has a lifetime of 600 ns in water, making it an ideal candidate for calibration of slower streak speeds. When performing calibrations, the fluorescence lifetime of the molecule was taken into account so that technically any molecule whose lifetime is well known can be used. There are two reasons for using long-lived species. First, it is more desirable to have even illumination across the streak camera trace, and thus uniform uncertainties, when making intensity corrections. Second, because picosecond spectroscopy is still in its early stages of development, there are few short-lived species whose lifetimes are known with sufficient accuracy to act as a standard of calibration.

The excitation pulses used to perform the experiments were 25 ± 5 ps in duration. If great care was taken in alignment, and pulses late in the train were selected, it was possible to obtain much shorter pulses, on the order of 5 ps in duration. The pulses from the OPS tended to be somewhat shorter than average and the 266 nm pulses tended to be somewhat longer than average. The maximum pulse energy of the 532 nm beam at the sample was approximately 0.5 ± 0.3 mJ. The power at the sample, however, was adjusted with neutral density filters to insure that there were no artifacts due to saturation phenomena. Thus, studies were done to establish acceptable levels of excitation energy for each set of experiments. Since the OPS and 266 nm beams were considerably less intense than the 532 nm beam, attenuation of the excitation beam in these experiments was frequently unnecessary.

For each experiment it was necessary to signal average over many shots in order to get accurate, reproducible results. Each streak cam-

era trace was first examined by the computer to ascertain if the excitation pulse met a predetermined set of qualifications. The time marking pulse was used as a model to examine the characteristics of the excitation pulse. The computer checks the pulse intensity and width to determine if they fall within an acceptable range. If the pulse was accepted, then the data was corrected for the time and intensity non-linearities. There was a small amount of jitter in the triggering system for the streak camera system (on the order of tens of ps) which causes the time-marking pulse and the fluorescence signal to fluctuate to different positions in the streak camera trace. The time-marking pulse acted as a reference to synchronize the traces from each pulse during signal averaging. Although the laser runs at 10 Hz, data collection was limited by the time it took the computer to manipulate each trace. The effective rate of data collection was approximately 2-3 Hz using the LSI 11/73.

When the experimental decay times were comparable to the pulse duration, deconvolution of the data was necessary. The time-marking pulse was used as a model of the profile of the excitation pulse in the deconvolution of the data. The deconvolution was performed by a convolution and comparison technique using a simplex computer routine whereby the square of the sum of the residuals was minimized. More details concerning the fitting procedure are given in reference 2.

C. High Pressure Cell

Pressure can play an important role in understanding liquid phase dynamics in a variety of experimental applications. Pressure is often overlooked, however, as an experimental variable due to the lack of availability of simple high pressure technology. High pressure technology is further complicated for spectroscopic applications by the need for optical windows which can withstand high pressures. Temperature variation is often used in lieu of pressure variation due to the widespread knowledge of temperature variation techniques. Temperature variation may effect a complex combination of many of the characteristics of a given chemical system, such as activation energies. Thus, temperature may not always be the parameter of choice. Under many conditions, pressure may be employed as an experimental parameter which lends itself to simpler interpretation of experimental results. In addition, the simultaneous variation of both temperature and pressure enables one to perform constant density experiments. These added dimensions accessible through the use of high pressure are particularly useful in the study of liquid phase dynamics. Pressure has been successfully exploited in a number of laboratories for optical experiments⁴⁻¹¹. The applications of pressure have included a variety of vibrational and electronic spectroscopies employing a range of energies from infrared to ultra-violet. The success of these experiments demonstrate the value of pressure as an experimental variable.

The application of high pressure technology in our laboratory is coupled with picosecond laser spectroscopy for the study of liquid phase dynamics. High pressure measurements have been performed successfully on a number of chemical systems. Pressure has proven to be

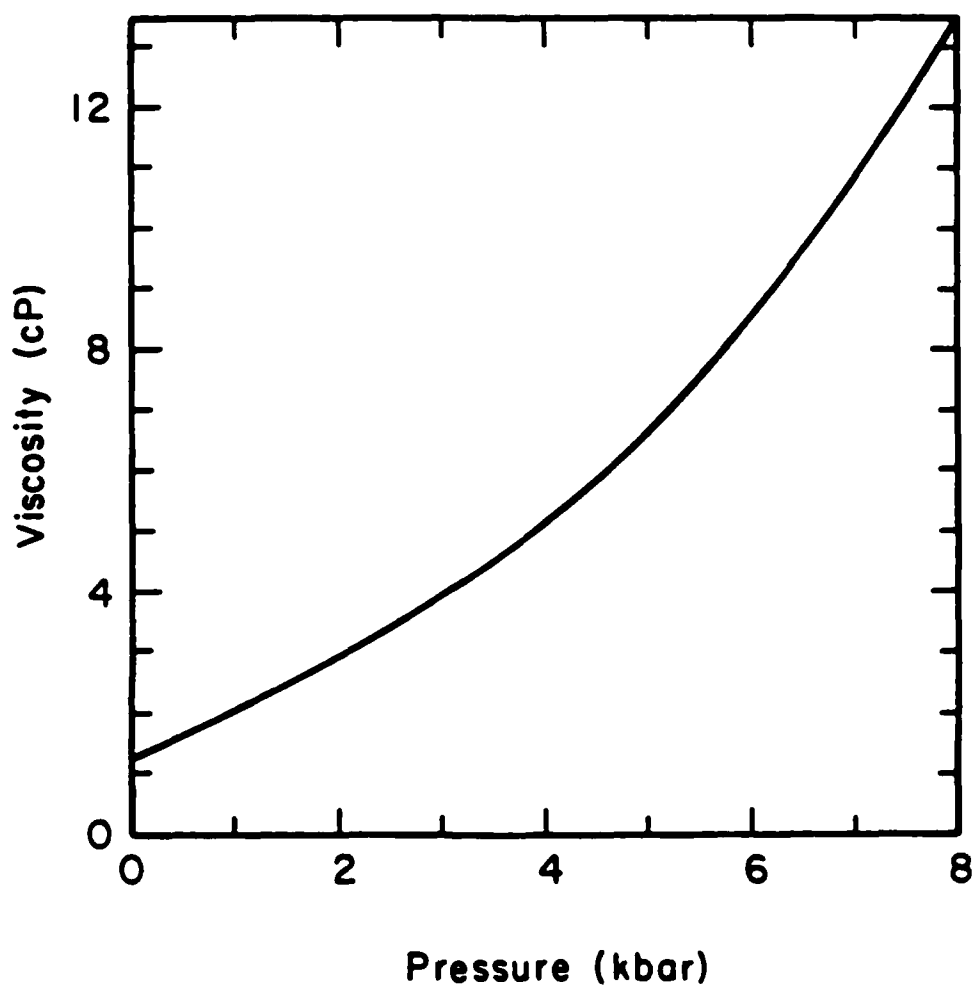


Figure 3 - Plot of viscosity versus pressure for ethanol. The viscosities under pressure are from Bridgman¹² corrected to 20°C. A smooth curve has been drawn through the experimental data points.

a useful experimental parameter to test predictive models, as well as to observe changes in behavior as a function of pressure. Pressure is used in some experiments as a clean way in which to vary bulk properties of the liquid such as the solvent viscosity.

The pressure dependence of the viscosity of ethanol is shown in Fig. 3. This plot is based on the results of Bridgman¹². An example of the effect of pressure on fluorescence properties is found in the triphenyl methyl dye, ethyl violet. The fluorescence lifetime of triphenyl methyl dyes is known to be dependent on the viscosity of the solvent¹³. If the viscosity is changed by increasing the pressure, the lifetime of the dye should increase. This effect has been observed in our laboratory for the case of ethyl violet in butanol. Fig. 4 shows the fluorescence decay of ethyl violet in butanol at 3 kbar, 2 kbar, and ambient pressure. The increase of the fluorescence lifetime with pressure is clear from the decays shown in the figure.

The dramatic role that pressure can play in such phenomena suggests that more widespread application of pressure as an experimental tool will yield valuable insight into liquid phase chemistry. To accomplish this goal, we developed a high pressure optical cell which is both easy to build and use.

The high pressure cell uses a hydrostatic press to generate the pressure. The pressure is then amplified from the large piston of the press to the small piston of the sample cell by the ratio of the areas of the two pistons. The cell and press were designed so that the sample cell could be kinematically mounted in the press. This arrangement allows for easy access to the sample cell for loading and exchanging samples. The compact cell may be filled away from the

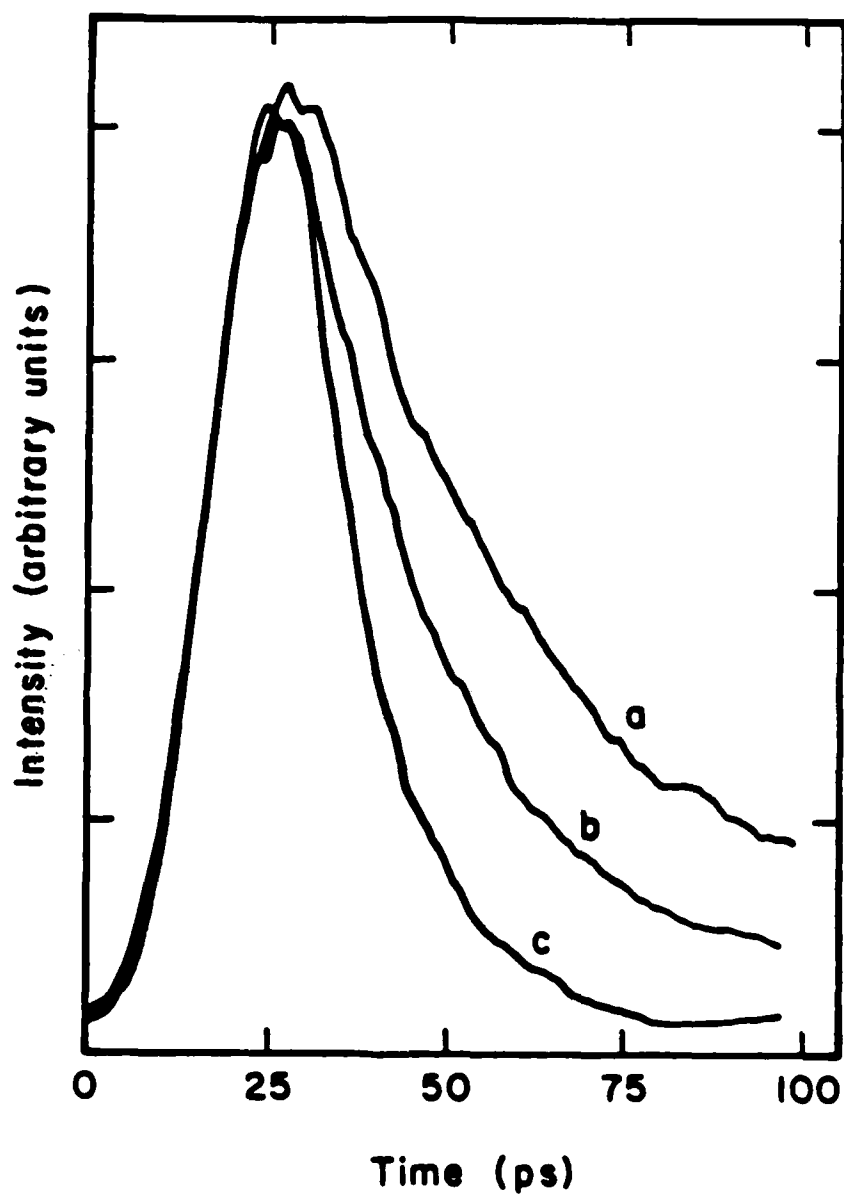


Figure 4 - Time resolved emission of ethyl violet in butanol. The three curves represent data taken at different pressures. Curves a, b, and c were taken at 3 kbar, 2 kbar and ambient pressure respectively.

Figure 5 - High pressure hydrostatic press. The piston in the diagram is 3 inches in diameter. A double O-ring seal contains the hydraulic oil in the reservoir above the piston. The high pressure seal connects to a hand pump which generates the pressure. Two of the four tie rods are depicted in the diagram. These rods are 0.75 inches in diameter and serve to hold the two iron blocks of the press together. The sleeves around the tie rods serve only as mechanical supports. An outline of the high pressure cell is shown in dotted lines.

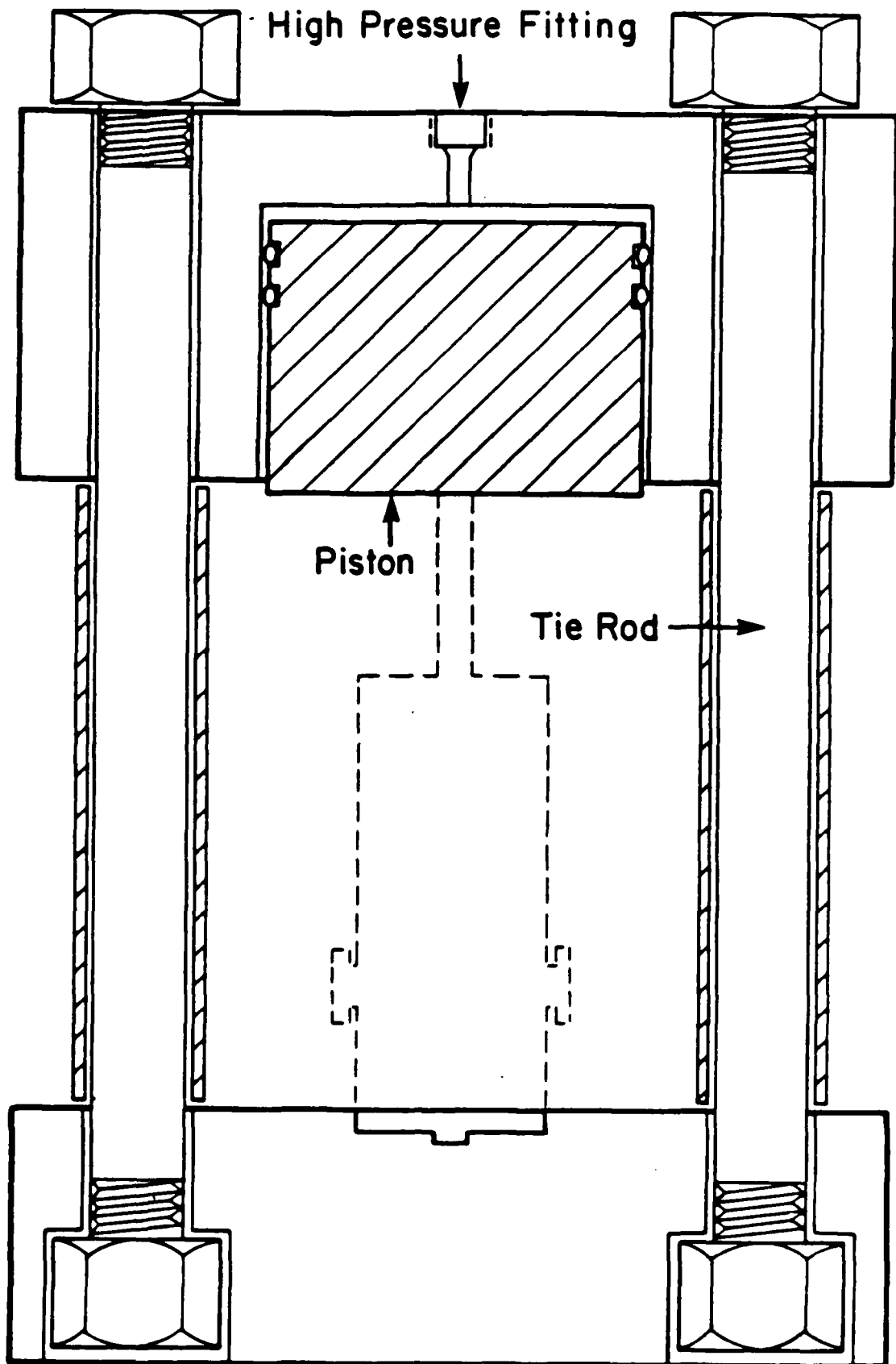


Figure 5

experimental apparatus in an isolated environment and then placed into the hydrostatic press as needed. We have found this arrangement to be extremely useful for running calibration samples and for exchanging different experimental samples with a minimum of laser realignment. In addition, the hydrostatic press itself is sufficiently compact that we are able to manually insert and remove it from the experimental set-up with great ease.

The hydrostatic press consists of a 1000 psi handpump (Enerpac, Model PH-39) and a home built piston press. A diagram of the press is shown in Fig. 5. The body of the press is 6 inches square and about 18 inches high. The body of the press was machined from cast iron, that was Kanigan plated to prevent rusting. The tie rods and keepers were made from steel. The piston was fabricated out of stainless steel. The pressure is transmitted from the hand pump to the press by hydraulic oil. More stable control of the pressure was accomplished by the addition of a Swagelock valve in the oil line. Since the oil never sees pressures above 600-1000 psi, Swagelock fittings and standard stainless steel tubing is sufficient to transfer the hydraulic oil. The piston is 3 inches in diameter and is sealed with a double O-ring seal.

A diagram of the sample cell itself is shown in Fig. 6, with an accompanying cross-section diagram shown in Fig. 7. The material used for most metal parts of the cell is Vascomex 350 (Vasco Pacific). This material is easy to machine. None of the special precautions required for some high pressure materials¹⁴⁻¹⁷ are required. After hardening to RC 58.4, the material has a tensile strength of 350,000 psi. These specifications are more than adequate to function at the required

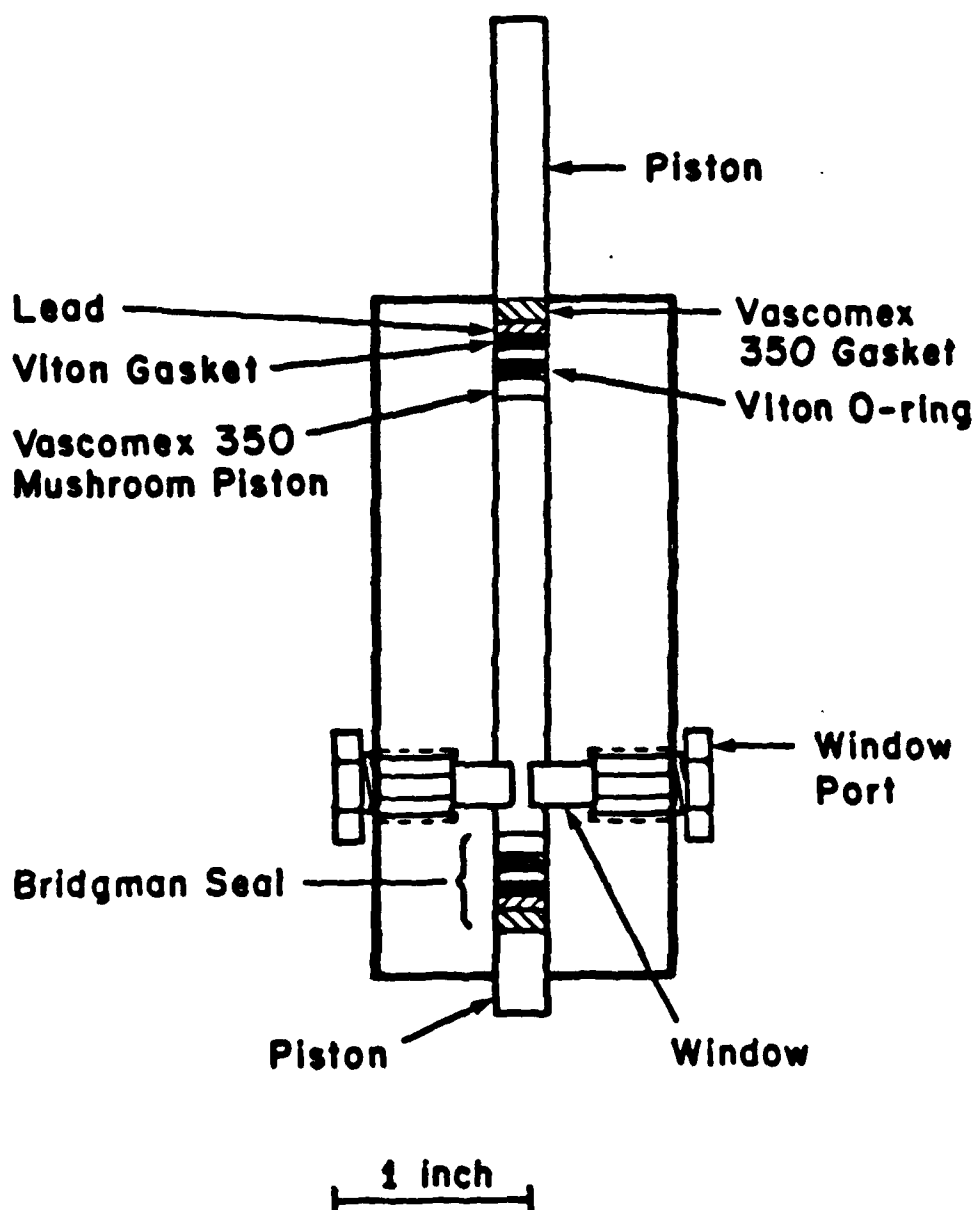


Figure 6 - High pressure cell. This side view of the high pressure cell shows two of the three window ports and the two Bridgman seals. The lower piston is stationary, while the upper piston moves down the cell as the pressure is increased. The high pressure Bridgman seals are in contact with both pistons. The seals consist of a sequence of three gaskets. An additional O-ring has been added as well. More detail of the window ports is shown in Fig. 7.

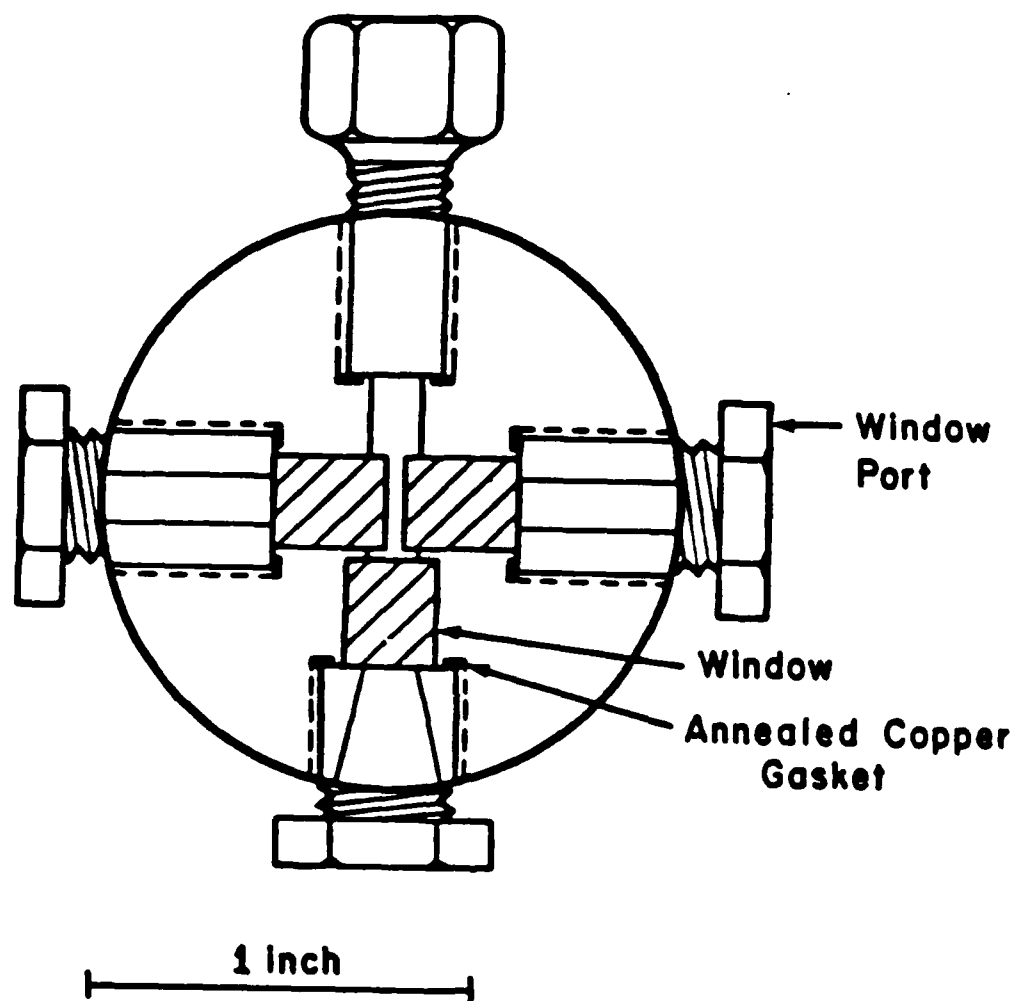


Figure 7 - High pressure cell cross section. The three window ports are depicted here. The ports are sealed into the main body of the cell by an annealed copper gasket. The forth port is at present blank, but could easily accomodate a manganin pressure gauge. The pathlength between the entrance and exit windows is approximately 1 mm. The windows themselves are 0.25 inches thick by 0.25 inches in diameter.

pressures of 6-10 kbar (80,000-150,000 psi).

High pressures are attained in the cell by the principle of area transfer of force from the large piston of the press to the smaller 0.25-inch-diameter piston in the cell. The ratio of the area of the large piston to the small piston creates an amplification in pressure of a factor of 144. The pistons at the top and bottom of the cell are sealed using Bridgman's design applying the principle of unsupported area¹⁸. The pistons and mushroom plugs are constructed of Vascomex 350. The seal is made with a sequence of gaskets starting with Viton, followed by lead, and finally by a Vascomex 350 gasket that acts as a keeper ring for the lead (see Fig. 6). In practice, we have found that an additional Viton O-ring at the mushroom plug insures good sealing for ambient and low pressure measurements before the lead flows into position. Bridgman seals are extremely easy to use and have been widely exploited in high pressure applications^{14,15,19,20}. For best sealing, care must be taken in machining the inner bore of the sample cell. The inner bore was machined roughly to the correct dimension of $0.25 \pm 0.000/-0.005$ inches and then ground to the final dimension. Grinding resulted in the most uniform inside diameter for the length of the cell as well as providing a good surface for sealing. The pistons and mushroom plugs were machined after grinding to match the final dimension of the bore.

The three window design of the cell lends itself to a variety of experimental applications. Two windows are positioned directly opposite one another to provide a path for a laser excitation source, in our case a passively modelocked Nd:YAG laser. The third window is positioned at 90° to the excitation source for collection of fluores-

cence or Raman scattered light. The clear aperture for all three windows is 0.125 inches. The design of the collection port differs from the other two window ports in that the bore of the window mount has an angle of 19° to improve collection efficiency. A 19° angle allows for a maximum collection efficiency of f3. By design, the windows are the weakest part of the cell. When rupture occurs, it is invariably due to a window cracking. Thus far, the cell has been used with BK7 and Suprasil windows 0.25 inches thick and 0.25 inches in diameter (Optics for Research). With these materials the cell has attained pressures of 7 kbar. Experiments have been performed using the cell at pressures of 6 kbar²¹. Sapphire windows have not yet been used because of birefringence problems. In applications where birefringence is not a concern one might expect a significant increase in attainable pressures with the use of sapphire windows.

The seal of the window to the window mount is patterned after the design originally introduced by Poulter²², and subsequently used in many other designs^{17,20,23,24}. The mount is polished optically flat after hardening. In principle, the contact of two optically polished surfaces is sufficient to create high pressure seals. In practice, for ease of handling and to insure sealing at ambient pressure, a thin layer of RTV cement is applied to the surface of the mount before applying the window. Clean, dust free surfaces are obviously of prime importance for best results, however, small surface scratches in the window mounts have not proven to be a problem. Laverne and Whalley²⁵ have shown that the shape of the sealing surface of the window mount may have profound effects on the working pressures of a given design. In particular, sharp edges on the sealing surfaces are undesirable.

Based on that work, our design of the window mount includes a radius on the inner bore of the window mount as well as beveled edges on the windows themselves. A simple radius is not the optimum design for the window mount (a gradual slope being the optimal design), however, it was the best compromise between performance and ease of construction for our purposes.

The window mount is sealed into the body of the cell by an annealed copper gasket. It is important that the inside diameter of the copper gasket be sufficiently large that it does not come into contact with the window and introduce stress when it becomes compressed. Behind the threads, the window mount is hexagonal in shape to accommodate a socket head torque wrench. The window mounts are tightened to 35 in. lbs. to make an initial seal. (Over tightening invariably led to leaks under pressure.) The window mounts are then retightened at approximately 1-2 kbar. This procedure gave the best results for leak free operation. On occasions when leaks did occur, in situ tightening of the window mounts was not difficult.

Originally, the cell was designed with two high pressure valves (Autoclave Engineers Model #AE60VM). These valves were used to flow sample into and out of the cell. One valve was placed opposite the collection window port and the other near the top of the cell. With use it was determined that loading of the cell was most easily accomplished through the top of the cell before loading the piston. The upper valve was retained for use in flushing the cell while loading, but the second valve was eliminated completely. Flushing sample through the cell upon loading eliminates any air from the cell which would interfere with experimental measurements. Since the valves were

limited to operating pressures below 60,000 psi, the elimination of the valve increases the pressure range of the cell. The upper valve does not encounter high pressures since the upper piston is moved beyond that valve before high pressures are attempted.

Pressure measurements are made above the large piston of the hydrostatic press in the hydraulic oil line. The pressure in the cell is then calculated by the area ratio of the pistons. The pressure is measured using a standard 1000 psi, dial pressure gauge (Ashcroft). Pressure measurements at the gauge are accurate to within 1%. Incorporating the errors introduced in translating this pressure into the pressure within the cell itself, including frictional forces, the accuracy in pressure measurement is considered to be within approximately 5 per cent²⁶. This error is well beneath the other errors inherent in our experiments. A test of the accuracy of the pressure measurement on a compression/decompression cycle was tested by performing identical experiments during both portions of the cycle. The results taken during compression and decompression were identical within our experimental error of approximately 10%. If better accuracy is required, then a manganin gauge may easily be incorporated in the design at the port opposite the collection window²⁶.

In addition to the present applications in our laboratory, this cell can be modified for use in variable temperature experiments. All of the materials used in the construction of the cell are able to tolerate a wide range of temperatures. Thus, minor modifications to control and monitor the temperature would result in a new dimension of flexibility of the cell¹⁹.

The high pressure cell described here has been demonstrated to be

Figure 8 - Picosecond time resolved Raman apparatus. SHG - Second harmonic generator (KDP crystal); THG - Third harmonic generator (KDP crystal); PD1 - Trigger photodiode to signal the computer and to synchronize data collection; PD2 - Monitoring photodiode to measure the laser intensity on a shot-to-shot basis.

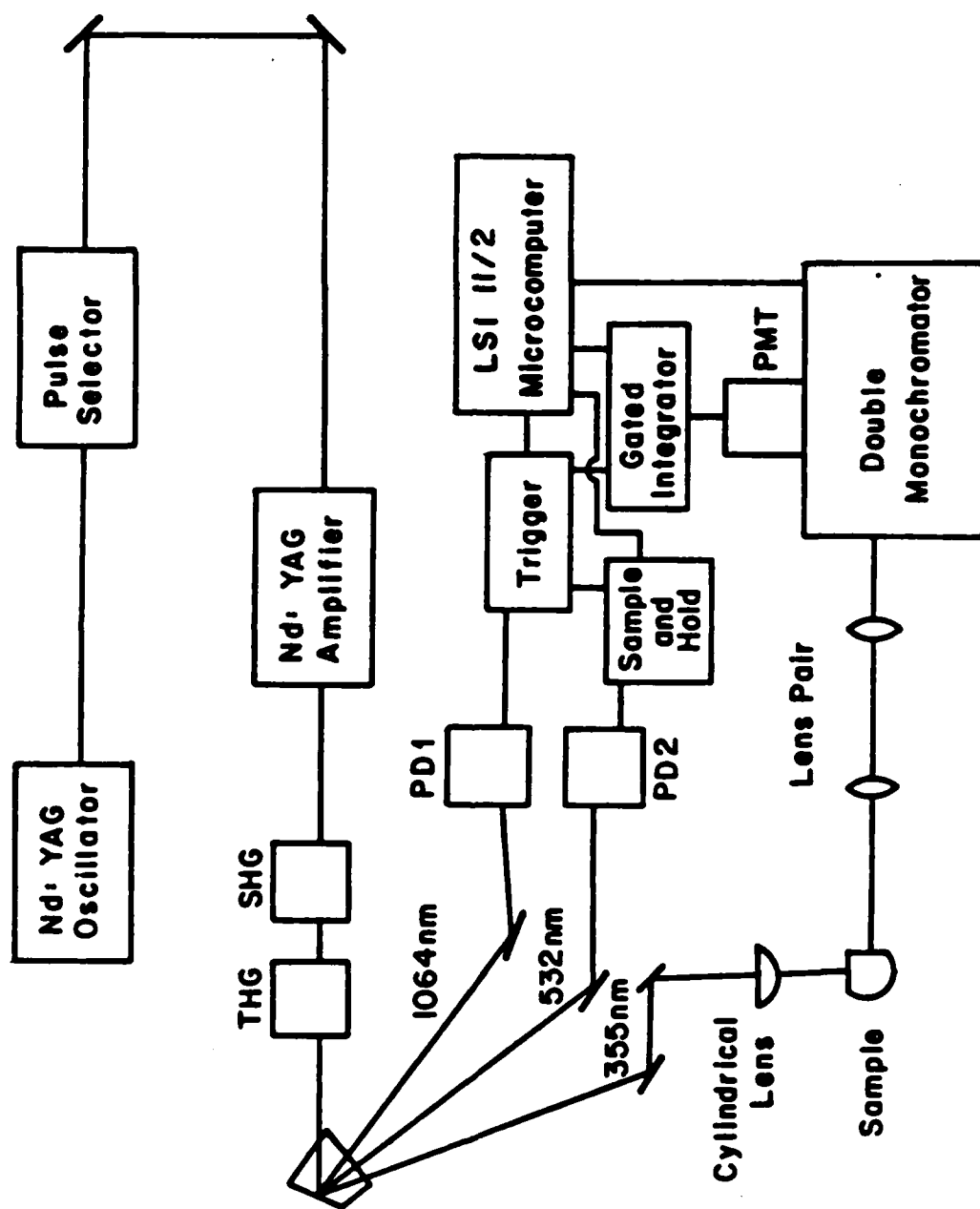


Figure 8

easy to construct, simple to use, and flexible in application. It is hoped that the introduction of such designs will help to extend the use of high pressure techniques.

D. Time Resolved Resonance Raman Apparatus

The picosecond, time resolved, resonance Raman (TR³) apparatus is shown in Fig. 8. As in the time resolved emission experiments, the various harmonics are separated at the Pellin-Broca prism. The 355 nm light was focused into a flowing sample cell by a 2 inch focal length cylindrical lens. The reservoir of the flowing cell was continuously purged with nitrogen. The cell itself consisted of a quartz capillary tube of inside diameter 2 mm and outside diameter 6 mm. The outside of the cell had two polished flat surfaces at right angles to one another. These surfaces served as an entrance window for the excitation pulse and as a collection window for the Raman scattered light. These flat "windows" minimized optical distortion of the beam and increased the ease of alignment of the imaging optics. The excitation beam was imaged onto the front edge of the sample, nearest the collection "window" to minimize the amount of the scattered light by the sample. The small inside diameter of the cell also helped to minimize this problem. The Raman scattered light from the sample was imaged onto the slits of a double monochromator (Spex, Model 1404) by the use of a lens pair. Light from the sample was collected by the first lens with an f1 collection efficiency. The second lens f matched into the monochromator. A 1P28 photomultiplier was used for signal detection. The output of the photomultiplier was gated at 100 ns intervals by a gated integrator (Evans Assoc.). The gated integrator signal was

monitored by an LSI 11/2 computer.

The 1064 nm beam was imaged onto a photodiode (Hewlett Packard, Model 5082-4220) that produces a trigger pulse. This photodiode is biased with a 90 V battery. The photodiode signal triggers a TTL circuit that in turn synchronously triggers the computer, the gated integrator, and a sample-and-hold unit. Neutral density filters were used to control the signal intensity, which was maintained just above the threshold necessary to trigger the TTL circuit. Operation just above threshold insured that only pulses with sufficient intensity would trigger the detection apparatus. In this manner, artifacts due to weak pulses, double pulse trains, or partially selected pulses were minimized. The 532 nm beam was imaged onto a second, unbiased photodiode. The photovoltaic signal from this photodiode was sent to a sample-and-hold unit to monitor the intensity of the excitation pulse.

The computer controlled the scanning of the monochromator, data collection, and signal averaging. Data was taken at wavelength intervals of 0.2 nm with a spectral resolution of 14 cm^{-1} . Each data point consists of an average of 500 laser shots. It was possible to normalize the signal to the laser intensity on a shot-to-shot basis. When 500 laser shots were averaged, however, normalization was unnecessary.

E. Solutions

1. Rhodamine 6G and p-Terphenyl

The absorption and emission spectra of rhodamine 6G (R6G) and p-terphenyl (PTP) are shown in Figs. 9 and 10. The appropriate excitation wavelengths were determined from the absorption spectra of these species. All studies of PTP were performed with 266 nm excita-

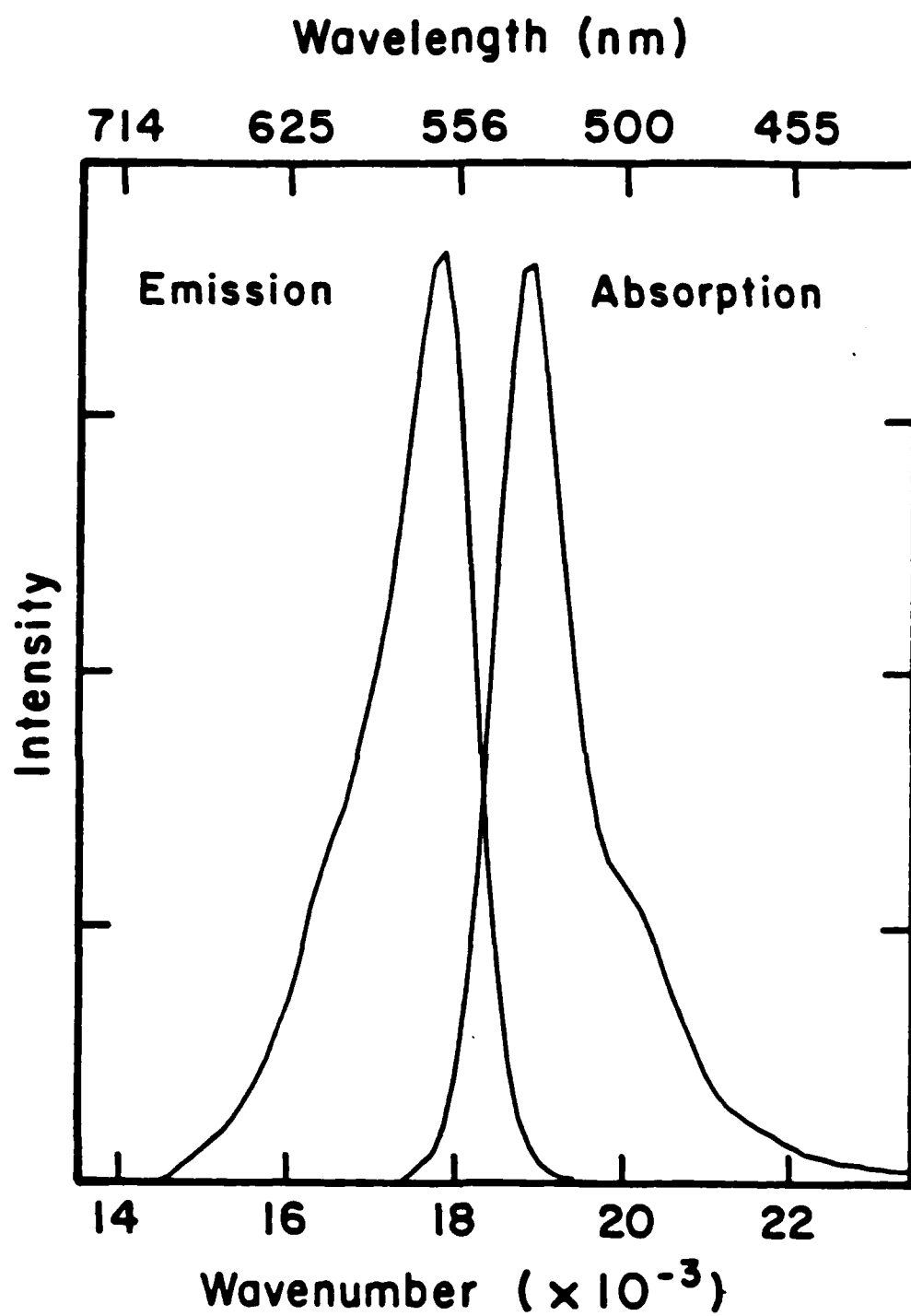


Figure 9 - Absorption and emission spectra of rhodamine 6G.

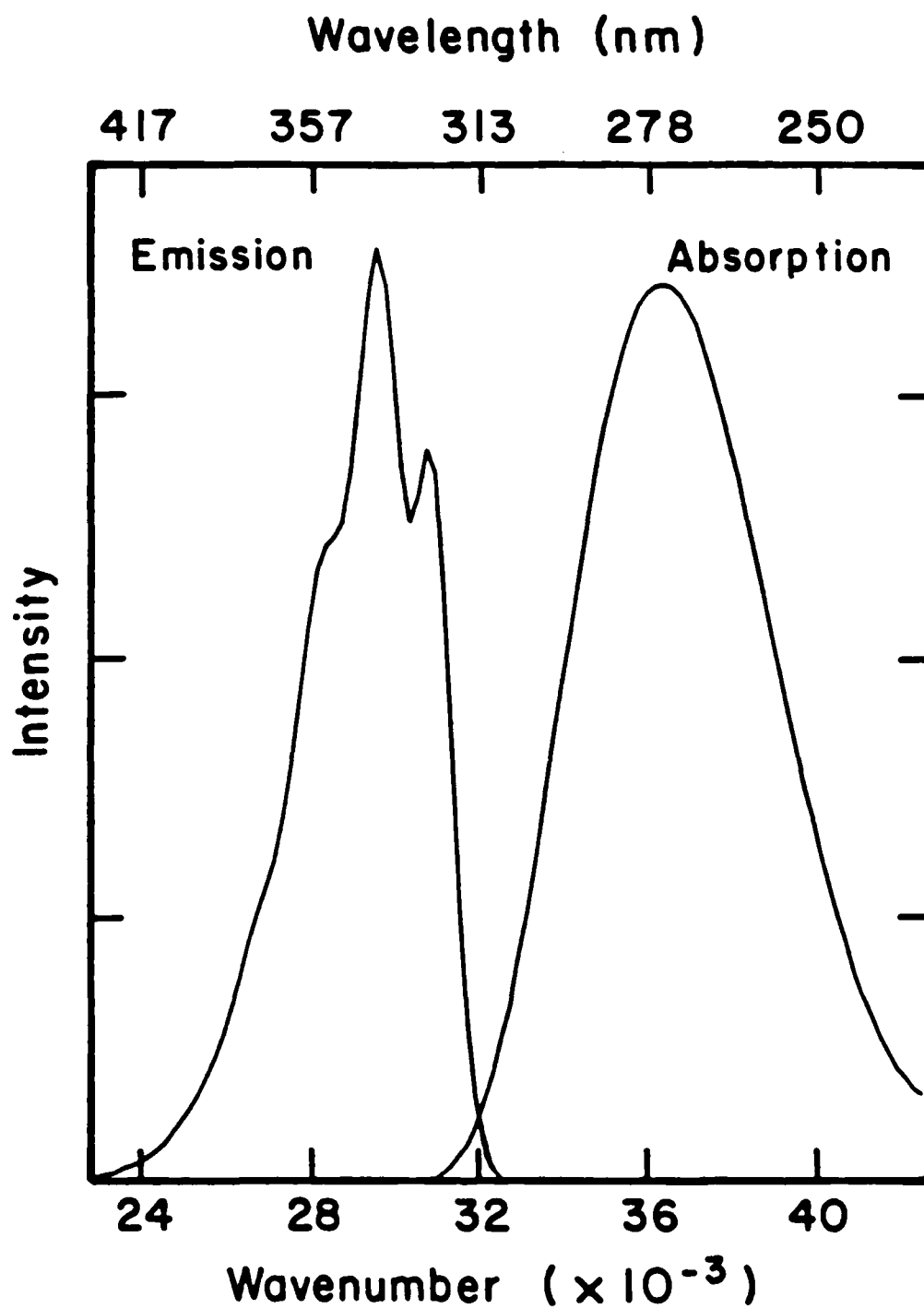


Figure 10 - Absorption and emission spectra of p-terphenyl.

tion. The majority of the R6G experiments were performed with 532 nm excitation. Additional experiments were performed on R6G to determine the excitation wavelength dependence of the rotational reorientation time. These experiments were performed at a series of wavelengths ranging from 450-550 nm, using the OPS as the excitation source (see Appendix A).

R6G (Eastman) solutions were 10^{-6} M and PTP (Aldrich) solutions were 10^{-5} - 10^{-4} M. These concentrations were determined to be sufficiently dilute to prevent artifacts resulting from reabsorption phenomena. All solvents were used as received. Whenever possible spectral grade solvents were used. Methanol, ethanol, propanol, butanol, octanol, hexane, heptane, nonane, cyclohexane, chloroform, dimethylformamide, and acetonitrile were available in this grade. The remaining solvents, pentanol, hexanol, decane, undecane, hexadecane, and dichloromethane, were reagent grade.

The viscosity of each solvent was determined at room pressure and temperature ($20 \pm 1^\circ\text{C}$) using a cone-plate viscometer (Brookfield, Model LVTDCP-40). High pressure viscosities were taken from Bridgman¹² and corrected to 20°C . The R6G experiments were performed at room pressure in water, methanol, ethanol, propanol, butanol, pentanol, and octanol. The excitation wavelength dependence study and the high pressure study were performed in ethanol. PTP experiments were performed in all of the above solvents including the additional solvents hexanol, hexane, heptane, octane, nonane, decane, undecane, hexadecane, cyclohexane, dichloromethane, chloroform, dimethylformamide, and acetonitrile. The high pressure experiments were performed in ethanol, hexane, octane, and chloroform.

2. $\text{Ru}(\text{bpy})_3^{++}$

Both 532 nm and 355 nm excitation were used in the emission experiments. Only 355 nm excitation was used in the Raman experiments. All emission was observed with the Glan prism polarizer set at 54.7° to eliminate any rotational effects. In addition, for the $\text{Ru}(\text{bpy})_3^{++}$ experiments, different wavelength filters were used in the emission experiments. In one set of experiments, high pass filters were used (Corning CS3-67, and Shott KV550). The alternate method used a 10 nm band pass filter centered at 600 nm (Corion). The signal level was much lower in experiments using the band pass filter, and there was no evidence of any difference in the two sets of experiments. Thus, the high pass filters were used preferentially.

Solutions were made of $\text{Ru}(\text{bpy})_3^{++}$ (Strem) as received at concentrations of 10^{-4} - 10^{-3} M in distilled water. Previous studies¹⁴⁰ have demonstrated that further purification is unnecessary. For Raman studies the solutions contained 0.5 M NaSO_4 . The SO_4^{2-} Raman mode at 904 cm^{-1} was used as an internal wavelength and intensity reference for the purpose of assigning and comparing the various Raman spectra. There was no evidence of a concentration effect in any of the experiments.

Chapter III

ROTATIONAL REORIENTATION

A. Introduction

Hydrodynamic models have been demonstrated to accurately describe rotational behavior of molecules in liquids in countless studies covering a wide range of experimental conditions²⁷. Since hydrodynamics is based on bulk properties, it is surprising that it is so effective in describing molecular motion. There are a number of experimental measurements, however, for which the results are not adequately predicted by simple hydrodynamic models²⁷⁻³⁹. The nature of these deviations provides a basis for the modification of existing models and may thus yield new information on the molecular interactions which influence rotational motion in liquids.

The classic model of rotational motion was derived in the early part of this century and is known as the Stokes-Einstein-Debye (SED) equation^{40,41}. While this model is based on the Brownian motion of macroscopic, non-interacting particles, it accurately predicts molecular behavior in many cases. Deviations from the predictions of the SED equation occur for the case of small solute molecules dissolved in a solvent of comparable size. These discrepancies have been almost completely eliminated by a variation of the SED equation that accommodates the behavior of small molecules⁴². Thus, the rotational motion of both large molecules and small molecules is well described by simple hydrodynamic models. The transition region between these extremes is less well understood. It is in this more complex region of intermediate sized molecules that the present study

was performed.

The SED equation is based on non-interacting solutes. It is therefore not surprising that deviations from the predictions of the SED equation have been observed in the case of charged solutes and hydrogen bonding solvents³⁵⁻³⁹. A variety of explanations have been proposed for the observed discrepancies, many involving the role of microscopic interactions between solute and solvent molecules. The focus of this study is to gain a better understanding of the cause of these discrepancies and to provide an experimental basis for the evaluation of some of the existing models.

Two very different solute molecules were studied here, p-terphenyl (PTP) and rhodamine 6G (R6G). Both molecules are in the intermediate size regime. PTP is a neutral, non-interacting solute molecule, while R6G is a highly interacting cation. Both molecules were studied in a number of different solvents and at different pressures. High pressure experiments furnish a unique means of varying macroscopic parameters such as viscosity over a large range using the same solvent. The study of PTP provides a test of hydrodynamic models for intermediate sized molecules over a wide range of solvents and pressures. This study also acts as a control experiment for the similarly sized, but highly interacting molecule R6G.

The similarities and differences between the results from the study of these two molecules establish a basis for the evaluation of existing models. In particular, it is of interest to determine the extent to which hydrodynamic models can be used to describe microscopic rotation. Departure from theoretical predictions establish criteria for the modification of hydrodynamic models. Alternatively,

a molecular model may be required to accurately fit the experimental results. In either case a better understanding of the molecular basis for the discrepancies is desired. The next section describes theoretical models previously presented in the literature that were used in the interpretation of the data in the present work. In turn, the data is used to evaluate the predictive power of the models themselves. This bridge between theory and experiment is the foundation through which an increased understanding of rotational motion in liquids is achieved.

B. Theory

1. Models

Since microscopic dynamics in liquids involves the simultaneous interaction of many molecules, liquids are extremely difficult to model theoretically. Explicit representation of the multitude of interactions is impossible. Simplifying approximations must be made in the interest of ease of calculation of experimentally measurable parameters. The predictive power of any model hinges on the validity of the approximations that are introduced.

A wide range of theories have been developed to describe rotational motion in solution. At one extreme is the hydrodynamic approach in which the solvent environment is described in terms of bulk properties alone. At the opposite extreme, the solvent and solute are described as individual molecules, and each solute-solvent interaction is treated as an isolated binary collision. Between these extremes there are many other approaches which attempt to incorporate molecular properties into the hydrodynamic formalism. A selection of some of the

more widely used models will be described here for later comparison with the results of the picosecond time-resolved measurements of rotational reorientation performed in the present study.

1) Hydrodynamic Models

As noted above, the foundation of many theoretical descriptions of rotational motion in liquids is the Stokes-Einstein-Debye (SED) equation⁴⁰⁻⁴¹. The SED equation is a diffusional model of rotation that predicts a linear relationship between rotational reorientation time and solvent viscosity. The SED equation is based on a hydrodynamic model which treats the solvent as a viscous continuum. In addition, the solute molecule is treated as a simple sphere. The SED equation is given by

$$D_R = \frac{k_B T}{8\pi\eta a^3} \quad (1)$$

where D_R is the rotational diffusion constant, k_B is Boltzmann's constant, T is the solvent temperature, η is the solvent viscosity, and " a " is the effective radius of the solute molecule. For a symmetric molecule, D_R is related to the rotational reorientation time (τ) by the equation

$$D_R = 1/6\tau \quad (2)$$

Combining Eqs. 1 and 2 gives

$$\tau = \frac{4a^3\pi\eta}{3k_B T} = \frac{V\eta}{k_B T} \quad (3)$$

where V is the volume of the solute molecule. The SED equation was derived for application to large solute molecules rotating in solvents consisting of molecules of much smaller dimensions. Under these conditions, Brownian motion provides an accurate description of solute move-

ment. In this regime a diffusional approach is appropriate.

Further, since the solvent size is much smaller than the solute, a continuum model approximation for the solvent is reasonable. It is no surprise that the SED equation presents a precise description of the rotational motion of symmetric macromolecules in solution. It is more shocking, however, to discover that with minor modifications, the SED equation accurately predicts the behavior of small molecules dissolved in solvents of comparable size.

Two modifications to the SED equation have greatly increased its range of application. The modifications deal with the shape of the solute molecule and the boundary conditions which describe the interactions between the solute and the continuum solvent. The SED equation may be rewritten as

$$\tau = \frac{V\eta}{k_B T} (fC) \quad (4)$$

In this modified SED equation, f is a variable parameter ($f > 1$), that is dependent on molecular shape, and C is a parameter which accounts for variable boundary conditions. This equation is from Kivelson^{27,28,39}. An excellent description of many of the modifications of the SED equation as well as other models is given by Dote, Kivelson, and Schwartz³². When the parameters f and C are both set equal to 1, Eq. 4 reduces to Eq. 3, the original form of the SED equation.

The SED equation was modified by Perrin⁴³ to extend the application of the SED equation to ellipsoids of arbitrary dimensions. Perrin derived an expression for f of Eq. 4 as a function of the axial ratio of the ellipsoid ($\rho = b/a$). Perrin's equation for f is given by

$$f = \frac{2}{3} \frac{1 - \rho^4}{(2 - \rho^2) \frac{\rho^2}{\sqrt{1-\rho^2}} \ln \frac{1 + \sqrt{1-\rho^2}}{\rho} - \rho^2} \quad (5)$$

for prolate ellipsoids ($\rho < 1$) and by

$$f = \frac{2}{3} \frac{1 - \rho^4}{(2 - \rho^2) \frac{\rho^2}{\sqrt{\rho^2-1}} \arctan \sqrt{\rho^2-1} - \rho^2} \quad (6)$$

for oblate ellipsoids ($\rho > 1$). Both of these equations apply to rotation of the symmetry axis about either of the other axes. Similar equations are given by Perrin for describing rotation about the symmetry axis but are omitted here, since only rotation of the symmetry axis was measured in the present study.

The SED equation and the Perrin-modified SED equation can be derived by solving the Navier-Stokes equation for slow, steady motion of a spheroid in a continuum solvent. The Navier-Stokes equation is given by^{42,44}

$$\eta \nabla^2 \mathbf{V} - \nabla p = 0 \quad (7)$$

where η is the fluid viscosity, $\mathbf{V}(\mathbf{r})$ is the relative velocity of the fluid with respect to the solute, and $p(\mathbf{r})$ is the pressure. In order to solve this differential equation, it is necessary to assume some boundary conditions.

Both the SED equation and the Perrin modification describe the rotation of a molecule that rotates with stick boundary conditions. Here one envisions that an infinitesimal layer of the solvent continuum at the surface of the solute molecule moves in unison with the surface of the solute (i.e. a layer of solvent sticks to the surface of the solute). The mathematical representation of this phenomena is given by the equation

$$\mathbf{V} = \boldsymbol{\omega} \times \mathbf{r} \quad (\text{on } S) \quad (8)$$

where $\boldsymbol{\omega}$ is the angular velocity of the solute, \mathbf{r} is a vector from the center of the solute, and S is the surface of the solute.

In contrast to the stick boundary conditions, an alternative approach may be taken, namely slip boundary conditions. With slip boundary conditions, the solvent moves independently of the solute and there is no adherence of the solvent to the solute. These conditions are manifested by the lack of any frictional force between the solute and solvent, as denoted by the equation

$$\mathbf{n} \times (\mathbf{n} \cdot \boldsymbol{\pi}) = 0 \quad (\text{on } S) \quad (9)$$

where " \mathbf{n} " is a vector normal to the surface and $\boldsymbol{\pi}$ is the stress tensor. For slip boundary conditions, the torque on a rotating ellipsoid is determined solely by the force required to displace the surrounding solvent molecules as the solute rotates. Although there are no frictional forces between the solute and solvent, friction is introduced when solvent displacement is required. Thus, for a sphere, where there is no fluid displacement, rotation is completely unaffected by the surrounding fluid and the frictional force is 0. As the solute molecule becomes less spherical, the frictional forces increase. Hu and Zwanzig⁴² have performed a numerical calculation of the frictional forces for both prolate and oblate ellipsoids as a function of axial ratio. Since the hydrodynamic friction (ζ) is proportional to the viscosity, the factor C in Eq. 4 is set equal to the ratio of

ζ_{slip} to ζ_{stick} (as compiled by Hu and Zwanzig) to convert the SED equation to slip boundary conditions.

With slip boundary conditions one would predict that the rotational reorientation time approaches zero as the molecular shape

becomes spherical. This result is clearly incorrect since even a free rotor has a rotational period. To correct the equation for highly symmetric molecules, some authors^{45,46} have added a term which provides for a non-zero intercept to Eq. 4. The physical meaning of the value of the intercept is not yet agreed upon, but its value tends to be similar to the free rotor lifetime of the solute molecule. Such times are small compared to rotational times observed for the molecules in this study, and this effect may therefore be safely ignored.

When using the above theory to interpret real experiments, approximations must be made with respect to the molecular shape and volume. Actual molecules seldom look like spheres or ellipsoids, and choosing an effective ellipsoid with which to represent the rotational dynamics is not a straightforward process. One method is to estimate the van der Waals volume of the molecule and then to redistribute that volume in such a manner as to approximate as closely as possible the general shape of the molecule with an ellipsoid. In this procedure, the true dimensions of the molecule are usually underestimated. Another alternative is to begin with the van der Waals radii of the molecule and calculate the effective volume of an ellipsoid with those dimensions. This procedure tends to overestimate the molecular volume. For small molecules, such discrepancies in the volume approximation are usually insignificant. For the solute molecules discussed in this study, the manner in which the volume and the axial ratio are calculated may change the predicted rotational reorientation time by a factor of 2.

Attempts have been made to approximate the shape of solute molecules by more complex shapes that more accurately depict various

solute molecules⁴⁷⁻⁵¹. Dote and Kivelson⁴⁸ calculated the slip and stick results for regular, but non-ellipsoidally shaped molecules. In particular, they modeled cylinders and cones with hemispherically capped ends, and two and three linear fused spheres. For the rotation of the symmetry axis of these shapes about the other axes, there was good agreement with the rotation time predicted for the equivalent ellipsoid. For very simple molecules, it is possible to model the solute in a more realistic fashion. Youngren and Acrivos modeled benzene by a hexagonal shape with hemispheres at its vertices and observed an improvement in the fit to experimental results⁴⁹⁻⁵⁰. Knauss, Evans, and Grant⁵¹ derived similar results for benzene when it was modeled as a sum of non-interacting spheres. Dote and Kivelson, however, warn of the dangers involved in the detailed modeling of the nooks and crevices of molecular shapes. A continuum solvent is able to access even the most minute crevice of a model molecule. In reality, an actual molecular solvent may not fit into many of the convex regions of the solute molecule. As a result, continuum calculations will overestimate the friction for a molecule of a complex shape. Given the above results and the complexity of the shape of the molecules used in this study, the solute molecules were approximated as ellipsoids.

Experimental results have been derived that support both the slip and the stick limits for rotational motion in solutions²⁷. The validity of each boundary condition depends on the characteristics of the specific system under examination. Since each of these extremes are appropriate in certain cases, it appears logical to invoke intermediate boundary conditions for some chemical systems. While such models have

been proposed^{31,52}, they typically contain an adjustable parameter that must be determined empirically. When attempting to measure subtle variations in boundary conditions, the presence of such an adjustable parameter is highly undesirable. Further, the variations one is attempting to measure may in fact be small compared to the errors involved in the volume approximation. Hence, unless the adjustable parameter can be calculated a priori from physical characteristics of the system under study, the practical utility of these models is greatly diminished. Since the volume calculations for the molecules in the present study have large uncertainties, models involving intermediate boundary conditions are not considered.

A series of other models have been proposed which attempt to depict more realistic boundary conditions by incorporating various aspects of the molecular nature of the solvent. Hydrodynamics is best suited to systems in which the solvent molecules are small compared to the solute. As the solvent molecules approach the size of the solute, effects due to the molecular nature of the solvent become more pronounced.

One theory was proposed by Gierer and Wirtz⁵³ in an attempt to correct for the size of the solvent relative to that of the solute. Instead of a structureless continuum, Gierer and Wirtz treat the solvent as a series of concentric shells surrounding the solute molecule. Angular momentum is transferred from the solute molecule to each successive solvent layer in a stepwise fashion. The fraction of momentum transferred to each successive layer decreases as the layers become more removed from the solute molecule. The size of the solvent layers is equated to the diameter of a solvent molecule. The angular

momentum of the solute is dependent on the diameter of the solute molecule. Thus, the relative sizes of the solute and solvent molecules play a decisive role in determining the boundary conditions. These boundary conditions can be incorporated into an expression for C in Eq. 4 as follows:

$$C = \sigma / C_0 \quad (10)$$

$$\sigma = \frac{1}{1 + \{6(V_S/V_T)^{1/3}\}/C_0} \quad (11)$$

$$C_0 = \frac{6(V_S/V_T)^{1/3}}{\{1 + 2(V_S/V_T)^{1/3}\}^4} + \frac{1}{\{1 + 4(V_S/V_T)^{1/3}\}^3} \quad (12)$$

where V_S is the solvent molecular volume and V_T is the volume of the solute molecules. In the limit where V_S is much smaller than V_T , C reduces to unity and the original SED equation is regained.

The Gierer-Wirtz theory strives for a more realistic description of the solvent by introducing structure to the continuum. The solvent layers correspond to molecular dimensions, representing the various solvation shells of the solvent. The correlation of the angular momentum of the solvation shells with the motion of the solute molecule is also included in the model. Each solvent shell, however, is itself a continuum. The continuum is merely broken down into specific regions. Further, the shape of each solvent shell is fixed and each shell moves as a complete unit. Thus, there is no representation of molecularity within the solvent shells. Since each layer of solvent is a continuum, there is no indication of the free space in the liquid.

As a result of the approximations made in the Gierer-Wirtz approach, there are some ambiguities involved in the application of the model. Equations 10-12 require knowledge of the molecular volumes of both the solute and the solvent molecules. The difficulties in deter-

mining the molecular volume of the solute was discussed above. Additional problems arise in the determination of the solvent volume. There are two dramatically different approaches to determining the molecular volume of the solvent. First, the solvent volume may be determined from the density of the solvent by

$$V_S = \frac{M}{\rho N_0} \quad (13)$$

where M is the molecular weight, ρ is the density, and N_0 is Avagadro's number. In this method, the "molecular volume" includes a substantial free volume contribution. This additional volume due to the free space in the liquid may be on the order of 40% of the excluded volume of the solvent molecule itself. Alternatively, the van der Waals volume of the solvent molecule may be used. In this case, the dimensions of the solvation layers will be underestimated since the free space is ignored in the volume calculation. Both of these methods of volume calculation are used in the present study. It is clear that an accurate representation of the solvent structure will not result if the free volume is omitted from the model.

The free space in a liquid may have important ramifications for the rotation of molecules in solution. Instead of continuous contact with the solvent continuum, a molecule in a real liquid contacts the solvent only at specific points. The remaining surface of the molecule is surrounded by free space. Both the torque on the molecule from the solvent and the concomitant transfer of angular momentum between the solute and solvent occur only at the contact points. Dote, Kivelson, and Schwartz³² include the concept of free space as well as relative solute/solvent size in their model of rotational reorientation in

liquids. The model of Dote et al. will be referred to as the free space model.

In the free space model, the parameter C in Eq. 4 is defined as the probability of contact between the solute and a neighboring solvent molecule. This modification of Eq. 4 may be thought of as reducing the amount of frictional force at the solute-solvent interface by the fraction of surface area of the solute which does not actually contact the solute. The evaluation of the equation for C by this method requires knowledge of a number of molecular and bulk parameters. The probability of contact is given by the ratio of the rotational volume of the solute to the rotational volume of solute plus the free space surrounding the solute.

The rotational volume of the solute is given by ϕV_T . ϕ is approximated by C_f for slip boundary conditions, where f is the Perrin value. This approximation for ϕ is valid when the interactions between the solute and solvent may be approximated as hard sphere interactions. The free space surrounding the solute is given by

$$\Delta V \{4(V_T/V_S)^{2/3} + 1\} \quad (14)$$

where ΔV is the free space per solvent molecule and the quantity in brackets is an approximation for the number of solvent molecules surrounding the solute. C may then be given as

$$\begin{aligned} C &= \frac{\phi V_T}{\phi V_T + \Delta V \{4(V_T/V_S)^{2/3} + 1\}} \\ &= \frac{1}{1 + (\Delta V/\phi V_T) \{4(V_T/V_S)^{2/3} + 1\}} \\ &= \frac{1}{1 + \gamma/\phi} \end{aligned} \quad (15)$$

The problems encountered in the applicaiton of Eq. 15 are the same

as those encountered for the Gierer-Wirtz model as described above. In addition, for the free space model one must also evaluate ΔV . The most straightforward method of evaluating ΔV is to use the equation

$$\Delta V = \frac{V_m}{N_0} - V_v \quad (16)$$

where V_m is the molar volume and V_v is the van der Waals volume of the solvent. Dote et al. suggest an alternate method based on a model of Frenkel⁵⁴. Frenkel expresses the isothermal compressibility(κ)_T as

$$\kappa_T = \frac{V_f}{V_0} \frac{\Delta V}{k_B T} \quad (17)$$

where V_f is the free volume of the liquid and V_0 is an empirically derived quantity that is loosely descriptive of the closest packing of the solvent that permits free rotation for all the solvent molecules. V_0 is determined from the empirical equation

$$\frac{1}{\eta} = \frac{B(V_m - V_0)}{V_0} \quad (18)$$

where B is a constant⁵⁴⁻⁵⁶. The inverse of the viscosity is plotted as a function of the molar volume to derive the constants V_0 and B . Early in this century Batschinski⁵⁵ made plots of over 80 liquids and determined that this relationship was linear for all of the non-associated liquids that he measured. All of the alcohols he studied were non-linear with the exception of methanol. Hildebrand⁵⁶ later provided the definition for V_0 . Dote et al. rewrite Eq. 18 as

$$\frac{1}{\eta} = \frac{B}{V_0} V_f \quad (19)$$

and substitute Eq. 19 into Eq. 17 to obtain an expression for ΔV

$$\Delta V = k_B T B \eta \kappa_T \quad (20)$$

Eq. 20 results in a very different value of ΔV than Eq. 16. In this

study both methods are used to predict rotation times whenever possible. It has been suggested that the values of B and V_0 from Eq. 18 are independent of temperature and pressure⁵⁶. In this study it is found that V_m becomes smaller than V_0 at high pressures, implying a negative viscosity, which is physically impossible. Thus, Eq. 20 is not used in the analysis of the results of the high pressure studies. Further, for alcohol solvents, Eq. 18 is non-linear. An attempt was made to determine B from the derivative of the curve at the required points, but the results were questionable.

Dote et al. point out the similarities between their theory and other theories. For example Ahn⁵² suggests that C should be a linear function of $1/\eta$. Vold et al.³⁴ demonstrate that their results support a linear relationship between rotation time and κ_T , and Goulay-Bize et al.³³ demonstrate a similar relationship between free volume and rotation time as a function of V_0/V_f . This ratio is determined from the equations⁵⁷

$$\frac{V_f}{V_0} = \frac{V_m}{V_0} - 1 \quad (21)$$

where

$$\frac{V_m}{V_0} = \left\{ 1 + (1/3)T\alpha/(1+T\alpha) \right\}^3 \quad (22)$$

and where α is the thermal expansion coefficient. As in Eq. 18, Eq. 21 is only valid for non-associated liquids. In the present study, the rotation time is plotted as a function of $V_m/\Delta V$, where ΔV is determined from Eq. 16. Conceptually, the two ratios, $V_m/\Delta V$ and V_0/V_f , are similar. The ratio $V_m/\Delta V$, however, avoids the use of vaguely defined empirical parameters, which are valid only under limited conditions.

Seeking correlations between the various parameters discussed

above provides a basis for understanding the relationship between bulk properties and microscopic dynamics. New insights based on these correlations can lead to modifications which extend the range of application of hydrodynamic models.

ii) Molecular Models

Given the approximate and general nature of hydrodynamic theories, it is amazing how well they have withstood the test of time. The success of hydrodynamics presents a precedent that is hard to surpass with molecular theories. Subtle deviations from hydrodynamic predictions suggest that the molecularity of the system is significant and provides impetus to derive molecular theories with predictive capabilities.

The most severe limitation of purely molecular theories is that the complex intermolecular interactions in liquids are at present impossible to model exactly. The major approximation universally employed in molecular theories is the representation of collisional events as isolated binary phenomena. In room temperature liquids, multi-body interactions occur continuously, this representation is therefore, incorrect. As a result of the binary collision approximation, the quantitative predictions of these theories may not be accurate, but the qualitative trends may still provide insight into some of the molecular phenomena which contribute to rotational motion.

Chandler has proposed a rough hard sphere Enskog model for rotational reorientation^{58,59}. Chandler derives this model for a liquid comprised of spherical or nearly spherical molecules which undergo uncorrelated binary collisions. Since the structure of these simple liquids is dominated by the short-range repulsive forces, it is as-

sumed that rotational motion of a single molecule will be controlled by these forces as well. Thus, long range forces are ignored. A collision between two smooth hard spheres results in the transfer of only translational momentum (i.e. there is no torque exerted on either molecule as a result of a collision). These conditions may be compared to slip boundary conditions in hydrodynamic models. If the surface of the hard sphere is made "rough", then angular momentum, as well as translational momentum, is transferred via collisions. The degree of roughness is a variable parameter which is adjusted in much the same manner as interpolating between slip and stick boundary conditions.

Evans et al. have modified the Chandler model to eliminate the adjustable parameter describing roughness and to extend the model to the treatment of a generalized convex body⁶⁰. In this model, the rotational reorientation time is expressed as

$$\tau = \frac{2\pi}{3} C^3 \epsilon^2 \rho \sqrt{I/2k_B T} \lambda_{AD} \quad (23)$$

where $\epsilon = (B^2 - C^2)/C^2$, B and C are the major and minor axes of the ellipsoid, respectively, ρ is the solvent density, I is the moment of inertia of the ellipsoid, and λ_{AD} is the reduced atom-diatom collision integral. To express τ as a function of the solvent viscosity, the Evans model uses the Enskog equation for viscosity. Keeping only the terms that are important at high density

$$\frac{\eta}{\rho} = \frac{5\pi A}{4} \sqrt{\pi k_B T/m} \rho_a^* g_{aa} \quad (24)$$

where A is the solvent radius, $\rho_a^* = (4/3)\pi A^3 \rho$, and g_{aa} is the atom-atom contact radial distribution function. Combining Eqs. 23 and 24 results in

$$\frac{\tau}{\eta/\rho} = \frac{2}{5\pi^2} \frac{\epsilon^2}{k_B T} \frac{\sqrt{mI/2}}{A^4} \frac{C^3}{A^4} \frac{\lambda_{AD}}{g_{aa}} \quad (25)$$

In this expression

$$\lambda_{AD} = g_{ad} \frac{2}{\sqrt{I/\mu_A C^2}} \langle g(x)s(x) \rangle \quad (26)$$

where

$$g(x) = \frac{x^2(1-x^2)}{\sqrt{(1+\epsilon x^2)(1+\epsilon x^2)/(1+\epsilon/R)}} \quad (27)$$

$s(x)$ is the surface area function of the atom-diatom collision pair, and $x = k \cdot e$, where " k " is a unit vector along the line of the collision perpendicular to the tangent of the surfaces of both collision partners, and " e " is a unit vector along the major axis of the ellipsoid. Eq. 25 is then rewritten as

$$\tau = \frac{\eta}{\rho} \frac{4}{5\pi^2} \frac{\epsilon^2}{k_B T} \frac{\sqrt{\mu_A m/2}}{A^4} \frac{g_{ad}(\rho_{aa}^*)}{g_{aa}(\rho_a^*)} \frac{C^4}{A^4} \langle g(x)s(x) \rangle \quad (28)$$

Many of the quantities in Eq. 28 are difficult to evaluate for real systems, but sufficient information is available to determine the trends predicted by this kinetic theory⁶¹.

The theory of Evans et al. as well as that of Chandler are designed to treat systems at the high densities present in normal, room temperature liquids. Other theories exist which are more appropriate at lower densities. For example the solute may be treated as a free rotor which is perturbed by collisions. These perturbations affect the angular momentum, of the rotating molecule. The direction of the angular momentum, or both the direction and the magnitude of the angular momentum may be altered by a collision as in the M and J diffusion models, respectively⁶². Although these models are most appropriate at low densities, they are sometimes applied to small solute molecules at higher densities as well⁶³. It is possible that small

solute molecules might be able to rotate in the pockets of free space in the solvent in a quasi-free rotor fashion. The quasi-free rotation of small molecules has been used to explain sub-slip behavior observed experimentally³².

In addition to the purely hydrodynamic models and the purely molecular models there are also models that attempt to incorporate molecular properties into hydrodynamic models. For example, it has been demonstrated that the success of hydrodynamic models can be emulated when the concept of boundary conditions is replaced by an intermolecular potential⁶⁴. Another study extends the SED equation into the molecular regime by incorporating a frequency dependent friction coefficient⁶⁵. Hynes, Kapral, and Weinberg⁶⁶ combine a rough sphere, binary collision model for short range interactions with a hydrodynamic model for the longer range interactions. In this model the diffusion constant is the sum of the molecular Enskog diffusion coefficient and the hydrodynamic diffusion coefficient given by the SED equation. Hynes et al. conclude that for small molecules, the molecular effects can play a dominant role in determining rotational reorientation times. If the role of microscopic parameters is ignored, erroneous conclusions may occur. The apparent linear relationship between the rotation time and the solvent viscosity may be the result of a simultaneous variation of both the rotation time and the microscopic friction with viscosity. The model of Hynes et al. is only directly applicable to spherical or nearly spherical molecules, but the conclusions of the model suggest that in general, apparent agreement of experimental results with hydrodynamic models should be viewed with caution. Due to the limitations and difficulties involved with

the application of the above models to real systems such as the molecules studied in these experiments, these models are not employed in the present study.

iii) Dielectric Friction Model

The final model to be considered focuses on an entirely new aspect of the problem - dielectric friction. Dielectric friction is the torque acting on a rotating polar molecule as a result of the induced polarization of the surrounding solvent. This frictional force occurs in addition to the viscous forces.

The role of dielectric friction on rotational reorientation times should be particularly important for the case of a charged molecule such as R6G in polar solvents such as alcohols. In contrast, dielectric friction should not be significant in the case of rotation of the non-polar PTP molecule. Both Hubbard and Wolynes⁶⁷ and Kivelson and Madden⁶⁸ have proposed methods of including dielectric friction in the description of rotational motion. Both of these models reduce to a result comparable to that of Nee and Zwanzig⁶⁹ in the zero frequency limit for the friction coefficient. In the Nee and Zwanzig equation the additional friction due to dielectric forces is

$$\zeta = \frac{6\mu^2 (\epsilon - 1)}{a^3 (2\epsilon - 1)^2} \tau_D \quad (29)$$

where ζ is the friction coefficient for dielectric friction, ϵ is the static dielectric constant, "a" is the cavity radius for the dipole moment, μ is the dipole moment, and τ_D is the Debye dielectric relaxation time. With the addition of this new term, the rotational reorientation time is given by

$$\tau = \frac{V\eta(fC)}{k_B T} + \frac{\zeta}{6k_B T} \quad (29a)$$

The dielectric friction is a frequency dependent parameter for all but macroscopic particles. Thus, quantitative agreement with experimental results may not occur when the zero frequency limit is used. The trends predicted by this model, however, provide a basis for understanding some of the similarities and differences observed under the variety of experimental conditions measured here.

The array of models described above demonstrates the wide variety of approaches that have been used to explain the dynamics of rotational reorientation. The success of any of these models is tested by their ability to predict experimental phenomena. The next section will describe the analysis required to determine rotational reorientation times from experiments. In Section B.3 we present some previous experimental results in the context of the theories discussed above.

2. Methods for Determining Rotational Reorientation Times

There are many kinds of experiments which measure rotational reorientation times(τ). The different methods may be separated into two categories. These two categories are: (1) frequency domain measurements, and (2) time domain measurements. In principle these two approaches are equivalent since the operation of Fourier transform converts between these two regimes. In practice, however, there are always approximations involved in performing a Fourier transform because information is never available at infinite times or over infinite frequencies. In many cases the approximations are small. Nevertheless, direct, time domain measurements avoid this complication.

Frequency domain measurements suffer from other, more severe limi-

tations as well. It is necessary to deconvolve the lineshape in the frequency domain to extract the portion of the lineshape that is due solely to rotational reorientation. In order to separate out the rotational lineshape, the rotation must be separable from the translational and vibrational relaxation processes⁷⁰. If any of these processes are coupled to one another, rotational reorientation times are extremely difficult to obtain. This limitation restricts frequency domain measurements to small symmetric molecules. An advantage in the study of small symmetric molecules is that theoretical calculations are easier to perform. Thus, there has been a great deal of complementary work between theory and frequency domain experiments.

Time domain measurements provide a more direct method of measuring rotational reorientation times. Since measurements are made directly in time, no assumptions or models are required to extract the desired numerical result. Thus, picosecond spectroscopy is well suited to the study of rotational reorientation of molecules in solution. The most severe limitation in time-domain measurements is the time resolution of the experimental apparatus. The time scale of standard picosecond experiments is slow compared to the time scales of the rotation times of the small molecules studied in the frequency domain. For a molecule the size of benzene, the rotation time in a liquid is on the order of a single picosecond per centipoise. The time resolution of the studies presented here is an order of magnitude slower, on the order of 10 ps. Thus, this study was limited to larger molecules with slower rotation times. The disadvantage of studying larger molecules is that they are more difficult to model theoretically.

Picosecond, time-resolved fluorescence measurements were performed

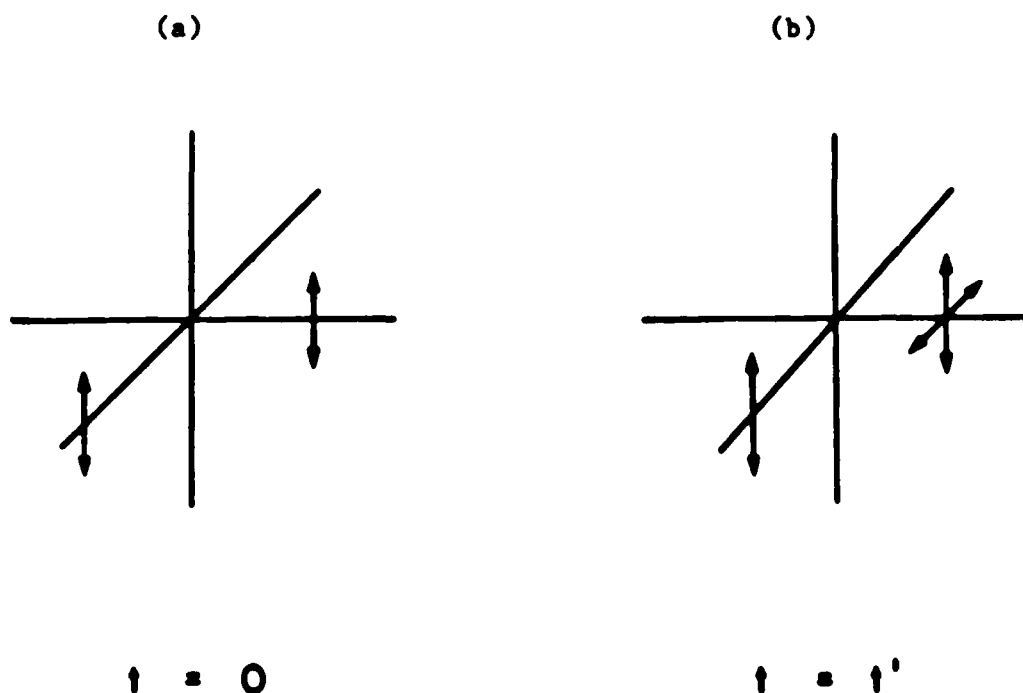


Figure 11 - Diagram of time resolved rotational reorientation experiments. (a) At time zero, excitation occurs with vertically polarized light. Excitation occurs preferentially to molecules with transition moments oriented vertically. Thus, an anisotropic distribution of excited state species is created. At early times, that is times short compared to rotational reorientation times, emission is rich in the vertical component. As the molecules rotate, the horizontal component grows in and the vertical component decays. (b) At times long compared to the rotational reorientation time ($t=t'$), the emission is isotropic.

in this study to determine rotational reorientation times. The conceptual basis for the experiment is shown diagrammatically in Fig. 11. The details of the analysis of the experiment have been given in depth elsewhere⁷¹, and thus will be described only briefly here. Initially, the sample is excited at time zero with vertically polarized light (Fig. 11a). The probability of excitation of any given molecule in solution is proportional to the projection of its transition moment vector along the vertical (z) axis, and is given by

$$P = |\mu \cdot z|^2 = \mu^2 \cos^2 \theta \quad (30)$$

where μ is the transition dipole of the molecule, P is the probability distribution of excitation, and θ is the polar coordinate which describes the angle of μ with respect to the z axis. The probability must be normalized and may be represented in terms of a second order Legendre polynomial,

$$P_2(\cos \theta) = (1/2)(3\cos^2 \theta - 1) \quad (31)$$

The probability distribution at time zero is then given by

$$P(t=0, \theta, \phi) = (1/4\pi)[1 + 2P_2(\cos \theta)] \quad (32)$$

At later times,

$$P(t, \theta, \phi) = (1/4\pi)[1 + 2c_{2,0}(t)P_2(\cos \theta)] \quad (33)$$

where $c_{2,0}(t)$ is an expansion coefficient of the Green's function operator for the time evolution of $P(t)$. Initially there is a non-random distribution of excited states in which the transition dipoles are preferentially oriented along the z direction as described by Eq. 32. The system relaxes towards a random orientation by rotational reorientation. The molecular orientation of an excited state molecule is reflected in the polarization of its emission. At time zero, just after excitation, there is a preferential orientation of the transi-

tion moments along the z axis. Thus, the emission at time zero will be rich in vertically polarized emission. The horizontal component of the emission will be correspondingly weak (Fig. 11a). As rotational diffusion occurs the vertical component decays and the horizontal component grows in (Fig. 11b). In any distribution of excited state species, the polarization of the emission is proportional to the projection of the transition moment along the axis of polarization. In addition, the intensity of emission along any given polarization vector must be weighted by the proportion of molecules which remain excited at time t. The resulting intensities of emission are given by:

$$\text{vertical: } F(t)|\mu \cdot z|^2 = \mu^2 F(t) \cos^2 \theta \quad \text{and} \quad (34)$$

$$\text{horizontal: } F(t)|\mu \cdot x|^2 = \mu^2 F(t) \sin^2 \theta \cos^2 \phi \quad (35)$$

where $F(t)$ is the fluorescence lifetime of the excited state species.

To get the time dependent intensity of emission of the vertical and horizontal components, Eqs. 34 and 35 are multiplied by the time dependent probability distribution given in Eq. 33 and integrated over all orientations. The resulting expressions are

$$I_{\parallel}(t) = [(1/3) + (4/15)c_{2,0}(t)]F(t) \quad \text{and} \quad (36)$$

$$I_{\perp}(t) = [(1/3) + (2/15)c_{2,0}(t)]F(t) \quad (37)$$

The rotational reorientation time of the system is given by

$$r(t) = \frac{I_{\parallel}(t) - I_{\perp}(t)}{I_{\parallel}(t) + 2I_{\perp}(t)} = \frac{2}{5} c_{2,0}(t) \quad (38)$$

For an arbitrary angle of observation (ω), Eq. 34 and 35 are replaced by the expression

$$\mu^2 F(t) (\sin \omega \sin \theta \cos \phi - \cos \omega \cos \theta)^2 \quad (39)$$

When Eq. 39 is multiplied by Eq. 33 and integrated over all space, the generalized expression for the emission intensity is given by

$$I_{\omega}(t) = [(1/3) + c_{2,0}(t)\{(4/15)\cos^2\omega - (2/15)\sin^2\omega\}]F(t) \quad (40)$$

Notice that when

$$(4/15)\cos^2\omega = (2/15)\sin^2\omega \quad (41)$$

the only time dependence in the fluorescence decay curve is the fluorescence lifetime of the excited species. The angle that satisfies Eq. 41, 54.7° , is known as the magic angle. Magic angle detection is necessary to measure the fluorescence lifetime independent of any rotational effects.

Implicit in the above formalism is the assumption that the absorbing and emitting dipoles are parallel. If this assumption is not valid, Eq. 38 becomes

$$r(t) = (2/5)P_2(\cos\lambda)c_{2,0}(t) \quad (42)$$

where λ is the angle between the emission and absorption dipoles. (When $\lambda=0^\circ$, Eq. 42 reduces to Eq. 38.) In this case, the equations corresponding to Eqs. 36 and 37 are

$$I_{\parallel}(t) = P_2(\cos\lambda)[(1/3)+(4/15)c_{2,0}(t)]F(t) + \frac{\sin^2\lambda F(t)}{2} \quad (43)$$

and

$$I_{\perp}(t) = P_2(\cos\lambda)[(1/3)+(2/15)c_{2,0}(t)]F(t) + \frac{\sin^2\lambda F(t)}{2} \quad (44)$$

When $\lambda=90^\circ$, that is when the emitting dipole is perpendicular to the absorption dipole, then the rotational anisotropy is given by

$$r(t) = -(1/5)c_{2,0}(t) \quad (45)$$

Finally, when $\lambda=54.7^\circ$

$$I_{\parallel}(t) = I_{\perp}(t) \quad \text{and} \quad r(t) = 0 \quad (46)$$

That is, there is no time dependent component due to rotational motion.

The value of $r(t)$ at time zero, $r(0)$, is of particular importance. The function $c_{2,0}(t)$ is normalized to unity at time zero, making $r(0)$

equal to $(2/5)P_2(\cos\lambda)$. For parallel absorption and emission transition moments, $r(0) = 2/5$. Any departure from this ideal case will be reflected in a deviation of $r(0)$ from $2/5$. The value of $r(0)$ is also dependent on the polarization of the input beam. If the excitation source is not completely vertically polarized, then $r(0)$ will deviate from the $2/5$ value as well. Finally, molecular dynamics calculations⁷² indicate that an $r(0)$ value less than $2/5$ may result from coupling between translational and rotational motion in liquids. In practice, there is some uncertainty in the determination of $r(0)$ from the experiments. Time zero is not perfectly well defined, and some estimation is involved in the measurement. A conservative estimate of the uncertainty of the measurement of $r(0)$ from these experiments is 10%.

The function $r(t)$ is dependent on the function $c_{2,0}(t)$. In order to evaluate these functions, it is necessary to make some assumptions about the molecular shape and symmetry. In a molecule that is a symmetric top, $c_{2,0}(t)$, and therefore $r(t)$, is a single exponential for the rotation of the symmetry axis about the other axes. For molecules with a more complex shape, $r(t)$ may be a function of a sum of up to five exponentials. In many experiments, the molecular shape is approximated as a symmetric top and the decay of $r(t)$ is fit to a single exponential. This procedure yields an appropriate value for the rotational reorientation time of an equivalent symmetric top, not the rotation time about a specific molecular axis. Fluorescence measurements are specific in that they directly measure the rotation of the transition moment of the molecule. When the transition moment of a symmetric top molecule coincides with the symmetry axis in the molecule, a single exponential decay accurately describes rotation of

the symmetry axis about the other axes. When the transition moment does not coincide with the symmetry axis the results are more complex. For a symmetric top, $r(t)$ is described by a sum of three exponentials when the transition moment does not coincide with the symmetry axis. When the transition moment is perpendicular to the symmetry axis, the expression for $r(t)$ simplifies to a sum of two exponentials given by

$$(1/4)\exp[-t/\tau'] + (3/4)\exp[-t/(\tau'/3 + 2\tau/3)] \quad (47)$$

where τ' is the rotation about the symmetry axis and τ is rotation of the symmetry axis. For a prolate top, $\tau > \tau'$ and this equation must be used explicitly. For an oblate top using stick boundary conditions, $\tau = \tau'$, and Eq. 47 reduces to a single exponential⁷³. Thus, in these two special cases ((1) rotation of the symmetry axis of any symmetric top and (2) rotation of an oblate top) rotational reorientation may be expressed as a single exponential.

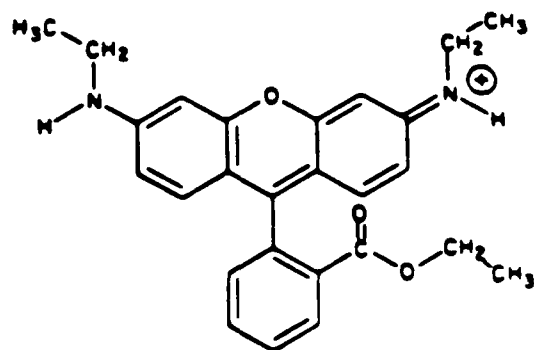
The molecules R6G and PTP were chosen because they have complementary properties that provide interesting comparisons. PTP is a neutral prolate top molecule, while R6G is a charged oblate top molecule. R6G as well as other similar molecules have been widely studied in the past by time resolved techniques. Thus, R6G acts as a link for comparison of data from this study with the existing data in the literature. The next section reviews some previous results for the purpose of comparison with the results presented here.

3. Literature Review

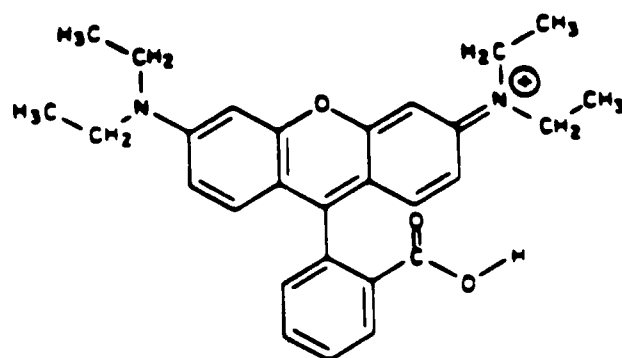
In the last decade numerous studies of the rotational reorientation of intermediate sized molecules have been made, employing a variety of techniques^{35-38,74,76-94}. Many of these studies used picosecond spectroscopy. Picosecond experiments may be further subdivided into a number of different methods including fluorescence depolarization^{38,76-86}, transient dichroism^{35-37,73,74,87-92}, and transient grating^{93,94} experiments. In general, these studies have focused on dye molecules with large absorption cross sections. Many of these dyes, such as R6G, are xanthene dyes. In addition to xanthene dyes, a number of other molecules have been studied such as DODCI, BBOT, and diphenylbutadiene (DPB). The structures of most of the more commonly studied dye molecules are shown in Figs. 12-15.

The dye molecules shown in Figs. 12-15 are designated according to shape and charge. The molecules in Fig. 12 are all cations of similar shape, and are treated as oblate symmetric tops. The molecules in Fig. 13a are also cationic xanthene dyes, but do not have a phenyl group at the 9 position. These molecules are treated as prolate symmetric tops. The molecules in Fig. 13a are very similar to those in Fig. 13b except that they contain an additional, fused, six-membered ring at the 1,2 position. The additional ring makes the shape of these dyes highly asymmetric.

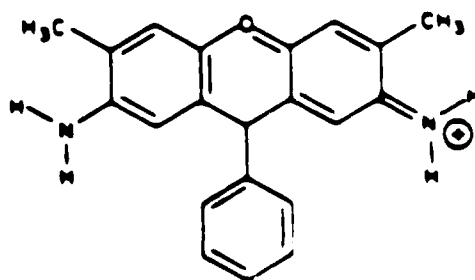
The molecules shown in Fig. 14 are very similar in shape to those shown in Fig. 12, but are dianions instead of cations. Finally, the molecules in Fig. 15 are not xanthene dyes. These molecules, with the exception of DODCI, are treated as prolate tops. DODCI is thought to exist in a cis configuration and, as such, is better approximated as



Rhodamine 6G (R6G)

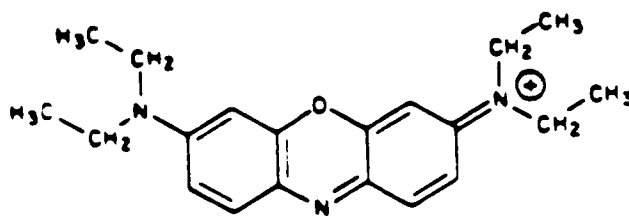


Rhodamine B (RhB)

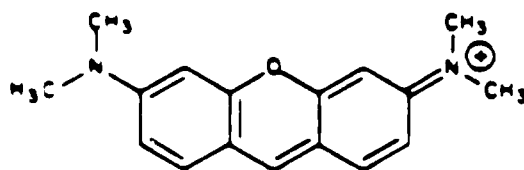


Safranin T (ST)

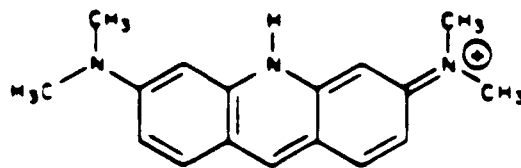
Figure 12 - Molecular structures of some oblate, cationic, xanthene dyes.



Oxazine 725 (Ox)

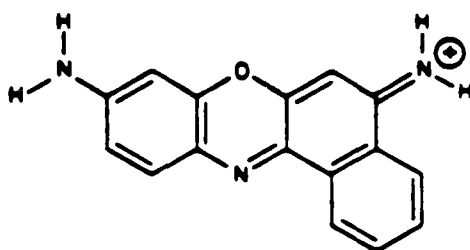


Pyronine G (PG)

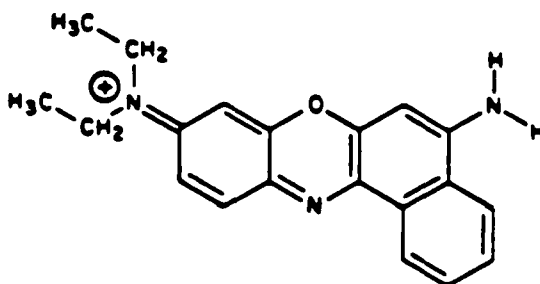


Acridine Orange (AO)

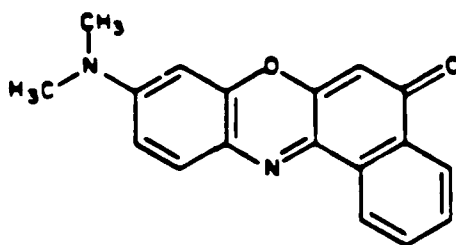
Figure 13a - Molecular structures of some prolate, cationic xanthene dyes.



Cresyl Violet (CV)

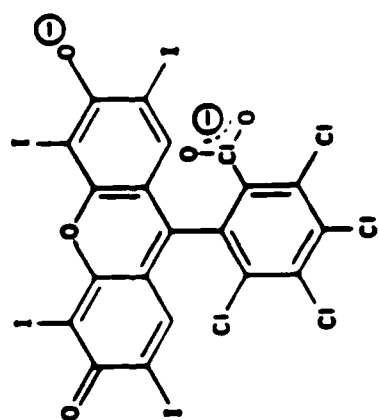


Nile Blue (NB)

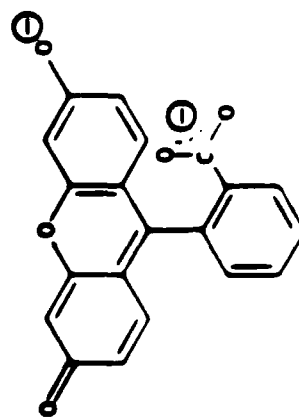


Phenoxazone 9 (P9)

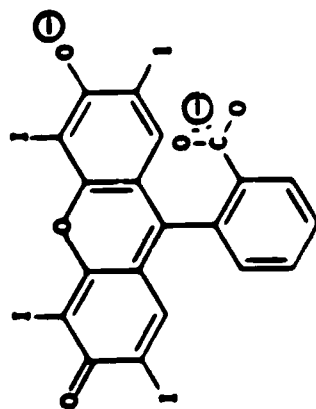
Figure 13b - Molecular structures of some asymmetric xanthene dyes.



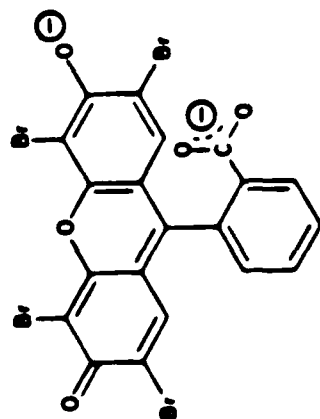
Rose Bengal (RB)



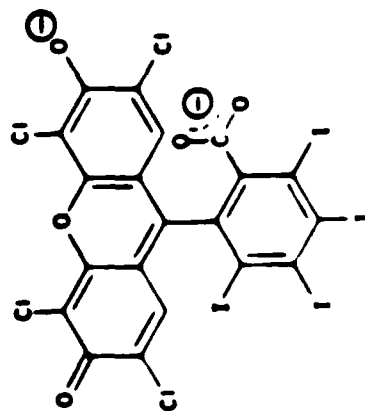
Fluorescein (Fl)



Erythrosin B (EB)

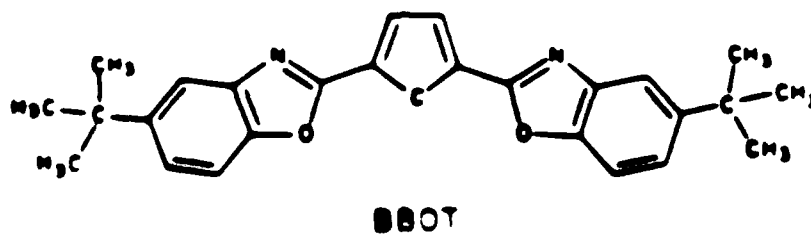


Eosin (E)



TCYTF

Figure 14 - Molecular structures of some dianionic xanthene dyes.



Diphenylbutadiene (DPB)



p-Terphenyl (PTP)

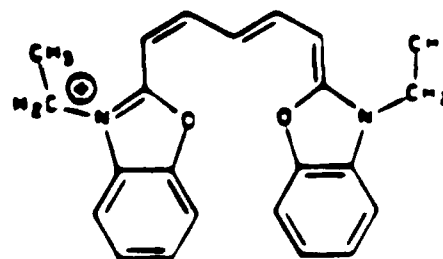


Figure 15 - Molecular structures of some non-xanthene dyes.

an oblate top. Of the molecules in Fig. 17, BBOT, DPB and PTP are neutral molecules, and DODCI is a cation.

The rotational reorientation times of many of the above molecules have been studied as a function of solvent. Results from a number of different studies are summarized in Tables 1-5. Table 1 presents the rotational reorientation times measured by different workers for three of the more widely studied dye molecules, R6G, RhB, and RB. This table is intended to demonstrate relatively good agreement generally found in the literature, although some exceptions do occur (see Table 1). In Tables 2-5, the rotation times have been normalized to the solvent viscosity to facilitate direct comparison among solvents. When more than one result is available from the literature, the average value is taken, unless it is deemed appropriate to omit specific values from the average due to experimental uncertainties. Table 2 presents all of the oblate and asymmetric cationic xanthene dyes. In Table 3 results are given for the prolate, cationic xanthene dyes. Table 4 includes similar information for the dianionic xanthene dyes. The results for the remaining molecules are given in Table 5. The results in Tables 2-5 can be used to evaluate the SED equation.

Any model which assumes constant boundary conditions will predict a constant value of τ/η with solvent. Thus, the SED equation with either slip or stick boundary conditions predicts a constant value of τ/η . A glance at Tables 2-5 clearly demonstrates that this prediction is not born out by the experimental results. Contradiction of the SED equation is particularly dramatic in the case of the dianions.

In some studies in which a limited number of molecules were studied in a few solvents, the discrepancies observed in Tables 2-5

Table 1

Rotational Reorientation Times of R6G, RhB, and RB from Previous Work

	Water	Methanol	Ethanol	Propanol	Decanol	Reference
<u>R6G</u>						
---	---	100	300	450	2300	76a
---	---	140	300	500	---	93
196	---	---	---	---	---	85
230	---	---	270	---	---	89
---	95	---	195	---	---	97
---	---	---	250	---	---	82
---	---	---	310	490	3400	36,37
---	---	---	255	---	---	88
<u>RhB</u>						
---	---	---	265	480	3800	94
230	---	---	270	---	---	89
---	---	---	196	---	---	90
---	---	---	218	---	---	80
---	---	---	260	460	3050	36,37
<u>RB</u>						
---	---	180	680	---	---	77
---	---	680	---	---	---	82
---	---	190	450	---	---	38
---	---	---	420	830	6200	36,37

Rotational reorientation times are given in picoseconds for rhodamine 6G(R6G), rhodamine B(RhB), and rose bengal(RB). The results are from selected literature data.

Table 2
Rotational Reorientation Times Normalized to Solvent Viscosity for
Oblate and Asymmetric Cationic Xanthene Dyes

Solvent	R6G	RhB	ST	CV	NB
Methanol	190	---	---	150	---
Ethanol	230	200	225	208	180
n-Propanol	200	200	180	320	150
i-Propanol	190	---	---	---	---
Butanol	200	---	---	350	---
Pentanol	240	---	---	370	---
Decanol	250	250	240	290	---
Water	210	230	---	75	---
Formamide	180	---	---	180	---
NMF	---	---	---	203	---
DMP	---	---	---	170	---
DMSO	220	---	---	194	---
Chloroform	170	---	---	---	---

Rotational reorientation times are normalized to the solvent viscosity and are given in units of ps/cP. The references for the data are as follows - Rhodamine 6G(R6G): 36, 37, 76a, 82, 85, 88, 89, 93, and 97; Rhodamine B (RhB): 36, 37, 80, 89, 90, and 94; Safranin T(ST): 36 and 37; Cresyl violet (CV): 36, 37, 73, and 90; Nile blue (NB): 36 and 37.

Table 3

Rotational Reorientation Times Normalized to Solvent Viscosity for
Prolate Xanthene Dyes

Solvent	Ox	AO	PG
Methanol	---	90	75
Ethanol	120	120	70
n-Propanol	---	85	60
i-Propanol	---	---	---
Butanol	---	100	60
Pentanol	---	160	60
Decanol	---	90	100
Water	---	---	105
Formamide	---	65	60
NMF	---	80	70
DMF	---	90	90
DMSO	---	90	70

Rotational reorientation times are normalized to the solvent viscosity and are given in units of ps/cP. The references for the data are as follows - Oxazine (Ox): 36, 37 and 90; Acridine orange(AO) and Pyronine G (PG): 36 and 37.

Table 4

Rotational Reorientation Times Normalized to Solvent Viscosity for
Oblate, Dianionic Xanthene Dyes

Solvent	RB	E	Fl	EB	TCTIF
Methanol	308	---	230	---	383
Ethanol	430	350	308	320	400
n-Propanol	390	370	350	350	398
i-Propanol	360	---	---	---	---
Butanol	---	---	380	---	350
Pentanol	460	---	510	400	---
Decanol	460	270	320	430	---
Water	---	550	90	---	340
Formamide	180	---	120	160	---
NMF	303	---	150	---	---
DMP	200	---	150	---	---
DMSO	180	120	100	200	---

Rotational reorientation times are normalized to the solvent viscosity and are given in units of ps/cP. The references for the data are as follows - Rose bengal(RB): 36, 37, 38, 82, and 77; Eosin(E): 36, 37 and 77; Flourescein(Fl): 36 and 37; Eosin B(EB): 36 and 37; TCTIF: 84.

Table 5

Rotational Reorientation Times Normalized to Solvent Viscosity for
Non-Xanthene Dyes

Solvent	DODCI	DPB	BBOT
Ethanol	140	---	175
1-Propanol	135	---	---
Butanol	147	---	---
Decanol	132	---	---
Cyclohexane	---	---	180
Tetradecane	---	66	---

Rotational reorientation times are normalized to the solvent viscosity and are given in units of ps/cP. The references for the data are as follows - DODCI: 81, 82, 83, 90, and 92; Diphenylbutadiene(DPB): 91; BBOT: 78.

were not apparent. The difficulty in observing deviations from the SED equation predictions are augmented by the fact that results from different dye molecules are not directly comparable. The rotation times must be normalized by the hydrodynamic volume of the solute. The effective rotational volume and shape of these complex dye molecules are difficult to estimate, as discussed in previous sections. Comparison of results from different dye molecules is limited by the accuracy with which their volumes can be calculated and compared. Based on the limitations imposed by the complexity of the systems studied, it is imperative that studies of rotational reorientation dynamics be performed under a variety of experimental conditions. In some previous studies the scope of the experiments were sufficient to observe the apparent discrepancies between experimental results and the SED predictions. In fact, a variety of conflicting hypotheses have evolved to explain these apparent discrepancies. Most explanations invoke variable boundary conditions in an attempt to reconcile the results with the predictions of the SED equation.

Extensive studies with interesting interpretations have been presented by Eisinger et al.⁷⁶, Lessing and Von Jena^{35-37,74,87}, Fleming and coworkers^{77-83,88-92}, and Spears and Cramer³⁸. Much of the data presented in Tables 1-5 are from these four groups. A more detailed account of some of the hypotheses that have been presented by these groups will be described in the following paragraphs.

Some of the first measurements of rotational reorientation times were performed by Eisinger and Drexler^{76b}. Eisinger and Chuang later studied the rotation of R6G in a series of linear alcohols as well as formamide, chloroform, and ethylene glycol^{76a}. The main

focus of this study was to examine the effects of hydrogen bonding on rotational reorientation dynamics. Saturation effects were also observed in the study of Eisinger et al. These effects are a topic of current controversy. Briefly, it was concluded that as the size of the solvent molecule approaches the size of the solute, a saturation effect is observed. Beyond this point, if the solvent size is further increased, the rotation time is no longer accurately predicted by the SED equation. The original goal of this work was to observe non-hydrodynamic behavior. Hydrogen bonding solvents were chosen with the expectation that their strong and specific interactions would make molecular aspects important. A linear dependence of τ on n was observed for the linear alcohols. The results in formamide and chloroform also fell on this line. Hydrogen bonding in the former solvents is dramatically different than in the latter solvents, yet the rotational behavior appears to be quite similar. This observation led to the conclusion that hydrogen bonding does not cause deviations from SED behavior. Eisinger et al. further argued that the hydrodynamic volume of hydrogen bonded complexes between R6G and solvent molecules would vary with the size of the solvent molecule. Since the size of the hydrogen bonded complex varies with solvent size, a non-linear dependence of τ on n would be expected. The authors thus concluded that rigid complexes of R6G and solvent molecules did not form. This conclusion is consistent with the concept that hydrogen bonds are both flexible and dynamic in alcohol solutions. The Eisinger et al. study makes no mention of the shape of the solute molecule. They present their results as being consistent with isotropic diffusion and stick boundary conditions.

Extensive work in the field of rotational reorientation has been performed by Lessing and von Jena^{36,37,74,87}. Their work has included both a wide variety of solutes and solvents. In a study of rotational reorientation dynamics of xanthene dyes in series of alcohols, Lessing and von Jena observed a general trend in the ordering of rotation times for the various solute structures. They noted that the rotation time decreased for solutes in the order: dianions > oblate cations > asymmetric cations > prolate cations. In conflict with the conclusions of Eisenthal et al., Lessing and von Jena propose the formation of specific hydrogen bonding complexes to explain their data. The dianions which were studied all contain an exposed, negatively charged oxygen atom at the 3,6 position, highly accessible for hydrogen bonding to solvent molecules. The amino groups on the cations are also hydrogen bonding species, but the authors argue that they are less accessible due to steric hindrance. The series of oblate cations included molecules with and without carboxyl groups. There was little difference between the various cations, hence the conclusion that this group does not play a significant role in determining rotation times.

The difference between the hydrodynamic volumes and shapes of the prolate versus the oblate cations is not sufficient to explain the dramatic difference in rotation times. Lessing and von Jena invoke the "paddle wheel effect", originally proposed by Fleming et al.⁷⁷, to explain this discrepancy. In this model the additional phenyl group on the oblate cations acts like a paddle wheel sweeping out solvent molecules. This concept is only possible for solvent molecules which are able to become entangled in the projecting phenyl group, and is not consistent with a continuum description. This model would also explain

the results obtained for the asymmetric molecules CV and PG. CV and PG also have an additional phenyl group, but it is attached in a more compact manner, fused at the 1,2 position in the xanthene structure. The rotational reorientation times of CV and PG fall correspondingly between those of the prolate and oblate cations.

The model of Lessing and von Jena includes rigid, hydrogen bonded complexes for oblate dianions, whereas steric effects are proposed as being predominant in the case of oblate cations, even though hydrogen bonding effects certainly also occur for cations. Additional support for the model was found in their results from studies in non-alcohol solvents. DMSO has proton-accepting but not proton-donating capabilities, and is of a similar viscosity to propanol. Oblate dianions which are only proton accepting rotate more rapidly in DMSO than in propanol. The oblate cations play the role of both proton acceptor and proton donor, consistent with the result that they have similar rotational reorientation times in both DMSO and propanol. Formamide and pentanol have similar viscosities and either solvent can serve as a proton donor and as a proton acceptor. All of the molecules studied rotated more rapidly in formamide than in pentanol. Since formamide is smaller than pentanol, the solvent-solute hydrogen bonded complex would be expected to have a faster rotation time. This rationale also explains the intermediate rotation time in N-methylformamide (NMF), and the faster rotation time in water. This explanation, however, is in direct conflict with the results of Eisinger et al. To test their hypothesis, Lessing and von Jena repeated the Eisinger experiment with the more strongly hydrogen bonding species Fl. They observed curvature of the plot of τ versus η for the series of linear alcohols,

as would be expected for a solute-solvent complex model.

As noted above for other intermediate-sized molecules, quantitative comparison of these experimental results to the predictions of the SED equation is difficult due to the uncertainties in the calculation of the hydrodynamic volume of the dyes. The general qualitative conclusions made by Lessing and von Jena are summarized here. The more regularly shaped, prolate molecules fit the SED model somewhere between slip and stick boundary conditions. The more complex shapes such as the oblate molecules often rotate too slowly to accommodate the SED equation even in the stick limit. The dianions are an extreme example of this kind of disagreement. The discrepancies are partially resolved by invoking hydrogen bonded complexes and steric effects, but anomalies remain. For example, CV is an asymmetric cation but rotates much more slowly than predicted. Further, only specific hydrogen bonding sites appear to play a role in controlling the dynamics of rotational motion. The nature of the differences between the various hydrogen bonding sites is not clear.

Spears and Cramer³⁸ offer an alternative model of the effect of solvent-solute interactions on rotational lifetimes. Instead of hydrogen bonded complexes between specific solvent molecules and the solute, they suggest that a polar solvent exerts a torque on the solute molecule. Dye molecules are assumed to rotate under slip boundary conditions but rotation is slowed by the electrostatic forces between the ionic solute and the polarized solvent environment. The results of dianion rotation in alcohols is explained by the interaction of the highly polarizable alcohol environment with the two negatively charged oxygen atoms. The faster rotation times in NMF are explained by the

fact the the nitrogen atoms (the positive end of the solvent dipole) in NMF are less polarizable and therefore exert less torque due to solvation. The faster rotation times of oblate cations are a result of the fact that these solutes have only half of the total charge, so less solvent torque is expected. This model is a good qualitative rationale for observed experimental results, but has limited predictive value.

Extensive work has been performed by Fleming and coworkers in a series of experiments. For cationic xanthene dyes as well as for DODCI, Fleming et al. conclude that the SED equation for ellipsoid shaped molecules with stick boundary conditions is an accurate model of their experimental results^{81,90,92}. For dianionic dyes these authors favor the solvent attachment concept⁷⁷. As a further probe of the role of hydrogen bonding between solute and solvent, Fleming et al. also studied the neutral molecules BBOT⁷⁸ and DPB⁹¹. These molecules are both modeled as prolate symmetric tops. DPB was studied in tetradecane, and BBOT in ethanol and cyclohexane. These studies indicated that both molecules rotated as predicted by the SED equation with slip boundary conditions. The dramatically different behavior of dianionic, cationic, and neutral molecules was explained in terms of hydrogen bond strengths. The authors noted that hydrogen bonds in RB are much stronger than those in R6G or DODCI, which in turn were much stronger than hydrogen bonds to BBOT. Hydrogen bonds are both flexible and dynamic. Fleming et al. suggest that the rate of hydrogen bond formation and dissolution is related to the strength of the hydrogen bond itself. Thus, the dianions may have hydrogen bonds that are sufficiently strong to remain intact on the timescale of molecular rotation. Rotation times for these molecules may be calculated using slip boun-

dary conditions, but the hydrodynamic volume is that of the solute-solvent bound complex. The hydrogen bonds in cations are presumed to break and reform on the timescale of molecular rotation. The net effect is that hydrogen bonds exert a drag on the solute which is equivalent to stick boundary conditions. In neutral molecules containing electronegative atoms, the hydrogen bond formation rate is fast compared to rotation times and slip boundary conditions are observed. The studies of neutral molecules were performed in a limited number of solvents, but appear to be consistent with the model presented.

Another interesting study performed by the Fleming group was to observe the rotational reorientation time of DODCI as a function of temperature⁹². For comparison with the temperature measurements, the rotational times of DODCI were also measured at a fixed temperature in a series of linear, normal alcohols, including methanol through hexanol, octanol, and decanol. The authors observe a discrepancy between the solvent variation study and the temperature variation study which they attribute to a saturation effect in the solvent study. Fleming et al. propose that the saturation effect does not occur when viscosity is changed via temperature variation. They conclude that anomalies due to solvent variation lead to non-hydrodynamic effects which are not present in the temperature variation studies.

The role of hydrogen bonding in rotational phenomena in solution is not clear. The experimental results from the literature argue both in favor of and against the formation of solute solvent complexes. Clear trends exist for charged solute molecules, but questions remain concerning a quantitative explanation of the results. Finally, the influence of solute shape and boundary conditions have been studied,

but again our understanding is far from complete.

Although more extensive work has been performed using steady state techniques on simple molecules, it does not provide a basis for understanding the existing time-resolved results. For simple systems in non-associated liquids, extensive steady state experiments support the model of slip boundary condition theories^{27,30,101}. This conclusion is supported by molecular dynamic simulations^{95,96}. In more complicated interacting systems (e.g. hydrogen bonding systems), intermediate or stick boundary conditions may apply^{30,46,98}. Larger molecules fall into the stick boundary condition regime^{99,100}. As in the experiments described above, predicting the behavior of these systems is difficult.

An additional parameter has been varied in some steady state rotational measurements that has not yet been exploited in time-resolved measurements. Jonas and coworkers have monitored rotational reorientation times as a function of pressure. In these experiments slip boundary conditions accurately described the data for non-associated (although polar) liquids¹⁰². In hydrogen bonded systems, anomalous effects occurred which suggested to the authors that hydrogen bonded complexes were formed¹⁰³. These complexes were postulated to undergo non-diffusional librations even at very high pressures. Studies of the hydrogen bonded liquid, glycerol, at high pressures supplied additional interesting results. It was found¹⁰⁴ that the hydrogen bonded network in glycerol was relatively insensitive to density changes, whereas temperature changes caused more dramatic effects. These intriguing results clearly demonstrate the value of pressure as an experimental parameter in the study of rotational reorientation times.

The use of pressure in time resolved measurements of the rota-

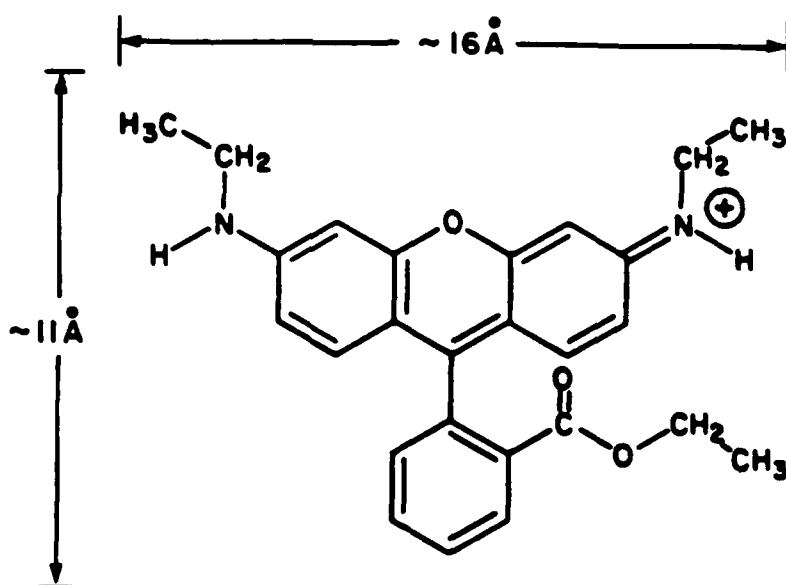
tional reorientation times of intermediate sized molecules seemed promising based on the above results. Ambient pressure, steady state measurements indicate that intermediate sized molecules may fall in an interesting regime between slip and stick boundary conditions. Further study of intermediate sized molecules with solvent variation as well as pressure variation is warranted. Steady state results at both ambient and elevated pressures, as well as time-resolved measurements suggest that further information is required on charged and hydrogen bonding systems to gain a better understanding of these complex systems.

C. Results

The fluorescence lifetimes (τ_f) and the rotational reorientation times (τ) of PTP and R6G are presented in this section. These parameters were determined under a variety of different experimental conditions for each of the solute molecules under consideration. Before the results are presented, there is a brief discussion of the molecular structure of these molecules.

1. Molecular Structure

The molecules in this study were approximated by symmetric top ellipsoids. The structures and approximate dimensions of R6G and PTP are shown in Fig. 16 and 17. R6G was modeled as an oblate ellipsoid and PTP as a prolate ellipsoid. R6G has a transition moment in the plane of the conjugated ring system⁷⁴. This transition moment is perpendicular to the symmetry axis of the ellipsoid. It has been suggested, however, that there is a small angle between the absorption and emission transition moments in R6G. The molecule is somewhat flexible due to rotation of the ethylamine groups at either end of



Rhodamine 6G (R6G)

Figure 16 - Molecular structure of rhodamine 6G. The dimensions given are only approximate, because of the complexity of the molecule. Although the charge is shown localized on one of the nitrogens, the charge actually resonates between both of the amino groups. The phenyl group is rotated slightly out of the plane due to steric hindrance.

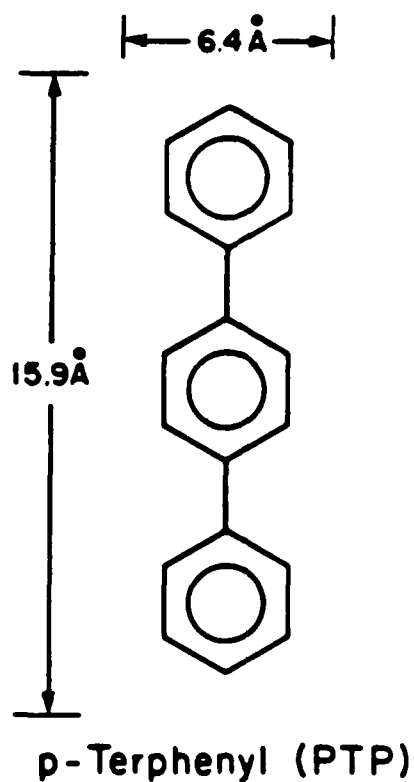


Figure 17 - Molecular structure of p-terphenyl. The dimensions given represent the van der Waals radii of the molecule. The phenyl groups are slightly twisted with respect to one another due to steric hindrance. The van der Waals thickness of a phenyl group is approximately three and a half angstroms.

the three ring system and twisting of the phenyl ring. The preferred orientation of the phenyl ring is thought to be canted at approximately 10° with respect to the main ring system as a result of steric hindrance. Although R6G is irregularly shaped, and has some flexible groups, the overall structure of the molecule is still essentially planar in nature. An oblate ellipsoid should provide a reasonable approximation to the actual structure. The positive charge can be assigned to either of the amine groups. Hydrogen bonding can occur at the oxygens or the nitrogens. Thus, there are many possible interactions between solvent molecules and R6G.

PTP makes an interesting comparison to R6G. PTP has two low lying singlet-singlet transitions one to the 1L_a state and the other to the 1L_b state. Transitions to the 1L_a state are polarized along the long axis of the molecule, whereas those to the 1L_b state are polarized perpendicular to this axis⁷². Absorption occurs to both states, but is dominated by the strong absorption to the 1L_a state. The absorption to the 1L_b state is weak by comparison and contributes little to the absorption cross section. Emission occurs from the 1L_a state since it is lower in energy than the 1L_b state.

The geometry of PTP is such that the three phenyl rings are slightly twisted with respect to one another due to steric hindrance⁷⁵. Both the twisted conformation of the molecule and the additional bulk of the π clouds on the rings give PTP roughly cylindrical symmetry. PTP is thus approximated by a prolate ellipsoid with a transition moment along the long axis of the molecule. In addition to the difference in shape, PTP is dramatically different than R6G in other aspects as well. PTP is uncharged and does not hydrogen bond to

solvent molecules. Since PTP is non-interacting, but is moderately polarizable, it will dissolve in a wide variety of solvents, thus facilitating the study of the role of the solvent structure in rotational phenomena. In this work, both R6G and PTP are treated as symmetric tops and $r(t)$ is assumed to be a single exponential decay.

2. Fluorescence Lifetimes

The magnitude of the fluorescence lifetime plays an important role in the analysis of the rotational reorientation data presented in this study. After the $I_{\parallel}(t)$ and $I_{\perp}(t)$ components are independently measured, Eq. 38 is used to determine $r(t)$. Equation 38 requires that $I_{\parallel}(t)$ and $I_{\perp}(t)$ are appropriately normalized to one another. Since a large number of laser shots are averaged, shot-to-shot fluctuations should average out over time. Due to small systematic deviations in each experimental run, it is nonetheless necessary to normalize $I_{\perp}(t)$ to $I_{\parallel}(t)$. The technique used to normalize is known as tail-matching⁷⁷. Tail-matching consists of normalizing the two data sets at times long compared to the rotational time of the molecule. At these long times, the signal is due solely to the fluorescence lifetime (i.e. $F(t)$ in Eqs. 36 and 37) and should be equivalent in both the horizontal and vertical components.

In order to make accurate determinations of rotational times by the method of tail-matching, it is imperative that the fluorescence lifetime (τ_F) be longer than the rotational reorientation time (τ). The value of τ_F is not used in the calculation of τ , however, the magnitude of τ_F is an important aspect to consider when performing the tail-matching procedure. In addition, any unusual quenching

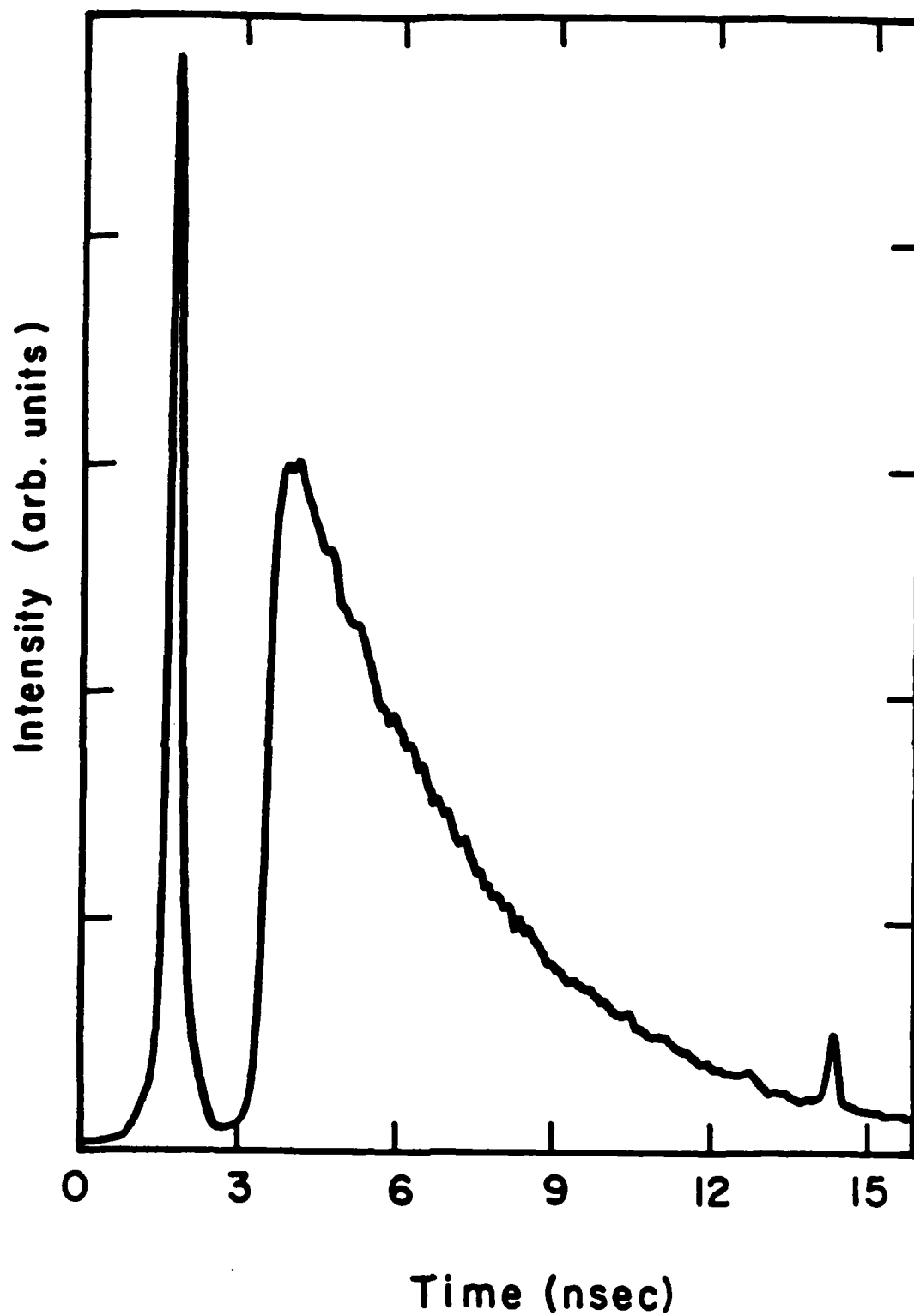


Figure 18 - Fluorescence decay of rhodamine 6G in ethanol. A typical streak camera trace of intensity versus time is shown, including the time marking pulse.

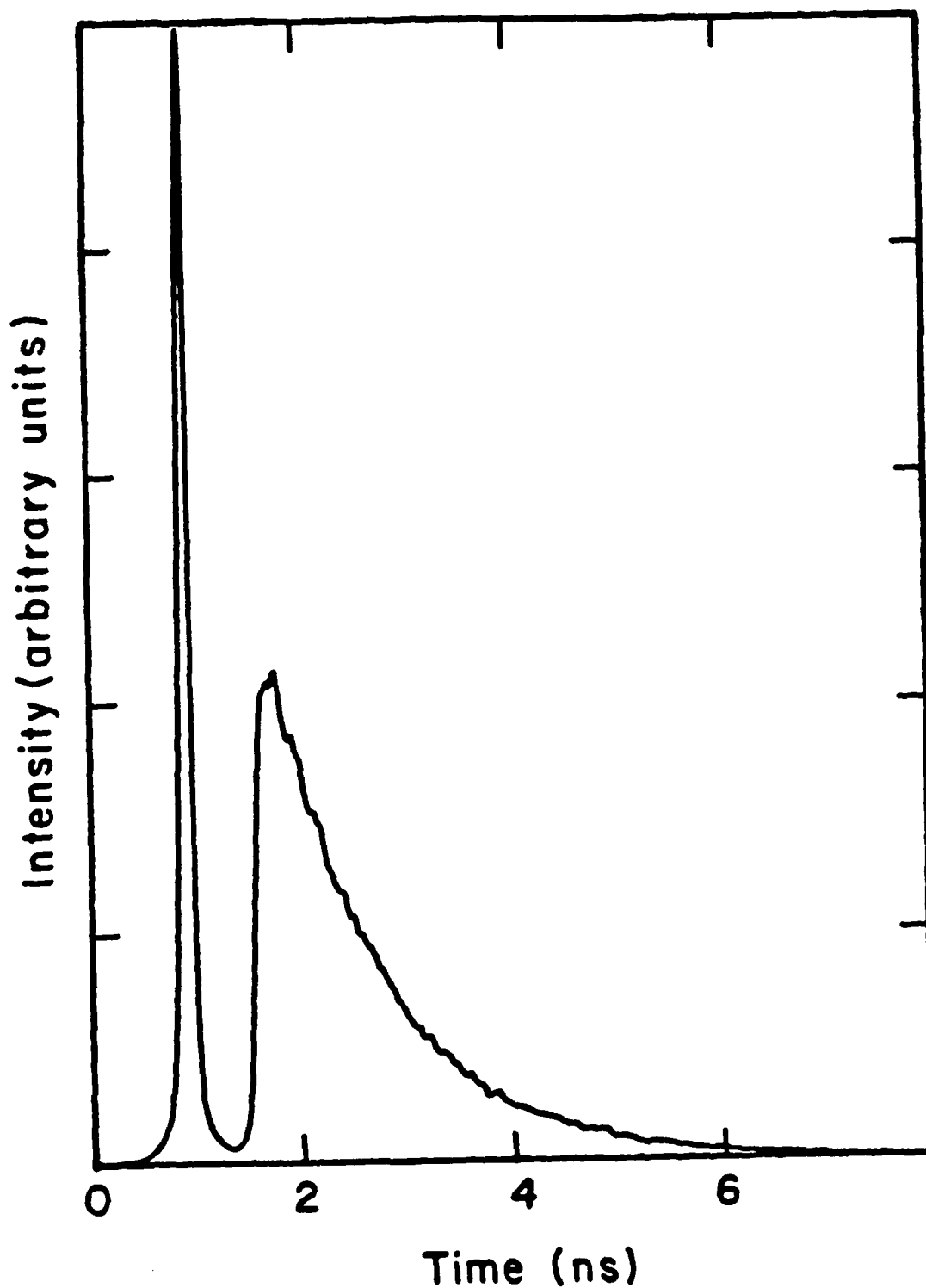


Figure 19 - Fluorescence decay of p-terphenyl in octanol. Notice that for p-terphenyl, the timescale is expanded compared to the rhodamine 6G data in Fig. 18. Higher time resolution is necessary since the lifetime of p-terphenyl is shorter than rhodamine 6G.

of these lifetimes may have ramifications in the quenching of τ as well. Thus, τ_F was determined in all sets of experiments.

τ_F was determined from the decay of fluorescence polarized at the magic angle. Under these conditions, all rotational effects are eliminated. For the solute molecules in this study, the fluorescence decay is single exponential, and the slope of the logarithm of the exponential decay yields the value of τ_F .

Examples of typical data used in obtaining τ_F are given in Figs. 18 and 19. Figure 18 shows the fluorescence decay of R6G in ethanol. Figure 19 shows similar data for PTP in octanol. Notice that the timescale for the R6G decay is much longer than the timescale for the PTP decay. The data in Fig. 18 was taken at a streak rate of 17.4 ps/ch, and that in Fig. 19 of 8.80 ps/ch. The initial, left-most pulse in each of the streak camera traces shown in Figs. 18 and 19 is the time-marking pulse mentioned in Section II.B., hereafter termed the prepulse. The prepulses in both Figs. 18 and 19 appear to have similar widths, although the timescales in each figure are quite different. In addition, the prepulse appears to be much longer than the known laser pulsewidth of ~ 25 ps. On these slow streak speeds the temporal width of the prepulse is solely determined by the instrument response function. In the case of PTP and R6G dissolved in the solvents used in this study, τ_F is much longer than either the temporal width of the excitation pulse or the instrument response function. The relative intensity of the fluorescence decay to the prepulse is not meaningful, because the intensity of each signal is attenuated independently.

Another interesting contrast between Figs. 18 and 19 is the small peak which occurs at the tail of the fluorescence decay in Fig. 18 but

not in Fig. 19. The peak occurs approximately 10 ns after the prepulse, which is the round trip cavity time of the laser. The peak is a fraction of an additional pulse which has been extracted from the pulse train by the pulse selector. This second pulse occurs at times long compared to τ_p and therefore does not interfere with analysis.

The value of τ_p is determined from a plot of $\log(\tau_p)$ versus time, such as the one shown in Fig. 20. The semi-log plot shown in Fig. 20 is of the decay of PTP in acetonitrile, and is linear for over five lifetimes of the decay. The value of τ_p was determined from the slope of the line to be 1120 ps.

Table 6 gives results for the determination of τ_p for R6G under the various experimental conditions studied here. Table 7 gives similar results for PTP. The uncertainties for all of the results given in Tables 6 and 7 are $\pm 10\%$. For the R6G results, all values of τ_p are equivalent to within the experimental uncertainties, regardless of solvent or pressure. The average of these values, 3.6 ns, is significantly longer than any of the observed rotation times.

There is a larger variation in τ_p for PTP in different solvents, as seen in Table 7. The average value of τ_p for PTP dissolved in alcohol or n-alkane solvents is 1070 ps. The only significant deviation from this result occurs for the solvents containing chlorine atoms. From Table 7, one observes that τ_p appears to be related to the number of chlorine atoms per solvent molecule for the series methylene chloride (950 ps) and chloroform (700 ps). In addition, when the solvent carbon tetrachloride (not shown) was used, τ_p was less than 100 ps. Carbon tetrachloride was eliminated from the study because the lifetime of PTP was too short in this solvent to enable proper

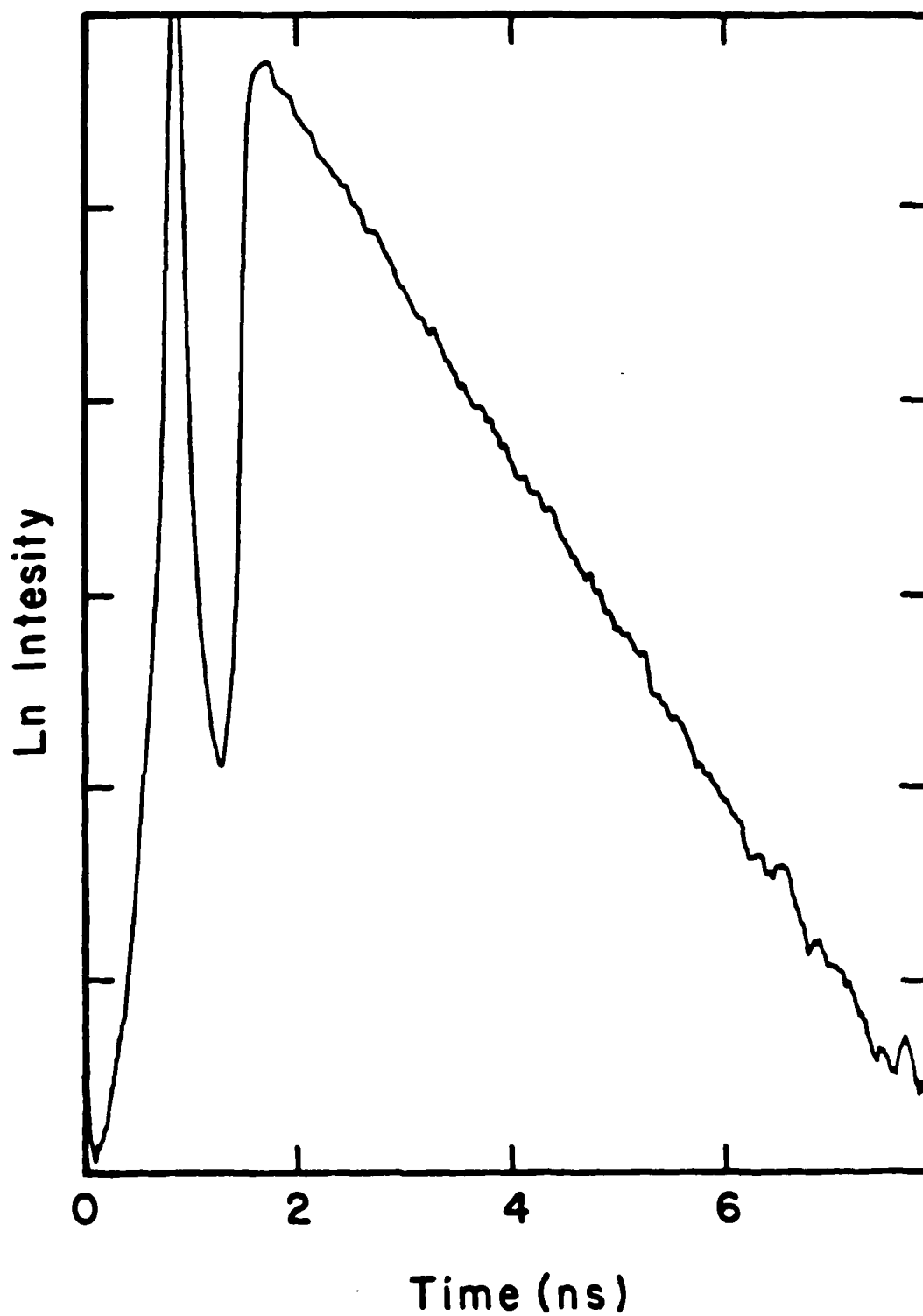


Figure 20 - Semi-log plot of the fluorescence decay of p-terphenyl in acetonitrile. τ is determined from the slope of the line shown here. The plot is linear over five lifetimes.

Table 6

Flourescence Lifetimes of R6G as a Function of Solvent and Pressure.

Solvent	τ_p (ns)
Methanol	3.9
Ethanol	3.6
Propanol	3.7
Butanol	3.6
Pentanol	3.6
Octanol	3.5
Ethanol(5.5 kbar)	3.4

All of the data is at ambient pressure unless otherwise specified.
The uncertainty in the data is $\pm 10\%$.

Table 7

Flourescence Lifetimes of PTP as a Function of Solvent and Pressure.

Solvent	τ_F (ps)
Methanol	1140
Ethanol	1070
Pentanol	1020
Octanol	1100
Hexane	970
Undecane	1100
Acetonitrile	1120
DMF	1140
Cyclohexane	980
Methylene Chloride	950
Chloroform	700
Ethanol	
3.44 kbar	1010
3.86 kbar	1010
Octane	
3.48 kbar	1020
3.99 kbar	1020
Chloroform	
2.58 kbar	510
2.94 kbar	500
3.46 kbar	480
3.95 kbar	460

All of the data is at ambient pressure unless otherwise specified.
 The uncertainties in the data are $\pm 10\%$.

tail-matching. Chloroform was used in high pressure experiments. Table 7 shows that quenching was observed in this solvent as a function of pressure. At the highest pressure, τ_F remained long enough to obtain accurate rotation times. No quenching of τ_F was observed in any of the other solvents used in high pressure experiments.

2. Rotational Reorientation Times

Rotational reorientation times were calculated by the procedure described in Section III.B.2. An example of the vertical and horizontal components of fluorescence decay is shown in Fig. 21. The vertical component has an additional decaying exponential superimposed on the fluorescence lifetime in accordance with Eq. 36. The horizontal component has a corresponding risetime superimposed on the fluorescence lifetime. At times long compared to the rotation time, the anisotropic portion of the decay in both the vertical and the horizontal components becomes insignificant and the decay is dominated by the fluorescence lifetime. In this region, the two curves are tail-matched. After three rotational lifetimes the anisotropic portion of the decay comprises less than 5% of the total fluorescence, and less than 2% after 4 rotational lifetimes.

In Fig. 21 the curves are tail-matched at slightly less than three lifetimes in the region between 4.2 and 5.1 ns. The value of τ was also determined for these experimental conditions at a slower streak speed where it was possible to tail-match at longer times. The results agreed within experimental uncertainty. Most experiments were performed at two different streak speeds and good agreement was found between data taken at different streak speeds. All of the data was

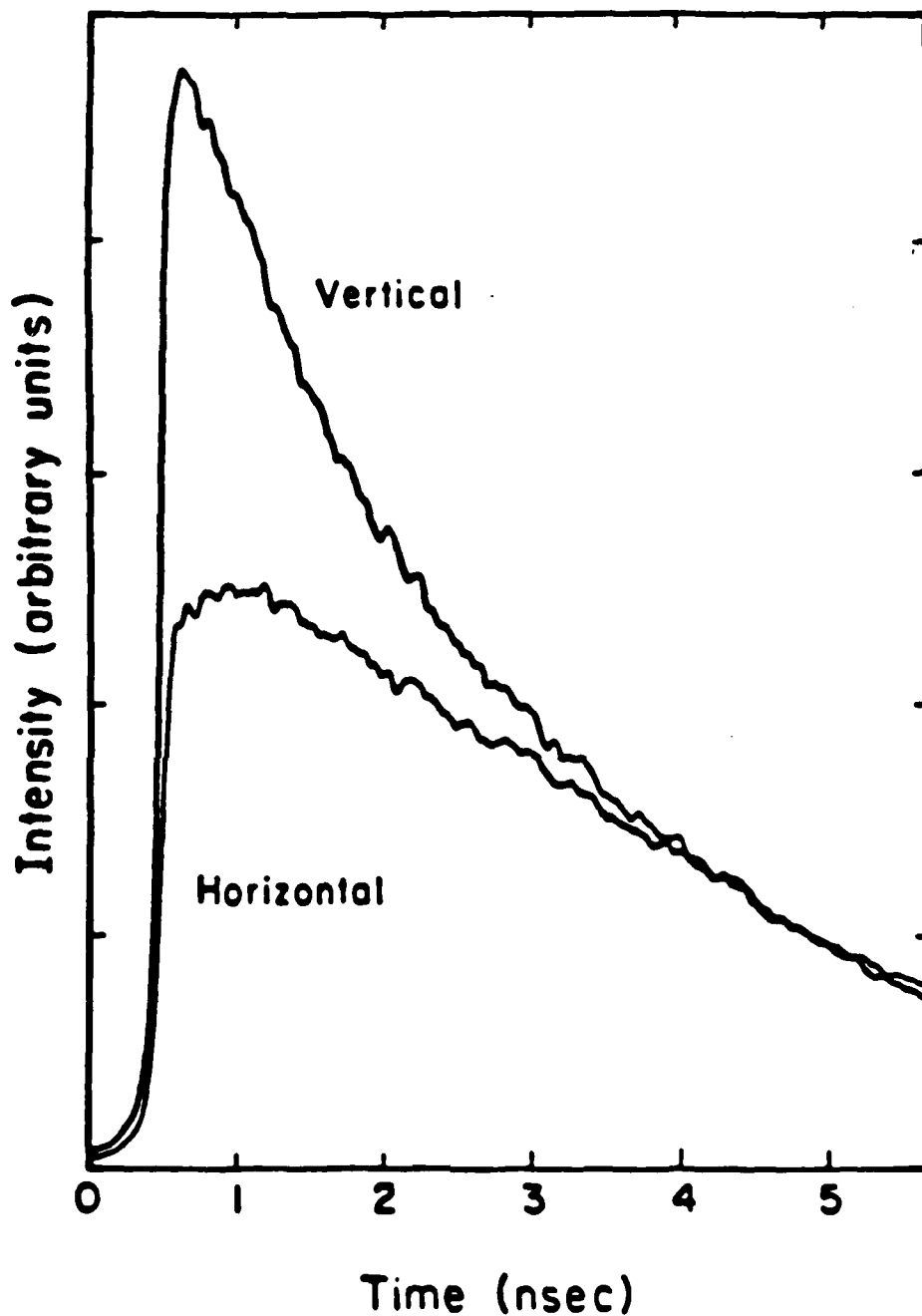


Figure 21 - Vertical and horizontal components of the fluorescence decay of rhodamine 6G in ethanol. This data was taken at 5.4 kbar. The two data sets were tail-matched between 4.2 and 5.1 ns.

checked at streak speeds where tail-matching could be performed at times longer than four rotational lifetimes.

Figures 22 and 23 each show a sequence of pairs of vertical and horizontal components of fluorescence decays. PTP is the fluorescing species for all of the decays shown in these two figures. In Fig. 22 a, b, and c, PTP is dissolved in butanol, ethanol, and methanol, respectively. Figure 23 a, b, and c show data from PTP in ethanol at 1.5 kbar, 0.74 kbar, and ambient pressure, respectively. In all six cases, the vertical and horizontal components were tail-matched over the region of the last 20 ps of the time period illustrated in the figures. Notice that although all traces were normalized over the same region, the anisotropy decays more slowly in Fig. 22a than in 22c. In Fig. 22c, the anisotropy becomes insignificant (i.e. the vertical and horizontal components of the decay become indistinguishable) by ~ 275 ps. In Fig. 22b the two curves coincide at ~ 325 ps, and not until ~ 400 ps for the data in Fig. 22a. This trend is a graphic illustration of the increase of rotation time over the sequence of solvents methanol, ethanol, and butanol. A similar trend is observed for increasing pressure, as demonstrated in Fig. 23.

To obtain the rotational reorientation time, the rotational anisotropy function $r(t)$ is derived from the vertical and horizontal components according to Eq. 38. The function $r(t)$ for the data depicted in Fig. 21 is shown in Fig. 24. The decay in Fig. 24 is well described by a single exponential. The rotational reorientation time is determined from the slope of a semi-log plot of $r(t)$ as in the calculation of τ_p . A sequence of five semi-log plots of $r(t)$ for R6G in ethanol as a function of pressure is shown in Fig. 25. The five

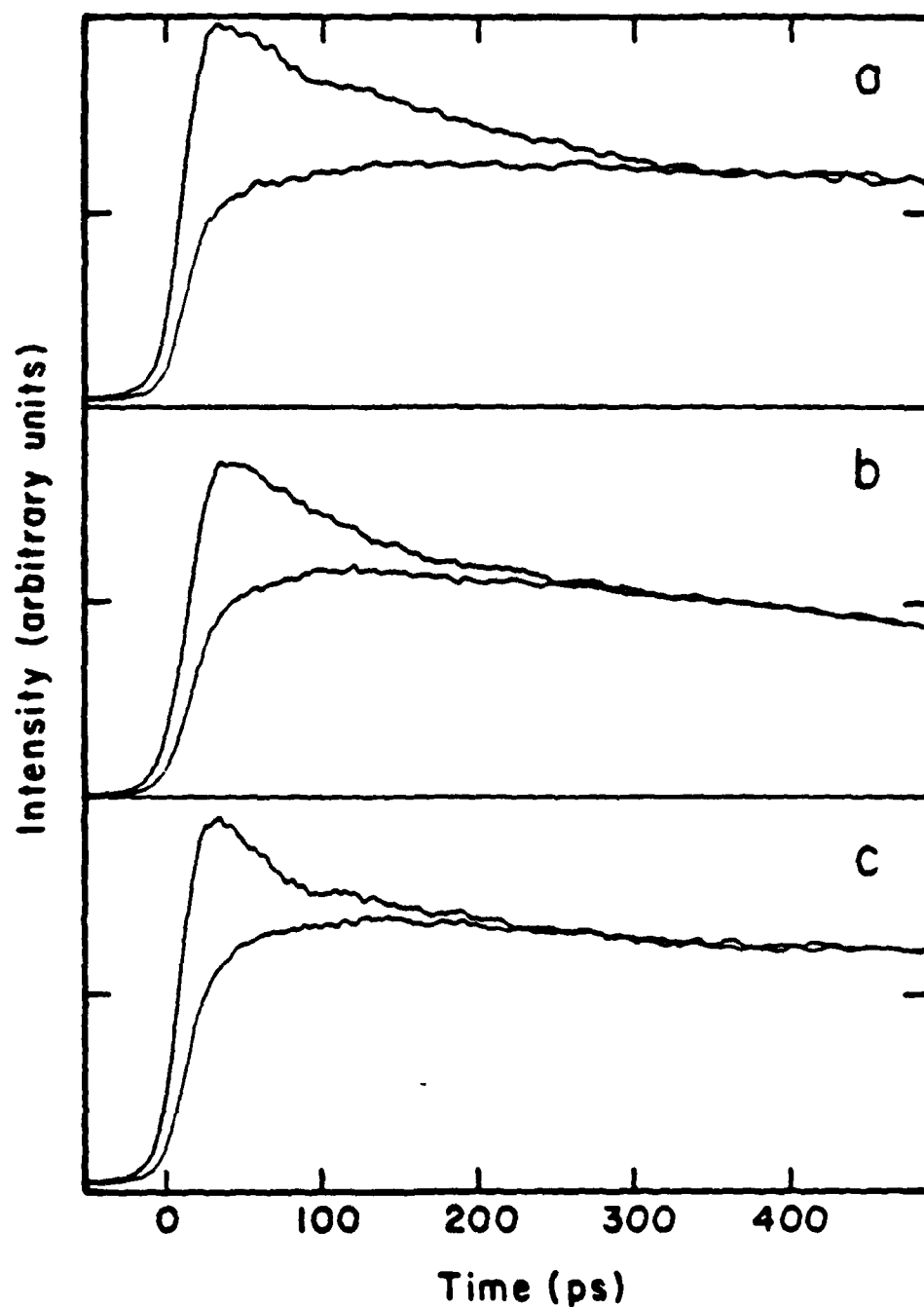


Figure 22 - Vertical and horizontal components of the fluorescence decay of p-terphenyl in various solvents. The solvents in a, b and c were butanol, ethanol, and methanol respectively. In all three cases, the vertical and horizontal components were tail matched over the last 20 ps depicted in the figure. The rotational reorientation time decreases over the sequence from a to c.

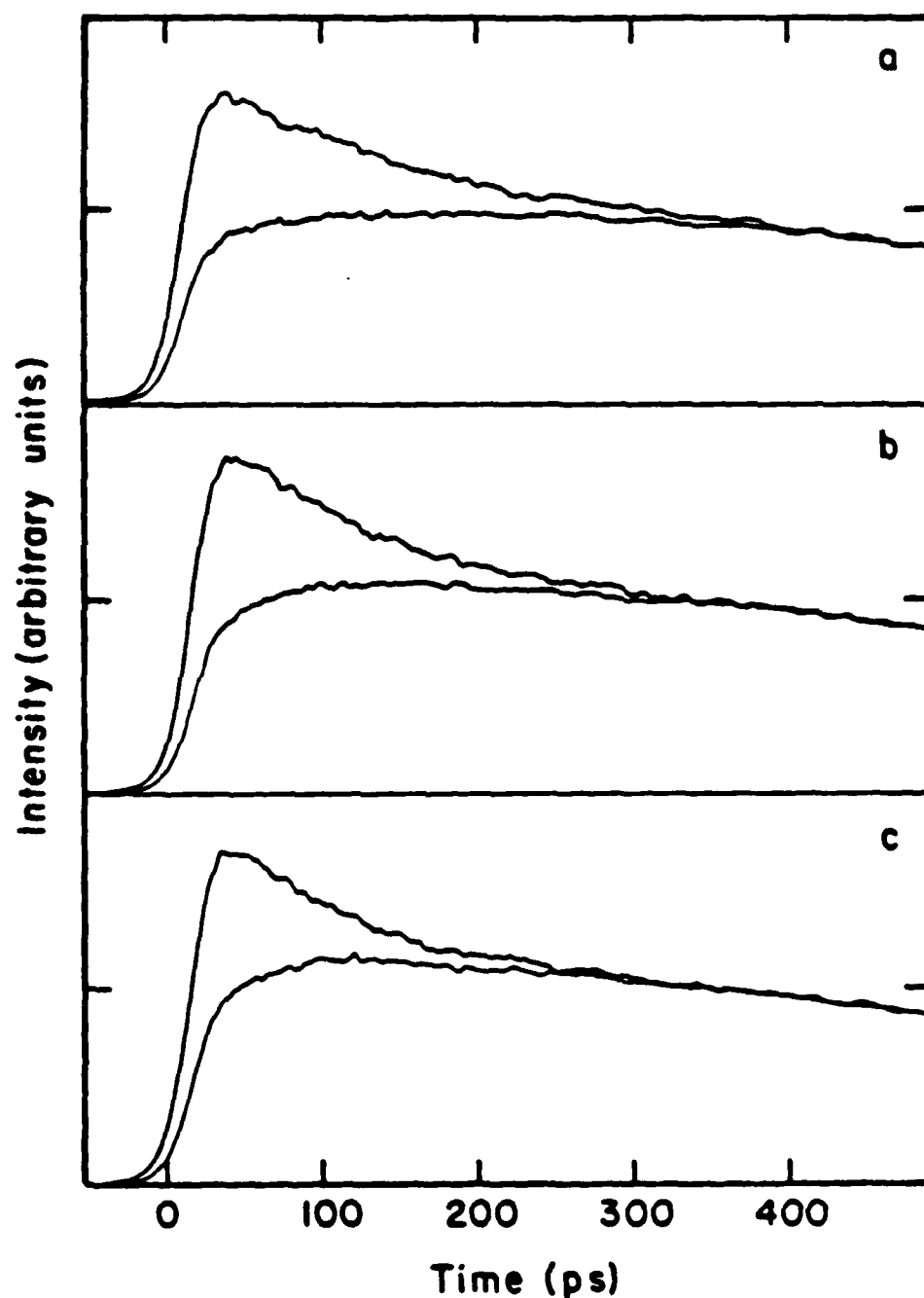


Figure 23 - Vertical and horizontal components of the fluorescence decay of p-terphenyl in ethanol at various pressures. The data in a, b, and c were taken at 1.5 kbar, 0.74 kbar and ambient pressure respectively. The data in all three cases were tail-matched over the last 20 ps depicted in the figure. As in the previous figure, the rotational reorientation times decrease over the sequence from a to c.

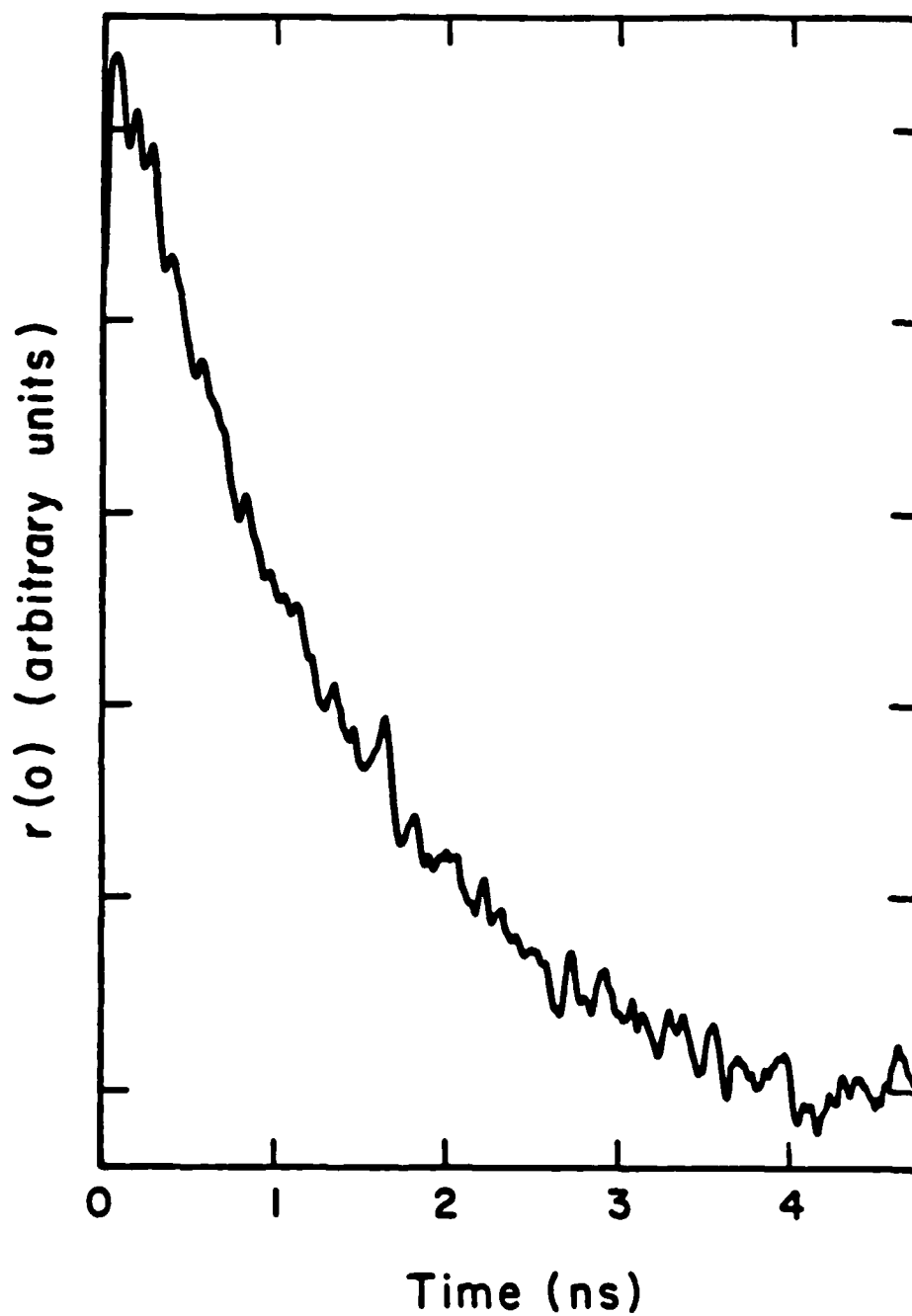


Figure 24 - Rotational anisotropy for rhodamine 6G in ethanol at 5.4 kbar. The plot here is derived from the data shown in Fig. 21, using Eq. 38.

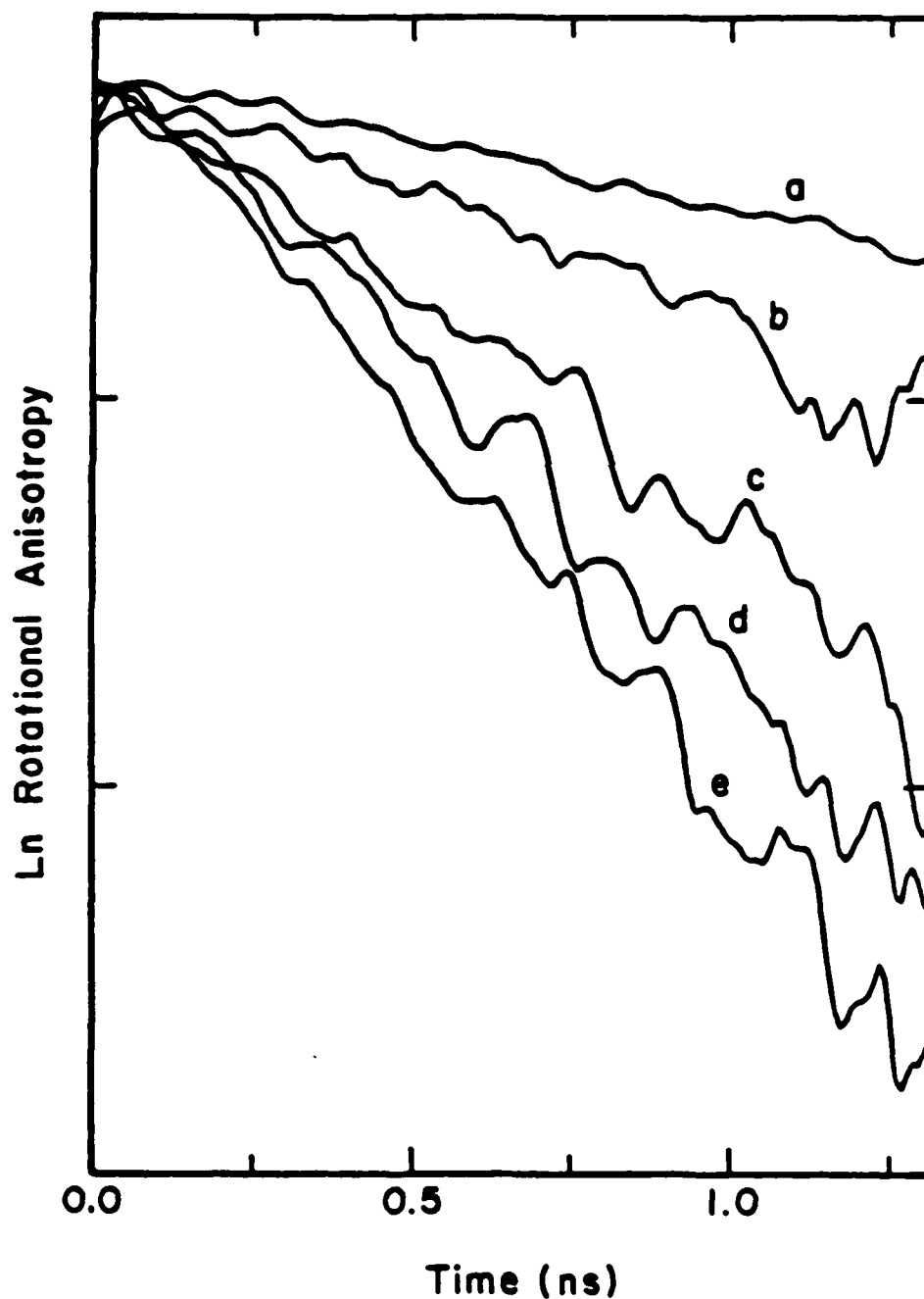


Figure 25 - Semi-log plots of the rotational anisotropy of rhodamine 6G in ethanol at various pressures. The plots depicted here are from data taken at five different pressures. The experimental pressures were: a) 5.4 kbar; b) 4.0 kbar; c) 3.3 kbar; d) 2.5 kbar; e) 2.0 kbar. τ is determined from the slope of these lines.

plots in Fig. 25 are from data taken at pressures of 5.4 kbar, 4.0 kbar, 3.3 kbar, 2.5 kbar, and 2.0 kbar. The slope of the lines increase with pressure, indicating an increase of τ with pressure.

A tabulation of τ and η for R6G may be found in Tables 8 and 9. Table 8 contains the values of τ and η for R6G dissolved in a series of linear alcohols at room pressure. The results for R6G in ethanol at a series of different pressures is found in Table 9. Tables 10-14 contain similar information for the PTP experiments. Table 10 presents the values of τ and η for PTP dissolved in a series of normal alcohols, a series of normal alkanes, and five other solvents. The results of high pressure experiments are given in Tables 11-14 for the solvents hexane, octane, ethanol, and chloroform, respectively. The values of η were determined directly for the room temperature experiments. For the high pressure experiments the viscosity values are taken from Bridgman¹², corrected to 20°C.

In an effort to determine the limits of the accuracy of the experimental results, a series of computer simulations were performed. Many of the τ values in Tables 8-14 approach the 25 ps pulsewidth of the laser at one extreme or the fluorescence lifetime of the solute molecule at the other extreme. Computer simulated data at both of these extremes were analyzed by the methods used in this study. Values of τ on the order of 10 ps could be determined accurately, if care was taken to measure the slope of the semi-log plot of $r(t)$ at times greater than the pulsewidth. The limitation of time resolution is caused by limitations in the signal-to-noise ratio. If the pulse width is 25 ps, and τ is 10 ps, then after 25 ps of the decay, two and a half rotational lifetimes have transpired. Thus, there is little

Table 8
Rotational Reorientation Times of R6G as a Function of Solvent

Solvent	$\eta(\text{cP})$	$\tau(\text{ps})$
Methanol	0.53	110 ± 20
Ethanol	1.1	280 ± 20
1-Propanol	2.0	575 ± 75
1-Butanol	2.6	875 ± 50
1-Pentanol	3.5	1200 ± 100
1-Octanol	8.2	3000 ± 300

Table 9
Rotational Reorientation Times of R6G in Ethanol as a Function of Pressure

Pressure(kbar)	$\eta(\text{cP})$	$\tau(\text{ps})$
ambient	1.2	280 ± 50
1.98	2.75	500 ± 50
2.53	3.3	580 ± 60
3.32	4.2	900 ± 50
4.09	5.1	950 ± 100
5.46	7.2	1500 ± 240
6.05	8.4	1660 ± 300

Viscosities are taken from Bridgman¹², corrected to 20°C.

Table 10

Rotational Reorientation Times of PTP as a Function of Solvent

Solvent	$\eta(\text{cP})$	$\tau(\text{ps})$
Normal Alcohols		
Methanol	0.53	40 ± 5
Ethanol	1.1	69 ± 7
Propanol	2.0	113 ± 12
Butanol	2.6	120 ± 12
Pentanol	3.5	150 ± 15
Hexanol	4.6	206 ± 20
Octanol	8.2	277 ± 30
Normal Alkanes		
Hexane	0.28	25 ± 5
Heptane	0.40	30 ± 5
Octane	0.51	36 ± 5
Nonane	0.68	39 ± 5
Decane	0.88	55 ± 6
Undecane	1.13	79 ± 8
Hexadecane	3.27	175 ± 35
Other Solvents		
Acetonitrile	0.35	29 ± 5
Methylene Chloride	0.40	33 ± 5
Chloroform	0.55	48 ± 5
DMF	0.85	73 ± 7
Cyclohexane	0.93	62 ± 6

Table 11
Rotational Reorientation Times of PTP in Hexane as a Function of
Pressure

Pressure(kbar)	η (cP)	τ (ps)
ambient	0.30	24 ± 5
0.695	0.46	38 ± 5
1.13	0.62	39 ± 5
1.50	0.75	60 ± 10
2.03	0.98	65 ± 5
2.52	1.2	69 ± 10
3.02	1.5	87 ± 9
3.55	1.8	101 ± 10
3.99	2.1	115 ± 20

Viscosities taken from Bridgman¹², corrected to 20°C.

Table 12
Rotational Reorientation Times of PTP in Octane as a Function of Pressure

Pressure(kbar)	η (cP)	τ (ps)
ambient	0.43	42 \pm 5
0.596	0.75	60 \pm 6
1.08	1.0	74 \pm 8
1.51	1.3	105 \pm 10
1.99	1.8	121 \pm 12
2.50	2.4	170 \pm 17
2.99	3.2	177 \pm 18
3.48	3.9	194 \pm 50
3.99	4.9	249 \pm 25

Viscosities taken from Bridgman¹², corrected to 20°C.

Table 13
Rotational Reorientation Times of PTP in Ethanol as a Function of
Pressure

Pressure(kbar)	η (cP)	τ (ps)
ambient	1.2	66 ± 7
0.74	1.75	77 ± 8
1.11	2.0	96 ± 10
1.50	2.4	114 ± 12
2.00	2.8	145 ± 15
2.49	3.3	175 ± 18
2.96	3.8	200 ± 20
3.44	4.4	209 ± 21
3.86	4.9	240 ± 50

Viscosities taken from Bridgman¹², corrected to 20°C.

Table 14

Rotational Reorientation Times of PTP in Chloroform as a Function of Pressure

Pressure(kbar)	η (cP)	τ (ps)
ambient	0.48	50 \pm 10
0.99	0.66	64 \pm 6
0.66	0.79	66 \pm 7
1.51	1.0	96 \pm 10
2.03	1.3	97 \pm 10
2.58	1.5	109 \pm 10
2.94	1.6	131 \pm 13
3.46	1.8	153 \pm 13
3.95	2.1	160 \pm 30

Viscosities taken from Bridgman¹², corrected to 20°C.

difference between the vertical and horizontal components of the fluorescence. The smallest value of τ observed in this study is 25 ps, which is well within the detection limit.

At the other extreme, large values of τ , the problems in analysis are different. If τ is close to the value of τ_p , then after three lifetimes of τ , most of the excited state population has decayed away as well. Thus, the total fluorescence signal is small and accurate tail-matching is limited by the signal-to-noise ratio. The only data taken near this extreme occur in the case of R6G in octanol. Computer simulation of this data reveals that these results are reliable to within 5-10% accuracy.

Another source of error in the data is scrambling of the polarization due to stress birefringence induced in the cell windows by high pressure. Experiments were performed to determine the extent of polarization scrambling at high pressures. The vertically polarized laser was passed through the cell containing ethanol. The polarization of the output beam was monitored as the cell was pressurized. These experiments were performed with BK7 windows in the cell. The polarization scrambling was insignificant at pressures up to 2 kbar. By 3 kbar, the scrambling was $\sim 5\%$ per window, and by 5.5 kbar the scrambling was 15% per window. Computer simulations of the data were performed assuming that the polarization was scrambled equally by all three windows. The effect of scrambling was a variation in τ of less than 2% over this pressure range, but that the value of $r(0)$ would be expected to decrease by up to 20% at a pressure of 6 kbar. In the data taken for R6G using BK7 windows, the maximum observed variation of $r(0)$ was approximately 10% over the course of any given

experimental run. This result suggests that pressure-induced scrambling does not seriously decrease the accuracy of the measurement of τ for any of the experiments on R6G presented here.

Experiments on PTP were performed using Suprasil windows. Pressure induced birefringence was found to be more extreme for this window material. Similar criteria for the variation of $r(0)$ values were used to determine the suitable pressure range for these experiments. Accordingly, data taken with Suprasil windows were included in this study only for pressures less than 4 kbar.

The values of $r(0)$ observed in all of the PTP experiments were uniformly less than those from the R6G experiments, both at room pressure and at the high pressures. The lower values of $r(0)$ for PTP may be understood by considering the nature of the relevant electronic states involved. As noted in Section III.B.2., a small component of the absorption of PTP at 266 nm is due to occurs to the 1L_b excited state. The transition moment of this state is perpendicular to that of the emitting 1L_a state. Perpendicular absorption and emission transition moments result in an $r(0)$ value of -0.2 (see Eq. 45). A small contribution from this pathway would decrease the value of $r(0)$, while having an insignificant effect on τ . An additional explanation for low $r(0)$ values is found by considering the conformation of the excited 1L_a state. While PTP is slightly twisted in the ground state due to steric hindrance, the 1L_a state is thought to be completely planar⁷⁵. A conformational change upon excitation may cause a small change in the direction of the transition moment resulting in a decrease in $r(0)$. Neither of these proposed mechanisms significantly affects the accuracy of the values of τ . For a further discussion of the significance of

the value of $r(0)$ for the case of R6G see Appendix A.

D. Discussion

The results of the PTP studies are discussed in the Section D.1. That section includes a comparison of the PTP results with calculations based on various models. That discussion also provides a foundation for the discussion of the R6G results which is presented in Section D.2. Anomalous behavior of R6G presents a dramatic contrast to that of PTP. The predictions of a number of different models are evaluated in an attempt to explain the R6G results (Sections D.3. and D.4.). Following this analysis of the R6G results, a comparison is made between the results of the present study and the results of previous work. Our conclusions are summarized in Section D.6.

1. p-Terphenyl

PTP is an intermediate sized, non-polar molecule. Small, non-polar molecules are known to conform to slip boundary conditions. In contrast, large non-polar molecules are accurately described by stick boundary conditions²⁷. The transition point between these two extremes is not yet clear.

SED plots of the measured values of τ for PTP as a function of η are given in Figs. 26 and 27. Figure 26 contains plots for the series of alcohol solvents, alkane solvents, and other additional solvents. Figure 27 shows similar plots for the four different solvents in which τ for PTP was studied as a function of pressure. For clarity, the points in the plots for each solvent and each class of solvents are connected. Also shown in Figs. 26 and 27 are calculations of τ using the SED equation with slip and stick boundary conditions. Due to the

Figure 26 - Plot of τ versus n for p-terphenyl in various solvents. (\blacktriangle) - Normal alcohol solvents; (\blacksquare) - Normal alkane solvents; (\bullet) - acetonitrile, methylene chloride, chloroform, DMF, and cyclohexane (see Table 10). The solid lines are calculated using SED equation with slip and stick boundary conditions for a volume of 224 \AA^3 , and the dashed lines are the for a volume of 341 \AA^3 . The latter is thought to be the more accurate approximation. In both cases the upper line is the stick limit and the lower line is the slip limit.

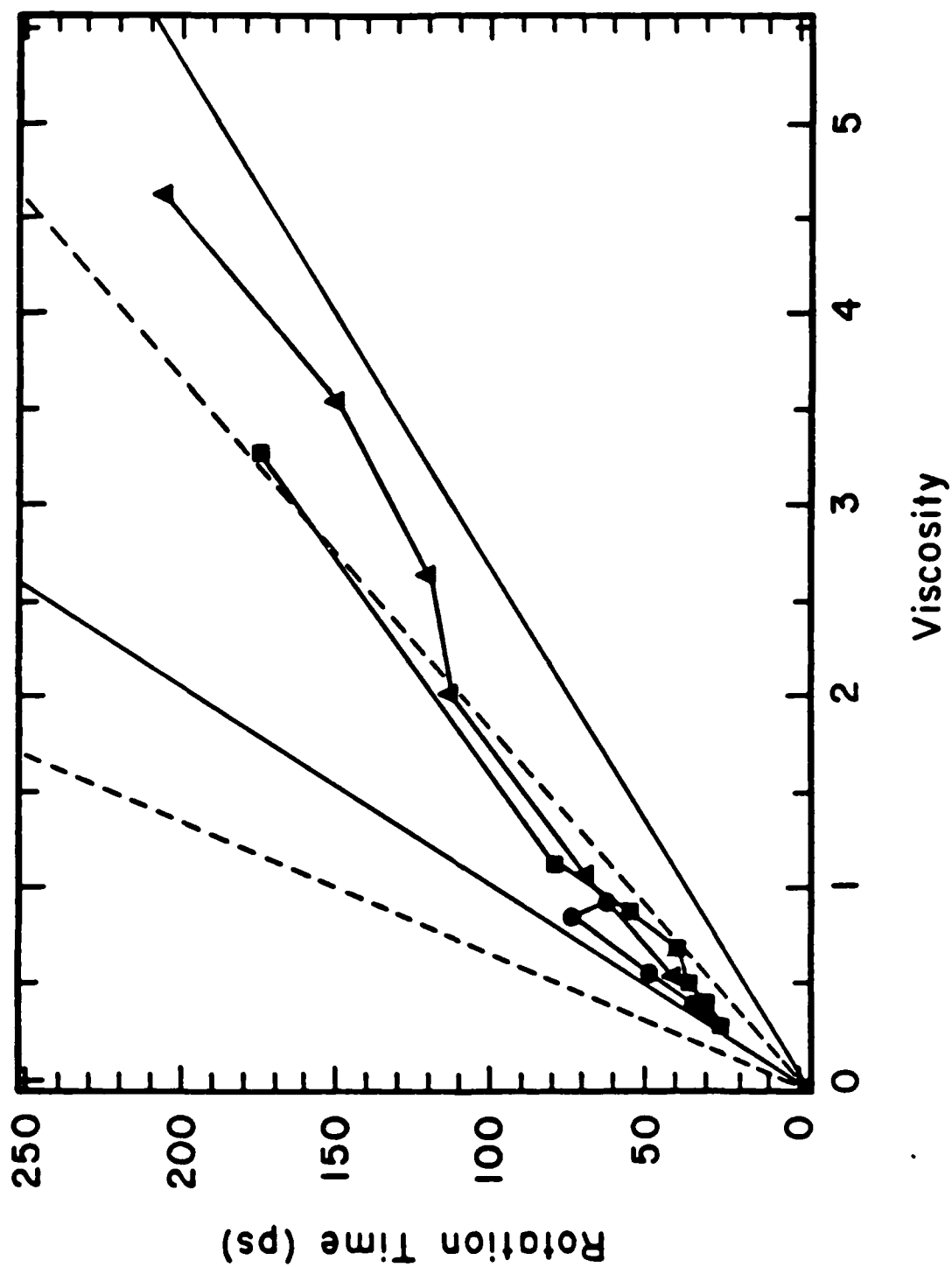


Figure 26

Figure 27 - Plot of τ versus η for p-terphenyl at various pressures.
(*) - Hexane; (\square) - Octane; (Δ) - Ethanol; (\circ) - Chloroform
(see Tables 11-14). The solid and dashed lines are identical to
those shown in Fig. 26.

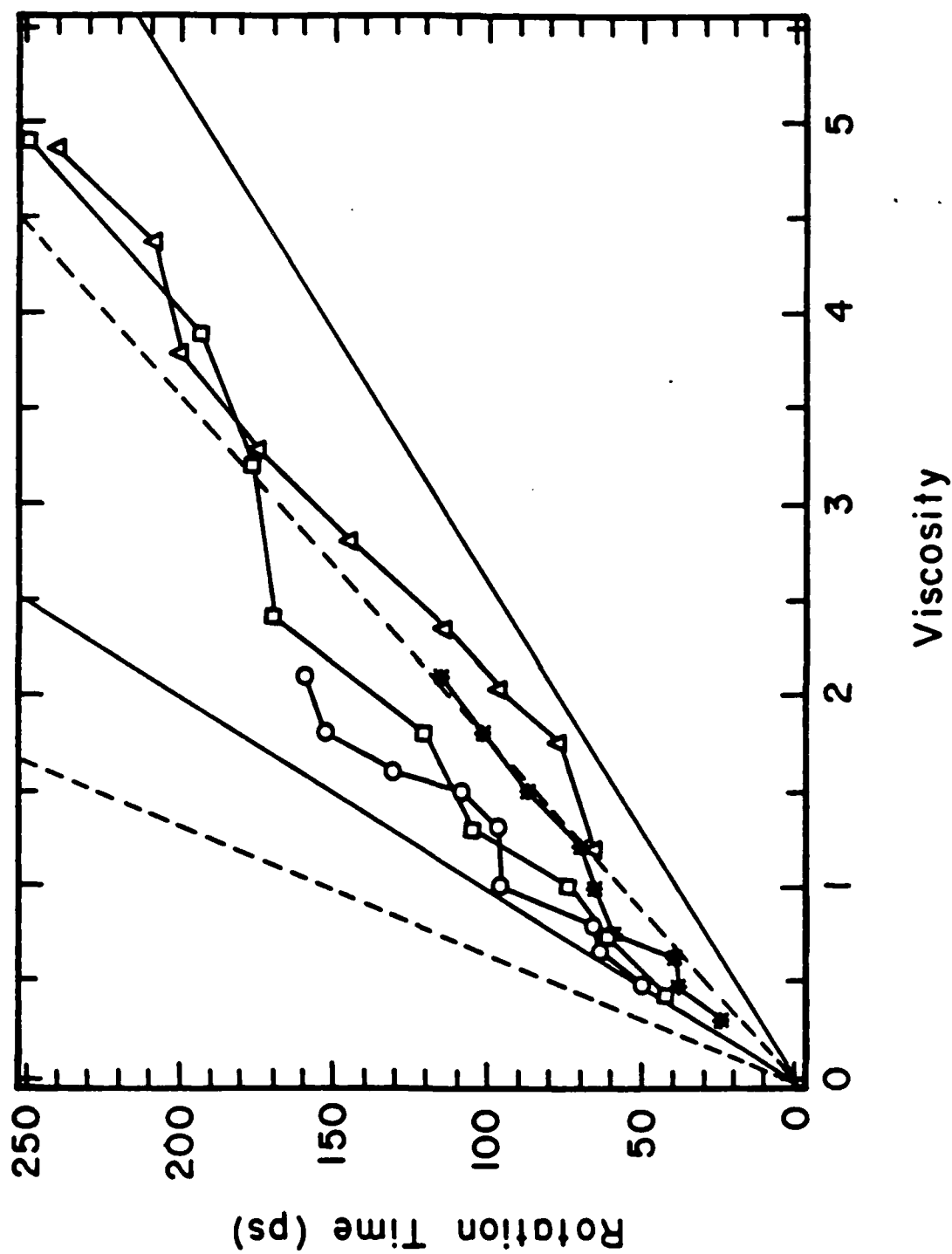


Figure 27

uncertainties in calculation of the hydrodynamic volume, two separate calculations were performed. In both calculations, PTP was treated as a prolate ellipsoid. The factor f in Eq. 4 was calculated from Eq. 6. Thus, both the volume, V , and the axial ratio, ρ , must be estimated. In the first method, V was determined by calculating the van der Waals volume according to the method of Bondi¹⁰⁵. The result is 224 \AA^3 . The axial ratio was determined from the approximate dimensions given in Fig. 13, based on the van der Waals radii of the molecule. Based on this hydrodynamic volume and an axial ratio of 0.4, the axes of the ellipsoid are given by 13.8 \AA and 5.6 \AA . The dimensions of R6G, based on the estimates of the van der Waals radii, as given in Fig. 13, are 15.9 \AA and 6.4 \AA . Using these dimensions, one obtains the volume 341 \AA^3 . Calculations based on both of these molecular volumes were performed. The calculations for the slip and stick limits of the SED equation are given in Figs. 26 and 27. In both cases the value ρ , and therefore f , are equal. In Figs. 26 and 27, the slip limit is the lower line and the stick limit is the upper line, for both sets of calculations.

From Figs. 26 and 27, one sees that the results in general are more closely approximated by the predictions of the calculations made using the slip boundary condition limit than those using the stick limit. The two methods of calculating the hydrodynamic volume do not represent extremes, but do serve as an indication of the uncertainties involved in this kind of calculation. Within the uncertainty of the calculation, most of the data are well characterized by slip boundary conditions. The exceptions appear to be the cases of chloroform and octane as a function of pressure. The data from these two sets of experiments fall in

the region intermediate between slip and stick boundary conditions.

Additional insight is provided by linear regression fits to the various sets of data. The results of the linear fits to the data are given in Table 15. With two exceptions, the slopes of all of the plots are the same within the experimental uncertainty. The two exceptions are: 1) the results obtained in the series of alcohol solvents where the slope is less than that of the other data sets; 2) the results obtained in chloroform under pressure where the slope is larger. The physical significance of these differences is not obvious. An additional feature of the results shown in Table 15 is that there is a wide spread in the values of the intercept, ranging from 0 to 25 ps. The SED equation predicts a zero intercept. As discussed in Section III.B.1, models exist which include an intercept in the SED equation. Small systematic errors could lead to deviations in the intercept on the order of the size of the variations observed here. Since the significance of the value of the intercept in the present data is not clear, the matter was not pursued further.

From the slope linear regression fits to the data, the quantity VfC may be calculated (Eq. 4). These results are also shown in Table 15. For comparison, the calculated values for VfC using the two estimates for the hydrodynamic volume given above are also shown for the stick and slip boundary conditions. The slopes are accurately represented by slip boundary conditions to within the uncertainty of the volume calculations in all but one case. The results for PTP in chloroform as a function of pressure fall between the two extremes.

Tables 16-18 contain the experimentally determined values of the

Table 15
Linear Regression Results of PTP Data

Data Set	Slope($VfC/k_B T$)	Intercept	$VfC(\text{\AA}^3)$
Alcohol Solvents	35.9 ± 2.6	26.4 ± 5	145
Alkane Solvents	54.6 ± 7.3	7.7 ± 4.8	220
Hexane/pressure	51.1 ± 5.1	11.5 ± 4.4	207
Octane/pressure	51.4 ± 3.8	23.4 ± 4.8	208
Ethanol/pressure	49.7 ± 4.7	-0.4 ± 10	201
Chloroform/pressure	68.4 ± 7.6	16.7 ± 8.1	277

Model Calculations of VfC :

Boundary Conditions	Volume = 341 \AA^3	Volume = 224 \AA^3
Stick	641	421
Slip	230	151

This table compares the results of linear regression fits of the PTP data to calculations based on the SED equation with slip and stick boundary conditions. The calculated quantity is the product ' VfC ', which is derived from the slope of the linear regressions.

Table 16

Rotational Reorientation Times of PTP Normalized to Solvent Viscosity

Solvent	η (cP)	τ/η (ps/cP)
Normal Alcohols		
Methanol	0.53	76
Ethanol	1.1	65
Propanol	2.0	57
Butanol	2.6	46
Pentanol	3.5	43
Hexanol	4.6	45
Decanol	8.2	39
Normal Alkanes		
Hexane	0.28	89
Heptane	0.40	75
Octane	0.51	71
Nonane	0.68	57
Decane	0.88	63
Undecane	1.13	70
Hexadecane	3.27	54
Other Solvents		
Acetonitrile	0.35	83
Methylene Chloride	0.40	83
Chloroform	0.55	88
DMF	0.85	86
Chyclohexane	0.93	67

Table 17

Rotational Reorientation Times of PTP Normalized to Solvent Viscosity
for Solvents Under Pressure: Hexane and Octane

Solvent	Pressure (kbar)	η (cP)	τ/η (ps/cP)
Hexane	ambient	0.30	81
	1.13	0.62	83
	1.50	0.75	63
	2.03	0.98	80
	2.52	1.2	66
	3.02	1.5	58
	3.55	1.8	58
	3.99	2.1	56
Octane	ambient	0.43	98
	0.596	0.75	82
	1.08	1.0	74
	1.51	1.3	81
	1.99	1.8	67
	2.50	2.4	71
	3.00	3.2	55
	3.48	3.9	50
	3.99	4.9	51

Table 18

Rotational Reorientation Times of PTP Normalized to Solvent Viscosity
for Solvents Under Pressure: Ethanol and Chloroform

Solvent	Pressure (kbar)	η (cP)	τ/η (ps/cP)
Ethanol	ambient	1.2	55
	0.74	1.75	44
	1.11	2.0	47
	1.50	2.4	49
	2.00	2.8	52
	2.49	3.3	53
	2.96	3.8	53
	3.44	4.4	48
	3.86	4.9	49
Chloroform	ambient	0.48	105
	0.646	0.66	97
	0.99	0.79	84
	1.51	1.0	96
	2.03	1.3	75
	2.58	1.5	73
	2.94	1.6	82
	3.43	1.8	85
	3.95	2.1	76

rotation time of PTP normalized to the solvent viscosity for PTP. With a single exception, τ/η decreases as viscosity increases. The decrease in τ/η with viscosity could be explained as a saturation effect that occurs at high viscosities. Such saturation phenomena have been proposed previously^{76,92,106}, as discussed in Section III.B.3. The proposed mechanism for saturation is based on the relative sizes of the solute and solvent molecules. This mechanism does not explain the results presented here, since the same phenomena is observed when the solvent molecule is held constant and the viscosity is increased via pressure variation. An alternative mechanism for a saturation effect would be required to describe the present results.

In an attempt to better understand some of the subtle variations among the various sets of data, calculations were performed based on the models of Gierer and Wirtz⁵³ and of Kivelson and Dote³². The details of these models were described in section III.B.1. The calculations using the Gierer-Wirtz model were performed using Eqs. 10-12. Calculations based on the Kivelson and Dote model were carried out using Eqs. 14-15. Both models require a value for the molecular volume of the solvent (V_s). As discussed previously, V_s may be derived either from the solvent density (see Eq. 13), or from the van der Waals volume by the method of Bondi¹⁰⁵. Both methods were used in each model. The different methods of calculating V_s significantly changed the calculated values of τ , but did not effect the qualitative trends predicted by the models. Because of the large uncertainty in the hydrodynamic volume of the solute molecule, the validity of the different methods of calculating V_s could not be evaluated. In addition, the Kivelson-Dote model calls for the calculation of the free space in the liquid (ΔV).

The value of ΔV can be determined from Eq. 16, based on the van der Waals volume of the solvent molecules, or from Eq. 20, using empirically derived quantities. Equation 20, however, is only applicable for the case of the series of alkane solvents.

Only the qualitative trends predicted by these two models are discussed and compared with the experimental results. Extensive tables of the results and the parameters used in the calculations may be found in Appendix B. Figures 28-34 show the predictions of the Gierer-Wirtz and the Kivelson-Dote models, respectively. Figures 28-29 and 30-31 are plotted so that they may be directly compared to the experimental results presented in Figs. 26 and 27. The calculations represented in Fig. 28-30 were made using a solute volume of 341 \AA^3 and based on the van der Waals volume of the solvent molecules. The slip limit of the SED equation are shown also in Figs. 28-30.

For the Gierer-Wirtz model calculations shown in Figs. 28 and 29, the slopes calculated for both the series of alkane and the series of alcohol solvents decrease with increasing viscosity. This trend is also observed empirically. As shown in Fig. 28, the predicted results for the series of alkanes are significantly faster than those predicted for the alcohols. This trend was not observed in the experimental data. In fact, at the higher viscosities the experimentally observed rotation in the alkane solvents are slower than those in alcohol solvents. Since the van der Waals volume of the solvent is used for V_s , this parameter does not change as a function of pressure. Thus, the calculations made for comparison with the high pressure results predict a linear dependence of τ on η . When V_s is calculated from the solvent data, a small insignificant curvature can be seen in the plot of τ versus η . Calculations for ethanol and chloroform under pressure

Figure 28 - Results of calculations using the Gierer-Wirtz model. Plot of τ versus η for p-terphenyl in various solvents. The points plotted correspond to viscosity values for the experimental data presented in Fig. 26. (\blacktriangle) - normal alcohols; (\blacksquare) - normal alkanes; (\bullet) - other solvents. A volume of 341 \AA^3 was used in the calculations. The line is the slip limit of the SED equation for a solute volume of 341 \AA^3 .

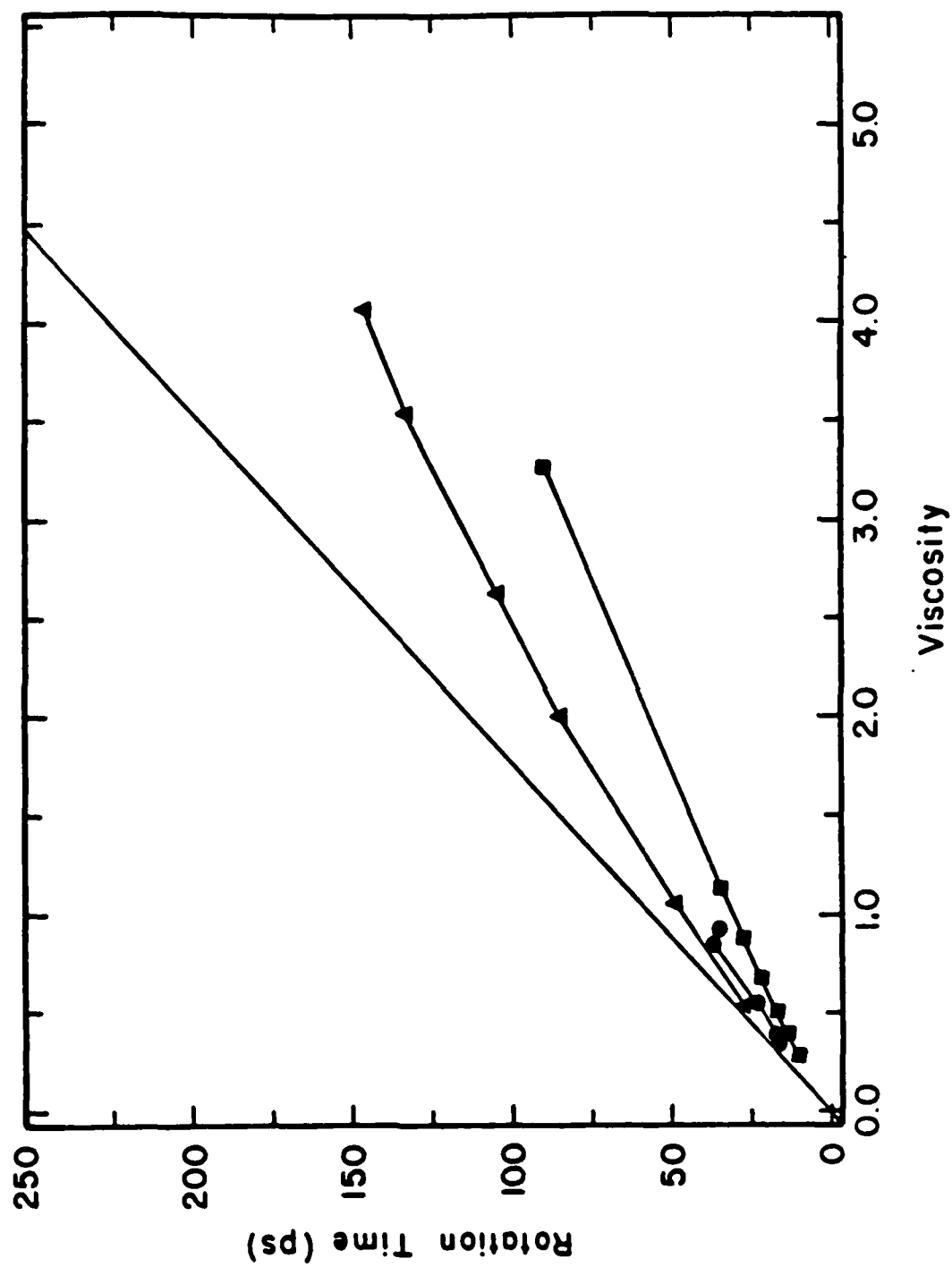


Figure 28

Figure 29 - Same as Fig. 28, except the points correspond to the viscosity values for the experimental data presented in Fig. 27 for PTP at various pressures. (*) - Hexane; (□) - Octane; (△) - Ethanol; (○) - Chloroform. The calculation was performed as in figure 28 with a volume of 341 \AA^3 . The line is identical to that drawn in figure 28.

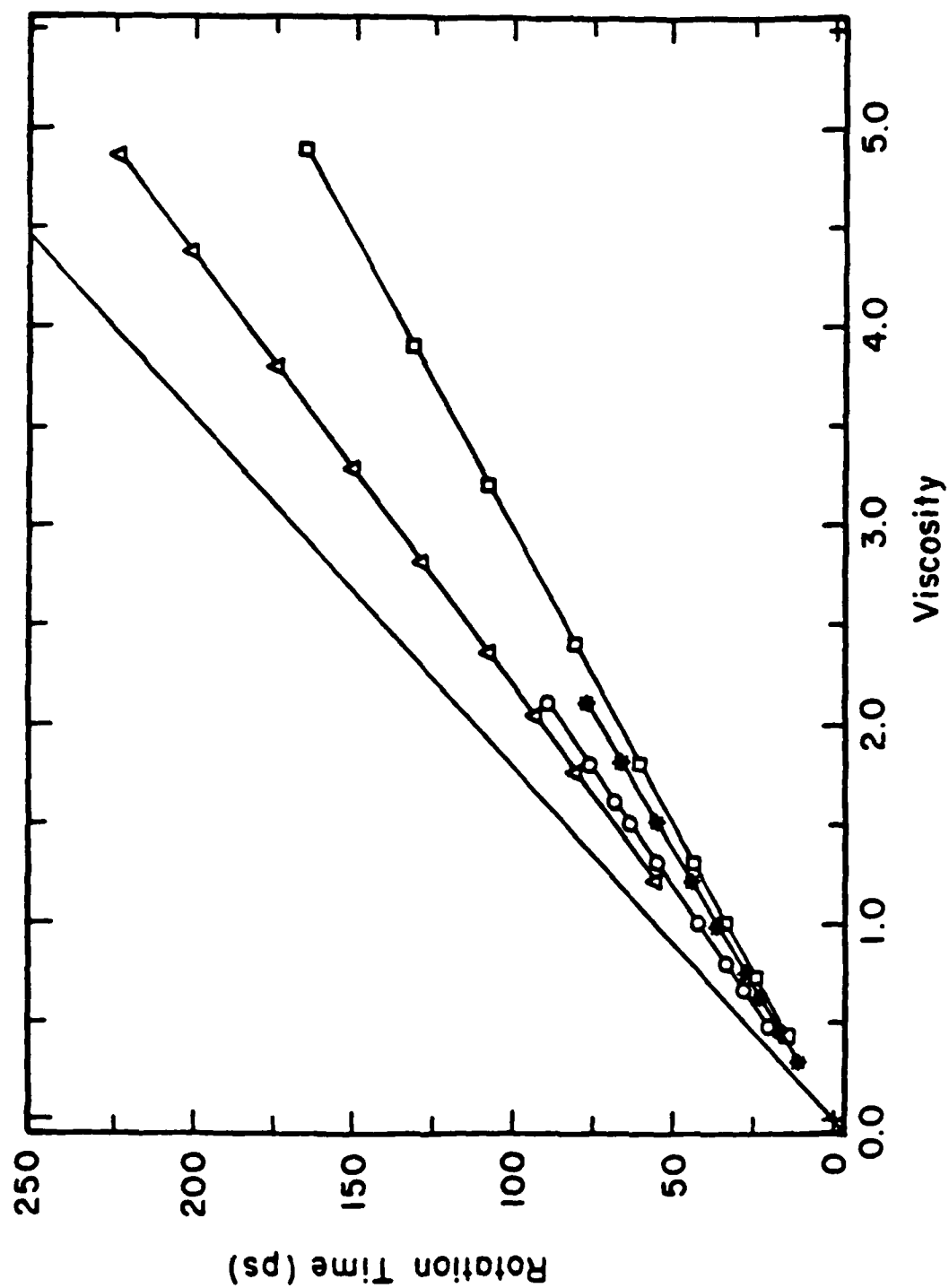


Figure 29

Figure 30 - Same as Fig. 28, except based on the Kivelson-Dote model. As in Figs. 27 and 28, the volume used was 341 \AA^3 . (\blacktriangle) - Normal alcohols; (\blacksquare) - Normal alkanes; (\bullet) - Other solvents. The line is the slip limit of the SED equation for this volume.

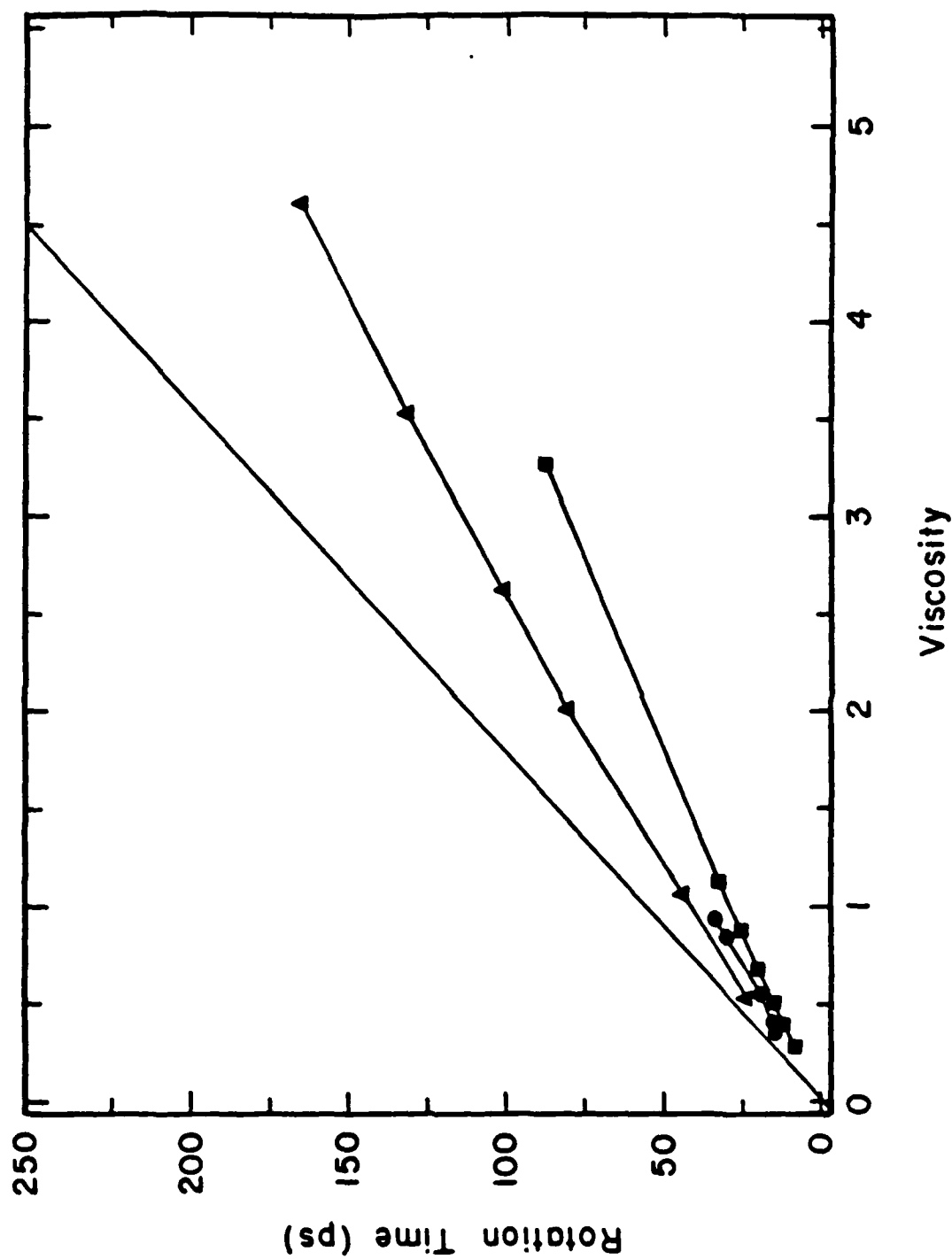


Figure 30

Figure 31 - Same as Fig. 29 except using calculations based on the Kivelson-Dote model. The points correspond to the data plotted in Fig. 27. (*) - Hexane; (□) - Octane; (Δ) - Ethanol; (○) - Other solvents. The calculation was performed as for the plots in Fig. 30, and the line is identical to that appearing in Fig. 28-30.

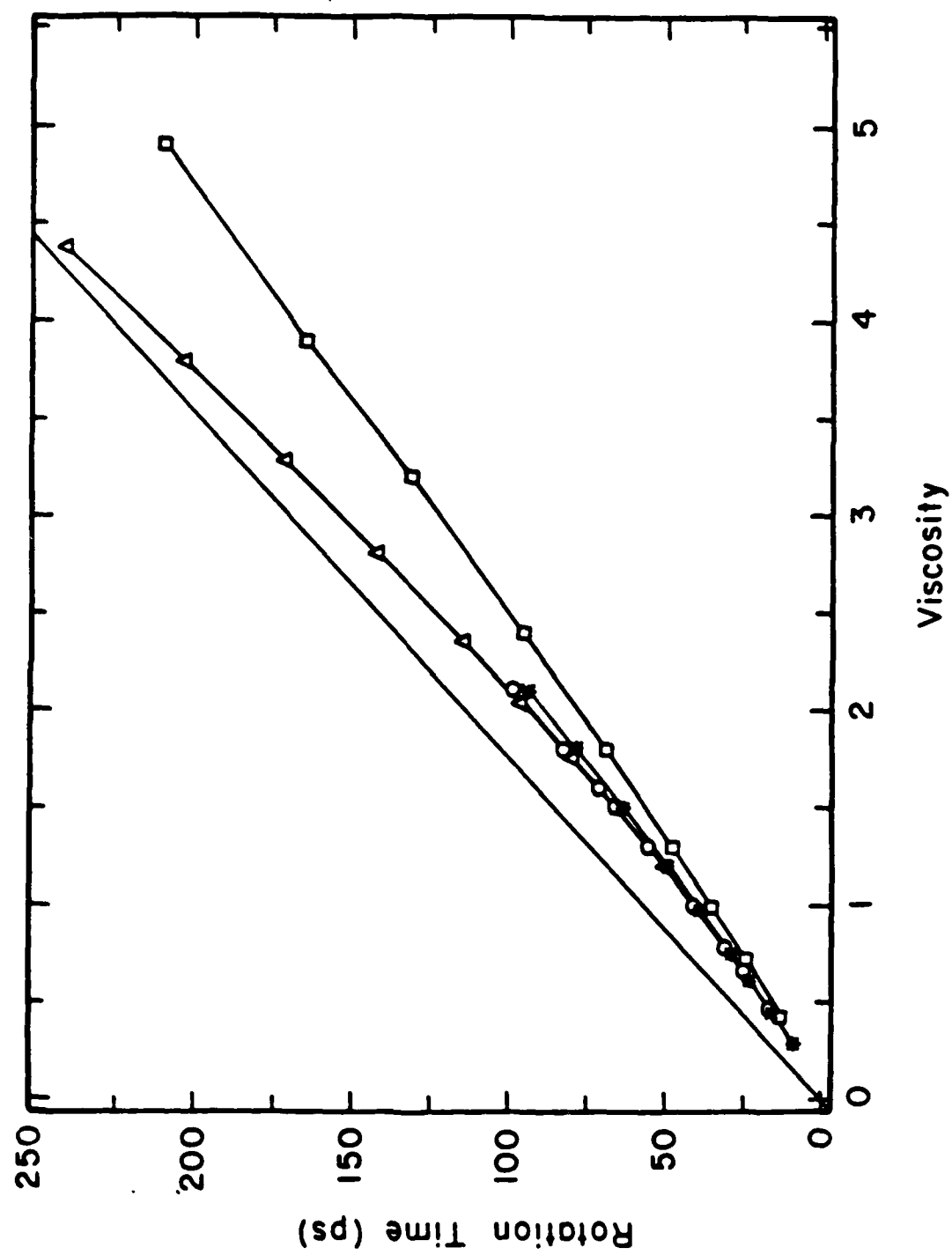


Figure 31

predict that these solvents should have a larger slope than hexane and octane under pressure. A larger slope was observed experimentally for the case of chloroform but not for ethanol. For the other solvents studied the predictions of the Gierer-Wirtz model are qualitatively correct. For example, for cyclohexane and DMF, which have nearly equal viscosities, the calculations yield slightly different values of τ , in agreement with experiment. Thus, the Gierer-Wirtz model is able to explain fairly subtle deviations from the SED equation. The model also accurately predicts the curvature in the τ versus η plots for different solvents and the large slope in these plots for the high pressure chloroform data. The accurate predictions of the Gierer-Wirtz model suggest that the relative sizes of the solute and solvent are important in determining rotational behavior. This model, however incorrectly predicts the relative rates of rotational reorientation in many of the alkane and alcohol solvents. It also incorrectly predicts the slope of the data from ethanol under pressure. These discrepancies suggest that certain features of the solvent environment that affect the dynamics of rotational reorientation which are not adequately treated by the Gierer-Wirtz model.

The calculations based on the Kivelson-Dote model show most of the same trends as those using the Gierer-Wirtz model (see Figs. 30 and 31). There is a similar curvature in the plots for the alkane and alcohol solvents, and the values for the alkane data are again underestimated. The main difference in the Kivelson-Dote model calculations, compared to the Gierer-Wirtz model calculations, is that there is a pronounced increasing slope with viscosity for all of the high pressure results (see Fig. 31). As shown in Fig. 27, this trend is not seen in

the experimental data. Also, the predicted rotation times are slower than those observed in high pressure ethanol. When Eq. 20 is used to calculate the free volume as used in Eqs. 14-15, there is much better agreement between the calculations and the experimental data for the alkane solvents. This observation suggests that significant physical properties of the solvent are described by the empirically-derived variable B in Eq. 20. Since this parameter, B , is only applicable for the series of alkanes, it is difficult to evaluate its physical significance. For the other solvents studied, the experimental results are less accurately predicted by the Kivelson-Dote model than by the Gierer-Wirtz model. The Kivelson-Dote model is an improvement, however, over the SED equation. These results may indicate that the amount of free space in the liquid has a significant effect on the rotational behavior of the solute.

Goulay-Bize et al.³³ find that a linear relationship exists between the rotation time and the normalized inverse free volume ($V_g/\Delta V$) of the liquid. Plots of τ versus $V_g/\Delta V$ are given in Figs. 32 and 33. The ratio $V_g/\Delta V$ was calculated using the van der Waals volume of the solvent for V_g and the definition of ΔV given in Eq. 16. Goulay-Bize et al. use the expression $V_0/(V_m - V_0)$ in place of $V_g/\Delta V$ where V_0 is an empirically derived quantity applicable only for non-interacting liquids at low pressures. The foundation of the Goulay-Bize approach rests on the same empirical equations that form the basis of the Kivelson-Dote model. From Figs. 32 and 33, it is apparent that the plot of τ vs $V_g/\Delta V$ does not give a uniform linear correlation. The contrast between our results and those of Goulay-Bize et al. again suggests that the empirical approach incorporates significant physical properties

Figure 32 - Plot of τ versus $V_S/\Delta V$ for p-terphenyl in various solvents. (\blacktriangle) - Normal alcohols; (\blacksquare) - Normal alkanes; (\bullet) - Other solvents.

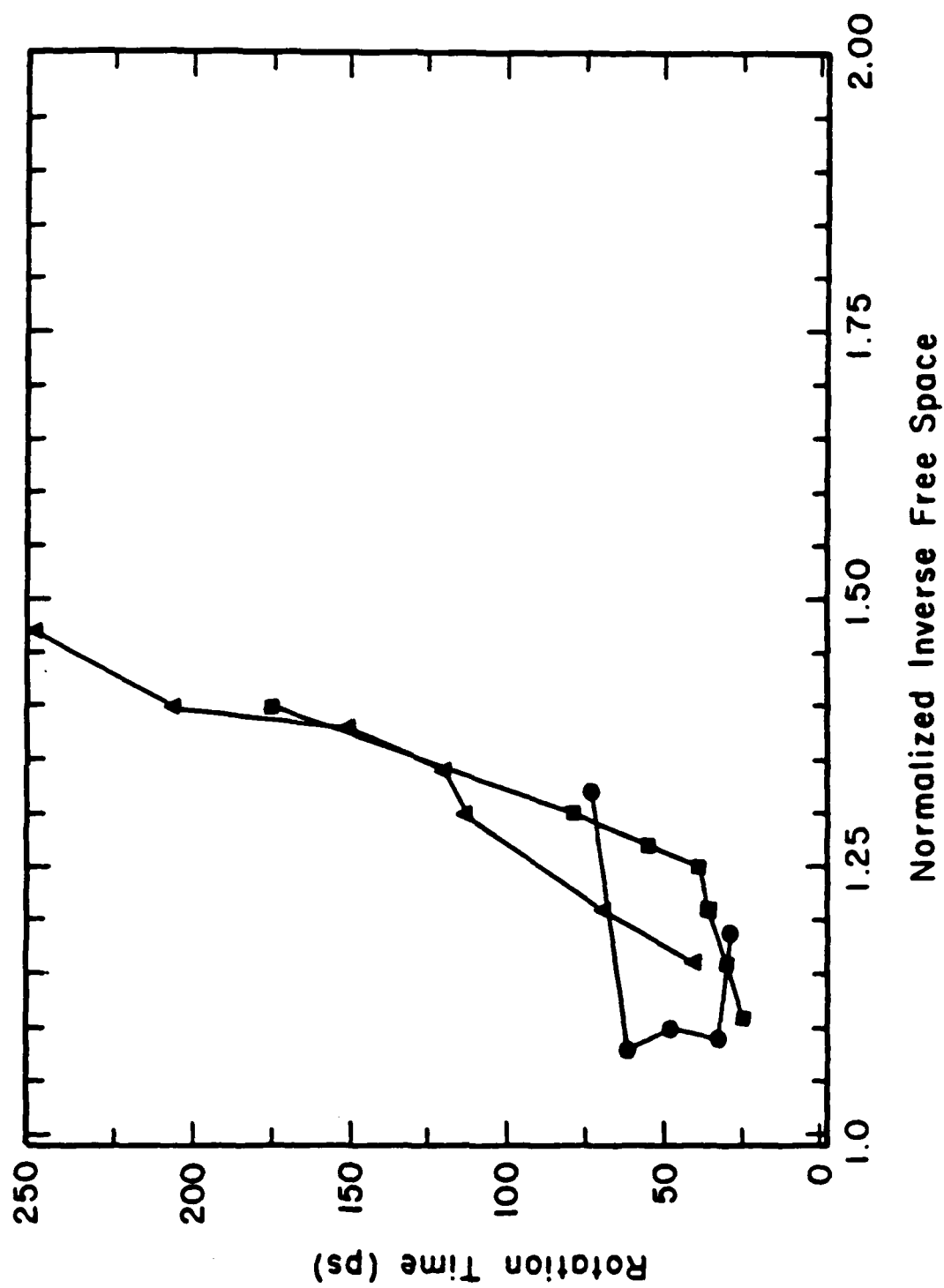


Figure 32

Figure 33 - Plot of τ versus $V_S/\Delta V$ for p-terphenyl at various pressures. (*) - Hexane; (\square) - Octane; (Δ) - Ethanol; (\circ) - Chloroform.

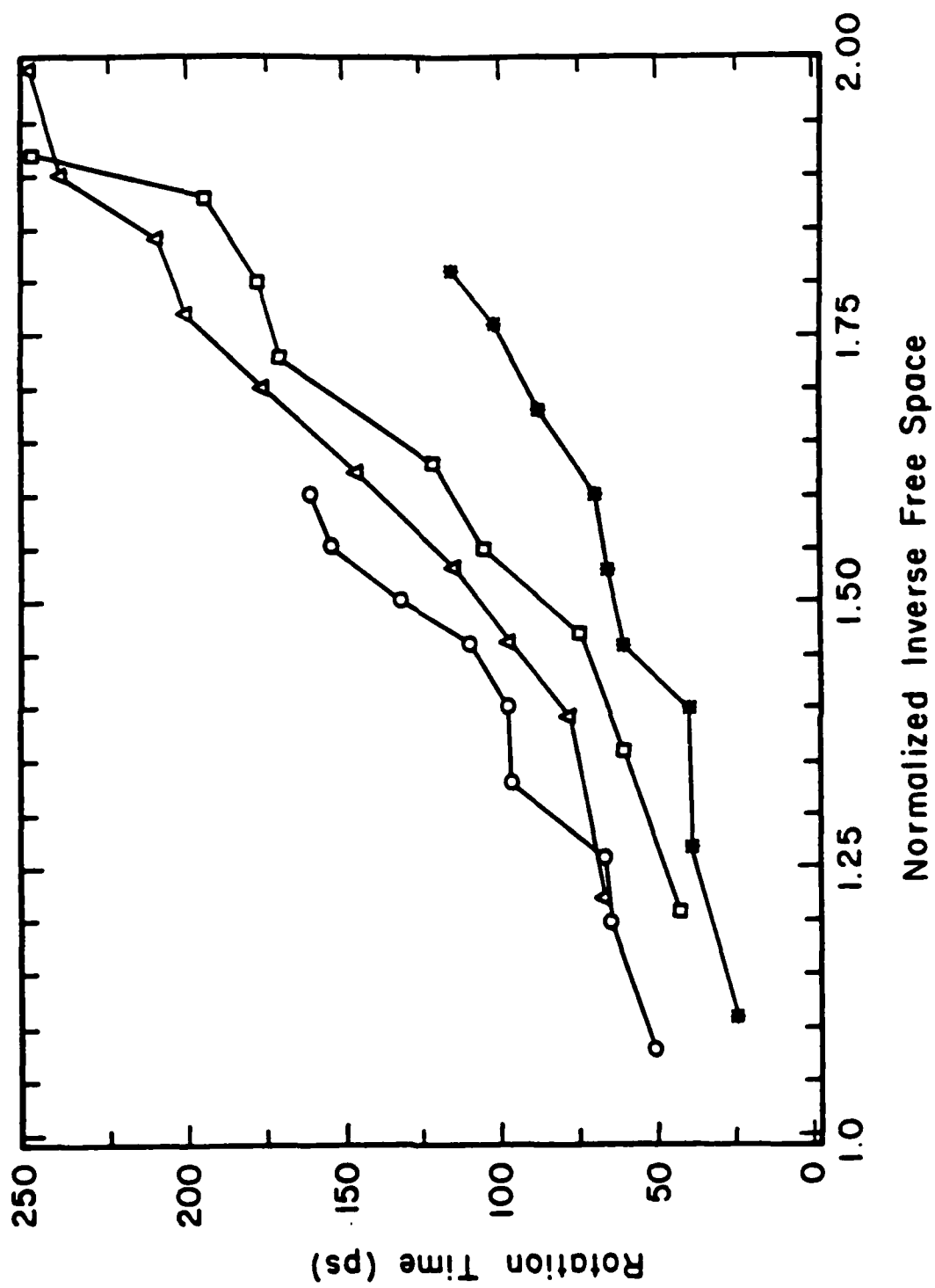


Figure 33

which are not present in the more direct approach used here.

Examination of Figs. 32 and 33 suggests another approach that might lead to an improved correlation in the experimental data. The plots in Figs. 32 and 33 show an increasing slope with $V_g/\Delta V$, whereas the plots in Figs. 26 and 27 show the opposite curvature. These observations suggest that a plot of τ as a function of the product of η and $V_g/\Delta V$ might be of interest. These plots are shown in Figs. 34 and 35. The correlation between the various sets of experimental data is not significantly improved in the plots of Figs. 34 and 35 over that of Figs. 26 and 27. Some improvement does occur for the data taken in the series of alcohols and for that taken in the additional solvents.

The experimental results demonstrate that the Gierer-Wirtz and Kivelson-Dote models are an improvement over the SED equation for non-associated solvents. These models give qualitatively accurate descriptions of subtle deviations from the SED equation in many cases. Models based on the empirically-derived quantities B or V_0 give better quantitative agreement for non-associated liquids at ambient pressure. The physical basis of these empirical quantities must be determined in order to extend such treatments to associated liquids and to liquids under pressure.

Models to interpret the data are essential since the variations in the data are subtle, sometimes within the experimental uncertainties. Deviations in the experimental data from the results predicted by the various models in turn help point out the limitations in the theoretical treatments. As evidenced by the data, better descriptions are needed particularly for the case of associated liquids under pressure.

Figure 34 - Plot of τ versus $\eta \times V_S/\Delta V$ for p-terphenyl in various solvents. (\blacktriangle) - Normal alcohols; (\blacksquare) - Normal alkanes; (\bullet) - Other solvents.

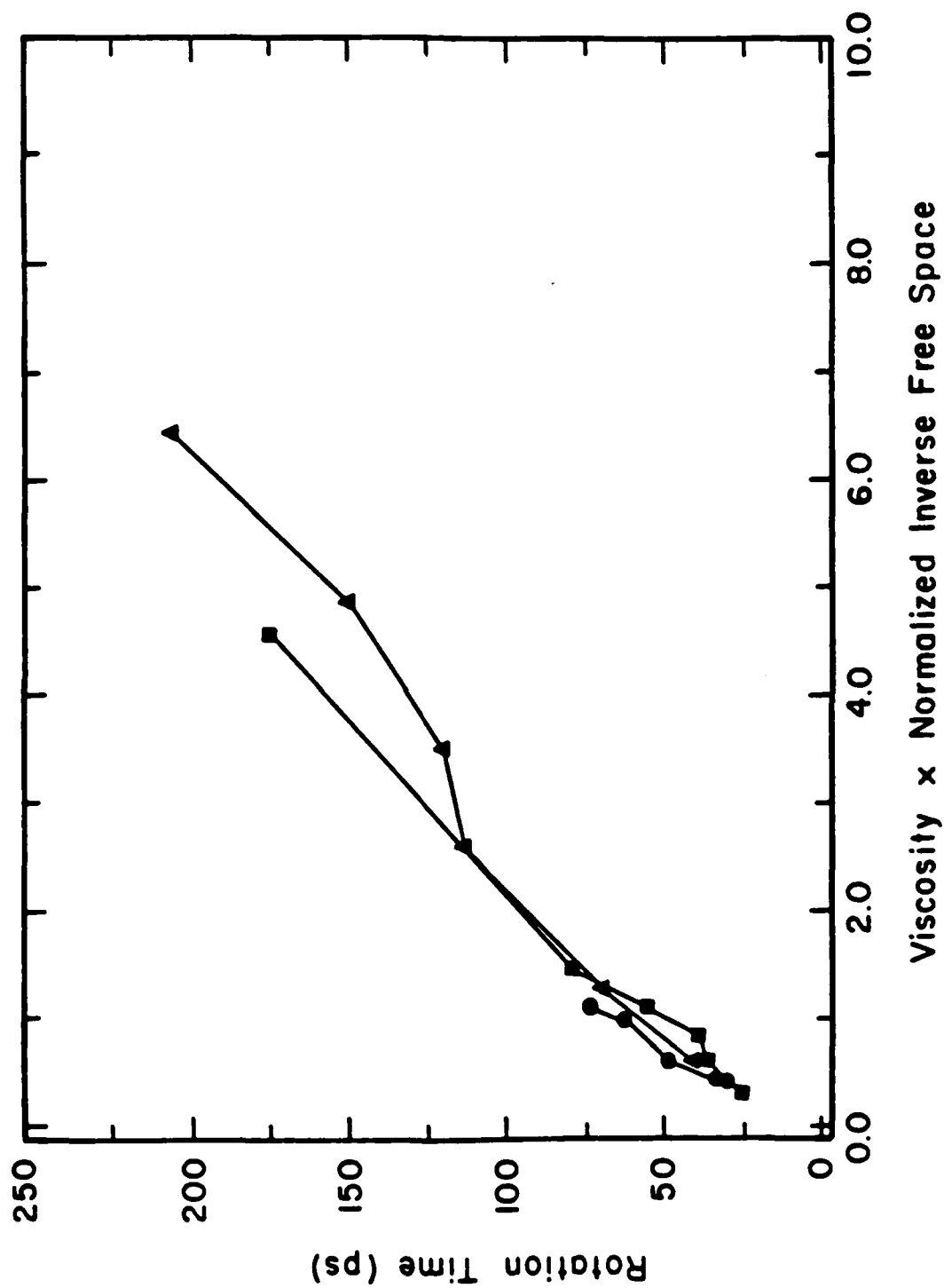


Figure 34

Figure 35 - Plot of τ versus $n \times V_S/\Delta V$ for p-terphenyl at various pressures. (*) - Hexane; (\square) - Octane; (Δ) - Ethanol; (\circ) - Chloroform.

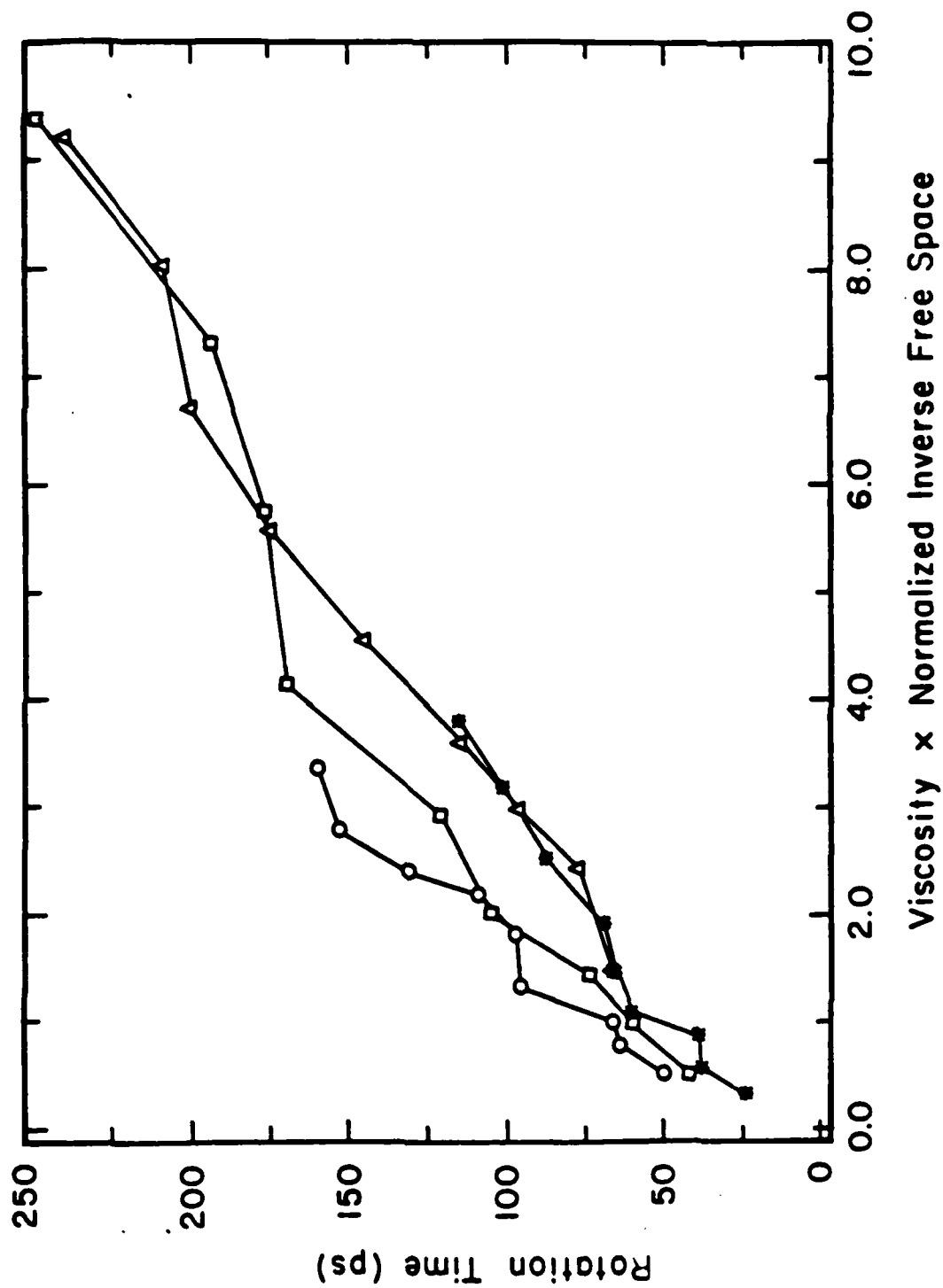


Figure 35

2. Rhodamine 6G

More dramatic departures from SED predictions are present in the data for R6G. The results from the experiments on R6G provide an extreme example which demonstrates the limitations of the SED equation. Plots of τ as a function of η are given in Fig. 36 for R6G in a series of alcohol solvents and in ethanol as a function of pressure. The lines in Fig. 36 are SED calculations using stick and slip boundary conditions for an oblate ellipsoid of dimensions 15.2 Å by 3.8 Å. The approximate van der Waals radii of R6G are given in Fig. 12 as ~11 Å by ~16 Å. The third dimension of the molecule is approximately 3.8 Å. The volume of this equivalent ellipsoid is also close to the van der Waals volume as calculated by the Bondi method (460 Å³). The value of f for an oblate ellipsoid with an axial ratio of 4, is 1.84. The Hu and Zwanzig value for the slip/stick ratio is 0.664.

Fig. 36 shows that the results for the series of alcohol solvents are well above the stick limit, beyond the uncertainty in the volume approximation. Such "super stick" results have been reported previously as described in Section III.B.3. The models used in the previous section to describe the behavior of PTP cannot account for such behavior. In fact, both the Gierer-Wirtz model and the Kivelson-Dote model predict that the results from the series of alcohol solvents should be close to the slip limit. Both models also predict that the high pressure ethanol data should fall above the data from the series of alcohol solvents. In reality, the results for ethanol as a function of pressure fall between the slip and stick limits, and below the alcohol solvent variation data. Thus, the predicted values of the rotational reorientation time are consistently shorter than the experimentally

Figure 36 - Plot of τ versus η for rhodamine 6G. (\blacktriangle) - Normal alcohol solvents; (\triangle) - Ethanol as a function of pressure. The lines are the calculations using the SED equation with slip and stick boundary conditions for a volume of 460 \AA^3 . The upper line is the stick limit and the lower line is the slip limit.

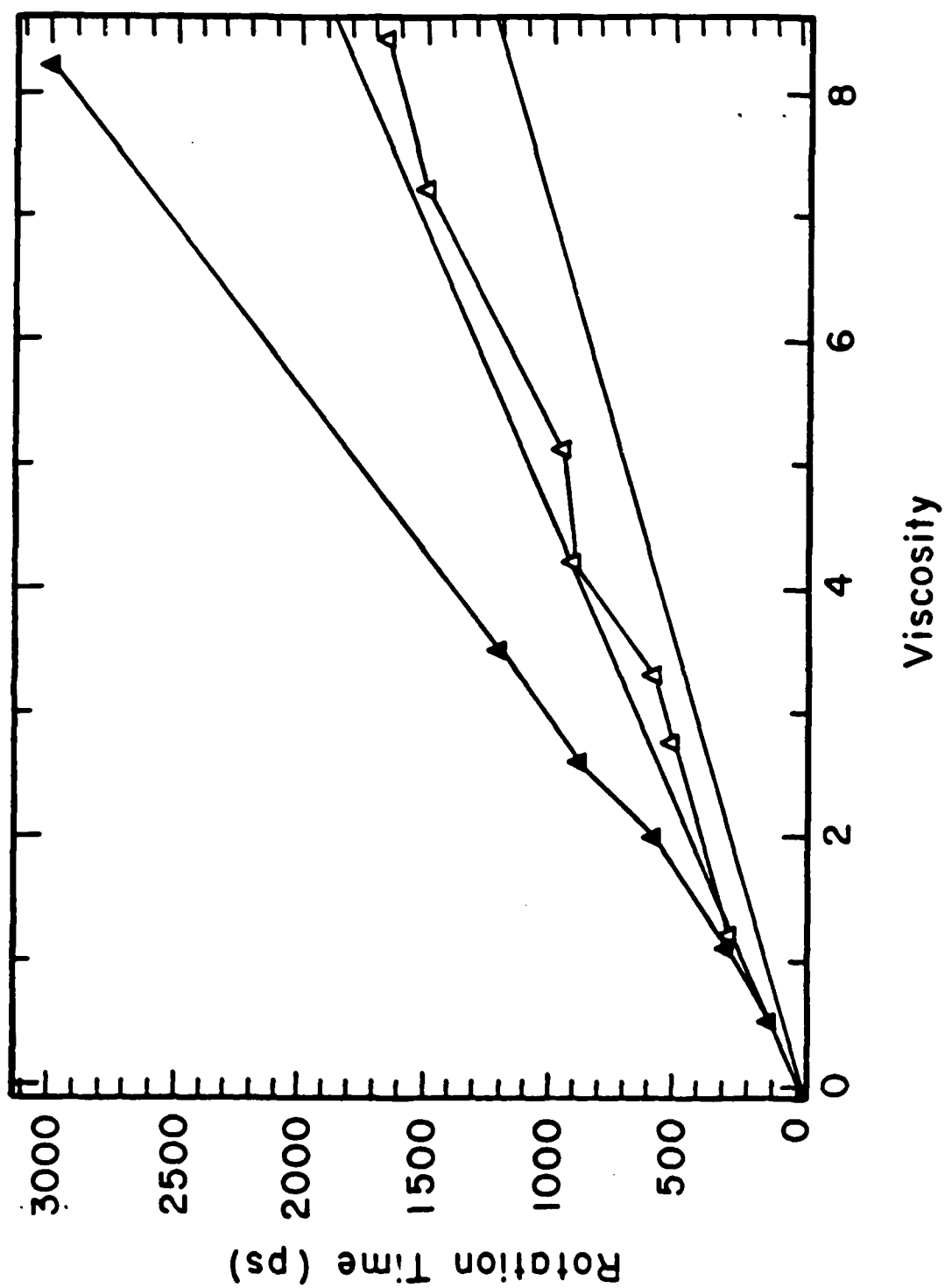


Figure 36

determined values. These two models predict a decreasing slope with viscosity for the series of alcohols for R6G as in the case of PTP. Although this trend was observed experimentally with PTP, it is not apparent in the R6G results.

Tables 19 and 20 give the rotation times normalized to the viscosities for R6G in various solvents and at high pressures, respectively. The high pressure data show a constant slope with viscosity to within the experimental uncertainty, as predicted by the SED equation, and in agreement with the results from the study of PTP in ethanol as a function of pressure. In contrast, the results for the series of solvents show an increasing slope with viscosity, dramatically different than any of the results observed for PTP. Tables 19 and 20 also contain the results from linear regression fits of the data. As is expected from inspection of Fig. 36, the slope of the fit to the data in the series of alcohol solvents for stick boundary conditions predicts a hydrodynamic volume which is too large by a factor of 2. The slope of the fit to the pressure data predicts a hydrodynamic volume which is commensurate with stick boundary conditions.

The results of the R6G study disagree with the predictions of the SED equation. First, the linear alcohols exhibit behavior well outside the range predicted by the SED equation regardless of boundary conditions. Further, identical macroscopic viscosities give rise to dramatically different microscopic behavior. The striking departure from SED behavior in R6G suggests that an alternative approach is necessary to adequately model the data. The model of Evans et al. described in Section III.B.1, is based on kinetic theory and provides a molecular description of rotational motion. As already mentioned, quantitative

Table 19

Rotational Reorientation Times of R6G Normalized to Solvent Viscosity

Solvent	η (cP)	τ/η (ps/cP)
Methanol	0.53	208
Ethanol	1.1	264
Propanol	2.0	288
Butanol	2.6	334
Pentanol	3.5	340
Octanol	8.2	366

Linear Regression Results:

Slope = $367 \pm 16 = V_f C / k_B T$
Intercept = -103 ± 22
 $V_f C = 1484$
 $V_{stick} = 807 \text{ \AA}^3$

Table 20

Rotational Reorientation Times of R6G Normalized to Solvent Viscosity
for Ethanol Under Pressure

Pressure (kbar)	η (cP)	τ/η (ps/cP)
ambient	1.2	233
1.98	2.75	182
2.53	3.3	176
3.32	4.2	214
4.09	5.1	186
5.46	7.2	208
6.05	8.4	198

Linear Regression Results:

Slope = $198 \pm 18 = V_f C / k_B T$
 Intercept = 7.8 ± 61
 $V_f C = 793$
 $V_{stick} = 422 \text{ \AA}^3$

calculations are difficult and potentially inaccurate, therefore only trends predicted by this model will be considered. The variables used in the theory that are sensitive to either solvent or pressure variation are (see Eq. 28)

$$\frac{C^4}{A^4} \langle g(x)s(x) \rangle \frac{g_{ad}(\rho^*)}{g_{aa}(\rho^*)}$$

When pressure is varied, the density of the solvent is varied. $\frac{C^4}{A^4}$ is

a constant with pressure. The density dependence of $\langle g(x)s(x) \rangle$ is difficult to estimate. In the limit of small solvent molecules, the ratio of the radial distribution functions is approximated by $\sim \frac{1 + \rho^*}{1 - \rho^*/2}$,

which is an increasing function of density. For solvent variation,

$\frac{C^4}{A^2} \langle g(x)s(x) \rangle$ may be approximated by $\frac{C^2}{A^4} (1 + C/A)^2 \langle x^2(1-x^2) \rangle$, which

is a decreasing function of solvent size. Similarly, the ratio of the radial distribution functions also decreases with solvent size. Thus, although some parameters are not well defined, it appears that this theory predicts that the plot of the pressure variation data should lie above that of the solvent variation data⁶¹. The trends predicted by the theory of Evans et al. are consistent with the predictions of the hydrodynamic approaches discussed above and, as in those models, it does not accurately predict the experimental results. Unless the erroneous predictions are a result of unusual effects in the unknown parameters, a further explanation is required to understand the experimental results.

3. Dielectric Friction

The difference between the R6G and PTP results is consistent with the previously reported results discussed in Section III.B.3. It is apparent that there is some correlation between τ and the charge on the solute molecule. The behavior of charged solute molecules has been observed to deviate from the predictions of the SED equation. Various explanations have been proposed for these anomalies. Through the use of pressure as an experimental variable it has been possible to examine the behavior of R6G under a much wider range of conditions than in previous work. The results presented here point toward a new explanation of the deviations from SED behavior that occur for charged solutes. The comparison of results at high pressures and ambient pressure indicate that dielectric friction is an important factor for modelling rotational motion of charged molecules in liquids.

Dielectric friction has been included in models of rotational reorientation by both Hubbard and Wolynes⁶⁷ and by Kivelson and Madden⁶⁸. In order to explain the difference between the pressure and solvent results, it is necessary to invoke a physical effect that does not have a simple linear dependence on viscosity. Previous studies of dielectric phenomena have demonstrated that in solvents such as propanol and glycerol, dielectric properties have a different pressure dependence than the solvent viscosity^{106,107}. Thus, dielectric friction behaves in a manner appropriate for the explanation of these results.

The additional contribution to τ due to dielectric friction will be called $\Delta\tau$. Combining Eqs. 29 and 30, $\Delta\tau$ can be written as

$$\Delta\tau = \frac{\mu^2}{k_B T a^3} \frac{(\epsilon - 1)}{(2\epsilon + 1)^2} \tau_D \quad (49)$$

There are a number of problems involved in the quantitative solution of Eq. 49. For a complex molecule such as R6G, it is difficult to determine the quantities μ and "a". These quantities, however, are constants throughout the range of experimental conditions, thus, they will only enter the equation as a scale factor. As a charged species, R6G should have a large effective dipole moment. Twenty Debye is a reasonable estimate for the dipole moment of a very polar molecule⁸⁸. Using 20 Debye as an approximation for the dipole moment, and 5 Å as the cavity radius (a), an order of magnitude estimate is

$$\frac{\mu^2}{k_B T a^3} \approx 13, \quad (50)$$

and thus

$$\Delta\tau \approx 13 \frac{(\epsilon - 1)}{(2\epsilon + 1)^2} \tau_D = 13 A \tau_D \quad (51)$$

where ϵ and τ_D characteristics of the solvent.

The static dielectric constants (ϵ) are readily available in the literature. Tables have been compiled of ambient pressure dielectric constants¹⁰⁸, and the static dielectric constants of selected solvents, including ethanol, have been studied as a function of pressure¹⁰⁹.

The dielectric relaxation times are more difficult to obtain. The value for ethanol was determined in a study by Sagal¹¹⁰, and Garg and Smyth¹¹¹ performed a study of the dielectric relaxation times for a series of linear alcohols from propanol to octanol. In their study, Garg and Smyth determined three dielectric relaxation times for each solvent. It is the longest relaxation time that is of interest here.

Measurements of τ_D for alcohol solvents as a function of pressure are much less extensive. Two different studies were performed on

octanol isomers¹¹⁵ and heptanol¹¹⁴. In both studies a linear correlation was found between $\ln(\tau_D)$ and pressure at pressures greater than 0.5 kbar. Below this pressure, a slight curvature was noticed in one of the studies¹¹⁵. In the only directly comparable isomers studied, 3-octanol and 3-heptanol, identical slopes were obtained. Since no pressure dependent data is available for ethanol, this similarity among isomers is assumed to hold for ethanol as well. The slope of the plot of $\ln(\tau_D)$ versus pressure for 1-heptanol was thus used to extrapolate values of τ_D for ethanol as a function of pressure. Values for the solvent parameters used in this analysis are given in Tables 21 and 22. Table 21 contains the values for ϵ and τ_D taken from references 111 and 108 for the linear alcohol solvents at ambient pressures. Table 22 contains the values of ϵ from reference 109 and the extrapolated values of τ_D for ethanol as a function of pressure. Also contained in Tables 21 and 22 are the calculated values of A and $\Delta\tau$ from Eq. 51.

Figure 37 contains plots of $\Delta\tau$ versus η for the series of alcohol solvents and for ethanol as a function of pressure. The striking similarity between the trends presented in Fig. 37 and the experimental data is immediately apparent (see Fig. 36). The actual values of τ would be calculated by adding $\Delta\tau$ to the value of τ predicted by the SED equation. The results of the PTP study showed that non-interacting molecules of a size similar to that of R6G show behavior that is in general better described by slip boundary conditions. If one starts with the predictions of the SED equation with slip boundary conditions and adds the appropriate increment of $\Delta\tau$ from Fig. 37, quantitative agreement with the experimental data is not achieved. The values of $\Delta\tau$ are, however, the appropriate order of magnitude. Given the

Table 21

Component of Rotational Reorientation Time of R6G Due to Dielectric Friction for Alcohol Solvents

Solvent	ϵ^a	A (x100) ^b	τ_D^c (ps)	$\Delta\tau$ (ps)	η (cP)
Ethanol	25.1 ^d	0.919	197 ^d	23.7	1.2
Propanol	20.8	1.09	430	61.5	2.2
Butanol	17.8	1.25	668	109.4	2.9
Pentanol	14.3	1.52	927	185	3.5
Hexanol	13.8	1.56	1210	288	4.6
Octanol	10.3	1.99	1980	464	8.2

a) From reference 108, unless otherwise specified

b) Defined in the text

c) From reference 111, unless otherwise specified

d) From reference 110

Table 22

Component of Rotational Reorientation Time of R6G Due to Dielectric Friction for Ethanol Under Pressure

Pressure(kbar)	ϵ^a	A ($\times 100$) ^b	τ_D^c (ps)	$\Delta\tau$ (ps)	η (cP)
ambient	24.1	0.933	197	24	1.2
0.5	25.9	0.893	252	33	1.6
1.0	26.6	0.871	308	35	1.9
2.0	27.8	0.837	460	51	2.8
4.0	30.0	0.779	1024	105	5.1
6.0	31.5	0.745	2333	228	8.4

a) From reference 109

b) Defined in the text

c) Extrapolated based on data in reference 114

Figure 37 - Plot of $\Delta\tau$ versus η for rhodamine 6G. (\blacktriangle) - Normal alcohol solvents; (\triangle) - Ethanol as a function of pressure. $\Delta\tau$ is calculated from Eq. 30 as described in the text.

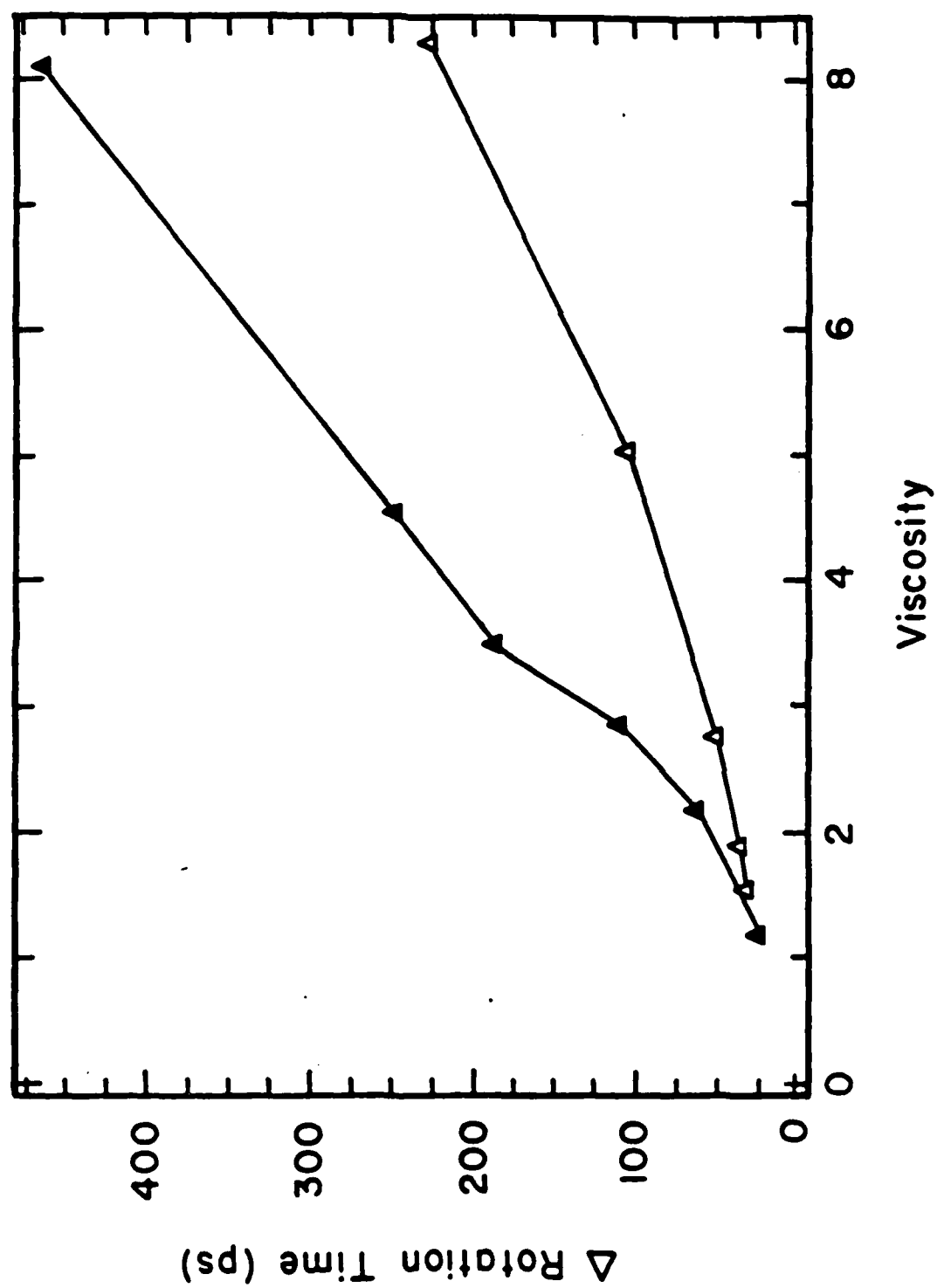


Figure 37

approximations made in the calculation, better agreement is not expected. In fact, the remarkable qualitative agreement is quite compelling considering the extent of the approximations involved. Furthermore, the dielectric friction model is the only model considered here which accurately predicts the trends observed experimentally.

Additional insight into the molecular phenomena associated with rotational motion is found in an examination of the physical basis of τ_D . In alcohol solvents, the primary dielectric relaxation time has been interpreted in a variety of ways by different authors¹¹³. The major difference between the various interpretations is the role of the breaking and forming of hydrogen bonds. Many authors have suggested that the breaking of hydrogen bonds is the primary mechanism for the unusually long dielectric relaxation times found in alcohols^{111, 112}. Others suggest that hydrogen bonding plays a more indirect role in the determination of dielectric relaxation times. It has been suggested that the relaxation mechanism consists of the concerted reorientation of groups of solvent molecules. In this mechanism, the hydrogen bonded superstructure controls the relaxation process of the individual molecules. In the course of the reorientation of a single molecule, hydrogen bonds may be broken and reformed many times. Thus, although the hydrogen bonded superstructure hinders the motion of individual molecules, the breaking of hydrogen bonds is not the rate determining step^{114, 115}. Bottcher¹¹⁶ argues in favor of the latter mechanism based on the observation that dielectric relaxation times in alcohols do not correlate well with the hydrogen bond strength of the solvent molecules. In any of the above interpretations, it is clear that the hydrogen bonding structure of the solvent plays an

important role in determining the dielectric relaxation times.

Although the dielectric friction model is based on bulk dielectric properties of the solvent, it provides information concerning specific intermolecular interactions. The predictions of the dielectric friction model stem from variations in solvent-solvent interactions rather than solvent-solute interactions. This fact suggests that interactions between the solvent and solute such as hydrogen bonding are not the dominant factor dictating rotational motion. Thus, the dielectric friction model argues against models involving solute-solvent complex formation. A better understanding of the molecular properties of the solvent that determine dielectric behavior would in turn increase our understanding of the molecular basis of rotational reorientation.

4. Salt Effect

An additional test of the dielectric friction model is provided by a study of rotational reorientation of PTP and R6G in ethanol as a function of added salt¹¹⁷. A study by Cachet et al.¹¹⁸ demonstrated that the dielectric relaxation lifetime in alcohols is unaffected by the addition of salts, but that there is a strong dependence of the static dielectric constant on the salt concentration. These results applied for the series of salts, $\text{Mg}(\text{ClO}_4)_2$, LiClO_4 , LiCl , and LiI , at concentrations up to 1M. The salt selected for our study was LiCl .

The data in Tables 23 and 24 demonstrate the effects of added salt on rotation times. Addition of salt to ethanol also increases the viscosity of the solvent. The measured rotation times, viscosities and rotation times normalized to the viscosity are given in Tables 23 and 24 for R6G and PTP, respectively. For PTP the behavior of τ/η is

Table 23

Rotational Reorientation Times of R6G in Ethanol as a Function of LiCl Concentration

[LiCl]	η (cP)	τ (ps)	τ/η (ps/cP)
0.0	1.2	270	225
0.25	1.5	323	215
0.47	1.8	295	164
0.94	2.5	359	144

Table 24

Rotational Reorientation Times of PTP in Ethanol as a Function of LiCl Concentration

[LiCl]	η (cP)	τ (ps)	τ/η (ps/cP)
0.0	1.2	70	58
0.2	1.4	74	53
0.4	1.7	78	46
0.8	2.3	97	42
1.6	4.0	150	38

very similar to that observed in most of the other series of PTP experiments. This result is not surprising since PTP is a neutral, non-polar molecule. The effects of dielectric friction are therefore not expected to be significant. In contrast, the results of the R6G experiments with added salt are quite different than those for either the solvent or the pressure experiments. The value of τ/η decreases as a function of η , in contrast to the solvent experiments in which τ/η increases, or the high pressure experiments, where it is constant.

The values of $\Delta\tau$ as a function of LiCl concentrations were calculated from Eq. 51 for the R6G experiments and are presented in Table 25. The values of $\Delta\tau$ versus η are plotted in Fig. 38. Figure 38 is an expanded version of Fig. 37 where data for temperature variation has also been added (see discussion below).

The plot of $\Delta\tau$ as a function of salt concentration shows a negative curvature. Since τ has a linear dependence on viscosity in the SED equation, the relative importance of $\Delta\tau$ will decrease with added salt. This prediction is born out in the experimental data, in the form of a decrease in the value of τ/η with increasing η . The physical implication of this prediction is that dielectric friction is diminished by the addition of salt. Thus, at high salt concentrations, the rotation time should approach the value of τ predicted by the SED equation. At 0.94 M LiCl, the value of τ/η is 144 as compared to 344 in butanol, which has a similar viscosity. The plot in Fig. 38 shows that there is a large relative contribution of $\Delta\tau$ to τ for butanol as compared to 0.94 M LiCl. Thus, one expects better agreement with the SED equation for 0.94 M LiCl. The hydrodynamic volume predicted by the value of $\tau/\eta=144$ is 310 \AA^3 for stick boundary conditions and 467 \AA^3

Table 25

Component of Rotational Reorientation Time of R6G Due to Dielectric Friction for Ethanol with Added LiCl

[LiCl]	ϵ^a	A ($\times 100$) ^b	$\Delta\tau$ (ps)	η (cP)
0.0	25.1	0.933	24.3	1.2
0.16	20.8	1.09	28.6	1.36
0.25	19.0	1.18	31.1	1.5
0.30	18.3	1.22	31.9	1.55
0.50	16.3	1.35	35.5	1.8
0.80	13.8	1.56	40.9	2.3

a) From reference 118

b) Defined in the text

Figure 38 - Expanded plot of Δt versus η for rhodamine 6G. This plot is an expanded version of the plot shown in Fig. 37. Additional data has been added in this plot as well. (\blacktriangle) - Normal alcohols; (\triangleleft) - Ethanol as a function of pressure; (\circ) - Ethanol as a function of temperature; (\blacksquare) - Ethanol as a function of added LiCl concentration.

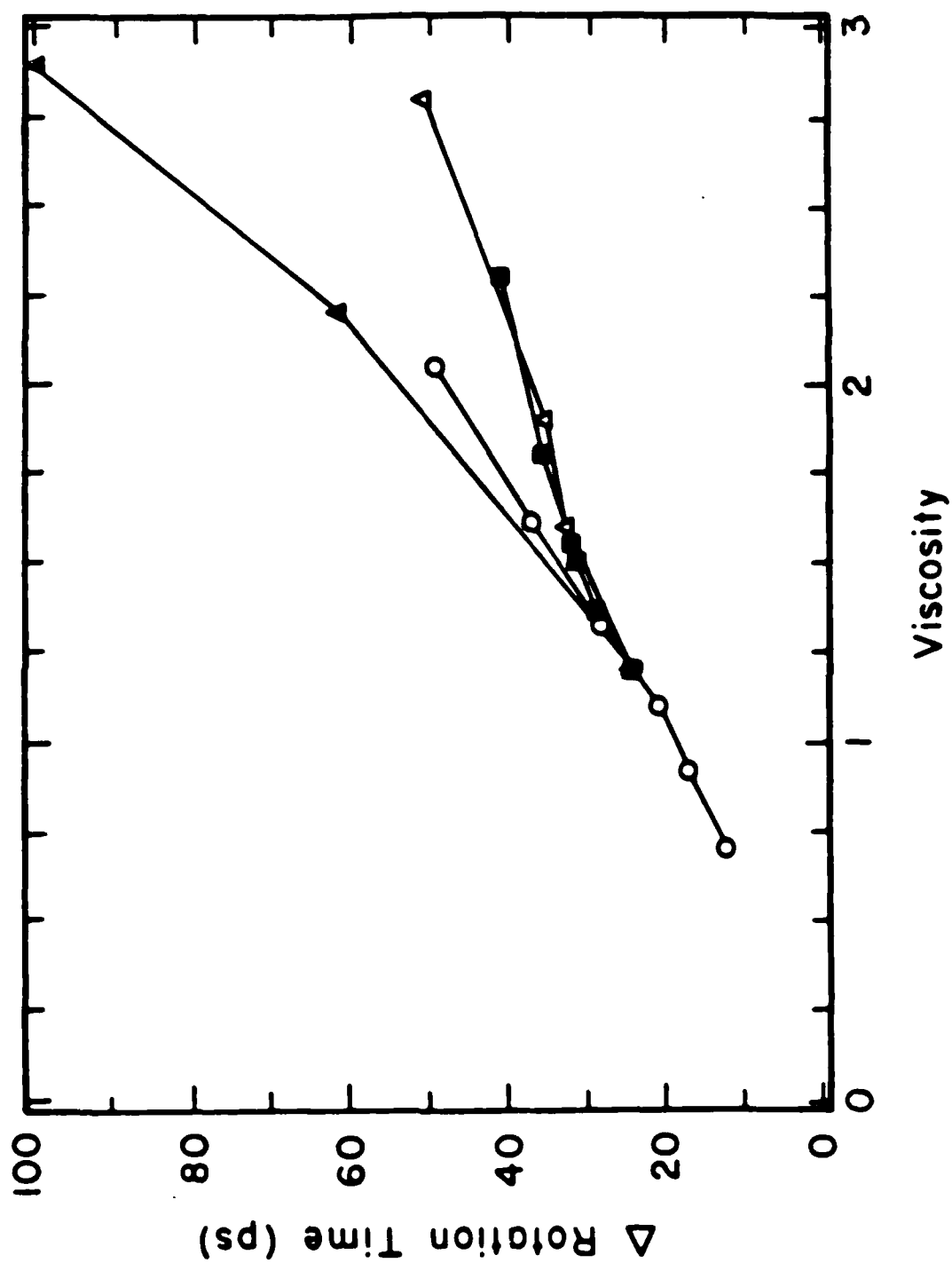


Figure 38

for slip boundary conditions. Thus, at high salt concentrations the rotation time falls within the range predicted by the SED equation. Conversely, as the salt concentration decreases, the relative importance of the contribution of dielectric friction increases and the SED equation is no longer adequate to describe the rotational behavior.

The results from this study of the effect of added salt are consistent with the dielectric friction model. The results presented here are a preliminary indication of the potential value of the study of salt effects. More data on the effect of added salt on rotation times would be useful to help quantify the contribution of dielectric friction.

5. Previous Results and the Dielectric Friction Model

A further test of the dielectric friction model can be made using the literature data presented in Tables 2-5. The variety of techniques employed in the different studies may have different systematic errors and experimental uncertainties, particularly for the longer rotational reorientation times. Thus, only preliminary conclusions should be drawn from such an analysis.

The series of linear alcohols from Tables 2-5 are considered first. The only xanthene cations that have been studied in a sufficient number of solvents to observe trends are R6G, CV, AO, and PG. The trend in R6G is not as pronounced in the literature-averaged values as it is in the present study, although a small increase in the value of τ/η with viscosity is still observed. The trend in CV is more dramatic, except for the case of decanol. This discrepancy is not troublesome because longer rotation times are in general subject to large uncertainties,

and saturation effects may occur in more viscous solvents as well.

Clear trends are not apparent in the molecules AO and PG. Both PG and AO are symmetric molecules in which the charge may be localized at either end of the molecule. The resonance of the charge between the two extremes precludes a static dipole moment of the molecule⁷⁴, thereby eliminating dielectric friction. In the oblate molecules (e.g. R6G) a similar resonance is possible, but the additional phenyl group generates the possibility of a dipole moment perpendicular to the xanthene system. Thus, the effective dipole moment of the prolate molecules is significantly smaller than the oblate molecules.

The most dramatic effects of dielectric friction are found in the case of the dianions. Since these molecules are doubly charged, it is expected that the effective dipole moments would be significantly larger than the similar, singly charged cations. The effect is most pronounced in the case of F1 and least pronounced for TCTIF. This difference is attributed to the fact that F1 has the least electron withdrawing groups, which serve to delocalize the charge and diminish the effective dipole moment. Consistent with this explanation is the fact that TCTIF has the most electron withdrawing groups.

Associated liquids are known to have anomalously large dielectric relaxation times, and the alcohol solvents are a particularly extreme example. As expected, dielectric friction causes large deviations from SED behavior in these solvents. The non-associated liquids, DMF, DMSO, chloroform, and acetone do not have unusually long dielectric relaxation times. As a result, these solvents would not be expected to generate a large amount of dielectric friction. Again, this prediction is verified by the data in Tables 2-5.

Other solvents that have a similar, albeit less extreme dielectric behavior, compared to that of the alcohols, are the amides. In particular the N-methylamides have very large dielectric relaxation times¹¹⁹. Surprisingly, the dielectric relaxation times in the N-methyl derivatives are longer than the dielectric relaxation times in the unmethylated analogs. This trend correlates with the experimental data of von Jena and Lessing^{36,37} and that of Spears and Cramer³⁸. In both of these studies, rotation times in NMF were longer than those expected, based on the rotation times in DMF and formamide.

Finally, we consider the case of the temperature variation experiments of Fleming et al. using the molecule DODCI. Values of τ_D and ϵ for ethanol as a function of temperature are given in Table 26¹¹⁰. Table 26 also contains the values of A and $\Delta\tau$ as calculated for the previous tables. The plot of $\Delta\tau$ vs η is shown in Fig. 38 along with the pressure, solvent, and salt effect data. From Fig. 38 one observes that the difference in the behavior due to temperature variation is much less extreme than in the case of either pressure variation or added salt concentration. Fleming et al.⁹² observe small deviations over limited regions, but the effect is opposite to that predicted by the dielectric friction model. The results may be rationalized by attributing the difference to errors due to approximations in the calculation of $\Delta\tau$. The differences are small, so that approximation errors may not be important for the molecule DODCI. Currently, this rationalization is purely speculative. Further temperature dependent work is clearly warranted.

Table 26

Component of Rotational Reorientation Times of R6G Due to Dielectric Friction for Ethanol Temperature Variation

Temperature(°C)	ϵ^a	A (x100) ^b	τ_D^a (ps)	$\Delta\tau$ (ps)	η (cP)
-5	29.5	0.792	432	49.1	2.05
5	27.7	0.839	318	36.9	1.62
15	25.9	0.893	236	28.1	1.33
25	24.4	0.944	170	20.6	1.10
35	22.9	1.000	135	16.8	0.915
50	20.9	1.086	93.9	12.1	0.702

a) From reference 110

b) Defined in the text

6. Conclusions

Experiments on PTP demonstrated that uncharged molecules of this size are roughly described by simple hydrodynamic models as embodied by the SED equation. Only subtle deviations from SED behavior are observed when either the solvent or the pressure is varied. Many of these subtle deviations can be accounted for by simple modifications of the SED equation such as the Gierer-Wirtz model or the Kivelson-Dote model. The improvement in fitting experimental data using these models argues that the finite size of the solvent molecules and the free space in the liquid do influence the rotational motion of solute molecules. Discrepancies between the predictions of the models and the experimental data suggest that other properties may also be important, particularly for the case of associated liquids under pressure.

The introduction of pressure as an experimental parameter has important ramifications for future work. The power of studies using pressure variation at constant temperatures has been demonstrated here. Previous work revealed that temperature variation at constant pressure also leads to valuable conclusions⁹². The combination of these two techniques would allow one to perform constant density experiments. This new dimension may help to resolve the remaining riddles in the existing results.

The trends predicted by the dielectric friction model explain the dramatic difference in the behavior of the charged R6G molecule compared to that of the neutral PTP molecule. This model also explains the changes in the rotational behavior of R6G for a variety of different experimental conditions, thereby elucidating the cause of deviations from SED behavior. More evidence in support of the dielectric

friction model is found from existing data in the literature. Many previously observed, anomalous effects are accurately described by invoking dielectric friction. It should be noted that the concept of dielectric friction is similar to the torque model proposed by Spears and Cramer. The torque model, however, was purely qualitative and had limited predictive capabilities. At this stage the dielectric friction model is only qualitative as well. It has been demonstrated, however, to be a useful predictive model for qualitative trends. Further, the framework exists to build a more quantitative model of dielectric friction. Experiments aimed at developing a better physical comprehension of dielectric properties of liquids in general will undoubtedly aid in a more quantitative model. More measurements of τ_D and ϵ as a function of solvent, pressure, temperature, and added salt would also be invaluable.

Additional studies of rotational reorientation as a function of dielectric friction are warranted. Both high pressure experiments and experiments with added salts have been demonstrated in this work to be effective methods of performing such experiments. The correlation between the variation of rotational behavior and the dielectric properties of the solvent suggests that hydrogen bonding between solvent and solute is not the dominant factor controlling rotational reorientation times. Intermolecular forces between solvent molecules in the surrounding environment appear to be more important in determining the dynamics of rotational motion. A better understanding of the role of dielectric friction in molecular rotation could provide a basis for understanding the molecular behavior responsible for the anomalous dielectric behavior

Chapter IV

ULTRAFAST CHARGE TRANSFER PHOTOPHYSICS IN $\text{Ru}(\text{bpy})_3^{++}$

A. Introduction

Transition metal complexes participate in a variety of complicated and diverse chemical processes. Such chemistry includes schemes for solar energy conversion, electron transfer reactions, acid/base reactions, and energy transfer processes¹²⁰⁻¹²³. $\text{Ru}(\text{bpy})_3^{++}$ has become a primary model for many of the phenomena that occur in transition metal complexes. In particular, the study of $\text{Ru}(\text{bpy})_3^{++}$ photophysics has provided insight into the characterization of electronically excited states of a broad class of transition metal complexes. Understanding the photophysics of $\text{Ru}(\text{bpy})_3^{++}$ has been difficult because of possible alternative mechanisms of energy reorganization among various excited electronic states. In many cases, the difficulties are compounded by the fact that experimental results yield only indirect or circumstantial evidence of the phenomena under examination. In spite of the complexity, the excited state dynamics of $\text{Ru}(\text{bpy})_3^{++}$ has proven to be a fertile, challenging area of research in recent years. As a result of extensive study, a great deal of information has been gathered concerning the nature of excited state processes in $\text{Ru}(\text{bpy})_3^{++}$.

In order to understand the excited state processes in $\text{Ru}(\text{bpy})_3^{++}$ it is necessary to obtain some information about the absorption spectrum of the molecule. The intense visible absorption band of $\text{Ru}(\text{bpy})_3^{++}$ was originally assigned by Palmer and Piper¹²⁴ to be a $d \rightarrow \pi^*$ metal-to-ligand-charge-transfer band. Since that time other studies have confirmed that assignment by both experiment and theoretical

models¹²⁵⁻¹³¹. Also present in the visible region and extending into the UV are $\pi \rightarrow \pi^*$ transitions localized on the bipyridine ligands, and $d \rightarrow d^*$ transitions localized on the central ruthenium atom. Crosby et al. used the information contained in the absorption spectrum to identify the nature of the emitting state in $\text{Ru}(\text{bpy})_3^{++}$.

By comparing the emission and absorption spectra of a series of ruthenium complexes, Crosby et al.¹²³ were able to assign the emission to a $d \rightarrow \pi^*$ transition. The series of ruthenium complexes consisted of molecules in which one bipyridine ligand was replaced by other ligands. The frequency shift and the intensity of the fluorescence in these different complexes did not follow the progression predicted by crystal field theory for a $d \rightarrow d^*$ transition. Thus, they were able to rule out the possibility of emission occurring from an excited d state on the ruthenium atom. In addition, they observed that the emission characteristics followed exactly the patterns observed for the metal-to-ligand-charge-transfer (MLCT) absorption band. This evidence led Crosby to assign conclusively the emission to a $d \rightarrow \pi^*$ ligand to metal charge transfer transition. The emission also remained constant regardless of what wavelength of light was used to excite the molecule. The conclusion drawn from this behavior was that rapid relaxation occurs via $\pi \rightarrow \pi^*$ or other $d \rightarrow \pi^*$ transitions prior to radiative relaxation from the lowest π^* level.

Although the emission from $\text{Ru}(\text{bpy})_3^{++}$ is now known to occur from a $d \rightarrow \pi^*$ transition, the role of spin multiplicity of the state remains in question. It is generally agreed that due to the heavy central atom, spin orbit coupling will play a role in mixing the singlet and triplet excited π^* states. The extent of spin-orbit mixing of the

states is not clear. Models have been proposed that cover a wide range of possibilities. For many years it was believed that the states were of singlet and triplet character, perturbed by spin-orbit coupling^{126,128,129,133 136}. Alternatively, it has been proposed that spin labels are inappropriate and that the states are completely mixed states¹³⁷⁻¹³⁹. The rate of transfer of population between the singlet and triplet states is an indication of the degree to which a transition is allowed. Thus, the timescale of the crossing between states should provide evidence as to the extent of spin-orbit coupling. If emission occurs from both the "singlet" and the "triplet" states, then time resolved emission studies should provide the timescale of the crossing time between the states. In an attempt to derive the crossing time between these states picosecond time-resolved emission experiments were performed.

There exists another area of interest concerning the lowest electronically excited state of $\text{Ru}(\text{bpy})_3^{++}$, that focuses on the distribution of the electron density in the excited state. One model proposes that the MLCT electron density is delocalized over all three bipyridine ligands, while other data suggests that the MLCT electron density is localized on a single ligand. Although nanosecond time resolved resonance Raman (TR^3) studies by Woodruff et al. suggest that a localized state is formed within 7 nsec of excitation, nanosecond time resolution is not sufficient to time resolve the formation of the emitting state. Picosecond TR^3 experiments were performed in order to gain more information concerning the nature of the emitting state, as well as the early time dynamics of the formation of that state.

B. Results

1. TR^3 Spectral Data

As in the Woodruff et al.¹⁴⁰ experiments, a single 355 nm pulse was used to both populate and Raman scatter from the electronically excited state of $Ru(bpy)_3^{++}$. The absorption spectrum of the ground state as well as the excited state absorption and emission spectra are shown in Fig. 39. The emission lifetime is 600 ns, which is four orders of magnitude longer than the laser pulses. At 355 nm the ground state absorption cross section, coupled with the long emission lifetime, is sufficient to insure complete bleaching of the ground state at our pulse energies. The excited state absorption spectrum has an absorption maximum at approximately 360 nm which acts to resonantly enhance the Raman scattering in the excited state¹⁴⁹. The initial fraction of the 25 ps laser pulse bleaches the ground state molecules. The remainder of the pulse Raman scatters from the newly formed excited state. The initial fraction of the pulse Raman scatters from the ground state as well. The net Raman signal is then the integral of the Raman processes which occur throughout the duration of the laser pulse. Since complete bleaching of the ground state is achieved in the first fraction of the pulse at our pulse energies, and since Raman scattering from the excited state is strongly resonantly enhanced, the dominant features in the TR^3 spectrum are due to electronically excited molecules. The TR^3 results are shown in Fig. 40. As seen in Fig. 39, the emission spectrum is significantly red shifted from the Raman wavelengths. Thus, luminescence from the excited state does not interfere with the Raman measurements. The baseline slope is due to two effects, the drift of the gated integrator over time (the spectra were taken

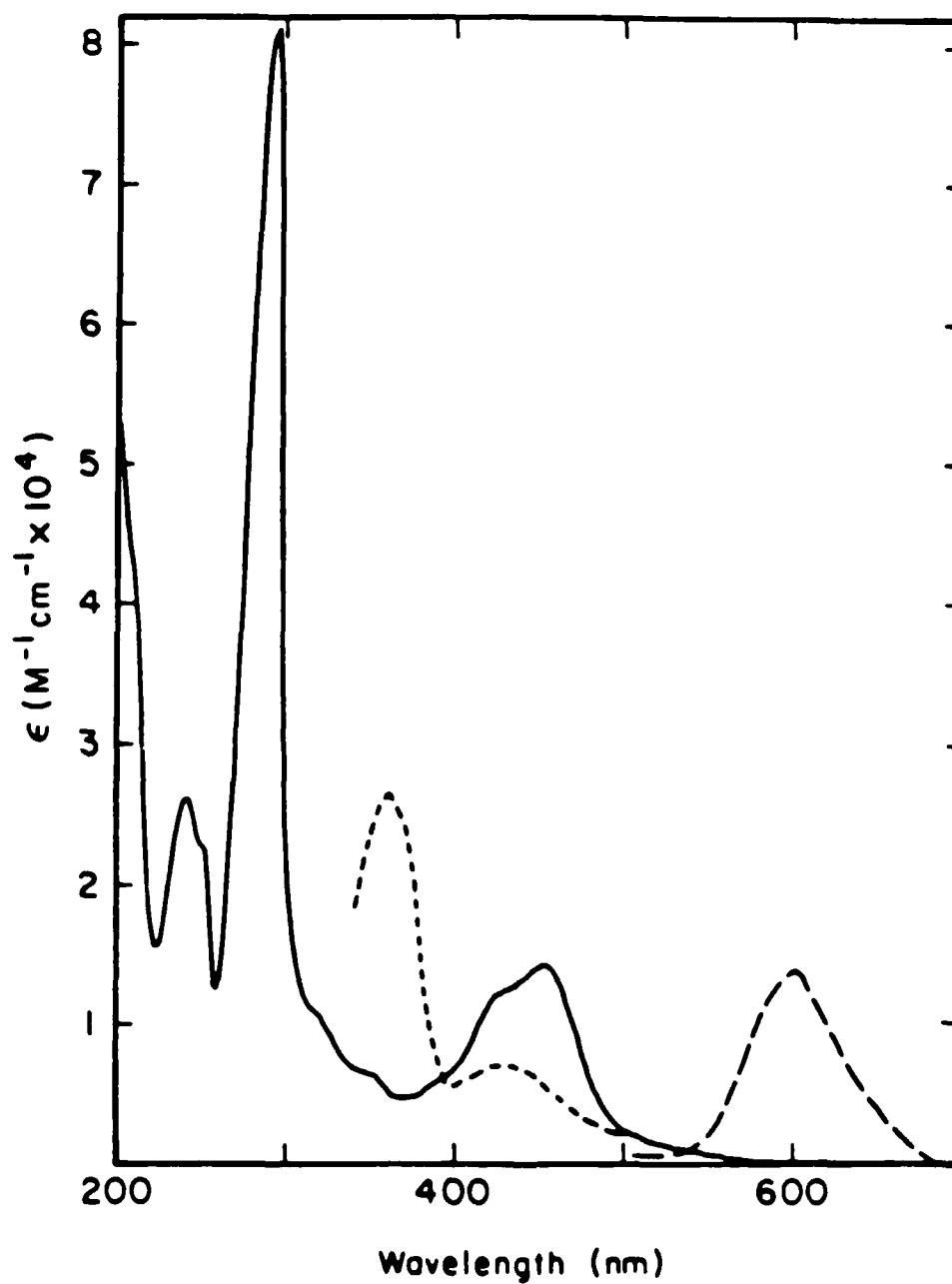


Figure 39 - Absorption and emission spectra of $\text{Ru}(\text{bpy})_3^{++}$. The solid line is the ground state absorption spectrum. The short dashed line is the excited state absorption spectrum. The long dashed line is the emission spectrum.

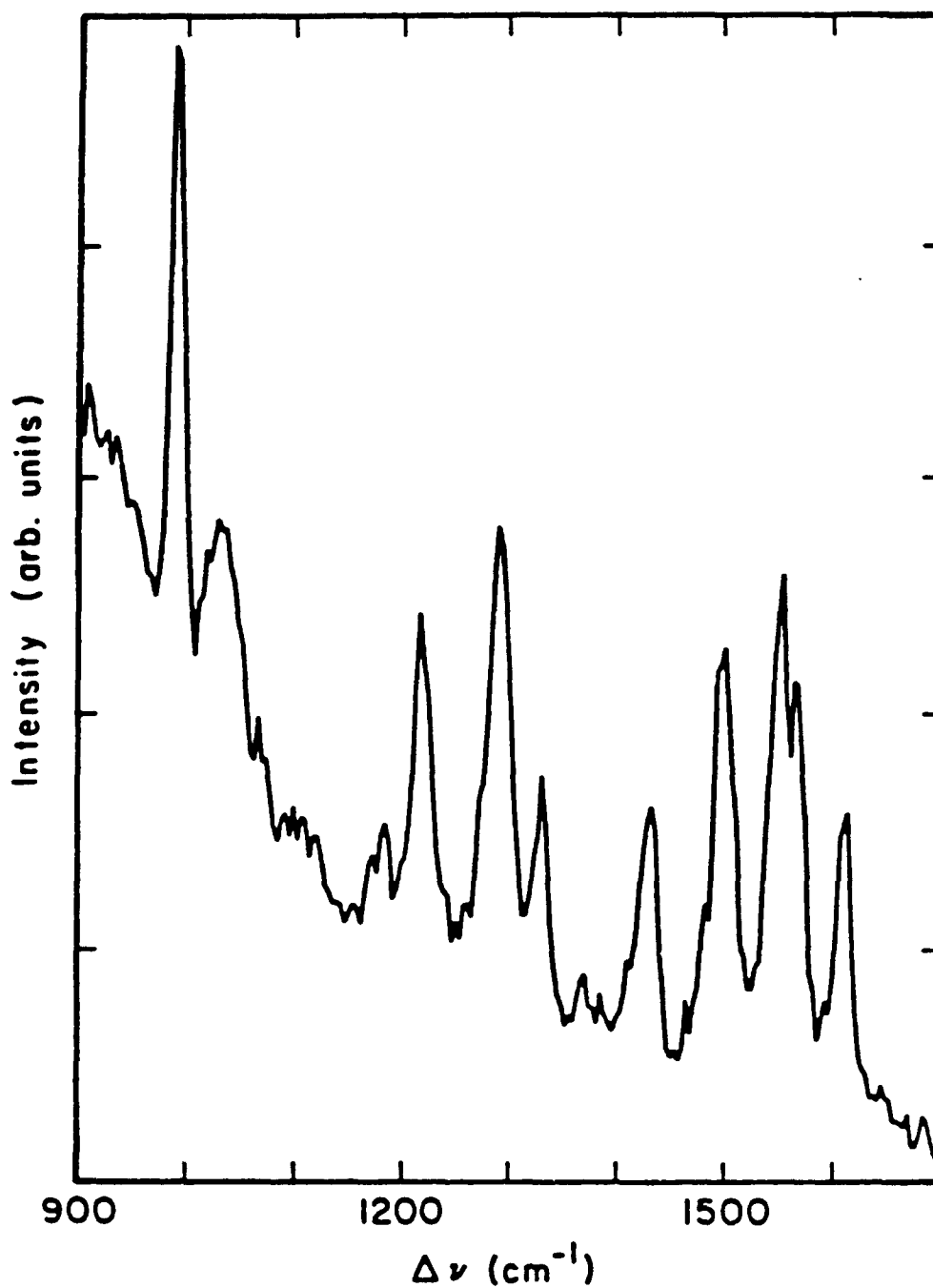


Figure 40 - Picosecond time resolved resonance Raman spectrum of $\text{Ru}(\text{bpy})_3^{++}$. A single 25 ps, 355 nm pulse was used to both excite the molecule and to Raman scatter from the electronically excited state.

over the course of several hours) and the presence of a broad quartz fluorescence from the sample cell upon 355 nm excitation. The peak at 984 cm^{-1} is a wavelength reference peak from the symmetric stretching mode of the 0.5 M SO_4^{2-} in aqueous solvent.

2. Time-Resolved Emission Data

Figure 41a shows a typical time resolved emission profile of $\text{Ru}(\text{bpy})_3^{++}$. The time resolved emission profiles were taken with a time resolution of 0.3 ps per channel on the diode array. The important feature of this data is the rise time of the emission. The rise time of the fluorescence is a measure of the rate of formation of the emitting species. The onset of the fluorescence was fast enough so as to require picosecond temporal resolution. In order to quantify the rate of formation of the emitted species it was necessary to calculate computer fits to the data. Multiexponential fits were made to the data and the best fit was found to be a single exponential rise accompanied by an exponential fall held at 600 ns, the luminescence lifetime. Figure 41a shows the best computer fit to the data. This fit gives a rise time of $< 5\text{ psec}$. The example in Fig. 41a is a result of 355 nm excitation and using a 600 nm bandpass filter for detection. These conditions give the best spectral resolution for the emission while sacrificing the signal-to-noise ratio. Other examples of similar data are shown in Figs. 41b and 41c. The conditions for Figs. 41b and 41c were high pass fluorescence filters ($> 570\text{ nm}$) for both, and 355 nm and 532 nm excitation, respectively. All three sets of data in Fig. 41 are shown with the same computer fit. It is clear that all of the data are consistent with a risetime of $< 5\text{ ps}$.

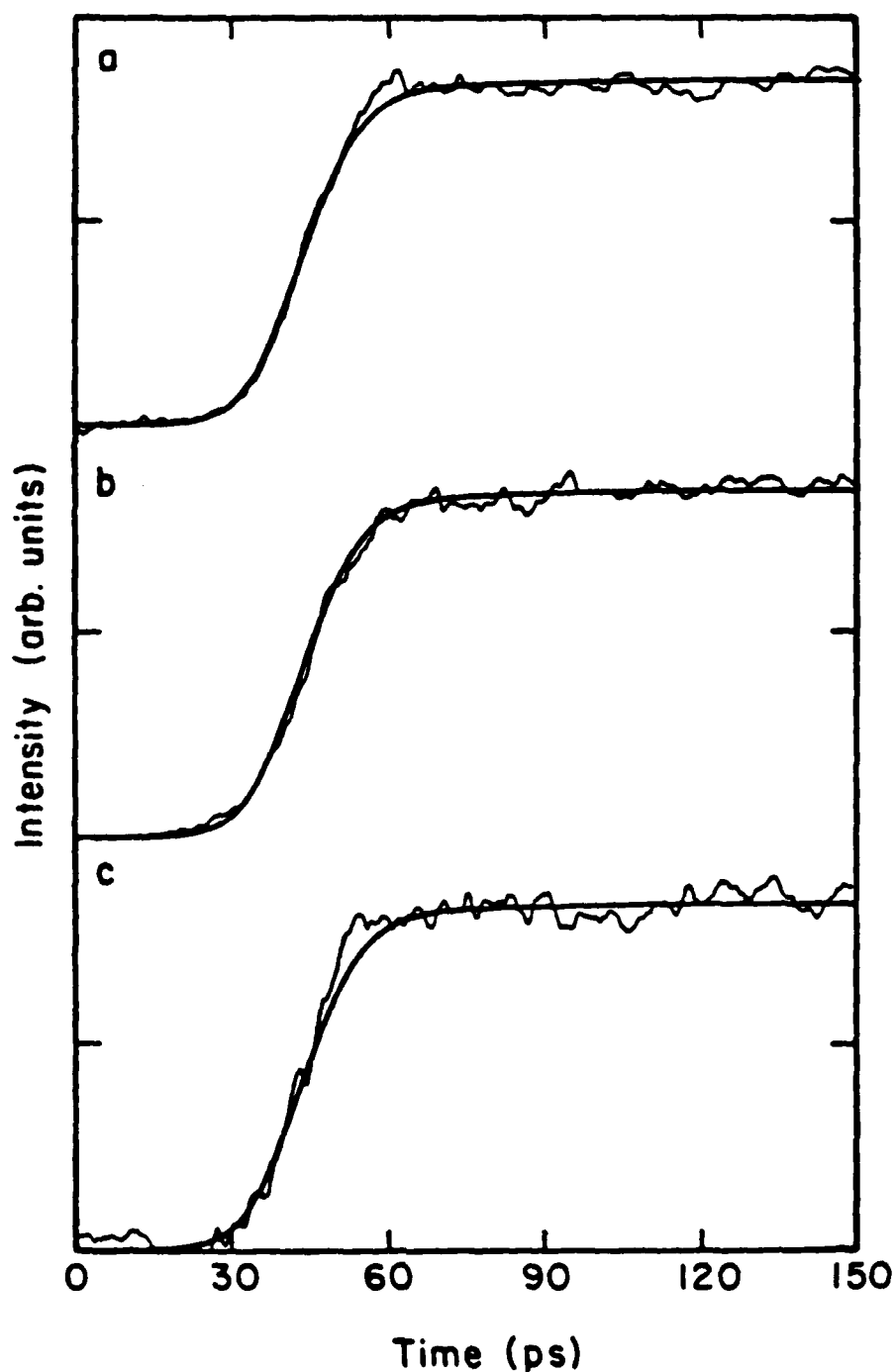


Figure 41 - Time resolved emission profiles of $\text{Ru}(\text{bpy})_3^{2+}$
 a) 355 nm excitation with detection through a 600 nm band-pass filter. b) 355 nm excitation with detection through high pass cutoff filters (> 570 nm). c) 532 nm excitation with detection through high pass cutoff filters as in b). All three sets of data are shown with the same computer generated fit to the data. The computer fit has a rise time of 0.041 ps and a fall time held at 600 ns.

The errors in fitting the data from Figs. 41a and 41c were much larger than for the data shown in Fig. 41a, due to less signal intensity. An additional problem with 532 nm excitation is the presence of a water Raman band in the emission wavelength region for $\text{Ru}(\text{bpy})_3^{++}$. Blanks were taken in conjunction with each emission spectrum. The intensity of the blanks were matched to the experimental spectra and the water Raman band was subtracted out of the experimental data. The 532 nm excitation occurs at a wavelength that is thought to result in direct excitation to the "triplet" state^{126,128,129,131}. In contrast, 355 nm is in a complex region of the spectrum involving the overlap of many transitions. Some transitions that may be involved in this region include MLCT states, $\pi \rightarrow \pi^*$ transitions localized on the ligands, and $d \rightarrow d^*$ transitions localized on the central metal atom^{126,128,129,131}.

C. Discussion

The TR^3 spectrum presents evidence that the localized state observed by Woodruff et al. within 7 ns, is already formed within 25 ps after excitation at 355 nm. The work of Woodruff et al. provides some of the strongest evidence for the localized model. In their study, Woodruff et al. looked at the C-C and C-N stretching modes of electronically excited $\text{Ru}(\text{tbp})_3^{++}$ in the region of 900 cm^{-1} to 1700 cm^{-1} within 7 ns of excitation. There are seven prominent C-C and C-N stretching modes of the bipyridine ligands in this region. If the MLCT electron were delocalized over all three ligands, one would expect to see a uniform perturbation in the spectra of all three ligands. In contrast, if the electron is localized on a single ligand, the perturbation would occur as a shift in the vibrational

frequencies of only one ligand, leaving the spectra of the other two ligands relatively unchanged. In this case the spectrum may be thought of as emanating from a species represented as $[\text{Ru(III)}(\text{bpy})_2(\text{bpy}^-)]^{++}$. Instead of seven peaks in the region $900\text{ cm}^{-1} - 1700\text{ cm}^{-1}$, this species would have 14 peaks—the seven original peaks plus seven additional shifted peaks. Woodruff et al. presented two other spectra to argue in favor of this representation of the emitting state. The ground state Raman spectrum, obtained using CW excitation at 351 nm, demonstrated the location of the seven unshifted bipyridine C-C and C-N stretching modes. In addition, Woodruff et al. provided the CW Raman spectrum of (bpy^-) in the form of the radical anion $\text{Li}^+(\text{bpy}^-)$. This spectrum should be a good model of what would be expected from a bipyridine ligand which contains an extra electron (i.e., the MLCT localized electron). Woodruff was able to assign all 14 peaks in his nanosecond spectrum. Seven peaks corresponded to the peaks in the CW Raman spectrum of $\text{Ru}(\text{bpy})_3^{++}$, and seven were analogous to the peaks in the spectrum of $\text{Li}^+(\text{bpy}^-)$. For comparison, our picosecond TR^3 spectrum from this study is shown in Fig. 42 (curve a) along with Woodruff's nanosecond TR^3 spectrum (curve b). There is complete peak-by-peak agreement between the two spectra, demonstrating that the two spectra arise from the same species. Since our TR^3 spectrum can be identified as emanating from the same species as Woodruff observes at longer times, we conclude that the emitting species is formed and is localized within 25 ps of 355 nm excitation.

Other evidence exists which argue in favor of a localized model. Braterman et al.¹⁴¹ obtained the absorption spectrum of the electronically excited state of $\text{Ru}(\text{bpy})_3^{++}$ and demonstrated that bands due to

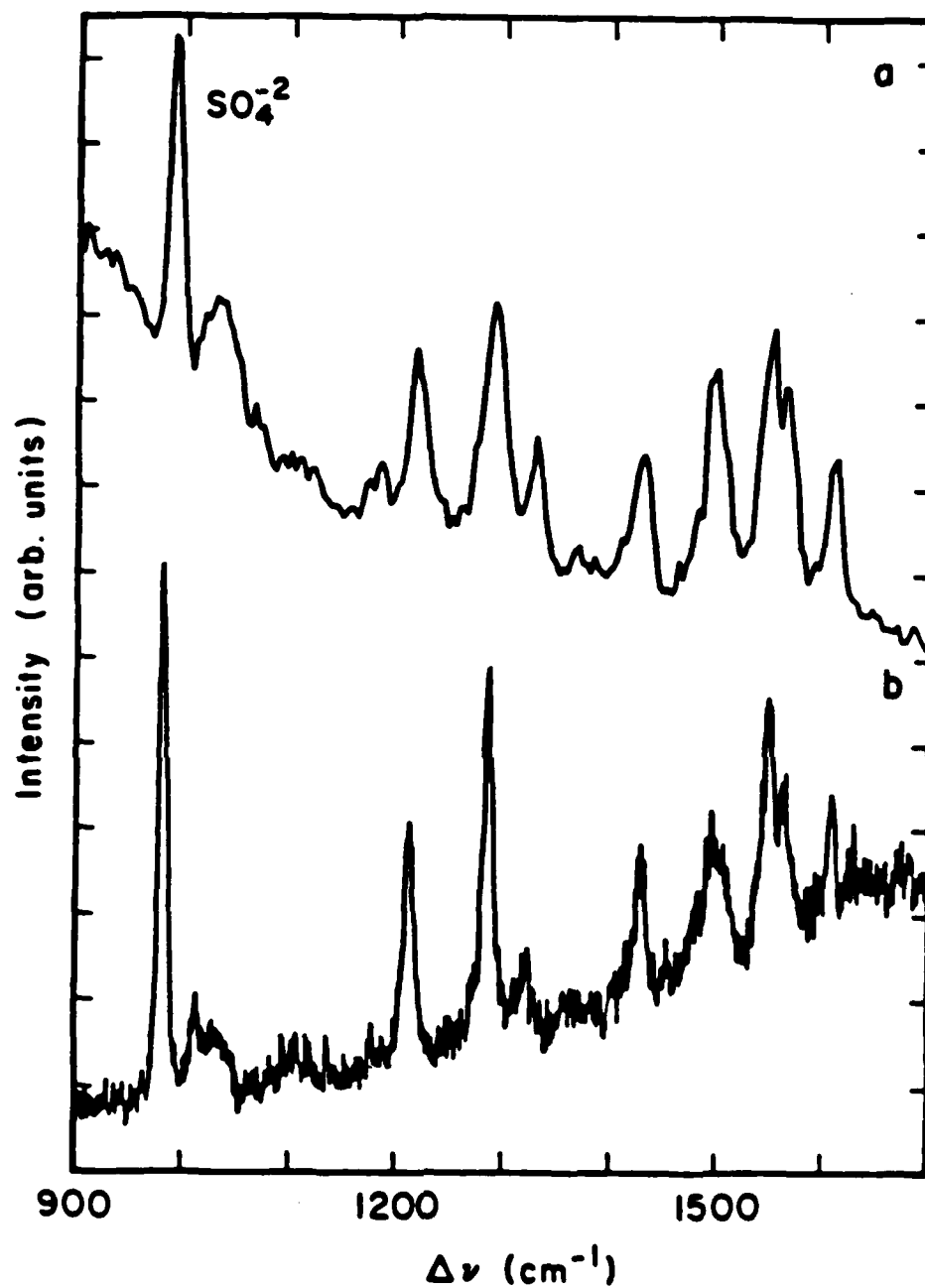


Figure 42 - Comparison of picosecond and nanosecond Raman spectra of $\text{Ru}(\text{bpy})_3^{2+}$.
 a) Picosecond data from Fig. 40. b) Nanosecond data from reference 140.
 The similarity of the spectra suggests that they are produced by the same species.

both (bpy) and (bpy⁻) exist simultaneously in the same spectrum. The presence of these bands suggest the formal representation of Ru(bpy)₃⁺⁺ as [Ru(III)(bpy)₂(bpy)⁻]⁺⁺. Hipps¹⁴², as well as Calvin and De Armond¹⁴³, argue on the basis of photoselection data that the symmetry of the excited species must be lower than the ground state D_{3h} symmetry in order to account for the large value of the polarization ratio of the emission. A localized model would reduce the symmetry to C_{2v}. Temperature dependent broadening of ESR spectrum of Ru(bpy)₃⁺⁺ was observed by Motten et al.¹⁴⁴, suggesting that the extra electron is localized on one ligand and hops between ligands on the ESR timescale (10⁻¹⁰ sec). In contrast, Crosby and Elfring¹³⁸ proposed a delocalized model based on the emission and proton NMR of a series of mixed ligand (bpy and phenanthroline) ruthenium complexes of the form [Ru(bpy)_n(phen)_{3-n}]⁺⁺. A series of experimental parameters, including the chemical shifts of the 3,3' protons of the bipyridine ligands and the 4,7 protons of the phenanthroline ligands, show a monotonic dependence on viscosity based on Crosby's data. Similar experiments were performed by Baggott et al.¹⁴⁵, but with different results. They found that the NMR spectra were more complex than Crosby's interpretation indicated and that there was not a monotonic dependence on viscosity. Further, they found that there was a more dramatic effect introduced upon changing solvents than in changing ligands. The Baggott et al. results suggest a localized model. In conjunction with other results in the literature, the results presented here provide conclusive evidence that a localized model is most appropriate for electronically excited Ru(bpy)₃⁺⁺. Our results further suggest that this state is formed in less than 25 ps. Although there is no evidence

of a second emitting state in the TR^3 spectrum, such a state cannot be ruled out. A second state may exist which is not discernable at our signal-to-noise ratio or spectral resolution. In addition, the 25 ps time resolution does not appear to be sufficient to time resolve the formation of the emitting state.

Better time resolution is achieved in the time resolved emission study which give additional information as to the kinetics of the formation of the emitting state. In Fig. 41, the experimental data is shown with the best calculated fit to the data. The fit is a single exponential risetime and a single exponential decay. The exponential risetime indicates that the onset of the emission occurs within 5 ps of excitation. Other descriptions are possible, however, if one introduces the existence of other fluorescing states. One possible alternative is that there exists another short-lived emitting state which decays to a second emitting state. In early work, it was proposed that excitation occurs to a singlet π^* state which then undergoes intersystem crossing to a triplet π^* state which then radiatively decays to the ground state. In particular, Lytle and Hercules¹³³ proposed an energy level diagram incorporating this relaxation scheme. They used the integrated intensity of the MLCT absorption band to calculate the lifetime of the initially excited π^* state. From this calculation the lifetime of the initial state should be 87 ns. The measured luminescence lifetime is on order the of microseconds. Assuming that the luminescence was from a triplet state, they expected the lifetime for this spin forbidden transition to be six orders of magnitude slower than the allowed process. The discrepancy of four orders of magnitude is explained by the introduction of spin-orbit

coupling from the interaction with the ruthenium atom. If spin-orbit coupling is able to enhance a spin-forbidden, radiative process, it should similarly enhance a spin-forbidden, non-radiative process. They reasoned that a typical intersystem crossing rate for a molecule with no spin-orbit coupling is 10^{-7} - 10^{-8} sec^{-1} , therefore, with the additional spin-orbit enhancement the upper limit of the intersystem crossing time is 10 ps. In this scheme, at times short compared to the intersystem crossing time, emission would occur from both the initially pumped state as well as the final emitting state. At long times the emission occurs only from the final state.

Alternative descriptions of the excited state manifold have also been proposed. Crosby et al.¹³⁷ have suggested a model in which spin labels of the excited state are inappropriate. Instead of triplet and single states, the excited state manifold consists of mixed spin-orbit states. A study by Harrigan and Crosby¹⁴⁶ and a second study by Harrigan, Hager and Crosby¹⁴⁷ measured the lifetimes and quantum yields of a series of ruthenium II complexes at temperatures from 2 - 77 K. The lifetimes of the complexes increase as the temperature is lowered. This effect becomes particularly dramatic at temperatures below 10 K. As the lifetime increases there is a concomitant decrease in the quantum yield. The data from these studies were empirically fit to a multiple state model. Crosby et al. found that a minimum of three levels were necessary to fit the experimental data. The spacing of the energy levels were found to be such that the second level is 10 cm^{-1} and the third level is 79 cm^{-1} above the lowest excited states. The lifetimes of the first, second, and third states are 217, 19 and 0.6 μsec , respectively. This empirical model

suggests that even at low temperatures there is sufficient thermal energy to populate all three levels. Most of the luminescence would occur from the level that has the shortest lifetime, which in this case is the state that is highest in energy. The assumptions implicit in the model proposed by Crosby et al. are that the population of the three excited states remain in Boltzmann equilibrium, each level radiatively and non-radiatively couples to the ground state, and the luminescing state(s) is populated with unit quantum efficiency from more highly excited states. The symmetry of the three excited states were assigned based on the D_{3h} symmetry group to be A_1 , E, and A_2 .

Additional evidence was provided for the Crosby model by a study by Baker and Crosby¹⁴⁸. They observed the change in spectral band shape and intensity with temperature (2 - 10 K) and with the application of a magnetic field. At 1.65 K, the luminescence should occur virtually exclusively from the lowest (A_1), electronically excited state. In contrast at a temperature of 10 K, the luminescence will occur preferentially from the highest level (E) which is symmetry allowed. The A_1 transition is only made vibronically allowed by a vibrational quantum of A_2 or E symmetry in the ground electronic state. The spectral shifts and intensity reflect the allowed character of the transition as well as the additional ground state vibrational energy. A magnetic field was applied to the 1.65 K sample to mix, in accord with this symmetry assessment, the E and A_2 states with the A_1 state, making this state more allowed. Further, the E state should be shifted so as to decrease the energy difference between the A_1 and E states, thereby increasing the population of the E state. The results of this experiment are consistent with the above expectations. With the

application of a magnetic field, the 1.65 K spectrum shifts so as to more closely resemble the higher temperature spectra without the magnetic field. Further, the intensity increases a great deal upon application of the field, reflecting the increased allowedness of the transition.

Other models have also been suggested which accurately describe the Crosby et al. data. Extensive work has been done by Ferguson et al.¹²⁸⁻¹³¹, which includes the temperature dependence of absorption, circular dichroism and luminescence spectra. Polarized absorption spectra suggest^{126,128-131} that it is necessary to include spin multiplicity in any description of the excited electronic state of $\text{Ru}(\text{bpy})_3^{++}$, although they may be highly mixed by spin/orbit coupling. The luminescing state is interpreted to originate from a triplet state, but carries significant intensity due to mixing with other states. The Ferguson model claims that the lowest energy, emitting states are all C states. They agree with the Crosby model that there must be a series of closely spaced energy levels in order to explain the low temperature emission data. The mechanism of emission at low temperatures conflict with the Crosby model in that Boltzmann equilibrium between the lower energy states does not occur. Instead, separate radiationless relaxation pathways are assumed to populate the different low energy states. The relaxation processes to the lower levels is blocked at low temperature (i.e., < 6 K), which results in the observed changes in the emission. At temperatures above 10 K, however, Ferguson et al. also predict thermal equilibration and emission predominantly from the highest energy level of the series of closely spaced C states.

The model of Crosby et al. requires a prompt rise in emission followed by a single exponential decay. Similarly, the model of Fergusen et al. is consistent with this description of the emission time profile. If emission occurs from a second short-lived state, as in the model of Lytle and Hercules, then a more complex description of the emission time profile is required. An emission scheme involving a second short-lived emitting state is shown in Fig. 43. τ_A is the natural lifetime of the initial state A, and τ_B , and τ_B' are, respectively, the fluorescence lifetime and natural lifetime of state B. τ_{AB} is the non-radiative transfer time from state A to state B. State A need not be excited directly, but may also be populated by rapid radiationless decay from more highly excited states. If one assumes that the emission from the initial state is prompt, as is indicated by the data, then a two state emission scheme can be represented by a sum of three exponentials:

$$I(t) = \frac{1}{\tau_A} [\exp(-t/\tau_A + t/\tau_{AB})] + \frac{1}{\tau_B} [\exp(-t/\tau_B + t/\tau_B') - \exp(-t/\tau_A + t/\tau_{AB})] \quad (52)$$

The first exponential represents the decay of the initial state, while the second two exponentials describe the risetime and subsequent decay of the final state. Since the decay of the second state is known to be 600 ns and its natural lifetime is 6.6 μ s, the decay time of the second state may be held constant¹⁴⁹. The variable parameters are the natural lifetime of the initial state (τ_A) and the inter-state transfer time(τ_{AB}). Calculated fits were made to the data using a three exponential fit with τ_B and τ_B' held constant, but there was

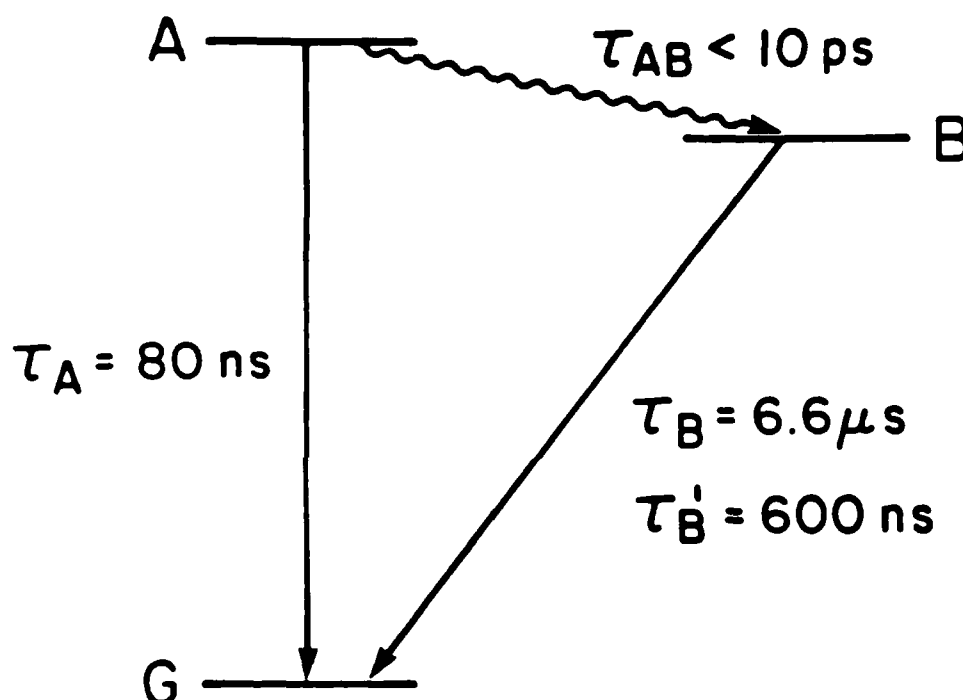


Figure 43 - Kinetic model of emission. This diagram depicts the standard representation of separate singlet and triplet manifolds, in which transfer of population between the two manifolds occurs through intersystem crossing. The natural lifetime of state B (τ_B) is known to be 6.6 μsec . The radiative lifetime of state B (τ_B') is 600 ns. The estimates of the natural lifetime of state A (τ_A), and the intersystem crossing time (τ_{AB}) given in this figure are from reference 133.

no significant improvement in the fit to the data. From our data, additional exponentials do not appear to be warranted, and a single emitting state is sufficient to describe the data. Our signal-to-noise is such, however, that we cannot completely rule out the presence of a second emitting state. Various curves were calculated from Eq. 51 in order to set some boundaries on possible values for the parameters τ_A and τ_{AB} . Figures 44 and 45 show a series of calculated curves varying τ_A and τ_{AB} . The Lytle and Hercules estimate of the lifetime of the initially pumped state based on the integrated absorption coefficient was 87 ns. Using comparable numbers to that study of $\tau_{AB} = 10$ ps and $\tau_A = 90$ ns, the calculated curve is dramatically different from the experimental data. Determination of τ_A from the integrated absorption coefficient is difficult, particularly from such a complex spectral region. It is very likely that the estimate has a large uncertainty, and that it is an overestimate of the absorption cross section. Assuming that τ_A is approximately an order of magnitude larger, 600 ns, the calculations are still inaccurate, for $\tau_{AB} = 10$ ps. If τ_{AB} is decreased to < 1 ps, while τ_A is maintained as 600 ns, then the calculated curve approached the experimental data. The curve calculated based on this set of parameters, could fit the data based on our experimental uncertainty (see Fig. 45). Thus, if a second emitting state exists, it must be very shortlived (< 1 ps) and will play only a small role in the emission photophysics or any subsequent photochemistry.

Persuasive evidence that the role of a short-lived state is not significant is also contained in Fig. 41. Regardless of the excitation energy, 532 nm or 355 nm, the time resolved emission profiles are

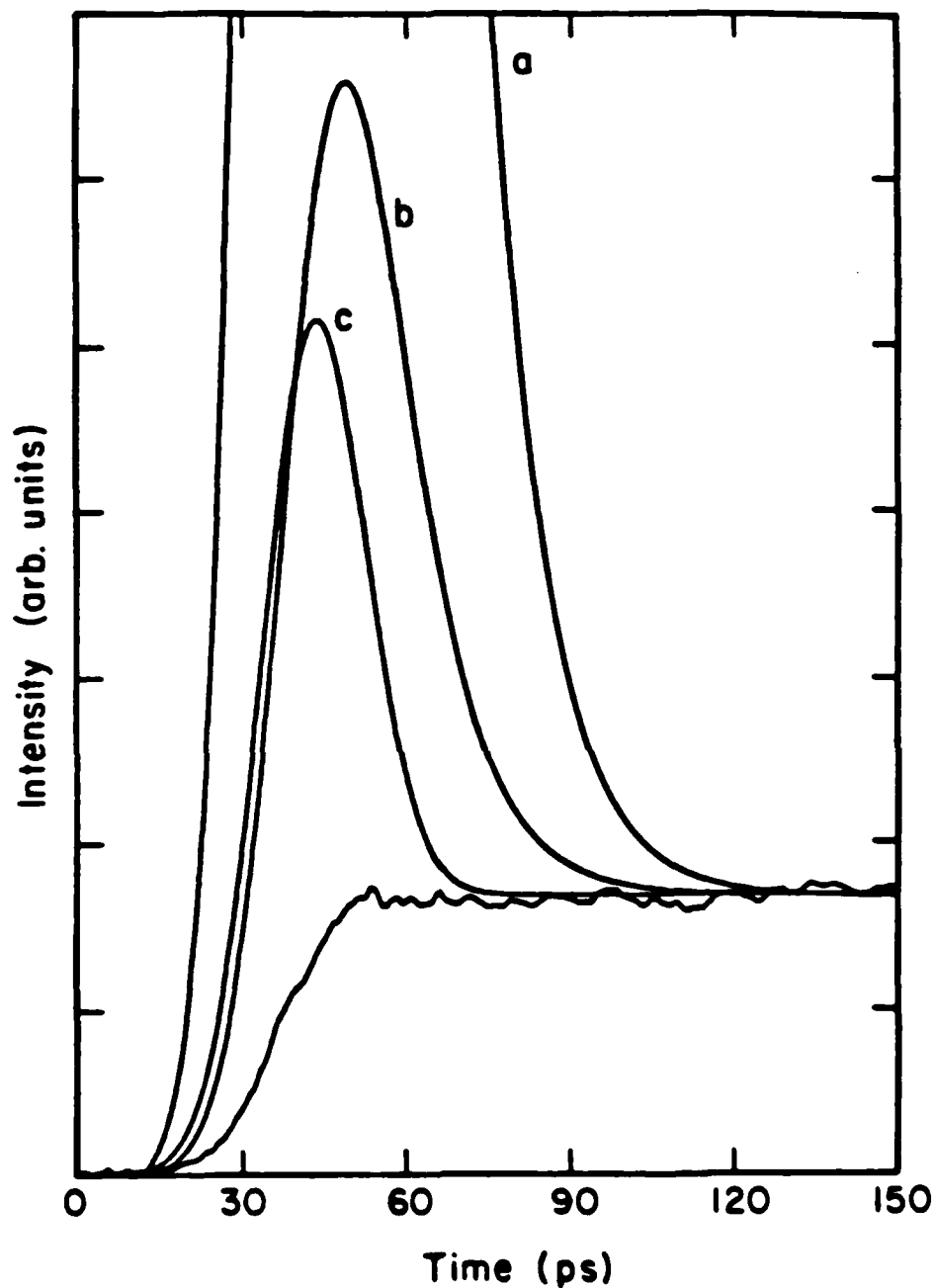


Figure 44 - Kinetic model fits to the experimental data. The experimental data from Fig. 41b is shown with three calculated curves. The curves are calculated from Eq. 52. In all cases, $\tau_B = 6.6 \mu\text{sec}$, and $\tau_B' = 600 \text{ ns}$. a) $\tau_A = 90 \text{ ns}$, $\tau_{AB} = 10 \text{ ps}$. b) $\tau_A = 600 \text{ ns}$, $\tau_{AB} = 10 \text{ ps}$. c) $\tau_A = 90 \text{ ns}$, $\tau_{AB} = 1 \text{ ps}$.

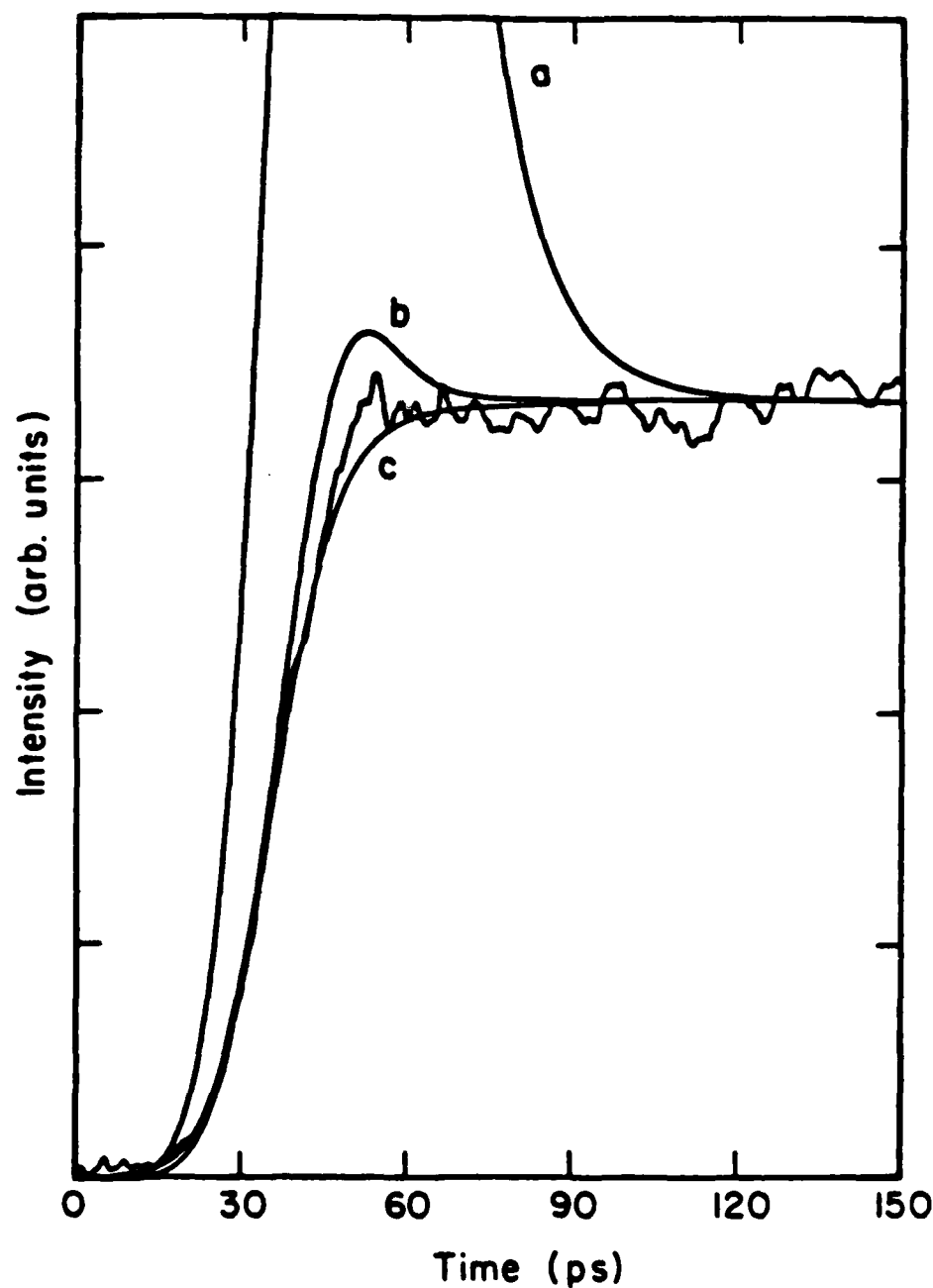


Figure 45 - Kinetic model fits to the experimental data. This figure is an expanded view of Fig. 44, with additional calculated curves. The experimental data is the same as that in Fig. 44. Curve a is the same as curve b in Fig. 44, that is for curve a: $\tau_A = 600$ ns, $\tau_{AB} = 10$ ps. Curve b) $\tau_A = 600$ ns, $\tau_{AB} = 1$ ps. Curve c is the computer fit to the data shown in Fig. 41, with a single exponential fall of 600 ns and an instantaneous rise time.

identical within the experimental uncertainty. Excitation in these experiments occurs to vastly different states. The state pumped with 355 nm is thought to be of singlet parentage, while 532 nm excitation is thought to directly pump a state of triplet parentage, yet the emission kinetics appear the same.

From the calculated fits to the experimental data, it is clear that the transfer time between an initial and final emitting state must be faster than 1 ps. When higher energy states are pumped, the emission kinetics are experimentally indistinguishable from the results when the lower energy states are directly pumped. The rapid transfer between these states as demonstrated by these experiments reflect the dominant role of spin-orbit coupling in transition metal complexes which contain a heavy central metal atom such as ruthenium.

Chapter V

CONCLUSION

Two different techniques coupled with picosecond laser technology have been demonstrated to add new insights into two different areas of chemical physics. A high pressure cell introduced a new method for varying the solvent parameters in the study of the dynamics of rotational motion. The structural specificity of Raman spectroscopy coupled with picosecond time resolution allowed for the identification of the states involved in the ultrafast excited state dynamics of the transition metal complex $\text{Ru}(\text{bpy})_3^{++}$.

The study of the rotational reorientation times of PTP and R6G focused on evaluating various models for rotational motion in liquids. Simple hydrodynamic models of rotational motion, such as the SED eq., gave results consistent with all of the PTP data. Modifications of the SED equation including the Kivelson-Dole and Gierer-Wirtz models accurately described some of the more subtle variations in the data. The correlations between the predictions of these models and the data suggest that the molecular structure of the liquid plays a role in determining rotational motion. The remaining, albeit subtle, discrepancies between predictions and data warrant closer examination. The explanation of these discrepancies may reside in either the theory or the experiment. The deviations in the data are small, often close to the limits of detection. More data would help verify conclusions. The theory is also similarly limited. Both of the models mentioned above specifically account for the free space on the liquid or the relative solute/solvent sizes. They do not, however, include inter-

molecular interactions between solvent molecules. This omission may be particularly important in the highly structured alcohol solvents. The models also do not include interactions between solute and solvent molecules. Such interactions are not pronounced in the case of the neutral, non-polar PTP molecule, hence the good agreement with the PTP data. In contrast, the results of the R6G studies expose some of the limitations of these models.

Pressure has proven to be a particularly useful parameter in the study of the rotational reorientation times of R6G. Through the use of high pressure it was possible to demonstrate that identical macroscopic viscosities have different microscopic rotational reorientation times. This result is in clear conflict with the predictions of simple hydrodynamic models. The discrepancy led to the incorporation of solvent induced dielectric friction in the description of rotational motion for highly interacting molecules such as R6G. The dielectric friction model accurately depicted the experimental trends observed here, as well as many anomalous results previously reported in the literature. A preliminary study on the effect of added salt further substantiated the dielectric friction model. The application of the model is presently limited by the paucity of data in the literature on the dielectric properties of solvents, particularly solvents under pressure. A further limitation is the difficulty in determining the effective dipole moment of complex molecules such as R6G. More work on simpler, highly polar molecules in a wide range of solvents of varying dielectric properties such as the alcohols and the amides as well as non-associated solvents would provide more information. Since dielectric properties vary markedly under pressure, high pressure

experiments are a stringent test of the model. The preliminary results from the experiments with added salts indicate the value of further, similar experiments.

Although the interpretation of the data in terms of the dielectric friction model are qualitative in nature, it is possible to gain specific information concerning intermolecular interactions. Since the trends in the data correlate with the dielectric properties of the solvent alone, it is concluded that interactions between solute and solvent such as hydrogen bonding are not the dominant effect controlling rotational motion. Rather, an effective torque induced by the response of the solvent environment to the motion of the solute governs the process. Thus, although the dynamics of rotational reorientation are accurately described in terms of bulk properties of the solvent, specific molecular information has been determined.

In the second study, the combination of picosecond, time resolved Raman and emission spectroscopies allowed the determination the time-scale of charge localization in electronically excited $\text{Ru}(\text{bpy})_3^{++}$. The structural specificity of Raman spectroscopy enabled us to determine that the charge localized state previously observed on the nanosecond timescale has already formed within 25 ps of the initial excitation.

Further studies using time resolved emission spectroscopy provided increased time resolution, and showed that the emitting state was formed in less than one picosecond. The emitting state is the same localized state observed in the Raman experiments. The use of different excitation wavelengths, including 532 nm and 355 nm, demonstrated that the relaxation time of the emitting state was identical in both cases within the time resolution of the experiments.

The results from these experiments were used to evaluate existing models of the role of spin multiplicity in the ultrafast photophysics of $\text{Ru}(\text{bpy})_3^{++}$. In classical models of singlet and triplet states, a barrier exists for transition between states of different multiplicity. It was determined that these models predict intersystem crossing times which are longer than those observed here. Thus, it was concluded that the spin-orbit coupling induced by the large central ruthenium atom acts to strongly mix the states. The high degree of mixing allows for rapid relaxation in the excited state manifold, which accounts for the ultrafast intersystem crossing times that were observed. These results should also be applicable to the excited state processes in a range of transition metal complexes that contain a heavy central metal atom.

It is hoped that the results presented here stimulate further investigation into the mechanism of rotational motion in solution and into the ultrafast photophysics of transition metal complexes. The power of the techniques employed in the study of these problems has been clearly demonstrated. The potential for further application of these techniques to a variety of other systems is almost unlimited. The study of dynamics in liquids is indeed complex. This thesis represents an attempt to increase our understanding in this complicated field of study.

Appendix A

EXCITATION WAVELENGTH STUDY OF ROTATIONAL REORIENTATION

1. Introduction

Rotational motion of molecules in solution has been widely studied as a probe of the microscopic interactions between solute molecules and their solvent environments^{37,38,73,76,77,94,150,150-152}. Rotational reorientation measurements have also been used as a probe of such solute characteristics as molecular shape, molecular charge, and vibrational relaxation^{36,37,74,88,89,150,153,154}. These various studies have employed a range of different experimental methods including both nanosecond and picosecond time resolved techniques of fluorescence depolarization, absorption recovery, and transient grating measurements. Although the techniques are varied, the choices of solute molecules have been very similar. Intermediate sized dye molecules of the xanthene family have been a popular choice because of their large absorption cross sections and their ubiquitous presence in laser laboratories. Further, there are an assortment of isomers within the xanthene dyes which cover a range of absorption and emission wavelengths easily accessible with generally available laser apparatus. In general, the results of previous studies have been in agreement, but the validity of making such comparisons has not been thoroughly investigated.

One potential source of disagreement among previous experiments is the influence of excitation wavelength on measured rotational reorientation times. Some results in the literature suggest that certain molecules have rotation times that are sensitive to the excitation

wavelength in emission experiments¹⁵⁰⁻¹⁵⁴, or to the probe wavelength in absorption recovery experiments^{88,155}. In some cases^{153,154}, these effects are thought to result from excitation into different electronic states that have transition moments oriented in different directions. If the molecule is asymmetric, then anisotropic rotational motion will result. Thus, different transition moments access different components of the rotational diffusion tensor.

It is more difficult to understand the variation of the rotation time with excitation wavelength when excitation occurs to different vibrational levels within the same electronic state. Various theories have been proposed in the literature to explain this phenomenon. Deviations in the transition moment with vibrational level¹⁵⁵ would cause changes in rotation times for asymmetric molecules. It has also been proposed that rapid vibrational relaxation deposits energy in the local environment. This sudden energy increase might induce a local change in temperature causing a variation in the rotational reorientation time¹⁵². Previous studies have not provided sufficient data to thoroughly evaluate the proposed models, or to validate the comparison of results from different experimental investigations. The experimental evidence is particularly limited in the case of the xanthene dyes. The present study has been performed to investigate the effect of excitation wavelength on the dynamics of rotational motion of the xanthene dye rhodamine 6G (R6G) in ethanol.

2. Experimental

These experiments were performed using picosecond, time resolved, fluorescence depolarization techniques. The experimental apparatus

will be described in detail elsewhere², and is described only briefly here. The excitation source was the output of a tunable, picosecond, optical parametric source (OPS)³, pumped by the 355 nm third harmonic of a single amplified pulse from an active/passive mode-locked Nd:YAG laser system (Quantel, YG400AP). The OPS output typically consisted of 50-100 μ J, 10-15 ps pulses at a repetition rate of 10 Hz. The OPS wavelength could be continuously tuned from 450 to 630 nm by adjusting the angle of the KDP crystals. The excitation wavelengths selected for this study were 464 nm, 476 nm, 495 nm, 503 nm, 510 nm, 520 nm, 532 nm, and 545 nm. Figure 9 shows the absorption and emission spectra for R6G in ethanol. Notice that the selected wavelengths span the absorption spectrum of the ground state of R6G.

An ultrafast streak camera (Hadland Photonics, Imacon 500) with diode array readout (Tracor Northern, IDARSS) was used to time resolve the emission. The sample was excited with vertically polarized light and the emission was observed through a Glan prism polarizer to select polarizations at the desired orientation. The emission was measured at polarizations parallel, perpendicular, and 54.7° with respect to the vertical input polarization. Each data set represents the signal accumulated from 200-500 individual laser pulses. For all excitation wavelengths, the emission was passed through high pass cut off filters (Shott, KV550) before detection. An example of the vertical and horizontal components of the emission are shown in Fig. 46. The vertical and horizontal components were normalized by the procedure of tail-matching⁷⁷ at times longer than five rotational lifetimes. The rotational anisotropy, $r(t)$, was derived from the vertical and horizontal components by standard methods⁷¹ and is given by

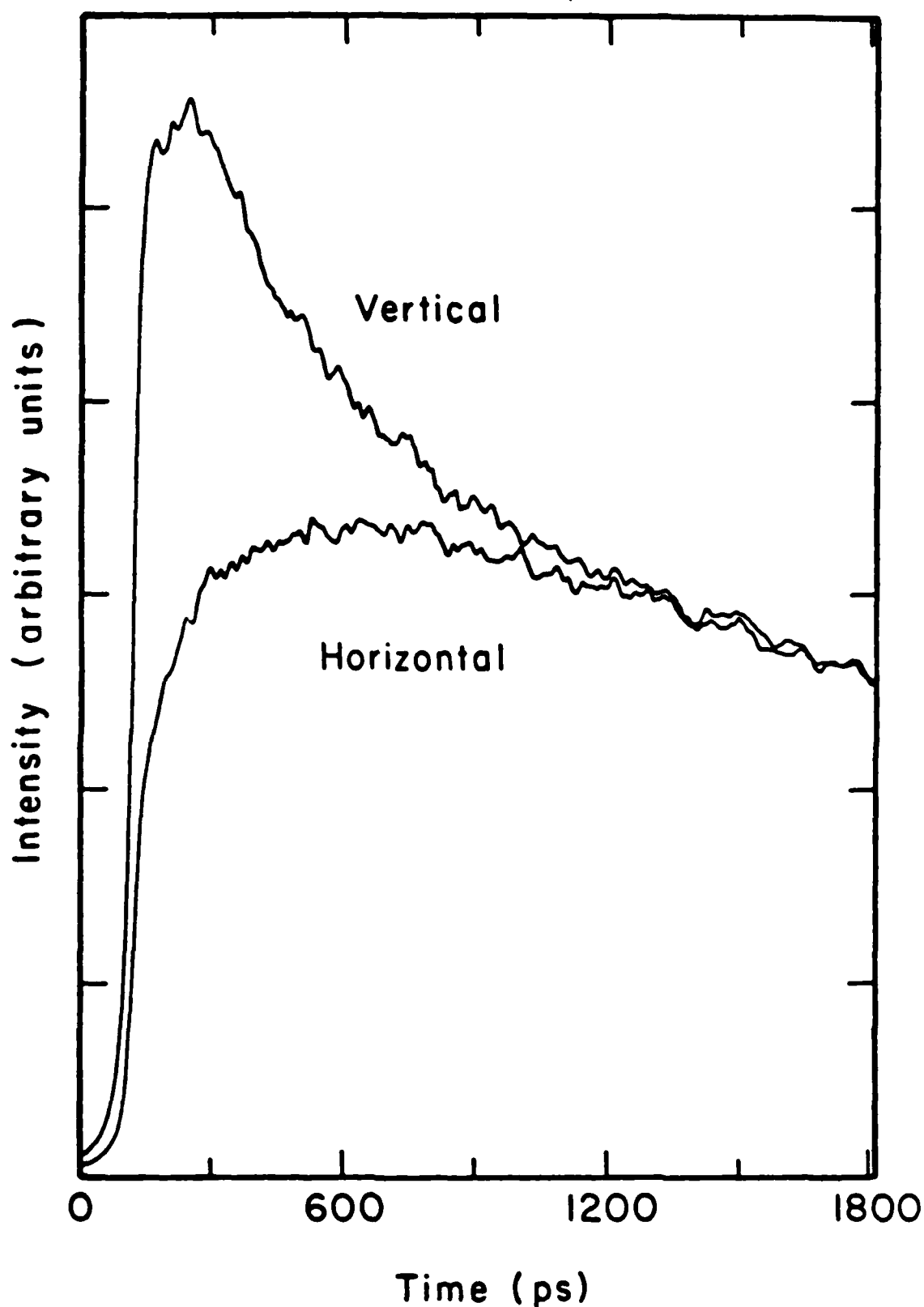


Figure 46 - Vertical and horizontal components of the fluorescence decay of rhodamine 6G in ethanol, for 476 nm excitation. The two sets of data were tail-matched (see text) over the last 100 ps depicted in the figure.

$$r(t) = \frac{I_{\parallel}(t) - I_{\perp}(t)}{I_{\parallel}(t) + 2I_{\perp}(t)} \quad (53)$$

All solutions were prepared using laser grade R6G (Eastman) and spectral grade ethanol at concentrations of 10^{-6} M. The laser power was attenuated sufficiently to ensure that saturation or stimulated emission artifacts were eliminated.

3. Results and Discussion

Semi-log plots of the rotational anisotropy versus time for all of the data sets were linear, indicating a single exponential decay. For any symmetric top molecule with its transition moment parallel to its symmetry axis, a single exponential decay will be observed. This is not the case for R6G, however. The structure of R6G, given in Fig. 12, is approximately an oblate ellipsoid, but the transition moment is in the plane perpendicular to the symmetry axis. For an oblate top molecule and stick boundary conditions, the two unique diffusion constants would be expected to be very similar⁷⁴. Thus, it is not surprising that the decays in this study appear single exponential. The values of the rotational reorientation times derived from the semi-log plots are given in Table 27. At all wavelengths, the fluorescence lifetime was found to be 3.6 ± 0.2 nsec.

A plot of the rotational reorientation time as a function of excitation wavelength is given in Fig. 47. From this plot it is clear that no systematic variation in the rotation time was observed as a function of excitation wavelength. The line in Fig. 47 is the average value of the rotation time. The uncertainties given in Table 27 and in the figure are not the standard deviations from the average, but rather encompass the total estimated random and systematic errors.

Table 27

Rotational Reorientation Times of R6G in Ethanol as a Function of
Excitation Wavelength

λ (nm)	$r(0)$ ($\pm 10\%$)	τ (ps) ($\pm 10\%$)
464	0.33	292
476	0.34	278
495	0.33	306
503	0.36	307
510	0.36	301
520	0.33	277
532	0.34	315
545	0.36	320

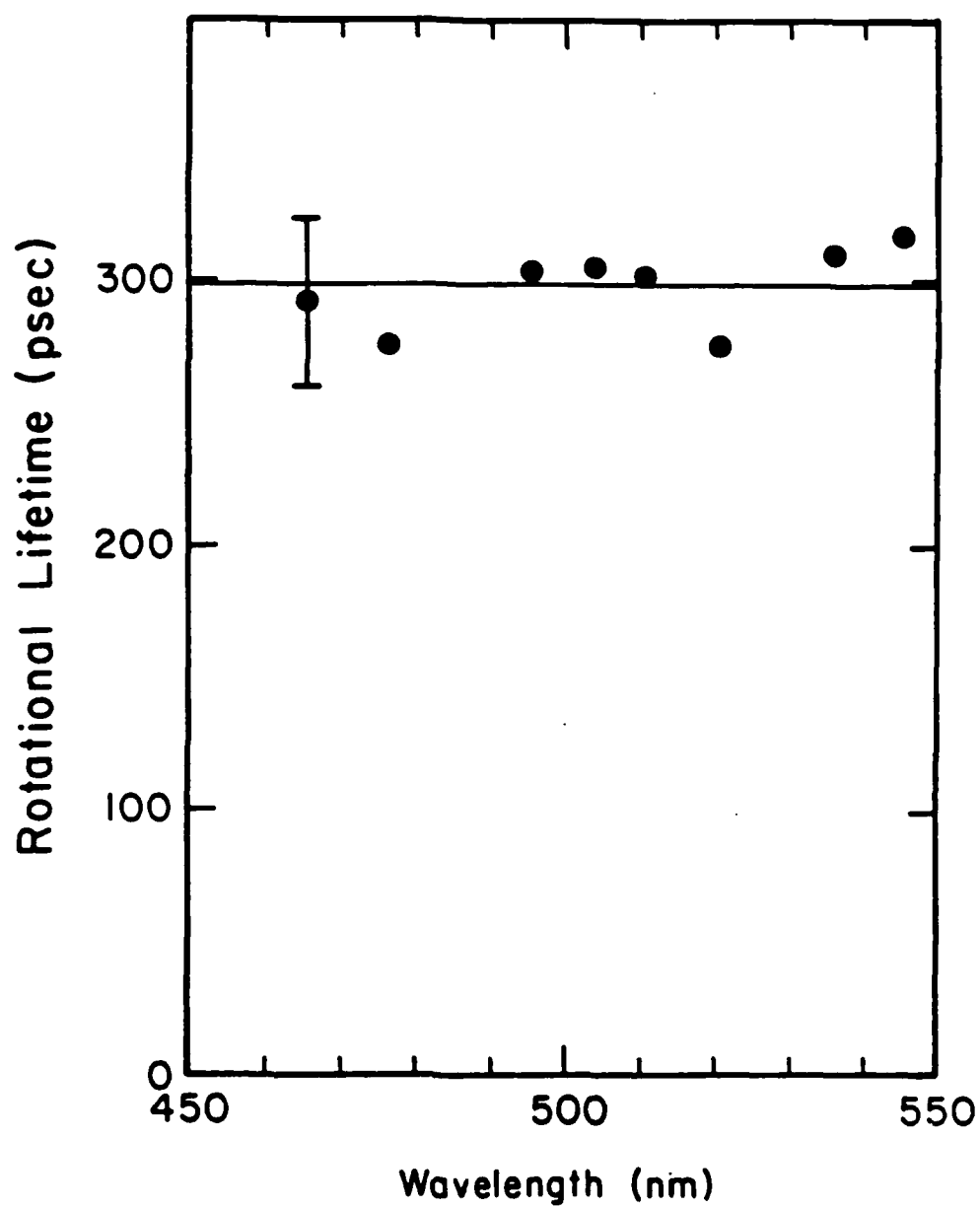


Figure 47 - Plot of τ versus excitation wavelength. The error bars represent systematic as well as random uncertainty in the data.

The results given here are in conflict with other results in the literature for R6G as well as for other molecules^{150-152,155}. Local thermal effects that occur on the timescale of molecular rotation as proposed by Heiss would result in a decrease in the rotational reorientation time with decreasing excitation wavelength. This effect has been reported previously. The present results are in conflict with these previous investigations^{151,152}. In other experiments which specifically studied R6G, the solvents used had viscosities that were an order of magnitude larger than ethanol. It is possible that this difference is the reason for the discrepancies.

The present results challenge the concept of local thermal "melting" of the solvent cage which occurs on the timescale of molecular rotation, but do not address thermal effects that may take place on a timescale much faster than molecular rotation. If excess energy is rapidly deposited in the local environment and then rapidly dissipated, the rotational lifetime may not be affected. Even on a very short timescale, however, the heating caused by the dissipation of the excess energy could allow increased librational motion of the solute that would cause a rotational displacement of the molecule. The outcome of this process would appear identical to a molecule that has an angle between the absorption and emission transition moments. If librational motion was occurring, this apparent angle would be expected to vary with the amount of energy deposited in the local environment.

The disagreement between the present results and the previous results on different molecules may be explained in terms of characteristics which are specific to the particular molecules under investigation^{150,152,155}. For example, Blanchard and Wirth studied the

molecule cresyl violet. Cresyl violet has less symmetry than R6G and must be treated as an asymmetric rotor. In this case, the function $r(t)$ is expected to be the sum of three exponentials, each of which are a function of the diffusion constants about different molecular axes. Since the sum is dominated by one of the terms, the experimental results appear to be single exponential. The presence of the other two terms has the effect of varying the lifetime of the apparent single exponential decay. It is suggested by Blanchard and Wirth that different wavelengths access excited vibronic states with varying transition moments. The different transition moments have different linear combinations of the three different exponentials which yield different measured lifetimes for the apparent single exponential decay. In R6G, the diffusion constants are very similar, as mentioned above. When the relative contribution from the two different exponential decays is varied, no difference in the measured single exponential decay is detected. Thus, anisotropic diffusion would not be expected to be manifested in the measured rotation times of R6G as it is in cresyl violet. The rotational reorientation results do not preclude the possibility that the orientation of the transition moment varies with excitation wavelength. Further measurements were performed to address this issue.

An experimental observable which is sensitive to the angle between the absorption and emission transition moments is the value of $r(t)$ at time zero, $r(0)$. The value of $r(0)$ was measured for all of the data in the present study. The values of $r(0)$ are presented in Table 27 and are plotted as a function of wavelength in Fig. 48. It is clear from the figure that the value of $r(0)$ is independent of

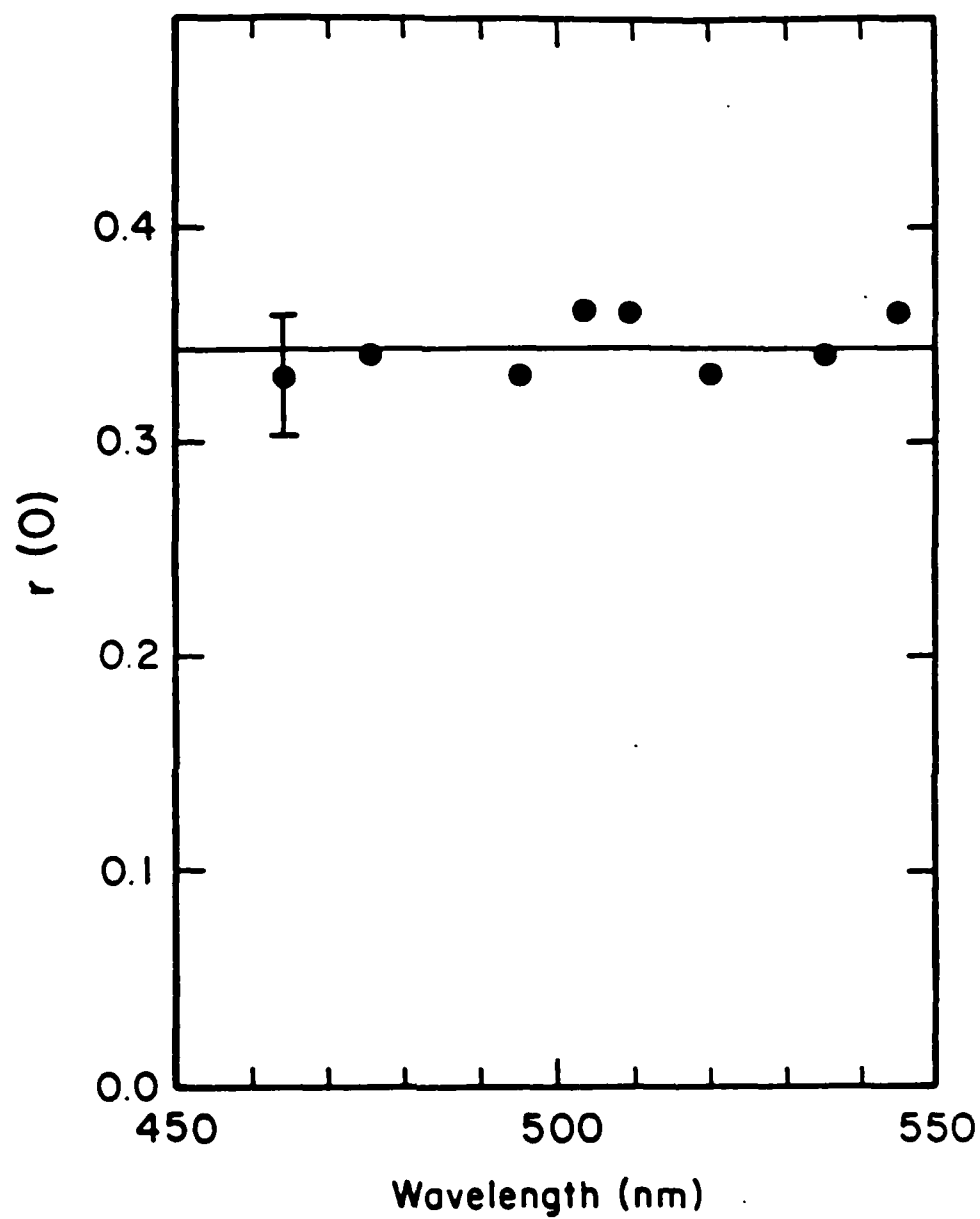


Figure 48 - Plot of $r(0)$ versus excitation wavelength. The error bars represent systematic as well as random uncertainty in the data.

excitation wavelength. Again, the line in this figure is the average value and the uncertainties shown represent the sum of the estimated systematic and random errors.

In the ideal case where the absorption and emission transition moments are parallel, the value of $r(0)$ is 0.4⁷¹. The values obtained in this study are below this ideal value. Some systematic error may result in these experiments because it is difficult to assign the location of time zero. It is estimated that this uncertainty would not exceed 10% of the measured values. Allowing for this maximum uncertainty would still place the value of $r(0)$ below the ideal value of 0.4. Low values of $r(0)$ have been previously reported in the literature^{74,89,150}, and have been attributed to the transition moment in the excited state being at a different angle than the initial ground state transition moment.

Penzkofer and Falkenstein⁸⁹ also observed a decreased value of $r(0)$ for R6G, which they attributed to the fact that excitation occurs simultaneously to a number of vibronic states that have a distribution of transition moments. In contrast, von Jena and Lessing⁷⁴ favor the model of Heiss et al.¹⁵² (see also Zinsli¹⁵⁰) which states that the displacement of the excited state transition moment is due to short time librational motion of the solute induced by local thermal effects. Local thermal effects would be sensitive to the excitation wavelength. At shorter wavelengths, excitation would take place to states higher in the vibrational manifold. The excess vibrational energy would be dissipated in the local environment leading to higher local temperatures, and therefore larger rotational displacements due to librational effects. This wavelength dependence of $r(0)$ is not observed in the

present study. Other mechanisms of angular displacement of the excited state transition moment not based on thermal effects, such as that suggested by Penzkofer and Falkenstein, must be the cause of the reduced value of $r(0)$. Another alternative mechanism for reduced values of $r(0)$ is suggested by molecular dynamics calculations⁷². In these calculations, reduced $r(0)$ values are found to result from coupling of rotational and translational motion.

In conclusion, the results presented here demonstrate that the variation of excitation wavelength does not affect the dynamics of the rotational motion of R6G in solution. The apparent similarities in behavior observed for symmetric oblate cationic xanthene dyes in solution suggest that the present results should also be applicable to a range of other dye molecules. These results also demonstrate the comparability of the results of different experimental investigations involving different excitation wavelengths. Finally, the constant values of $r(0)$ with excitation wavelength argues against short-lived local heating effects playing a role in determining rotational behavior in solution.

Appendix B

TABLES

The tables here consist of the constants used in the calculations performed using the Gierer-Wirtz model and the Kivelson-Dote model. The results of these calculations are also presented. The constants contained in Tables B1 and B2 are from the following references:

R. C. Weast, ed., Handbook of Chemistry and Physics, 52nd ed., (The Chemical Rubber Co., Cleveland, 1971).

E. W. Washburn, ed., International Critical Tables, (McGraw-Hill, New York, 1928).

A. J. Batchinski, Z. Phys. Chem., 84, 643 (1913).

J. H. Hildebrand, Science, 174, 490, (1971).

P. W. Bridgman, Proc. Am. Acad. Arts Sci., 61, 57 (1926).

Table B1
Thermodynamic Constants of Solvents at Ambient Pressure

Solvent	η (cP)	B	κ_T	V_ρ ^a	V_{vdw} ^b	ΔV ^c
Hexane	0.28	18.0	16.0	216	113	103
Heptane	0.40	18.8	13.9	242	130	112
Octane	0.51	17.1	11.6	269	147	122
Nonane	0.68	16.5	11.9	296	164	131
Decane	0.88	15.2	11.3	324	181	143
Undecane	1.13	16.0	9.6	351	198	152
Hexadecane	3.27	13.4	7.4	485	283	202
Methanol	0.53	20.0	12.1	67.3	36.1	31.2
Ethanol	1.06	19.3	11.1	96.8	53.1	43.8
Propanol	2.00	11.0	9.9	124	70.1	53.9
Butanol	2.62	9.3	8.9	152	87.0	64.8
Pentanol	3.53	5.1	8.6	179	104	75.4
Hexanol	4.60	----	8.1	208	121	86.6
Octanol	8.20	----	7.5	261	155	106
Acetonitrile	0.35	----	----	86.7	47.1	39.6
Methylene Chloride	0.40	----	9.7	106	55.6	50.5
Chloroform	0.55	14.0	9.9	133	69.2	64.1
DMF	0.85	----	----	128	66.5	61.2
Cyclohexane	0.93	----	10.8	179	102	77.4

a) Volume calculated from the solvent density.

b) Van der Waals volume from reference 105.

c) Calculated from the difference: $V_\rho - V_{vdw}$
All of the volumes are in Å³.

Table B2

Thermodynamic Constants of Solvents as a Function of Pressure

Solvent	Pressure (kbar)	η (cP)	V_ρ^a	V_{vdw}^c	ΔV^c
Hexane	ambient	0.30	216	113	103
	0.695	0.46	203		89
	1.13	0.62	194		81
	1.50	0.75	191		78
	2.03	0.98	189		74
	2.52	1.2	184		71
	3.02	1.5	181		68
	3.55	1.8	178		64
	3.99	2.1	176		63
Octane	ambient	0.43	269	147	123
	0.596	0.73	256		108
	1.08	1.0	247		100
	1.51	1.3	243		95
	1.99	1.8	238		90
	2.50	2.4	233		85
	2.99	3.2	229		82
	3.48	3.9	226		79
	3.99	4.9	224		77
Ethanol	ambient	1.2	96.7	53.1	43.6
	0.74	1.8	91.4		38.3
	1.11	2.0	89.4		36.3
	1.50	2.4	87.8		34.7

Table B2
(continued)

Solvent	Pressure (kbar)	η (cP)	V_p^a	V_{vdw}	ΔV^c
Ethanol	1.98	2.8	86.1	53.1	33.0
	2.00	2.8	85.9		32.8
	2.49	3.3	84.4		31.3
	2.53	3.3	84.2		31.2
	2.96	3.8	83.1		30.0
	3.32	4.2	82.2		29.2
	3.44	4.4	81.9		28.8
	3.86	4.9	81.1		28.0
	4.09	5.1	80.4		27.3
	4.49	5.8	79.6		26.5
	4.93	6.5	78.9		25.8
	5.46	7.2	78.1		25.0
	6.05	8.4	77.2		24.2
Chloroform	ambient	0.476	133	69.2	64.1
	0.646	0.66	127		57.6
	0.99	0.79	124		54.9
	1.51	1.0	121		51.9
	2.03	1.3	118		49.3
	2.58	1.5	116		47.3
	2.94	1.6	115		46.1
	3.43	1.8	114		44.5
	3.95	2.1	112		43.1

a), b), c) See notes in Table B1. All volumes are in Å³.

Table B3

Calculations of PTP Rotational Reorientation Times as a Function
of Solvent for a Solute Volume of 341 \AA^3

Solvent	GW_{ρ}^a	GW_{vdw}^b	KD^c	KD^d	KD^e
Hexane	8.4	10.3	23.1	8.5	11.4
Heptane	11.6	14.1	29.9	12.1	16.0
Octane	14.3	17.3	40.0	15.3	20.0
Nonane	18.5	22.3	47.2	20.2	26.2
Decane	23.3	28.0	58.6	25.6	33.0
Undecane	29.2	35.0	71.1	32.5	41.7
Hexadecane	76.1	90.4	152.5	87.8	110.5
Methanol	22.8	27.3	21.4	23.4	30.5
Ethanol	41.0	48.9	32.7	43.6	56.5
Propanol	71.7	85.1	71.6	80.1	102.3
Butanol	88.2	104.5	103.5	100.9	128.2
Pentanol	112.8	133.4	189.2	131.4	166.2
Hexanol	140.4	146.6	-----	165.0	208.3
Octanol	232.8	274.2	-----	281.8	352.2
Acetonitrile	14.0	16.7	-----	14.7	19.1
Methylene Chloride	15.0	18.2	-----	15.1	20.1
Chloroform	19.3	23.5	40.5	19.2	25.7
DMF	30.2	36.7	-----	30.1	40.3
Cyclohexane	29.7	35.4	-----	33.6	42.9

a) Gierer-Wirtz model using V_{ρ} as the solvent volume.

b) Gierer-Wirtz model using V_{vdw} as the solvent volume.

c) Kivelson-Dote model using Eq. 20 for ΔV and $V_S = V_{\rho}$.

d) Kivelson-Dote model using Eq. 16 for ΔV and $V_S = V_{vdw}$.

e) Kivelson-Dote model using Eq. 16 for ΔV and $V_S = V_{\rho}$.

All of the rotation times are in ps.

Table B4

Calculations of PTP Rotational Reorientation Times as a Function
of Solvent for a Solute Volume of 224 Å³

Solvent	GW _ρ ^a	GW _{vdw} ^b	KD ^c	KD ^d	KD ^e
Hexane	4.8	5.9	13.8	4.9	6.5
Heptane	6.6	8.1	17.7	6.9	9.1
Octane	8.2	9.9	23.7	8.7	11.3
Nonane	10.6	12.8	27.7	11.5	14.8
Decane	13.3	16.0	34.1	14.5	28.6
Undecane	16.7	20.0	41.2	18.4	23.4
Hexadecane	43.4	51.6	85.9	49.0	61.3
Methanol	13.2	15.8	12.5	13.7	18.0
Ethanol	23.5	28.3	18.7	25.4	33.1
Propanol	41.1	49.1	41.1	46.5	61.3
Butanol	50.5	60.1	59.4	58.3	74.3
Pentanol	64.6	76.7	110.	75.7	95.8
Hexanol	80.3	95.3	---	94.7	119.5
Octanol	113.	157.	---	161.	201.
Acetonitrile	8.0	9.7	---	8.6	11.2
Methylene Chloride	8.6	10.5	---	8.8	11.7
Chloroform	11.1	13.5	8.6	11.1	14.9
DMF	17.3	21.2	---	17.4	23.4
Cyclohexane	17.0	20.3	---	19.4	24.7

a)-e) See notes for Table B3.
All rotation times are given in ps.

Table B5

Calculations of PTP Rotational Reorientation Times as a Function
of Pressure for a Solute Volume of 341 Å³

Pressure(kbar)	GW _ρ ^a	GW _{vdw} ^b	KD ^d	KD ^{-e}
Solvent - <u>Hexane</u>				
ambient	8.9	10.9	9.0	12.0
0.695	14.1	16.9	15.6	20.2
1.13	19.3	22.8	22.8	28.7
1.50	23.5	27.6	28.4	35.5
2.03	30.9	36.1	38.4	47.5
2.53	38.0	44.2	48.7	60.1
3.02	47.8	55.2	63.0	76.4
3.55	57.7	66.3	78.4	94.2
3.99	67.5	77.3	93.3	111.5
Solvent - <u>Octane</u>				
ambient	12.1	14.6	12.9	16.9
0.596	20.9	24.8	24.1	30.6
1.08	28.9	34.0	35.1	43.8
1.51	37.8	44.2	47.4	58.6
1.99	52.6	61.2	68.4	83.5
2.50	70.7	81.5	95.2	115.0
2.99	94.6	108.7	130.7	156.7
3.48	115.9	132.5	164.4	195.5
3.99	145.9	166.4	209.7	248.4

a), b), d), e) See notes for Table B3.
All rotation times are given in ps.

Table B6

Calculations of PTP Rotational Reorientation Times as a Function
of Pressure for a Solute Volume of 341 Å³

Pressure(kbar)	GW _ρ ^a	GW _{vdw} ^b	KD ^d	KD ^e
Solvent - <u>Ethanol</u>				
ambient	46.4	55.4	49.5	64.1
0.74	68.8	80.8	79.3	99.5
1.11	80.3	93.7	95.6	118.4
1.50	93.5	108.5	114.4	140.0
2.00	112.2	129.3	141.4	171.3
2.49	132.1	151.4	171.0	205.2
2.96	153.3	175.0	203.3	241.8
3.44	177.6	201.7	240.7	284.2
3.86	198.1	224.4	272.7	320.2
Solvent - <u>Chloroform</u>				
ambient	16.7	20.3	16.6	22.2
0.646	23.5	28.2	25.0	32.6
0.99	28.3	33.8	31.0	39.9
1.51	36.1	42.7	40.9	52.0
2.03	47.2	55.5	55.3	69.3
2.58	54.8	64.1	65.7	81.7
2.94	58.6	68.4	71.4	88.3
3.43	66.2	76.9	82.4	101.0
3.95	77.6	89.7	98.3	119.8

a), b), d), e) See notes for table B3.
All of the rotation times are in ps.

Table B7

Calculations of PTP Rotational Reorientation Times as a Function
of Pressure for a Solute Volume of 224 Å³

Pressure(kbar)	GW _p ^a	GW _{vdw} ^b	KD ^d	KD ^e
Solvent - <u>Hexane</u>				
ambient	5.1	6.3	5.1	6.9
0.695	8.1	9.7	9.0	11.6
1.13	11.1	13.1	13.1	16.5
1.50	13.4	15.9	16.4	20.4
2.03	17.7	20.7	22.1	27.4
2.53	21.8	25.4	28.1	34.3
3.02	27.4	31.7	36.4	44.2
3.55	33.0	38.1	45.4	54.6
3.99	38.6	44.4	54.0	64.7
Solvent - <u>Octane</u>				
ambient	6.9	8.4	7.3	9.6
0.596	11.9	14.2	13.7	17.4
1.08	16.5	19.5	20.0	25.0
1.51	21.6	25.3	27.2	33.5
1.99	30.1	35.0	39.2	47.9
2.50	40.4	46.7	54.7	66.0
2.99	54.1	62.3	75.2	90.1
3.48	66.3	75.9	94.6	112.6
3.99	83.4	95.4	120.8	143.2

a), b), d), e) See notes for Table B3.
All of the rotation times are given in ps.

Table B8

Calculations of PTP Rotational Reorientation Times as a Function
of Pressure for a Solute Volume of 224 \AA^3

Pressure(kbar)	GW_p^a	GW_{vdw}^b	KD^d	KD^{*e}
Solvent - <u>Ethanol</u>				
ambient	26.7	32.0	28.9	37.6
0.74	39.6	46.7	46.4	58.5
1.11	46.2	54.2	56.1	69.8
1.50	57.9	62.7	67.1	82.6
2.00	64.5	74.7	83.2	101.3
2.49	76.0	87.5	100.7	121.5
2.96	88.2	101.1	119.9	143.4
3.44	102.2	116.6	142.2	168.8
3.86	114.0	129.6	161.2	190.3
Solvent - <u>Chloroform</u>				
ambient	9.6	11.7	9.6	12.9
0.646	13.5	16.3	14.5	18.9
0.99	16.2	19.5	18.0	23.3
1.51	20.7	24.6	24.0	30.3
2.03	27.1	32.0	32.2	40.5
2.58	31.5	36.9	38.3	47.8
2.94	33.6	39.4	41.7	51.7
3.43	38.0	44.3	48.1	59.2
3.95	44.5	51.7	57.5	70.3

a), b), d), e) See notes for Table B3.
All rotation times are given in ps.

Table B9

Calculations of R6G Rotational Reorientation Times as a Function
of Solvent for a Solute Volume of 463 Å³

Solvent	GW _ρ ^a	GW _{vdw} ^b	KD ^c	KD ^d	KD ^e
Methanol	32.9	39.2	45.9	49.0	59.9
Ethanol	59.2	70.4	73.8	92.9	113.5
Propanol	103.8	122.8	157.7	171.8	208.1
Butanol	127.8	151.0	223.8	218.5	264.0
Pentanol	163.6	193.0	381.1	286.5	346.0
Octanol	338	398	-----	627	752

a)-e) See notes for Table B3.

All rotation times are given in ps.

Table B10

Calculations of R6G Rotational Reorientation Times in Ethanol
as a Function of Pressure

Pressure(kbar)	GW _ρ ^a	GW _{vdw} ^b	KD ^d	KD ^e
ambient	67.1	79.8	105.4	128.7
1.98	159.1	182.8	281.3	324.5
2.53	192.1	219.3	347.3	396.7
3.32	246.2	279.1	456.5	515.9
4.09	300.9	338.9	572.3	640.2
5.46	428.4	478.5	840.9	929.1
6.05	501.5	558.3	995.1	1094.4

a), b), d), e) See notes for Table B3.

All rotation times are given in ps.

References

1. H. Nathel, D. Guthals, J. H. Clark, (to be submitted).
2. S. P. Webb, S. W. Yeh, L. A. Philips, M. A. Tolbert, J. H. Clark, Rev. Sci. Instrum., (to be submitted).
3. D. M. Guthals, C. C. Hayden, H. Nathel, D. W. Anthon, J. H. Clark, (to be submitted).
4. J. Jonas, Ann. Rev. Phys. Chem. 26, 167 (1975).
5. Y. Ebisuzaki, T. J. Taylor, J. T. Woo, M. F. Nicol, J. Chem. Soc. Faraday Trans. 2, 73, 253 (1977).
6. Y. Hara, M. F. Nicol, Bul. Chem. Soc. Jpn., 51, 1985 (1978).
7. H. W. Offen, D. E. Hein, in Molecular Luminescence, ed. E. C. Lim, (New York, Benjamin, 1969).
8. H. G. Drickamer, Ann. Rev. Phys. Chem., 33, 25 (1982).
9. H. G. Drickamer, Rev. Phys. Chem. Jpn., 50, 1 (1980).
10. G. Weber, H. G. Drickamer, Q. Rev. Biophys., 16, 89 (1983).
11. M. F. Mirbach, M. J. Mirbach, A. Saus, Chem. Rev., 82, 59 (1982).
12. P. W. Bridgman, Proc. Am. Acad. Arts Sci., 61, 57 (1926).
13. V. Sundstrom, T. Gillbro, H. Bergstrom, Chem. Phys., 73, 439 (1982).
14. D. B. Fitchen, Rev. Sci. Instrum., 34, 673 (1963).
15. D. R. Dawson, H. W. Offen, Rev. Sci. Instrum., 51, 1349 (1980).
16. P. Mazzinghi, M. Zoppi, Rev. Sci. Instrum., 54, 1585 (1983).
17. M. Yamada, V. H. Schmidt, Rev. Sci. Instrum., 49, 1226 (1978).
18. P. W. Bridgman, The Physics of High Pressure (Bell, London 1931).
19. R. Landau, A. Wurflinger, Rev. Sci. Instrum., 51, 533 (1980).
20. G. S. Chryssomallis, H. G. Drickamer, G. Weber, J. Appl. Phys., 49, 3084 (1978).
21. L. A. Philips, S. P. Webb, S. W. Yeh, J. Phys. Chem., 89, 17 (1985).
22. T. C. Poulter, F. Buchley, Phys. Rev., 41, 364 (1932).
23. E. Whalley, A. Lavergne, P. T. T. Wong, Rev. Sci. Instrum., 47, 845 (1976).

24. K. Ishihara, S. Funahashi, M. Tanaka, *Rev. Sci. Instrum.*, 53, 1231 (1982).
25. A. Lavergne, E. Whalley, *Rev. Sci. Instrum.*, 50, 962 (1979).
26. R. Boehler, I. C. Getting, G. C. Kennedy, *J. Phys. Chem. Solids*, 38, 233, (1977).
27. For a Review see D. Kivelson, P. A. Madden, *Ann. Rev. Phys. Chem.*, 31, 523 (1980).
28. D. Kivelson, M. G. Kivelson, I. Oppenheim, *J. Chem. Phys.*, 52, 1810 (1970).
29. G. R. Alms, D. R. Bauer, J. I. Brauman, R. Pecora, *J. Chem. Phys.*, 58, 5570 (1973).
30. D. R. Bauer, J. I. Brauman, R. Pecora, *J. A. C. S.*, 96, 6840 (1974).
31. K. Tanabe, *Chem. Phys.*, 31, 319 (1978).
32. J. L. Dote, D. Kivelson, R. N. Schwartz, *J. Chem. Phys.*, 85, 2169 (1981).
33. A. M. Goulay-Bize, E. Dervil, J. Vincent-Geisse, *Chem. Phys. Lett.*, 69, 319 (1980).
34. R. R. Vold, R. L. Vold, N. M. Szeverenyi, *J. Chem. Phys.*, 70, 5213 (1979).
35. H. E. Lessing, A. von Jena, *Chem. Phys. Lett.*, 42, 213 (1976).
36. A. von Jena, H. E. Lessing, *Chem. Phys. Lett.*, 78, 187 (1981).
37. A. von Jena, H. E. Lessing, *Chem. Phys.*, 40, 245 (1979).
38. K. G. Spears, L. E. Cramer, *Chem. Phys.*, 30, 1 (1978).
39. D. Kivelson, *Discuss. Faraday Soc.*, 11, 7 (1977).
40. A. Einstein, *Ann. Phys. (Leipzig)*, 19, 371 (1906).
41. P. Debye, Polar Molecules (Dover, New York, 1928).
42. C. M. Hu, R. Zwanzig, *J. Chem. Phys.*, 60, 4354 (1974).
43. F. Perrin, *J. Phys. Rad.*, 5, 497 (1934).
44. J. P. Boon, S. Yip, Molecular Hydrodynamics (McGraw-Hill, New York, 1980).
45. G. R. Alms, D. R. Bauer, J. I. Brauman, R. Pecora, *J. Chem. Phys.*, 59, 5310 (1973).

46. G. R. Alms, D. R. Bauer, J. I. Brauman, R. Pecora, J. Chem. Phys., 59,5321,(1973).
47. T. Yoshizaki, H. Yamakawa, J. Chem. Phys.,72,57(1980).
48. J. L. Dote, D. Kivelson, J. Phys. Chem.,87,3889(1983).
49. G. K. Youngren, A. Acrivos, J. Chem. Phys.,63,3846(1975).
50. G. K. Youngren, A. Acrivos, J. Fluid Mech.,69,377(1975).
51. D. C. Knauss, G. T. Evans, D. M. Grant, Chem. Phys. Lett.,71,158 (1980).
52. M. Ahn, Chem. Phys. Lett.,52,135(1977).
53. A. Gierer, K. Wirtz, Z. Naturforsch. A,8,532(1953).
54. J. Frenkel, Kinetic Theory of Liquids(Dover, New York, 1955).
55. A. J. Batchinski, Z. Phys. Chem.,84,643(1913).
56. J. H. Hildebrand, Science,174,490(1971).
57. R. A. Orwoll, P. J. Flory, J. A. C. S.,89,6814(1967).
58. D. Chandler, J. Chem. Phys.,60,3500(1974).
59. D. Chandler, J. Chem. Phys.,60,3508(1974).
60. G. T. Evans, R. G. Cole, D. K. Hoffman, J. Chem. Phys.,77,3209 (1982).
61. The derivations and calculations of the Evans model are from private communications with G. T. Evans.
62. W. G. Rothchild, Dynamics of Molecular Liquids(John Wiley and Sons, New York, 1984).
63. R. A. Assink, J. Jonas, J. Chem. Phys.,57,3329(1972).
64. R. Peralta-Fabi, R. Zwanzig, J. Chem. Phys.,70,504(1979).
65. A. J. Masters, P. A. Madden, J. Chem. Phys.,74, 2460(1981).
66. a) J. T. Hynes, R. Kapral, M. Weinberg, J. Chem. Phys.,69,2725 (1978); b) J. T. Hynes, R. Kapral, M. Weinberg, J. Chem. Phys., 67,3256(1977).
67. J. B. Hubbard, P. G. Wolynes, J. Chem. Phys.,69,998(1978).
68. P. Madden, D. Kivelson, J. Phys. Chem.,86,4244(1982).

69. T. Nee, R. Zwanzig, J. Chem. Phys., 52, 6353(1970).
70. W. A. Steele, Adv. Chem. Phys., 34, 1(1976).
71. T. Tao, Biopolymers, 8, 609(1969).
72. D. J. Adams, Chem. Phys. Lett., 85, 131(1982).
73. D. P. Millar, R. Shah, A. H. Zewail, Chem. Phys. Lett., 66, 435(1979).
74. A. von Jena, H. E. Lessing, Ber. Bunsenges. Phys. Chem., 83, 181(1979); K. H. Drexage, in Dye Lasers, ed. F. P. Schafer, (Springer-Verlag, Berlin, 1978).
75. I. Baraldi, M. C. Bruni, F. Momicchioli, Chem. Phys., 33, 393(1978).
76. a) T. J. Chuang, K. B. Eisenthal, Chem. Phys. Lett., 11, 368(1971).
b) K. B. Eisenthal, K. H. Drexhage, J. Chem. Phys., 51, 5720(1969).
77. G. R. Fleming, J. M. Morris, G. W. Robinson, Chem. Phys., 17, 91(1976).
78. G. R. Fleming, A. E. W. Knight, J. M. Morris, R. J. Robbins, G. W. Robinson, Chem. Phys. Lett., 51, 399(1977).
79. G. W. Robinson, J. M. Morris, R. J. Robbins, G. R. Fleming, J. Mol. Struct., 47, 221(1978).
80. P. J. Sadkowski, G. R. Fleming, Chem. Phys. Lett., 57, 526(1978).
81. G. R. Fleming, A. E. W. Knight, J. M. Morris, R. J. Robbins, G. W. Robinson, Chem. Phys. Lett., 49, 1(1977).
82. G. R. Fleming, A. E. W. Knight, J. M. Morris, R. J. Robbins, G. W. Robinson, Chem. Phys., 23, 61(1977).
83. G. R. Fleming, A. W. E. Knight, J. M. Morris, R. J. S. Morrison, G. W. Robinson, J. A. C. S., 99, 4306(1977).
84. G. Porter, P. J. Sadkowski, C. J. Tredwell, Chem. Phys. Lett., 49, 416(1977).
85. U. K. A. Klein, H.-P. Haar, Chem. Phys. Lett., 58, 531(1978).
86. M. J. Sanders, M. J. Wirth, Chem. Phys. Lett., 101, 361(1983).
87. H. E. Lessing, A. von Jena, M. Reichert, Chem. Phys. Lett., 36, 517(1975).
88. D. Reiser, A. Laubereau, Ber. Bunsenges. Phys. Chem., 86, 1106(1982).
89. A. Penzkofer, W. Falkenstein, Chem. Phys. Lett., 44, 547(1976).

90. D. Waldeck, A. J. Cross, D. B. McDonald, G. R. Fleming, J. Chem. Phys., 74, 3381(1981).
91. D. H. Waldeck, W. T. Lotshaw, D. B. McDonald, G. R. Fleming, Chem. Phys. Lett., 88, 297(1982).
92. D. H. Waldeck, G. R. Fleming, J. Phys. Chem., 85, 2614(1981).
93. D. W. Phillion, D. J. Kuizenga, A. E. Siegman, App. Phys. Lett., 27, 85(1975).
94. R. S. Moog, M. D. Ediger, S. G. Boxer, M. D. Fayer, J. Chem. Phys., 86, 4694(1982).
95. a) B. J. Alder, D. M. Gass, T. E. Wainwright, J. Chem. Phys., 53, 3813(1970); b) W. E. Alley, B. J. Alder, Phys. Rev. A, 27, 3158(1983).
96. J. A. Montgomery, B. J. Berne, J. Chem. Phys., 67, 4580(1977).
97. R. W. Wijnaendts Van Resandt, L. De Maeyer, Chem. Phys. Lett., 78, 219(1981).
98. S. G. Stanton, R. Pecora, B. S. Hudson, J. Chem. Phys., 78, 3365(1983).
99. B. Kowert, D. Kivelson, J. Chem. Phys., 64, 5206(1976).
100. K. B. Eisenthal, Acc. Chem. Res., 26, 62(1975).
101. D. R. Bauer, J. I. Brauman, R. Pecora, Ann. Rev. Phys. Chem., 27, 443(1976).
102. M. Fury, J. Jonas, J. Chem. Phys., 65, 2206(1976).
103. S. Perry, T. W. Zerda, J. Jonas, J. Chem. Phys., 75, 4214(1981).
104. M. Wolfe, J. Jonas, J. Chem. Phys., 71, 3252(1979).
105. A. Bondi, J. Phys. Chem., 68, 441(1964).
106. S. A. Rice, G. A. Kenney-Wallace, Chem. Phys., 47, 161(1980).
107. a) G. E. McDuffie, M. V. Kelley, J. Chem. Phys., 41, 2666(1964); b) A. Gilchrist, J. E. Earley, R. H. Cole, J. Chem. Phys., 26, 196(1957).
108. A. A. Maryott, E. R. Smith, "Table of Dielectric Constants of Pure Liquids"(NBS circular 514, 1951).
109. W. E. Danforth, Phys. Rev., 38, 1224(1931).
110. M. W. Sagal, J. Chem. Phys., 36, 2437(1962).

111. S. K. Garg, C. P. Smyth, J. Phys. Chem., 69, 1294 (1965).
112. a) D. J. Denney, R. H. Cole, J. Chem. Phys. 23, 1767 (1955).
b) C. Brot, M. Magat, J. Chem. Phys., 39, 841 (1963).
113. E. Jakusek, L. Sobzyk, in Dielectric and Related Molecular Processes, 3, 108, ed. M. Davies, (The Chemical Society, London, 1977).
114. J. K. Vij, W. G. Scaife, J. H. Calderwood, J. Phys. D, 14, 733 (1981).
115. G. P. Johari, W. Danhauser, J. Chem. Phys., 50, 1862 (1969).
116. C. J. F. Bottcher, P. Bordewijk, Theory of Electric Polarization, (Elsevier Scientific, Amsterdam, 1978).
117. J. C. Lestrade, J. P. Badali, H. Cachet, in Dielectric and Related Molecular Processes, 2, 106, ed. M. Davies, (The Chemical Society, London, 1975).
118. H. Cachet, I. Epelboin, J. C. Lestrade, Electro. Acta, 11, 1759 (1966).
119. S. J. Bass, W. I. Nathan, R. M. Meighen, R. H. Cole, J. Phys. Chem., 68, 509 (1964).
120. K. Mandel, T. D. Pearson, J. N. Demas, J. Chem. Phys., 73, 2507 (1980).
121. M. K. DeArmond, Acc. Chem. Res., 7, 309 (1974).
122. N. Sutin, J. Photochem., 10, 19 (1979).
123. F. Bolletta, M. Maestri, L. Moggi, V. Balzani, J. Phys. Chem., 78, 1374 (1974).
124. R. A. Palmer, T. S. Piper, Inorg. Chem., 5, 864 (1965).
125. U. Lachish, P. P. Infelta, M. Gratzel, Chem. Phys. Lett., 62, 317 (1979).
126. E. M. Kober, T. J. Meyer, Inorg. Chem., 21, 3967 (1982).
127. B. Mayoh, P. Day, Theoret. Chim. Acta, 49, 259 (1978).
128. F. Felix, J. Ferguson, H. U. Gudel, A. Ludi, Chem. Phys. Lett., 62, 153 (1979).
129. F. Felix, J. Ferguson, H. U. Gudel, A. Ludi, J. A. C. S., 102, 4069 (1980).
130. J. Ferguson, F. Herren, Chem. Phys. Lett., 89, 371 (1982).

131. F. Ferguson, F. Herren, Chem. Phys.,76,45(1983).
132. D. M. Klassen, G. A. Crosby, J. Chem. Phys.,48,1853(1968).
133. F. E. Lytle, D. M. Hercules, J. A. C. S.,91,253(1969).
134. J. N. Demas, G. A. Crosby, J. Molec. Spect.,26,72(1968).
135. J. N. Demas, G. A. Crosby, J. A. C. S.,93,2841(1971).
136. F. Bolletta, M. Maestri, V. Balzani, J. Phys. Chem.,80,2499(1976).
137. G. A. Crosby, K. W. Hipps, W. H. Elfring, J. A. C. S.,96,630(1974).
138. G. A. Crosby, W. H. Elfring, J. Phys. Chem.,80,2206(1976).
139. W. H. Elfring, G. A. Crosby, J. A. C. S.,103,2683(1981).
140. a) P. G. Bradley, N. Kress, B. A. Hornberger, R. F. Dallinger, W. H. Woodruff, J. A. C. S.,103,7441(1981); b) R. F. Dallinger, W. H. Woodruff, J. A. C. S.,101,4391(1979).
141. P. S. Braterman, A. Harriman, G. A. Geath, L. J. Yellowlees, J. Chem. Soc. Dalton Trans.,1801(1983).
142. K. W. Hipps, Inorg. Chem.,5,1391(1980).
143. C. M. Carlin, M. K. DeArmond, Chem. Phys. Lett.,89,297(1982).
144. A. G. Motten, K. Hanck, M. K. DeAmond, Chem. Phys. Lett.,79,541(1981).
145. J. E. Baggott, G.K. Gregory, M. J. Pilling, S. Anderson, K. R. Seddon, J. E. Turp, J. Chem. Soc., Faraday Trans. 2,79,195(1983).
146. R. W. Harrigan, G. A. Crosby, J. Chem. Phys.,59,3468(1973).
147. R. W. Harrigan, G. D. Hager, G. A. Crosby, Chem. Phys. Lett.,21,487(1973).
148. D. C. Baker, G. A. Crosby, Chem. Phys.,4,428(1974).
149. C. Creutz, M. Chou, T. L. Netzel, M. Okamura, N. Sutin, J. A. C. S.,102,1309(1980).
150. P. E. Zinsli, Chem. Phys.,20,299(1977).
151. M. Scholz, K. Teuchner, M. Nather, W. Becker, S. Dahne, ACTA Phys. Pol.,A54,823(1978).
152. A. Heiss, F. Dorr, I. Kuhn, Ber. Bunsenges.,79,294(1975).

153. M. D. Barkley, A. A. Kowalczyk, L. Brand, J. Chem. Phys., 75, 3581(1981).
154. a) E. R. Pantke, H. Labhart, Chem. Phys. Lett., 23, 476(1973);
b) E. R. Pantke, H. Labhart, Chem. Phys. Lett., 23, 482(1973).
155. G. J. Blanchard, M. J. Wirth, J. Chem. Phys., 82, 39(1985).